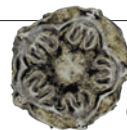


# THIS WEEK

## EDITORIALS

**WORLD VIEW** Cuts to the US disaster response are a false economy **p.7**

**HEADACHE?** The brain stress signals that produce migraine pain **p.8**



**FOSSILS** Preserved remains of the half-billion-year-old jellyfish **p.8**

## Science for all

*Many women are deterred from pursuing a career in science at the highest levels. Much more must be done to address the reasons behind this potential waste of human talent.*

Whether female scientists will want to celebrate International Women's Day on 8 March may depend on how far they look back in time. Things have changed, and if you talk in terms of decades, there are considerable victories to cheer about. But despite those victories, progress now seems to have stalled.

That is clear from the package of articles in this week's *Nature* (see page 21) that exposes the dismaying extent to which sexism still exists in science. In the United States and Europe, around half of those who gain doctoral degrees in science and engineering are female — but barely one-fifth of full professors are women. Women are not invited in significant numbers to sit on the scientific advisory boards of start-up companies. A scientific conference at which half of the keynote speakers are women stands out simply because of that.

Why has progress stalled? Childcare is one major factor that blocks the career of many women. But that is a practical issue, theoretically easy to fix given political will. Even the most enlightened childcare policies will not fix a second, more insidious major problem: overt or unconscious gender bias. It can be detected even in female scientists, and even, according to neurobiologist Jennifer Raymond (see page 33), in those who actively promote women within science.

### POLITICS

The fate of women in science can be influenced for good and bad by political systems. In communist China, women and men had a fairly equal presence in science until recently, when its tottering attempts to open up to the capitalist world led to a disproportionate recruitment of young men returning from research training abroad. This sets the stage for gender imbalance in the future. At the other end of the political spectrum, Portugal's twentieth-century dictatorship similarly managed to secure a healthy balance of female professors. That may have been for the wrong reasons, such as that those jobs were of low salary and prestige, or because a bellicose foreign policy sent male graduates to fight in colonial wars. Most of those men chose to stay abroad, leaving the academic field open for women. The role models were therefore in place when Portugal became a democracy in 1974 and began to invest in research in the 1990s. A healthy gender balance continues there.

The worrying gender bias in mature democracies won't be resolved by the flick of a master switch. As in most professions, it is locked in place by male dominance at all the levels of decision-making that affect academic careers — from journal editorial boards, to grant-reviewing boards, to academic selection committees. Women are barely visible at these levels, fixing the subconscious idea that science belongs to men. There are many ways to chip away at this invisibility and they should all be tried, with the results published so that others can learn from them.

One serious proposal is the imposition of quotas. In certain contexts, such as academic promotions, this would be a good way to ensure that



### WOMEN IN SCIENCE

The gender gap and how to close it  
[nature.com/women](http://nature.com/women)

young female scientists have female role models. Some argue that setting a quota for women in leading academic positions such as professorships will result in mediocre female candidates being promoted. But there is a gap in reasoning

here. Women and men are equally talented, so if men occupy a large majority of high-level posts, there must be an awful lot of mediocrity among their number. Is mediocrity more acceptable in men? Quotas on decision-making committees, however, do come with the inbuilt problem of overburdening the few women who already hold top positions. The solution here would be to keep the quota realistically low for now.

### PROFILE RAISING

Individuals — from Nobel prizewinners to lowly postdocs — have a part to play. Some laureates have contributed with foundations. The Rita Levi-Montalcini Foundation supports young women in Africa who wish to become scientists. The Christiane Nüsslein-Volhard Foundation supports young female scientists with children. And other scientists engage in various consciousness-raising activities.

At the institutional level, several European research agencies and institutions have special funding programmes for women, allowing them to establish their own labs. Last November, *Nature* made a public challenge to itself by reporting that only 14% of its reviewers and 19% of its invited Comment and World View authors were female (see *Nature* **491**, 495; 2012). We vowed to improve, and have asked our editors to try harder to engage with women. In time, we will make our progress public.

One useful tool is the online platform AcademiaNet (<http://academianet.info>), created by the Stuttgart-based Robert Bosch Foundation in Germany in cooperation with *Spektrum der Wissenschaft*, the German edition of *Scientific American* (which is owned by the Nature Publishing Group). AcademiaNet gives a web presence to high-achieving female scientists, making them visible to conference-programme committees seeking female speakers, journalists seeking experts to quote, head-hunters seeking board members and the like. The network will become even more important as work to address gender imbalance accelerates. With successful women being both fewer and less likely to push themselves forward than their male counterparts, they can be hard to find for even the most enthusiastic gender-balancer.

AcademiaNet was opened in 2010 by German chancellor Angela Merkel, a former physicist, who stressed how important it is to preserve half of a country's scientific potential. She recalled her own difficulties training with men who would rush impulsively to try to solve practical-class problems. Her style was to think and then try out, by which time the equipment was occupied or broken. Might an option for separate training in some areas be useful for women, she pondered? Merkel knows a thing or two about being a successful woman, so let's add her idea to that list of things to try. It's a long list. It's time to get started. What are you waiting for? ■



## A central agency is crucial for disaster response

*The United States must not follow through with its plans to scale back its Federal Emergency Management Agency, argues Donald Moynihan.*

Superstorm Sandy did more than rock the eastern coast of the United States last year. It also damaged Mitt Romney's chances in the presidential election. Quotes from Republican primaries, where Romney called for responsibility for disaster response to shift from the federal government to state and local authorities, suddenly looked foolish as those local authorities were quickly overwhelmed. Yet, even as the aftermath of Sandy demonstrates the need for federal help, the Federal Emergency Management Agency (FEMA) in New York is losing US\$1.3 billion — roughly 5% of its budget — in government cutbacks.

The cut to FEMA is a false economy. If we do not prepare for the growing threats that FEMA deals with, we will pay more when disaster strikes. Worse, there is a political effort under way to delegate its responsibilities to regional and local authorities.

Discussions on FEMA largely fail to acknowledge the agency's crucial functions. Climate change, combined with more human development in vulnerable areas, will lead to more Sandy-like events. The question that many countries face is not whether they need a national agency to manage crises, but how to run such an agency in an era of catastrophic risk.

FEMA provides a classic public good. It offers services that the market will not and in which state and local governments under-invest. It makes more sense, and is cheaper, to develop high-level risk expertise at the national rather than local level. This was, in fact, the rationale for the creation of FEMA in 1979. Governors were tired of dealing with a confusing federal approach to disaster response, and convinced then-president Jimmy Carter of the need for a single central agency.

A coordinated response is essential because large-scale crises cut across governmental boundaries and can quickly exceed the capacity of local responders. FEMA fills the unique role of lead coordinator. Much of the public may think of it as a national response agency, but this is not really the case. It is too small to do that, and by law becomes involved only when local and state responders become overwhelmed.

Crisis-response networks of different public, non-profit and private organizations coordinate more effectively if responders speak the same language and follow the same general principles. Only a national government can enforce common standards, and so avert the confusion when multiple approaches conflict in their attempts to manage hazards. After the terrorist attacks of 11 September 2001, FEMA and the Department of Homeland Security forced states and local governments to adopt common preparation and response principles. This approach is not perfect, but it establishes role expectations before a crisis and is flexible enough to deal with different hazards and response networks. Other countries, including

Australia, the United Kingdom and China, have followed the US lead.

FEMA also helps states to recover, through measures that include providing money for disaster relief. This is the part of FEMA's function that provides direct and tangible benefits to individuals and is subject to close attention by elected officials. Studies from both the United States and India suggest that incumbent politicians tend to lose support after natural disasters, but that cash for relief efforts can minimize the political damage. This provides a strong incentive for governors and congressional delegations to seek emergency declarations that trigger federal disaster relief, and for the president to provide them. The result has been a marked rise in the number of presidential emergency declarations made since the 1990s, including declarations for events not traditionally seen as disasters.

Disaster relief has become politicized, and this drains attention

from FEMA's other main function — to mitigate and prepare for disasters. Such investments are made in the absence of a particular threat, and so seem abstract and of limited value to voters. But estimates suggest that every dollar invested in mitigation creates long-term savings of between \$4 and \$15. We need FEMA to drive the revision of building codes to make buildings more resilient to extreme weather, and to encourage states to build climate change into their hazard plans.

Although Congress was happy to find \$60 billion for disaster relief in the wake of Sandy, it is unwilling to invest a similar amount to reduce the impact of the next superstorm. Historically, such investments are made only when FEMA takes the lead to set national standards and share costs. To transfer power from FEMA

to local officials would neuter this ability.

To prepare for disaster means building strong working relationships between the organizations that form the crisis-response network. Training and simulation exercises build trust, which is essential in an emergency. Yet cutting them is seen as an easy way to save money. Before Hurricane Katrina hit New Orleans, Louisiana, in 2005, a planned exercise to test hurricane responses was postponed, and a follow-up workshop was cancelled. Without such investments, we can expect more responses that look like those to Katrina — responders disagreeing about who is in charge, and failing to work together.

The public has come to expect that a large-scale crisis will be met with a competent national response. Politicians can help if they enable FEMA to better manage long-term risk. They must, because, however much they want to, they cannot wish away the next Sandy. ■

THE PUBLIC  
HAS COME TO  
**EXPECT**  
THAT A LARGE-SCALE  
CRISIS WILL BE MET  
WITH A  
**COMPETENT**  
NATIONAL RESPONSE.

➔ **NATURE.COM**  
Discuss this article  
online at:  
[go.nature.com/2hizmi](http://go.nature.com/2hizmi)

**Donald Moynihan** is a professor at the La Follette School of Public Affairs at the University of Wisconsin-Madison.  
e-mail: [dmoynihan@lafollette.wisc.edu](mailto:dmoynihan@lafollette.wisc.edu)



# RESEARCH HIGHLIGHTS

Selections from the  
scientific literature

## NEUROSCIENCE

### How migraines begin

Researchers have pinpointed a brain stress signal that may spark migraine pain.

Migraines are thought to be caused by a wave of cellular depolarization that travels through the brain's cortex. Turgay Dalkara and his colleagues at the Hacettepe University in Ankara induced depolarizing waves in the exposed brains of mice by pricking the cortex with a pin or by applying potassium chloride to it.

The authors then used molecular and pharmacological tools to document the cascade of molecular events that led to activation of the trigeminal nerves, which innervate the face and are implicated in migraines.

*Science* 339, 1092–1095 (2013)

## PALAEONTOLOGY

### Fine anatomy of earliest animals

Internal structures of embryonic jellyfish-like organisms have been found in limestone that formed more than 530 million years ago.

Basic animal body plans were established over half a billion years ago, and their origins are often murky. Differing hypotheses have tied one relatively common specimen, *Olivoides*, to three disparate phyla, of which penis worms, sea stars and jellyfish are modern examples. A team led by Philip Donoghue at the University of Bristol,



UK, found three specimens in which the internal anatomy (pictured) of late-stage *Olivoides* embryos had been preserved, revealing details that place it with Cnidaria, which includes jellyfish. The authors argue that assigning ancient organisms to the correct group is crucial to our understanding of how changes in embryonic development led to the formation of current animal phyla.

*Proc. R. Soc. B* 280, 20130071 (2013)



## ECOLOGY

### Fish migration reduces predation

Fish in Danish lakes substantially reduce their risk of being eaten by making annual migrations. Thus, predation — alongside food and weather — may drive such movements.

Christian Skov at the Technical University of Denmark in Silkeborg and his team implanted 2,219 roach (*Rutilus rutilus*, pictured) with tags during a 4-year period, and monitored individuals' migratory behaviour. Most of the tags recovered from a nearby colony of

cormorants (*Phalacrocorax carbo*) were from fish that were last recorded as being in lakes. Roach that spent most time in the lakes during winter were substantially more likely to be eaten by cormorants than those that moved to streams.

This study provides direct evidence that animals can benefit from migration by reducing their risk from predators.

*Biol. Lett.* 9, 20121178 (2013)

## INFECTIOUS DISEASE

### Worm signal for river blindness

A newly identified chemical could help to monitor the treatment of a tropical disease that afflicts tens of millions of people.

Onchocerciasis, commonly known as river blindness, is caused by the parasitic worm *Onchocerca volvulus*. The worm can persist in the body in nodules, even after treatment.

Kim Janda at the Scripps Research Institute in La Jolla, California, and his colleagues studied urine from people with the disease, aiming

to find a marker of active infection. The team found a previously unknown molecule called *N*-acetyltyramine- $\text{O},\beta$ -glucuronide by using liquid chromatography–mass spectrometry. The molecule — which is derived from one of the worm's neurotransmitters — was present at high levels in the urine of infected people, but at much lower levels in healthy people and patients who were receiving antibiotic treatment.

The authors suggest that a similar approach could be used to find biomarkers for other tropical diseases.

*Proc. Natl Acad. Sci. USA*  
<http://dx.doi.org/10.1073/pnas.1221969110> (2013)

JANIS BRODERSEN

## CHEMICAL BIOLOGY

## Protein caught in the act

A technique that can track proteins at atomic resolution in live cells could help to show how proteins fold and mature into functional forms.

A protein's environment strongly influences its maturation, but most analyses of protein dynamics require purified components. Radu Aricescu of the University of Oxford, UK, Lucia Banci of the University of Florence, Italy, and their groups used nuclear magnetic resonance spectroscopy to track the structure of the protein SOD1 in human cells.

The technique showed that another protein helps SOD1 to bind zinc and copper, and form internal disulphide bonds that aid stability. The method also showed that disulphide bonds can form even when SOD1 has not bound copper, a result that has not been seen using purified proteins.

*Nature Chem. Biol.* <http://dx.doi.org/10.1038/nchembio.1202> (2013)

## FLUID DYNAMICS

## Tying fluids in knots

Vortex loops, of which smoke rings are a familiar example, occur when a fluid or gas spins in a tornado-like funnel that turns back on itself. The behaviour of 'knots' that can form in vortex loops is hard to study, but these important, complex objects have now been created experimentally.

Dustin Kleckner and William Irvine of the University of

Chicago in Illinois generated vortex loops in water (pictured) by using precisely shaped plastic wings produced with a three-dimensional printer. They watched how these loops change over time; flows in vortices break and reconnect, causing knots to unknot. The evolution of knots is important to our understanding of energy transfer in solar plasmas, electromagnetic fields and turbulent fluids.

*Nature Phys.* <http://dx.doi.org/10.1038/nphys2560> (2013)  
For a longer story on this research, see [go.nature.com/jjtthk](http://go.nature.com/jjtthk)

## MICROBIOLOGY

## Before the bacterial cell wall

Much of the machinery in cells is devoted to division, but in the earliest cells this process may have been governed by changes in the ratio of surface area to volume.

Although all bacteria either have cell walls or are thought to have evolved from ancestors that did, Jeff Errington and his colleagues at Newcastle University, UK, found that excess production of cell membrane in mutants of the bacterium *Bacillus subtilis* drives them into a state without cell walls. Non-mutant bacteria forced into a shape with a greater surface-to-volume ratio also lost their cell walls. In both cases, cells divided through irregular bulges, rather than dedicated cell-division machinery.

In addition to providing a model for early cells, this work could help to explain how some infectious bacteria resist antibiotics.

*Cell* 152, 997–1007 (2013)

## COMMUNITY CHOICE

The most viewed papers in science

## CHEMISTRY

## X-rays read beer's bitter chemicals

**HIGHLY READ**  
on <http://onlinelibrary.wiley.com> in January

A technique developed in the twentieth century has helped researchers to pin down the conformations of the compounds that flavour one of the

world's oldest beverages.

A team led by Werner Kaminsky at the University of Washington in Seattle used X-ray crystallography to study the bitter-tasting chemical humulone — a component of the beer additive hops — and its derivatives.

The authors purified acids recovered during beer-making and grew them into salt crystals that were then analysed with X-rays. This showed the exact position of the chemicals' molecular side chains, contradicting previous assumptions made from easier but less-rigorous techniques.

Now the arrangements of the humulone compounds are known, their purported health benefits can be better explored, the authors suggest.

*Angew. Chem. Int. Edn* 52, 1553–1555 (2013)

## MEDICAL SCIENCES

## Sleepless nights affect gene activity

Sleep deprivation alters the expression of hundreds of genes, including some whose activity normally varies depending on the time of day.

Derk-Jan Dijk and his team at the University of Surrey in Guildford, UK, allowed study participants to sleep for up to 10 hours every night for one week and up to 6 hours a night another week. At the end of each week, all 26 participants were asked to stay awake for about 40 hours.

Genes affected by sleep deprivation included those involved in DNA packaging, gene-expression regulation, metabolism, and inflammatory, immune and stress responses. The authors suggest that studying the effects of sleep on gene expression can help to show how sleep deficits are linked to problems, such as cognitive impairment and obesity.

*Proc. Natl Acad. Sci. USA* <http://dx.doi.org/10.1073/pnas.1217154110> (2013)

## ASTRONOMY

## Hot star with a cool layer

The nearby star  $\alpha$  Centauri A has a relatively cool layer above its visible surface and beneath its superhot corona, one of several characteristics it shares with the Sun.

A team led by René Liseau at Chalmers University of Technology in Onsala, Sweden, looked at  $\alpha$  Centauri A in far-infrared wavelengths with the Herschel Space Observatory and a ground-based telescope. They compared the star's light with a model of the stellar atmosphere to show a minimum temperature of 3,920 kelvin just above the surface — the first minimum observed on a Sun-like star.

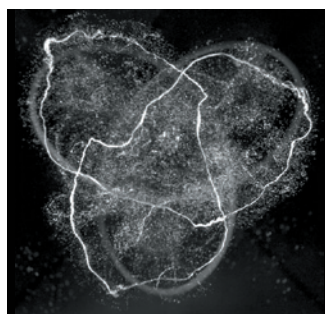
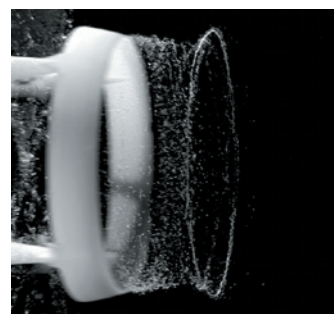
Knowledge that this cool layer exists in other stars could help astronomers to understand how widespread such stellar atmospheric phenomena are.

*Astron. Astrophys.* 549, L7 (2013)

**NATURE.COM**

For the latest research published by Nature visit:

[www.nature.com/latestresearch](http://www.nature.com/latestresearch)



DUSTIN KLECKNER/WILLIAM T. M. IRVINE

# SEVEN DAYS

The news in brief

## POLICY

### US science cuts

After US lawmakers failed to reach a budget compromise, federal science programmes took a 5% hit to their annual budgets on 1 March — part of across-the-board government cutbacks known as sequestration. National Science Foundation director Subra Suresh said that the agency would probably maintain funding for currently approved research grants, and eliminate about 1,000 new grants. At the National Institutes of Health, director Francis Collins said that the agency would probably not complete funding for some multi-year grants this year. See [go.nature.com/8vdcht](http://go.nature.com/8vdcht) for more.

### European advisers

The president of the European Commission, José Manuel Barroso, announced on 27 February the establishment of a council to advise him on where research could support social and economic growth in the European Union (EU). The Science and Technology Advisory Council comprises 15 high-ranking scientists and will meet several times a year under the chairmanship of Barroso's chief scientific adviser, Anne Glover, to promote the public acceptance of science and technology and to support 'evidence-based' EU policy-making. Members include Swiss molecular biologist Susan Gasser, head of the Friedrich Miescher Institute in Basel, and neuroscientist Tamás Freund, director of the Institute of Experimental Medicine in Budapest.

### India budget

Indian scientists were disappointed for a second year by budget allocations for science and technology in the government's 2013–14

budget request. Nine research departments share some US\$6.9 billion, a mere 4% more than budgeted for 2012–13, and below the rate of inflation. India's prime minister, Manmohan Singh, had promised large increases in science spending from 2012 to 2017, but these have not yet materialized. C. N. R. Rao, who heads the prime minister's science advisory council, says that he is glad that science at least escaped big cuts.

### Patent reform

The UK government has revealed plans to change national patent law to ensure that clinical trials do not count as a breach of existing drug patents. To obtain marketing approval, new drugs must be compared with medicines already on the market, but

such comparison trials could infringe the patents of existing drugs. Under rules announced on 26 February, which are still subject to parliamentary approval, clinical trials will be exempt from these patent restrictions. Other countries, including the United States and Canada, already have such exemptions in place. See [go.nature.com/rpuunl](http://go.nature.com/rpuunl) for more.

### Pipeline push

The US Department of State has identified no major concerns in its draft environmental assessment of a controversial 1,400-kilometre pipeline proposed to link oil sands in Alberta, Canada, to existing pipelines in Nebraska. Opponents argue that the Keystone XL project would encourage the development of carbon-intensive energy.

But the analysis, issued on 1 March, concludes that approval or denial of the project is "unlikely to have a substantial impact" on the rate of development of the oil sands. Many analysts expect the US government to approve the pipeline, although it denied an initial proposal last January.

## RESEARCH

### HIV cure

An infant born with HIV has been "functionally cured", a multi-institute team reported on 3 March at a conference on retroviruses in Atlanta, Georgia. The child received a combination of antiviral drugs within 30 hours of birth and for the next 18 months, at which point doctors lost track of the infant for 10 months and treatment ceased. Subsequent



STEVEN KAZLOWSKI/SCIENCE FACTION/CORBIS

## Polar bear stays on US endangered list

The US Court of Appeals for the District of Columbia has upheld a 2008 decision to list the polar bear as threatened under the Endangered Species Act. The Fish and Wildlife Service's 2008 listing relied in part on climate-model projections indicating that the animals' summer sea-ice habitat may disappear in

the future, making this the first time that a species has been listed primarily on the basis of the threat of global warming. On 1 March, the appeals court rejected a challenge filed by the state of Alaska and others, ruling that the underlying science is "adequately explained and uncontested".



ALEX BRANDON/AP

blood tests found no sign of the virus. Quick treatment, the doctors believe, prevented the formation of dormant infected cells in which the virus can persist. It is the first time that a cure has been reported in a child with HIV.

## Fukushima review

The World Health Organization released on 28 February its report on the health impacts of the 2011 catastrophe at the Fukushima Daiichi nuclear power plant in Japan. The report concludes that the accident will have little health impact apart from small, but significant, increases in cancers among populations in a few hotspots exposed to higher doses of radioactivity. But the health consequences would have been much worse had prevailing winds during the accident not blown most of the massive release of radioactive elements out to sea. See [go.nature.com/fkp9vb](http://go.nature.com/fkp9vb) for more.

## PEOPLE

## Obama's new team

After weeks of speculation, on 4 March US President Barack Obama nominated Ernest Moniz, a physicist at the Massachusetts Institute of Technology in Cambridge, to succeed Steven Chu as secretary of Energy (see *Nature* **494**, 409–410; 2013).



Obama also named Gina McCarthy (**pictured**) to replace Lisa Jackson as head of the Environmental Protection Agency. McCarthy currently leads the agency's office of air and radiation and previously served as commissioner of the Connecticut Department of Environmental Protection, where she worked on a regional greenhouse-gas trading initiative.

## Nobel physicist dies

Donald Glaser, a Nobel prizewinning physicist and inventor of the bubble chamber used to track elementary particles, died on 28 February, aged 86. Glaser won the 1960 Nobel Prize in Physics for his realization — in 1952, aged just 25 — that a vat of superheated liquid could detect electrically charged particles better than the vapour-filled 'cloud chambers' in use at the time. He later switched to molecular biology, then to studies

of human vision. He also co-founded Cetus in Berkeley, California, one of the first biotechnology companies.

## BUSINESS

## Drug-trial data

The Swiss drug giant Roche announced last week that it would give researchers access to anonymized clinical-trial data. Requests for data would need to be approved by an independent panel of experts, the Basel-based company said. The move follows that made last month by GlaxoSmithKline to make data from all its future trials publicly accessible (see *Nature* **490**, 322; 2012). The European Medicines Agency intends from next year to make public all trial data submitted to it by industry for drug approvals.

## Arctic drilling pause

Royal Dutch Shell announced on 27 February that it is suspending its Arctic drilling programme this year. Work commenced on two oil wells in Alaska's Beaufort and Chukchi seas less than a year ago, but one drilling rig lost its moorings in July, and a second ran aground in December, sparking a federal review of the programme. Shell says that it plans to tow the rigs to Asia for maintenance and repairs as the company prepares for future drilling efforts.

## COMING UP

### 10 MARCH

Comet C/2011 L4 (PANSTARRS), which is coming into view in the Northern Hemisphere, brightens as it reaches the point in its orbit closest to the Sun. [go.nature.com/bpf2yy](http://go.nature.com/bpf2yy)

### 11–12 MARCH

At the Royal Society in London, researchers aim to set the agenda for the next decade of extrasolar-planet science. [go.nature.com/a5cxah](http://go.nature.com/a5cxah)

## Dragon docking

An unmanned Dragon spacecraft docked with the International Space Station on 3 March, arriving a day late because of thruster problems that were resolved. Built by California-based firm SpaceX, the space freighter carries supplies, equipment and scientific experiments. After completing its delivery — SpaceX's second — Dragon is scheduled to return and splash into the Pacific Ocean on 25 March, bringing back more than 1,300 kilograms of spent supplies and research samples. See page 18 for more on private spaceflight.

## FACILITIES

## Museum fire

A large fire on 4 March gutted much of an iconic science centre: the 12,000-square-metre City of Science exhibition centre and museum in Naples, Italy, which opened in 2001. No one was hurt — the museum was closed at the time — but media reports say that the fire destroyed four of the complex's five buildings. City authorities had not ruled out arson as *Nature* went to press.

► [NATURE.COM](http://NATURE.COM)

For daily news updates see: [www.nature.com/news](http://www.nature.com/news)

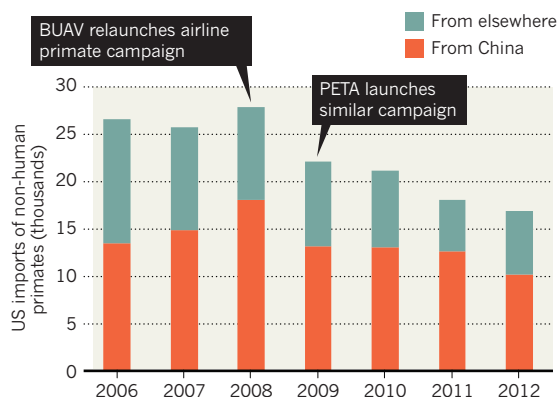
SOURCE: US FWS/PETA

## TREND WATCH

The number of non-human primates being imported into the United States for research purposes has dropped sharply since the British Union for the Abolition of Vivisection (BUAV) in London and People for the Ethical Treatment of Animals (PETA) in Norfolk, Virginia, started pressuring major airlines to stop the activity (see *Nature* **489**, 344–345; 2012). All but a few have acquiesced, including Air China and China Southern, which had been transporting large numbers of animals.

## US PRIMATE IMPORTS DECLINE

The number of non-human primates imported for research has fallen by 36% between 2006 and 2012.



# NEWS IN FOCUS

**ASTRONOMY** From fireball to fragments, a portrait of the Siberian meteor **p.16**

**PHYSICS** A material advance for energy-efficient transistors? **p.17**

**NEUROSCIENCE** Masterminds of the US Brain Activity Map project **p.19**



**WOMEN IN SCIENCE** A *Nature* special looks at barriers and success stories **p.21**

OREGON PARKS AND RECREATION DEPT./AP PHOTO



A worker in Newport, Oregon, burns debris off a Japanese concrete dock that washed across the Pacific.

## ECOLOGY

# Tsunami triggers invasion concerns

*Biologists track species on flotsam from Japan to US shores.*

BY VIRGINIA GEWIN

When a 165-tonne block of concrete and steel crashed into the central Oregon coast last June, Jessica Miller was shocked to find that the structure — a dock that had washed across the Pacific from Misawa, Japan — was teeming with life after 15 months at sea. “It was surreal,” says Miller, a marine ecologist at Oregon State University’s Hatfield Marine Science Center in Newport. She found tens of thousands of organisms on the structure in layers up to 15 centimetres thick, including brown algae, pink barnacles and shrimp-like creatures called caprellids. In

December 2012, a second large Japanese dock landed in Washington state laden with species. Other debris, including derelict boats and buoys harbouring live organisms, continues to wash up on the shores of Oregon, Washington and, most recently, Hawaii.

Almost two years after the Tohoku earthquake triggered a devastating tsunami, North American shores are awash in debris swept from the Japanese coastline some 8,000 kilometres away. The flotsam constitutes floating islands of species — some of which could

➔ **NATURE.COM**  
For more on the Tohoku tsunami, see the *Nature* special: [nature.com/japanquake](http://nature.com/japanquake)

potentially be invasive. According to estimates from the Japanese government, the tsunami carried about 1.5 million tonnes of debris out to sea. “We expect to see tsunami debris for years to come,” says Peter Murphy of the National Oceanic and Atmospheric Administration (NOAA) in Silver Spring, Maryland, who is the Alaska coordinator for NOAA’s marine debris programme.

The tsunami has sparked several unanticipated experiments. Biologists have seized on the unprecedented opportunity to track a potential species invasion from the beginning, and oceanographers have used the debris sightings to refine their models of the effects of winds and currents on debris. Marine ecologists, meanwhile, are tracing fish migrations using radioisotopes released from the tsunami-triggered accidents at the Fukushima nuclear reactors.

“The tsunami debris is an unparalleled scientific opportunity, specific in time and place,” says Susan Williams, a marine ecologist at the University of California, Davis.

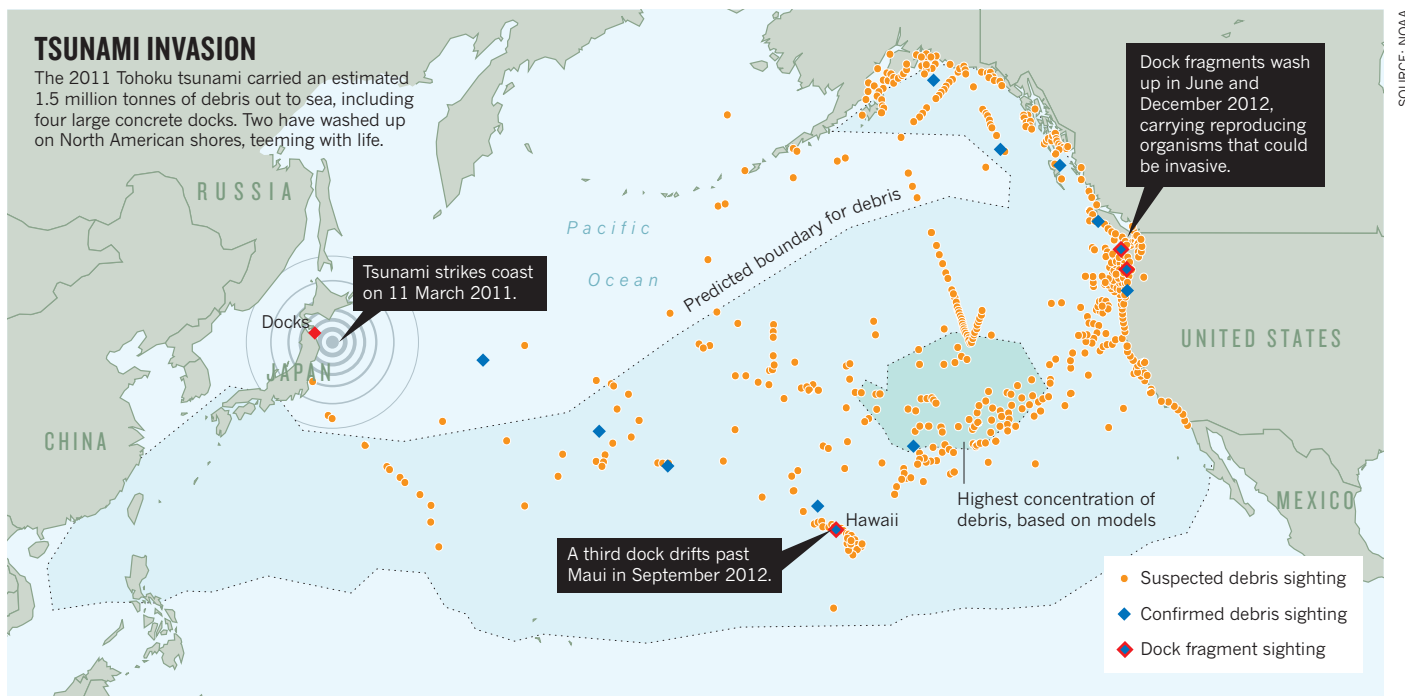
The invasion biologists have perhaps had the most urgent call to action, because no one anticipated that coastal species would survive such a long journey across the open sea. “This is an event so rare we simply don’t expect to see it,” says James Carlton, an invasive-species expert from Williams College in Williamstown, Massachusetts, who has teamed up with Miller and other colleagues to study the arrivals.

Researchers must first confirm that the debris they are studying really is from the tsunami. Water bottles with Japanese characters offer a clue. Registration numbers on boats can be traced back to those that were reported missing. But of the 1,500 or so reported items that have washed up in recent months, only 21 have been confirmed by the Japanese consulate, according to Murphy.

The arrival of potentially invasive species is not a new concern on the Pacific coast. Organisms can be transported on transoceanic boats or in their ballast water. But boats do not typically recruit whole communities, and they move too fast between ports for many organisms to hang on. The resident coastal communities transported on slow-moving tsunami debris therefore look very different — and can arrive along the whole North American coastline rather than just at heavily monitored ports. No invasions have yet been detected ►

## TSUNAMI INVASION

The 2011 Tohoku tsunami carried an estimated 1.5 million tonnes of debris out to sea, including four large concrete docks. Two have washed up on North American shores, teeming with life.



► from the tsunami debris, but it is unlikely that Carlton, Miller and their team are aware of every single landfall, so a potentially invasive species could well have been missed.

The team's next step is to determine which organisms survived the journey across the Pacific, and how. In the nine months since the first dock made landfall, the team has identified roughly half of the 175 species found so far on all debris items. John Chapman, a marine biologist also at Hatfield Marine Science Center, will go to Misawa later this month to document which species reside on docks there in early spring, the season when the tsunami struck.

The results so far suggest a real risk of invasion. For example, three of the best-known algal invaders have been among the debris, says Gayle Hansen, a marine-algae expert at Oregon State University who is based in Newport. She says that 75% of the 46 algal species she has collected from the debris so far have been reproductively active, dropping spores. That gives them a good chance of getting established and possibly displacing native species in the Pacific Northwest.

State officials, who are usually first on the scene, are often quick to destroy any organisms

clinging to debris to avert potential invasions. That can make it challenging for Carlton's team to get samples. But the problem is easing, Carlton says, as more responders become aware of the need to sample the arrivals. He adds that there have been few reports of debris with living Japanese species from Alaska, British Columbia and California, which could represent a lack of reporting, or an artefact of oceanography.

The recent spike in debris landings is to be expected during winter and spring, owing to large-scale patterns of currents and winds. The path of debris flows north of Hawaii (see 'Tsunami invasion') and was predicted by NOAA models, which have incorporated sightings from mariners. But Nikolai Maximenko, an oceanographer at the University of Hawaii in Honolulu, says that the exact landfall for the concrete docks was difficult to predict because they are buoyant enough that the effects of winds and currents are comparable in strength.

Maximenko is also helping to sample the plume of Fukushima radioisotopes, which lags behind the debris and is slowly moving east. The radioisotopes are assisting ecologists. In February, Nicholas Fisher, a marine

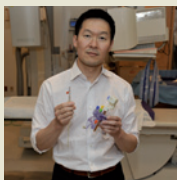
scientist at Stony Brook University in New York, and his colleagues showed that two radioisotopes, caesium-134 and caesium-137, could be used to trace the past movements of bluefin tuna between Japan and California (D. J. Madigan *et al. Environ. Sci. Technol.* <http://doi.org/kn9>; 2013). Fisher's team confirmed the presence of both caesium isotopes in bluefin tuna arriving from Japan — although the levels pose no health risk to humans. "We see evidence that fish might cross the Pacific in about one month, which we found amazing," says Fisher.

Other researchers from Oregon State University in Corvallis and NOAA are using the technique to determine whether there are two different stocks of North Pacific albacore tuna, which would be reflected in each population's isotopic profile. Fisher's team also wants to use this method to track the migratory patterns of other large marine animals, such as albatrosses, loggerhead turtles and salmon sharks.

Even as researchers track species using radioisotopes and count them on debris, they bear in mind the tsunami's staggering human toll. "This is the experiment that never should have taken place," says Chapman. ■

## MORE ONLINE

## TOP STORY

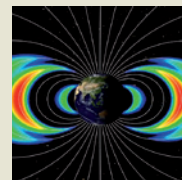


Bendable needles could facilitate delivery of stem cells to the brain [go.nature.com/radv2c](http://go.nature.com/radv2c)

## MORE NEWS

- Intercontinental mind-meld links rats and sparks scepticism [go.nature.com/5sttji](http://go.nature.com/5sttji)
- Richard I's heart shows Christians practised embalming [go.nature.com/ocfslz](http://go.nature.com/ocfslz)
- Having sons can shorten a woman's life expectancy [go.nature.com/wctpgf](http://go.nature.com/wctpgf)

## VIDEO



Third ring of radiation makes surprise appearance around Earth, then disappears [go.nature.com/iqvogh](http://go.nature.com/iqvogh)



## EARTH MONITORING

# ESA's climate-eye dilemma

Scientists face difficult choice for Europe's next Earth-observation mission.

BY QUIRIN SCHIERMEIER

Now, trees or the air we breathe? Europe's environmental research community is facing the difficult task of settling which of the three should be the priority for Europe's next Earth-observing satellite.

Around 250 Earth scientists and climate researchers will meet in Graz, Austria, this week to weigh up the scientific benefits of projects proposed for the roughly €300-million (US\$390-million) seventh Earth Explorer mission of the European Space Agency (ESA). They face a choice between three projects — Biomass, PREMIER and CoReH<sub>2</sub>O (an acronym referring to cold regions and water) — preselected through peer review from more than 20 proposals. The scientists behind the missions have been preparing their proposals for years.

The Biomass project aims to take radar measurements of global forest biomass to assess terrestrial carbon stocks and fluxes. CoReH<sub>2</sub>O, also a radar mission, would measure snow cover and snow-melt rates in cold regions around the world. Finally, PREMIER would use infrared and microwave sounding to measure atmospheric composition and temperature in the upper troposphere and lower stratosphere, a region particularly important for climate.

No satellites currently in orbit can match the sensitivity of the proposed missions. Neither NASA's Landsat programme, which has captured images of Earth since 1972 (see *Nature* **494**, 13–14; 2013), nor Japan's Advanced Land Observing Satellite-2 — to be launched later

this year — have sensors that can measure forest biomass with the precision of Biomass, for example. And climate scientists have been warning of an impending data crisis after the 2010 retirement of NASA's ICESat mission, which among other things monitored ice sheets and vegetation, and the failure of the agency's Orbiting Carbon Observatory and the solar monitoring and aerosol mission Glory (see *Nature* <http://doi.org/bqjhn7>; 2011).

Once ESA has decided which it will back, a satellite could be ready for launch by the end of the decade. Science will be the main criterion for the decision, but cost and the maturity of the technology will also play a part. The stakes are high, says Thomas Stocker, a climate researcher at the University of Bern, and a co-chair of a working group of the Intergovernmental Panel on Climate Change. "Findings such as those concerning ice-sheet changes in Greenland and Antarctica would have been impossible without space observations," he says.

Europe currently has three Earth Explorer satellites in orbit: GOCE is mapping tiny variations in Earth's gravity field, which can reveal changes in ice mass and ocean circulation; SMOS is measuring soil moisture and ocean salinity; and CryoSat-2 is monitoring variations in sea-ice thickness and changes in the mass of large ice sheets and glaciers. Three further missions — Swarm, ADM-Aeolus and EarthCARE — are scheduled for launch over the next three years, and will, respectively, monitor Earth's magnetic field; global wind profiles; and clouds, aerosols and radiation.

The seventh Earth Explorer mission will

provide scientists with yet another set of global data that are hard to come by on the ground. The extent of seasonal snow cover, for instance, is an important feedback in climate change because snow reflects sunlight, cooling Earth's surface, and affects the supply of fresh water.

"More than 1 billion people rely on glaciers and seasonal snow packs for their water supply," says Helmut Rott, a meteorologist at the University of Innsbruck in Austria and lead scientist on the CoReH<sub>2</sub>O project. "They will want to know what the future might hold for them. That's why we need these data."

But data on global forest biomass — a major store of land carbon and a key indicator of biodiversity — are no less important, says Shaun

**"They will want to know what the future might hold for them. That's why we need these data."**

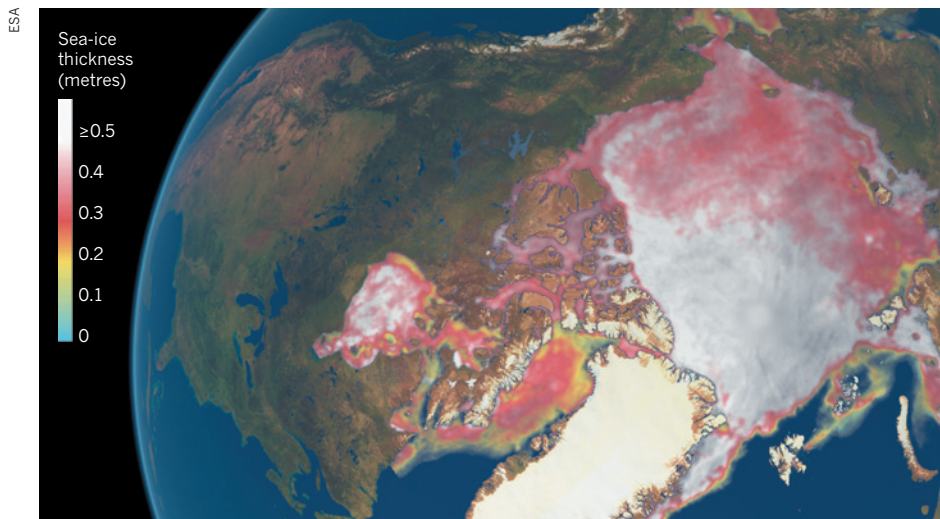
Quegan, a carbon-cycle researcher at the University of Sheffield, UK, who is part of the Biomass assessment group. In particular, he says, satellite observations are needed to quantify

global carbon emissions for tropical forests, for which no reliable ground inventories exist.

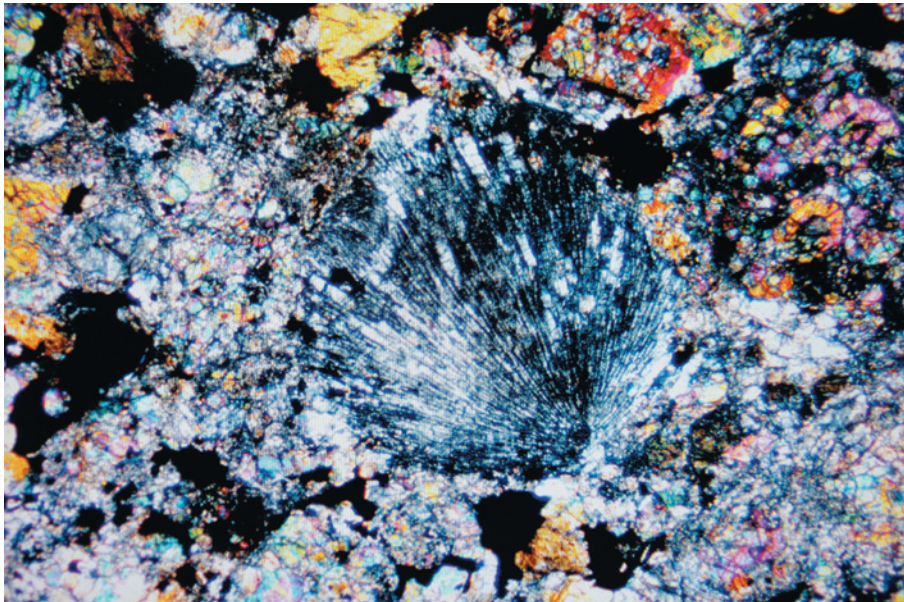
Supporters of the PREMIER mission are just as emphatic. It promises knowledge that "is absolutely vital," says Michaela Hegglin, an atmospheric scientist at the University of Reading, UK, and a member of the mission's advisory group. To improve regional climate predictions, she says, "we need to better understand how the atmospheric circulation responds to rising greenhouse-gas concentrations".

No clear front runner has emerged. Which-ever proposal prevails at the Graz meeting is almost certain to be funded by ESA. A final decision is expected at the agency's board meeting in May in Svalbard, Norway, but ESA has backed the verdict of the scientists in the past.

"If I had my way, I would love to see all three missions fly," Stocker says. But with the economic crisis casting a shadow over Europe's Earth- and climate-observation plans, there is little chance of that. Spain, France and Italy last year reduced their contributions to ESA, leaving the agency with €600 million less for its 2013–17 Earth-observation budget than it had hoped for. The seventh Earth Explorer mission is safe, says Volker Liebig, director of ESA's Earth-observation programmes. But tight budgets are likely to shrink the size and ambition of future missions. "We need to make future missions cheaper without impairing the science," he says. ■



Measurements from ESA's SMOS mission show the thickness of seasonal sea ice.



Polarized light shows that the Chebarkul meteorite contains melted and recrystallized material.

## ASTRONOMY

# The death of the Chebarkul meteor

*Scientists reconstruct a battered traveller's final moments.*

BY QUIRIN SCHIERMEIER

The city of Chelyabinsk was once a secret Soviet weapons centre, then a poor Siberian backwater. But a few minutes after sunrise on 15 February, the largest meteor blast in more than 100 years lifted the region from obscurity. Since then, scientists have been scrutinizing fragments of the meteorite and studying videos of its final moments to pin down its origin and how it got to Earth.

The picture so far is of a garden-variety envoy from the asteroid belt between Mars and Jupiter, the size of a house and weighing 9,000 tonnes, that had a hard life even before its chance encounter with Earth. "It was a rather fragile body," says Pavel Spurný, a meteor expert at the Ondřejov Observatory near Prague, a member of one of the teams doing the analysis.

His team examined seven videos of the fireball — the largest since the 1908 Tunguska meteorite, which also hit Siberia. The analysis reveals that the meteor first became visible around 92 kilometres above ground. Just over 11 seconds later, at a height of nearly 32 kilometres, it exploded spectacularly under the stress of heating and air drag, damaging thousands of homes and injuring more than 1,000 people in and around Chelyabinsk.

Before its cataclysmic encounter with Earth's atmosphere, the object — dubbed Chebarkul after the small town and lake where some of the largest fragments have been found — seems to have been on an elliptical orbit around the Sun. Stretched between Venus and the centre of the asteroid belt between Mars and Jupiter, the Earth-crossing orbit was just slightly inclined relative to the plane of Earth's orbit around the Sun, the team says in its report to the International Astronomical Union's Central Bureau for Astronomical Telegrams in Cambridge,

Massachusetts. (NASA scientists have ruled out any relation between the Chebarkul meteor and the asteroid 2012 DA14, which skimmed by Earth just hours later.)

A team assigned by the Russian Academy of Sciences to comb the snowy countryside has collected more than 50 fragments measuring 0.5–1 centimetre in diameter. A second group, led by Viktor Grokhovsky of the Urals Federal University in Ekaterinburg, has found another 50 or so pieces, one of which weighs almost 2 kilograms. The samples are being sent to the Russian Academy of Science's Vernadsky Institute of Geochemistry and Analytical Chemistry in Moscow, which has also asked locals for photographs of any fragments they have found.

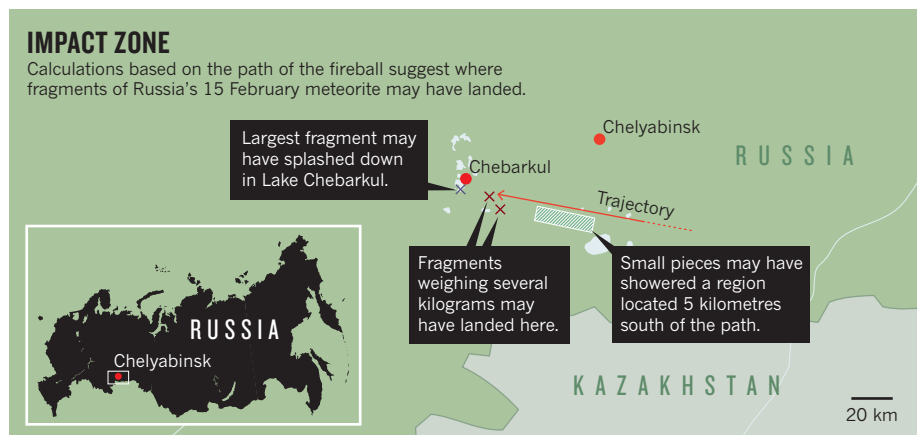
Inside some of the rocky shards are glassy veins, perhaps created during the impact that broke the object away from its mother asteroid many million years ago. Preliminary geochemical analysis suggests that Chebarkul was a stony meteor with low iron content — a chondrite — made of material that had been partially melted and recrystallized from the dust and gas cloud of the early solar nebula.

A sturdier body might have reached the surface without exploding, but this one probably took a beating after its genesis, having collided with other celestial bodies, says Timothy Spahr, director of the Smithsonian Astrophysical Observatory's Minor Planet Center in Cambridge, Massachusetts. "This could have caused cracks which then resulted in such a powerful blast," says Erik Galimov, director of the Vernadsky Institute.

The search is on for bigger pieces that hold more clues to the meteor's origin and history. Spurný and his colleagues have calculated the final part of the meteor's 254-kilometre flight through the atmosphere and where the largest fragments probably landed (see 'Impact zone').

The fireball zipped through the upper atmosphere at an initial velocity of 17.5 kilometres per second, the team thinks. In the denser air near the ground, the fragments would have slowed to about 180 metres per second, cooled and vanished, says Jiri Borovicka, a co-author of the report.

But calculations based on the fireball's





observed path and on wind profiles suggest that chunks weighing tens of kilograms probably landed close to the village of Travniki, and one weighing around 1 kilogram may have hit northwest of the village of Shchapino, Borovicka says. Thousands of smaller pieces may be hiding in a 25-kilometre-long swathe south of the final point of the trajectory.

The largest single fragment, a piece of rock that could weigh up to half a tonne, may have landed smack in Lake Chebarkul. A 6-metre-wide hole found in the lake's frozen surface the morning after the impact "almost certainly" marks the spot where the whopper came down, says Borovicka.

Russian military divers are busy searching

the shallow lake. But Spahr, who discussed the impact with other scientists at a meeting of the United Nations Committee on the Peaceful Uses of Outer Space in Vienna last month, isn't so sure. "From what we've seen on pictures, the 'crater' just doesn't look right," he says. "It looks more like a hole someone has cut in the lake with an axe." ■

## PHYSICS

# Metal oxide chips show promise

*Materials that flip from insulator to conductor could make energy-efficient transistors.*

BY EUGENIE SAMUEL REICH

The switches in most electronic circuits are made of silicon, one of the commonest elements. But their successors might contain materials that, for now, are lab-grown oddities: strongly correlated metal oxides.

The allure of these materials lies in the outer shells of electrons surrounding their metal atoms. The shells are incomplete, leaving the electrons free to participate in coordinated quantum-mechanical behaviour. In some materials, electrons pair up to produce superconductivity, or coordinate their spins to produce magnetism. Other materials can switch from being an insulator to a conductor.

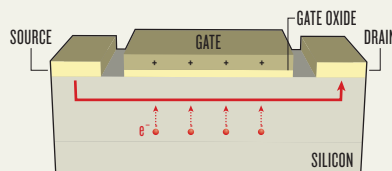
Unlike transitions to superconductivity, which happen as temperatures approach absolute zero, the insulating-to-conducting transition typically happens as temperature increases, and sometimes occurs near room temperature. That has raised hopes that metal oxides could be used instead of silicon to make transistors. A spate of results is now making that look feasible. "People are interested in seeing if oxides can make it to applications," says Manuel Bibes, a physicist at the Joint Physics Unit in Palaiseau, France, which is run by the French National Research Centre and electronics company Thales.

Metal oxide transistors have the potential to consume less power than silicon switches, because the phase transition frees electrons from their localized state near each atom, without moving them through the bulk material. By contrast, silicon switches work by pulling electrons through the material to a channel where they conduct current (see 'Go with the flow').

In the past 5–10 years, researchers have succeeded in growing high-quality thin films of the metal oxides — overcoming one of the major barriers to applications. In July 2012, for example, a group in Japan reported<sup>1</sup> that it had deposited a thin film of vanadium dioxide that underwent a phase transition in response to an

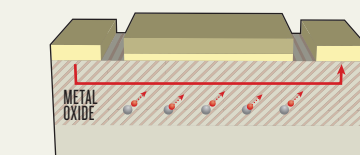
## GO WITH THE FLOW

Metal oxide transistors have the potential to consume less power than silicon ones, because switching does not require the atoms to be relocated.



### Silicon transistor

A positive charge at the gate draws electrons into a surface channel, allowing current to flow between the source and the drain.



### Metal oxide transistor

An applied electric field at the gate causes electrons on metal atoms to become conductive, letting current flow between source and drain.

applied electric field — proof that the material could be used as an electronic switch.

And last month, a group led by Shriram Ramanathan, a materials scientist at Harvard University in Cambridge, Massachusetts, addressed a fabrication challenge by growing a thin film of samarium nickelate on top of a substrate made of silicon and silicon dioxide<sup>2</sup>.

The nickelate was deposited at a relatively low temperature that did not disturb the underlying silicon layers, raising the possibility of manufacturing metal oxides on top of silicon wafers to form three-dimensional chips, says Andrew Millis, a solid-state theorist at Columbia University in New York. Not only would that allow computing power to be packed much more densely, says Millis, but it would also permit metal oxide switches to be built on top of existing circuit architectures.

Other groups are trying to understand the

nature of the phase transition. In January, Ivan Schuller, a solid-state physicist at the University of California, San Diego, and his colleagues showed<sup>3</sup> that in vanadium oxide, the transition is in large part caused by micrometre-scale heating by the applied electric field.

Some point to Schuller's work as evidence that metal oxides will never make fast switches, because heating effects are usually quite slow. But Ramanathan says that his own measurements on vanadium oxide demonstrate that the phase transition is quite fast — less than a few nanoseconds — and that it should not hinder applications.

Some physicists are finding further examples of potentially useful materials. Bernhard Keimer at the Max Planck Institute for Solid State Research in Stuttgart, Germany, alternates thin layers of metal oxides to form composites that often turn out to have serendipitous properties. His group layered conducting lanthanum nickelate and insulating lanthanum aluminate and found<sup>4</sup> that the composite underwent a transition between the two properties.

The highest phase-transition temperature for the composite was 150 kelvin above absolute zero — too low for practical applications. But the group is now trying to replicate the phenomenon in other materials that might have higher transition temperatures.

Sandip Tiwari, an applied physicist at Cornell University in Ithaca, New York, acknowledges that metal oxides are not yet close to competing with silicon. But given recent progress, he feels that researchers need to start trying to implement them in devices. That way, he says, all the properties needed for a good transistor will be developed in tandem. "If you just look at whatever property is your favourite, you won't get them all." ■

1. Nakano, M. *et al. Nature* **487**, 459–462 (2012).
2. Jaramillo, R., Schoofs, F., Ha, S. D. & Ramanathan, S. *J. Mater. Chem. C* <http://dx.doi.org/10.1039/C3TC00844D> (2013).
3. Zimmers, A. *et al. Phys. Rev. Lett.* **110**, 056601 (2013).
4. Boris, A. V. *et al. Science* **332**, 937–940 (2011).





A successful engine test last month means that the Antares rocket can proceed to its inaugural launch.

## SPACE FLIGHT

# Commercial space race heats up

*Antares test could challenge dominance of Falcon 9 rocket.*

BY DEVIN POWELL

The Falcon 9 rocket, which made its fifth successful flight on 1 March, has stolen the spotlight in the commercial space race. Built by SpaceX, a young company based in Hawthorne, California, the rocket has become NASA's choice for hauling cargo to the International Space Station (ISS). But it may soon have competition from a rocket that has kept a low profile (see 'Battle of the rockets').

After years of delays, Orbital Sciences of Dulles, Virginia, has slated the first test flight of its Antares rocket for April. If that goes well, its second mission could carry an unmanned Cygnus spacecraft to the ISS within months. "There's no one main problem, no show-stopper," says Orbital spokesman Barron Beneski. "In hindsight, this has just taken us longer to do than we thought it would."

Both companies have received hundreds of millions of dollars from NASA's Commercial Orbital Transportation Services (COTS) programme. With the space shuttle retiring in 2011, the agency wanted alternatives to paying for ISS deliveries aboard the Russian Progress and Soyuz craft. NASA deliberately put two companies in competition with each other to keep prices down over the long run and to attract other customers. "The government is the necessary anchor tenant for commercial cargo, but it's not sufficient to build a new economic ecosystem," says Scott Hubbard, an aeronautics researcher at Stanford University in

California and former director of NASA's Ames Research Center in Moffett Field, California.

With 30 years of experience in making satellites and rockets, Orbital once seemed the safer bet. Instead of assembling its vehicles from scratch like SpaceX, Orbital uses parts made by companies with proven track records. The core of the first stage of Antares was designed

and built by veterans KB Yuzhnoye and Yuzhmash, both based in Dnipropetrovsk, Ukraine. Cygnus's sensors come from Mitsubishi Electric in Tokyo and its pressurized cargo module was built at a Thales Alenia Space plant in Turin, Italy. "Orbital used more heritage technology," says Alan Lindenmoyer, manager of NASA's commercial crew and cargo programme. "That was less risky for us."

But the company did not enter COTS until 2008, two years after SpaceX. With the clock ticking, NASA allocated less money for Orbital and ordered a simpler ship. Unlike SpaceX's Dragon capsule, Cygnus can't carry sensitive biological experiments, such as those that grow protein crystals in microgravity. It burns up on re-entry, so it can't return samples to Earth. And it can't be modified to carry humans.

Nor has it yet flown. Orbital chose to launch from NASA's Wallops Flight Facility in Virginia; less crowded than Cape Canaveral in Florida, which hosts most NASA rocket launches, Wallops usually caters for smaller vehicles such as scientific balloons and sounding rockets. The facility's Mid-Atlantic Regional Spaceport had to build a new launch pad for Antares, which took longer than expected. Originally scheduled for 2010, the demonstration launch slipped to 2012, and then to 2013, after Hurricane Sandy hit the spaceport last October.

Antares' engines, built half a century ago for Russia's Moon programme and recently refurbished, have also proven finicky. A test on 13 February was aborted when pressure anomalies were detected in one of the engines. A successful test on 22 February means that Orbital can now proceed to a launch in April.

Having another cargo carrier would provide a safety net for the ISS. That need was made clear when Dragon's thrusters initially failed during the flight last week, almost preventing the spacecraft from docking with the station. But there is scepticism about whether competition will drive down prices. "This is a mixed-up crazy business and a small market that isn't all that price sensitive," says Henry Hertzfeld, a space-policy expert at George Washington University in Washington DC.

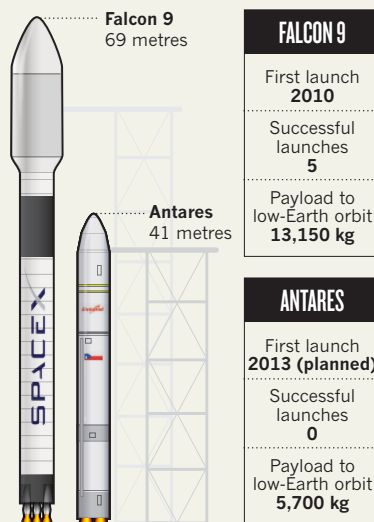
Factors such as political or military concerns often shape demand, he says. And reliability is as much of a concern as price. The market could grow: private space stations, orbiting fuel depots and asteroid-mining operations have all been proposed as future clients for commercial rockets. But for now, supplying the ISS and launching satellites are the major niches.

SpaceX is making inroads with the latter: it has contracts for launches with the US Air Force and commercial operators in Israel, Thailand, Luxembourg and Mexico. Orbital, too, wants to develop business beyond NASA, but it has not yet booked any launches. "Right now, we're focused on getting the rocket launched," says Frank Culbertson, executive vice-president of Orbital's advanced-programmes group. "Then we can talk to other customers." ■

ORBITAL SCIENCES CORPORATION

## BATTLE OF THE ROCKETS

Next month, Orbital Sciences plans to launch its Antares rocket, which could provide an alternative to SpaceX's Falcon 9 for supplying the International Space Station.



## NEUROSCIENCE

# Behind the scenes of a brain-mapping moon shot

*Critics fear that a proposed megaproject could crowd out other biological research.*

BY MEREDITH WADMAN

Ron Kalil, a neuroscientist at the University of Wisconsin–Madison, didn't expect to see his son among the 28,500 attendees at the meeting of the Society for Neuroscience in New Orleans last October. And he wondered why Tom Kalil, deputy director for policy at the White House's Office of Science and Technology Policy (OSTP), was accompanied by Miyoung Chun, vice-president of science programmes at the Kavli Foundation in Oxnard, California.

Tom Kalil told his father that the Kavli Foundation had wanted his help in bringing nanoscientists together behind an ambitious idea. Ron Kalil says he thought: "Why are you talking about it at a neuroscience meeting?"

He understands now. These two people, neither of them a working scientist, had been quietly pushing into existence the Brain Activity Map (BAM), the largest and most ambitious effort in fundamental biology since the Human Genome Project — and one that would need advances in both neuroscience and neuroscience to achieve its goals.

This is the kind of science — big and bold — that politicians like. President Barack Obama praised brain mapping in his State of the Union address on 12 February. Soon after, Francis Collins, director of the US National Institutes of Health (NIH) in Bethesda, Maryland, which will be the lead agency on the project, talked up the idea in a television appearance.

The Obama administration is expected to provide more details about the initiative this month, possibly in conjunction with the release of the federal 2014 budget request. But already, some scientists are wondering whether the project, a concept less than two years old and still evolving, can win new funding from Congress, or whether it would crowd out projects pitched by individual scientists. "Creative science is bottom-up, not top-down," says Cori Bargmann, a neurobiologist at the Rockefeller University in New York. "Are we talking about central planning inside the Beltway?"

The idea was born at a meeting of neuroscientists and nanoscientists that Chun helped to convene in September 2011 at the Kavli Royal Society International Centre at Chicheley Hall, an elegant country house in Buckinghamshire, UK. There, a handful of scientists drafted

a white paper laying out their ambitions to illuminate what they would soon call the "impenetrable jungles" of brain function, by mapping and stimulating neural circuits with cellular and millisecond-level resolution. Functional magnetic resonance imaging can provide the big picture, and electrodes can trigger single and small groups of neurons, but this project called for the mapping of thousands of neurons simultaneously, using new tools such as nanoprobe and optogenetics, which manipulates neurons using light. Chun suggested sending the paper, which eventually appeared in *Neuron* (A. P. Alivisatos *et al.* *Neuron* 74, 970–974; 2012), to the OSTP.

Chun, a molecular geneticist known for being extraordinarily persistent, had already been in touch with Tom Kalil, who had been

**"Creative science is bottom-up, not top-down."**

the prime mover behind a major nanotechnology initiative during the Clinton administration. Kalil had urged Chun to bring him "out-of-the-box, great and progressive ideas", she recalls.

In December 2011, Chun brought the Chicheley Hall group to Washington DC to present its vision to the OSTP. Led by Rafael Yuste, a biologist at Columbia University in New York and co-director of the Kavli Institute for Brain Science, the group at first had modest plans. They would deploy the new tools in simple model organisms — worms, flies and leeches — before graduating to zebrafish, mice and rats.

When the scientists returned to Washington in May 2012, OSTP officials "wanted us to think bigger", Yuste says. They pushed the group to expand the project to human brains — and to the study of possible interventions for brain disorders.

That goal has some observers cautioning against the selling of a basic-science project as a way to find cures for Alzheimer's disease and Parkinson's disease. "Don't overpromise," says Arthur Caplan, a medical ethicist at the New York University Langone Medical Center. "The genome mapping I think was worth doing. But it has left many in Congress and some on the industry side saying: 'where are the goodies?'"

With the genome project, the goal was relatively fixed: a sequence of 3 billion base pairs.

But Donald Stein, a neuroscientist at Emory University in Atlanta, Georgia, points out that brain anatomy and chemistry are constantly shifting. Mapping structure and measuring electrical activity at a particular moment doesn't necessarily mean that answers will "miraculously appear", he says.

Critics also wonder who will pay for the project at a time when budgets are stretched thin. The NIH has US\$545 million in its Common Fund, a flexible source of money for new projects — but last year, all but \$30 million of it was tied up in existing projects. The BAM would probably cost several billion dollars over the course of a decade or more. "What motivates people to pursue these big projects is not the belief that they will solve problems," says Michael Eisen, a biologist at the University of California, Berkeley. "It's the belief that this is the way to get money."

However, two other agencies are expected to help support the project: the National Science Foundation and the Department of Defense, which has an interest in treatments for traumatic brain injuries and in mind-controlled prosthetics. And private foundations, such as the Howard Hughes Medical Institute in Chevy Chase, Maryland, have already spent hundreds of millions of dollars on brain-mapping research. Yuste wants to leverage that work, and make BAM a private–public partnership rather than a competition between the government and private funders, as the genome project was. "We are trying to learn from the Human Genome Project, the mistakes they made," says Yuste.

Whatever becomes of the BAM, one thing is clear: it has a powerful advocate in the Obama administration. Ron Kalil recalls once asking his son what he actually did in the OSTP. His answer was simple: "I'm the make-it-happen guy." ■

## CORRECTION

The News story 'Tusk tracking will tackle illegal trade' (*Nature* 494, 411–412; 2013) gave the wrong dates for the ivory seizures in the map — they were all 2006. It also omitted a reference to the statistical models: Wasser, S. K. *et al.* *Proc. Natl Acad. Sci. USA* 104, 4228–4233 (2007).



Science remains institutionally sexist. Despite some progress, women scientists are still paid less, promoted less, win fewer grants and are more likely to leave research than similarly qualified men. The reasons range from overt and covert discrimination to the unavoidable coincidence of the productive and reproductive years.

In this special issue, *Nature* takes a hard look at the gender gap and at what is being done to close it. A survey of the data (see page 22 and [go.nature.com/ytmyhf](http://go.nature.com/ytmyhf)) reveals where progress has been made and where inequalities still lie, from salary to tenure. A News Feature (see page 25) reveals a particular dearth of women in some commercial spheres, such as on the scientific advisory boards of biotechnology firms, and an article by historian Patricia Fara (see page 43) traces the wearying stereotypes perpetuated by the biographers of women scientists.

A series of Comment articles looks at possible solutions. Neuroscientist Jennifer Raymond (see page 33) calls on both sexes to recognize and reduce their biases against women in science, and eight researchers from around the world offer their prescriptions (see page 35), from equalizing the retirement age in China, to liberalizing travel restrictions in Saudi Arabia, to boycotting conferences that lack female speakers. We catalogue some of the ambitious moves being made in Europe to get more women into top positions (see page 40) and explore some surprising statistics about mandatory quotas (see page 39). Finally, profiles of four successful 30-something women (see page 28) show how ambition and talent can trump obstacles.

This special issue is dedicated to the memory of Maxine Clarke. In the 28 years that Maxine spent championing the highest scientific standards as an editor at *Nature*, she was all too often the only one to ask, "Where are the women?" ■

# WOMEN'S WORK

A special section of *Nature* finds that there is still much to do to achieve gender equality in science.



## WOMEN IN SCIENCE

The gender gap and how to close it  
[nature.com/women](http://nature.com/women)



# MIND THE GENDER GAP

*Despite improvements, female scientists continue to face discrimination, unequal pay and funding disparities.*

BY HELEN SHEN

**A**s an aspiring engineer in the early 1970s, Lynne Kiorpes was easy to spot in her undergraduate classes. Among a sea of men, she and a handful of other women made easy targets for a particular professor at Northeastern University in Boston, Massachusetts. On the first day of class, “he looked around and said ‘I see women in the classroom. I don’t believe women have any business in engineering, and I’m going to personally see to it that you all fail.’”

He wasn’t bluffing. All but one of the women in the class ultimately left engineering; Kiorpes went on to major in psychology.

Such blatant sexism is almost unthinkable today, says Kiorpes, now a neuroscientist at New York University. But Kiorpes, who runs several mentoring programmes for female students and postdoctoral fellows, says that subtle bias persists at most universities. And it drives some women out of science careers.

By almost any metric, women have made great gains in closing the scientific gender gap, but female scientists around the world continue to face major challenges. According to the US National Science Foundation, women earn about half the doctorates in science and engineering in the United States but comprise only 21% of full science professors and 5% of full engineering professors. And on average, they earn just 82% of what male scientists make in the United States — even less in Europe.

Scientific leaders say that they continue to struggle with ways to level the playing field and entice more women to enter and stay in science. “We are not drawing from our entire intellectual capital,” says Hannah Valentine,

dean of leadership and diversity at the Stanford School of Medicine in California. “We’ve got to put on the accelerator to evoke social change.”

One of the most persistent problems is that a disproportionate fraction of qualified women drop out of science careers in the very early stages (see ‘Women in science’). A 2006 survey of chemistry doctoral students by the Royal Society of Chemistry in London, for example, found that more than 70% of first-year female students said that they planned a career in research; by their third year, only 37% had that goal, compared with 59% of males<sup>1</sup>.

Many experts say that a big factor driving this trend is the lack of role models in the upper divisions of academia, which have been slow to change. The Royal Society of Chemistry has found, for instance, that female chemistry students are more likely than males to express low self-confidence and to report dissatisfaction with mentorship<sup>2</sup>. Female students “conclude consciously and unconsciously that these careers are not for them because they don’t see people like them”, suggests Valentine. “That effect is very, very powerful — this sense of not belonging.”

The attrition continues at later stages. In biology, for example, women comprised 36% of assistant professors and only 27% of tenure candidates in a 2010 study by the US National Research Council<sup>3</sup>. “We’re not talking about a lack of talent here. Part of the story is that

women leave earlier. In a sense, they give up on an academic career,” says Curt Rice, vice-president of research and development at the University of Tromsø in Norway, who has studied gender equality in US and European universities.

## FAMILY VALUES

Many of the UK chemistry students viewed research as an all-consuming endeavour that was incompatible with raising a family. Meeting the demanding schedule of academic research can seem daunting for both mothers and fathers. But family choices seem to weigh more heavily on the career goals of women.

Law professor Mary Ann Mason at the University of California, Berkeley, and her colleagues have found<sup>4</sup> that male and female postdocs without children are equally likely to decide against research careers, each leaving at a rate of about 20%. But female postdocs who become parents or plan to have children abandon research careers up to twice as often as men in similar circumstances.

“The plan to have children in the future, or already having them, is responsible for an enormous drop-off in the women who apply for tenure-track jobs,” says Wendy Williams, a psychologist at Cornell University in Ithaca, New York. Furthermore, women who do become faculty members in astronomy, physics and biology tend to have fewer children than their male colleagues — 1.2 versus 1.5, on average — and also have fewer children than they desire<sup>5</sup>.

In response to these concerns, many universities have taken steps to establish family-friendly policies such as providing child-care assistance and extending tenure clocks for new



## WOMEN IN SCIENCE

The gender gap and how to close it  
nature.com/women

# WOMEN IN SCIENCE: MANY HURDLES AHEAD

The number of women studying and practising science has risen sharply, but women are disproportionately driven away from scientific careers.



MEN

WOMEN

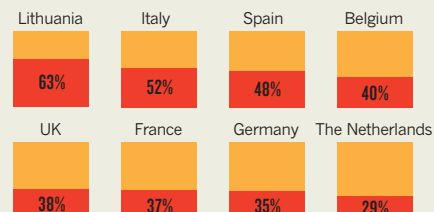
## GRADUATE SCHOOL

The fraction of women gaining doctorates in science has more than doubled in the United States since 1980 and is now nearing equity. In some European countries, women outnumber men in science degrees but there is significant variation between nations and fields.

### US FEMALE DOCTORAL RECIPIENTS IN SCIENCE AND ENGINEERING



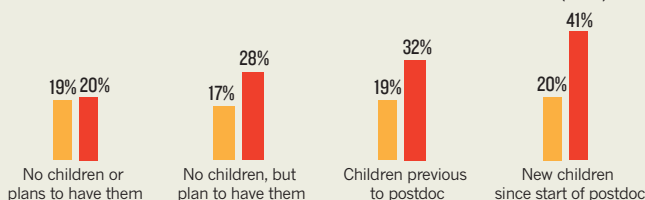
### FEMALE DOCTORAL RECIPIENTS IN SCIENCE IN EUROPE (2006)



## POSTGRADUATE POSITIONS

A 2009 survey of postdoctoral fellows at the University of California showed that women who had children or planned to have them were more likely to consider leaving research.

### POSTDOCS WHO DECIDED AGAINST CAREERS AS RESEARCH FACULTY MEMBERS (2009)



**"The plan to have children in the future, or already having them, is responsible for an enormous drop-off in the women who apply for tenure-track jobs."**

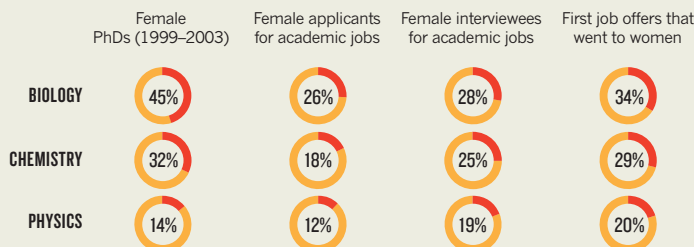
Wendy Williams, Cornell University

## EARLY CAREER

Female representation among science and engineering faculty members in the United States has lagged behind gains in graduate education, in part because many women do not apply for tenure-track jobs. But women who do apply are more likely than men to receive interviews and offers.

**"At least part of the lack of applications is due to the fact that women look at these careers and don't see people like themselves."**

Hannah Valentine, Stanford University

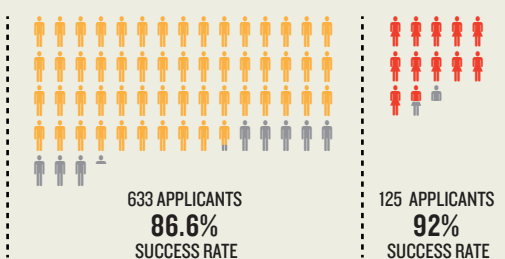


## RISING IN THE RANKS

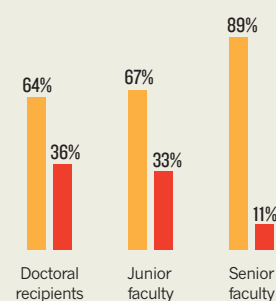
A study of US science departments showed that women were more successful than men in gaining tenure between 2002 and 2004. In Europe as in the United States, the gender gap is greater among senior than among junior faculty members.

### US TENURE DECISIONS 2002-04

♂ / ♀ = 10 PEOPLE



### GENDER GAP AMONG SCIENTISTS IN EUROPEAN UNIVERSITIES (2006)



SOURCE: NSF/REF. 12

SOURCE REF. 4

SOURCE: NSF/WEBCASPAR

SOURCE: REF. 3/REF. 12

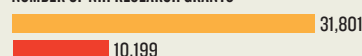
## THE FUNDING GAP

Women are earning an increasing share of research grants from the US National Institutes of Health (NIH) but the average size of their awards has consistently lagged behind what men receive.



2002

NUMBER OF NIH RESEARCH GRANTS

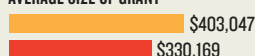


24%

Proportion going to women

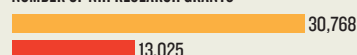
2002

AVERAGE SIZE OF GRANT



2012

NUMBER OF NIH RESEARCH GRANTS



30%

Proportion going to women

2012

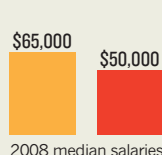
AVERAGE SIZE OF GRANT



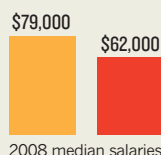
## THE SALARY GAP

Female scientists in the United States earn much less than men, on average, with the difference varying strongly by field.

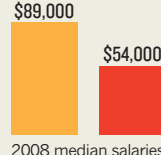
## BIOLOGY



## CHEMISTRY



## PHYSICS AND ASTRONOMY



18% AVERAGE PAY GAP ALL POSITIONS

parents. Shirley Tilghman, president of Princeton University in New Jersey, believes that such initiatives provide crucial support for women, but that other solutions are still needed. "I don't think there's a single obstacle," she says. "I think there's a whole series of phenomena that add up."

## LIVE ISSUE

At Yale University in New Haven, Connecticut, microbiologist Jo Handelsman is one of many researchers who think that gender discrimination continues to be a significant part of the problem. In a much-talked-about experiment last year<sup>6</sup>, her team showed that science faculty members of both sexes exhibit unconscious biases against women. Handelsman's group asked 127 professors of biology, chemistry and physics at 6 US universities to evaluate the CVs of two fictitious college students for a job as a laboratory manager. The professors said they would offer the student named Jennifer US\$3,730 less per year than the one named John, even though the CVs were identical. The scientists also reported a greater willingness to mentor John than Jennifer. "If you extrapolate that to all the interactions that faculty have with students, it becomes very frightening," says Handelsman.

Her findings match well with the results of a survey<sup>7</sup> done in 2010 by the American Association for the Advancement of Science. Of the 1,300 or so people who responded, 52% of women said that they had encountered gender

bias during their careers, compared with just 2% of men.

Still, other concrete evidence of bias is hard to find. Some measures show female scientists outperforming male rivals in landing interviews and job offers early in their careers. The National Research Council study<sup>3</sup> showed that women accounted for 19% of the interview pool and received 32% of job offers for tenure-track electrical-engineering positions. Women fared just as well as men in tenure evaluations, but female assistant professors in many disciplines seemed less likely to reach tenure consideration compared with men.

Women face even more daunting odds in Spain. Men are 2.5 times more likely to rise to the rank of full professor than female colleagues with comparable age, experience and publication records<sup>8</sup>.

Disparities can also be found in grant funding in some countries. In one frequently cited study<sup>9</sup>, Christine Wennerås and Agnes Wold at the University of Gothenburg in Sweden found in 1997 that female applicants for postdoctoral fellowships had to score 2.5 times higher on an index of publication impact to be judged the same as men.

Several groups, such as the UK Medical Research Council and biomedical research charity the Wellcome Trust, have since investigated their grant programmes and found negligible or very subtle effects of gender<sup>10</sup>. The Canadian Medical Research Council found no differences in success rate in most of its research

grant programmes, but reported lower success rates for women in some training grants<sup>11</sup>. In the United States, women are slightly more successful than men in obtaining grants from the National Science Foundation, but the trend is reversed for the National Institutes of Health (NIH). The NIH also gives women smaller awards on average (see 'The funding gap').

Information provided to *Nature* by the NIH through a Freedom of Information Act request indicates that the percentage of women on review panels has improved marginally over the past decade, from 25% in 2003 to 30% in 2012. Those figures roughly parallel the percentage of women applying for and receiving grants in that time.

## PAY PROBLEMS

The inequalities also extend to salaries. In the European Union, female scientists earned on average between 25% and 40% less than male scientists in the public sector in 2006 (ref. 12). Although the average pay gap is smaller in the United States, the disparity is particularly large in physics and astronomy, where women earn 40% less than men.

For young academic scientists, however, those differences may be fading. The National Research Council found an 8% pay gap at the level of full science and engineering professors but no significant differences among junior faculty members<sup>3</sup>. Some experts argue, however, that the salary gap may reflect other continued trends, such as the fact that a disproportionate share of women move into non-tenure positions or faculty jobs at lower-status universities.

Tilghman says that Princeton and many other universities have grown increasingly conscious of the need to track and rectify gender gaps in salary and other institutional support. "Absolutely, it needs eternal vigilance," she says. "But we're in a much better place." ■

**Helen Shen** is an intern with *Nature* in Washington DC.

1. Royal Society of Chemistry *Change of Heart* (RSC, 2008).
2. Newsome, J. L. *The Chemistry PhD: The Impact on Women's Retention* (RSC, 2008).
3. National Research Council *Gender Differences at Critical Transitions in the Careers of Science, Engineering, and Mathematics Faculty* (National Academies, 2010).
4. Goulden, M., Frasch, K. & Mason, M. A. *Staying Competitive* (Center for American Progress, 2009).
5. Ecklund, E. H. & Lincoln, A. E. *PLoS ONE* **6**, e22590 (2011).
6. Moss-Racusin, C. A., Dovidio, J. F., Brescoll, V. L., Graham, M. J. & Handelsman, J. *Proc. Natl Acad. Sci. USA* **109**, 16474–16479 (2012).
7. Cell Associates *Barriers for Women Scientists Survey Report* (AAAS, 2010).
8. Women and Science Unit *White Paper on the Position of Women in Science in Spain* (UMYC, 2011).
9. Wennerås, C. & Wold, A. *Nature* **387**, 341–343 (1997).
10. Grant, J., Burden, S. & Breen, G. *Nature* **390**, 438 (1997).
11. Friesen, H. G. *Nature* **391**, 326 (1998).
12. European Commission. *She Figures 2009* (European Communities, 2009).



# BARRED FROM THE BOARDROOM

The number of women in scientific research is going up — but where academia crosses into industry, **men still rule.**



BY ALISON MCCOOK

**N**ancy Hopkins started Googling her colleagues in spring 2012. She mentally scanned the hallways of her institution at the Massachusetts Institute of Technology (MIT) in Cambridge — along with the campuses of other elite institutions — for the offices of men she knew who had founded companies. Then she clicked on the websites of their firms, and counted the number of men

and women serving on their scientific advisory boards (SABs), a prestigious position for researchers who steer the company's scientific direction.

It was an informal exercise, rather than a systematic survey. But Hopkins, a molecular biologist at MIT and a long-time campaigner for women in science, found the results shocking. A sample of 12 of the companies she examined had a

VIKTOR KOEN



## WOMEN IN SCIENCE

The gender gap and how to close it  
[nature.com/women](http://nature.com/women)

total of 129 SAB members; only 6 were women. “I was completely stunned,” says Hopkins. “And it made me sad. I thought, ‘gee, why don’t these men want to work with [MIT] women?’ We have such incredible women faculty.”

The proportion of women in industrial and academic science has shot up over the past 20 years. According to the US National Science Foundation, women make up 25% of tenured academics in science and engineering and more than 25% of industry scientists in research and development. But when it comes to academics engaging in commercial work — patenting their discoveries, starting biotech companies or serving on SABs — the picture is less progressive. Studies have confirmed Hopkins’ impression that even leading female scientists are often absent from these roles. “The secret club [of men] used to be going to the lab and conferences,” says Fiona Murray, who studies life-sciences entrepreneurship at MIT. “That world has changed a lot, but we have a new venue where it is still difficult for women to play a similar role.”

Experts in industry and academia speculate that the disparity could reflect the small numbers of women in certain specialized fields; the demands of family life; or a residual male clubbiness. Whatever the reasons, this stubborn gender gap hurts everyone, says Bonnie Bassler, a molecular biologist at Princeton University in New Jersey. “I think the companies would do better science by having the best people on their board. And I think these women, who are great scientists, would do better science in their labs by having access to these ideas.”

“Everybody’s losing,” says Bassler.

### HIDDEN PROBLEM

For much of the 1980s and 1990s, there were more than 11 men for every one woman in the science faculty at MIT. Things started to change 20 years ago, when Hopkins, as the first chair of MIT’s Committee on Women Faculty in the School of Science, and her team drove through major increases in the hiring of women. By 2006, one out of every five biology faculty members on the MIT campus was a woman.

At a dinner last April to honour these achievements and mark her retirement from the lab, Hopkins spoke about the work still to be done. She talked about a list she had been given by a graduate of Harvard Business School in Boston, Massachusetts, showing the names of scientists in the area who had received funding from a local venture-capitalist firm. Among 100 names, only one was a woman. The list would not have surprised Hopkins more than 30 years ago, when she had been told by a colleague that “women aren’t allowed” to found biotech companies. But to see such a dearth of academic women in modern biotechnology was upsetting.

Around that time, Hopkins embarked on her Google search. She was particularly interested in SABs because they consist mainly of working scientists who are often invited by the company’s academic founders — a social process that could reveal conscious or unconscious biases against female academics. And membership in advisory boards comes with advantages: it can tip members off to promising tools and areas of research, and lead to other lucrative prospects, such as consulting. Plus, for a few meetings per year, board members are paid a sometimes-substantial fee, given stock options, or both.

The first name Hopkins looked up was Eric Lander, founding director of the Broad Institute of MIT and Harvard. She typed “Eric Lander companies” into the search engine. Scrolling through the results, she came upon Verastem, a cancer stem-cell company founded in 2010 by Lander and others, including Robert Weinberg, a cancer researcher at the Whitehead Institute in Cambridge. She counted 14 people on Verastem’s SAB; all were men.

Entering “Phil Sharp companies” brought up Alnylam Pharmaceuticals, a Cambridge-based firm co-founded by the Nobel prize-winning molecular biologist at MIT in 2002. The company, which is developing therapies based on RNA interference, had one woman on its 11-person SAB. “Bob Langer companies” yielded a handful of the 20-plus firms that the MIT bioengineer has helped to launch,

including Taris Biomedical in Lexington, Massachusetts, which focuses on genitourinary conditions, and the biopharmaceutical company Blend Therapeutics in Watertown, Massachusetts. Neither SAB included any women. (Weinberg and Lander say that they were not involved in selecting the SABs at Verastem, and Langer that he was not involved with the process at Blend or Taris. Sharp says that at Alnylam, choosing the SAB required “agreement between” the founders, chief executive, venture capitalists and other people already brought into the company.)

Hopkins included in her search a few scientists from other institutions, such as Harvard University in Cambridge and Memorial Sloan-Kettering Cancer Center in New York. Overall, among the full-time professors affiliated with a sample of 14 companies she reviewed, only 5% of founders or SAB members were women. Although boards change over time, that fraction was much the same as of last month.

Last July, Hopkins began circulating her results to a handful of faculty members at MIT and to scientists further afield. Vicki Sato, a professor of biology and management at Harvard with a long career in the biotechnology industry, says she could not believe what she was seeing. “I was stunned by the sampling she had done, and told her she had to be wrong,” says Sato. “But I knew deep down she was right.”

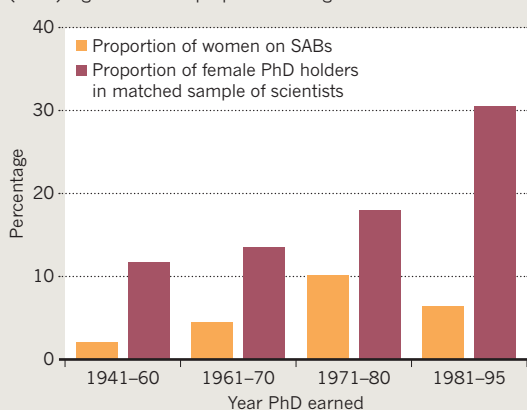
### GLOBAL CONCERN

More rigorous studies have reached similar conclusions. In a paper published last October<sup>1</sup>, Murray, Toby Stuart at the University of California, Berkeley, and Waverly Ding at the University of Maryland in College Park reviewed all publicly available lists of US biotech SABs, starting in the 1970s and including about 500 companies. Although women represented between 12% and 30% of academically active PhD holders over that time period, the percentage of women on SABs never exceeded 10.2% (see ‘Inequality on board’). Even when the researchers compared male and female faculty members with similar levels of achievement, measured by factors such as publication and citation counts, male scientists were roughly twice as likely to join SABs as female ones.

SABs are not the only commercial forum in which academic women seem to be disadvantaged. US women also receive patents about 40% as often as men<sup>2</sup>, start businesses half as often<sup>1</sup> and receive significantly less funding for the start-ups that they do launch<sup>3</sup>. This is not just a US problem: a study released in April 2012 by the Royal Society of Edinburgh found that women

### INEQUALITY ON BOARD

The proportion of women on biotech scientific advisory boards (SABs) lags behind the proportion of eligible female candidates.



SOURCE: REF. 1



are underrepresented on the boards of UK science, technology, engineering and mathematics companies<sup>4</sup>. That is despite the fact that including women seems to be beneficial: a 2012 report from Credit Suisse in Zurich, Switzerland, found that worldwide, companies with women on the board have higher share prices than those with all-male boards<sup>5</sup>.

## INVITATION ONLY

So what is going on? For SABs, Hopkins thinks that the answer is simple: women are not asked. When she noticed the stark patterns in board memberships, Hopkins asked some of her female colleagues — including one she believed was an “absolute star” — if they had ever been invited to serve on boards. All of them said no. “In the end, these stories are very sad,” says Hopkins. “People know they’re excluded, and it’s costly professionally. They’re embarrassed to talk about it. It’s like not being asked to dance.”

But the picture is not so simple, says Paul Schimmel, a former colleague of Hopkins who is now based at the Scripps Research Institute in La Jolla, California, and is a co-founder of Alnylam. He says that he has tried to ensure equal gender participation in his lab and his companies for the past 20 years. “There’s no lack of effort, I tell you,” says Schimmel. But serving on a board “can be a lot of work” — conference calls, e-mails, travel several times a year and thick documents to review — and women often bear the majority of domestic work and child care. At least one woman has turned down Schimmel’s invitation to serve on an SAB because of family responsibilities, he says. Indeed, research has shown that female academics with children are less likely than those without to patent their discoveries<sup>6</sup>.

Some prominent female scientists disagree. Carolyn Bertozzi, a chemical biologist at the University of California, Berkeley, who has two young children and one on the way, says that she is always willing to make time to serve on the research advisory board at GlaxoSmithKline, which entails attending two-day meetings twice a year for “generous” compensation. The meetings teach her about what it takes to make a drug, including medicinal chemistry, regulatory issues and intellectual property; that helps with her start-up, Redwood Bioscience in Emeryville, California, which has two female SAB members out of four. Bertozzi acknowledges that her situation is unusual: her female partner is a stay-at-home mother. But Bassler, too, says that the work involved in SABs is worth the sacrifices. “If I were asked to serve on a board, I wouldn’t do something else,” she says. Bassler has been invited to serve on two SABs in her career, but “of course” would accept another invitation if it arose.

Research seems to support the idea that it is a lack of invitations — not a lack of time — that reduces female membership in biotech SABs. Murray, Stuart and Ding found that both men and women tend to join SABs on average around the 20th year after completing their PhDs<sup>1</sup> — often a time when the major strain of child rearing is over. This suggests that family obligations are not holding back women more than men. And in interviews at a leading institution that Murray declined to name, women consistently reported they had rarely been invited to serve on their colleagues’ SABs — which was not the case in a matched sample of men<sup>7</sup>.

Stuart says that the disparity is most likely to be a result of social connections and unconscious bias among men. “If you’re male, you’re slightly more comfortable shooting the shit with your male colleagues, and they’re who come first to mind when you’re putting these boards together. You may assume — ‘oh, she’s got two kids, she’s not going to be interested’ — and then not invite her.”

**“People know  
they’re excluded.  
They’re  
embarrassed to  
talk about it. It’s  
like not being  
asked to dance.”**

But companies say that they can have difficulty finding women with the right experience, because there are fewer women than men in academia overall. At Alnylam, says Schimmel, the type of science and the diseases it hopes to treat “considerably narrow the size of the pool of highly qualified senior investigators, regardless of gender”. (A statement from the company notes that women represent “nearly 30%” of Alnylam’s management team.) At Taris, says Langer, the SAB had to include mostly clinical experts in urology, who are generally men. And Verastem found that there were few prominent female biologists who focus on cancer stem cells, says chief medical officer Joanna Horobin. At least one woman declined the offer to join the SAB, Horobin says, because she was already working with a competing company.

The academics and biotech companies interviewed for this story say that they hope the situation will change. At Alnylam, people have “discussed openly the issue of gender and the SAB”, says Schimmel. “All of us support strongly the idea of addressing the ‘gender problem’ in a thoughtful way and are actively working on it.” In Lander’s opinion, more important than the make-up of the SAB is the selection of the company’s board of directors — who “control the entire company”. Two out of seven directors at Verastem are women.

Women can also make the first move, says Helen Blau, a stem-cell biologist at Stanford University in California, who has served on the advisory boards for several start-ups. She broke into commercialization by patenting discoveries and talking to companies at conferences about her work. The effort paid off: companies have licensed at least a dozen of her patents, which helped Blau to get consulting jobs, board invitations and now her own start-up, Didimi in Berkeley, California.

Hopkins, meanwhile, has not let the issue lie. After she discussed her data with MIT colleagues, the group decided to forward the findings to the university’s provost, Chris Kaiser. It turned out that Lydia Snover, director of institutional research at MIT, had already started mining faculty CVs across the entire institution for information about activities such as patenting, technology licensing and participation in SABs. If MIT finds gender differences and can help to do something about them, it will, says Snover. “We want all [faculty members] to be involved in the same way.”

Hopkins wants to see all institutions follow MIT’s example. In academia, people used to believe that “time would fix things naturally”, and that women would eventually move up the ranks, she says — and this attitude may still exist when it comes to academics moving into industry. “I think [the gender disparity in SABs] is what universities would look like if we hadn’t stopped, analysed what was going on, and changed it. If you don’t put attention to it, it doesn’t happen.” ■

*Alison McCook is a freelance writer and editor in Philadelphia, Pennsylvania.*

1. Ding, W., Murray, F. & Stuart, T. *Acad. Mgmt. J.* <http://dx.doi.org/10.5465/amj.2011.0020> (2012).
2. Ding, W. W., Murray, F. & Stuart, T. E. *Science* **313**, 665–667 (2006).
3. Robb, A. M. & Coleman, S. *Sources of Financing for New Technology Firms: A Comparison by Gender* (Ewing Marion Kauffman Foundation, 2009); available at [go.nature.com/hdfa6q](http://go.nature.com/hdfa6q).
4. *Tapping All Our Talents: Women in Science, Technology, Engineering and Mathematics: A Strategy for Scotland* (Royal Society of Edinburgh, 2012); available at [go.nature.com/b8xrkb](http://go.nature.com/b8xrkb).
5. Credit Suisse Research Institute *Gender Diversity and Corporate Performance* (Credit Suisse, 2012); available at [go.nature.com/vw2rsa](http://go.nature.com/vw2rsa).
6. Whittington, K. B. *Work Occup.* **38**, 417–456 (2011).
7. Murray, F. & Graham, L. *Ind. Corp. Change* **16**, 657–689 (2007).

# 30 something science

What's being female got to  
do with anything, ask the  
scientists who are starting  
labs and having kids.



**WOMEN IN SCIENCE**

The gender gap and how to close it  
[nature.com/women](http://nature.com/women)



DANA SMITH

## KAY TYE: POWER MOVER

*The neuroscientist break-dancing down the tenure track.*

BY HEIDI LEDFORD

**B**eing five months pregnant comes with a series of concessions: no booze, no sushi, no double-shot espressos. Less appreciated, perhaps, is the havoc it can wreak on a break-dancer's moves. "My dancing is definitely limited now," says Kay Tye, neurobiologist, award-winning b-girl and assistant professor at the Picower Institute for Learning and Memory at the Massachusetts Institute of Technology (MIT) in Cambridge. "I can't do windmills — I can't do anything that might cause me to fall. Which is, like, everything."

It is one of the few limitations that Tye, 31, has been willing to accept. Striving to make her mark in optogenetics, one of the hottest fields in neuroscience, Tye thought nothing of working past midnight, getting by on four or five hours sleep a night and maintaining a constant, trans-continental travel schedule. She has had to dial back a little in recent weeks, and she knows that life may change further once her daughter is born. But she is ready. "I've been preparing for this my entire life," she says. "I chose a career path that's family friendly."

An assistant professorship at MIT, where the tenure rate hovers at around 50% and the faculty is still about 80% male, may not strike many as particularly family friendly. But Tye, the daughter of a theoretical physicist father and a biochemist mother, grew up in her mother's lab, where she was paid 25 cents per box to rack pipette tips. With her mother as a role model, Tye says that she was in her teens before it occurred to her that her gender could hold back her career. "And by then, my brain was already fully formed," she says with a smile.

Even so, Tye wasn't sure that science was for her. After graduating from MIT, where she first took up break-dancing, she travelled to



JOHNNY TANG

Australia to live on a cattle farm, in a yoga ashram and finally in a beach tent in an art commune. Her goal was to live moment-to-moment and write a novel based on her experiences. But Tye found her new lifestyle unfulfilling — and, she adds, the novel wasn't very good. She flew back home and started graduate school at the University of California, San Francisco. After rotating through the usual three labs without finding a suitable home, she begged neurobiologist Patricia Janak for the chance to do one last placement in her lab. "If you don't let me rotate, I'm going to drop out," Tye tearfully told her.

Tye got the place and a new mentor: Janak, a successful female scientist with two children. And Janak watched Tye bloom. "Her insecurities rapidly disappeared," she says. "She started to get amazing results." In Janak's lab, Tye published her first *Nature* paper after finding that in rats learning to associate a cue with a reward, there was a boost in the activity and synaptic strength of neurons in the amygdala, a brain region that in humans is associated with processing emotions (K. M. Tye *et al.* *Nature* **453**, 1253–1257; 2008). But Tye wasn't satisfied: she wanted to be able to switch neurons on or off directly. That led her to optogenetics, a way to activate or inhibit specific neurons in rodent brains using light.

After a two-year postdoc learning the technique in Karl Deisseroth's lab at Stanford University in California, Tye landed at the Picower. She plans to use the approach to map the neural circuits that govern whether an animal forms a positive or a negative association with a given environmental cue. Ultimately, she hopes that her studies can be used to devise ways to treat disorders such as anxiety, depression and addiction.

Over the past five years, the Picower has recruited a number of young female faculty members, several of whom have since started families. (MIT opened a day-care facility across the street from Tye's office in 2004 and uses it as a recruitment tool.) It definitely helps to know they have paved the way, says Tye.

Since her return to MIT a year ago, Tye has recruited four graduate students and four postdocs, applied for 13 grants, extended her list of top-tier papers and begun to prepare herself for the impact of motherhood. Some decisions are easy: the exercise bike in her office will be replaced with "a crib, or playpen, or whatever" for the times that her daughter accompanies her to work. Some are more difficult, like a trip to Tokyo to speak at a conference a month after the baby is due. Tye can't say no, not yet.

And tenure remains near the top of her list. "I never thought that my life had to be limited to anything," she says. "And I want to set that example for my daughter." ■



"I NEVER THOUGHT THAT MY LIFE HAD TO BE LIMITED TO ANYTHING, AND I WANT TO SET THAT EXAMPLE FOR MY DAUGHTER."

KARINE MARAFIJO DE AMÍCIS



## KEITY SOUZA SANTOS: VENOM DETECTIVE

*An immunologist who studies allergic shock receives a shock of her own.*

BY ANNA PETHERICK

W

hat should have been an ordinary Thursday for Keity Souza Santos turned out to be anything but. It was 4 a.m. when she woke up on 22 November 2012, tired but alert. She had been meaning to take a pregnancy test for days; now she decided she couldn't put it off any longer, and headed to the bathroom. Later, at work at the University of São Paulo Medical School's allergy and immunology department in Brazil, Santos, 33, told none of her colleagues why she had felt like screaming for joy hours earlier. She kept her secret even when one of them called to tell Santos that she had won the prestigious Young Investigator Award from the São Paulo Research Foundation. That meant that she would be starting her own lab at about the same time as her baby was due. Only it will not be just one baby; Santos is expecting twins.

Santos studies life-threatening allergens in foods and insects, a serious threat in Brazil. Well known for its stunning biodiversity, the country ▶



► has more than 400 species of wasp compared with the Northern Hemisphere's 30-odd. One species, *Polybia paulista*, causes hundreds of hospitalizations in Brazil every year. But doctors often have trouble pinpointing the cause of the allergic reactions. "Sometimes patients even bring the wasp to the hospital, but even then we cannot treat them properly because we don't know what allergens are in the sting," Santos says.

During a PhD at the University of São Paulo, Santos worked on an antivenom against the sting of the Africanized honeybee or 'killer bee' (*Apis mellifera* L.). As a postdoc, she studied the proteins responsible for anaphylactic reactions to cassava (*Manihot esculenta*), a staple food in north Brazil, and to the sting of several wasps. From *P. Paulista* alone, she and her colleagues separated out and identified 84 venom proteins — including some that had previously been found only in snake venom — and showed how they can trigger devastating tissue damage (L. D. dos Santos *et al. J. Proteome Res.* **9**, 3867–3877; 2010). Now she is trying to identify the offending proteins in other insect venoms.

To learn the mass spectrometry and other molecular techniques

required for the task, Santos spent months in labs in the United States and Austria. While abroad, she heard tales of sexism, something she says she did not encounter when growing up in Brazil. Santos says that her family was shocked when she announced (after reading about the cloning of Dolly the sheep) that she wanted to become a biologist, but not because of her gender. No one in her family was a scientist, and such a career was different from the world they knew.

Now working largely independently, Santos's goal is to create kits that will help doctors to quickly identify the allergens to which a person has been exposed and how to detoxify them. But first she is focused on the challenges that this summer will bring. "My boss is a little bit worried," she says. "But I already have a PhD student and a technician. We can Skype a lot [during my maternity leave]."

"I think she will manage," says immunologist Jorge Kalil, Santos's head of department, before adding after a pause, "but they are twins". Santos has no such qualms. "I want to increase my group of students and collaborators," she says. "Why would I give up my scientific career now?" ■

## MÓNICA BETTENCOURT-DIAS: CELL MECHANIC

*A biologist who explores and shares the intricacies of the cell.*

BY ALISON ABBOTT

**M**ónica Bettencourt-Dias grew up surrounded by role models. Despite being relatively poor, Portugal has an excellent record within Europe for appointing women to top positions in academia and other professions. Some think that the situation traces back to the 1960s and 1970s, when educated young men were sent to fight in Angola and Mozambique, leaving room to promote women and spawning a gender blindness in academia. On top of that, Bettencourt-Dias was raised by a supportive mathematician father and social-scientist mother, and she came of scientific age just as her country was introducing an innovative, government-paid doctoral programme, for which she was selected in 1996. "We had some of the world's best scientists teaching us," she recalls, "and I was able to learn that my destiny was cell biology and development."

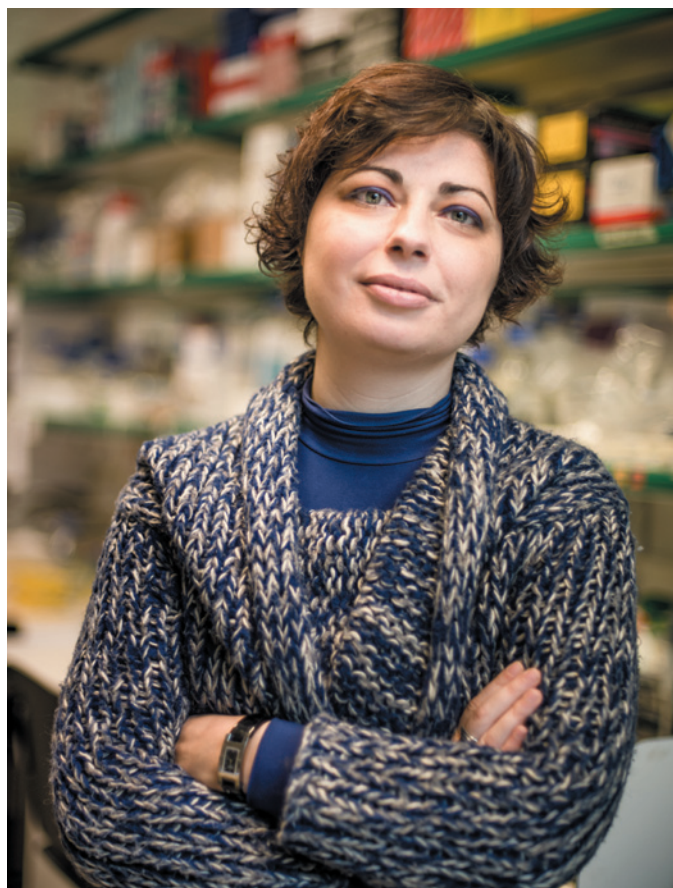
Bettencourt-Dias travelled to University College London to study the regenerative properties of salamanders as part of her PhD. Later, as a postdoc at the University of Cambridge, UK, she discovered a master regulator of the centrosome, an organelle that organizes some of the key structures and machinery involved in the cell cycle, bagging her first *Nature* paper (M. Bettencourt-Dias *et al. Nature* **432**, 980–987; 2004). She returned to Portugal in 2006 to start her own laboratory at the Gulbenkian Institute of Science in Oeiras and the money has flowed generously ever since — including a prestigious €1.5-million (US\$2-million) Starting Grant from the European Research Council.

Now 39, Bettencourt-Dias's life changed a few months ago with the long-awaited arrival of her adopted one-year-old daughter. But Portugal has abundant professional child-care places, and family members tend to be close by to help out. Bettencourt-Dias's husband, also a scientist, does his share of the child-raising, and the couple has hired help for their domestic chores.

In the lab, Bettencourt-Dias still focuses on the tight communication and organization imposed by cellular-signalling pathways and centrosomes. There are parallels in her own life. Being well-organized has been essential to her career, she says, and she developed a drive for communicating science to the public that has led to regular participation in workshops in Portugal's former colonies. Last year, she organized a molecular biology workshop in the west African island nation of Cape

Verde, which in 2008 became the first country in Africa to have a government comprising a majority of women. The workshop had a similar number of men and women, Bettencourt-Dias says, and the attendees "told me they wanted to learn science to help their country — you don't hear this in Western countries".

Sharing is a life philosophy for Bettencourt-Dias; her discoveries are recalled in those terms. One of her first such moments came in Cambridge when she and her first PhD student showed that an enzyme called PLK4 is important for the structure of fly centrosomes (M. Bettencourt-Dias *et al. Curr. Biol.* **15**, 2199–2207; 2005). Together, they watched scores of tiny centrosomes forming under the microscope. "It is beautiful to share that moment with someone you are teaching," she says. ■



ROBERTO KELLER-PÉREZ





## AMANDA WELTMAN: DRIVING FORCE

*A cosmologist who probes dark energy and ignores stereotypes.*

BY LINDA NORDLING

W

hen Amanda Weltman discovered physics as an undergraduate at the University of Cape Town in South Africa, she thought that “understanding the way the Universe worked was just about the coolest job anyone could have”.

Weltman was just 24 when she shot to fame with a proposal about how the Universe works at the grandest scales. Her breakthrough paper, ‘Chameleon Cosmology’ (J. Khoury and A. Weltman *Phys. Rev. D* **69**, 044026; 2004), published when she was graduate student at Columbia University in New York, gave rise to a popular theory to explain the phenomenon of dark energy — the mysterious force that is hypothesized to be speeding up the expansion of the Universe.

Weltman and her colleague Justin Khoury suggested that a new force that changes according to its environment could explain many observations about the Universe’s expansion. This ‘chameleon’ force would be weak when particles are packed together, such as on Earth or in the early Universe. But as galaxies fly apart the force would grow, and accelerate the growth. What makes their theory popular is its testability: it predicts that a photon will sometimes decay into a chameleon ‘particle’ when travelling through a strong magnetic field. Experimental physicists have begun looking for this effect, but haven’t yet found anything conclusive (see *Nature* <http://doi.org/b96z3f>; 2009).

In 2009, after finishing her PhD at Columbia and a postdoc at the University of Cambridge, UK, Weltman moved back to South Africa. This enabled her to start a life with her husband, string theorist Jeff Murugan, whom she had met a decade earlier. Until that point, their courtship had been a typical case of academia’s ‘two-body problem’ — mostly conducted at great distances. Their return to South Africa was also driven by idealism. After years learning from the best in their disciplines, they wanted to bring that expertise home. “We thought we could

be better put to use here to grow the country’s science and knowledge,” Weltman says.

Back at the University of Cape Town, she is part of a large research group, but is also building her own — she has one student and one post-doc so far — to extend and test the chameleon theory. Last year she received a ‘P’ rating from the country’s National Research Foundation, a distinction given to a handful of young researchers who are on their way to becoming international leaders in their field.

Weltman thinks that early barriers for women — the expectations that girls are better at soft sciences than hard ones, or that mathematics

**“I DON’T THINK GIRLS NECESSARILY NEED GIRL ROLE MODELS, BUT I THINK THEY NEED GOOD ROLE MODELS.”**

is more for boys than girls — are the most harmful. She was raised in a family in which such stereotypes did not exist, she says, and is grateful to have had role models, many of whom were men. “I don’t think girls necessarily need girl role models, but I think they need good role models,” she says.

Having her husband down the hall was handy after the arrival of their two children, now 2 years old and 8 months

old. Weltman, who is now 33, kept her research going through her four-month bouts of maternity leave, which in practice were only a leave from teaching. She admits that it was tough at times. Her husband, she says, “looked after the children as much as possible, so I could work. Together we make it work by finding the cracks in the day.” They go to conferences as a family and take turns looking after the children.

Academia offers flexibility, but it can still be a daunting place to start a family, Weltman says. “When I was pregnant, I felt a little bit defensive and guilty, like I was admitting that my personal life was important to me by having a child,” she says. “In physics, you are supposed to be life, blood, flesh, dedicated 100% to your research.” ■

# COMMENT

**WOMEN** Quotas could overburden already-stretched science stars **p.39**

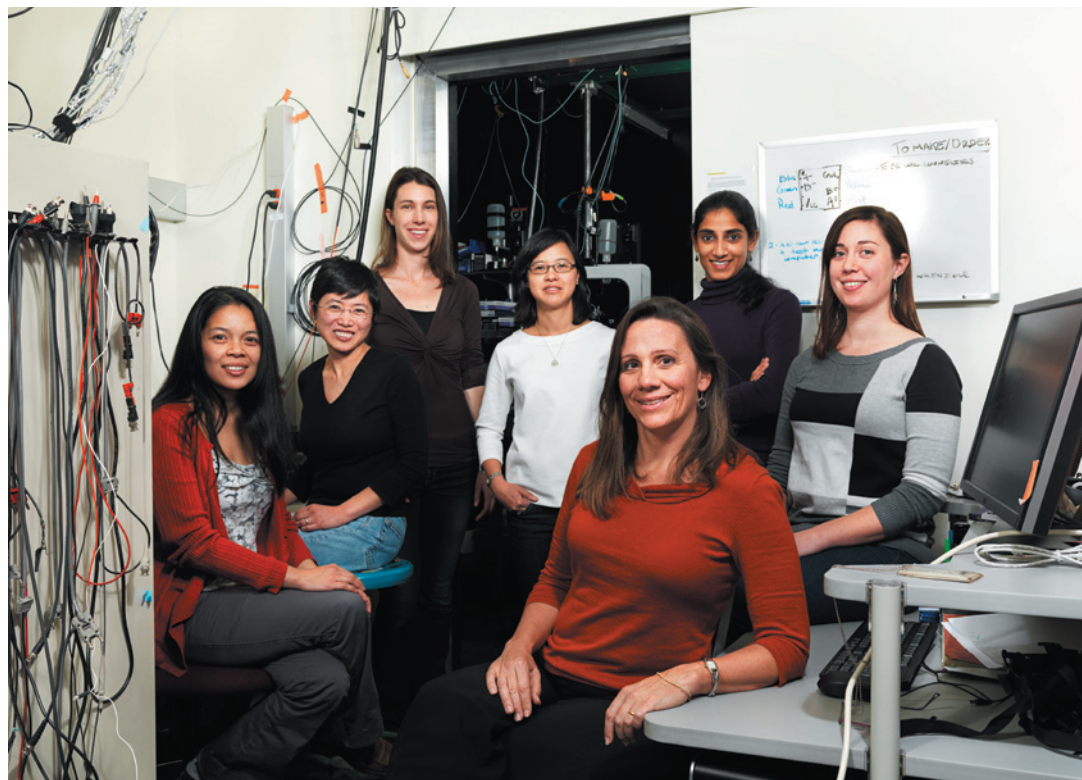
**WOMEN** Europe must build on its impressive efforts to close the gender gap **p.40**

**WOMEN** Why do biographers stereotype female scientists as weird? **p.43**



**TECHNOLOGY** Two takes on why the Internet is no cure-all for social ills **p.45**

CODY PICKENS



Neurobiologist Jennifer Raymond (front) and her colleagues in their lab at Stanford University in California.

## Most of us are biased

Let's move beyond denial, own up to our prejudices against women and retrain our brains to overcome them, says **Jennifer Raymond**.

I have a bias against women in science. Please don't hold this against me. I am a woman scientist, mentor and advocate for women in science, and an associate dean in my school's Office of Diversity, with a budding field biologist as a daughter. Yet my performance on the Implicit Association Test (<https://implicit.harvard.edu/implicit/demo>), which measures unconscious associations between concepts, revealed that I have a tendency to associate men with science and career, and women with liberal arts and family. I didn't even need to wait for my score; I could feel that my responses were slower and that I made more mistakes when I had to group science words such as 'astronomy'

with female words such as 'wife' rather than male words such as 'uncle'.

The results from hundreds of thousands of people indicate that I am not an outlier — 70% of men and women across 34 countries view science as more male than female<sup>1</sup>.

Gender bias is not just a problem in science. A host of studies shows that people tend to rate women as less competent than men across many domains, from musical abilities to leadership<sup>2</sup>, and that many individuals

hold biases about competency on the basis of other irrelevant attributes, such as skin colour, body weight, religion, sexual orientation and parental status.

Such biases have important consequences in the workplace. One study showed that mothers are 79% less likely to be hired and are offered US\$11,000 less salary than women with no children<sup>3</sup>. By contrast, the same study shows that parenthood confers an advantage to men in the workplace.

A 2012 study by Jo Handelsman of Yale University in New Haven, Connecticut, and her colleagues shook the scientific community by reporting that science faculty members have a pervasive bias against female ▶



**WOMEN IN SCIENCE**

The gender gap and how to close it  
[nature.com/women](http://nature.com/women)



## BIAS BUSTERS

*Ways to conquer gender assumptions*

- **Raise awareness of gender bias as a first step to overcoming it.** Call for transparency in salaries, hiring, leadership and editorial decisions. Organize a discussion of implicit bias in science, and what can be done locally to address it. At Stanford University, we have a Gender Issues in Neuroscience discussion group that brainstorms ways to overcome challenges such as competition, response to failure, networking and speech and body language. We include men in these discussions because they are also affected by gender stereotypes and are an essential part of the solution.
- **Use gender-blind review<sup>5</sup> or other processes to mitigate bias** when reviewing applicants for a job, award, speaking engagement, grant or manuscript. Define measurable review criteria in advance to avoid a gut response, which is most vulnerable to bias. Be vigilant for rationalizations that could reflect an unconscious bias, such as “she’s great, but seems awfully young/is not a good fit/is working in such a competitive area”. Create an environment in which it is acceptable to question colleagues when bias might be influencing their behaviour. It is easier to detect bias in others than ourselves<sup>8</sup>, so we need to help each other without judgement. It is especially helpful if men initiate conversations about gender bias so that women don’t bear the full responsibility.
- **Make a conscious effort to offer women mentoring and other support,** including an equal salary to male peers, to overcome the documented tendency to offer women

less<sup>4</sup>. Trumpet the achievements of female colleagues, because biases have the greatest influence when there is a dearth of specific information<sup>9</sup>.

● **Women should overcome their own gender bias** because it could make them less likely to compete for prestigious jobs or awards<sup>10</sup>. Be proactive in seeking mentorship, and negotiate for salary and other resources. Offer your talent to employers who have programmes to help level the playing field for women. Join or start a women-in-science group, especially within your own scientific subspeciality, because such groups can provide speaking invitations, tenure letters, advice about the key issues and players in the field, and reviews of papers and grants. For about 15 years, women in my subspeciality have got together at our national neuroscience meeting for an annual event that we irreverently call the Babes of the Vestibular/Oculomotor System Dinner.

● **Fund pilot projects** to test innovative interventions to mitigate the effects of bias, and create a central repository for sharing strategies. These programmes will more than pay for themselves if they help to retain the best talent. Considerable resources are being invested in training each young scientist — if we want to be good stewards of that investment, we need to provide everyone, male and female, with a fair shot at success. Institutions should provide incentives, such as salary support or alleviation of other duties, to individuals who spearhead efforts to address implicit bias.

► scientists<sup>4</sup>. This prevents us from doing our job of promoting the best scientists, and society is paying a price in terms of the advancement of science.

There is now sufficient evidence to move us beyond the denial phase of dealing with gender bias. Yet in talking to colleagues around the world, I find continued resistance to the idea that scientists, who take pride in being rational and objective, could be influenced by bias. One colleague was convinced that gender bias could affect the hiring of a lab manager, but he still doubted that it would affect a faculty-level hiring decision or the evaluation of a manuscript, even though the evidence suggests otherwise<sup>5</sup>. And I have seen junior colleagues shake their heads disapprovingly at the gender bias of older science faculty members, yet resist the idea that their generation might also have such bias.

Unfortunately, young people are not

immune to gender bias. Many studies have been conducted on college-age subjects, and gender bias has even been reported in pre-school children<sup>6</sup>. I tried to protect my own children from gender bias by doing things such as changing the gender of the characters in the children’s books I read to them to reverse gender stereotypes, and using the feminine pronoun wherever possible — “Look at the elephant; she is so strong.” Despite these efforts, my daughter had a bias against women in leadership positions by the age of three. One day in the park, she announced, “I am the captain; I’m a girl captain,” suggesting that she knew she had to violate a gender stereotype to assume that leadership position. And although she has a scientist mum who runs a lab full of women, when my daughter took the implicit association test at age 8, it revealed a bias against women in science. My presence as a role model and other efforts at countering gender

stereotypes were not enough to overcome the powerful cultural transmission of bias. Thus, it seems unlikely that unconscious gender bias will be eradicated any time soon, and the best we can do in the near term is to suppress its symptoms.

If we are vigilant, we can reduce the influence of bias on our decisions. Unconscious biases are mental habits that tend to dominate our gut reactions, but we also have more-rational decision processes, which compete with our biases for control of behaviour. Just as one can overcome physical habits such as biting one’s fingernails or saying ‘umm’ when one speaks, one can suppress undesirable mental habits such as gender bias through deliberate, conscious strategies (see ‘Ways to conquer gender assumptions’). By enabling more women to succeed, despite the existence of unconscious bias, this will gradually eliminate the stereotype of the successful scientist as male, which is the root of gender bias.

However, if left unrecognized and unchecked, bias can commandeer both our behaviour and our rational thought processes. Our brains are skilful at creating seemingly rational justifications for our behaviour, even when it is driven by bias. People who had to rate two ‘applicants’ for police chief — one who had more education and the other who had more experience — always chose the man over the woman, but justified their choice as arising from the value they placed on either education or experience, whichever factor was assigned to the man<sup>7</sup>.

Denial that bias exists gives it more power. I am not proud of my unconscious bias against women in science. However, I know that I must first recognize my own bias to overcome it with deliberate practices that suppress its effects. I urge you to join me. ■

**Jennifer Raymond** is associate professor of neurobiology and associate dean in the Office of Diversity and Leadership at the Stanford University School of Medicine, Stanford, California 94305-5125, USA. e-mail: jennifer.raymond@stanford.edu

1. Nosek, B. A. *et al.* *Proc. Natl Acad. Sci. USA* **106**, 10593–10597 (2009).
2. Eagly, A. H. & Karau, S. J. *Psychol. Rev.* **109**, 573–598 (2002).
3. Correll, S. J., Benard, S. & Paik, I. *Am. J. Sociol.* **112**, 1297–1339 (2007).
4. Moss-Racusin, C. A., Dovidio, J. F., Brescoll, V. L., Graham, M. J. & Handelsman, J. *Proc. Natl Acad. Sci. USA* **109**, 16474–16479 (2012).
5. Budden, A. E. *et al.* *Trends Ecol. Evol.* **23**, 4–6 (2008).
6. Del Río, M. F. & Strasser, K. *Sex Roles* **68**, 231–238 (2012).
7. Uhlmann, E. L. & Cohen, G. L. *Psychol. Sci.* **16**, 474–480 (2005).
8. Pronin, E. *et al.* *Pers. Soc. Psychol. Bull.* **28**, 369–381 (2002).
9. Carter, N. M. & Silva, C. *The Myth of the Ideal Worker: Does Doing All the Right Things Really Get Women Ahead?* (Catalyst, 2011).
10. Niederle, M. & Vesterlund, L. *J. Econ. Perspect.* **24**, 129–144 (2010).

# Scientists of the world speak up for equality

Eight experts give their prescriptions for measures that will help to close the gender gap in nations from China to Sweden.



TOP TO BOTTOM: JIM SPENCER (FROM PHOTO BY ASHOK PRASAD); VIKTOR KOEN



**LIHADH AL-GAZALI**

## Remove social barriers

*Clinical geneticist at the United Arab Emirates University in Al-Ain*

Just 1% of Saudi Arabia's researchers were women in 2011, according to the International Labour Organization. This low number is particularly surprising given that 65% of the nation's bachelor's science degrees go to women. Similar patterns are evident in the rest of the Arab Middle East. Women are clearly interested in science. But many cannot continue their careers because of limiting social attitudes in traditional Arab societies.

The expected role for women — graduates included — is housewifery. In some areas, women must ask the permission of the men of the household even to leave their house. Conservative families may not allow their daughters to work in mixed-gender workplaces. To pursue advanced training in research often requires postgraduate study elsewhere. If a woman wishes to do this, the household patriarch may mandate that a male family member accompanies her abroad.

Despite these restrictions, the pool of highly qualified women scientists continues to grow in some Arabic countries. According to the Organisation of Islamic Cooperation in Jeddah, Saudi Arabia, women now represent 19% of researchers in the occupied Palestinian territories and 22% in Libya. Few of these women are university presidents, ►



### WOMEN IN SCIENCE

The gender gap and how to close it  
[nature.com/women](http://nature.com/women)



► directors or department heads.

Having more women in these positions would help to shift cultural expectations. Leading Arab women scientists should continue to get involved in the political life of their countries, where they can be strong advocates for other women scientists. Developments such as the inclusion of leading women academics in the Shura council, Saudi Arabia's highest advisory council (which is now 20% female), and in the Federal National Council of the United Arab Emirates (22% female), are steps in the right direction. Highlighting success stories will encourage qualified Arab women to pursue careers in science. Role model and mentoring initiatives are also important. Examples of such programmes include the Stars of Science initiative by the Qatar Foundation for Education, Science and Community Development, and the TechGirls Exchange Program of the US Department of State.

Universities and professional organizations must help to educate the public about what science entails by inviting families to join conferences, careers days or networking events that include presentations of the achievements of women scientists.



## VIRGINIA VALIAN

### Invite women to talk

*Psychologist at Hunter College and the Graduate Center, City University of New York*

In 2003, I was invited to give the keynote speech at an event held annually by the Sigma Xi scientific-research society to honour scientists' achievements. I was asked to speak about women in science. During dinner, I scanned a list of the event's previous speakers, from 1964

on, to count how many women had given the keynote. Most were listed only by surname and first initial, so between courses, I walked around the room asking people whether they knew anyone on the list. Eventually, I found an older scientist who reviewed the list, recognizing every name, then turned to me with a surprised, rueful smile: in nearly 40 years, I was the only woman to speak at this event. He had heard nearly every lecture but had never noticed that they were all given by men.

At the beginning of my talk, I used that story as an example of how hard it would be for organizers and attendees to detect such a pattern, given only one data point a year. The pattern isn't a product of discrimination or intentional exclusion of women. Rather, few people — men or women — think of women when they picture 'top' scientists who might headline an event.

Are men still disproportionately featured at conferences? Determining an expected number is hard, but it is still relatively rare to find women giving plenary or keynote speeches at conferences. At the American Chemical Society's upcoming spring meeting, for example, all four of the planned plenary speakers are male. That doesn't send an optimistic message to young female chemists. The blog Feminist Philosophers lists nearly 20 recent philosophy conferences — many of which focus on science — featuring only male speakers.

At a language-processing conference I attended recently, I went to 15 or so talks, making note of who asked questions in each one. Women were more likely to ask questions in sessions chaired by women, regardless of the speaker's gender. If that is a general pattern, bringing more women into prominent positions in conferences will increase women's overall participation in scientific discourse. Many organizations strive to include scientists who are from non-English-speaking countries — the same can be done for women.

To that end, my colleague Dan Sperber, a cognitive scientist at the Central European University (CEU) in Budapest, and I have created an online petition ([go.nature.com/sj4yed](http://go.nature.com/sj4yed)) whose signatories commit to accepting talk invitations only from conferences that have made good-faith efforts to include women. So far, we have more than 450 signatures — but few of them are from senior male scientists, and even fewer are from scientists in the United States.

What counts as a good-faith effort? There is no single prescription, but Sperber and I have adopted a few suggestions from Feminist Philosophers. For one, organizers should seek out women in relevant fields to speak at conferences — and keep looking if the first woman they ask says no. Other examples include extending invitations early so that women have time to make

arrangements, and offering child-care services at meeting sites.

But efforts should go beyond the individual. Conference funders should be mindful of gender equity for invited speakers. Similarly, universities should follow the example of the CEU, which now requires that organizers of university-funded events show good-faith efforts to include qualified female speakers ([go.nature.com/ym81ws](http://go.nature.com/ym81ws)).



## BEN BARRES

### Allow time for postdoc babies

*Neurobiologist at Stanford University in California*

Three decades ago, when Nobel laureate Rosalyn Yalow spoke to a women in science group at a major university, her opening statement was: "The primary problem is childcare. Everything else is secondary." Fortunately, many universities now recognize the huge amount of time needed to raise children and help to offset this by providing an extension of 1 year to assistant professors who have a child while seeking tenure. Increasingly, however, scientists are having babies during graduate or postdoctoral training, which together can now total 10 years or more.

I propose that universities modify their tenure-clock extension rules to cover children born at any stage in a career. So even if people already have children when starting out as assistant professors, they should be offered an additional year per child (up to two children, perhaps) to obtain tenure. Even though women typically provide more of the child care than do men, it seems only fair to provide the same extension to men. In the modern world, both parents often work and like to eat dinner with their children (and so cannot write grant applications and papers until midnight).



This change would remove a persistent, if unintentional, form of discrimination that deters many young scientists, particularly women, from choosing tenure-track jobs, and would increase the chance that those who do will make tenure. At Stanford, our provost routinely grants tenure-clock extensions when requested. Why not just make it the rule at every university?

The main argument against extending tenure clocks is that it might help men more than women, because men may use the extra time to amass papers whereas women use it to raise children. If so, one could argue that this is also true of the tenure-clock extensions already granted. Yet most agree that these have been beneficial to all involved. If universities wish to achieve a more diverse faculty, we must continue to remove obviously discriminatory policies.



## LING-AN WU

### Equalize the retirement age

*Physicist at the Institute of Physics, Chinese Academy of Sciences, Beijing, China*

There are two things that China can and should do to make it easier for women to succeed in science: enforce laws that grant equal opportunities to women in the workplace, and make the retirement age the same for men and women.

In some ways, it is harder to be a woman in

science in China today than it was 50 years ago, before the Cultural Revolution. Then, under the socialist system, men and women were given jobs based purely on their performance, so sex ratios were relatively fair. Now that more-capitalist principles infiltrate job placement, it has become more difficult for women to find work. I benefited from the socialist system. After working on a farm for three years, I was assigned a job doing translations at Beijing's Institute of Physics, Chinese Academy of Sciences, because I was fluent in English. This enabled me to go to the United States and obtain a PhD in physics. On returning to the institute with my new skill set, I became a researcher.

Now, women face discriminatory practices that make it harder for them to succeed. For example, in most Chinese institutions, women who are not full professors are required to retire by age 55, 5 years before men. The earlier retirement age was originally established to protect women performing manual labour. In science it essentially prevents them from reaching the same career goals as men, particularly if they had to take time off to raise children. In the past, this practice was not compulsory for academia. It was put into effect at the turn of the twenty-first century to open up positions for young returnees from abroad, who were mostly men. This led to a fast drop in the proportion of women holding lab or department directorships — for example, at my institute, that percentage fell from around 20% before the 1990s to 6% in 2003. (The proportion of female associate scientists has risen to the original level of 27%, but they still make up only 13% of the full-scientist ranks.)

Furthermore, bias now plays a major part in job recruitment. Even in academia, I frequently hear faculty members — even women — saying that they would prefer to hire male students. Private companies advertise for men only, or decline to interview female candidates. Although a 1995 law prohibits discrimination by employers based on gender in China, this is often completely disregarded.

Still, the country has made progress. In 2011, the National Natural Science Foundation of China, which oversees the largest source of government funding for fundamental research, raised the age of its young investigators' awards from 35 to 40 for women, to give them time off to raise children. This allows women to compete more fairly with their male counterparts, especially important because the number of day-care centres has plummeted owing to rising costs. Today, Western and old feudal perceptions spread by the media have led to the saying: "It is more worthwhile to find a good husband than a good job." But no one says: "It is more worthwhile to find a good wife than a good job." This saddens me.



## EVA Y. ANDREI

### Inspire our daughters

*Physicist at Rutgers University in New Jersey*

As a female physicist I am a 'rare bird' — a member of a tiny minority, scarcer than in any other field of science and engineering. Women's representation in physics at major US research universities hovers at about 13%, for many reasons. In my view, these demographics alone make it hard to find female plenary speakers, conference organizers and journal reviewers.

It would be counterproductive to restore the gender balance by burdening the 13% with more refereeing or committee work. Instead, the solution needs to be sought through inspiring and mentoring high-school girls and undergraduate students.

We must also ask whether girls are less inclined towards physics than boys. Is there something in the discipline or its culture that turns them away? Can this be changed?

I am somewhat heartened to see that the fraction of physics PhDs earned by women has increased from 2% in 1966 to 18% in 2010. The percentage of women faculty members at every rank matches the numbers who graduated in the respective years. Still, we are not there yet, and the decline since 2002 in the number of women earning a bachelor's degree in physics is a further cause for concern.

When I polled my women colleagues, almost all agreed that a dearth of guidance and mentorship early on was the main reason for the lack of female physicists.

The rising tide of women joining the profession will encourage more young women into physics. In the meantime, we should showcase successful female physicists through lectures and prizes, and retain young scientists by offering travel bursaries and by stopping tenure clocks. But to really solve the problem, we must inspire our high-school daughters.



## JO HANDELSMAN & CORINNE MOSS-RACUSIN

### Institute training to reduce bias

*Microbiologist, and social psychologist, Yale University, New Haven, Connecticut*

In 2012, we published a study showing that scientists of all ranks and both genders are more likely to hire, mentor and pay more to a 'John' than a 'Jennifer'. Soon afterwards, we were contacted by the office of US congresswoman Louise Slaughter about ways that policy-makers might help to promote gender equity in science.

We proposed that the ethics training now required for students funded by grants from the US National Institutes of Health be expanded to include gender-bias training. Indeed, we feel that all scientists should go through such training. It has been shown that students who undergo diversity training score markedly lower on tests of implicit bias than students who do not (L. A. Rudman *et al.* *J. Pers. Soc. Psychol.* **81**, 856–868; 2001).

Other approaches can also make a difference — the board game *Wages*, designed by Stephanie Shields, a psychologist at Pennsylvania State University in University Park, and her colleagues, shows players how subtle disadvantages to women can have enormous cumulative impact on their careers.

Visual priming works too — for example, people who have viewed images of disliked white people and admired African Americans within the past 24 hours are less likely to show automatic pro-white attitudes (N. Dasgupta & A. G. Greenwald *J. Pers. Soc. Psychol.* **81**, 800–814; 2001).

For more sustained effects, we could paint murals of admired female scientists throughout the halls of universities. A large image of, say, Rosalind Franklin, viewed daily by students in an introductory molecular-biology class, might be even more powerful than explicit instruction on implicit bias. Scientists have agreed on standards and training to ensure proper treatment of animal and human research subjects. The people doing the research are just as important. Striving for equality should be a core aspect of being a scientist.



## LIISA HUSU

### Recognize hidden roadblocks

*Professor of gender studies at the GEXcel Centre of Gender Excellence, Örebro University, Sweden*

In researching women in science and academia, I have found that it is not only the things that happen to women — such as recruitment discrimination or belittling remarks — that affect them in pursuing a

career in science or that slow their career development. It is also the things that do not happen: what I call 'non-events' (L. Husu *Adv. Gender Res.* **9**, 161–199; 2005).

Non-events are about not being seen, heard, supported, encouraged, taken into account, validated, invited, included, welcomed, greeted or simply asked along. They are a powerful way to subtly discourage, sideline or exclude women from science. A single non-event — for example, failing to cite a relevant report from a female colleague — might seem almost harmless. But the accumulation of such slights over time can have a deep impact.

Non-events can be manifold. Superiors or colleagues might ignore or bypass women's research and performance; fail to invite or welcome them to important informal and formal networks; bypass them for awards, prizes or invitations; fail to give them merit-advancing tasks such as representing the research group in public forums; not ask them to design or participate in scientific meetings, conferences, panels or as keynote speakers; or simply stay silent when it comes to career support, advice and mentoring. Even supposedly small non-events can send a powerful message, such as when a female postdoc publishes a high-profile article that generates no reaction from senior local colleagues, while her male counterpart's parallel article is celebrated with high-fives all round.

Non-events are challenging to recognize and often difficult to respond to. Nothing happened, so why the fuss? Often, non-events are perceived only in hindsight or when comparing experiences with peers. Learning to recognize various non-events would help women scientists to respond to them, individually or collectively, with confidence and without embarrassment. Anonymous pooling of non-event experiences would be an eye-opener and a good start to understanding how non-events work in various scientific settings.

All scientists — leaders, gatekeepers, rank and file — need to be aware of how they might inadvertently exclude women from crucial collegiality. Monitoring the practices of support, encouragement, inclusion and exclusion in research groups, projects, networks, conferences and science institutions from a gender perspective would be a first step forward. Addressing this issue in management and supervisor training and early-career coaching is key. ■

**“Non-events are a powerful way to subtly discourage, sideline or exclude women from science.”**

LEFT TO RIGHT: JO HANDELSMAN BY TIFFANY TSANG; JIM SPENCER (FROM PHOTO OF HANDELSMAN BY ULLA-CARIN EKBLOM)



# Quotas are questionable

Measures to give women a fair chance in science should be based on evidence, warns **Isabelle Vernos**, or they could make matters worse.

**I**n Europe, only 36% of mid-ranking professors, and 18% of full professors, are women, despite equal proportions of men and women at the undergraduate level<sup>1</sup>. To address the problem of gender imbalance, the European Commission (EC) has committed to reaching 40% female participation in its advisory structures for Horizon 2020, the European Union's research-funding programme for 2014–20. The EC has also proposed a mandatory quota of 40% for women on non-executive boards of public companies.

But statistics collected by the European Research Council (ERC) suggest that quotas are no magic wand to bring about gender equality in research and academia (despite tentative successes elsewhere, such as for company boards in Norway). Quotas might even make matters worse by overworking already-stretched female scientists. Instead, a range of bottom-up and top-down measures are needed to effect lasting change in the structures and culture of science.

## THE ERC EXPERIENCE

The ERC, launched in 2007, provides up to five years of funding for scientific-research projects chosen by peer reviewers through a transparent competition system. So far, women make up a disheartening 19% of the ERC's 3,500 grantees and account for just 25% of the nearly 35,000 applications received by the ERC to date; 29% of applicants for early-career grants, and only 15% of those for advanced grants, are female.

In 2010, the ERC implemented some recommendations — made by its gender-balance working group (GBWG) under the excellent leadership of outgoing chairwoman Teresa Lago — such as increasing the window of grant eligibility for applicants who have children (the US National Science Foundation adopted similar measures in 2011). The number of female applicants for ERC grants has increased, but so has the number of male applicants — the gap has not narrowed.

Another concern is the lower success rate of female applicants for ERC grants: 10% on average, versus 12% for men. This general trend has been observed in other funding schemes, including the European Molecular Biology Organization<sup>2</sup> and the international

Human Frontier Science Program<sup>3</sup>. Despite several studies on the issue, the reasons for these disparities are still elusive<sup>2,4</sup>. The dearth of women in academia's upper ranks

creativity and productivity, and scientific excellence requires steely focus and lots of time. Female scientists are more likely than males to bear domestic duties<sup>2,5</sup>, making their time already stretched. My estimate, based on the proportion of ERC grantees who are women, is that the burden of panel participation would be three or more times higher for these women than for men in equivalent positions. That said, concerted efforts should be made to identify qualified women for all posts.

Given that measures taken to date have had limited impact, some argue that mandatory quotas are the best way to accelerate gender balance in research (see page 42). I disagree. There are many pockets of good practice — such as mentorship programmes, family-friendly policies and transparency in recruitment — and these should be expanded. Further solutions must also be sought. The GBWG has commissioned a study, called ERCAREER, to examine the career paths of young female and male scientists. Another study, to begin this year, will look into possible sources of

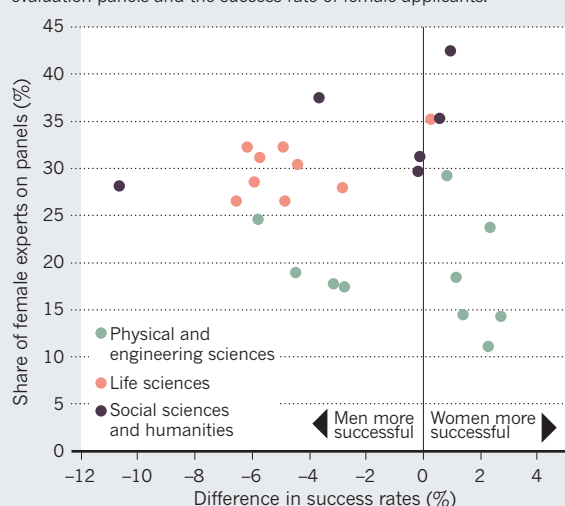
gender bias in the ERC's evaluation processes.

Progress towards improving women's representation in science is too slow. More efforts are needed to understand the reasons for gender disparities and to recruit, retain and promote excellent female scientists — and thus increase the research talent pool and power scientific progress. Europe's future success requires a society that recognizes talent and offers equal opportunity to all — through evidence-based measures. ■

**Isabelle Vernos** is chair of the ERC GBWG and is ICREA Research Professor at the Centre for Genomic Regulation, 08003 Barcelona, Spain.  
e-mail: [isabelle.vernos@crg.eu](mailto:isabelle.vernos@crg.eu)

## GRANT GAP

Aggregating data for 2008–12, the European Research Council found no correlation between the percentage of women on its evaluation panels and the success rate of female applicants.



translates into their scarcity on committees, and it has been argued that this gender imbalance could be feeding back into the lower success rate of female applicants for funding schemes and positions.

I do not think this is so — at least not at the ERC. We have found no correlation between the success rates of female applicants and the gender balance of evaluation panels (see 'Grant gap'). Nor have we found that female applicants are more successful when the panels are chaired by women. Other studies have found that women fare worse than men in evaluations<sup>4</sup>, even when applicant gender is undisclosed to evaluators<sup>5</sup>. These findings suggest that a quota system for staffing evaluation panels will not lead to more grants for women.

Worse, quotas would place greater demand on the small pool of female scientists who would serve on these panels — possibly enough to hamper their career progress. Scientists are evaluated on the basis of



## WOMEN IN SCIENCE

The gender gap and how to close it  
[nature.com/women](http://nature.com/women)

1. European Commission. *She Figures 2009: Statistics and Indicators on Gender Equality in Science*. (European Communities, 2009).
2. Ledin, A., Bornmann, L., Gannon, F. & Wallon, G. *EMBO Rep.* **8**, 982–987 (2007).
3. Langfeldt, L. *Review of the Human Frontier Science Program's Initiatives 2000–2005*. Working Paper 26/2006 (NIFU STEP, 2006).
4. Moss-Racusin, C. A., Dovidio, J. F., Brescoll, V. L., Graham, M. J. & Handelsman, J. *Proc. Natl Acad. Sci. USA* **109**, 16474–16479 (2012).
5. Martinez, E. D. *et al. EMBO Rep.* **8**, 977–981 (2007).





At the European Parliament in Brussels, the European Platform of Women Scientists is calling for binding gender targets.

# Only wholesale reform will bring equality

Providing equal opportunities for women in science requires change at every level, argue **Brigitte Mühlenbruch** and **Maren A. Jochimsen**.

**G**ender-equality policy in science at European regional and national level has come a long way, thanks to more than 20 years of efforts by women scientists and far-sighted politicians. Yet progress is slow. The pipeline is still leaking and female researchers still hit glass ceilings.

In 2007, in the 27 countries that comprise the European Union (EU), women scientists accounted for 38% of active researchers and only 19% of full professors, on average<sup>1</sup>. In 2009, 45% of doctorates were awarded to female students<sup>2</sup>. Although the number of women PhD graduates is growing — up by an average of 4.9% per year between 2004 and 2009, compared with 3.2% for men<sup>2</sup> — this is not enough to suggest that science's

gender imbalance is self-correcting.

When it comes to women in decision-making positions in science and research, Europe is a long way from its 2001 target of 40%. With the exception of Sweden, Finland and Norway, women in Europe are still significantly under-represented on the boards of research institutions, funding organizations, scientific councils and academies, and are rarely found among the heads of higher-education institutions in the majority of European countries<sup>2</sup>. In short, Europe could do better.



**WOMEN IN SCIENCE**

The gender gap and how to close it  
[nature.com/women](http://nature.com/women)

The persistent gender gap has prompted great changes in equal-opportunities strategies at European and member-state level, particularly since the launch of the EU's Women and Science activities in 1998. At first, policy concentrated on individual programmes to equip women scientists with the necessary soft skills to advance, such as networking, mentoring, stipends, training and the provision of role models. These remain indispensable instruments for encouraging individuals.

However, impediments to women scientists have deep institutional roots. The lack of full female participation in academic careers is often a systemic consequence of the culture and organization of higher-

education institutions. Consequently, attention is shifting in the EU to encouraging structural changes in research organizations. Measures include increasing diversity in recruitment; introducing promotion and retention policies; updating management and research-assessment standards; developing course content to successfully attract women as well as men; policies for dual-career couples; and schemes that allow women to return to work after career breaks<sup>3</sup>.

To achieve lasting equality, science needs a culture that is sensitive to gender and diversity in all its endeavours: individual and social, structural, institutional and political. We need transparency, accountability and monitoring in decision-making, evaluation, recruitment, attribution and funding. We need to secure the interest and collaboration of highly qualified women and men by offering predictable academic careers, attractive working places and conditions that enable work and life to be reconciled<sup>4</sup>.

Furthermore, we need to agree that gender is indispensable to research itself. For example, given that there are important sex differences in responses to many drugs and therapies, the underrepresentation of women in clinical trials must be fixed. This applies to animal studies too: laboratory experiments in mice predominantly use male animals, limiting what can be inferred from findings. Gender should be addressed from proposals to papers and beyond<sup>5</sup>.

### BEST PRACTICE

Changing the academic culture will take a mixture of voluntary commitments and binding regulations — all backed up by funding. Here we describe some examples of measures that are having good effects and that should be replicated elsewhere.

In 2008, the member organizations of the German Research Foundation (DFG; Germany's largest research-funding body) committed to a set of structural and personal guidelines called Research-Oriented Standards on Gender Equality. These call on member institutions to make gender equality integral to management, human resources, organizational development, strategy and content, resource allocation and quality-assurance procedures. The standards also demand that institutions publish data on gender equality at all organizational levels and academic career stages. The guidelines require that institutions design procedures in a transparent, structured and formal manner, that they counter outdated gender stereotypes, accommodate individual life plans and empower men and women to combine family life and academic careers.

Responsibility for implementing the standards lies with each member institution, and the DFG uses incentives and evaluation

reports to ensure adherence. To help, the foundation also provides an online toolbox of practical examples (see [go.nature.com/dojcsz](http://go.nature.com/dojcsz); in German). Implementing the standards is voluntary but is a condition of DFG funding.

These standards have led to progress. For example, most DFG member institutions now have flexible working schedules, childcare facilities and other family services. Most member universities have implemented transparent, structured and formalized procedures for the unbiased evaluation of scientific quality and the hiring of professors. Other positive developments include the endeavour to replace stipends, especially PhD grants, with employment contracts that include social-security benefits.

The University of Duisburg-Essen, where one of us (M.A.J.) manages the Essen College of Gender Studies, is particularly notable for its pro-women activities. These include a university-wide mentoring system; a nationwide network on university course development and teaching for sharing expertise in gender issues; and an online portal of gender information for staff. The institution even has a vice-rector for diversity management — the first post of its kind at a German university.

At European level, the European Research Council (ERC) published a gender-equality plan in 2011 (ref. 6). Each process within the ERC — from advertising to grant signing — is designed to give equal opportunities to men and women (see page 39). Among other measures, the ERC sets goals for and monitors the gender balance of its panels of peer reviewers on the basis of information from relevant scientific

communities and its pool of applicants. If a goal is not reached this must be reported, with an analysis of how the situation can be improved<sup>6</sup>. The ERC also commits to challenging potential sources of gender bias in the evaluation process, for example by publishing men and women's submission rates, success rates and granted amounts. The council offers gender-equality training to ERC scientific officers and discusses gender awareness with evaluation panels, highlighting how they should evaluate career breaks and unconventional research career paths<sup>6</sup>.

### MEASURES OF MERIT

Other gratifying recent measures include a 2011 recommendation by the European Science Foundation (ESF) for its member organizations to attain a gender ratio of at least 40% women among grant reviewers. When selecting experts, the ESF also encourages the consideration of individual non-standard career paths affected by changes or interruptions caused by professional mobility or family reasons<sup>7</sup>. Among university associations at European level, the League of European Research Universities took the lead in mapping out what universities and their affiliated institutions can do to bring about change<sup>8</sup>.

Germany's Programme for Women Professors, launched in 2007, is an exemplary blend of state prescription and voluntary institutional commitment. The programme funds universities for appointing women to the rank of full tenured professor. To be selected, a university must produce a coherent gender-equality plan. So far, the programme has led to more than 260 new female professorships at 109 universities



A chemistry student at Germany's University of Duisburg-Essen, notable for its pro-women activities.



(see [go.nature.com/imunpf](http://go.nature.com/imunpf); in German). It has also funded measures such as increasing the number of women in decision-making positions, providing career development for young female researchers and boosting the proportion of women in disciplines that have low female participation, such as engineering, computer science and physics.

Although voluntary targets can achieve much, binding regulations are the only way to effect change in some cases. Quotas, as contested as they are, are another way to counter the under-representation of women scientists in decision-making positions in research organizations. In the Nordic countries and Austria, for example, quotas of at least 40% of each gender are mandated in the administrative parts of research organizations.

From this year, the German Leibniz Association, a high-profile umbrella organization of 86 non-university research institutions, has become one of the first research organizations to introduce binding, merit-based quotas to encourage equal opportunities. The quotas use a 'cascade model': each level of university hierarchy in each discipline must, by 2017, reach at least the same proportion of women as is present at the level below. Such flexible quotas are sensitive to varying numbers of men and women in different scientific disciplines.

#### BEYOND ACADEMIA

The structural measures outlined above should be applied to other leading institutions, such as academic publishers, which should publicize the number of female editors and reviewers (see page 47). More women scientists should be invited to write editorials, reviews and survey articles. Journals and funding agencies should mandate that researchers account for gender in experiments and that they disaggregate gender data in all submitted and accepted papers where relevant, and in clinical trials and cohort studies as a matter of routine. The *Canadian Medical Association Journal* and the *Journal of the American College of Cardiology* already follow such good practice, and *Nature* and *The Lancet* are considering adopting similar policies<sup>9,10</sup>.

Against this background, the European Platform of Women Scientists, which represents more than 12,000 female researchers in Europe and beyond, has urged the European Commission (EC) to do six things with respect to Horizon 2020, the upcoming EU Framework Programme for Research and Innovation<sup>5</sup>.

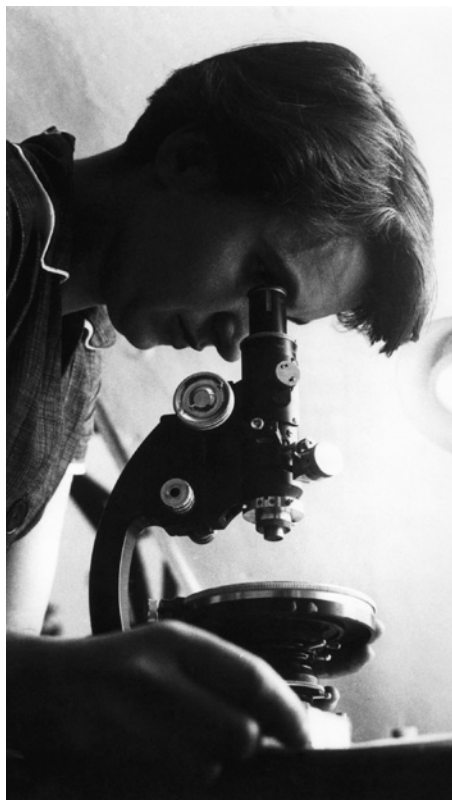
First, the EC needs to introduce binding gender-evaluation criteria in EU

research-funding programmes. Second, it should set targets for the participation of women in EU-funded research projects at all levels (young and senior scientists, project leaders, consortium managers) at the proposal stage, sanctioning missed targets and publishing results. Third, the EC needs to set indicators for gender sensitivity in the research design of proposed projects. Fourth, it should extend the 40% target for women's participation beyond advisory groups and evaluators' panels to all structures related to Horizon 2020 — including the ERC, Joint Research Centre, European Institute of Innovation and Technology, steering and expert groups and the like. Fifth, it needs to train evaluators in gender issues. Finally, the EC must increase funding for research into improving societal structures as part of its innovation strategy (see [go.nature.com/y7vygb](http://go.nature.com/y7vygb)).

Motivation and participation are the basis of high-quality results in research — not biased evaluation criteria, job insecurity and glass ceilings. An academic culture that is transparent, democratic and sensitive to gender and diversity will benefit all scientists. Much has been achieved; a lot remains to be done. ■

**Brigitte Mühlenbruch** is president of the European Platform of Women Scientists, Brussels, Belgium. **Maren A. Jochimsen** is managing director of the Essen College of Gender Studies, University of Duisburg-Essen, D-45117 Essen, Germany. e-mails: [brigitte.muehlenbruch@epws.org](mailto:brigitte.muehlenbruch@epws.org); [maren.a.jochimsen@uni-due.de](mailto:maren.a.jochimsen@uni-due.de)

1. European Commission. *She Figures 2009: Statistics and Indicators on Gender Equality in Science*. (European Communities, 2009); available at <http://go.nature.com/pfifex>.
2. European Commission. *She Figures 2012: Gender in Research and Innovation* (European Union, 2012); available at <http://go.nature.com/muybtr>.
3. European Commission. *Structural Change in Research Institutions: Enhancing Excellence, Gender Equality and Efficiency in Research and Innovation* (European Union, 2012); available at <http://go.nature.com/ryd24j>.
4. Jochimsen, M. A. & Mühlenbruch, B. in *Encouragement to Advance — Supporting Women in European Science Careers* CEWS Beiträge No. 5 (ed. Lipinsky, A.) 11–24 (Kleine, 2009); available at <http://go.nature.com/5wfmgl>.
5. European Platform of Women Scientists. *EPWS Position Paper on the EU Framework Programme for Research and Innovation Horizon 2020* (EPWS, 2012); available at <http://go.nature.com/hwlq71>.
6. European Research Council. *ERC Scientific Council Gender Equality Plan 2007–2013* (ERC, 2011); available at <http://go.nature.com/cfap9o>.
7. European Science Foundation. *Member Organisation Forum European Peer Review Guide: Integrating Policies and Practices into Coherent Procedures* (ESF, 2011); available at <http://go.nature.com/gpkasaa>.
8. League of European Research Universities. *Women, Research and Universities: Excellence Without Gender Bias* (LERU, 2012).
9. *Nature* **491**, 495 (2012).
10. *Lancet* **378**, 1826 (2011).



Rosalind Franklin, Marie Curie and Marie Tharp (from left to right).

## WOMEN IN SCIENCE

# Weird sisters?

Biographies of female scientists perpetuate stereotypes, laments **Patricia Fara**.

James Watson was thrilled to catch an illicit glimpse of Rosalind Franklin's X-ray photograph suggesting the double-helical structure of DNA. He was much less impressed by her personal appearance. "There was never lipstick to contrast with her straight black hair," he wrote in *The Double Helix*, "while at the age of thirty-one her dresses showed all the imagination of English blue-stocking adolescents." Had he been more aware of European fashion, he might have appreciated the care Franklin took to adopt designer Christian Dior's iconic 1947 New Look — although she presumably never revealed to him that her underwear was hand-made from parachute silk to her own specifications.

Watson was far from alone in believing that it is impossible for someone to be both a normal woman and a first-class scientist. To safeguard her reputation as a serious researcher, PhD student Jocelyn Bell — who discovered pulsars in 1967 — removed her engagement ring every morning before she went into the laboratory. Decades later, when president of Britain's Royal

Astronomical Society, she complained that "As a woman in physics, you certainly need to be a superwoman".

In the past, biographers and their publishers routinely squeezed female scientists into stereotypical roles — the frump, the whore, the enchantress, the underdog or the power behind the throne. Even Brenda Maddox, who criticizes Watson for his chauvinistic attitudes, played on gender stereotypes in choosing the subtitle *The Dark Lady of DNA* for her biography of Franklin. Is it not sufficiently fascinating that Franklin's skilled research was crucial for Watson's fame?

Current writers, male and female, are keen to distance themselves from old-fashioned approaches. Still, to boost their book's appeal, they emphasize the singularity of their subjects. It seems that being an ordinary woman with a stellar scientific career is simply not enough: to be marketable, she

## Marie Curie and her Daughters: The Private Lives of Science's First Family

SHELLEY EMLING

Palgrave Macmillan: 2012. 256 pp. \$26.00

## Soundings: The Story of the Remarkable Woman who Mapped the Ocean Floor

HALI FELT

Henry Holt: 2012. 352 pp. \$30

## Rosalind Franklin: The Dark Lady of DNA

BRENDA MADDOX

HarperCollins: 2002. 304 pp. \$29.95

## Hedy's Folly: The Life and Breakthrough Inventions of Hedy Lamarr, The Most Beautiful Woman in the World

RICHARD RHODES

Doubleday: 2011. 272 pp. \$26.95

## I Died For Beauty: Dorothy Wrinch and the Cultures of Science

MARJORIE SENECHAL

Oxford University Press: 2012. 312 pp. \$34.95

must also be odd. Dust jackets entice purchasers by rebranding an overlooked character as a unique female individual — in other words, as a weird woman.

Converting female scientists into publishing opportunities may sell books, but it ▶



## WOMEN IN SCIENCE

The gender gap and how to close it  
[nature.com/women](http://nature.com/women)



► does the cause of equality in science no favours. Take the recent biography of Marie Tharp, the American geologist and cartographer who, with colleague Bruce Heezen, produced the first systematic map of the ocean floor in 1977. In *Soundings*, author Hali Felt imagines Tharp walking along the streets of New York, her coat unbuttoned, shoes scuffed and frizzy hair unbrushed. “She does not look like the other women,” Felt writes — reinforcing sweeping generalizations that female scientists are a race apart.

Even sympathetic authors perpetuate the prejudice that brains and beauty never go together. Describing the film star Hedy Lamarr as *The Most Beautiful Woman in the World*, Richard Rhodes deliberately provokes a shiver of surprise by reporting that she also made breakthrough inventions. With composer George Antheil, she devised spread-spectrum radio, a technology now used in many applications, including cordless phones. “Any girl can be glamorous,” Lamarr is reported to have said. “All you have to do is stand still and look stupid.” Despite her intelligence, Lamarr’s remarkable looks and glamorous career occluded her innovations for decades.

Science’s most famous heroine is surely Marie Curie. Over the decades, biographers have caricatured her as various unrealistic and undesirable ciphers, most notably the adulterous opportunist and the martyr to science. When her husband was killed — according to some such romances — she ensured her continuing success by latching on to his married colleague, Paul Langevin. Meanwhile, eulogies of the pioneer who dared to behave differently stress that she was often too absorbed in her work to eat, sacrificing her health as well as her appearance to the higher cause of research. Downplaying Curie’s theoretical achievements, they portray her as a dedicated worker who spent months systematically sieving tonnes of pitchblende — a mindless, repetitive task with echoes of domestic drudgery.

Modern biographers may have abandoned such facile renderings, but they behave as if it were unthinkable to criticize an icon. Thus, in *Marie Curie and Her Daughters*, Shelley Emling presents the physicist as a doting mother to Eve and Irène, even though the evidence suggests otherwise. Birthday after birthday, Curie chose to be away, sending letters that overflowed with love and regrets, yet enclosed extra homework. Eve reported that her parents regarded radium as their

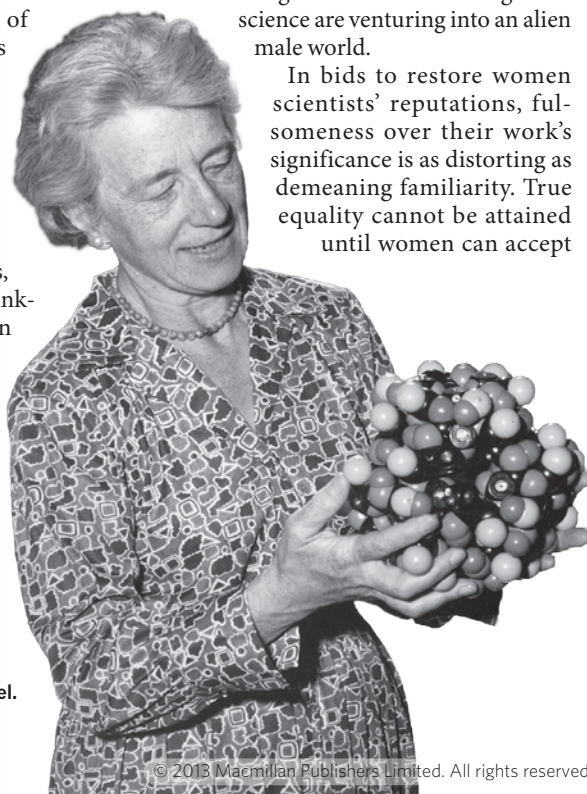
third child, and they seem to have treated their human offspring as an experimental research project. Marie remained physically and emotionally remote, while meticulously recording the girls’ clothes, diet and academic progress in her notebooks.

A less familiar name is that of mathematician Dorothy Wrinch, often labelled a harridan because of her forceful manner among her male peers. Like Curie, she was censored for behaving like a man — with ruthless ambition. The first woman to receive a doctor of science degree from the University of Oxford, UK, Wrinch developed a theory about the molecular structure of proteins that, although later discredited, ultimately contributed to genetics.

In contrast with Felt’s book about Tharp, Wrinch’s name does at least appear on the cover of Marjorie Senechal’s biography, although relegated to the subtitle in favour of the eye-catching but misleading *I Died for Beauty*. Wrinch was indeed fascinated by the aesthetic appeal of mathematical truths, so the title and the pink cover motif implicitly trivialize her intellectual abilities.

Another infuriating feature of many biographies about women scientists is their use of first names and gushing prose. Senechal adopts the nickname ‘Dot’ for Wrinch — but presumably she would not have converted Michael Faraday into Mike, or Albert Einstein into Al. Similarly, although Maddox writes in an accessible yet dignified style, she insists on calling Franklin ‘Rosalind’. So why does she use surnames for Watson and his male colleagues? Presumably, this patronizing practice is intended to foster an impression of cosy familiarity, but it signals once again that women who go into science are venturing into an alien male world.

In bids to restore women scientists’ reputations, fulsomeness over their work’s significance is as distorting as demeaning familiarity. True equality cannot be attained until women can accept



Dorothy Wrinch with her protein model.



Hedy Lamarr co-invented spread-spectrum radio.

criticism without taking the easy route of complaining about gender bias. Ideas are often rejected simply because they are not good enough: the US Navy may have been justified in dismissing Lamarr’s projected guidance system as too bulky to be valuable. And failing to win a Nobel prize need not mean that a woman is a wronged genius: Franklin’s X-ray photograph proved crucial in the race to find the structure of DNA, but Crick and Watson did get there before her.

By perpetuating stereotypes, books affect how people think. When I was in my early twenties, I resolved never to confess that I had a degree in physics from the University of Oxford: I knew from experience that any potential suitor would immediately assume I slotted into one or other of the ‘strange woman scientist’ categories. And schoolgirls are still being steered, as I was, into mathematical and technical subjects by teachers serving the cause of political correctness. I migrated immediately after graduating not because I was incapable of tackling physics or because I was intimidated by being in an environment dominated by men, but because I was bored by the repetitive practical work.

Biographers can shift attitudes, but they need to celebrate their subjects for being special scientists, not marvel at them as weird women. Just like men, female scientists have individual personalities and idiosyncrasies, and they have weaknesses as well as extraordinary capabilities — not because they are women, but because they are human beings. ■

Patricia Fara is a historian of science at the University of Cambridge, UK.  
e-mail: pf10006@cam.ac.uk

## TECHNOLOGY

# Techno-fix troubles

Two analyses challenge the idea of the Internet as a panacea for social ills, finds **Nicholas Carr**.

In his introduction to the 1995 edition of *Engines of Culture* (Transaction), social scientist Daniel Fox lamented the rise of “technocratic solutionism”. Frustrated by the messiness of politics, intellectuals were retreating to a simplistic view of social progress, predicated on a belief that “problems have technical solutions even if they are the result of conflicts about ideas, values and interests”. In technology’s promise of the quick fix, disheartened thinkers found comfort.

Some 20 years on, the appeal of solutionism is stronger than ever, thanks to rapid advances in the analytical and communicative powers of computers. The hopes of today’s solutionists centre on the Internet. In its decentralized, ‘peer-to-peer’ architecture, they see a model for a more democratic polity. And in its bulging databases, they see a digital Rosetta Stone that, once decoded, will allow us to decipher the causes of social ills from obesity to government corruption. If we can just get the algorithms right, the thinking goes, we’ll be able to solve our most intractable problems in an illuminating burst of statistical analysis.

The Internet has been around for long enough to put its curative powers to the critical test. Two authors — social theorist Evgeny Morozov and computer scientist Jaron Lanier — argue independently that the Net is too blunt an instrument to solve complex societal problems. Far from being a cure-all, the network actually aggravates some maladies, such as the concentration of economic power, that many assumed it would remedy.

In *To Save Everything, Click Here*, Morozov provides an astute, if sometimes shrill, critique of contemporary solutionists and their reductive assumptions. He describes the way in which “Internet centrism” has skewed our discussions of everything from law enforcement to public health. It may be tempting, he writes, to recast complicated cultural and political phenomena as “transparent and self-evident processes that can be easily optimized”,

but this usually culminates in simplistic prescriptions that do more harm than good. Painstaking analyses are replaced by vague

**To Save Everything Click Here: Technology, Solutionism and the Urge to Fix Problems That Don't Exist**

EVGENY MOROZOV

Allen Lane: 2013. 432 pp. £20

**Who Owns the Future?**

JARON LANIER

Allen Lane: 2013. 384 pp. £20

bromides: embrace “openness”, “sharing” and “virality”, let information do its thing, and our problems will solve themselves.

Morozov points to the rise of ‘crowd-funding’ as an example. Online exchanges such as Kickstarter broaden the reach of venture capitalism by allowing people to make small investments in commercial and creative projects being undertaken by individuals and small businesses. The US singer Amanda Palmer, for example, raised more than a million dollars on Kickstarter to fund the recording of a solo album. The combination of automated transactions and an open marketplace is intoxicating to today’s efficiency-minded technophiles, who have been quick to promote such sites as replacements for cash-strapped arts councils.

But, Morozov contends, crowd-funding is in thrall to the herd instinct. It funnels money towards endeavours that generate buzz rather than demonstrate merit, and it encourages artists to act as marketers and hucksters. He points to a recent study of documentary film-making in Britain that suggests that online contributors tend to concentrate their money in polemical features that promote a fashionable “activist agenda”. They are much less likely to back documentaries that seek to explore contentious issues objectively and in depth. Crowd-funding is a solution only if you misjudge the problem.

Although Morozov is right to stress how technological determinism can warp political debates, he ends up going too far in the opposite direction. He claims that “the Internet” — his quotation marks — is largely a rhetorical construct, a sort of popular myth, and that it lacks any inherent qualities that might shape the behaviour of its users.

**Wealth concentrates around those who control the servers and databases.**

Digital technologies, he asserts, “are not the causes of the world we live in but rather its consequences”. This is a naive view of large-scale networks, and it lets Morozov sidestep difficult questions about the way the Net, like the highway system and the electric grid before it, moulds our economy and culture in its own image.

Lanier offers a more searching examination of the Internet’s defects in *Who Owns the Future?*. The Net’s workings, he argues, have been shaped by an ideology that, although well-intentioned, has deformed our commercial and social relationships. By mistaking free information for freedom, the network’s designers and defenders have inadvertently created a system that centralizes power and profit. Companies such as Google and Facebook take in billions of dollars by hosting online exchanges, but the people who actually create whatever is being exchanged — words, ideas, works of art — often get nothing. The joy of participation, they’re told, should be compensation enough.

As digital networks come to regulate more of the economy, Lanier sees a perverse dynamic taking hold. Wealth concentrates around those who control the servers and databases, whereas risk spreads outwards to the masses. He points to the banking crisis of 2008 as an example. By erasing local market boundaries and controls, computerized financial systems helped to funnel riches to a handful of bankers and traders — yet when the system collapsed, it was ordinary citizens who paid the bill.

The only way to change the dynamic is to redesign our computer networks to be a little less efficient and a little more egalitarian. Lanier imagines a “symmetrical” web, in which every piece of information is linked back to the person who created it. Copying the information triggers a “micropayment” to its creator. By placing a price on information, you constrain a company’s ability to track and manipulate people and to reap windfalls by exploiting massive data stores.

Many of Lanier’s proposals, including his call to assign everyone “a universal online identity”, will be controversial. And some of them, such as the micropayments scheme — which would require the value of every Facebook update and blog comment to be calculated — seem far-fetched. But, like Morozov, Lanier does a service by challenging us to address societal problems as humanists, not engineers. ■

**Nicholas Carr** writes on technology and culture. His book *The Shallows: What the Internet Is Doing to Our Brains* was a finalist for the 2011 Pulitzer Prize in General Nonfiction.  
e-mail: ncarr@mac.com

➔ **NATURE.COM**

For a review of Nicholas Carr’s *The Shallows*, see: [go.nature.com/y9lftw](http://go.nature.com/y9lftw)





Anna Maria Luisa de Medici bequeathed her family's legacy to the city of Florence in Italy.

## HISTORY

# Medicean secrets

**Alison Abbott** enjoys a scientific history of the family who ruled Florence during the Renaissance.

**T**he Medici clan held sway over Florence and Tuscany during the Italian Renaissance and well beyond. They created one of Europe's most powerful banks, ruled Florence and produced four Popes. Today they are best remembered for their patronage of science, art and architecture. We have them to thank for Florence's enduring beauty — including the magnificent Basilica of San Lorenzo. Designed by the architect Filippo Brunelleschi, this is where most of the family were buried, several after violent deaths.

Tombs were shuffled around within San Lorenzo four times between the fifteenth and nineteenth centuries, as successive generations tried to improve the presentation of their dynasty. Some remains got jumbled; some labelling got lost. Then, in 1945, anthropologist Giuseppe Genna disinterred 23 skeletons to make measurements that he hoped would support fashionable 'anthropometric' theories of psychological traits. The research was scientifically misguided and damaging: Genna removed all traces of flesh from the bones before returning them to their graves. Today's molecular biologists could have made much of those scraps.

Now the exhibition *The Medici* at the Reiss-Engelhorn Museum in Mannheim, Germany, charts the family's rise and fall, from founding father Giovanni di Bicci (1360–1429) to

Anna Maria Luisa de Medici, the last of the clan, who died in 1743. It is Anna Maria Luisa whose crowned skull graced international news media last month (see <http://go.nature.com/gws6g3>).

The exhibition has the familiar round-up of formal portraits, many on loan from the Uffizi in Florence, the world-famous art museum built for the Medici. The family was known from contemporary documents to have been plagued by disfiguring illnesses such as psoriasis, syphilis and arthritis, which, unsurprisingly, the flattering portraits do not reflect.

But the paintings are complemented by casts of the skulls of each of those pictured. Some were made by Genna, others after more systematic exhumations — of both bones and the pots in which the Medici interred the entrails of the deceased — carried out since 2004, when the Medici Project was launched. This project was a collaboration of Italian scientists and the culture ministry to assess any damage caused by the catastrophic flooding of the city in 1966, to identify which remains belonged to whom and to try to work out, using molecular biology, what the various individuals died from.

The exhibition weaves stories about each Medici from these scientific results and from

**The Medici: People, Power and Passion**

REISS-ENGELHORN MUSEUM, MANNHEIM, GERMANY.

Until 28 July 2013

analyses of contemporaneous documents. A couple involve murder. Beautiful, flirtatious Isabella (1542–76) was strangled by her jealous husband, with the apparent encouragement of her brother. Her bones were thrown into a mixed grave. Researchers managed to identify which skull was likely to be hers, and used forensic techniques to make a facial reconstruction for the exhibition that closely matches a contemporaneous portrait. It stands startlingly apart from the other oil portraits in its modernity and humanity.

Project scientists also managed to tentatively identify the entrails pot of Bianca Cappello, long-term mistress and then second wife of Francesco I (1541–87), whose bones have disappeared. Bianca and Francesco died within hours of each other. Scientists found traces of arsenic in their remains, lending substance to the historical claim that they were poisoned rather than dying of malaria as autopsy doctors declared at the time.

But it is the exhibition's centrepiece — the exhumation of Anna Maria Luisa — that propelled it into the headlines recently. When project scientists at the University of Florence opened the wooden coffin of Anna Maria Luisa last October, they were startled. Her skeleton was almost undamaged by the floods and topped by a crown — not the expected Medici death crown, but that of her husband's principality of Palatinate, in what is now Germany's Rhineland, where the museum is located.

The scientists used a three-dimensional scanner to replicate the skull for palaeo-forensics, one of the first such applications of the technology. They removed a small fragment of bone to analyse carbon and nitrogen isotopes that might illuminate how rich the Medicis' diets were in meat and fish, and for DNA analysis to determine her cause of death. Documents from the time suggest it could have been syphilis or breast cancer. Researchers also took samples for DNA testing from an unlabelled pot of entrails that they suspect belongs to her. The exhibition will be updated should results arrive.

A final thrill for scientists visiting the exhibition is a relic of Galileo Galilei (1564–1642), on display for the first time outside Italy. Galileo depended on Medici patronage. To keep things sweet, he named the moons of Jupiter, which he discovered in 1610, the Medicean Planets. The relic — the astronomer's fifth lumbar vertebra — has spent decades in a safe box at the University of Padua. It was brought out in 2010 when NASA requested a fragment for its Juno mission to Jupiter. The Italian Space Agency, apparently fearing Vatican disapproval, declined. After the Medici exhibition, the relic will go on permanent display at the university. ■

**Alison Abbott** is Nature's senior European correspondent.

# Correspondence

## Corrected numbers for fish on Red List

Kelly Swing gives inaccurate numbers for marine fish species on the International Union for Conservation of Nature (IUCN) Red List of Threatened Species. He also mistakenly conflates the scientific process of species assessment for the Red List with the separate political process of IUCN member voting (*Nature* **494**, 314; 2013).

About one-quarter, or 4,337, of some 17,000 species of marine fish are on the IUCN Red List (not fewer than 100 species out of 25,000, as Swing writes). Of those, 416 species have been placed in a threatened category (Critically Endangered, Endangered or Vulnerable) and 1,180 species were classed as Data Deficient.

The IUCN Tuna and Billfish Specialist Group has assessed all 10 species of billfish and 51 species of tuna and mackerel through a series of regional workshops, unhindered by the “IUCN’s worldwide voting procedures”. Seven species meet the IUCN threshold for a threatened category (B. B. Collette *et al. Science* **333**, 291–292; 2011). The sale of billfish has since been banned in the continental United States.

The IUCN Marine Biodiversity Unit’s Global Marine Species Assessment programme is now evaluating all remaining marine fish, and aims to finish within 5 years (<http://sci.odu.edu/gmsa>).

**Bruce B. Collette** *National Marine Fisheries Service, Washington DC, USA.*  
[collett@si.edu](mailto:collett@si.edu)

**Beth Polidoro** *Arizona State University, Phoenix, USA.*

**Kent Carpenter** *Old Dominion University, Norfolk, Virginia, USA.*

## Regulating stem-cell therapies worldwide

Japan’s drive to regulate experimental stem-cell treatments is a welcome step (*Nature* **494**, 5; 2013). However,

it could be hard to define universally applicable criteria that ensure the safety and effectiveness of such treatments worldwide.

There is a risk that the social and economic circumstances of patients and researchers might blur or compromise crucial criteria, such as evidence-based support (including adequate preclinical and clinical testing), ethical review and no-fee experimental treatment.

Stem-cell therapies are all too often unsupported by scientific evidence, but many patients are prepared to accept the risks. And nations with inadequate health-care resources may expect patients to pay for experimental treatments.

Proliferation of experimental stem-cell therapies may even be indirectly encouraged in countries such as China, where ultra-light regulation through official notification (see [www.moh.gov.cn](http://www.moh.gov.cn)) has uncertain regulatory value.

**Margaret Sleeboom-Faulkner** *University of Sussex, Brighton, UK.*  
[m.sleeboom-faulkner@sussex.ac.uk](mailto:m.sleeboom-faulkner@sussex.ac.uk)

## Order health systems in developing world

Governments and policy-makers are aiming to improve health markets in developing countries as they take up the challenge of last year’s United Nations resolution to move towards universal health coverage (see [go.nature.com/acsmss](http://go.nature.com/acsmss)). We caution that they must do more than simply legislate their way to a more orderly health system.

We have highlighted the risks associated with unregulated health-care services and products in developing countries (*Nature* **487**, 163–165; 2012). We now wish to draw governments’ attention to improvements proposed at a conference on securing international agreements on future health markets.

A small group of health policy-makers, entrepreneurs, academics

and funders met in Bellagio, Italy, at the end of last year. Among their recommendations were that countries should establish systems for collecting better basic health-market data for incorporation into local policy and management processes, and that they should organize funds to promote sound regulatory practice (see [go.nature.com/npsdvg](http://go.nature.com/npsdvg)).

The group called for a major effort by all market players to test innovative regulatory approaches and business models to improve access to safe and effective health services in the developing world.

**David H. Peters** *Johns Hopkins Bloomberg School of Public Health, Baltimore, Maryland, USA.*

[dpeters@jhsph.edu](mailto:dpeters@jhsph.edu)

**Gerald Bloom** *University of Sussex, Brighton, UK.*

## Modelling genetics within ecosystems

Safeguarding genetic diversity is one of the Convention on Biological Diversity’s main targets, because genetics underpins ecosystems. General models of whole ecosystems (D. Purves *et al. Nature* **493**, 295–297; 2013) therefore need to incorporate genetic data if they are to represent natural systems and guide conservation policy.

Yet it is important to understand that species diversity and genetic diversity do not always correlate; that the interplay between phylogenetic and functional diversity can be highly complex and regulated by interactions between cornerstone species; and that ecosystem resilience is tied to evolutionary history and genetic diversity. An ecosystem’s full genetic potential, as represented by ancient lineages and maximally diverse taxa and key species, must be realized.

**Niall McCann, Pablo Orozco Wengel, David Stanton** *Cardiff University, Cardiff, UK.*  
[mccannnp@cardiff.ac.uk](mailto:mccannnp@cardiff.ac.uk)

**Drew Purves *et al.* reply:** It could be useful to incorporate genetics into general ecosystem models (GEMs), along with complexities such as stoichiometry or long-range migrations. Genetically based GEMs could interface with the increasing amounts of genetic data available to capture the effects of individual-scale adaptation, although this can be approximated without explicit genetics (for example, traits mutate in the Madingley model we describe in our Comment). However, such complexities bring greater computational demands and increased model freedom, which might lead to the model producing almost any output unless properly constrained with data.

## Evaluate gender equality in journals

The European Association of Science Editors established a gender policy committee last year to develop a set of standards for adoption by scientific journals. As co-chairs of the committee, our first step is to invite science editors to contribute to a survey of gender-equality policies in their journals (see [go.nature.com/wor7ks](http://go.nature.com/wor7ks); survey closes on 10 April).

In this survey, we ask editors for their views on considering sex and gender in experimental design and data analysis, and on presenting data that are broken down by sex. Information is also requested on gender balance and its promotion among editorial staff, editorial boards and peer reviewers.

Our hope is that all journals will eventually follow *Nature*’s example in promoting gender equality in science (see [www.nature.com/women](http://www.nature.com/women)).

**Shirin Heidari** *Journal of the International AIDS Society, Geneva, Switzerland.*

[shirin.heidari@iasociety.org](mailto:shirin.heidari@iasociety.org)

**Tom Babor** *University of Connecticut School of Medicine, Farmington, Connecticut, USA.*



## BIOTECHNOLOGY

# Rewriting a genome

**A bacterial enzyme that uses guide RNA molecules to target DNA for cleavage has been adopted as a programmable tool to site-specifically modify genomes of cells and organisms, from bacteria and human cells to whole zebrafish.**

EMMANUELLE CHARPENTIER  
& JENNIFER A. DOUDNA

In a 1987 paper, researchers at Osaka University in Japan reported an apparently minor finding. While investigating the sequence of a bacterial gene that encodes the enzyme alkaline phosphatase, they discovered an unusual segment of neighbouring DNA that consisted of short, directly repeating nucleotide sequences flanked by short unique segments<sup>1</sup>. They noted that “the biological significance of these sequences is not known”. Fast-forward almost three decades, and what initially seemed to be an obscure observation is now being used to open the door to easy manipulation of the genomes of a multitude of organisms. Five papers published within a month of each other, in *Science*<sup>2,3</sup> and *Nature Biotechnology*<sup>4–6</sup>, report the application of such bacterial sequences — now referred to as CRISPR–Cas systems<sup>7</sup> — as a simple and versatile tool for genomic editing.

As whole-genome sequencing became routine in recent decades, regions containing CRISPR (clustered regularly interspaced short palindromic repeat) sequences and CRISPR-associated (Cas) genes were found in a wide variety of bacteria and archaea<sup>8–12</sup>. The discovery<sup>10,11</sup> that the short unique sequences in these arrays matched DNA sequences from viruses or plasmids (small non-chromosomal DNA molecules that can be transferred among bacteria and archaea) hinted that CRISPR–Cas systems encode ‘adaptive’ immune systems, providing specific defences against invaders. Subsequent genetic and biochemical experiments confirmed this speculation by showing that CRISPR–Cas systems allow detection of and protection against mobile genetic elements<sup>13</sup>.

Although some CRISPR–Cas systems require multiple proteins to function<sup>14</sup>, the type II systems found in many bacteria<sup>13,15,16</sup> use a single endonuclease, Cas9 (Fig. 1). This enzyme acts together with guide RNA to locate and cleave invading DNA at sites demarcated by conserved sequences called proto-spacer adjacent motifs (PAMs)<sup>7,17,18</sup>. To form a functional DNA-targeting complex, Cas9 requires two distinct RNA transcripts, CRISPR RNA (crRNA) and *trans*-acting CRISPR RNA (tracrRNA)<sup>7,15</sup>.

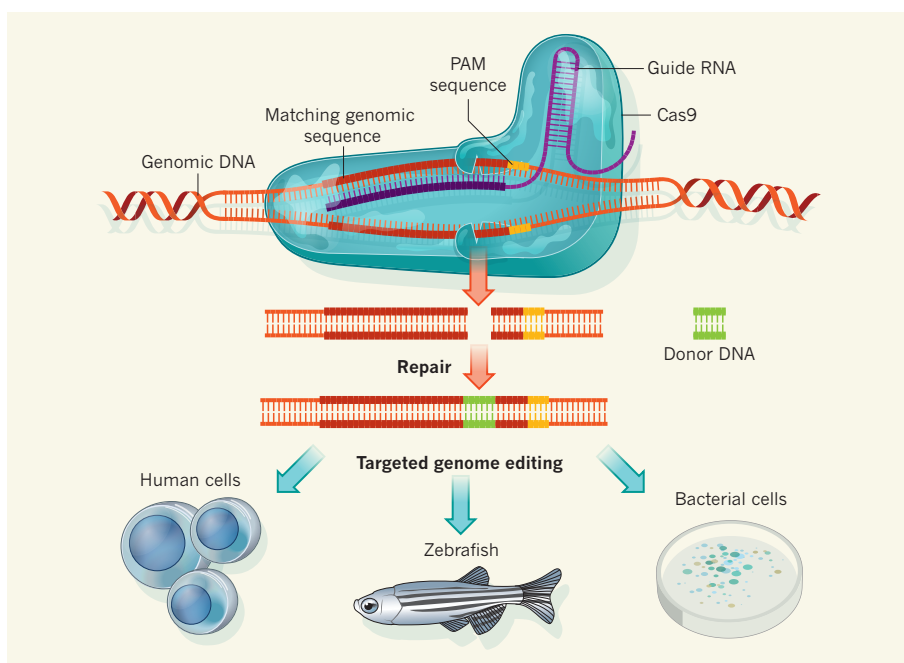


**Figure 1 | Targeted genome editing with RNA-guided Cas9.** The enzyme Cas9 is a DNA endonuclease found in many bacteria, in which it functions as part of a defence system against invading DNA molecules, such as viruses. Cas9 has two active sites that each cleave one strand of a double-stranded DNA molecule. The enzyme is guided to the target DNA by an RNA molecule that contains a sequence that matches the sequence to be cleaved, which is demarcated by PAM sequences. RNA-guided Cas9 activity creates site-specific double-stranded DNA breaks, which are then repaired by either non-homologous end joining or homologous recombination. During homologous recombination, the addition of donor DNA enables new sequence information to be inserted at the break site. Several recent papers show that RNA-guided Cas9 systems can be used to engineer the genomes of human and mouse cell lines<sup>2–4,19</sup>, bacteria<sup>5</sup> and — by modifying one-cell-stage embryos — zebrafish<sup>6</sup>.

However, it was recently shown<sup>7</sup> that this dual RNA can be reconfigured as a single-guide RNA (sgRNA) that includes sequences that are sufficient to program Cas9 to introduce double-stranded breaks in target DNA. As the new publications show, RNA-guided Cas9 can function in a variety of cells and organisms to cleave intact genomes at specific sites. And this is the point at which the potential for genome editing comes in. When the double-stranded breaks are repaired by standard cellular repair mechanisms, either by homologous recombination (the exchange of genetic information between DNA molecules with similar sequences) or non-homologous end joining (NHEJ; the introduction of insertions or deletions into the sequence), the sequence at the

repair site can be modified or new genetic information inserted.

Three of the studies demonstrate that RNA-programmed Cas9 can function in human cells. Cong *et al.*<sup>2</sup>, Mali *et al.*<sup>3</sup> and Cho *et al.*<sup>4</sup> engineered versions of the Cas9 enzyme from the bacterium *Streptococcus pyogenes* so that it would be active in the nucleus of human cells, and designed dual RNAs or sgRNAs that included a 20-nucleotide sequence complementary to human target DNA sequences. When the researchers expressed the ‘humanized’ Cas9 together with these guide RNAs in various human cell lines, including induced pluripotent stem cells, they observed the expected alterations to the target DNA — achieved through the introduction of

double-stranded breaks followed by repair. The gene-targeting achieved up to 38% success and was accompanied by only a low level of Cas9 toxicity. The RNA-guided Cas9 was also efficient at triggering targeted gene replacement at normal genomic sites in human cells. In another paper published in the same month, Jinek *et al.*<sup>19</sup> show that RNA-programmed Cas9 functions in human cells to trigger site-specific genome modifications, and that the ability of Cas9 to assemble with guide RNA in cells is a limiting factor in this activity.

On the basis of earlier observations that single-stranded DNA breaks can favour homologous recombination and reduce off-target mutagenesis, Mali *et al.*<sup>3</sup> and Cong *et al.*<sup>2</sup> also tested versions of Cas9 that have been shown<sup>7</sup> to act as a nickase enzyme — one that breaks only one strand of a DNA molecule. The mutated enzymes had lower rates of NHEJ but were as efficient as the wild-type endonuclease at gene replacement triggered by homologous recombination. Both groups also demonstrated further functionality of the system in ‘multiplexed’ targeting; the expression of sgRNA-programmed Cas9 that can bind to two different genomic sequences led to sequence disruption at more than one independent target site. In addition, Cong and colleagues show that gene-disruption efficiency could be improved upon independent expression of the two RNA components of the original dual-tracrRNA–crRNA combination. This finding implies that improved design of sgRNAs may allow them to better mimic the dual RNA structure<sup>7</sup>.

In addition to these results in cell lines, RNA-guided Cas9 can be used to engineer genomic changes in intact organisms. Jiang and colleagues<sup>6</sup> show that the system can be used in bacteria to modify multiple sites by programming Cas9 with several different guide RNAs in a single cell. This technology could be exploited to engineer microorganisms that are otherwise genetically intractable to harbour pathways for producing biofuels and molecules of therapeutic value. Working with zebrafish, Hwang and colleagues<sup>5</sup> show that injection of one-cell-stage embryos with Cas9-encoding mRNA and appropriate guide RNAs produced high frequencies (24–59%) of targeted insertions and deletions at eight of ten sites in all embryos tested. These findings hint that RNA-guided Cas9 might be useful for engineering other multicellular organisms, including mammals and plants. One of the most exciting potential uses of such technology would be to provide a straightforward means of generating animal models of human disease.

Genome engineering by RNA-programmable Cas9 promises to have broad applications in synthetic biology, direct and multiplexed perturbation of gene networks, and targeted *ex vivo* and *in vivo* gene therapy<sup>2–7</sup>. The next challenges will be to

analyse and address possible off-target effects and improve the efficiency and specificity of the system, while expanding its use to other organisms. In this regard, it will be important to compare RNA-programmed Cas9 with existing genome-editing tools<sup>18</sup>, including meganucleases, ZFNs (zinc-finger nucleases) and TALENs (transcription activator-like effector nucleases). In addition to genome editing, this approach offers the exciting possibilities of transcriptional gene silencing using an inactive Cas9 (ref. 20) or engineering Cas9 to have new functions, such as transcriptional activation. The discovery and application of bacterial systems, such as restriction enzymes and thermostable polymerases, have revolutionized molecular biology in the past. With RNA-guided Cas9 enzymes, bacteria now offer a versatile tool for rewriting genomic sequence information that has the potential to reshape the genome-engineering landscape in biotechnology and medicine. ■

**Emmanuelle Charpentier** is at the Helmholtz Centre for Infection Research, Department of Regulation in Infection Biology, 38124 Braunschweig, Germany, in the Laboratory for Molecular Infection Medicine Sweden, Umeå University, Sweden, and at the Hanover Medical School, Hanover, Germany. **Jennifer A. Doudna** is at the Howard Hughes Medical Institute, Departments of Molecular and Cell Biology

and of Chemistry, University of California, Berkeley, Berkeley, California 94720, USA, and in the Physical Biosciences Division, Lawrence Berkeley National Laboratory, Berkeley.

e-mails: [emmanuelle.charpentier@helmholtz-hzi.de](mailto:emmanuelle.charpentier@helmholtz-hzi.de); [doudna@berkeley.edu](mailto:doudna@berkeley.edu)

1. Ishino, Y., Shinagawa, H., Makino, K., Amemura, M. & Nakata, A. *J. Bacteriol.* **169**, 5429–5433 (1987).
2. Cong, L. *et al. Science* **339**, 819–823 (2013).
3. Mali, P. *et al. Science* **339**, 823–826 (2013).
4. Cho, S. W., Kim, S., Kim, J. M. & Kim, J. S. *Nature Biotechnol.* **31**, 230–232 (2013).
5. Hwang, W. Y. *et al. Nature Biotechnol.* **31**, 227–229 (2013).
6. Jiang, W., Bikard, D., Cox, D., Zhang, F. & Marraffini, L. A. *Nature Biotechnol.* **31**, 233–239 (2013).
7. Jinek, M. *et al. Science* **337**, 816–821 (2012).
8. Jansen, R., Embden, J. D., Gaastra, W. & Schouls, L. M. *Mol. Microbiol.* **43**, 1565–1575 (2002).
9. Haft, D. H., Selengut, J., Mongodin, E. F. & Nelson, K. E. *PLoS Comput. Biol.* **1**, e60 (2005).
10. Mojica, F. J., Díez-Villasenor, C., García-Martínez, J. & Soria, E. *J. Mol. Evol.* **60**, 174–182 (2005).
11. Pourcel, C., Salvignol, G. & Vergnaud, G. *Microbiology* **151**, 653–663 (2005).
12. Makarova, K. S., Grishin, N. V., Shabalina, S. A., Wolf, Y. I. & Koonin, E. V. *Biol. Direct* **1**, 7 (2006).
13. Barrangou, R. *et al. Science* **315**, 1709–1712 (2007).
14. Brouns, S. J. *et al. Science* **321**, 960–964 (2008).
15. Deltcheva, E. *et al. Nature* **471**, 602–607 (2011).
16. Garneau, J. E. *et al. Nature* **468**, 67–71 (2010).
17. Sapranasauskas, R. *et al. Nucleic Acids Res.* **39**, 9275–9282 (2011).
18. Carroll, D. *Mol. Ther.* **20**, 1658–1660 (2012).
19. Jinek, M. *et al. eLife* <http://dx.doi.org/10.7554/eLife.00471> (2013).
20. Qi, L. S. *et al. Cell* **152**, 1173–1183 (2013).

## ASTROPHYSICS

# An accurate distance to the nearest galaxy

**By having a highly accurate value for the distance to the Large Magellanic Cloud galaxy, astronomers can get a better measure of cosmic ‘dark energy’. Using binary stars, they have now achieved a value accurate to 2.2%. SEE LETTER P.76**

BRADLEY E. SCHAEFER

**D**istances to celestial bodies are crucial in astronomy. They allow astronomers to understand the structure of the Universe; for example, to see the organization of the Solar System and to recognize that galaxies lie beyond the Milky Way. The derived physical sizes of bodies scale with the distances adopted for them, whereas their energetics scale with the square of the distances. A current hot enterprise is to use distance measurements to the farthest supernovae to map out the expansion history of the Universe and to uncover the nature of the Universe’s mysterious dark energy. Distances are deduced

by means of a ‘distance ladder’: knowledge of the distances to nearby bodies is used to determine the distances of bodies farther out, and so on to yet more remote objects. On page 76 of this issue, Pietrzyński *et al.*<sup>1</sup> claim to provide a much-needed, highly accurate measure of the distance to the Large Magellanic Cloud galaxy — the bottleneck in the ascent of the distance ladder.

Historically, the lowest ‘rung’ of the distance ladder, the size of Earth, was used to calibrate the timings of the transit of Venus across the Sun, and so to climb to the second rung, the Earth–Sun distance. The method of parallax — watching stars wobble back and forth as Earth orbits the Sun — was used to climb





**Figure 1 | The Large Magellanic Cloud.** Pietrzyński *et al.*<sup>1</sup> have determined an accurate distance to the Large Magellanic Cloud galaxy, the 'anchor' point from which distances to other galaxies can be measured.

to the third rung, the distance to nearby stars. For cosmology and extragalactic astronomy, almost all ways of climbing the distance ladder pass through the rung of the Large Magellanic Cloud (LMC; Fig. 1), which is the evocatively named nearest galaxy to the Milky Way. So if the LMC distance is off by 10%, then the distances to all galaxies (as quantified with the Hubble constant, the expansion rate of the Universe) will be in error by the same 10%. When combined with measures of far-off supernovae, a highly accurate distance to the LMC will also substantially improve measurements of the properties of dark energy, and thereby potentially reveal its nature.

The distance to the LMC has long been a contentious question. Published values over the decades have been scattered, with values from the decade before 2001 alone having a scatter of 36%, despite the fact that the reported error bars are much smaller than this scatter<sup>2</sup>. So it is clear that the many methods used to determine the LMC distance had large and unidentified systematic errors. In 2001, the influential Hubble Space Telescope Key Project presented a middle value of the previous scatter with a reasonable error bar ( $50.1 \pm 2.3$  kiloparsecs, or  $163,400 \pm 7,500$  light years)<sup>3</sup>. But its publication created a bandwagon effect, and for the next six years the astronomy community

published distances that slavishly followed this value<sup>4</sup>. The 2011 Nobel laureate Adam Riess and the SH0ES project have since adopted a method pioneered by a group centred at Villanova University in Pennsylvania<sup>5–8</sup> (involving four eclipsing binary stars) to obtain an LMC distance of 49.8 kiloparsecs, with an accuracy to 3% (ref. 9).

Now Pietrzyński *et al.*, as part of the international Araucaria Project, derive a value that is accurate to 2.2%. They achieved this by measuring the distances to eight eclipsing binaries in the LMC. (Eclipsing binaries are two-star systems whose component stars regularly pass directly in front of each other as viewed from Earth.) They measured accurate sizes for both stars in each binary (from the durations of the eclipses and the measured velocities) and their surface temperatures (from spectra of the stars), thereby deriving the total intrinsic luminosity of each binary system. By comparing the total luminosity and the observed brightness, and using the inverse square law of light, they then determined the distances to the binaries. This method inspires confidence because it uses only undergraduate astronomy and physics (but very carefully done), and completely jumps over all the lower rungs of the distance ladder. The authors' new distance to the LMC, which is based on the average of the distances to the eight binaries, is  $49.97 \pm 1.13$  kiloparsecs.

A comparison of the new LMC distance with previously published values reveals three disturbing issues. First, the Araucaria Project had previously reported one of its eclipsing binaries to have a distance of  $50.1 \pm 1.4$  kiloparsecs<sup>10</sup>, but it now quotes  $49.3 \pm 0.5$  kiloparsecs for that binary, with no indication of how its analysis has changed. Second, and much more disturbingly, the four eclipsing binaries reported by the Villanova group<sup>5–8</sup> have an average distance of  $47.1 \pm 1.4$  kiloparsecs, which is substantially different. The main difference between the groups' techniques is the use of cool stars by the Araucaria Project, together with an empirical surface-brightness-versus-colour relation to determine the stars' surface temperature, as opposed to the use of hot stars by the Villanova group and theoretical models to infer the temperature. Third, the new distance is remarkably close to the value obtained by the Key Project, with a difference of only one-tenth of the error bar quoted by Pietrzyński *et al.*, so we should recall the history of the bandwagon effect.

What can we expect in the future? Studies of roughly a dozen more eclipsing binaries are in the pipeline, with results expected soon. Also, extensions of the technique will be made to the eclipsing binaries in the galaxy M33, in the constellation Triangulum. But the entire scene will change when the Gaia spacecraft is launched later this year, with its awesome capability for measuring accurate distances by means of the parallax, even out to the LMC. Gaia will provide definitive calibration of various 'standard candles' used to climb rungs above the LMC on the distance ladder, thereby eliminating the bottleneck at the LMC. Indeed, Gaia will obtain parallax data for many stars in the LMC with the resultant average accurate to 1%, and will map out its structure. So the time spent by the LMC's eclipsing binaries at the forefront of astrophysics will be limited to only the next few years. ■

**Bradley E. Schaefer** is in the Department of Physics and Astronomy, Louisiana State University, Baton Rouge, Louisiana 70803, USA.

e-mail: schaefer@lsu.edu

1. Pietrzyński, G. *et al.* *Nature* **495**, 76–79 (2013).
2. Benedict, G. F. *et al.* *Astron. J.* **123**, 473–484 (2002).
3. Freedman, W. L. *et al.* *Astrophys. J.* **553**, 47–72 (2001).
4. Schaefer, B. E. *Astron. J.* **135**, 112–119 (2008).
5. Guinan, E. F. *et al.* *Astrophys. J.* **509**, L21–L24 (1998).
6. Fitzpatrick, E. L. *et al.* *Astrophys. J.* **564**, 260–273 (2002).
7. Ribas, I., Fitzpatrick, E. L., Maloney, F. P., Guinan, E. F. & Udalski, A. *Astrophys. J.* **574**, 771–782 (2002).
8. Fitzpatrick, E. L., Ribas, I., Guinan, E. F., Maloney, F. P. & Claret, A. *Astrophys. J.* **587**, 685–700 (2003).
9. Riess, A. G. *et al.* *Astrophys. J.* **730**, 119 (2011).
10. Pietrzyński, G. *et al.* *Astrophys. J.* **697**, 862–866 (2009).

## STEM CELLS

# A unifying theory for the crypt

A long-standing ambiguity has been whether quiescent cells located in intestinal crypt structures are stem cells. The answer seems to be yes and no, depending on how one defines the term stem cell. [SEE ARTICLE P.65](#)

HANS CLEVERS

The epithelial cell layer that covers the small intestine is the self-renewal champion of the mammalian body — the life cycle of its cells is only 4–5 days. As a result, this epithelium, combined with its characteristic architecture of crypt–villus units, has become the model-of-choice for studying adult mammalian stem cells. The relationship between, and the functions of, two stem-cell populations (one rapidly cycling, the other quiescent) at intestinal crypts has been a matter of great interest and debate. On page 65 of this issue, Buczacki *et al.*<sup>1</sup> use an ingenious strategy to genetically mark quiescent crypt cells and thus shed light on these issues\*.

The operational definition of adult stem cells has only two criteria. Such cells must be capable of self-renewal and persistence over the lifetime of an animal, and be multipotent — have the capacity to generate all cell types of a tissue. In addition, all types of stem cell have been tacitly assumed to be quiescent ever since haematopoietic stem cells of the blood system were noted to divide infrequently<sup>2</sup>. The ability of stem cells to retain molecules that have been introduced experimentally, to label their DNA or chromatin (DNA–protein complexes), has made detection of the non-proliferative state easy, and has made label retention a popular surrogate stem-cell marker.

After their formation from stem cells at crypt bottoms, young epithelial cells proliferate intensely for 2 days before differentiating and exiting the crypts. The cells then move onto the villus flanks to process nutrients and finally die at the villus tips on days 4–5. Paneth cells also derive from stem cells, but persist for 1–2 months at the crypt base — in which they are thought to maintain stem-cell renewal and provide protection against bacteria.

Two alternative identities for crypt stem cells were defined decades ago. On the one hand, it was proposed<sup>3</sup> that small proliferative cells that are wedged between the Paneth cells represent the crypt stem cells. Much later, the protein Lgr5 was discovered<sup>4</sup> to be an exquisite marker for these cells, allowing formal, experimental proof of their ‘stemness’ *in vivo*. Subsequently,

single Lgr5-expressing (Lgr5<sup>+</sup>) cells were shown<sup>5</sup> to form ever-expanding, transplantable ‘mini-guts’ *in vitro*. On the other hand, the presence of DNA-label-retaining cells (LRCs) was noted<sup>6</sup> directly above the Paneth cells, at position +4 (counting Paneth-cell nuclei from the bottom of the crypt). Several molecular markers were reported for these quiescent ‘+4 LRCs’, including the protein Bmi1 (ref. 7). Confusingly, however, Lgr5<sup>+</sup> cells also robustly express these +4 markers<sup>8</sup>.

Buczacki and colleagues reassess the nature of crypt LRCs. The authors labelled all crypt cells (except the long-lived Paneth cells) by briefly expressing in them the stable chromatin marker histone 2B fused to the yellow fluorescent protein (YFP). What happened over time was intriguing. After this pulse, all of the dividing cells rapidly diluted out the label. A week later, cells still carrying the label — the LRCs — were seen only near the crypt base, and included Paneth cells. In the initial weeks after labelling, non-Paneth-cell LRCs were also evident and surprisingly co-expressed Lgr5, Paneth-cell markers and +4 markers. Buczacki *et al.* concluded that this second LRC class represents non-dividing

precursors of Paneth cells (Fig. 1).

To test the properties of these cells, the authors devised a strategy that directly exploits the quiescent state to genetically mark the non-dividing LRCs. Specifically, they briefly expressed histone 2B fused to the amino-terminal segment of the enzyme Cre recombinase, CreA, and found that — like histone-2B–YFP — this fusion protein was retained only in the chromatin of non-dividing Paneth cells and their presumed precursors. The other part of the enzyme, CreB, was expressed constitutively in all cell types.

Reassociation of CreA and CreB into functional Cre recombinase depends on the presence of an injectable small chemical. Two weeks after the pulse, Buczacki *et al.* injected this chemical into mice to genetically mark the LRCs with the now-intact Cre recombinase. In healthy mice, the marked cells failed to divide. When crypts were damaged, however, these LRCs generated large, persistent crypt–villus ribbons — the telltale signature of crypt stem cells.

The authors’ genetic-labelling approach is original, allowing documentation of LRC behaviour over time. Because this technology for the first time directly exploits the label-retention trait to mark stem cells, it will be broadly applicable to the study of other quiescent stem cells. Indeed, it will now be possible to investigate the dynamics of stem-cell compartments in other tissues in which quiescent stem cells have been postulated to act at the base of the self-renewal hierarchy, including bone marrow, hair follicle, muscle and brain.

Buczacki *et al.* also show that isolated LRCs form mini-guts in culture, confirming the conclusions from their Cre-recombinase data that these cells can regain a stem-cell-like behaviour. Similar observations have been made<sup>9</sup> for

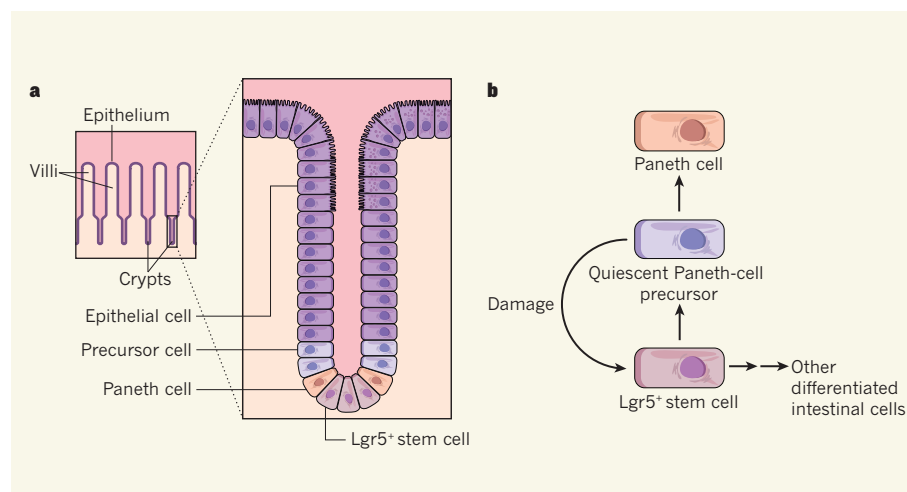


**Figure 1 | Complexities of intestinal stem cells.** **a**, The intestinal epithelium follows the distinct contours of villus–crypt units in the intestine. **b**, Normally, Lgr5-expressing stem cells (Lgr5<sup>+</sup>) lead to the production of precursor cells that further differentiate into the various types of crypt epithelial cell. Buczacki *et al.*<sup>1</sup> report that precursors of one type of differentiated intestinal cell, Paneth cells, can persist for several weeks in a quiescent state before maturing into Paneth cells. Intriguingly, these quiescent precursors can revert back into Lgr5<sup>+</sup> stem cells following crypt damage.

\*This article and the paper under discussion<sup>1</sup> were published online on 27 February 2013.



the proliferative, more primitive, Dll1-expressing cells, which are precursors to all intestinal secretory cells.

The current study unifies earlier theories about the identity of crypt stem cells<sup>3,6</sup>. The cycling Lgr5<sup>+</sup> stem cells are the engines of crypt self-renewal. They generate a transient population of non-dividing daughter cells that are destined to differentiate into relatively long-lived Paneth cells. These daughter cells express Lgr5, as well as markers for the proposed quiescent +4 stem cells; they probably, therefore, represent the +4 cells. As individual cells, LRCs disappear over a few weeks and so cannot be considered stem cells. However, LRCs are constantly being generated by the cycling Lgr5<sup>+</sup> stem cells and so — as has also been proposed elsewhere<sup>10</sup> — LRCs are always available as ‘reserve stem cells’ that can be called into action if tissue is damaged (Fig. 1). This surprising design of the crypt stem-cell hierarchy reconciles many of the paradoxical

observations that have been seen in this adult stem-cell compartment. ■

**Hans Clevers** is at the Hubrecht Institute, Royal Netherlands Academy of Arts and Sciences, University Medical Center Utrecht, the Netherlands.  
e-mail: h.clevers@hubrecht.eu

1. Buczacchi, S. J. A. *et al. Nature* **495**, 65–69 (2013).
2. Lajtha, L. G., v. Pozzi, L., Schofield, R. & Fox, M. *Cell Prolif.* **2**, 39–49 (1969).
3. Cheng, H. & Leblond, C. P. *Am. J. Anat.* **141**, 537–561 (1974).
4. Barker, N. *et al. Nature* **449**, 1003–1007 (2007).
5. Sato, T. *et al. Nature* **459**, 262–265 (2009).
6. Potten, C. S. *Nature* **269**, 518–521 (1977).
7. Sangiorgi, E. & Capecchi, M. R. *Nature Genet.* **40**, 915–920 (2008).
8. Barker, N., van Oudenaarden, A. & Clevers, H. *Cell Stem Cell* **11**, 452–460 (2012).
9. van Es, J. H. *et al. Nature Cell Biol.* **14**, 1099–1104 (2012).
10. Roth, S. *et al. PLoS ONE* **7**, e38965 (2012).

at ambient temperatures, could be easily distributed using the existing infrastructure for petroleum. The development of chemical methods for extracting hydrogen from methanol is crucial to the success of this strategy. Currently, the best systems use platinum-based catalysts operating at temperatures above 200 °C, which limits the efficiency of methanol-based fuel cells to about 40%.

Nielsen *et al.* now report ruthenium-based molecules that catalyse the highly efficient liberation of hydrogen from methanol in water at less than 100 °C. The ruthenium catalysts ensure that, for each molecule of methanol and water consumed, three molecules of hydrogen are generated, along with one molecule of carbon dioxide (Fig. 1a). The authors observed that the reaction is facilitated in strongly basic solution, which also sequesters the CO<sub>2</sub> almost quantitatively as carbonate or formate salts. Using such strongly basic conditions, the researchers found that the ratio of hydrogen to CO<sub>2</sub> in the evolved gas is consistently greater than 500:1.

To optimize the reaction conditions, Nielsen and colleagues studied the effects of catalyst concentration, the ratio of methanol to water, the basicity of the solution, and temperature. In the best case, the authors found that as little as 1.8 parts per million (p.p.m.) of the catalyst produced hydrogen from a 9:1 mixture of methanol to water, using a high concentration (8.0 moles per litre) of the base potassium hydroxide at 91 °C. Under these conditions, approximately 2,700 equivalents of hydrogen per equivalent of the catalyst were liberated every hour. This ‘turnover frequency’ rose to 4,700 equivalents per hour if pure methanol was used as the solvent, with just 1.6 p.p.m. of catalyst. However, for real-world applications in fuel cells, methanol–water mixtures and lower concentrations of base will be required.

To test their catalysts in real-world conditions, Nielsen *et al.* decreased the ratio of methanol to water to 4:1, used a much lower concentration of a different base (0.1 moles per litre of sodium hydroxide) and increased the catalyst concentration (to 21 p.p.m.). Under these conditions, the initial catalyst-turnover frequency decreased to about 800 equivalents per hour. The researchers observed that the pH of the solution fell from 13 to 10 during the first 4 hours of reaction and that the ratio of hydrogen to CO<sub>2</sub> in the produced gas changed from 9:1 to 3:1 over the same period. However, the composition of the gas mixture then remained stable for up to a further 3 weeks of operation, equivalent to a remarkable 350,000 turnovers of hydrogen from the catalyst.

The authors did not test their catalyst in methanol fuel cells, but their findings suggest that the catalysts will improve the energy capacity of such cells. In the short term, this augurs well for applications such as portable electronic devices. For transportation

## CATALYSIS

# A step closer to a methanol economy

**A ruthenium catalyst has been developed that, at a few parts per million, releases hydrogen gas from methanol, a simple bulk chemical. The advance might allow methanol to be used as a hydrogen source for fuelling vehicles. SEE LETTER P.85**

DOUGLAS W. STEPHAN

Fossil fuels are a worry. For example, the phenomenon of global warming is linked to the presence of atmospheric greenhouse gases arising from their use<sup>1</sup>. Combustion of these fuels has provided convenient energy for centuries, and so there are also questions about the extent of remaining, accessible oil supplies<sup>2</sup>. Combine these issues with environmental concerns, and with humans’ seemingly insatiable thirst for energy, and the result is a strong motivation to seek alternative energy sources. In this issue (page 85), Nielsen *et al.*<sup>3</sup> report a dramatic advance that might pave the way to the practical use of one such alternative: hydrogen gas derived from the solvent methanol<sup>4</sup>.

The use of ‘traditional’ alternatives to fossil fuels, such as hydroelectricity and nuclear power, has increased, and technologies that exploit nature’s wind, solar and tidal power are also being developed to supplement the energy needs of stationary users. For transportation applications, the advent of hybrid technologies — such as cars that use electric

motors alongside petroleum-driven combustion engines — may reduce fossil-fuel consumption. However, a longer-term alternative to fossil fuels has been the subject of speculation by scientists, business leaders and futurist visionaries alike<sup>4</sup>.

A leading candidate for a ‘clean’ energy source is hydrogen, because the only product of its combustion is water<sup>5</sup>. This would seem to offer a solution to energy, pollution and greenhouse-gas problems in one fell swoop. But there are downsides. Public acceptance of hydrogen-based technologies is undermined by the gas’s flammable nature — a fact indelibly linked to the explosion of the *Hindenburg* passenger airship in 1937. Finding a way to store large quantities of hydrogen in a portable volume is also a challenge. And even if these issues were overcome, distributing hydrogen to the millions of potential users would require massive new infrastructure.

Nobel laureate George Olah and his colleagues have advocated methanol (CH<sub>3</sub>OH) as an alternative fuel, and have proposed the development of a ‘methanol economy’<sup>6</sup>. Perhaps the most compelling aspect of their vision is the fact that methanol is hydrogen-rich (12.6% by weight) and, because it is a liquid

\*This article and the paper under discussion<sup>3</sup> were published online on 27 February 2013.

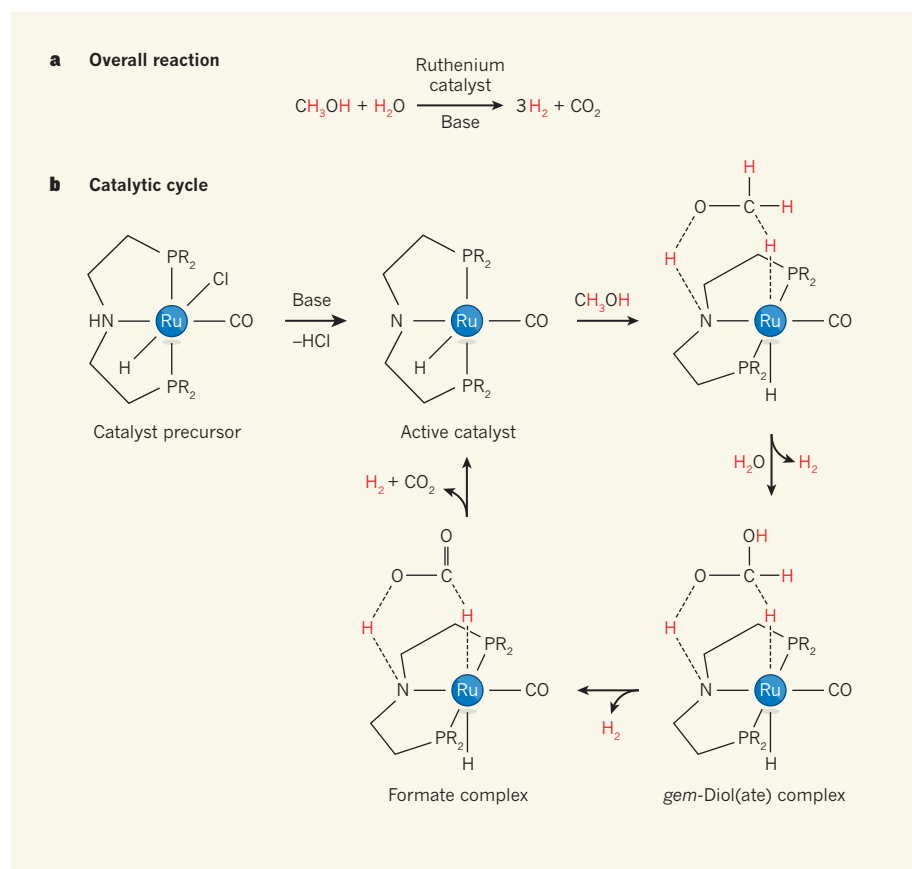


**Figure 1 | Simplified mechanism for the catalytic generation of hydrogen from methanol.** **a**, Nielsen *et al.*<sup>3</sup> describe ruthenium complexes that catalyse the dehydrogenation of methanol (CH<sub>3</sub>OH) in basic solution, yielding three equivalents of H<sub>2</sub> and an equivalent of CO<sub>2</sub>. **b**, The active catalyst is generated from a catalyst precursor when the base removes hydrogen chloride (HCl) from the complex. Methanol forms a complex with the active catalyst and then loses a molecule of hydrogen. In the presence of water, a *gem*-diol(ate) complex forms. This loses another hydrogen molecule, forming a formate complex, which loses a third hydrogen molecule and a molecule of carbon dioxide, regenerating the active catalyst. Ru, ruthenium; R can be phenyl (C<sub>6</sub>H<sub>5</sub>) or isopropyl (CH(CH<sub>3</sub>)<sub>2</sub>). Broken lines indicate interatomic bridging interactions through hydrogens.

applications, however, the catalyst-turnover frequencies will have to rise substantially.

The active form of the catalyst is generated *in situ* from a precursor complex in which ruthenium is bound by the nitrogen and phosphorus atoms of a 'tridentate' ligand molecule, HN(CH<sub>2</sub>CH<sub>2</sub>PR<sub>2</sub>)<sub>2</sub> (where R is either a phenyl group, C<sub>6</sub>H<sub>5</sub>, or an isopropyl group, CH(CH<sub>3</sub>)<sub>2</sub>). The ruthenium is also bound by a hydrogen atom, a chloride ion and a molecule of carbon monoxide. Nielsen and co-workers probed the mechanism of action of their catalyst, and found that the dissolved base removes a proton (H<sup>+</sup>) from the nitrogen of the tridentate ligand to generate the active catalyst (Fig. 1b). This nitrogen and the ruthenium atom then interact with methanol to liberate a hydrogen molecule (H<sub>2</sub>), transiently generating formaldehyde (O=CH<sub>2</sub>). In the presence of water, the formaldehyde forms a *gem*-diol(ate) species (CH<sub>2</sub>(OH)<sub>2</sub>)<sup>-</sup>, and then becomes a formate intermediate (HCO<sub>2</sub><sup>-</sup>) by losing another hydrogen molecule. Loss of CO<sub>2</sub> and of a third hydrogen molecule from the formate and the nitrogen of the ligand on ruthenium regenerates the active form of the catalyst.

Nielsen and colleagues' work is a seminal finding, because it demonstrates the viability of a soluble catalyst for the efficient and long-lived generation of hydrogen from methanol. Chemists know a great deal about the design and optimization of molecular catalysts, and so they will undoubtedly embark on further studies aimed at improving the catalytic activity of ruthenium complexes. They could thereby discover innovations that will bring us even closer to the methanol economy. ■

**Douglas W. Stephan** is in the Department of Chemistry, University of Toronto, Toronto, Ontario M5S 3H6, Canada. e-mail: dstephan@chem.utoronto.ca

1. Karl, T. & Trenberth, K. *Science* **302**, 1719–1723 (2003).
2. Owen, N. A., Inderwildi, O. R. & King, D. A. *Energy Policy* **38**, 4743–4749 (2010).
3. Nielsen, M. *et al.* *Nature* **495**, 85–89 (2013).
4. Demirbas, A., Sahin-Demirbas, A. & Demirbas, A. H. *Energy Sources* **26**, 191–204 (2004).
5. Züttel, A. *et al.* in *Hydrogen as a Future Energy Carrier* (eds Züttel, A., Borgschulte, A. & Schlappbach, L.) Ch. 6 (Wiley-VCH, 2008).
6. Olah, G. A., Prakash, G. & Goepfert, A. *Chem. Eng. News* **81** (38), 5 (2003).



# The units of a song

Exactly when motor-planning neurons function to produce a bird's song is debatable. New data suggest that bursts of activity in these cells mark sudden changes in the commands to the vocal organ. [SEE ARTICLE P.59](#)

TODD W. TROYER

What is the basic unit of speech? The word? The syllable? The phoneme? This question has been vexing speech and language researchers for decades, and similar questions have challenged those who study songbirds. Whereas behavioural evidence<sup>1</sup> supports the grouping of songs into 100–250-millisecond vocalizations called syllables, neurophysiological data suggest<sup>2</sup> that the premotor areas at high levels in the hierarchy of motor neurons in the brain act more like a clock, providing a continuous stream of activity on a 10-millisecond timescale. On page 59 of this issue, Amador *et al.*<sup>3</sup> reconcile these data by providing evidence that the song code generated by motor neurons of zebra finches (*Taeniopygia guttata*) is indeed broken into discrete 'gestures', which are significantly shorter than song syllables\*.

The study has roots in two research programmes that started at opposite ends of the motor-coding problem. One group studied the highest levels of the motor system, in which sensory signals about a song's acoustics change the song motor program during learning. The researchers discovered<sup>4</sup> that, for every rendition of the bird's song, individual neurons produce short bursts of activity with incredible regularity and precision. They also demonstrated<sup>5</sup> a remarkable correspondence between the motor activity that was recorded when the bird was singing and the auditory activity that resulted from playing the bird's song back to it when it was asleep.

The other team investigated how sound is generated by the avian vocal organ, the syrinx. They developed a simplified biophysical model of the syrinx with two dynamic parameters: the pressure in the bird's air sac and the spring-like tension on a vibrating membrane controlled by the muscles surrounding the syrinx. Analysis of the model showed that small changes in pressure and tension can lead to output that is a passable imitation of the sounds produced by several species of songbird<sup>6,7</sup>. This work also

\*This article and the paper under discussion<sup>3</sup> were published online on 27 February 2013.

suggested that, to sing, birds may not need precise control over a large ensemble of muscles. Rather, two basic signals may suffice, as long as the signals are controlled in a temporally precise manner.

Combining their previous approaches, the two research programmes now come together. Amador *et al.* focus on a high-level cluster of neurons called the HVC, which is essential for singing, but — in terms of synaptic connections between neurons — is the most distant from the syrinx. They recorded the activity of individual HVC cells either while the birds sang or during playback of the bird's own song while it slept. They also tuned the syrinx model to reproduce each bird's song. By defining a vocal gesture as a period of time when both the pressure and tension parameters were either unchanged or strictly increasing or decreasing, they could divide the song into a sequence of distinct gestural units.

On aligning the neural and behavioural data, the authors found that activity bursts in HVC neurons occurred at specific time points in the song, namely at the boundaries between gestures. The results suggest that the gesture — which is longer than a burst but shorter than a syllable — might be the basic unit of song production.

This finding contrasts with the reigning view of the motor code for birdsong that was originally developed<sup>2,8</sup> to account for the precise bursting activity of HVC neurons (Fig. 1). Finding no clear relationship between burst timing and the division of song into syllable-base units, researchers proposed that the HVC acted more like a clock: bursting in one set of HVC neurons triggered a burst in the next set, forming a continuous set of 'ticks' throughout the song.

Although the clock and gesture hypotheses lead to different views of the motor code for song, it is entirely possible that whereas bursting activity in HVC neurons tends to align with gesture transitions, a sufficient number of HVC neurons is active throughout each gesture to sustain clock-like functionality. Because ruling out this variation on the clock hypothesis would require demonstrating a negative — that there are no HVC neurons active during gestures — the debate over the status of the two hypotheses will probably linger for some time.

Amador and colleagues' results also contain a deeper mystery, the resolution of which may yield insight into how a bird learns its song (Fig. 2). The mystery stems from their observation that the average delay between an HVC burst and its associated gesture transition was near zero milliseconds. However, neural signals in the HVC must be relayed through several stages before they can alter the contraction of respiratory and syringeal muscles, a process estimated to take 20 milliseconds<sup>8</sup>. Thus, the bursts recorded during singing occur too late to actually cause gesture transitions. Similarly, the sound signal that arrives at the bird's ears has to traverse several synapses, causing an estimated delay of 15 milliseconds, before a sensory representation of it is registered in the HVC. This means that the bursts recorded during sleep, which align to sound with a zero-millisecond delay, occur too early to be caused by the auditory detection of a gesture transition.

Although we cannot yet expect definitive answers to the question of how high-level motor representations determine the control signals for song production, the syringeal-modelling approach pursued by Amador *et al.*

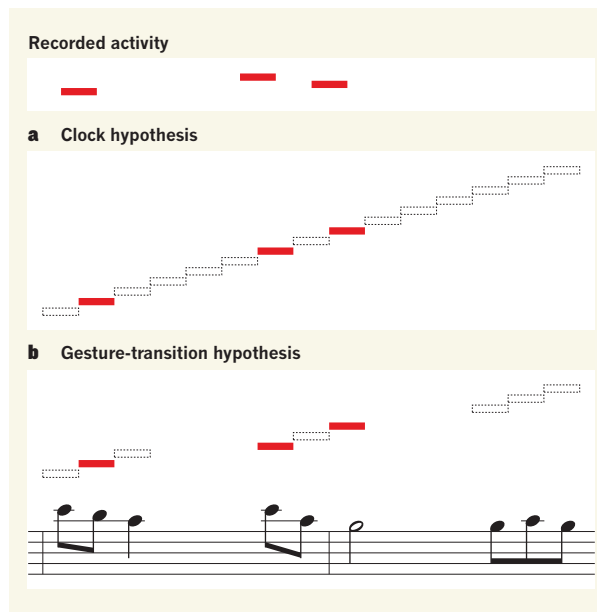


**Figure 1 | The clock and gesture hypotheses.** In the premotor cluster of HVC neurons, which is essential for singing, each neuron produces a single burst of activity (bars) precisely locked to the song output. Recordings are possible from only a few neurons (red) in any given bird. **a**, It was proposed that the unrecorded neurons (open) are continuously active throughout the song, acting like a clock to pace the song output. **b**, By building a model of the bird's vocal organ, Amador *et al.*<sup>3</sup> produce a new set of 'sheet music' for the song that specifies the motor commands needed to make any given sound. They find that every burst they recorded fell near a transition point between gestures (start times for notes in the sheet), suggesting that song is encoded as a series of distinct units.



**Figure 2 | The singer under investigation<sup>3</sup>.** The zebra finch *Taeniopygia guttata*.

provides both a method for breaking the song down into its basic units and evidence that HVC bursts are related to specific events in a bird's song. With a better understanding of the basic units, these results provide a foundation for understanding how birds learn to string these pieces back together to produce a whole song. ■

**Todd W. Troyer** is in the Department of Biology, University of Texas at San Antonio, San Antonio, Texas 78249, USA.  
e-mail: todd.troyer@utsa.edu

#### CELL BIOLOGY

## A fable of too much too fast

**A bacterium and a fungus both use gene sequences that fail to optimize the production of circadian-clock proteins. Two studies reveal different reasons for the advantages of producing less protein. SEE LETTERS P.111 & P.116**

JENNIFER M. HURLEY & JAY C. DUNLAP

**T**his is a tale of two organisms from two kingdoms that hail from very different habitats and that have nothing in common other than their ability to keep time, albeit using wholly distinct circadian systems. In this issue, Xu *et al.*<sup>1</sup> (page 116) and Zhou *et al.*<sup>2</sup> (page 111) respectively studied a freshwater cyanobacterium and a fungus. What these studies share is the fact that each organism has exploited the phenomenon of codon-usage bias to produce less of certain proteins and thereby build a more useful circadian clock. This modern fable features model organisms

1. Cynx, J. J. *Comp. Psychol.* **104**, 3–10 (1990).
2. Hahnloser, R. H. R., Kozhevnikov, A. A. & Fee, M. S. *Nature* **419**, 65–70 (2002).
3. Amador, A., Perl, Y. S., Mindlin, G. B. & Margoliash, D. *Nature* **495**, 59–64 (2013).
4. Yu, A. C. & Margoliash, D. *Science* **273**, 1871–1875 (1996).
5. Dave, A. S. & Margoliash, D. *Science* **290**, 812–816 (2000).
6. Mindlin, G. B. & Laje, R. *The Physics of Birdsong* (Springer, 2005).
7. Laje, R., Gardner, T. J. & Mindlin, G. B. *Phys. Rev. E* **65**, 051921 (2002).
8. Fee, M. S., Kozhevnikov, A. A. & Hahnloser, R. H. *Ann. NY Acad. Sci.* **1016**, 153–170 (2004).

used in clever ways to reveal something new and confirm something old, and it reminds us that the goal of evolution is not necessarily to do more of something, but to do it better\*.

First the cast of characters. The cyanobacterium is *Synechococcus elongatus*, in which three proteins, KaiA, KaiB and KaiC, self-assemble into a feedback loop that can keep time without the need for additional gene transcription or protein translation<sup>3</sup>. The fungus is *Neurospora crassa*, an exemplar of the circadian clocks found in fungi and animals<sup>4</sup> that operate using transcription-translation-based

\*This article and the papers under discussion<sup>1,2</sup> were published online on 17 February 2013.

feedback loops. In these systems, heterodimeric transcription factors drive the expression of one or more 'negative-element' proteins — after a lag, these negative elements turn down the activity of their transcriptional activator. The *Neurospora* heterodimeric activator is formed from WC-1 and WC-2, and the negative element is FRQ, a protein that can be inactivated by phosphorylation at more than 100 amino-acid residues, consistent with its long-predicted propensity for inherent structural disorder<sup>5,6</sup>.

The two research groups respectively assessed codon usage in the genes encoding KaiB–KaiC (KaiBC) and FRQ (codons are the three-nucleotide messenger RNA sequences that code for different amino acids). They found that both genes lack strong codon-usage biases, meaning that the codons used to encode the amino acids are not those that would optimize abundant protein expression. The authors demonstrate that this lack of bias is advantageous to the organism in both cases, although for different reasons.

Codon-usage bias stems from the fact that there is redundancy in the process of protein coding. Twenty standard amino acids are used to form proteins, but because the three-letter codon code gives 64 possible combinations (the four nucleotide bases taken three at a time), there is the potential for more than one codon for each amino acid. Transfer RNA (tRNA) molecules recognize codons and carry the appropriate amino acid to the ribosome (the cellular machine that synthesizes proteins), and tRNAs can be expressed at different levels. It is thought that highly used codons correlate with abundant matching tRNA molecules, and that genes evolve to optimize the efficiency of protein translation on the rationale that faster protein synthesis yields more protein and that this is good. According to this concept, the translation rate depends on the codons used by the encoding gene, and *in vitro* studies suggest that this can not only affect the amount of protein made, but also influence the process of folding a polypeptide chain into the correct three-dimensional protein structure<sup>7</sup>. But until now, few studies have provided *in vivo* demonstrations of the biological significance of non-optimal codon usage.

Xu *et al.* and Zhou *et al.* sought to understand the surprising finding that neither *kaiBC* nor *frq* use optimal codons, by expressing versions of the genes in which all or some of the codons were optimized. As expected, in both cases the optimized versions made more protein, but in neither case was 'more protein' actually more useful.

Zhou and colleagues found that FRQ that was expressed from a gene in which either rare codons or all codons near the amino terminus of the protein were optimized could not function in the *Neurospora* clock despite the presence of adequate cellular FRQ levels. Further probing revealed that this forced codon usage



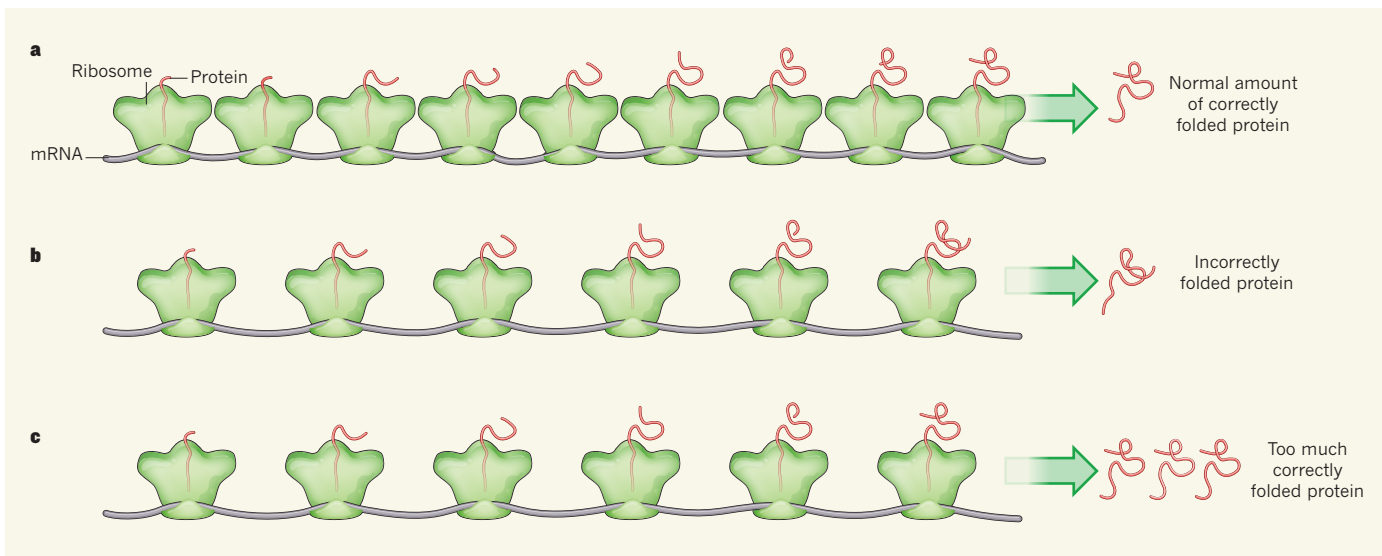


**Figure 1 | Balancing quality and quantity.** Ribosomes are cellular machines that produce proteins by translating messenger RNA codons of three nucleotides into the corresponding amino acids. Some codons are known to facilitate more-rapid protein production than others, but it seems that producing more protein more rapidly is not always advantageous. **a**, Zhou *et al.*<sup>2</sup> and Xu *et al.*<sup>1</sup> find that both the fungus *Neurospora* and the cyanobacterium *Synechococcus* adopt non-optimal codon usage for their circadian-clock genes — *frq* and *kaiBC*, respectively. This produces normal amounts of correctly folded protein. **b**, Zhou *et al.* show that, for production of FRQ protein in *Neurospora* (assuming that the initiation of protein translation is the limiting step and that protein elongation then proceeds rapidly),

forced codon optimization causes its mRNA to be translated so fast that protein folding fails, resulting in a misformed and non-functional protein that does not support a rhythm. **c**, By contrast, Xu *et al.* show that, in *Synechococcus*, optimized codon usage in the *kaiBC* gene leads to a more robust rhythm and enhanced clock-protein production (also assuming limiting initiation and rapid elongation). Surprisingly, at low temperatures, the bacterium actually grows better using the non-optimized codon usage that yields lower clock-protein production and a weakened clock. Thus, it seems that both organisms have evolved non-optimal codon usage to produce a reduced number of properly folded clock proteins that are adaptive to natural conditions.

induced constant, rather than rhythmic, FRQ expression, and also led to hyperphosphorylation of the protein and impaired interactions with WC-2. This 'optimized' FRQ also seemed to be more sensitive to degradation by protease enzymes, leading the authors to suggest that codon optimization in *frq* leads to an increased translation rate that affects protein folding and that thereby changes FRQ structure (Fig. 1).

Interestingly, optimizing codon usage at a region that encodes the middle of FRQ and that contains many phosphorylation sites was also disruptive, yielding arrhythmic protein expression and FRQ that displayed altered protease sensitivity and inadequate phosphorylation, again indicating that proper protein folding was not attained. The reasonable conclusion from these findings is that the non-optimal codon usage for the wild-type version of this gene in *Neurospora* is a mechanism to allow the proper co-translational folding of FRQ by reducing the translation rate.

Working with *Synechococcus*, Xu *et al.* also found that optimizing codon usage in *kaiBC* led to the cells forming more protein. Surprisingly, however, codon optimization produced a more robust clock than seen in the wild type, especially when the bacteria were grown at low temperatures (which they may normally encounter). So why has the organism not evolved to optimize codon usage, if this produces a more robust clock across different temperatures? The authors show that, despite their weaker rhythm, the

wild-type strain grew better under light–dark cycles (to mimic natural growing conditions) than the codon-optimized strain at low temperatures.

The explanation for this goes back to circadian first principles: clocks are evolutionarily advantageous because they help to coordinate activities in organisms such that they happen at appropriate times of day (for an example, see ref. 8). In this case, the bacterium's natural rhythm at low temperature can be as long as 30 hours. Circadian-entrainment theory and practice both show that when a 30-h clock is entrained to a 24-h light–dark cycle, it must do so with a significantly later phase angle — so late that clock-regulated activities are driven to later and inappropriate times<sup>9</sup>. Thus, the temperature conditionality of the wild-type system, in which rhythms are weakened or lost at low temperatures, is good: no clock is better than a maladaptive clock (Fig. 1). This may suggest a rationale for the conditional loss of rhythms previously reported in other organisms unable to control their internal body temperatures, including cyanobacteria, fungi<sup>10</sup>, dinoflagellates<sup>11</sup> and higher plants<sup>12</sup>.

These findings suggest that the lack of codon optimization in the two organisms probably reflects two different factors. In *Synechococcus*, *kaiBC* mRNA is extremely abundant and KaiBC is a highly structured protein, so codon optimization has its impact on the amount of functional protein that is made. By contrast, *frq* mRNA in *Neurospora* is rare and FRQ is

predicted to be disordered, so the choice of codons is aimed at producing a limited amount of protein with the correct structure. But in both cases, the moral of the story is: less can be more, and quality is more important than quantity. ■

**Jennifer M. Hurley and Jay C. Dunlap** are in the Department of Genetics, Geisel School of Medicine at Dartmouth, Hanover, New Hampshire 03755, USA. J.C.D. is also at the Texas A&M University Institute for Advanced Studies, College Station, Texas. e-mails: jennifer.hurley@dartmouth.edu; jay.c.dunlap@dartmouth.edu

1. Xu, Y. *et al.* *Nature* **495**, 116–120 (2013).
2. Zhou, M. *et al.* *Nature* **495**, 111–115 (2013).
3. Kondo, T. *Cold Spring Harb. Symp. Quant. Biol.* **72**, 47–55 (2007).
4. Baker, C. L., Loros, J. J. & Dunlap, J. C. *FEMS Microbiol. Rev.* **36**, 95–110 (2012).
5. Baker, C. L., Kettenbach, A. N., Loros, J. J., Gerber, S. A. & Dunlap, J. C. *Mol. Cell* **34**, 354–363 (2009).
6. Tang, C.-T. *et al.* *Proc. Natl Acad. Sci. USA* **106**, 10722–10727 (2009).
7. Plotkin, J. B. & Kudla, G. *Nature Rev. Genet.* **12**, 32–42 (2011).
8. Johnson, C. H., Golden, S. S. & Kondo, T. *Trends Microbiol.* **6**, 407–410 (1998).
9. Johnson, C. H. *et al.* in *Chronobiology: Biological Timekeeping* (eds Dunlap, J. C., Loros, J. J. & DeCoursey, P. J.) 67–105 (Sinauer, 2004).
10. Liu, Y., Garceau, N. Y., Loros, J. J. & Dunlap, J. C. *Cell* **89**, 477–486 (1997).
11. Njus, D., McMurtry, L. & Hastings, J. W. *J. Comp. Physiol. B* **117**, 335–344 (1977).
12. Bünning, E. *The Physiological Clock: Circadian Rhythms and Biological Chronometry* 3rd edn (Springer, 1973).

# Elemental gesture dynamics are encoded by song premotor cortical neurons

Ana Amador<sup>1†</sup>, Yonatan Sanz Per<sup>1</sup>, Gabriel B. Mindlin<sup>2</sup> & Daniel Margoliash<sup>1</sup>

**Quantitative biomechanical models can identify control parameters that are used during movements, and movement parameters that are encoded by premotor neurons. We fit a mathematical dynamical systems model including subsyringeal pressure, syringeal biomechanics and upper-vocal-tract filtering to the songs of zebra finches. This reduces the dimensionality of singing dynamics, described as trajectories (motor ‘gestures’) in a space of syringeal pressure and tension. Here we assess model performance by characterizing the auditory response ‘replay’ of song premotor HVC neurons to the presentation of song variants in sleeping birds, and by examining HVC activity in singing birds. HVC projection neurons were excited and interneurons were suppressed within a few milliseconds of the extreme time points of the gesture trajectories. Thus, the HVC precisely encodes vocal motor output through activity at the times of extreme points of movement trajectories. We propose that the sequential activity of HVC neurons is used as a ‘forward’ model, representing the sequence of gestures in song to make predictions on expected behaviour and evaluate feedback.**

For a given set of movements, sets of movement parameters tend to be correlated with each other, so that it is difficult to resolve whether motor cortical neurons encode different sets of static parameters (for example, position, velocity and direction), or even to distinguish between static and time-dependent parameters (for example, path trajectory)<sup>1</sup>. In principle, the motor coding problem can be addressed by developing quantitative models that describe the biomechanics of the movements<sup>2</sup>. To the extent that such models capture the actual control elements used to produce a movement, this permits motor cortical neuron activity to be evaluated in a natural framework. We examined motor control in the avian song system from this perspective, creating a dynamical systems model of the avian vocal organ (syrinx) that captures many of the rich set of vocal behaviours that characterize bird songs<sup>3</sup>.

We assessed predictions of the biomechanical model by taking advantage of a neuronal replay phenomenon<sup>4–6</sup>. Neurons in the nucleus HVC, a secondary motor or association cortex structure (among the structures that are essential for singing, this is the most synaptically distant from the syrinx), emit precise premotor activity when a bird sings<sup>5–7</sup>. Interestingly, when a bird listens to playback of its own song, the same HVC neurons have responses that are very similar in timing and structure to their responses during singing<sup>6</sup>, and that are highly selective for the bird’s own song (BOS)<sup>8,9</sup>. In zebra finches, there is a notable state-dependent neuronal replay phenomenon<sup>4</sup> associated with song learning<sup>10</sup>, so that the strongest and most selective auditory responses are recorded in sleeping birds. We used the responses of HVC neurons in sleeping adult zebra finches to evaluate the responses to BOS and artificial BOS variants, and then tested emerging hypotheses by recording from singing birds.

## Validating a song model and estimating static parameters

The avian vocal organ is a nonlinear device<sup>11–13</sup> that is capable of generating complex sounds even when driven by simple instructions<sup>14,15</sup>. We extended a low-dimensional model of the avian syrinx and vocal tract that can capture a variety of acoustic features such as the precise relationship between fundamental frequency and spectral

content of zebra finch song<sup>16,17</sup>. The model used here is summarized in Fig. 1. A two-dimensional set of equations describes the labial dynamics (Fig. 1; see Methods). Flow fluctuations are fed into a vocal tract, generating an input sound ( $P_{in}(t)$ ). The tract filters the sound and is characterized as a trachea, modelled by a tube, which connects to the oro-oesophageal cavity (OEC), modelled here as a Helmholtz resonator<sup>18</sup> (see Methods). The output of the model is a time trace representing the uttered sound ( $P_{out}(t)$ ).

Using this model, we created synthetic versions of the songs that our test birds sang. Time-dependent parameters of the model describing the labial dynamics were reconstructed to account for the time-dependent acoustic properties of the sound (see Methods). Following procedures described previously<sup>3,16,17</sup> for each bird’s song we used an algorithmic procedure to reconstruct unique functions for the air-sac pressure ( $\alpha(t)$ ) and the tension of syringeal labia ( $\beta(t)$ ). The result of the procedure for one song is illustrated in Fig. 2, showing that many features observed in the spectrograph of the recorded song (Fig. 2a) were also present in the synthesized song (Fig. 2b). Relatively simple time traces of reconstructed pressure and tension arose from fitting the bird’s song (Fig. 2c). These two functions drove the nonlinear equations for the labia to produce a wide range of diverse acoustic features. The parameter space of pressure versus tension was organized by bifurcation curves (Fig. 2d); curves in the parameter space that separated regions in which the model presented qualitatively different dynamics (sound patterns). Only one region (Fig. 2d) corresponded to oscillatory behaviour in which labial oscillations resulted in sound-pressure fluctuations. Two features of the pressure–tension trajectories resulting in sound output were apparent (Fig. 2d). First, most of the control parameters were maintained close to bifurcation curves, facilitating rapid changes in the quality of sound output with small changes in parameter values; and second, there were many sounds that were characterized principally by movements in pressure or tension, but not both.

Song was described by the sequence of these pressure–tension trajectories, which we call gestures, with gesture onsets and offsets

<sup>1</sup>Department of Organismal Biology and Anatomy, University of Chicago, 1027 East 57th Street, Chicago, Illinois 60637, USA. <sup>2</sup>Department of Physics, FCEN, University of Buenos Aires, Intendente Guiraldes 2160, Pabellón 1, Buenos Aires 1428, Argentina. †Present address: Department of Physics, FCEN, University of Buenos Aires, Intendente Guiraldes 2160, Pabellón 1, Buenos Aires 1428, Argentina.



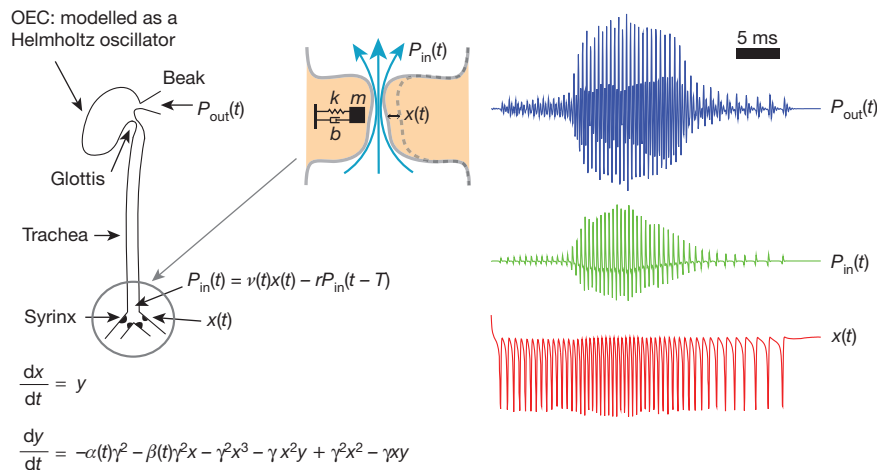


**Figure 1 | Schematized view of a dynamical systems model describing syringeal labial dynamics and tracheal vocal-tract filtering.** The syringeal membrane was modelled as a mass ( $m$ ) with damping ( $b$ ) and a restitution (spring) force ( $k$ ). Normal form equations for labial position ( $x(t)$ , red line) were integrated, computing the input pressure at the vocal tract ( $P_{in}(t)$ , green

line), filtered by the oro-oesophageal cavity (OEC), and ultimately the total output pressure ( $P_{out}(t)$ , blue line).  $\gamma$ , time constant;  $r$ , reflection coefficient of the trachea;  $T$ , propagation time along trachea;  $v$ , proportional to the mean velocity of the flow;  $y$ , velocity (see Methods).

defined as discontinuities in either the pressure or tension functions (Fig. 2c). Gestures include movements that do not result in phonation, such as pressure patterns associated with mini-breaths between syllables<sup>19</sup>, but our recordings were limited here to airborne sounds. In a sample of 8 modelled songs, there were  $13 \pm 4$  gestures per motif (largest basic unit of song, a repeated sequence of syllables). The distribution of gesture durations (mode =  $22.5 \pm 2.5$  ms, range 4–142 ms) was non-Gaussian, with 33% of the gestures lasting less than 30 ms, and it had a long tail corresponding to slowly varying sounds, such as constant-frequency harmonic stacks (Fig. 2e).

This simple model captured the essential features of sound production in a framework of labial tension and subsyringeal pressure over which birds have direct motor control<sup>20–22</sup>. Although the syrinx has considerable additional complexity, the model described the vocal system in a low-dimensional space, enabling us to capture a wide range of acoustic features using a small set of time-dependent parameters.

We tested the model by comparing responses of HVC neurons to the broadcast of the modelled song (mBOS) with the BOS in sleeping birds (Fig. 3). Responses to a grid of mBOS stimuli with identical timing but different spectra from BOS identified optimal estimates for two remaining free static parameters (Supplementary Fig. 1). In sleeping birds, song-system neurons are exceptionally selective and it was difficult to induce a response: for example, mBOS generated without the OEC component failed to elicit responses. On one occasion we mis-estimated the duration of a component of BOS by 5 ms, and found one neuron that responded strongly to the BOS but not at all to the synthetic song (Supplementary Fig. 2b). Over a population of 30 neurons, the best mBOS elicited  $58\% \pm 8\%$  of the response to BOS (Supplementary Note 1). Phasic projection neurons ( $HVC_p$ ;  $n = 15$ ) and tonic interneurons ( $HVC_{ii}$ ;  $n = 15$ ) both responded selectively to mBOS over non-BOS stimuli (Supplementary Note 1). These results show that a low-dimensional model representing an approximation of peripheral mechanics is sufficient to capture behaviourally relevant features of song.

### Projection neurons burst at gesture extrema

We next evaluated the activity of HVC neurons relative to model dynamics, by analysing the timing of spike bursting relative to the pressure–tension trajectories used to synthesize the mBOS. This identified a compelling relationship between the timing of  $HVC_p$  spikes and the pressure–tension trajectories. For example, in Fig. 4a the spiking of two neurons (coded with different colours) is shown relative to the BOS spectrograph, oscillograph and reconstructed pressure and tension

time series. One of the neurons burst once, at the transition between descending frequency modulations and a constant frequency ‘high note’. The other neuron burst twice, once when the pressure during a high note reached a maximum, and once at the transition between a high frequency chevron and a broadband frequency-modulated sound. Similar relationships between spike-burst timing and gestures were seen for 14 of the 15  $HVC_p$  (Supplementary Figs 2 and 3). In one case, a neuron emitted bursts in the interval between syllables. We propose that this pattern might arise if the bursts are associated with mini-breaths during singing<sup>19</sup>. Only the 17 bursts occurring during phonation were considered for further analysis.

Examination of the responses of the  $HVC_p$  using pressure versus tension plots showed that neurons burst preferentially at gesture-trajectory extrema (GTE) associated with gestures (Fig. 4b). A gesture has at least two GTE, at its beginning and end, and up to two additional GTE, if the absolute maxima of pressure and/or tension represent unique and distinct time points. In cases in which the absolute maximum is not distinct in time, no additional GTE result (for example, if there are multiple local maxima with the same magnitude). Of the 17 bursts (14  $HVC_p$ ), 11 (65%) were aligned with onsets or offsets, and 6 (35%) were aligned with pressure or tension maxima. In a sample of 5 songs, there were  $28 \pm 4$  GTE per song (165 GTE in total). From a total of 60 gestures, 20 (33.4%) had only onset and offset GTE; in addition, 30 (50%) had a unique peak in pressure (3 GTE per gesture), 5 (8.3%) had a unique peak in tension (3 GTE per gesture); and 5 (8.3%) had unique peaks in both pressure and tension. The distribution of time intervals between successive GTE (mode =  $9 \pm 1$  ms, range 4–116 ms) was non-Gaussian, and 66% of the intervals had a duration of less than or equal to 30 ms (Fig. 4c). Most gestures corresponded to notes (the smallest unit of song organization recognized by ornithologists), but motor activity at GTE maxima could subdivide notes; for example, at the point at which a neuron burst and the pressure reached a maximum in the middle of a constant-frequency harmonic stack (Supplementary Fig. 2). These examples highlight that for some  $HVC_p$ , the patterns of activity would not be interpretable with a purely spectrographic analysis of song<sup>5</sup>. We also observed cases in which  $HVC_p$  burst at the onset of relatively pure pressure-only or tension-only trajectories, with a tendency towards pressure-only trajectories (Fig. 2d). If such neurons project to distinct regions of the HVC’s afferent targets, which are organized based on the syringeal muscles and interactions with respiratory system, such observation could help to resolve the long-standing riddle of the HVC’s topographic organization.

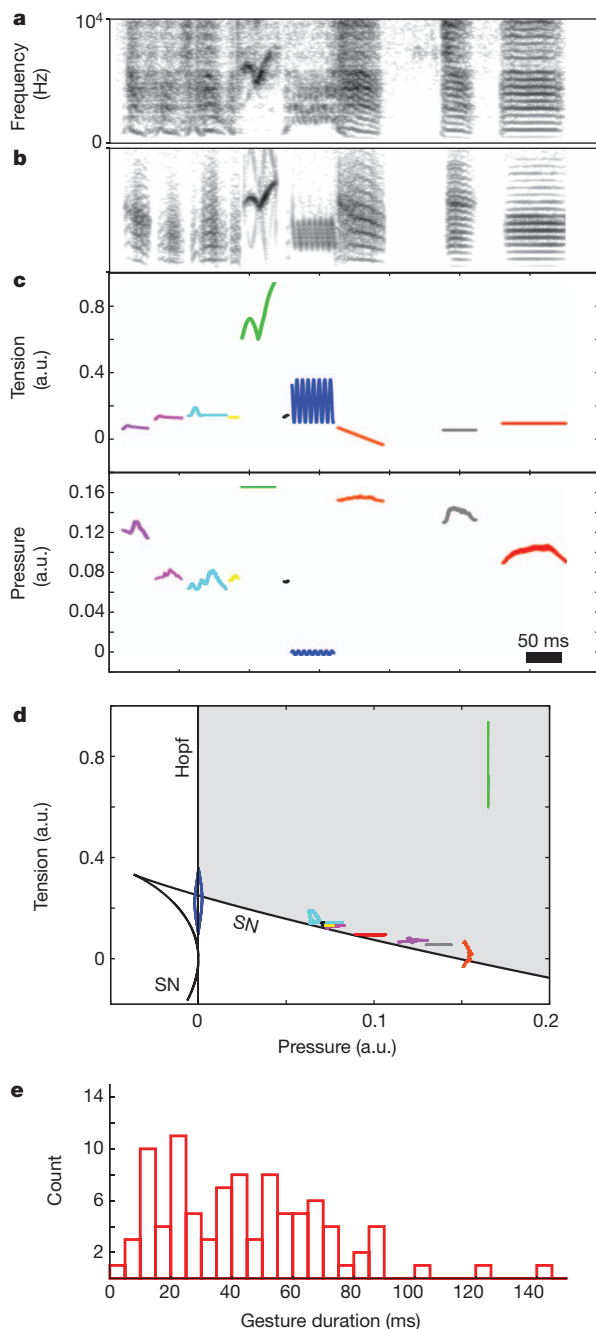


**Figure 2 | A low-dimensional model for reconstructing gestures.**

**a–e**, Spectrograms of a bird's song (**a**) and a model synthetic song (**b**). Song is described by fitted parameters  $\alpha(t)$  and  $\beta(t)$ , proportional to air-sac pressure and labial tension, respectively (**c**; each distinct sound is colour coded). Each sound (same colour code as in **c**) is generated by a continuous curve in the parameter space of the model, that we define as a 'gesture' (**d**). Oscillations in the vicinity of a Hopf bifurcation are almost tonal, whereas oscillations near a saddle-node (SN) bifurcation present rich spectra, typical of zebra finch song. Note that the spectrally poor 'high note' (green) is distant from the SN bifurcation. The grey area indicates the region of phonation. The distribution of gesture durations for five birds is displayed in **e**. a.u., arbitrary units.

To quantify these observations, we calculated the time between each spike in each burst to the closest GTE for all 17 bursts. The resulting distribution was approximately Gaussian and, on average, the bursts preceded the closest GTE (mean =  $-5.6 \pm 0.3$  ms,  $\sigma = 6.7 \pm 0.3$  ms; Fig. 4d). A bootstrap procedure (Supplementary Note 2) confirmed that the correspondence to the closest GTE was statistically significant ( $F$ -test,  $P < 0.045$ ). This indicates that the timing of HVC<sub>p</sub>

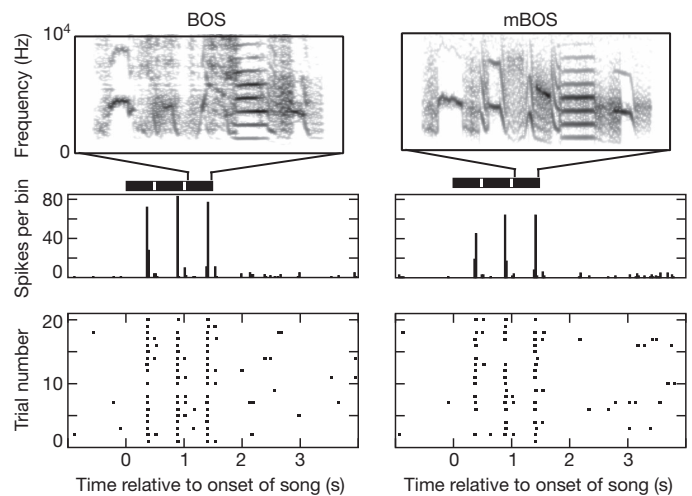


**Figure 3 | Testing the low-dimensional model.** The activity of HVC-selective neurons of sleeping birds in response to the presentation of BOS and mBOS was similar. The timing of the three repeated motifs that were presented is indicated by the bold horizontal lines.

bursts is associated with the timing of GTE. Given a minimal delay between activity of HVC<sub>p</sub> and sound production estimated between 25–50 ms<sup>23</sup>, the minimal 15-ms delay for auditory feedback to HVC<sub>i</sub><sup>8</sup>, and that the duration of intervals between GTE varied greatly (Fig. 4c), it is notable that the timing of HVC<sub>p</sub> bursting was synchronized with a near-zero time lag to a model of actual behavioural output.

### Interneurons are suppressed at GTE

HVC<sub>i</sub> show local minima and maxima in their tonic activity throughout song, and we noted that there was a relationship between the minima and the timing of GTE. To characterize this, for each interneuron we binned the spikes in 10-ms windows for each acoustic presentation. The resultant average response traces were smoothed and the minima in the smoothed traces were identified (see Methods; an example neuron is shown in Fig. 5a, bottom panel). Each HVC<sub>i</sub> did not have minima at all GTE, but across all neurons we observed a close alignment between the times of the minima and the times of GTE (a non-significant relationship was observed for maxima of HVC<sub>i</sub> activity; Supplementary Fig. 4). Computing the differences between the time of each minimum that occurred during phonation and the closest GTE resulted in a distribution that was approximately Gaussian (mean =  $-0.82$  ms  $\pm$  0.60 ms,  $\sigma = 7.3 \pm 1.4$  ms; Fig. 5b). We compared this distribution to the distribution of randomly positioned minima within each motif using the bootstrap procedure and found them to be significantly different ( $F$ -test,  $P < 0.016$ ; Supplementary Note 2). Additional tests identified marginally significant timing of minima relative to GTE for one of four birds (Supplementary Note 3). Thus, the precise activity of HVC<sub>i</sub> (ref. 7) can help to shape the timing of HVC<sub>p</sub>. This suggests a simple model in which bursts of activity of HVC<sub>p</sub> suppress activity in HVC<sub>i</sub>, whose ongoing activity helps to shape the next HVC<sub>p</sub> burst.

### A representation of gestures during singing

Given that our results were obtained by broadcasting songs to sleeping birds, it is natural to enquire whether the activity of HVC neurons are also locked to gesture transitions during singing. Previous results have shown similar patterns of spike bursts between the daytime singing activity and the auditory-driven responses during sleep of single neurons of the robust nucleus of the arcopallium (RA) in zebra finches<sup>4</sup>. HVC neurons in awake swamp sparrows and Bengalese finches, which respond to auditory stimulation, also show auditory-motor correspondence in their activity patterns<sup>6</sup>. However, similar



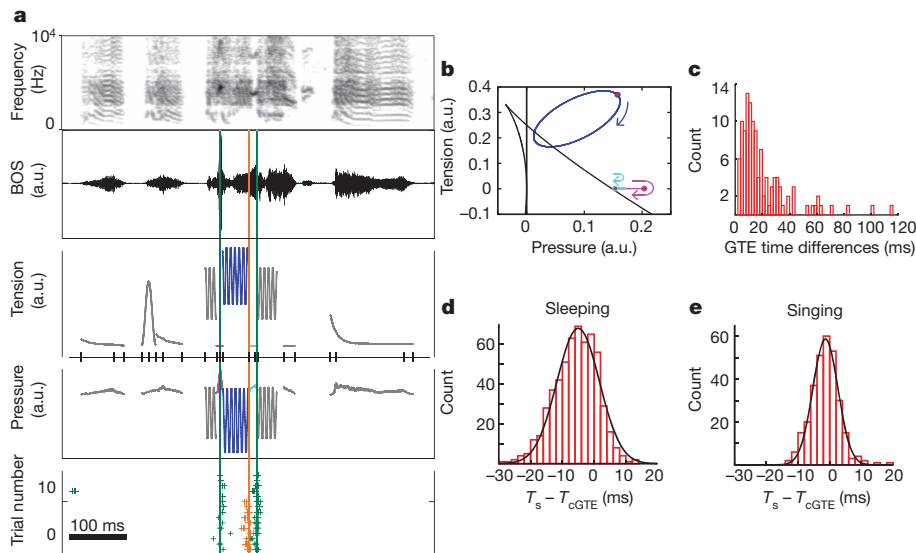


**Figure 4 | Timing of gestures relative to bursting of projection neurons.** **a**, Song spectrograph and oscillograph (top two panels); reconstructed parameters of pressure and tension (third and fourth panels; the gestures of interest are coloured magenta, blue and cyan), with tick marks indicating the times of all GTE; and raster plots of the responses of two neurons (bottom panel, coloured dark green and orange), together with their closest GTE, indicated with lines of the same colours. **b**, The trajectories in pressure–tension parameter space, with a point indicating the mean position of a burst, and arrows indicating the trajectory direction (the movement may follow and return along the same pressure–tension path, hence the curved arrows). Colours as in part **a**. **c**, Distribution of time differences between consecutive GTE occurrences ( $n = 5$  birds). **d**, Distribution of time differences between the time of each spike ( $T_s$ ) and the time of the closest GTE ( $T_{cGTE}$ ) in sleeping birds ( $n = 14$  HVC<sub>p</sub>, 5 birds). **e**, The same analysis of **d** but for singing birds ( $n = 5$  HVC<sub>p</sub>, 2 birds).

observations have yet to be reported for zebra finch HVC neurons. We made recordings from HVC in singing birds ( $n = 3$  birds), including ten tonic neurons, and five phasic neurons that burst during

phonation, recorded in two of the three birds (Fig. 6 and Supplementary Fig. 5); one phasic neuron had two bursts per motif. These recordings confirmed that during singing, all sparse bursts of HVC<sub>p</sub> occurred at gesture transitions (Fig. 4e). The same analysis that was used in sleeping birds was then used for singing birds (except that as each motif of song could vary, it was independently modelled here), and this showed that the timing of HVC<sub>p</sub> for singing birds was even more precise than during sleeping (see Fig. 4d, e). The Gaussian fit for the population of phasic neurons recorded during singing (mean =  $-1.35 \text{ ms} \pm 0.10 \text{ ms}$ ,  $\sigma = 4.0 \pm 0.1 \text{ ms}$ ; Fig. 4e) was significantly different from the bootstrapped random distribution ( $F$ -test,  $P < 0.025$ ; see Supplementary Note 2 and Supplementary Fig. 6). The minima activity of tonic neurons recorded during singing also showed precise timing relative to GTE (Gaussian fit for the minima: mean =  $-0.12 \text{ ms} \pm 0.4 \text{ ms}$ ,  $\sigma = 4.0 \pm 0.4 \text{ ms}$ ; Fig. 5c), and this was significantly different to the bootstrapped random distribution ( $F$ -test,  $P < 0.002$ ). Additional analyses showed significant locking of minima to GTE in two out of three singing birds (Supplementary Note 3). As for sleeping birds, the maxima of tonic neural activity showed no evidence of a significant locking to the GTEs (Supplementary Fig. 4c). Finally, examination of data from a previous study of zebra finches<sup>24</sup> showed that during singing the timing of HVC<sub>RA</sub> bursts were closely associated with the timing of the bursts of the other class of HVC projection neurons, which project to Area X (HVC<sub>X</sub>), the basal ganglia component of the song system (Supplementary Fig. 7). Our results support the hypothesis that all classes of HVC neurons are active in relation to the timing of gestures, although the multiple subtypes of HVC<sub>RA</sub>, HVC<sub>X</sub>, and HVC<sub>i</sub> have yet to be evaluated.

It was thought previously that the timing of song syllables was unrelated to the timing of HVC<sub>p</sub> discharge in singing birds<sup>5,24</sup>. Given the sparse bursting of these cells, this led to the idea that the output of HVC had a clock-like function with a nearly uniform ‘tick’ size of approximately 10 ms (ref. 23) supported by a ‘syn-fire’ chain of synaptic activity across HVC<sub>p</sub> (ref. 5). Instead, we find that the

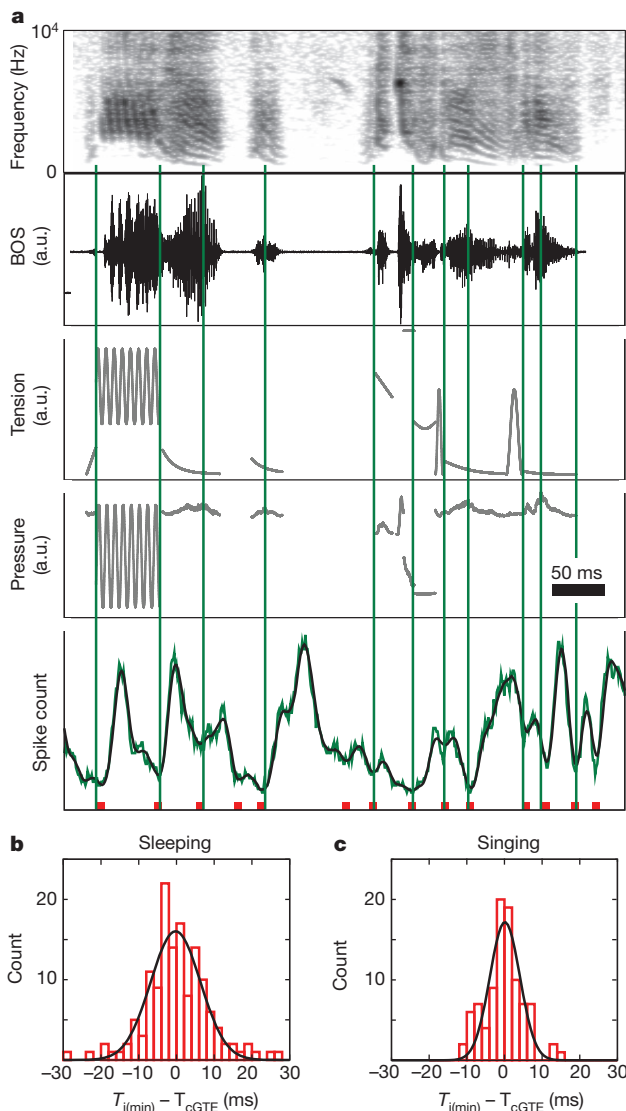


**Figure 5 | Suppressed interneuron activity is associated with GTE.** **a**, Song spectrograph and oscillograph, reconstructed parameters of pressure and tension, and raster plots, organized as in Fig. 4a, but with spike count response to the song (10-ms bin, 20 repetitions; green line) for one HVC<sub>i</sub>, and a smoothed measure of the response (black line; see Methods). Red squares indicate the time of the minima in the smoothed measure, and the vertical lines indicate the position of the closest GTE to each minima. **b**, distribution of time differences between spike response minima ( $T_{i(\min)}$ ) and their closest GTE ( $T_{cGTE}$ ) in sleeping birds ( $n = 15$  HVC<sub>i</sub>, 5 birds). **c**, Same analysis as **b** but for singing birds ( $n = 10$  HVC<sub>i</sub>, 3 birds).

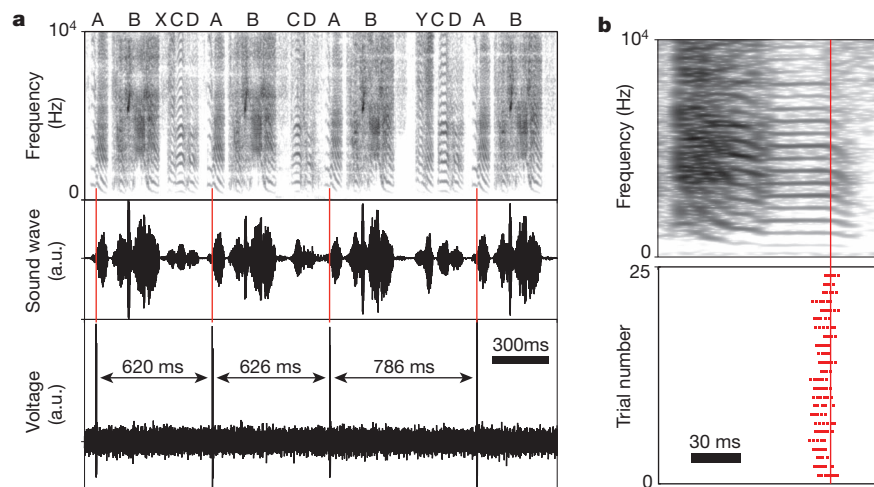


**Figure 6 | During singing, HVC projection neurons fired in the vicinity of GTE.** **a**, An HVC<sub>p</sub> neuron with spike bursting that is time-locked to the vicinity of a GTE, even as the syllable sequence and time-interval varies. Letters over the

sonograph identify the syllable types. **b**, For another bird, the bursts of a HVC<sub>p</sub> neuron are locked to a GTE in the vicinity of a subtle acoustic transition.

bursting of HVC<sub>p</sub> and modulation of HVC<sub>i</sub> activity is timed to particular time points of motor gestures. The sequential firing across the population of HVC<sub>p</sub> unfolds in an ordered fashion<sup>5</sup>, but time is not explicitly represented in HVC. Instead, the statistics of HVC activity are closely tied to syringeal-vocal tract mechanics. Given the broad distribution of times between GTE, if HVC activity is synchronized with GTE this is inconsistent with a syn-fire network that is active at every moment. The differences between these two models of HVC have additional broad implications for the functional organization of the song system, for song learning and for motor coding.

As gestures vary greatly in duration, and as the RA only has access to the times of GTE, downstream components of the motor pathway (the RA and presumably the brainstem) should generate independent dynamical information to sustain the detailed structure within each gesture (compare with refs 23, 25). Previous experiments—including examinations of the effects of electrical stimulation of HVC or RA during singing<sup>26</sup>, and lesions of nuclei afferent to the HVC<sup>27</sup>—implicate information in the HVC in the encoding of larger units of song. This might be explained, for example, if gestures at the start of syllables are overemphasized in HVC relative to gestures encoding mini-breaths preceding syllables. Finally, gestures are learned, and this is consistent with the physiological properties of HVC neurons: integration over hundreds of milliseconds and multiple syllables, nonlinear summation over syllables in a sequence preceding the excitatory response, and selective response to BOS<sup>4,8,9,28–30</sup>. The information on groupings of gestures, such as syllables, can be carried in these integrated signals. This also re-emphasizes that synaptic modification in HVC, not just changes at HVC–RA synapses, are associated with feedback-mediated sensorimotor learning (compare with ref. 23). The HVC also projects to the cortico-basal ganglia pathway, which contributes to learning-mediated synaptic modification in RA by introducing variance into song output<sup>31,32</sup>. This suggests the hypothesis that the variance is structured not in an auditory framework but around specific features of song motor gestures.

### A forward model for vocal motor control

If activity in the HVC is synchronized, with little time lag, with motor gestures occurring at the periphery, this would tend to bring it into temporal register with fixed (circa 15 ms) delayed auditory<sup>33</sup>, proprioceptive<sup>20</sup> feedback. This allows movements to be represented in the HVC by gestures of greatly varying duration (with dynamics generated principally through internal HVC interactions), and with each gesture referenced to a common time framework for evaluating feedback (with feedback arriving through distinct, extrinsic inputs).

This suggests that projection neurons represent a prediction of the actual behavioural output at that moment in time, constituting an unexpected form of a ‘forward’ or predictive model to resolve the problem of the delay in sensorimotor control<sup>35</sup>. Assuming that behaviour is subdivided into gestures, and that only the transitions (GTE) are represented by HVC output (HVC<sub>p</sub>), feedback information could accumulate in the intervals between the transitions by modifying the tonic activity of HVC<sub>i</sub> and subsequently, the spike bursting of HVC<sub>p</sub>. Indeed, HVC receives multiple sources of feedback, including input from the primary motor cortex RA<sup>36</sup>, thalamic input carrying brain-stem respiratory, auditory and proprioceptive information<sup>21,34,37</sup>, and forebrain auditory input<sup>38</sup>.

We have described song organization based on gestures, using the dynamical systems modelling framework to replace analysis of songs based on spectrographs. These features of motor systems organization may be represented in other systems and for other behaviors<sup>39</sup>. Our data support Sherrington’s long-standing hypothesis that the motor cortex is a synthetic organ, representing segments of whole movements<sup>1,40</sup>. In humans, the production of speech and the performance of athletes and musicians are an exceptional example of highly precise learned skilled behaviour that could have similar mechanisms to those described here. The development of corresponding models for human speech production should help to provide insight into speech and language pathologies in which sequential behaviour is disrupted.

### METHODS SUMMARY

Songs were recorded from 12 birds and electrophysiology was conducted on 9 adult male zebra finches (*Taeniopygia guttata*) bred in our colony. Birds were prepared for HVC extracellular recordings using standard techniques; by implanting a head pin (auditory experiments)<sup>10</sup> or motorized microdrive (singing experiments)<sup>5</sup>. Recordings were post-processed with a spike-sorting algorithm (Klusters, <http://klusters.sourceforge.net>) to separate the times of spike events for each unit. In sleeping birds, we picked the last (second or third) motif, which gave the strongest response, to analyse the timing of spikes relative to GTE. This minimized false peaks and troughs in the response profiles. The average response of each interneuron (1-ms resolution) was smoothed using a Savitsky Golay filter (polynomial local regression) and the minima were identified using a 21-point sliding window.

**Full Methods** and any associated references are available in the online version of the paper.

Received 28 February 2012; accepted 31 January 2013.

Published online 27 February 2013.

1. Hatsopoulos, N. G., Xu, Q. & Amit, Y. Encoding of movement fragments in the motor cortex. *J. Neurosci.* **27**, 5105–5114 (2007).



2. Nishikawa, K. *et al.* Neuromechanics: an integrative approach for understanding motor control. *Integr. Comp. Biol.* **47**, 16–54 (2007).
3. Perl, Y. S., Arnedo, E. M., Amador, A., Goller, F. & Mindlin, G. B. Reconstruction of physiological instructions from Zebra finch song. *Phys. Rev. E* **84**, 051909 (2011).
4. Dave, A. S. & Margoliash, D. Song replay during sleep and computational rules for sensorimotor vocal learning. *Science* **290**, 812–816 (2000).
5. Hahnloser, R. H. R., Kozhevnikov, A. A. & Fee, M. S. An ultra-sparse code underlies the generation of neural sequences in a songbird. *Nature* **419**, 65–70 (2002).
6. Prather, J. F., Peters, S., Nowicki, S. & Mooney, R. Precise auditory-vocal mirroring in neurons for learned vocal communication. *Nature* **451**, 305–310 (2008).
7. Yu, A. C. & Margoliash, D. Temporal hierarchical control of singing in birds. *Science* **273**, 1871–1875 (1996).
8. Margoliash, D. Acoustic parameters underlying the responses of song-specific neurons in the white-crowned sparrow. *J. Neurosci.* **3**, 1039–1057 (1983).
9. Margoliash, D. Preference for autogenous song by auditory neurons in a song system nucleus of the white-crowned sparrow. *J. Neurosci.* **6**, 1643–1661 (1986).
10. Shank, S. S. & Margoliash, D. Sleep and sensorimotor integration during early vocal learning in a songbird. *Nature* **458**, 73–77 (2009).
11. Amador, A., Goller, F. & Mindlin, G. B. Frequency modulation during song in a suboscine does not require vocal muscles. *J. Neurophysiol.* **99**, 2383–2389 (2008).
12. Elemans, C. P. H., Laje, R., Mindlin, G. B. & Goller, F. Smooth operator: avoidance of subharmonic bifurcations through mechanical mechanisms simplifies song motor control in adult zebra finches. *J. Neurosci.* **30**, 13246–13253 (2010).
13. Fee, M. S., Shraiman, B., Pesaran, B. & Mitra, P. P. The role of nonlinear dynamics of the syrinx in the vocalizations of a songbird. *Nature* **395**, 67–71 (1998).
14. Mindlin, G. B. & Laje, R. *The Physics of Birdsong*. (Springer Verlag, 2005).
15. Laje, R., Gardner, T. J. & Mindlin, G. B. Neuromuscular control of vocalizations in birdsong: A model. *Phys. Rev. E* **65**, 05192 (2002).
16. Sitt, J. D., Amador, A., Goller, F. & Mindlin, G. B. Dynamical origin of spectrally rich vocalizations in birdsong. *Phys. Rev. E* **78**, 011905 (2008).
17. Amador, A. & Mindlin, G. B. Beyond harmonic sounds in a simple model for birdsong production. *Chaos* **18**, 043123 (2008).
18. Riede, T., Suthers, R. A., Fletcher, N. H. & Blevins, W. E. Songbirds tune their vocal tract to the fundamental frequency of their song. *Proc. Natl Acad. Sci. USA* **103**, 5543–5548 (2006).
19. Hartley, R. S. & Suthers, R. A. Air-flow and pressure during canary song: direct evidence for mini-breaths. *J. Comp. Physiol. A* **165**, 15–26 (1989).
20. Suthers, R. A., Goller, F. & Wild, J. M. Somatosensory feedback modulates the respiratory motor program of crystallized birdsong. *Proc. Natl Acad. Sci. USA* **99**, 5680–5685 (2002).
21. Wild, J. M. Functional neuroanatomy of the sensorimotor control of singing. *Ann. NY Acad. Sci.* **1016**, 438–462 (2004).
22. Suthers, R. A., Goller, F. & Pytte, C. The neuromuscular control of birdsong. *Phil. Trans. R. Soc. B* **354**, 927–939 (1999).
23. Fee, M. S., Kozhevnikov, A. A. & Hahnloser, R. H. Neural mechanisms of vocal sequence generation in the songbird. *Ann. NY Acad. Sci.* **1016**, 153–170 (2004).
24. Kozhevnikov, A. A. & Fee, M. S. Singing-related activity of identified HVC neurons in the zebra finch. *J. Neurophysiol.* **97**, 4271–4283 (2007).
25. Fiete, I. R., Hahnloser, R. H. R., Fee, M. S. & Seung, H. S. Temporal sparseness of the premotor drive is important for rapid learning in a neural network model of birdsong. *J. Neurophysiol.* **92**, 2274–2282 (2004).
26. Vu, E. T., Mazurek, M. E. & Kuo, Y. C. Identification of a forebrain motor programming network for the learned song of zebra finches. *J. Neurosci.* **14**, 6924–6934 (1994).
27. Williams, H. & Vicario, D. S. Temporal patterning of song production: Participation of nucleus uvulaeformis of the thalamus. *J. Neurobiol.* **24**, 903–912 (1993).
28. Margoliash, D. & Fortune, E. S. Temporal and harmonic combination-sensitive neurons in the zebra finch's HVC. *J. Neurosci.* **12**, 4309–4326 (1992).
29. Nick, T. A. & Konishi, M. Neural auditory selectivity develops in parallel with song. *J. Neurobiol.* **62**, 469–481 (2005).
30. Prather, J. F., Nowicki, S., Anderson, R. C., Peters, S. & Mooney, R. Neural correlates of categorical perception in learned vocal communication. *Nature Neurosci.* **12**, 221–228 (2009).
31. Brainard, M. S. & Doupe, A. J. Interruption of a basal ganglia-forebrain circuit prevents plasticity of learned vocalizations. *Nature* **404**, 762–766 (2000).
32. Ölveczky, B. P., Andalman, A. S. & Fee, M. S. Vocal experimentation in the juvenile songbird requires a basal ganglia circuit. *PLoS Biol.* **3**, e153 (2005).
33. Konishi, M. The role of auditory feedback in the control of vocalization in the white-crowned sparrow. *Z. Tierpsychol.* **22**, 770–783 (1965).
34. Ashmore, R. C., Wild, J. M. & Schmidt, M. F. Brainstem and forebrain contributions to the generation of learned motor behaviors for song. *J. Neurosci.* **25**, 8543–8554 (2005).
35. Wolpert, D. M., Ghahramani, Z. & Jordan, M. I. An internal model for sensorimotor integration. *Science* **269**, 1880–1882 (1995).
36. Roberts, T. F., Klein, M. E., Kubke, M. F., Wild, J. M. & Mooney, R. Telencephalic neurons monosynaptically link brainstem and forebrain premotor networks necessary for song. *J. Neurosci.* **28**, 3479–3489 (2008).
37. Coleman, M. J., Roy, A., Wild, J. M. & Mooney, R. Thalamic gating of auditory responses in telencephalic song control nuclei. *J. Neurosci.* **27**, 10024–10036 (2007).
38. Bauer, E. E. *et al.* A synaptic basis for auditory-vocal integration in the songbird. *J. Neurosci.* **28**, 1509–1522 (2008).
39. Mulliken, G. H., Musallam, S. & Andersen, R. A. Forward estimation of movement state in posterior parietal cortex. *Proc. Natl Acad. Sci. USA* **105**, 8170–8177 (2008).
40. Leyton, S. S. & Sherrington, C. S. Observations on the excitable cortex of the chimpanzee, orangutan and gorilla. *Q. J. Exp. Physiol.* **11**, 135–222 (1917).

**Supplementary Information** is available in the online version of the paper.

**Acknowledgements** We are grateful to R. H. R. Hahnloser for help with the microdrives and techniques used to record from singing birds. We thank H. D. I. Abarbanel, T. Q. Gentner, H. C. Nusbaum and S. E. Palmer for valuable comments on the manuscript. This work was supported by a Human Frontiers Science Program cross-disciplinary fellowship award to A.A., NIDCD006876, ANCYT, CONICET and UBA awards to G.B.M. and Y.S.P., and NIDCD and NSF/CRCNS awards to D.M.

**Author Contributions** A.A., G.B.M. and Y.S.P. developed the syringeal model, G.B.M. and Y.S.P. modelled the songs, A.A. conducted surgeries, sound recordings and collected the electrophysiological data, A.A., G.B.M. and D.M. conceived and designed the experiments, and prepared the manuscript. All four authors participated in data analysis.

**Author Information** Reprints and permissions information is available at [www.nature.com/reprints](http://www.nature.com/reprints). The authors declare no competing financial interests. Readers are welcome to comment on the online version of the paper. Correspondence and requests for materials should be addressed to D.M. ([dan@bigbird.uchicago.edu](mailto:dan@bigbird.uchicago.edu)).

## METHODS

**Subjects, songs and surgeries.** All procedures were carried out in accordance with a protocol approved by the University of Chicago Institutional Animal Care and Use Committee. Songs were recorded from 12 birds and electrophysiology was conducted on 9 adult male zebra finches (*Taeniopygia guttata*) bred in our colony. Birds were prepared for recordings using standard techniques to implant a head pin (for auditory experiments)<sup>10</sup> or motorized microdrive (for singing experiments)<sup>5</sup>. For auditory experiments, adults were maintained on a 16 h–8 h reversed light cycle in sound-isolation boxes. Songs were recorded and filtered using custom software and then these were edited using Praat (<http://www.praat.org>). Edited songs included two or three repetitions of one motif, and were typically 2–4 s in duration. Birds were allowed to recover for 2 or 3 days before the first day of recordings, and were rested for at least 2 days between recording sessions.

**Electrophysiology, stimulus presentation and spike analysis.** HVC extracellular recordings were carried out using head-fixed sleeping or singing tethered birds. Recordings were post-processed with a spike-sorting algorithm (<http://klusters.sourceforge.net>) to separate the times of spike events for each unit. For experiments in singing birds, all well-isolated neurons are reported. For auditory experiments, only BOS-responsive neurons were recorded. The auditory stimuli were presented randomly with an interstimulus interval of  $7 \pm 1$  s. The neural response to each song is quantified in terms of the Z score<sup>25</sup>:

$$Z = \frac{\mu_S - \mu_{BG}}{\sqrt{\text{Var}(S) + \text{Var}(BG) - 2\text{Covar}(S, BG)}}$$

where  $\mu_S$  is the mean response during the auditory stimulus (S) and  $\mu_{BG}$  is the mean response during background activity (BG) (Covar is covariance, Var is variance). The denominator of the equation is the standard deviation of (S – BG). The background was estimated by averaging the firing rate during a 2-s period. The Z scores of the mBOS (model BOS), CON (conspecific song) and REV (reversed BOS) were normalized to the BOS Z score, and averages across neurons were reported as means of normalized responses  $\pm$  s.e.m. For interneurons, the strength of the response varied across the motifs<sup>41</sup>. To analyse the timing of spikes relative to GTE, we picked the last (second or third) motif, which gave the strongest response. This minimized false peaks and troughs in the response profiles. In singing birds, interneurons fired reliably for each motif and all motifs were incorporated into the analysis. The average response of each interneuron (1-ms resolution) was smoothed using a Savitsky Golay filter (polynomial local regression<sup>42</sup>) and the minima were identified using a 21-point sliding window.

**Reconstruction of motor gestures.** We assumed flow-induced oscillations of opposing labia as a sound-source model for bird song production<sup>14</sup>. This model assumes that for airflow values above a certain threshold, the labia start to oscillate with a wavelike motion. Assuming that two basic modes are active (a flapping-like motion and a lateral displacement of the tissues, appropriately out of phase), a system of equations describe the dynamics of the medial position  $x(t)$  of one of the opposing labia, at one of the sound sources. These read:

$$\begin{aligned} \frac{dx}{dt} &= y \\ \frac{dy}{dt} &= \left(\frac{1}{m}\right) (-k(x)x - (b(y) + cx^2)y + a_{\text{lab}}p_{\text{av}}) \end{aligned}$$

where the first term in the second equation is the restitution in the labium, the second term accounts for the dissipation, and the last term for the force due to the interlabial pressure, where  $a_{\text{lab}}$  is the labial area. The average pressure,  $p_{\text{av}}$ , can be written in terms of the displacement and its velocity<sup>3</sup>. These equations describe a set of qualitatively different dynamical regimes. To gain independence from the details of any particular model presenting these regimes, we worked with a normal form that unfolds into a saddle-node in limit-cycle bifurcation and a Hopf bifurcation. The normal form, which is analytically derived<sup>43</sup>, constitutes the simplest set of equations for any model in which oscillations arise in either of these two bifurcations. Once this reduction is carried out, the selection of parameters that enables a sound with specific acoustic features to be obtained gives rise to unique values. The normal form equations are shown in Fig. 1, and display the same set of dynamical regimes<sup>3</sup> as the physical model, with scaling through a time constant  $\gamma$ . Once  $x(t)$  is computed, the pressure at the input of the tract is

computed as  $P_{\text{in}}(t) = v(t)x(t) - rP_{\text{in}}(t - T)$  where  $T$  is the time for a sound wave to reach the end of the tube and return, and  $v(t)$  is proportional to the average mean velocity of the flow. The transmitted pressure fluctuation  $P_{\text{tr}}(t) = (1 - r)P_{\text{in}}(t - 0.5T)$  forces the air in the glottis, which is approximated by the neck of a Helmholtz resonator (used to model the OEC<sup>3,44</sup>); that is, a large container with a hole, such that the air in its vicinity oscillates owing to the springiness of the air in the cavity. A linear set of three ordinary differential equations accounts for the dynamics of the air flow and pressure in this linear acoustic device<sup>3</sup>, resulting in the final output pressure  $P_{\text{out}}(t)$  (Fig. 1).

We reconstructed the parameters driving the equations of the normal form ( $\alpha(t)$  and  $\beta(t)$ ), as well as the parameters describing the tracheal length and the OEC cavity in such a way that the synthesized sounds presented the same fundamental frequencies and spectral content as natural song. Reconstructions over sequential sound segments gave estimates of the time-dependence of physiological parameters used during song production. A linear integrator ( $\tau = 2.5$  ms) was used to compute the envelope of the sound signal. A threshold was used to identify phonating segments. For those longer than 20 ms, we decomposed the recorded songs into successive 20-ms segments (time between consecutive segments  $\Delta t = 1/20,000$  s). These were short enough to avoid large variation of the physiological gestures, and long enough to compute spectral content. For each segment, we computed the spectral content index (SCI)<sup>16</sup> and the fundamental frequency. A search in the parameter space  $\alpha(t)$ ,  $\beta(t)$  was performed over a grid so that the synthetic sounds produced would match the fundamental frequencies of the song segment being fitted. Over the set of  $\alpha(t)$ ,  $\beta(t)$  values selected, a search was carried out so that the SCI of the synthetic sounds matched the value of the song segment<sup>3</sup>. For sound segments shorter than 20 ms, the fundamental frequency was computed as follows: first, we selected the relative maxima of the sound signal that reached the sound envelope; next, the fundamental frequency was computed as the inverse of the time difference between the next two consecutive selected maxima; after this, the SCI at that time was estimated as the average value among all the possible SCI values, corresponding to that frequency in the framework of the model<sup>16</sup>. With those estimations of fundamental frequency and SCI,  $\alpha(t)$  and  $\beta(t)$  were computed. In general, brief segments were found to be fast trills. We modelled these as rapid oscillations of pressure and tension, with the amplitude of the pressure oscillations such that the maxima fell in the phonating region, and with the amplitude of the tension oscillations such that the frequency range of the vocalization was reproduced. We found that most of the parameters could be approximated well by fractions of sine functions, exponential decays, constants or a combinations of these.

Use of these analytic functions as parameters of the model to generate a synthetic copy of the recorded song resulted in a noiseless surrogate song (for example, Supplementary Fig. 1 ('Noise = 0')). The addition of noise allowed the gradual recovery of realistic timbre features. The dimensionless variable 'Noise' varied between 0 and 40, with Noise = 5 corresponding to a fluctuation size equal to 2.5% of the maximum range of the  $\beta(t)$  parameter. Note that the effect of timbre is more important for low-frequency sounds, which explore a small range of  $\beta(t)$ .

For each bird, the length of the trachea was chosen so that the frequencies close to 2.5 kHz and 7 kHz in the bird's song were the first and second resonances of a tube closed at one end. This corresponds to a length of 3.5 cm (ref. 45). Typically, zebra finch songs have a third important resonance at approximately 4 kHz. The parameters of the Helmholtz resonator were adjusted so that its resonant frequency would account for this resonance<sup>3</sup>. The synthetic songs for sleeping birds were generated before the electrophysiological experiments were carried out. For singing birds, all song reconstructions were also performed blind to the spike data.

41. Sutter, M. L. & Margoliash, D. Global synchronous response to autogenous song in zebra finch HVC. *J. Neurophysiol.* **72**, 2105–2123 (1994).
42. Press, W. H., Teukolsky, S. A., Vetterling, W. T. & Flannery, B. P. *Numerical Recipes: The Art of Scientific Computing* 3rd edn (Cambridge Univ. Press, 2007).
43. Guckenheimer, J. & Holmes, P. *Nonlinear Oscillations, Dynamical Systems, and Bifurcations of Vector Fields*. (Springer Verlag, 1997).
44. Fletcher, N. H., Riede, T. & Suthers, R. A. Model for vocalization by a bird with distensible vocal cavity and open beak. *J. Acoust. Soc. Am.* **119**, 1005–1011 (2006).
45. Daley, M. & Goller, F. Tracheal length changes during zebra finch song and their possible role in upper vocal tract filtering. *J. Neurobiol.* **59**, 319–330 (2004).



# Intestinal label-retaining cells are secretory precursors expressing Lgr5

Simon J. A. Buczacki<sup>1</sup>, Heather Ireland Zecchini<sup>1</sup>, Anna M. Nicholson<sup>1</sup>, Roslin Russell<sup>1</sup>, Louis Vermeulen<sup>1</sup>, Richard Kemp<sup>1</sup> & Douglas J. Winton<sup>1</sup>

**The rapid cell turnover of the intestinal epithelium is achieved from small numbers of stem cells located in the base of glandular crypts. These stem cells have been variously described as rapidly cycling or quiescent. A functional arrangement of stem cells that reconciles both of these behaviours has so far been difficult to obtain. Alternative explanations for quiescent cells have been that they act as a parallel or reserve population that replace rapidly cycling stem cells periodically or after injury; their exact nature remains unknown. Here we show mouse intestinal quiescent cells to be precursors that are committed to mature into differentiated secretory cells of the Paneth and enteroendocrine lineage. However, crucially we find that after intestinal injury they are capable of extensive proliferation and can give rise to clones comprising the main epithelial cell types. Thus, quiescent cells can be recalled to the stem-cell state. These findings establish quiescent cells as an effective clonogenic reserve and provide a motivation for investigating their role in pathologies such as colorectal cancers and intestinal inflammation.**

The epithelial lining of the small intestine is continuously renewed from a small number of stem cells including Lgr5-expressing crypt base cells that have been shown to be a rapidly cycling stem-cell population in homeostasis<sup>1</sup>. Alternative markers of intestinal stem cells have variously identified populations as rapidly cycling or quiescent with proposed roles for the latter as a parallel or reserve stem-cell population that act to replace rapidly cycling stem cells either periodically or after injury<sup>2–7</sup>. Periodic replacement however, implies a hierarchical relationship that contrasts with the recent demonstration that the ongoing loss and replacement of rapidly cycling stem cells explains all the cellular output of the crypt<sup>8,9</sup>. Hence, contemporary views consider the possibility of a reserve stem-cell population that is distinct from the rapidly cycling population responsible for homeostasis<sup>10,11</sup>. Quiescent or slowly cycling stem-cell populations are defined by the property of label retention. Under conditions of expansion of the stem-cell compartment (during the later stages of gut growth or during regeneration after epithelial damage), proliferating cells in the intestine can be labelled with nucleotide analogues. Small numbers of label-retaining cells (LRCs) persist for around 4 weeks after homeostasis is (re)established<sup>12</sup>. On subsequent regenerative challenge some LRCs can re-enter the cell cycle thereby demonstrating their proliferative potential<sup>13</sup>. Quiescent cells identified in this way are predominantly located in a supra-Paneth cell position within the crypt. Several candidate markers or regulators of quiescence with expression patterns that overlie this location have been identified. Bmi1-expressing cells in the proximal small intestine are capable of clonal expansion, have low Ki67 positivity and are responsible for repopulation of the Lgr5<sup>+</sup> stem-cell population after conditional Lgr5 cell deletion<sup>4,11</sup>. Wip1 phosphatase regulates stem-cell apoptosis in a p53-dependent manner and co-localizes with thymidine label-retaining cells in a supra-Paneth cell position<sup>14</sup>. The tumour suppressor Pten acts to limit the numbers of intestinal stem cells and its inactive phosphorylated form has been shown to co-localize with 5-bromodeoxyuridine (BrdU)-positive label-retaining cells<sup>15,16</sup>. It has also been shown that Hopx marks cells in the +4 position, a small proportion of which are label-retaining and that

are also capable of converting to a Lgr5 population and maintaining clonogenic growth<sup>6</sup>. Most recently two publications dispute the role of the negative regulator of ErbB, Lrig1. One proposes that it is a unique marker of quiescent stem cells distinct from the bulk Lgr5 population, whereas the other identifies it as a general regulator of the stem-cell compartment<sup>3,7</sup>. Furthermore, a recent report has demonstrated that all previously identified 'quiescent stem-cell' markers appear highly expressed by the Lgr5 population<sup>17</sup>. In summary, the exact nature of quiescent crypt cells remains unknown because candidate markers rather than the label-retaining population itself have been the focus of study.

## Identification of label-retaining cells

To study quiescence directly we identified cells retaining nuclear-localized fluorescent H2B-YFP during a chase period following a pulse of induced expression. Transgenic *Cypla1-H2B-YFP* mice were evaluated before and after a pulse of  $\beta$ -naphthoflavone (BNF) treatment (Fig. 1a, b). The *Cypla1* promoter has an established pattern of expression on induction in all cells of the crypt-villus axis with the exception of the mature Paneth cells<sup>18</sup>. Twenty-four hours after induction (T0) cells throughout the crypt to villus axis expressed H2B-YFP with, as expected, the exception of Paneth cells (Fig. 1b–d and Supplementary Video 1). By 7 days crypt expression was restricted to multiple cells of the crypt base (Supplementary Fig. 1a). These cells decrease in frequency with time, becoming absent by 12 weeks (Supplementary Fig. 1b–d). Confocal microscopy analysis after 1 week suggested that a number of positive cells were Paneth cells due to characteristic enlarged and rounded nuclear morphology; this was confirmed using Paneth cell markers (Supplementary Fig. 1e, f). Non-Paneth LRCs were selected as the population of interest and, from 10 days post-induction, were defined as YFP-labelled LRCs (YFP-LRCs) in accord with published definitions of intestinal LRCs (Fig. 1e)<sup>5,6,12</sup>. YFP-LRCs were present throughout the crypt base, slightly predominating in the +3 position, and were identifiable in decreasing numbers for up to 4 weeks (Fig. 1f, g). Subsequently, YFP<sup>+</sup> Paneth cells were seen up to 8 weeks after this time (that is 12 weeks

<sup>1</sup>Cancer Research UK Cambridge Research Institute, Li Ka Shing Centre, Robinson Way, Cambridge CB2 0RE, UK.

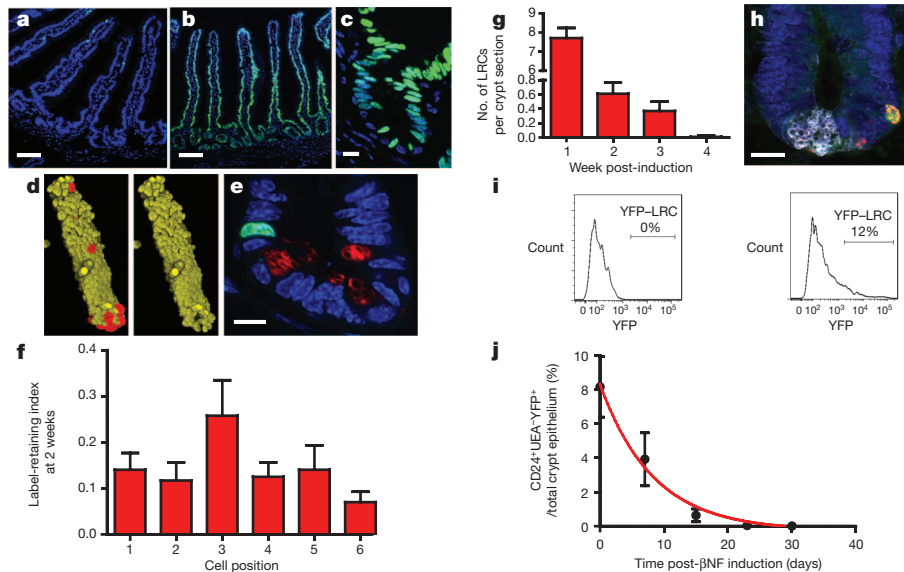


**Figure 1 | Identification and isolation of YFP-LRCs.** **a–f**, Time course images of intestinal epithelium from *Cyp1a1-H2B-YFP* mice after induction with βNF. **a**, Uninduced control. A very small number of background YFP<sup>+</sup> cells are present on duodenal villus tips (**b**, **c**) T0. **d**, T0 three-dimensional reconstructed z-stack image of an isolated crypt showing that Paneth cells identified with UEA (red) do not initially express YFP (yellow). **e**, Three weeks post-induction image demonstrating a typically positioned YFP<sup>+</sup> cell above UEA<sup>+</sup> (red) Paneth cells. **f**, Non-Paneth YFP<sup>+</sup> LRCs are distributed

post-induction) but not thereafter, which accords with the previously reported lifespan of terminally differentiated Paneth cells of 6–8 weeks<sup>18</sup>. By 3 weeks YFP-LRCs were reduced to  $0.4 \pm 0.13$  per crypt section, approximating to 2 per whole crypt. No YFP-LRCs were seen in the colon.

The above estimate for YFP-LRC number is 50 times higher than previously described for LRCs identified by retention of nucleotide analogues ( $0.008$  per crypt section)<sup>6</sup>. Confocal microscopy on dual pulse-chased EdU/H2B-YFP mice determined that EdU-LRCs were recognized at a frequency of  $0.009$  per crypt section and that EdU-LRCs (27 out of 30) are YFP<sup>+</sup>, demonstrating that the majority (90%) of EdU-LRCs can be identified by YFP label retention (Fig. 1h). The greater abundance of YFP-LRCs (2–3 per crypt) demonstrates that nucleotide labelling incompletely marks slowly cycling populations, presumably because the method only marks cells captured in S phase before acquiring quiescence<sup>19</sup>.

### LRCs have a combined secretory and stem-cell signature

After tissue dissociation, YFP-LRCs were isolated by flow sorting for transcriptional profiling. A strategy combining UEA lectin (for Paneth cell selection) and CD24 (lower crypt specific) was used to compare three populations independent of stem markers associating with cell cycle status (Fig. 1i, j and Supplementary Figs 1f, g and 2a, b)<sup>7</sup>. Expression microarray analysis showed that YFP-LRCs (CD24<sup>+</sup>UEA<sup>-</sup>YFP<sup>+</sup>) are distinct from both Paneth (CD24<sup>+</sup>UEA<sup>+</sup>) and cycling lower crypt cells (LCCs) (CD24<sup>+</sup>UEA<sup>-</sup>YFP<sup>-</sup>) (Supplementary Fig. 2c). Notably, transcripts associated with the Paneth and enteroendocrine lineages (*Mmp7*, *Kit*, *Chga*, *Gip*, *Pax6*) as well as stem-cell markers (*Lgr5*, *Lrig1*, *CD133*, *CD44*, *Peg3*) were more abundant in YFP-LRCs compared to LCCs. To establish that the YFP-LRC signature did not arise as a composite of the other two differentiated cell populations, we undertook single-cell profiling of 48 cells from each of the three groups for 47 transcripts selected either as stem cell/differentiation markers or YFP-LRC-specific from the array comparison (see Methods). Principal component analysis demonstrated that YFP-LRCs were a discrete homogeneous population separate from both Paneth cells and LCCs but with no internal structure

throughout the crypt base and occur maximally at cell position +3 (mean ± s.e.m.). **g**, Non-Paneth YFP<sup>+</sup> LRCs are present for up to 4 weeks after βNF induction (mean ± s.e.m.). **h**, Representative image of an EdU<sup>+</sup>YFP<sup>+</sup> non-Paneth LRC. EdU, red; YFP, green; lysozyme, white. **i**, FACS YFP histograms of single, live, UEA<sup>-</sup>CD24<sup>+</sup> cells in uninduced (left panel) and 10 days post-βNF-treated animals (right panel). **j**, The CD24<sup>+</sup>UEA<sup>-</sup>YFP<sup>+</sup> population decreases in number with time (mean ± s.e.m.). Scale bars: 50 μm (**a**, **b**); 10 μm (**c**, **e**, **h**).

(Fig. 2a). *Nfat3*, *CD83* and *Nfat5* were the top three principal components defining YFP-LRCs. It was confirmed that larger numbers of YFP-LRCs expressed higher levels of Paneth/enteroendocrine cell markers than LCCs including *Mmp7* and *Chgb* (Fig. 2b). Homogeneity of the YFP-LRC population was further validated using immunofluorescence for differentiation markers on flow-sorted populations (Supplementary Fig. 3).

Unexpectedly, given the quiescent status of YFP-LRCs, the microarray showed elevated expression of *Lgr5* in YFP-LRCs compared to the LCCs. To determine the degree of similarity with the *Lgr5* population, we used previously published microarray data<sup>20</sup> and found a highly significant degree of overlap in overexpressed genes between YFP-LRCs and *Lgr5*-GFP<sup>hi</sup> cells ( $P < 0.0001$ ) (Fig. 2c). Furthermore, quantitative polymerase chain reaction with reverse transcription (qRT-PCR) comparison of YFP-LRCs with *Lgr5*-GFP<sup>hi</sup> cells isolated from *Lgr5-EGFP-IRES-creERT2* mice demonstrated equivalent expression not only of *Lgr5* but also ‘quiescent’ stem-cell markers *Tert*, *Lrig1* and *Hopx*. In addition, there was upregulated expression of Paneth and enteroendocrine lineage genes in YFP-LRCs compared to *Lgr5*-GFP<sup>hi</sup> cells (Fig. 2d). These comparisons suggest that most YFP-LRCs are a subpopulation of *Lgr5*-expressing cells. This was confirmed using spectral detection confocal microscopy to overlay YFP and GFP fluorescence on *Cyp1a1-H2B-YFP/Lgr5-EGFP-IRES-creERT2* mice to confirm that 98% (40 out of 41) of YFP-LRCs also expressed *Lgr5* (Fig. 2e).

### Elevated *Lgr5* defines LRC maturation into Paneth cells

YFP-LRCs have a combined secretory and stem-cell signature, indicating that they may have a secretory fate. Confocal microscopy was first used to track YFP inheritance into the Paneth cell population from 10 days (when all YFP-LRCs are formally defined) to 21 days post-induction (Fig. 3a). YFP-LRCs decrease in number over time whereas the number of YFP<sup>+</sup> Paneth cells increases (Fig. 3b). This reciprocal relationship shows that one fate of YFP-LRCs is differentiation to Paneth cells. Moreover, the increasing number of YFP<sup>+</sup> Paneth cells over the 11-day chase accounts for 3.6 new Paneth cells per crypt (see Methods). This chase period is relatively short compared



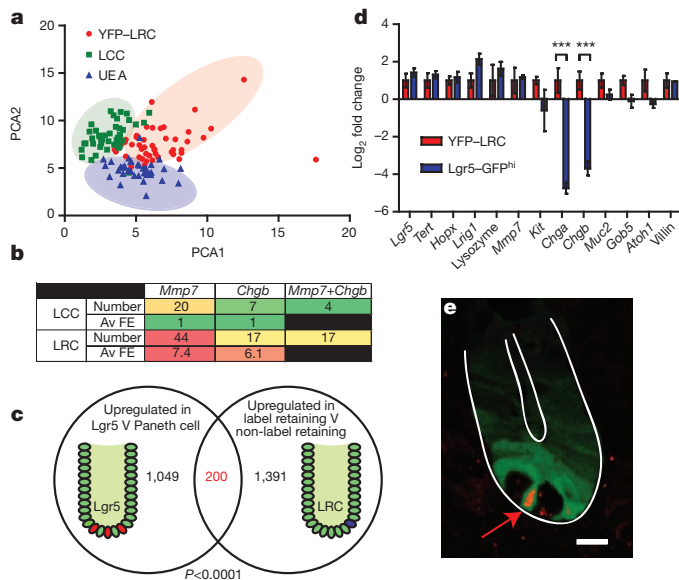


**Figure 2 | YFP-LRCs are a discrete Lgr5-expressing subpopulation.**

**a**, Principal component analysis (PCA) on single-cell Fluidigm qRT-PCR data from 48 single YFP-LRCs (red), LCCs (green) and CD24<sup>+</sup>UEA<sup>+</sup> (blue) cells. **b**, Summary table of single-cell data showing the number of cells expressing secretory cell transcripts ( $n = 48$ ) and the log fold change expression level of expressing cells (Av FE) relative to LCCs. **c**, Venn diagram demonstrating the overlap in overexpressed genes between YFP-LRCs and Lgr5<sup>+</sup> cells. **d**, qRT-PCR data comparing the expression patterns of YFP-LRCs and Lgr5<sup>+</sup> cells. Data are mean  $\pm$  s.e.m. \*\*\* $P < 0.005$ . Two-tailed Student's  $t$ -test. **e**, Representative confocal microscopy image of a Lgr5-GFP<sup>+</sup>/YFP-LRC cell. YFP, red; Lgr5, green. Scale bar, 10  $\mu$ m.

to the turnover time of Paneth cells (42 days), indicating that the direct conversion of LRCs to Paneth cells without any cell division could create around 14 ( $3.6 \times 42/11$ ) Paneth cells per crypt over this time. With an estimated 15 Paneth cells per crypt it is likely that most, if not all, Paneth cells originate via LRCs.

We next investigated whether a subset of Lgr5<sup>+</sup> cells could be identified with maturing Paneth cell features independent of the label-retaining marker and further differentiated in Paneth cell status to YFP-LRCs. A subset of Lgr5-GFP<sup>hi</sup> cells that stained with UEA as a marker of Paneth cells was identified and isolated by flow sorting and confirmed to be enriched for Paneth cell transcripts *Mmp7* and *Defa5* (Fig. 3c–f).

To determine alternative fates for YFP-LRCs, the upper crypt region was analysed at 14 days post-induction for the presence of YFP<sup>+</sup> cells transiting from the crypt base. Such cells are infrequent owing to the rapid rate of migration through the crypt (Fig. 3g)<sup>21</sup>. The vast majority of YFP<sup>+</sup> cells (24 out of 25) present above the crypt base were chromogranin A<sup>+</sup> enteroendocrine cells. This proportion effectively eliminates the numerically more abundant absorptive or Goblet cells as arising from YFP-LRCs. Overall, LRCs appear to be a Paneth cell precursor population but also capable of some enteroendocrine differentiation.

### LRCs possess multi-lineage growth potential

To determine whether YFP-LRCs are irreversibly committed to a secretory fate we functionally assessed their growth potential in organoid culture<sup>22</sup>. YFP-LRCs and Lgr5-GFP<sup>hi</sup> cells plated at the same densities were roughly equivalent in ability to form organoids (0.15% versus 0.25%). The organoids from YFP-LRCs demonstrated crypt budding at around 7 days and were found to resemble intact crypt-villus units as previously described (Supplementary Fig. 4). YFP-LRCs are therefore capable in a regenerative setting of acquiring stem-cell characteristics.

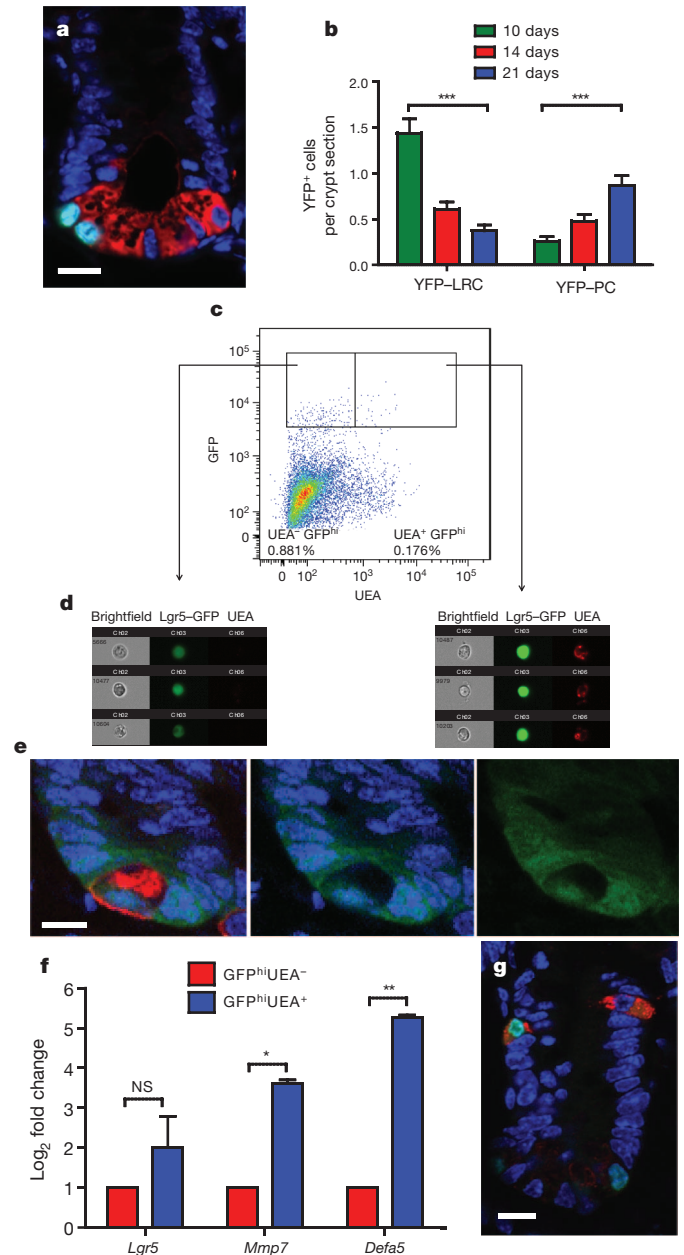


**Figure 3 | Acquisition of Paneth and enteroendocrine cell characteristics from YFP-LRCs.** **a**, Image demonstrating that after 4 weeks all YFP<sup>+</sup> cells are Paneth cells as confirmed by lysozyme staining. **b**, Assessment of the number of YFP<sup>+</sup> cells between 10 and 21 days demonstrates a reciprocal relationship in cell types: YFP<sup>+</sup> Paneth cells (YFP-PC) increase in frequency as YFP-LRCs decrease (mean  $\pm$  s.e.m.);  $n = 100$ . \*\*\* $P < 0.001$ . Mann-Whitney  $U$ -test. **c**, FACS analysis showing that around 15% of Lgr5-GFP<sup>hi</sup> cells are marked by UEA. **d**, Image-stream images showing examples of Lgr5-GFP<sup>hi</sup>UEA<sup>−</sup> and Lgr5-GFP<sup>hi</sup>UEA<sup>+</sup> cells from **c**. Note the greater intensity of GFP in the latter. **e**, Confocal image showing a GFP<sup>+</sup>UEA<sup>+</sup> cell. Left panel: UEA (red), Lgr5-GFP (green) and DAPI (blue). Middle panel: Lgr5-GFP and DAPI. Right panel: Lgr5-GFP alone. **f**, qRT-PCR data showing upregulation of Paneth cell transcripts *Mmp7* and *Defa5* in the GFP<sup>hi</sup>UEA<sup>+</sup> subpopulation. (mean  $\pm$  s.e.m.); \* $P < 0.05$ ; \*\* $P < 0.01$ . Two-tailed Student's  $t$ -test. NS, not significant. **g**, Representative image of rare YFP<sup>+</sup> chromogranin A<sup>+</sup> enteroendocrine cells in the upper crypt at 2 weeks post-induction. Scale bars: 10  $\mu$ m (**a**, **e**, **g**).

### LRCs contribute to the stem-cell pool only after injury

To functionally assess whether YFP-LRCs have stem-like characteristics *in vivo* we used a novel dimerizable Cre recombinase strategy (Fig. 4)<sup>23</sup>. *dicreAB* mice are capable of clonally marking cells when two

inactive Cre fragments heterodimerize to form functional recombinase by the binding of Ariad rapamycin analogues to FKHB-ligand-binding domains present in both fragments. The carboxy-terminal peptide of Cre (CreB) is expressed constitutively from the *Rosa26* locus whereas the amino-terminal peptide (CreA) is expressed as an H2B–CreA fusion protein under the control of the  $\beta$ NF inducible promoter, *Cyp1a1* (Fig. 4a, b). Treatment of double transgenic *Rosa26-creB* and *Cyp1a1-H2B-creA* mice with  $\beta$ NF induces expression of

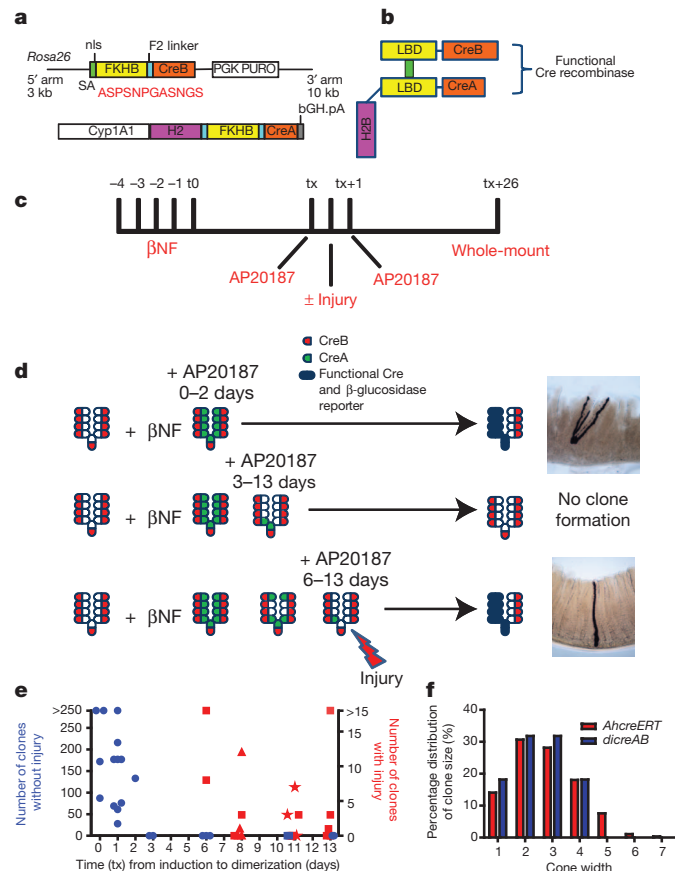


**Figure 4 | LRCs only demonstrate clonogenicity after injury *in vivo*.**

**a**, Diagrammatic representation of diCreAB construct showing position of FKHB dimerizing domain in protein fusions to both N terminus (*H2B-creA*) and C terminus (*creB*) regions of a split *cre* gene. **b**, Representation of the *in vivo* dimerization of CreA and CreB to form a functional Cre recombinase. Dimerizing agent (AP20187) (green) mediates dimerization of two FKHB domains thereby creating a functional Cre complex. **c**, Generic schematic of induction protocol to test *in vivo* clonogenicity of cells expressing *creA*.  $\beta$ NF induces *H2B-creA* against a background of constitutive *creB* expression. With time (tx) following  $\beta$ NF administration *H2B-creA* is first expressed and then becomes restricted. Expressing cells are tested for their ability to generate clones after treatment with dimerizing agent (AP20187) that allows a functional Cre complex to form and thereby mediate recombination of a *cre* reporter gene. **d**, Schematic showing conditions for clone formation. AP20187 is sufficient for clone formation 0–2 days post  $\beta$ NF (top row) but not between 3–13 days (middle row). Between 6–13 days combined injury and AP20187 are required for clone formation (bottom row). In the clone shown, the injury was hydroxyurea. **e**, Numbers of clones formed over the total murine intestinal tract in the absence of injury (blue) and in the presence of injury (red) and showing that treatment with AP20187 only generates clones in the absence of injury up to 2 days after  $\beta$ NF treatment. When AP20187 treatment is combined with injury, clones are generated up to 14 days post  $\beta$ NF induction of *H2B-creA* (squares, hydroxyurea; stars, irradiation; triangles, doxorubicin). **f**, Clone width (measured in cell diameters) comparisons from data acquired at 3 weeks after induction of clones with  $\beta$ NF in *AhcreERT* mice ( $n = 277$ )<sup>8</sup> and 3 weeks after dimerization of Cre with AP20187 in *dicreAB* mouse ( $n = 23$ ) induced with  $\beta$ NF and then dimerized and injured 13 days later.

*H2B-creA* throughout the epithelium on a background of constitutive *creB* expression. With time after  $\beta$ NF induction only LRCs retain H2B–CreA, in a manner analogous to H2B–YFP. Administration of intravenous dimerizing agent causes the two fragments of Cre to form a functional protein with subsequent downstream reporter expression.

By varying the interval between  $\beta$ NF induction and Cre dimerization we show that, in the absence of injury, crypt cells form clones only up to 3 days between  $\beta$ NF induction and dimerization (Fig. 4c, d). With longer induction and dimerization intervals (>3 days) clone formation is not observed. However, induction–dimerization intervals of up to 14 days induced clone formation when combined with intestinal injury (Fig. 4e). These clones were noted to contain all differentiated cell lineages at appropriate frequency (Supplementary Fig. 5). Clone size analysis compared to work we have previously published for pulse–chase clone induction after tamoxifen treatment demonstrates that LRC-derived clones occupy the predicted size distribution expected for clones of equivalent age (3 weeks) and that arises from clone expansion due to neutral drift and leads to clone fixation as clones occupy whole crypts (Fig. 4f)<sup>8</sup>.

These results demonstrate that rapidly cycling stem cells (not having diluted CreA within 3 days) are, as expected, competent to produce clonal progeny in the steady state. The lack of clone formation with longer induction–dimerization intervals could either be due to insufficient bioavailability of H2B–CreA for recombination or that H2B–CreA-retaining cells are not clonogenic. The injury models indicate the latter, demonstrating that LRCs do not maintain the stem-cell pool during homeostasis. Under conditions of injury/regeneration LRCs are capable of clonogenic growth by recall to the self-renewing pool of stem cells. To our knowledge this is the first demonstration of *in vivo* lineage tracing based on label retention in a mammalian system.

### Mature Paneth cells are not proliferative

The differentiation of YFP–LRCs into Paneth cells has the consequence that both cell types co-exist. To confirm that Paneth cells are indeed terminally differentiated and not able to proliferate after damage, H2B–YFP mice were induced with  $\beta$ NF in a pulse–chase experiment with a chase period (5 weeks) that extended beyond the lifespan of YFP–LRCs. These animals were then irradiated and the response of the residual population of YFP<sup>+</sup> Paneth cells determined. In control (non-irradiated) animals YFP<sup>+</sup> cells were invariably isolated Paneth cells. After radiation treatment (at 1, 2 and 7 days), intestinal sections were examined for the doublets or strings of YFP<sup>+</sup> cells that would arise if Paneth cells were undergoing post-irradiation division. The pattern of YFP<sup>+</sup> positivity remained unchanged from the controls, suggesting that Paneth cells do not divide (Supplementary Fig. 6).

### Discussion

There are a number of alternative functional roles for a quiescent population. First, they could be a stem population co-existing and in dynamic equilibrium with the rapidly cycling cells<sup>6</sup>. The dynamics of stem-cell renewal, however, have shown that the turnover of a single population of rapidly dividing cells is sufficient to drive changes in clone size distribution, leading to clones that occupy whole crypts<sup>8,9</sup>. Second, they could be a dormant or reserve stem-cell population that is only active under conditions of epithelial stress or injury<sup>10</sup>. Third, they could be terminally differentiated Paneth cells<sup>2</sup>. Last, and not previously described, they could be committed to differentiate and no longer contribute to stem-cell functions.

Our observations establish the functional role of LRCs. They are normally destined to become Paneth and enteroendocrine cells but retain the ability to reacquire stem-cell function and can be recruited to serve as a functional clonogenic stem population under conditions of regeneration. Historically it is accepted that following stem-cell ablation cells normally destined for differentiation can regenerate the stem-cell compartment<sup>12</sup>. However, the current findings demonstrate



directly that a committed precursor can be recalled to the stem-cell pool after damage in a similar manner to that shown recently for Dll1<sup>+</sup> secretory precursors<sup>24</sup>.

Our observations resolve the apparent paradox that quiescence markers are expressed within a population of Lgr5<sup>+</sup> cells that are viewed as rapidly cycling<sup>17</sup>. Around 20% of Lgr5<sup>+</sup> cells are largely quiescent and continue to express Lgr5 before Paneth cell maturation.

Lgr5<sup>+</sup> cells have been implicated as cancer stem cells in colonic cancers, and higher frequencies of Lgr5<sup>+</sup> cells in intestinal cancers correlate with more extensive Paneth cell differentiation<sup>25</sup>. Paneth cells may nurture cancer stem cells by niche generation as they do normal stem cells in culture. It will be important to determine the extent to which quiescent secretory intermediates retaining clonogenic potential are maintained in colon cancers and establish the factors that activate them.

## METHODS SUMMARY

**Mouse models and inductions.** *Cyp1a1-H2B-YFP* mice have previously been described<sup>8</sup>. *dicreAB* mice were generated as follows: *creA* and *creB* are two segments of the *cre* coding sequence comprising codons 19–59 and 60–343, respectively, and were fused to other protein motifs with flexible F2 linkers as described previously<sup>23</sup> (see Methods for details).

*Cyp1a1* was induced by ×3 intraperitoneal βNF injections over 24 h (80 mg kg<sup>−1</sup>). Dimerization of Cre fragments was performed by ×2 intravenous AP20187 (Ariad) injections (10 mg kg<sup>−1</sup>).

**Single-cell qRT-PCR.** FACS-sorted single cells underwent single-cell RNA amplification (see Methods for details). Generated cDNA libraries were then used for Fluidigm Biomark high-throughput qRT-PCR against custom-designed and validated primers (see Methods for details). Principal component analysis was carried out in R.

**Quantitative PCR.** qRT-PCR was performed using standard TaqMan or SybGreen assays. Custom primers were validated before use. For experiments where cell numbers were limiting, cDNA was amplified using a custom protocol (see Methods for details). Fluidigm qRT-PCR was performed as per the manufacturer's protocol.

**Full Methods** and any associated references are available in the online version of the paper.

Received 26 July 2012; accepted 30 January 2013.

Published online 27 February 2013.

1. Barker, N. *et al.* Identification of stem cells in small intestine and colon by marker gene Lgr5. *Nature* **449**, 1003–1007 (2007).
2. Roth, S. *et al.* Paneth cells in intestinal homeostasis and tissue injury. *PLoS ONE* **7**, e38965 (2012).
3. Powell, A. E. *et al.* The Pan-ErbB negative regulator Lrig1 is an intestinal stem cell marker that functions as a tumor suppressor. *Cell* **149**, 146–158 (2012).
4. Sangiorgi, E. & Capecchi, M. R. Bmi1 is expressed *in vivo* in intestinal stem cells. *Nature Genet.* **40**, 915–920 (2008).
5. Montgomery, R. K. *et al.* Mouse telomerase reverse transcriptase (mTert) expression marks slowly cycling intestinal stem cells. *Proc. Natl Acad. Sci. USA* **108**, 179–184 (2011).
6. Takeda, N. *et al.* Interconversion between intestinal stem cell populations in distinct niches. *Science* **334**, 1420–1424 (2011).
7. Wong, V. W. *et al.* Lrig1 controls intestinal stem-cell homeostasis by negative regulation of ErbB signalling. *Nature Cell Biol.* **14**, 401–408 (2012).

8. Lopez-Garcia, C., Klein, A. M., Simons, B. D. & Winton, D. J. Intestinal stem cell replacement follows a pattern of neutral drift. *Science* **330**, 822–825 (2010).
9. Snippert, H. J. *et al.* Intestinal crypt homeostasis results from neutral competition between symmetrically dividing Lgr5 stem cells. *Cell* **143**, 134–144 (2010).
10. Li, L. & Clevers, H. Coexistence of quiescent and active adult stem cells in mammals. *Science* **327**, 542–545 (2010).
11. Tian, H. *et al.* A reserve stem cell population in small intestine renders Lgr5-positive cells dispensable. *Nature* **478**, 255–259 (2011).
12. Potten, C. S., Hume, W. J., Reid, P. & Cairns, J. The segregation of DNA in epithelial stem cells. *Cell* **15**, 899–906 (1978).
13. Potten, C. S., Owen, G. & Booth, D. Intestinal stem cells protect their genome by selective segregation of template DNA strands. *J. Cell Sci.* **115**, 2381–2388 (2002).
14. Demidov, O. N. *et al.* Wip1 phosphatase regulates p53-dependent apoptosis of stem cells and tumorigenesis in the mouse intestine. *Cell Stem Cell* **1**, 180–190 (2007).
15. He, X. C. *et al.* BMP signaling inhibits intestinal stem cell self-renewal through suppression of Wnt-β-catenin signaling. *Nature Genet.* **36**, 1117–1121 (2004).
16. He, X. C. *et al.* PTEN-deficient intestinal stem cells initiate intestinal polyposis. *Nature Genet.* **39**, 189–198 (2007).
17. Muñoz, J. *et al.* The Lgr5 intestinal stem cell signature: robust expression of proposed quiescent '4' cell markers. *EMBO J.* **31**, 3079–3091 (2012).
18. Ireland, H., Houghton, C., Howard, L. & Winton, D. J. Cellular inheritance of a Cre-activated reporter gene to determine Paneth cell longevity in the murine small intestine. *Dev. Dyn.* **233**, 1332–1336 (2005).
19. Foudi, A. *et al.* Analysis of histone 2B-GFP retention reveals slowly cycling hematopoietic stem cells. *Nature Biotechnol.* **27**, 84–90 (2009).
20. Sato, T. *et al.* Paneth cells constitute the niche for Lgr5 stem cells in intestinal crypts. *Nature* **469**, 415–418 (2011).
21. Cheng, H. & Leblond, C. P. Origin, differentiation and renewal of the four main epithelial cell types in the mouse small intestine. V. Unitarian Theory of the origin of the four epithelial cell types. *Am. J. Anat.* **141**, 537–561 (1974).
22. Sato, T. *et al.* Single Lgr5 stem cells build crypt-villus structures *in vitro* without a mesenchymal niche. *Nature* **459**, 262–265 (2009).
23. Jullien, N., Sampieri, F., Enjalbert, A. & Herman, J. P. Regulation of Cre recombinase by ligand-induced complementation of inactive fragments. *Nucleic Acids Res.* **31**, e131 (2003).
24. van Es, J. H. *et al.* Dll1<sup>+</sup> secretory progenitor cells revert to stem cells upon crypt damage. *Nature Cell Biol.* **14**, 1099–1104 (2012).
25. Lewis, A. *et al.* Severe polyposis in *Apc*(1322T) mice is associated with submaximal Wnt signalling and increased expression of the stem cell marker Lgr5. *Gut* **59**, 1680–1686 (2010).

**Supplementary Information** is available in the online version of the paper.

**Acknowledgements** This research was supported by Cancer Research UK (S.J.A.B., H.I.Z., A.M.N., R.R., R.K. and D.J.W.). L.V. was supported by a KWF fellowship. We thank D. Tan for providing the single-cell RNA amplification protocol. We also thank M. de la Roche, R. von Furstenberg and S. Henning for advice with the *in vitro* culture work. We acknowledge the following core facilities at CRUK/CRI: The Transgenic Laboratory, Biological Resource Unit, Flow Cytometry, Histopathology, Microscopy, Genomics and Bioinformatics and the CRUK Paterson Institute Microarray Facility. We thank R. J. Davies, A. Klein and A. Ibrahim for manuscript discussions.

**Author Contributions** S.J.A.B. designed and performed experiments and wrote the paper. H.I.Z. designed and developed the H2B-YFP model and performed experiments. R.R. performed the bioinformatic analysis. A.M.N. and L.V. performed experiments. R.K. designed experiments and performed bioinformatic analysis. D.J.W. designed experiments, developed the diCreAB model and wrote the paper.

**Author Information** Data were deposited to the GEO database under accession number GSE43772. Reprints and permissions information is available at [www.nature.com/reprints](http://www.nature.com/reprints). The authors declare no competing financial interests. Readers are welcome to comment on the online version of the paper. Correspondence and requests for materials should be addressed to D.J.W. ([doug.winton@cruk.cam.ac.uk](mailto:doug.winton@cruk.cam.ac.uk)).

## METHODS

**Mice models.** *Cyp1a1-H2B-YFP* mice have previously been described<sup>8</sup>. Briefly, *Cyp1a1-H2B-YFP* mice were created using conventional cloning techniques involving removing the human *H2B* coding sequence from the pBOS-H2BGFP vector (BD Pharmingen) and then ligating this into pIRES-eYFP (BD Biosciences). *Lgr5-EGFP-IRES-creERT2* mice were purchased from the Jackson Laboratory.

*dicreAB* mice were generated as follows: *creA* and *creB* are two segments of the *cre* coding sequence comprising codons 19–59 and 60–343, respectively, and were fused to other protein motifs with flexible F2 linkers as described previously<sup>23</sup>. The FKBP dimerizing domain and AP20187 was a gift provided by Ariad Pharmaceuticals. *creA* was synthesized as a single fusion gene comprising in 5' to 3' order *H2B-F2 linker-FKBP-F2 linker-creA-pA* with flanking BglII sites to permit excision.

*H2B-F2 linker-FKBP-F2 linker-creA-pA* was subcloned using BglII into pAh1R1 such that the fusion gene was under the control of 12-kb of the rat *CYP1A1* promoter element<sup>26</sup>. The cassette comprising *Cyp1a1-H2B-F2 linker-FKBP-F2 linker-creA-pA* (or *Cyp1a1-H2B-LBD-creA*) was excised from the plasmid backbone using NotI and this fragment purified for pronuclear injection. Oocyte injection was performed by the Transgenic Lab, within the CRI.

*CreB* was synthesized as *FKB-F2 linker-creB-pA* with flanking NheI sites for excision (sequences available on request). This cassette was cloned in the NheI site of *ROSMEs13* as described previously<sup>27</sup>. The linearized plasmid was introduced into ES cells and selected with puromycin. The S6B6 ES cell line was derived from 129/sv/C57BL6/j hybrid embryos. Initial screening of ES-derived colonies was confirmed by long-range PCR and sequencing and mice generated as previously described<sup>28</sup>.

Mice were bred and housed according to UK Home Office guidelines. For induction of *Cyp1a1-H2B-YFP* mice, 3 intraperitoneal injections of 80 mg kg<sup>-1</sup> of  $\beta$ NF over a 36-h period were used. T0 was defined as the same day as the last  $\beta$ NF injection. For inductions of *dicreAB* mice, 5 daily intraperitoneal injections of 80 mg kg<sup>-1</sup>  $\beta$ NF were used. Dimerization of Cre was performed using two intravenous injections of AP20187 10 mg kg<sup>-1</sup> (Ariad Pharmaceuticals) over 2 days. Injury models involved single doses: of hydroxyurea (intraperitoneally, 1 g kg<sup>-1</sup>), doxorubicin (intraperitoneally, 10 mg kg<sup>-1</sup>) that target DNA replicating cells (by inhibition of nucleotide incorporation and topoisomerase respectively) and  $\gamma$ -irradiation (6 Gy) that preferentially kills rapidly cycling cell as they attempt to replicate damaged DNA template.

**Tissue preparation, immunofluorescence and whole-mounting.** Preparation of tissues for immunofluorescence was performed by fixation in 4% PFA for 48 h followed by 20% sucrose for a further 48 h. Tissue was then embedded in OCT and sectioned at 6  $\mu$ m. Antigen retrieval was performed using 1% SDS for 5 min and then blocked with 5% NDS for 30 min. Sections were stained overnight at 4 °C for all primary antibodies and 2 h at room temperature for UEA. Secondary antibodies were applied for 1 h at room temperature. Nuclear staining was achieved using ProLong Gold antifade reagent with DAPI (Invitrogen). Sections were visualized on a C1Si Nikon confocal microscope.

For UEA and lysozyme co-expression experiments, primary anti-lysozyme was incubated overnight at 4 °C followed by incubation with UEA-AF647 and an AF555-anti-rabbit secondary for 2 h at room temperature. Differentiated Paneth cells were seen to overlay with both markers but in addition UEA marked a subset of goblet cells in both the upper crypt and villus.

Whole-mounting of intestines and detection of SYN $\beta$ Glu activity was carried out as previously described<sup>8</sup>. Organoids were prepared for immunofluorescence as previously reported<sup>29</sup>. Clone sizes were measured as previously described<sup>8</sup>. Comparisons were made between *dicreAB* clones at 3 weeks and those analysed in this publication at the same time.

**Confocal counting experiments.** For assessment of YFP-LRC position, YFP-LRC number and YFP-Paneth cell number, 100 crypts were counted for each time point in the proximal small intestine. Position +1 was defined as the apical two cells in the crypt and subsequent positions followed superiorly. Illuminating laser intensity was set uniformly between all comparisons to allow for reproducible and comparable detection of YFP positivity. Paneth cells were identified based on cytoplasmic and/or membranous UEA positivity. Countable crypts were initially detected by DAPI confirmation of a complete half crypt. The crypt of interest was then assessed for UEA or YFP positivity up to position +6. Label-retaining index was calculated as the mean number of YFP-LRCs at crypt positions +1 to +6 2 weeks after  $\beta$ NF induction.

EdU and YFP dual labelling experiments were performed by injecting mice with three injections of 1 mg per mouse (intraperitoneal) EdU over 24 h followed by three (intraperitoneal)  $\beta$ NF (80 mg kg<sup>-1</sup>) injections over the next 24 h. Mice were killed 14 days later and EdU visualized using the Invitrogen Click-iT imaging detection kit as per the manufacturer's protocol.

The murine crypt has a population of 250 cells<sup>30</sup>. Confocal assessment of an optimally sectioned 2  $\mu$ m optical section of a small intestinal crypt shows  $39.3 \pm 1.1$  cellular nuclei. A single section through a crypt is therefore representative of 16% of the total number of crypt cells.

Images were acquired using a C1Si Nikon confocal microscope. Images were edited on EZ-C1 3.20 FreeViewer and Adobe Photoshop CS3. Volocity software was used to generate the H2B-YFP crypt three-dimensional reconstruction and video.

**Flow cytometry.** Intestinal epithelial single-cell preparation was performed as previously described<sup>31</sup>. Briefly, after dissection intestines were everted and fed onto either 3-mm (distal SI) or 4-mm (proximal SI) diameter glass rod spirals. They were then incubated in 50 ml of HBSS without Ca<sup>2+</sup> and Mg<sup>2+</sup> supplemented with 10  $\mu$ M EDTA and 10 mM NaOH at 37 °C for 1 h. Every 10 min the spirals were pulsed using a vibrating stirrer (Chemap AG, model CH-8604) and the HBSS collected and replaced with fresh HBSS. Fractions 2–6 were pooled and then re-suspended in  $1 \times 0.05\%$  Trypsin-EDTA at 37 °C for 7 min with regular agitation. Epithelial samples were filtered through a 70  $\mu$ m mesh into cold 2% FBS/PBS and washed twice more.

After staining with antibodies and UEA, samples were sorted or analysed using either a BD FACS Aria SORP or BD LSR II, respectively. Single stained and unstained controls were always used, and propidium iodide (2.5  $\mu$ g ml<sup>-1</sup>) was used to discriminate between live and dead cells.

For flow cytometric assessment of the percentage of YFP-LRCs, the denominator was defined as the number of single, live cells from analysis of 50,000 cells of pooled fractions 2–6 of a single cell epithelial preparation; that is, crypt enriched. The numerator was defined as the number of CD24<sup>+</sup> UEA<sup>-</sup> YFP<sup>+</sup> cells; that is, non-Paneth-cell, crypt-located YFP-LRCs from the same population.

Single-cell fluorescent images were acquired using an Amnis ImageStream. FACS data were analysed using FlowJo v7.5.5 (TreeStar).

**Affymetrix exon microarray and analysis.** Six age- and sex-matched *Cyp1a1-H2B-YFP* mice 10 days after  $\beta$ NF induction were used comparing three cell populations from each mouse. After flow sorting 30,000 cells from the respective populations, RNA extraction was performed using the RNeasy Micro kit (Qiagen) with on column DNase digestion. RNA quality was assessed using a 2100 Bioanalyzer (Agilent Technologies).

RNA amplification and hybridization was performed at the Paterson Institute, Manchester, UK, Microarray Facility using Nugen Ovation Pico WTA System for amplification and then hybridization to a Mouse Exon 1.0 ST Array. Arrays were scanned using an Affymetrix GeneChip scanner 3000 running GCOS software.

The raw data were RMA (robust multi-array average)<sup>32</sup> normalized using the Affymetrix Power Tools (APT) software package and the analysis was restricted to 'core' probe sets which are supported by Refseq<sup>33</sup> annotations. The data set was filtered on both the cross-hybridizing and undetected probe sets<sup>34</sup> and further processing was carried out in R<sup>35</sup> using a number of Bioconductor Packages<sup>36</sup>. Differential expression analysis was carried out in *limma*<sup>37</sup> and the hypergeometric test was used to test for significant overlap with Lgr5<sup>+</sup> cells. The Benjamini-Hochberg method for multiple correction was applied to *P* values from both methods. The data were deposited in the GEO database (accession number GSE43772).

**Organoid culture.** Culture of organoids was performed as previously described and including the use of Wnt3A (R&D) (100 ng ml<sup>-1</sup>) for the first 3 days after plating<sup>22</sup>. Cells were plated in 24-well plates at a density of ~50,000 cells in 50  $\mu$ l matrigel. Organoids were counted as budding organoids at 10 days post seeding.

**Single-cell expression profiling.** For single-cell expression profiling, single cells were flow-sorted into 96-well PCR plates (Star Lab) with 4  $\mu$ l of first-strand synthesis buffer in each well containing 1  $\mu$ l 5 $\times$  SuperScript III buffer (Invitrogen), 0.5  $\mu$ l 5% NP-40 (Pierce), 0.25  $\mu$ l 1 mM dNTP mix (Thermo Scientific), 0.075  $\mu$ l 1  $\mu$ M MO4d(T) primer (DNA Technology A/S), 0.05  $\mu$ l 0.1 M DTT (Invitrogen), 0.25  $\mu$ l SuperRNaseIN (Ambion), 0.25  $\mu$ l RNase OUT (Invitrogen), 1  $\mu$ l Spike *Arabidopsis* DNase treated total RNA 10<sup>-1</sup> pg  $\mu$ l<sup>-1</sup> (gift from A. Giakountis) and 0.625  $\mu$ l nuclease-free H<sub>2</sub>O (Ambion); and then incubated at 65 °C for 5 min followed by 45 °C for 2 min. Then 0.5  $\mu$ l of SuperScript III (Invitrogen) was added to each aliquot and incubated at 45 °C for 15 min and then 65 °C for 10 min.

One microlitre of exonuclease mix was then added containing 0.2  $\mu$ l exonuclease I (Thermo Scientific), 0.6  $\mu$ l 75 mM MgCl<sub>2</sub> (Ambion) and 0.2  $\mu$ l nuclease-free H<sub>2</sub>O (Ambion) and incubated at 37 °C for 30 min and 80 °C for 25 min.

Seven microlitres of a reaction mix was then added containing 2.6  $\mu$ l 5 $\times$  TdT buffer (Promega), 0.097  $\mu$ l 100 mM dATP (Thermo Scientific), 0.5  $\mu$ l RNase H (Invitrogen), 0.5  $\mu$ l TdT (Promega), 3.303  $\mu$ l nuclease-free H<sub>2</sub>O (Ambion) and incubated at 37 °C for 15 min and 70 °C for 10 min.

Sixteen microlitres of amplification mix 1 was then added to 4  $\mu$ l of polyadenylated cDNA in triplicate, containing 2  $\mu$ l 10 $\times$  ExTaq buffer (Takara),



0.13 µl 100 mM dATP/dGTP/dCTP/dTTP (Thermo Scientific), 1.65 µl 100 µM MO<sub>4</sub>(T) primer (DNA Technology A/S), 0.2 µl ExTaq polymerase (Takara) and 11.63 µl nuclease-free H<sub>2</sub>O (Ambion) and cycled for 94 °C for 1 min, 50 °C for 2 min and 72 °C for 2 min followed by 35 cycles of 94 °C for 30 s, 60 °C for 30 s and 72 °C for 2 min.

The triplicate products were then pooled and 2 µl of pooled product was added in duplicate to 18 µl of amplification mix 2 containing 2 µl 10× ExTaq buffer (Takara), 1.6 µl 2.5 mM dNTP mix (Takara), 0.4 µl 100 µM T7-MO4 primer (DNA Technology A/S), 0.2 µl ExTaq polymerase (Takara) and 13.8 µl of nuclease-free water (Ambion) and cycled for 35 cycles at 94 °C for 30 s, 60 °C for 30 s and 72 °C for 2 min. The duplicate samples were then pooled. Subsequent cDNA was then cleaned up using Zymo Clean and Concentrate kit and normalized based on Nanodrop quantification.

Normalized single-cell amplified cDNA was run on the Fluidigm Biomark EvaGreen qRT-PCR system against custom-designed primer pairs. Data were analysed using Fluidigm Real-Time PCR Analysis software (v3.0.2) and samples were normalized to spike *Arabidopsis* RNA primers LTP4 and TIM. Principal component analysis was carried using the prcomp function of the R statistical computing and graphics language. Cells were eliminated from PCA if the mouse housekeeping genes had failed to fire.

**RNA amplification.** For *Lgr5*/UEA qRT-PCR, cell numbers were limiting so a modified single-cell RNA amplification protocol was used<sup>38</sup>. Briefly, 1 µl of extracted total RNA underwent first-strand synthesis in a buffer containing 1 µl 5× SuperScript III buffer (Invitrogen), 0.5 µl 5% NP-40 (Pierce), 0.25 µl 1 mM dNTP mix (Thermo Scientific), 0.075 µl 1 µM MO<sub>4</sub>(T) primer (DNA Technology A/S), 0.05 µl 0.1 M DTT (Invitrogen), 0.25 µl SuperRNaseIN (Ambion), 0.25 µl RNase OUT (Invitrogen) and 0.625 µl nuclease-free H<sub>2</sub>O (Ambion); and then incubated at 65 °C for 5 min followed by 45 °C for 2 min. 0.5 µl of SuperScript III (Invitrogen) was then added to each aliquot and incubated at 45 °C for 15 min and then 65 °C for 10 min.

One microlitre of exonuclease mix was then added containing 0.2 µl exonuclease I (Thermo Scientific), 0.6 µl 75 mM MgCl<sub>2</sub> (Ambion) and 0.2 µl nuclease-free H<sub>2</sub>O (Ambion) and incubated at 37 °C for 30 min and 80 °C for 25 min.

Seven microlitres of a reaction mix was then added containing 2.6 µl 5× TdT buffer (Promega), 0.097 µl 100 mM dATP (Thermo Scientific), 0.5 µl RNase H (Invitrogen), 0.5 µl TdT (Promega), 3.303 µl nuclease-free H<sub>2</sub>O (Ambion) and incubated at 37 °C for 15 min and 70 °C for 10 min.

Sixteen microlitres of amplification mix was then added to 4 µl of polyadenylated cDNA in triplicate, containing 2 µl 10× ExTaq buffer (Takara), 0.13 µl 100 mM dATP/dGTP/dCTP/dTTP (Thermo Scientific), 1.65 µl 100 µM MO<sub>4</sub>(T) primer (DNA Technology A/S), 0.2 µl ExTaq polymerase (Takara) and 11.63 µl nuclease-free H<sub>2</sub>O (Ambion) and cycled at 94 °C for 1 min, 50 °C for 2 min and 72 °C for 2 min followed by 35 cycles at 94 °C for 30 s, 60 °C for 30 s and 72 °C for 2 min.

Subsequent cDNA was then cleaned up using Zymo Clean and Concentrate kit and normalized based on Nanodrop quantification. qRT-PCR was then performed as follows using custom-designed 3' orientated primers.

**qRT-PCR.** Sybr green qRT-PCR was performed under standard conditions using a Rotorgene RG3000 (Corbett Research) and data analysed using Rotorgene 6 software. Custom primers were validated before use using standard Sybr green qRT-PCR and agarose gel electrophoresis of PCR products. Samples were normalized to housekeeping genes β-actin or β2 microglobulin.

TaqMan qRT-PCR was performed under standard conditions as above. Samples were normalized to housekeeping genes ribosomal protein L19 or glyceraldehyde 3-phosphate dehydrogenase (*Gapdh*).

**Antibodies and lectin.** *Ulex europaeus* agglutinin I (UEA)-Alexa Fluor 647, 1:1,000 (custom conjugation; AbD Serotec). Anti-CD24-Pacific blue, 1:200 (Biolegend). Anti-substance P, 1:100 (Millipore). Anti-lysozyme, 1:1,000 (Dako). Anti-chromogranin A, 1:400 (Abcam). Anti-villin, 1:100 (Abcam).

**Primers used for single cell-expression profiling.** *Abca1* forward, 5'-TTGTTCCAAAGAGCCATGTG-3'; *Abca1* reverse, 5'-GGAATGAGGGCC AATGATAA-3'; *Apc* forward, 5'-TGGGAGATGGTTGCCAGGGT-3'; *Apc* reverse, 5'-GTCGGAAGATGCATCAATGGCCT-3'; *At1l* forward, 5'-TGATCAAAAATGCACAAAATTG-3'; *At1l* reverse, 5'-AGAGCCAGTGA GCATTTGGT-3'; β-actin forward, 5'-AGGTGACAGCATTTGCTTCTG-3'; β-actin reverse, 5'-AGGGAGACCAAGCCTTCAT-3'; β2 microglobulin forward, 5'-ATTCACCCCCACTGAGACTG-3'; β2 microglobulin reverse, 5'-GCTATTCTTTCTGCGTGCAT-3'; *Bmi1* forward, 5'-TCATGGTGTGTACCT AAGACAAAAGAC-3'; *Bmi1* reverse, 5'-GGTAAAAAGCCTCATCCAGAG-3'; *Cadps* forward, 5'-TCACATTTTGTCTTTCTGTTTCA-3'; *Cadps* reverse, 5'-CCAGGGTCGCTCAGTTACAG-3'; *CD133* forward, 5'-ATCGGGGAAAC GAAGAAGTT-3'; *CD133* reverse, 5'-ACAGCCGGAAGTAAGAGCAC-3'; *CD44* forward, 5'-CCCCCTTTCTTTTCCAGTT-3'; *CD44* reverse, 5'-ACTTTC

TGCCCCCTCTCCACT-3'; *CD82* forward, 5'-CAGGGTAGGCAATTCTTCCA-3'; *CD82* reverse, 5'-AGCTGCCAAGAAACACCAGT-3'; *Cdk5rap2* forward, 5'-TGCCAAGATGGATGTTCAAA-3'; *Cdk5rap2* reverse, 5'-AAGAGCTTCA GCAACCTGGA-3'; *Chga* forward, 5'-GCAGAGGACCAGGAGCTAGA-3'; *Chga* reverse, 5'-CAGGGGCTGAGAACAAGAGA-3'; *Chgb* forward, 5'-ACAGGAAGAAGGCAGACGAA-3'; *Chgb* reverse, 5'-TCCTTCAGTGAAG GGTCTGT-3'; *Csrnp1* forward, 5'-GCCCCCTCTGTAAGATGGTGA-3'; *Csrnp1* reverse, 5'-GGCACACACACACACACAAA-3'; *DCAMKL-1* forward, 5'-AGGTGGGCTGGGGACTTGACA-3'; *DCAMKL-1* reverse, 5'-TGCAGCAAG TGACAAGGGCA-3'; *Ddahl1* forward, 5'-CCAAACACTAAGGCCGTCAT-3'; *Ddahl1* reverse, 5'-CACACATTGGCTGGAAGATG-3'; *Defa5* forward, 5'-TCTGTCTCAACAATTCTCCA-3'; *Defa5* reverse, 5'-GACACAGCCTGGT CCTCTTC-3'; *Dill1* forward, 5'-TGAGCCAGTCTTCTCTTGAA-3'; *Dill1* reverse, 5'-AGACCCGAAGTGCCTTTGTA-3'; *Dill4* forward, 5'-CCCCTTTTGCCAGC CAGGGG-3'; *Dill4* reverse, 5'-AGGTTGGTCTCGGGGCGAGCA-3'; *Dvl3* forward, 5'-ACACCTTAAGCCACCCCTTT-3'; *Dvl3* reverse, 5'-GCTCTCTG GGGTCTGTATTG-3'; *EphB2* forward, 5'-TCCTCCCTGTCTGTCTCAT-3'; *EphB2* reverse, 5'-CTGGGGTGTACAGTGAATG-3'; *EphB4* forward, 5'-TCC TGACTTGTCTGTCACCAC-3'; *EphB4* reverse, 5'-GAACCAGGTGCCCTTT AACA-3'; *Fgfr2* forward, 5'-TCGAAGGATGGCAAAGCCAGC-3'; *Fgfr2* reverse, 5'-AGTGAGTGGGCGTATCCAAAGCA-3'; *Frs2* forward, 5'-TCTACAGTGGGACTACCATTGCCA-3'; *Frs2* reverse, 5'-ACAGTGGTTACG TTTGCCAAGCA-3'; *Gip* forward, 5'-GGGAAAGGAGGACAAAGAGG-3'; *Gip* reverse, 5'-AGCCAAGCAAGCTAAGGTCA-3'; *Kif20a* forward, 5'-ACAG GAACAGCAGTGGGAAC-3'; *Kif20a* reverse, 5'-CACTAAGTGGGTGCCA TGTG-3'; *Lgr5* forward, 5'-GGGCGTTAAGTCCACTGTGT-3'; *Lgr5* reverse, 5'-CGAACACCTGCGTGAATATG-3'; *Lrig1* forward, 5'-TTCCTTACCGGTG AGACTGG-3'; *Lrig1* reverse, 5'-CCATCACTGTGCCAACACTT-3'; *LTP4* forward, 5'-GTGCTGTGTCAGGAGTCAAAA-3'; *LTP4* reverse, 5'-TCTTCA GGCAAATGATGTCG-3'; *Mcm6* forward, 5'-CTGAAAGGCTCCAGTGAA GG-3'; *Mcm6* reverse, 5'-TCAAGCATTGCTCCAGACAC-3'; *Mctp2* forward, 5'-CATCTGGAGCGTAACCCCTA-3'; *Mctp2* reverse, 5'-CAGTCAAAAAG CAGGTGGA-3'; *Mmp7* forward, 5'-CCCGGTACTGTGATGTACCC-3'; *Mmp7* reverse, 5'-AATGGAGGACCCAGTGAGTG-3'; *Tert* forward, 5'-AGCC GCATTTGGCTCTGCT-3'; *Tert* reverse, 5'-TCGCCTCTGGGAGCTTCCGG-3'; *Muc2* forward, 5'-GTCCGAAGTGTACCCTGGA-3'; *Muc2* reverse, 5'-CCAGGAGTGGAGAAGGTCAG-3'; *Nfat5* forward, 5'-ACTGACCTGCCTT CTTCAT-3'; *Nfat5* reverse, 5'-TTGACTGTCAGCTGTTTACAGAAA-3'; *Nfatc1* forward, 5'-TCATTTGCTCTGCACCAGTC-3'; *Nfatc1* reverse, 5'-GAC GAGAGTCAGGGAAGCAG-3'; *Nfatc3* forward, 5'-TGGGCTCAAGATGA AACCTT-3'; *Nfatc3* reverse, 5'-TAACTGAGGAGGAGCCTGGA-3'; *Ngn3* forward, 5'-ATCTGCCGCGCTCCGACCAT-3'; *Ngn3* reverse, 5'-GCCTGG TCTCCCTTGGGGGA-3'; *Notch1* forward, 5'-TCAGTGTGACCAGACC TTG-3'; *Notch1* reverse, 5'-CAAAAGGCCAGAAAGAGCTG-3'; *Pax6* forward, 5'-GAACAACACAGGCTGTTGGA-3'; *Pax6* reverse, 5'-TGTGTGTGTGCC CAGGTTCA-3'; *Pbx1* forward, 5'-AGAAAGCCATGTGTTGGAC-3'; *Pbx1* reverse, 5'-TGAAAAGGGTGCCTTTCATC-3'; *Rfx6* forward, 5'-TTTTCTT CCTCTTTGGTTTC-3'; *Rfx6* reverse, 5'-GCACAGGGGTAGAAGGTCAA-3'; *Ssh2* forward, 5'-CCACAGCCCAAGTATTC-3'; *Ssh2* reverse, 5'-GGAAGGCCTCCTTCAGAACT-3'; *Tac1* forward, 5'-GATGAAGGAGCT GTCCAAGC-3'; *Tac1* reverse, 5'-TCACGAAACAGGAAACATGC-3'; *TIM* forward, 5'-ACGGAAATCGCTAGTCTCCA-3'; *TIM* reverse, 5'-TGTCAAAC CAGAGTCCAGCA-3'; *Tph1* forward, 5'-AATTTGCCAAGACCGTGAAG-3'; *Tph1* reverse, 5'-GCCCTGGCTCTAGACTGATG-3'; villin forward, 5'-ATT AGCGTCTGGGGGTTTCT-3'; villin reverse, 5'-CGTAGCAAACCCATGTT CCT-3'; *Zbtb48* forward, 5'-CACATGGAGATCCACGACAG-3'; *Zbtb48* reverse, 5'-CAGGAGCTCCACAATGACCT-3'. MO4(T) primer, 5'-AAGCA GTGGTATCAACGACAGATGGCCATTACGGCCGTACTTTTTTTTTTTTTTTT- TTTTTTTTTTTTTTTTTT-3'; T7-MO4 primer, 5'-GGCCAGTGAATTGTAA TACGACTACTATAGGGAGGCGGAAGCAGTGGTATCAACGCAGAGTG GCCATTACGGCCGTAC-3'.

**Taqman probes.** *Atoh1*, Mm00476035\_s1; *Chgb*, Mm00483287\_m1; *Chga*, Mm00514341\_m1; *Clca3*, Mm01320697\_m1; *Kit*, Mm03053277\_s1; *Gapdh*, Mm03302249\_g1; *Hoxp*, Mm00558630\_m1; *Lgr5*, Mm00438890\_m1; *Lrig1*, Mm00456116\_m1; *Lyz1*, Mm00657323\_m1; *Mmp7*, Mm00487724\_m1; *Muc2*, Mm00458299\_m1; *Rpl19*, Mm01606039\_g1; *Tert*, Mm00436931\_m1; villin, Mm00457074\_m1.

26. Campbell, S. J. *et al.* Regulation of the CYP1A1 promoter in transgenic mice: an exquisitely sensitive on-off system for cell specific gene regulation. *J. Cell Sci.* **109**, 2619–2625 (1996).

27. Vooijs, M., Jonkers, J. & Berns, A. A highly efficient ligand-regulated Cre recombinase mouse line shows that LoxP recombination is position dependent. *EMBO Rep.* **2**, 292–297 (2001).

28. McCutcheon, S. C. *et al.* Characterization of a heat resistant  $\beta$ -glucosidase as a new reporter in cells and mice. *BMC Biol.* **8**, 89 (2010).
29. Gracz, A. D., Ramalingam, S. & Magness, S. T. Sox9 expression marks a subset of CD24-expressing small intestine epithelial stem cells that form organoids in vitro. *Am. J. Physiol. Gastrointest. Liver Physiol.* **298**, G590–G600 (2010).
30. Potten, C. S. & Loeffler, M. Stem cells: attributes, cycles, spirals, pitfalls and uncertainties. Lessons for and from the crypt. *Development* **110**, 1001–1020 (1990).
31. Bjerknes, M. & Cheng, H. Methods for the isolation of intact epithelium from the mouse intestine. *Anat. Rec.* **199**, 565–574 (1981).
32. Irizarry, R. A. *et al.* Summaries of Affymetrix GeneChip probe level data. *Nucleic Acids Res.* **31**, e15 (2003).
33. Pruitt, K. D., Tatusova, T., Klimke, W. & Maglott, D. R. NCBI Reference Sequences: current status, policy and new initiatives. *Nucleic Acids Res.* **37**, D32–D36 (2009).
34. Lockstone, H. E. Exon array data analysis using Affymetrix power tools and R statistical software. *Brief. Bioinform.* **12**, 634–644 (2011).
35. R Development Core Team. *R: A Language and Environment for Statistical Computing* (2009).
36. Gentleman, R. C. *et al.* Bioconductor: open software development for computational biology and bioinformatics. *Genome Biol.* **5**, R80 (2004).
37. Smyth, G. K. in *Bioinformatics and Computational Biology Solutions using R and Bioconductor Solutions using R and Bioconductor* (eds Carey, V., Gentleman, R., Dudoit, S., Huber, W. & Irizarry, R.) 397–420 (Springer, 2005).
38. Jensen, K. B. & Watt, F. M. Single-cell expression profiling of human epidermal stem and transit-amplifying cells: Lrig1 is a regulator of stem cell quiescence. *Proc. Natl Acad. Sci. USA* **103**, 11958–11963 (2006).



# Crystal structure of an RNA-bound 11-subunit eukaryotic exosome complex

Debora Lika Makino<sup>1</sup>, Marc Baumgärtner<sup>1</sup> & Elena Conti<sup>1</sup>

**The exosome is the major 3′–5′ RNA-degradation complex in eukaryotes. The ubiquitous core of the yeast exosome (Exo-10) is formed by nine catalytically inert subunits (Exo-9) and a single active RNase, Rrp44. In the nucleus, the Exo-10 core recruits another nuclease, Rrp6. Here we crystallized an approximately 440-kilodalton complex of *Saccharomyces cerevisiae* Exo-10 bound to a carboxy-terminal region of Rrp6 and to an RNA duplex with a 3′-overhang of 31 ribonucleotides. The 2.8 Å resolution structure shows how RNA is funnelled into the Exo-9 channel in a single-stranded conformation by an unwinding pore. Rrp44 adopts a closed conformation and captures the RNA 3′-end that exits from the side of Exo-9. Exo-9 subunits bind RNA with sequence-unspecific interactions reminiscent of archaeal exosomes. The substrate binding and channelling mechanisms of 3′–5′ RNA degradation complexes are conserved in all kingdoms of life.**

RNA degradation serves a multitude of functions in all domains of life. RNA decay modulates the abundance of transcripts and is the ultimate step in quality control pathways that detect and eliminate defective RNA molecules<sup>1,2</sup>. Degradation is also used to partially trim RNA precursors to their mature form<sup>2</sup>. The main cellular machinery responsible for degrading RNA molecules in the 3′-to-5′ direction is the RNA exosome complex<sup>1–3</sup>. The exosome is conserved in all eukaryotes studied so far. Related complexes are also present in bacteria and archaea, highlighting the importance of this ancient molecular machine<sup>1</sup>.

The common core of eukaryotic and archaeal exosomes is a barrel-like structure of nine polypeptides (Exo-9)<sup>1,2</sup>. Exo-9 consists of six subunits with structural homology to RNase PH (a phosphorolytic 3′-to-5′ exoribonuclease), and a ring of three subunits with S1 and KH domains (folds typically found in RNA-binding proteins)<sup>4–6</sup>. In prokaryotes, RNA substrates use the central channel to reach the three active sites confined in the interior of the RNase PH barrel<sup>7–9</sup>. In yeast and human Exo-9, however, all RNase PH-like subunits contain amino acid changes in their putative active sites that renders them inactive<sup>4,6,10</sup>. The processive activity of eukaryotic exosomes resides in an additional subunit, Rrp44 (also known as Dis3)<sup>6,10</sup>. Rrp44 associates with Exo-9 to form the catalytically active Exo-10 complex that is ubiquitously present in the cytoplasm and nucleus of eukaryotic cells. Exo-10 recruits additional factors and regulators that act specifically in either the cytoplasm or the nucleus<sup>1,2</sup>.

All Exo-10 subunits are essential *in vivo* in yeast<sup>3,11,12</sup>. Yet, Rrp44 can bind and degrade RNAs *in vitro* in the absence of Exo-9 (refs 6, 10, 13), raising questions about the function of this catalytically inert scaffold. We previously reported *in vitro* biochemical experiments suggesting that the channel in yeast Exo-9 is used to deliver RNA substrates to the processive RNase site of the tenth subunit<sup>14</sup>. The Exo-9 channel was recently shown to be essential *in vivo* in yeast<sup>15</sup>. To shed light on the molecular mechanisms of RNA binding and processing, we have determined the atomic structure of a complete *S. cerevisiae* exosome core bound to an RNA substrate trapped in a pre-cleavage state within the complex.

## Rrp6 stabilizes an exosome–RNA complex

We reconstituted *S. cerevisiae* exosome complexes containing Exo-9 and an Rrp44 mutant lacking endonucleolytic and exonucleolytic

activities (Rrp44(D171N/D551N))<sup>6,14,16–18</sup> (Supplementary Fig. 1a, b). Within Exo-9, the RNase PH-like proteins (Rrp41, Rrp45, Rrp46, Rrp43, Mtr3 and Rrp42) and two of the S1/KH ‘cap’ proteins (Rrp40 and Rrp4) form a stable structural unit, whereas the third cap protein (Csl4) is a more labile component of the complex<sup>17,19,20</sup>. To stabilize the complex for structural analysis, we added an eleventh subunit, Rrp6 (refs 21, 22). In *in vitro* RNase protection assays, Rrp6 binding to Exo-10 slightly but reproducibly increased the intensity of the 31–33-nucleotide fragments that correspond to a long RNA-binding path in Exo-10 (ref. 14) (Supplementary Fig. 1c). Concomitantly, Rrp6 decreased the intensity of the 11–12-nucleotide fragments that reflect an alternative short RNA-binding path<sup>14</sup> (Supplementary Fig. 1c). A construct encompassing only the C-terminal region of Rrp6 (that is, lacking the nuclease region) had a similar stabilizing effect in RNase protection assays to the full-length protein (Supplementary Fig. 1c). We concluded that the C-terminal exosome-binding region of Rrp6 (ref. 23) contributes either directly or indirectly to the long RNA-binding path of Exo-10.

We narrowed down the exosome-binding region of Rrp6 to residues 518–693 (hereafter referred to as Rrp6<sub>C-term</sub>) (Supplementary Fig. 1c and data not shown). The reconstituted Exo-10 complex bound to Rrp6<sub>C-term</sub> crystallized in the presence of a 5′-CCCC CGAGAGGGGGU<sub>31</sub>-3′ RNA. This RNA substrate consists of a single-stranded 3′-overhang (designed to span the size of the fragments protected by Exo-10 in RNase protection assays<sup>14</sup>) and a 5′-CG duplex closed by a tetraloop (designed to stall at the narrow entrance of the Exo-9 channel<sup>24</sup>). We determined the structure of Exo-10–Rrp6<sub>C-term</sub>–RNA by molecular replacement using the coordinates of human Exo-9 (ref. 6) and yeast Rrp44–Rrp41–Rrp45 (ref. 14). The structure was refined to 2.8 Å resolution with good statistics (*R*<sub>free</sub> value of 22.4%) and stereochemistry (Supplementary Table 1). The atomic model is complete for most of the polypeptides (Supplementary Fig. 1a). RNA has defined electron density for 17 nucleotides in the single-stranded overhang (nucleotides 1–15 and 30–31, as numbered from the 3′-end), and 13 nucleotides in the duplex (32–44). Additional weak density is present that corresponds to partially disordered oligonucleotides in the wider parts of the channel.

<sup>1</sup>Department of Structural Cell Biology, MPI for Biochemistry, Am Klopferspitz 18, 82152 Martinsried, Germany.

## Structure of yeast Exo-10-Rrp6-RNA

The structure of the Exo-10-Rrp6<sub>C-term</sub>-RNA complex shows the canonical overall architecture of Exo-9, with the ring of the cap proteins bound on top of the RNase PH barrel (Fig. 1). Rrp6 folds into two separate stretches that bind S1/KH and RNase PH-like proteins (Fig. 1, right). The first (amino-terminal) stretch (residues 532–557) forms an  $\alpha$ -helix that binds to Csl4 and Mtr3 (Fig. 2a and Supplementary Fig. 2a). The second (C-terminal) stretch (residues 565–619) contains an unstructured region that is followed by a small  $\beta$ -hairpin and  $\alpha$ -helix that contact Mtr3, Rrp43 and approach Csl4 (Fig. 2a and Supplementary Fig. 2a). Although the exosome-binding region of Rrp6 shows altogether relatively weak sequence conservation, the second stretch of Rrp6 in particular docks onto a conserved surface of Exo-9 (Fig. 2a), suggesting that at least part of the Rrp6-binding site on the exosome is conserved across species. The C-terminal region of Rrp6 does not contact RNA directly. The structural analysis suggests that it indirectly contributes to the long RNA-binding path by stabilizing Csl4 in an appropriate RNA-binding conformation (Fig. 2b and Supplementary Fig. 2b). This also rationalizes previous reports that Rrp6 binding increases the exoribonuclease activity of Exo-10 independently of Rrp6 activity<sup>15</sup>.

Rrp44 contains an endoribonuclease (the PIN domain) and an exoribonuclease region (with the CSD1, CSD2, RNB and S1 domains typical of RNase II-like enzymes<sup>25</sup>) (Fig. 3a). Rrp44 binds the RNase PH

barrel on the opposite side from the S1/KH ring, but is offset from the central axis of Exo-9 by about 50° (Fig. 1, left). It adopts a closed conformation (in which the PIN domain contacts CSD2) that is different from the open conformation observed in the yeast Rrp41–Rrp45–Rrp44 structure (in which the PIN domain contacts CSD1 and S1)<sup>14</sup> (Fig. 3b, left). The PIN domain is anchored on the RNase PH proteins at a similar position as observed in the Rrp41–Rrp45–Rrp44 complex, with the endonuclease site exposed to solvent (Supplementary Fig. 3). The relative displacement of Rrp44 can roughly be described as large rigid-body rotations of the exoribonuclease region with respect to the Exo-9–PIN module (Fig. 3b). A helix of CSD1 seems to be uncoupled from the rest of the exoribonuclease region and obstructs the exit of the central channel at the bottom of the RNase PH barrel (Fig. 3b). Finally, the N-terminal region of Rrp44, which was disordered in previous structures<sup>14</sup>, forms a long  $\beta$ -hairpin that is wedged in between Rrp41–Rrp42 and approaches the N terminus of the cap protein Rrp4 (Supplementary Fig. 3b).

## RNA duplex unwinding at the entry pore

The RNA we used for crystallization binds Exo-10 with the 5'-duplex sandwiched between the cap proteins Rrp4 and Rrp40 (Fig. 2b). In comparison with the structure of human apo Exo-9 (ref. 6), Rrp4 and Rrp40 are only ~4 Å closer to the centre of the barrel and thus seem to be almost pre-positioned to bind the RNA duplex (Supplementary

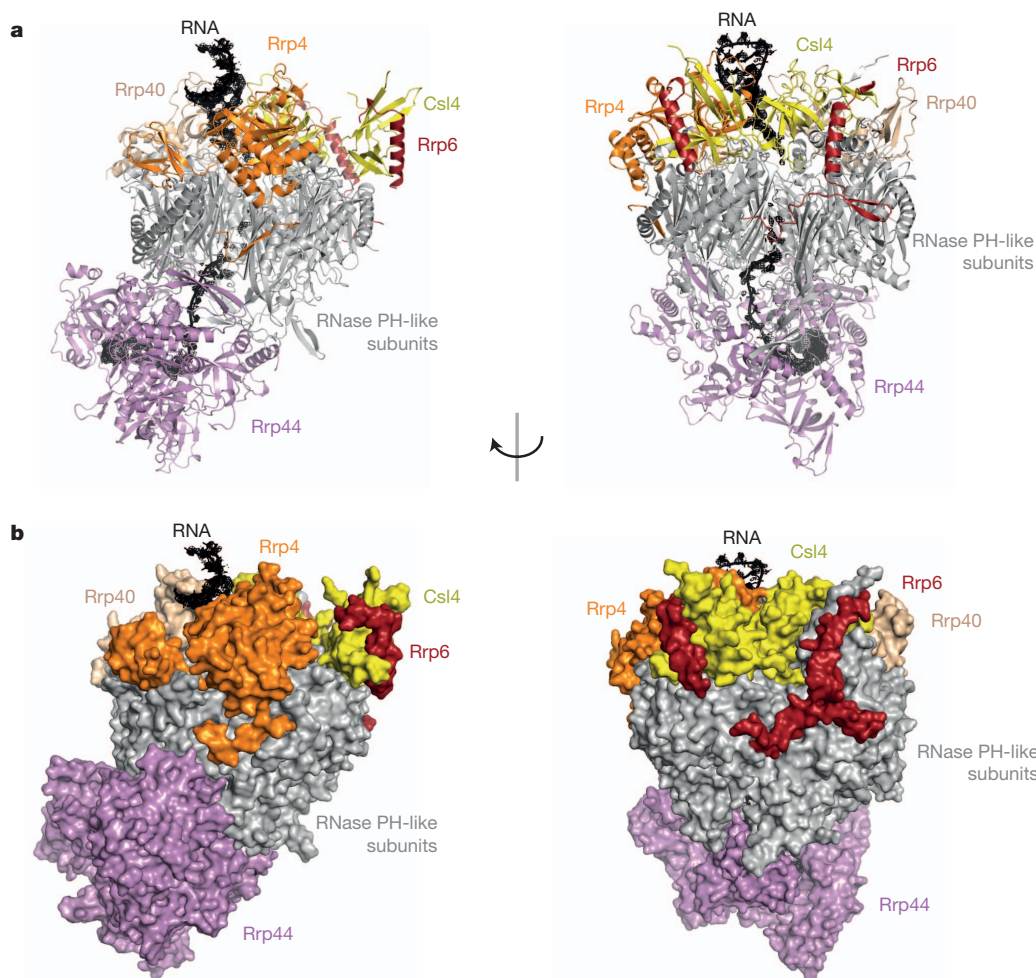


**Figure 1 | The crystal structure of a yeast exosome-RNA complex.** **a, b,** The structure of *S. cerevisiae* Exo10-Rrp6<sub>C-term</sub>-RNA is shown as ribbon (**a**) and surface (**b**) representations in two orientations related by a ~90° rotation around a vertical axis. RNA is in black, together with the simulated annealing

omit map (contoured at 2.5 $\sigma$ ). The exosome-binding region of Rrp6 wraps around Csl4 and contacts the RNase PH ring (right). The Rrp4 N-terminal tail reaches across the RNase PH-like barrel towards the N-terminal region of Rrp44 (left). RNA is enclosed in the complex (**b**).



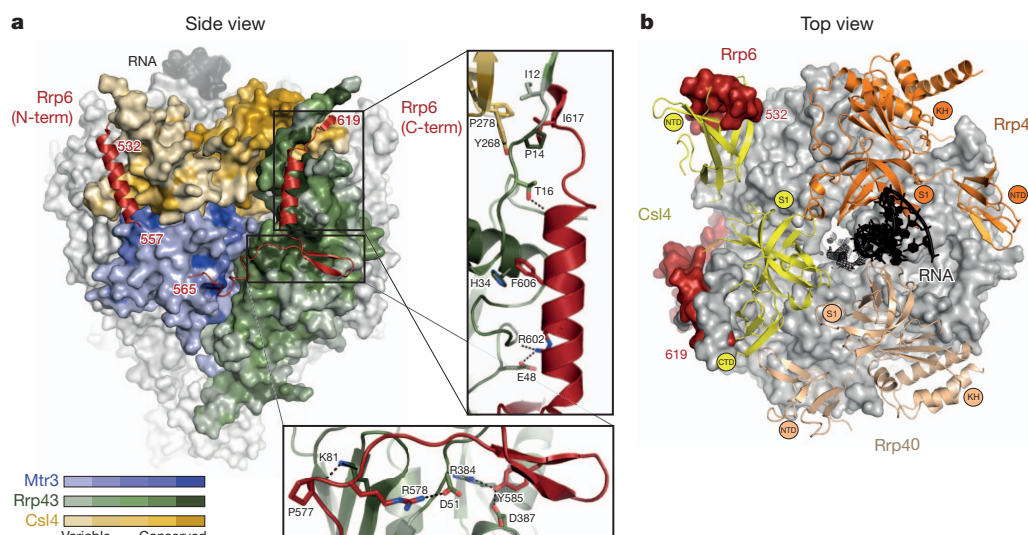


**Figure 2 | Interaction between Exo-9 and Rrp6.** **a**, Rrp6<sub>C-term</sub> binds to conserved surface patches of Exo-9. The surfaces of Csl4 (yellow), Mtr3 (blue) and Rrp43 (green) are coloured according to sequence conservation. The zoomed-in views show direct interactions between Exo-9 and Rrp6. **b**, The structure of yeast Exo10-Rrp6<sub>C-term</sub>-RNA is shown in a top-view orientation.

Fig. 2b). The cap protein Csl4 presents the largest (~10 Å) conformational difference compared to apo human Exo-9 (ref. 6). Csl4 does not contact the RNA duplex directly, but contacts the single-stranded RNA (ssRNA) at the entrance of the RNase PH channel (Fig. 2b).

Starting from the 5'-end of the RNA, the first direct interaction with the exosome occurs at the last base pair of the duplex (G32-C45)

The RNase PH ring and Rrp6 are shown as a surface in grey and red, respectively. The S1, KH, N-terminal (NTD) and C-terminal (CTD) domains of the cap proteins are indicated. The atomic model and additional density for RNA are in black.

(Fig. 4a). On the 3'-strand, the phosphate backbone of G32 binds Rrp4 Arg 123 and the base stacks against Rrp40 Arg 110 (Fig. 4b). The complementary nucleotide on the 5'-strand is almost completely disordered: in the base-pair conformation, C45 would stereochemically clash against a conserved loop of Rrp40 (Supplementary Fig. 4a). Thus, the first base pair of the duplex is melted just before entering the Exo-9 channel by the structural features of the cap proteins.

RNA is then threaded in a single-stranded conformation through the narrow entrance pore (10–12 Å across) by sequential base-stacking interactions and a base-flipping mechanism (Fig. 4a). The base of U31, the first nucleotide of the single-stranded overhang, flips out to be sandwiched by  $\pi$ - $\pi$  stacking interactions between the side chains of Rrp4 Phe 77 and Rrp41 Arg 119 (Fig. 4b). The base of the following nucleotide, U30, interacts with Rrp40 Phe 80 and a loop of Rrp41 (at Lys 62 and Ser 63) (Fig. 4b, c). Consistently, negatively charged substitutions at these residues in Rrp41 abolish the long RNA-binding path in *in vitro* assays<sup>14</sup> and a negatively charged insertion at this position is lethal *in vivo*<sup>15</sup>.

### Binding of ssRNA in the internal channel

After U30, the sparse density for ssRNA (left uninterpreted in the final atomic model) is in close proximity to positively charged residues of the Csl4 S1 domain and to loop regions of the Rrp41-like proteins Rrp46 and Mtr3 (Fig. 4c). This binding site corresponds to the position of a bound nucleotide in an archaeal exosome<sup>24</sup> (Supplementary Fig. 4b, left). Below this point, the internal cavity widens and the density for RNA becomes correspondingly more diffuse, suggesting the presence of multiple conformations and/or weak binding (Fig. 4d). We estimate that about eight nucleotides can span this part of the channel, which narrows again roughly halfway through the RNase PH barrel by the juxtaposition of positively charged residues of Rrp42 and of the N terminus of Mtr3 (Fig. 4d). The RNA channel then veers sideways. Here, the backbone of U15-U13 is bound by positively charged residues of Rrp41 (Arg 95) and Rrp45 (Arg 71, Arg 106, Arg 113 and Arg 114) (Fig. 4a, e). Consistently, charge-swap mutations or a negatively charged insertion at these residues abolish the long RNA-binding path in *in vitro* assays<sup>14</sup> or cause lethality *in vivo*<sup>15</sup>. In the archaeal exosome, this sideways channel ends with the phosphorolytic active site of Rrp41 (ref. 24) (Supplementary Fig. 4b, right). In the yeast exosome, the channel continues in Rrp44.

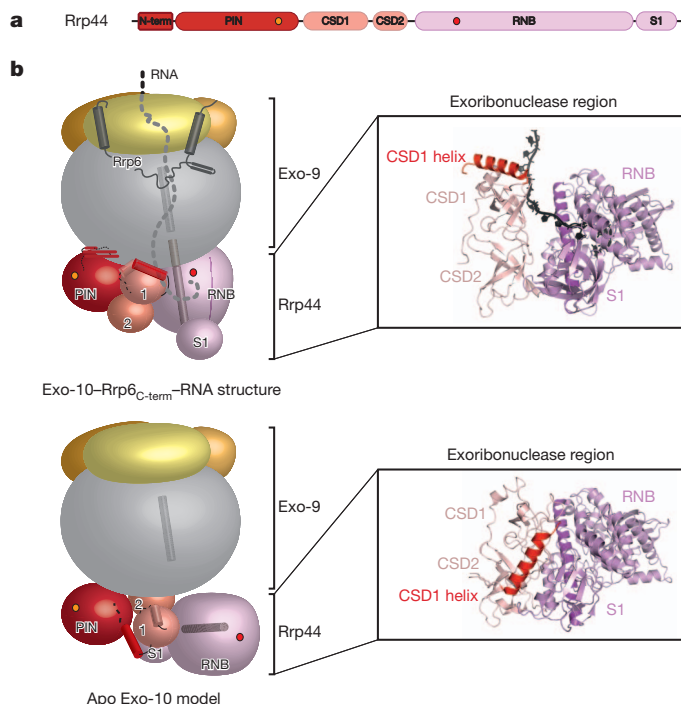


**Figure 3 | Conformational rearrangements of Rrp44.** **a**, Domain organization of Rrp44. The D171 endonuclease and D551 exoribonuclease sites are circled in yellow and red, respectively. **b**, On the left, schematics based on the crystal structure of Exo-10-Rrp6<sub>C-term</sub>-RNA (top) and a model of Exo-10 (refs 14, 20) (bottom). The cap proteins are in yellow or orange, the RNase PH core is in light grey and Rrp6 is in dark grey. The domains of Rrp44 are coloured as in **a**. Two helices of Rrp45 and Rrp44 are shown as a reference. On the right are the crystal structures of the corresponding Rrp44 exoribonuclease regions.

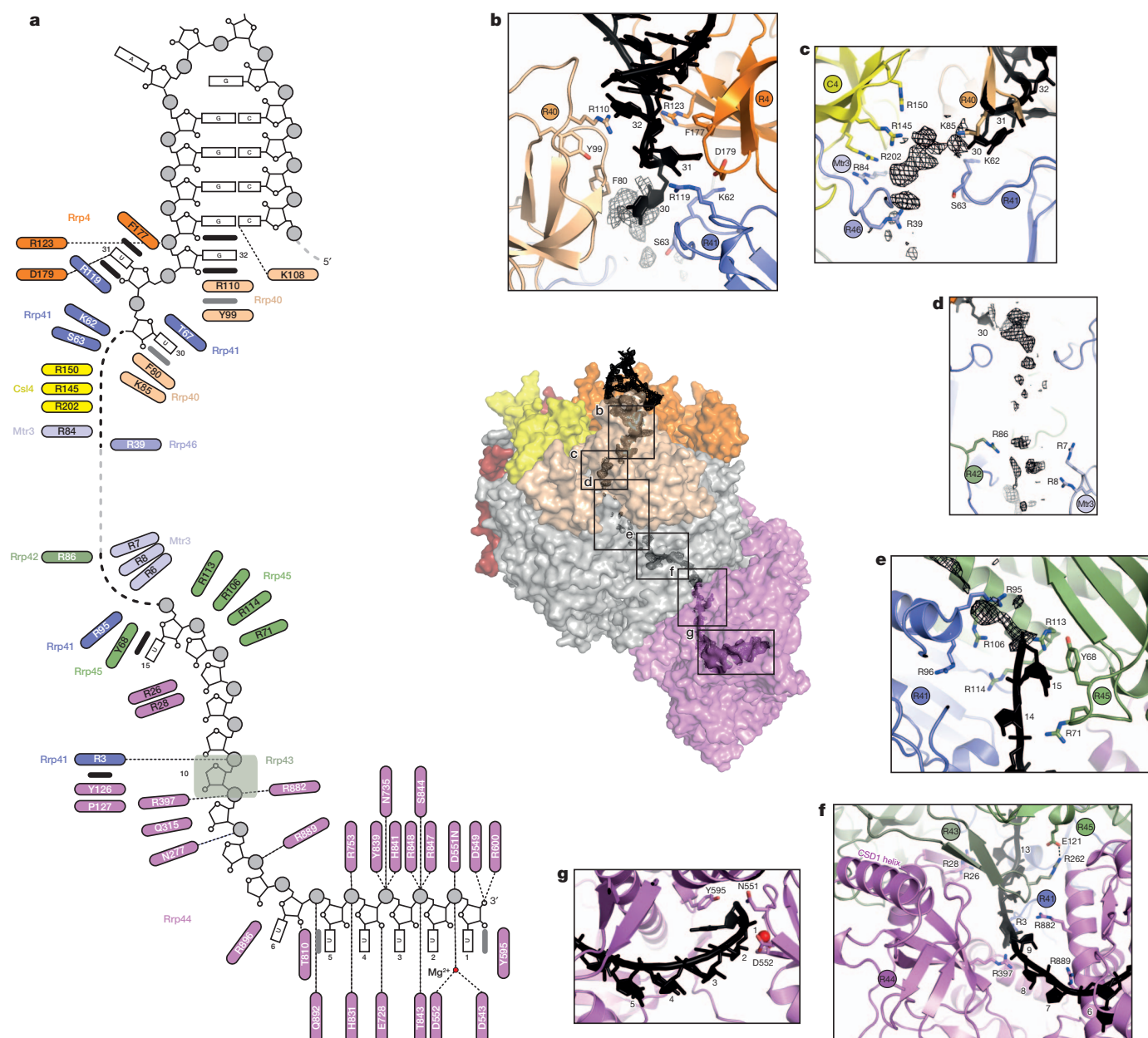


**Figure 4 | The RNA path through the exosome.** **a**, Schematics showing the protein-RNA interactions in the Exo-10-Rp6C-term-RNA structure. Polar interactions are highlighted with dotted lines, and stacking interactions with thick black lines. **b–g**, Zoomed-in panels relative to the overall structure shown in the centre. The subunits are indicated in coloured circles. Density not

interpreted in the final model is shown (as black mesh) as a difference omit map contoured at  $2.5\sigma$ . The RNA-binding sites at the entrance (**c**) and exit (**e**) of Exo-9 are similar to those observed with the archaeal exosome<sup>24</sup> (Supplementary Fig. 4).

The N-terminal region of Rrp41, a loop of Rrp43, the N-terminal region of Rrp44 (Arg 26 and Arg 28) and the PIN domain of Rrp44 (Tyr 126 and Pro 127) contact nucleotides U13–U10 (Fig. 4a, f). The finding that the PIN domain also contributes residues to the long RNA-binding path (albeit from a surface opposite to that of the endonuclease site) rationalizes recent *in vivo* cross-linking data suggesting that the exonuclease and PIN domains of Rrp44 act together to degrade RNA substrates<sup>26</sup>. The RNA channel ends in the exoribonuclease. Similar to the structure of Rrp44 in isolation<sup>13</sup>, the U6–U9 nucleotides bind at the interface between the CSD1 and catalytic domains of Rrp44 (Fig. 4a, f), and the five nucleotides at the 3'-end (U1–U5) bind in the catalytic region (Fig. 4a, g).

### The RNA-binding path through the exosome

The long RNA-binding path in the internal chamber of the exosome (between the entrance pore of Exo-9 and the exoribonuclease

site of Rrp44) extends over 160 Å and is spanned by a minimum of 25 nucleotides in a single-stranded conformation. In this path, the single-stranded overhang of the RNA is almost entirely embedded in the interior of the complex and shielded from solvent (Fig. 1b). A notable exception is at nucleotides U6–U7, which reside in a groove of Rrp44 that is accessible to solvent (Supplementary Fig. 5). It is possible that this surface groove allows RNA to access the exoribonuclease site directly, rationalizing the short 11–12-nucleotide-binding path observed in RNase protection assays<sup>14</sup> (Supplementary Fig. 1c).

Notably, all Exo-9 subunits in addition to Rrp44 contribute directly to bind the phosphate groups along the RNA backbone. The electrostatic interactions are not sequence specific, in line with the ability of the exosome to degrade a wide variety of substrates. The interactions with RNA are clustered at the substrate entry pore and degradation



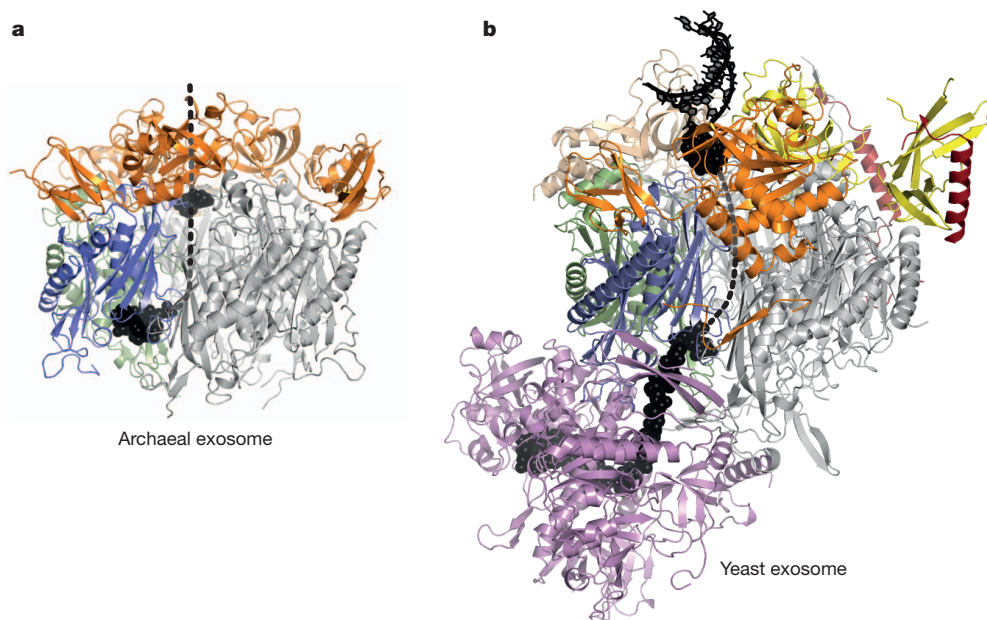


**Figure 5 | RNA channelling to degradation is a conserved mechanism.**

**a**, Archaeal exosome structure<sup>24</sup> with RNA (in black) with a nucleotide bound at a phosphorolytic site and at the entrance of the exosome (with the corresponding Rrp41 subunit in blue, Rrp42 in green, Rrp4 in orange, and the other subunits in grey for clarity). **b**, Yeast exosome structure shown in a similar

orientation to the archaeal exosome in **a**. Rrp41 is in blue, Rrp45 in green (an Rrp42-like subunit), Rrp4 in orange, the other RNase PH subunits are in grey, and RNA is in black. The eukaryotic and prokaryotic exosomes share the same RNA-binding path within Exo-9.

site. The central portion of the RNA in the channel lacks defined binding sites. Here, however, the barrel-like shape of the molecule confines the substrate. The presence of strong and weak binding sites as well as the topological restraints rationalize the processive nature of this molecular machine. Topological constraints also promote strand separation of a duplex RNA at the 5'-end of the binding path. Complete unwinding is achieved by translocation: RNA binding to Rrp44 at the U6–U7 pockets seems to be sufficient to drive a duplex through the unwinding pore even before 3'-end hydrolysis (Supplementary Fig. 6).

## Conclusions

The structure of the yeast exosome bound to a substrate trapped in a pre-cleavage state within the long RNA-binding path shows how the complex engages and prepares the ribonucleotide chain for degradation. RNA enters the internal chamber present in the exosome in an unwound conformation, reminiscent of how polypeptides are unfolded when entering the proteasome<sup>27</sup>. The nucleic acid traverses roughly half of the barrel-like structure of Exo-9 and is then channelled to the side, to the same binding path that in prokaryotic exosome-like complexes leads to a phosphorolytic site (Fig. 5a). In yeast, in the absence of such a catalytic site, the path continues uninterrupted within the Rrp44 nuclease, which curls up on the side of Exo-9 and grabs the RNA 3'-end (Fig. 5b). Although the chemistry of the reactions is different, the channelling mechanism of exosome complexes is remarkably conserved from prokaryotes to eukaryotes and parallels the mechanism used by the proteasome to confine and prepare polypeptides for processive degradation.

## METHODS SUMMARY

*S. cerevisiae* exosome subunits were expressed and purified to homogeneity with similar methods to those previously described<sup>6,14,28</sup> and detailed in the Methods. For crystallization, yeast exosome complexes were reconstituted by combining Exo-9, Rrp44 and His<sub>6</sub>-SUMO-Rrp6<sub>518–693</sub>. After cleavage of the His<sub>6</sub>-SUMO tag and further purification by size-exclusion and anion-exchange chromatography, Exo-10-Rrp6<sub>518–693</sub> was incubated in a 1:2 (mol:mol) stoichiometry with a pre-annealed 5'-CCCCGAGAGGGGGU<sub>31</sub>-3' RNA oligoribonucleotide

(Sigma Aldrich). Needle-like crystals of 20 × 50 × 2,500 μm<sup>3</sup> were grown as described in the Methods, and diffracted to 2.8 Å resolution (data processing statistics are summarized in Supplementary Table 1). The structure was solved by molecular replacement and extensive model building and refinement.

**Full Methods** and any associated references are available in the online version of the paper.

**Received 6 November; accepted 21 December 2012.**

**Published online 3 February 2013.**

- Lykke-Andersen, S., Brodersen, D. E. & Jensen, T. H. Origins and activities of the eukaryotic exosome. *J. Cell Sci.* **122**, 1487–1494 (2009).
- Houseley, J. & Tollervey, D. The many pathways of RNA degradation. *Cell* **136**, 763–776 (2009).
- Mitchell, P., Petfalski, E., Shevchenko, A., Mann, M. & Tollervey, D. The exosome: A conserved eukaryotic RNA processing complex containing multiple 3'→5' exoribonucleases. *Cell* **91**, 457–466 (1997).
- Lorentzen, E. *et al.* The archaeal exosome core is a hexameric ring structure with three catalytic subunits. *Nature Struct. Mol. Biol.* **12**, 575–581 (2005).
- Büttner, K., Wenig, K. & Hopfner, K.-P. Structural framework for the mechanism of archaeal exosomes in RNA processing. *Mol. Cell* **20**, 461–471 (2005).
- Liu, Q., Greimann, J. C. & Lima, C. D. Reconstitution, activities, and structure of the eukaryotic RNA exosome. *Cell* **127**, 1223–1237 (2006).
- Lorentzen, E. & Conti, E. Structural basis of 3' end RNA recognition and exoribonucleolytic cleavage by an exosome RNase PH core. *Mol. Cell* **20**, 473–481 (2005).
- Navarro, M. V. A. S., Oliverira, C. C., Zanchin, N. I. T. & Guimarães, B. G. Insights into the mechanism of progressive RNA degradation by the archaeal exosome. *J. Biol. Chem.* **283**, 14120–14131 (2008).
- Hardwick, S. W., Gubbey, T., Hug, I., Jenal, U. & Luisi, B. F. Crystal structure of *Caulobacter crescentus* polynucleotide phosphorylase reveals a mechanism of RNA substrate channelling and RNA degradosome assembly. *Open Biol.* **2**, 120028 (2012).
- Dziembowski, A., Lorentzen, E., Conti, E. & Séraphin, B. A single subunit, Dis3, is essentially responsible for yeast exosome core activity. *Nature Struct. Mol. Biol.* **14**, 15–22 (2007).
- Noguchi, E. *et al.* Dis3, implicated in mitotic control, binds directly to Ran and enhances the GEF activity of RCC1. *EMBO J.* **15**, 5595–5605 (1996).
- Allmang, C. *et al.* The yeast exosome and human PM-Scl are related complexes of 3'→5' exonucleases. *Genes Dev.* **13**, 2148–2158 (1999).
- Lorentzen, E., Basquin, J., Tomecki, R., Dziembowski, A. & Conti, E. Structure of the active subunit of the yeast exosome core, Rrp44: Diverse modes of substrate recruitment in the RNase II nuclease family. *Mol. Cell* **29**, 717–728 (2008).

14. Bonneau, F., Basquin, J., Ebert, J., Lorentzen, E. & Conti, E. The yeast exosome functions as a macromolecular cage to channel RNA substrates for degradation. *Cell* **139**, 547–559 (2009).
15. Wasmuth, E. V. & Lima, C. D. Exo- and endoribonucleolytic activities of yeast cytoplasmic and nuclear RNA exosomes are dependent on the noncatalytic core and central channel. *Mol. Cell* **48**, 133–144 (2012).
16. Lebreton, A., Tomecki, R., Dziembowski, A. & Séraphin, B. Endonucleolytic RNA cleavage by a eukaryotic exosome. *Nature* **456**, 993–996 (2008).
17. Schaeffer, D. *et al.* The exosome contains domains with specific endoribonuclease, exoribonuclease and cytoplasmic mRNA decay activities. *Nature Struct. Mol. Biol.* **16**, 56–62 (2009).
18. Schneider, C., Leung, E., Brown, J. & Tollervey, D. The N-terminal PIN domain of the exosome subunit Rrp44 harbors endonuclease activity and tethers Rrp44 to the yeast core exosome. *Nucleic Acids Res.* **37**, 1127–1140 (2009).
19. Wang, H.-W. *et al.* Architecture of the yeast Rrp44 exosome complex suggests routes of RNA recruitment for 3' end processing. *Proc. Natl Acad. Sci. USA* **104**, 16844–16849 (2007).
20. Malet, H. *et al.* RNA channelling by the eukaryotic exosome. *EMBO Rep.* **11**, 936–942 (2010).
21. Briggs, M. W., Burkard, K. T. & Butler, J. S. Rrp6, the yeast homologue of the human PM-Scl 100-kDa autoantigen, is essential for efficient 5.8S rRNA 3' end formation. *J. Biol. Chem.* **273**, 13255–13263 (1998).
22. Cristodero, M., Böttcher, B., Diepholz, M., Scheffzek, K. & Clayton, C. The *Leishmania tarentolae* exosome: purification and structural analysis by electron microscopy. *Mol. Biochem. Parasitol.* **159**, 24–29 (2008).
23. Callahan, K. P. & Butler, J. S. Evidence for core exosome independent function of the nuclear exoribonuclease Rrp6p. *Nucleic Acids Res.* **36**, 6645–6655 (2008).
24. Lorentzen, E., Dziembowski, A., Lindner, D., Séraphin, B. & Conti, E. RNA channelling by the archaeal exosome. *EMBO Rep.* **8**, 470–476 (2007).
25. Frazão, C. *et al.* Unravelling the dynamics of RNA degradation by ribonuclease II and its RNA-bound complex. *Nature* **443**, 110–114 (2006).
26. Schneider, C., Kudla, G., Wlotzka, W., Tuck, A. & Tollervey, D. Transcriptome-wide analysis of exosome targets. *Mol. Cell* **48**, 422–433 (2012).
27. Lupas, A., Flanagan, J. M., Tamura, T. & Baumeister, W. Self-compartmentalizing proteases. *Trends Biochem. Sci.* **22**, 399–404 (1997).
28. Greimann, J. C. & Lima, C. D. Reconstitution of RNA exosomes from human and *Saccharomyces cerevisiae* cloning, expression, purification, and activity assays. *Methods Enzymol.* **448**, 185–210 (2008).

**Supplementary Information** is available in the online version of the paper.

**Acknowledgements** We would like to thank the Max Planck Institute Biochemistry Core Facility and Crystallization Facility; the staff members at beamlines X10SA (Swiss Light Source) and ID23-2 (European Synchrotron Radiation Facility) for support; F. Bonneau for the assay in Supplementary Fig. 6; J. Ebert, J. Basquin and F. Bonneau for initial materials and reagents; and P. Birle and T. Krywcun for technical assistance. We also thank members of our laboratory for discussions and critical reading of the manuscript. This study was supported by the Max Planck Gesellschaft, the ERC Advanced Investigator Grant 294371 and the Deutsche Forschungsgemeinschaft (SFB646, SFB1035, GRK1721 and CIPSM) to E.C.

**Author Contributions** D.L.M. and E.C. designed the experiments. M.B. purified several exosome components. D.L.M. performed all other experiments and solved the structure. D.L.M. and E.C. wrote the manuscript.

**Author Information** Atomic coordinates and structure factors have been deposited at the Protein Data Bank under accession number 4IFD. Reprints and permissions information is available at [www.nature.com/reprints](http://www.nature.com/reprints). The authors declare no competing financial interests. Readers are welcome to comment on the online version of the paper. Correspondence and requests for materials should be addressed to E.C. ([conti@biochem.mpg.de](mailto:conti@biochem.mpg.de)).



## METHODS

**Expression and purification.** Bacterial expression and purification of Exo-9 subunits were primarily based on the procedures established previously<sup>6</sup>. Exosome proteins were overexpressed in BL21 (DE3) gold pLysS (Stratagene) or BL21 (DE3) T7 express I<sup>q</sup> (New England Biolabs) cells. Cells were grown at 37 °C in TB media and isopropyl-β-D-thiogalactoside (IPTG) induced overnight at 18 °C.

Protease inhibitors—phenylmethylsulphonyl fluoride (PMSF), 4-(2-aminoethyl) benzenesulphonyl fluoride hydrochloride (AEBSF), or cOmplete protease inhibitor cocktail (Roche Applied Science)—were added to cell lysate, which was loaded on to affinity column (GSH (GE Healthcare) or TALON cobalt (Takara Bio)). This was followed by an overnight tobacco etch virus (TEV) or small ubiquitin-like modifier (SUMO) protease cleavage (except for Rrp6 and Csl4 constructs) and loaded again on TALON cobalt a second time to remove uncleaved species. In-bead TEV cleavage was done on glutathione S-transferase (GST)–Rrp40 protein. After affinity purification, all samples were submitted to ion-exchange chromatography (HiTrapQ HP or HiTrapSP HP from GE Healthcare), and, with the exception of Csl4 and of Rrp40, proteins were further purified by size-exclusion chromatography (Superdex 200 or 75 from GE Healthcare). For Rrp44 purification, heparin and MonoQ 4.6/100 PE columns (both GE Healthcare) were added to the purification protocol. In particular, MonoQ chromatography was important to remove nucleic acid-bound Rrp44 species. All purifications were performed at pH 7.5.

**Exosome reconstitution.** Equimolar amounts of each Exo-9 component were combined, incubated at room temperature for 30 min, and concentrated for size-exclusion chromatography (Superdex 200, GE Healthcare) in buffer containing 20 mM Tris, pH 7.5, 100 mM NaCl, 10% glycerol and 2 mM dithiothreitol (DTT). The main peak was pooled and injected onto a MonoQ anion exchange column. A shallow linear gradient separated Exo-9 sub-complexes from the sample<sup>28</sup>. After quantifying the purified Exo-9 amounts, we added a 1.3-fold excess molar ratio of Rrp44 (pre-run on a MonoQ column to remove nucleic acid-bound species), a fourfold excess of SUMO-tagged Rrp6 and a 2.5-fold excess of Csl4. The mixture was then incubated in the presence of 1:50 (w/w) (protease:Rrp6) SUMO protease at room-temperature for over 1 h. We then added zinc acetate to a final concentration of 0.2 mM. A final round of Superdex 200 and MonoQ chromatography removed further protein excess, impurities and subcomplexes. The peak was pooled, buffer-exchanged to a final exosome solution containing 20 mM Tris, pH 7.5, 50 mM NaCl, 1 mM tris(2-carboxyethyl)phosphine hydrochloride (TCEP) and concentrated to 20–30 mg ml<sup>−1</sup> for storage at −80 °C. The entire reconstitution process was done under RNase-free conditions.

**RNase protection.** Exo-10 (500 nM) was added to [<sup>32</sup>P]-body-labelled ssRNA<sup>14</sup> (250 nM) and to increasing concentrations of SUMO-tagged Rrp6 (750, 1,000 and 2,000 nM). Reaction buffer contained 50 mM HEPES, pH 7.5, 50 mM NaCl, 5 mM EDTA, pH 8.0, 0.1% NP-40, 10% glycerol and 1 mM DTT to a final volume of 20 µl. After incubation at 4 °C for more than 1 h, unprotected RNA was digested with 0.5 µl RNase A/T1 Mix (Thermo Scientific, containing 2 mg ml<sup>−1</sup> of RNase A and 5,000 U ml<sup>−1</sup> of RNase T1) for 20 min at 20 °C. The reaction was quenched with 10 mM EDTA and 1% SDS. RNA products that were protected by the exosome were extracted by two rounds of phenol:chloroform:isoamyl alcohol (25:24:1 volume ratios from Invitrogen) and followed by ethanol precipitation. These reaction products were resolved by 20% (w/v) PAGE containing 7 M urea, and detected using Typhoon FLA 7000 (GE Healthcare). Band intensity profiles were evaluated using ImageJ<sup>29</sup>.

**Crystallization.** Exo-10–Rrp6<sub>C-term</sub> (18 mg ml<sup>−1</sup>) was incubated with twofold molar excess of pre-annealed RNA (5′-CCCCGAGAGGGGU<sub>31-3′</sub>) (Sigma-Aldrich) in buffer containing 20 mM Tris, pH 7.5, 50 mM NaCl, 1 mM MnCl<sub>2</sub>, 2 mM MgCl<sub>2</sub> and 1 mM TCEP. Crystallization conditions were optimized from PACT screen (Qiagen) (0.1 M Bis-Tris propane, pH 6.5, 0.2 M NaBr and 20% PEG3350) to 0.15 M MES, pH 6.5, 0.27 M NaBr and 11.4–12.2% PEG3350 using sitting-drop Cryschem plates (Hampton Research). Long needle-like crystals

(of up to 20 × 50 × 2,500 µm<sup>3</sup>) presenting best diffraction power grew within 2 weeks at 19 °C. Crystals are of monoclinic space group *P*<sub>2</sub><sub>1</sub> with cell dimensions of *a* = 154.09 Å, *b* = 107.44 Å, *c* = 150.46 Å and β = 110.63°.

**Data collection and processing.** Exo-10–RNA–Rrp6<sub>(518–693)</sub> crystals were flash-frozen in liquid nitrogen after exchanging mother liquor with 0.1 M MES, pH 6.5, 0.27 M NaBr, 25% (w/v) PEG3350 and 10% (v/v) glycerol. Data collection was carried out at beamline X10SA at the Swiss Light Source, equipped with Pilatus 6M detector (Dectris). The detector was set at a distance of 600 mm with adjusted beam stop position to allow detection of lower resolution spots and the wavelength was set to the Br edge of 13.478 keV (0.9199 Å). As crystals frozen at 100 K decayed rapidly under X-ray radiation, only 8–15° sweeps of contiguous data were typically possible to collect before resolution loss. More than 160 sub-data sets were collected, from which the best images were merged to a final 99.5% complete data set in the 3.5–3.2 Å resolution shell and 56.5% in the 3.0–2.8 Å highest resolution shell (Supplementary Table 1). In the final processed data, Bijvoet pairs were treated as identical despite the weak anomalous signal from bromide ions ( $|F(+)-F(-)|/\sigma = 1.192$  at 8 Å) observed when treated as unique. Statistical quality measures of the two data sets were basically unchanged with overall *R*<sub>merge</sub> values of 17.4% and 16.3% for the data treated as native and as anomalous, respectively. The structure was ultimately refined against data containing merged Bijvoet pairs, as there was a gain in completeness by near 10% at the highest resolution shell (3.0–2.8 Å). Data were processed using XDS<sup>30</sup>.

**Structure determination and refinement.** Initial phases were calculated by molecular replacement using subunits of human Exo-9 (ref. 6) (Supplementary Table 2), *Sulfolobus solfataricus* Rrp41/42 (ref. 24), *S. cerevisiae* Rrp41/45/44<sub>A25</sub> (ref. 14), *S. cerevisiae* Rrp44<sub>A251</sub> (ref. 13) and the C terminus of *S. cerevisiae* Rrp40 (ref. 31) crystal structures as search models. Not all protein components were found by likelihood enhanced rotation, and translation functions were applied by Phaser<sup>32</sup> from the CCP4 package<sup>33</sup>. Several domains, including the CSD2 and S1 domains of Rrp44, all domains of Csl4 and Rrp4 subunits, and the N-terminal domain of Rrp40, Rrp6 and the RNA were placed manually as phases were slowly improved by several cycles of model building (Coot<sup>34</sup>), rigid-body, group B-factor, and TLS refinements (PHENIX<sup>35</sup>). The final model includes all atom positional, TLS and individual B-factor refinements. Current refinement statistics stand at an *R*<sub>free</sub> value of 22.4% and an *R*<sub>work</sub> value of 18.3%, using data to 2.80 Å. Ramachandran plots indicate 0.12% (4 residues) in the disallowed, 4.06% (135 residues) in the allowed, and 95.82% (3,189 residues) in the favoured regions. Detailed statistics and other quality control measures can be found in Supplementary Table 1. Figures were prepared with PyMOL<sup>36</sup> and electrostatic potentials were calculated with APBS<sup>37</sup>. Surface conservation and Rrp6-interacting residues were calculated using Consurf<sup>38</sup> and AquaProt<sup>39</sup> servers, respectively.

29. Schneider, C. A., Rasband, W. S. & Eliceiri, K. W. NIH image to ImageJ: 24 years of image analysis. *Nature Methods* **9**, 671–675 (2012).
30. Kabsch, W. XDS. *Acta Crystallogr. D* **66**, 125–132 (2010).
31. Oddone, A. et al. Structural and biochemical characterization of the yeast exosome component Rrp40. *EMBO Rep.* **8**, 63–69 (2007).
32. McCoy, A. J. et al. Phaser crystallographic software. *J. Appl. Crystallogr.* **40**, 658–674 (2007).
33. Winn, M. D. et al. Overview of the CCP4 suite and current developments. *Acta Crystallogr. D* **67**, 235–242 (2011).
34. Emsley, P. & Cowtan, K. Coot: model-building tools for molecular graphics. *Acta Crystallogr. D* **60**, 2126–2132 (2004).
35. Adams, P. D. et al. PHENIX: a comprehensive Python-based system for macromolecular structure solution. *Acta Crystallogr. D* **66**, 213–221 (2010).
36. The PyMOL Molecular Graphics System. v. 1.2r3pre (Schrödinger, LLC).
37. Baker, N. A., Sept, D., Joseph, S., Holst, M. J. & McCammon, J. A. Electrostatics of nanosystems: application to microtubules and the ribosome. *Proc. Natl Acad. Sci. USA* **98**, 10037–10041 (2001).
38. Ashkenazy, H., Erez, E., Martz, E., Pupko, T. & Ben-Tal, N. ConSurf 2010: calculating evolutionary conservation in sequence and structure of proteins and nucleic acids. *Nucleic Acids Res.* **38**, W529–W533 (2010).
39. Reichmann, D. et al. Binding hot spots in the TEM1-BLIP interface in light of its modular architecture. *J. Mol. Biol.* **365**, 663–679 (2007).

# An eclipsing–binary distance to the Large Magellanic Cloud accurate to two per cent

G. Pietrzyński<sup>1,2</sup>, D. Graczyk<sup>1</sup>, W. Gieren<sup>1</sup>, I. B. Thompson<sup>3</sup>, B. Pilecki<sup>1,2</sup>, A. Udalski<sup>2</sup>, I. Soszyński<sup>2</sup>, S. Kozłowski<sup>2</sup>, P. Konorski<sup>2</sup>, K. Suchomska<sup>2</sup>, G. Bono<sup>4,5</sup>, P. G. Prada Moroni<sup>6,7</sup>, S. Villanova<sup>1</sup>, N. Nardetto<sup>8</sup>, F. Bresolin<sup>9</sup>, R. P. Kudritzki<sup>9</sup>, J. Storm<sup>10</sup>, A. Gallenne<sup>1</sup>, R. Smolec<sup>11</sup>, D. Minniti<sup>12,13</sup>, M. Kubiak<sup>2</sup>, M. K. Szymański<sup>2</sup>, R. Poleski<sup>2,14</sup>, Ł. Wyrzykowski<sup>2</sup>, K. Ulaczyk<sup>2</sup>, P. Pietrukowicz<sup>2</sup>, M. Górski<sup>2</sup> & P. Karczmarek<sup>2</sup>

**In the era of precision cosmology, it is essential to determine the Hubble constant to an accuracy of three per cent or better<sup>1,2</sup>. At present, its uncertainty is dominated by the uncertainty in the distance to the Large Magellanic Cloud (LMC), which, being our second-closest galaxy, serves as the best anchor point for the cosmic distance scale<sup>2,3</sup>. Observations of eclipsing binaries offer a unique opportunity to measure stellar parameters and distances precisely and accurately<sup>4,5</sup>. The eclipsing-binary method was previously applied to the LMC<sup>6,7</sup>, but the accuracy of the distance results was lessened by the need to model the bright, early-type systems used in those studies. Here we report determinations of the distances to eight long-period, late-type eclipsing systems in the LMC, composed of cool, giant stars. For these systems, we can accurately measure both the linear and the angular sizes of their components and avoid the most important problems related to the hot, early-type systems. The LMC distance that we derive from these systems ( $49.97 \pm 0.19$  (statistical)  $\pm 1.11$  (systematic) kiloparsecs) is accurate to 2.2 per cent and provides a firm base for a 3-per-cent determination of the Hubble constant, with prospects for improvement to 2 per cent in the future.**

The modelling of early-type eclipsing binary systems consisting of hot stars is made difficult by the problem of obtaining accurate flux calibrations for early-type stars and by the degeneracy between the stellar effective temperatures and reddening<sup>8,9</sup>. As a result, the distances determined from such systems are of limited ( $\sim 5$ – $10\%$ ) accuracy. More-accurate distances can be obtained using binary systems composed of cool stars; however, among the frequent dwarf stars in the LMC such systems are too faint to be accurately analysed with present-day telescopes.

The Optical Gravitational Lensing Experiment (OGLE) has been monitoring around 35 million stars in the field of the LMC for more than 16 years<sup>10</sup>. Using this unique data set, we have detected a dozen extremely scarce, very long-period (60–772-d) eclipsing binary systems composed of intermediate-mass, late-type giants located in a quiet evolutionary phase on the helium-burning loop<sup>11</sup> (Supplementary Table 1). These well-detached systems provide an opportunity to use the full potential of eclipsing binaries as precise and accurate distance indicators, and to calibrate the zero point of the cosmic distance scale with an accuracy of about 2% (refs 5, 12, 13).

To do so, we observed eight of these systems (Fig. 1 shows one example) over the past 8 yr, collecting high-resolution spectra with the MIKE spectrograph at the 6.5-m Magellan Clay telescope at the Las Campanas Observatory and with the HARPS spectrograph attached to the 3.6-m telescope of the European Southern Observatory on La

Silla, together with near-infrared photometry obtained with the 3.5-m New Technology Telescope located on La Silla.

The spectroscopic and OGLE V- and I-band photometric observations of the binary systems were then analysed using the 2007 version of the standard Wilson–Devinney code<sup>14,15</sup>, in the same way as in our recent work on a similar system in the Small Magellanic Cloud<sup>9</sup>. Realistic errors in the derived parameters of our systems were obtained from extensive Monte Carlo simulations (Fig. 2). The astrophysical parameters of all the observed eclipsing binaries were determined with an accuracy of a few per cent (Supplementary Tables 2–9).

For late-type stars, we can use the very accurately calibrated (2%) relation between their surface brightness and  $V$ – $K$  colour to determine their angular sizes from optical ( $V$ ) and near-infrared ( $K$ ) photometry<sup>16</sup>. From this surface-brightness/colour relation (SBCR), we can derive angular sizes of the components of our binary systems directly from the definition of the surface brightness. Therefore, the distance can be measured by combining the angular diameters of the binary components derived in this way with their corresponding linear dimensions obtained from the analysis of the spectroscopic and photometric data. The distances measured with this very simple but accurate one-step method are presented in Supplementary Table 12. The statistical errors in the distance determinations were calculated by adding quadratically the uncertainties in absolute dimensions,  $V$ – $K$  colours, reddening and the adopted reddening law. The reddening uncertainty contributes very little (0.4%) to the total error<sup>11,17</sup>. A significant change in the reddening law (from  $R_v = 3.1$  to 2.7, where  $R_v$  is the ratio of total to selective absorption) causes an almost negligible contribution, at the level of 0.3%. The accuracy of the  $V$ – $K$  colour for all components of our eight binary systems is better than 0.014 mag (0.7%). The resulting statistical errors in the distances are very close to 1.5%, and are dominated by the uncertainty in the absolute dimensions. By calculating a weighted mean from the individual distances to the eight target eclipsing binary systems, we obtain a mean LMC distance of  $49.88 \pm 0.13$  kpc.

Our distance measurement might be affected by the geometry and depth of the LMC. Fortunately, the geometry of the LMC is simple and well studied<sup>18</sup>. Because nearly all the eclipsing systems are located very close to the centre of the LMC and to the line of nodes (Fig. 3), we fitted the distance to the centre of the LMC disk plane, assuming its spatial orientation<sup>18</sup>. We obtained an LMC barycentre distance of  $49.97 \pm 0.19$  kpc (Fig. 4), which is nearly identical to the simple weighted mean value. This shows that the geometrical structure of the LMC has no significant influence on our present distance determination.

<sup>1</sup>Universidad de Concepción, Departamento de Astronomía, Casilla 160-C, Concepción, Chile. <sup>2</sup>Warsaw University Observatory, Aleje Ujazdowskie 4, 00-478 Warszawa, Poland. <sup>3</sup>Carnegie Observatories, 813 Santa Barbara Street, Pasadena, California 91101-1292, USA. <sup>4</sup>Dipartimento di Fisica Università di Roma Tor Vergata, Via della Ricerca Scientifica 1, 00133 Rome, Italy. <sup>5</sup>INAF-Osservatorio Astronomico di Roma, Via Frascati 33, 00040 Monte Porzio Catone, Italy. <sup>6</sup>Dipartimento di Fisica Università di Pisa, Largo B. Pontecorvo 2, 56127 Pisa, Italy. <sup>7</sup>INFN, Sezione di Pisa, Via E. Fermi 2, 56127 Pisa, Italy. <sup>8</sup>Laboratoire Lagrange, UMR7293, UNS/CNRS/OCA, 06300 Nice, France. <sup>9</sup>Institute for Astronomy, 2680 Woodlawn Drive, Honolulu, Hawaii 96822, USA. <sup>10</sup>Leibniz Institute for Astrophysics, An der Sternwarte 16, 14482 Potsdam, Germany. <sup>11</sup>Nicolaus Copernicus Astronomical Centre, Bartycka 18, 00-716 Warszawa, Poland. <sup>12</sup>Departamento de Astronomía y Astrofísica, Pontificia Universidad Católica de Chile, Vicuña Mackenna 4860, Casilla 306, Santiago 22, Chile. <sup>13</sup>Vatican Observatory, V00120 Vatican City, Italy. <sup>14</sup>Ohio State University, 140 West 18th Avenue, Columbus, Ohio 43210, USA.



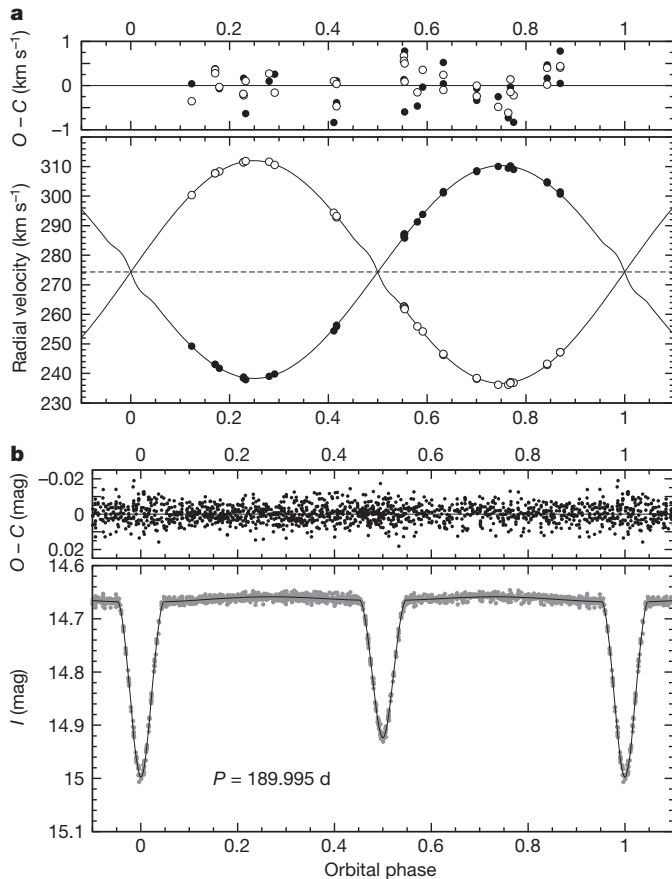


**Figure 1** | Change of the brightness of the binary system OGLE-LMC-ECL-06575 and the orbital motion of its components. **a**, The main panel shows the orbital motion of the two binary components in the system OGLE-LMC-ECL-06575. Filled circles, primary component; open circles, secondary component. The top panel shows the residuals of the fit (see below): observed radial velocities (O) minus the computed radial velocities (C). **b**, The main panel shows the I-band light curve (1,200 epochs collected over 16 yr) of OGLE-LMC-ECL-06575 together with the solution obtained using the Wilson-Devinney code.  $P$ , orbital period. The top panel shows the residuals of the observed magnitudes from the computed orbital light curve. All individual radial velocities were determined by the cross-correlation method using appropriate template spectra and spectra from the Magellan Inamori Kyocera Echelle (MIKE) and High Accuracy Radial Velocity Planet Searcher (HARPS) spectrographs, yielding in all cases velocity accuracies better than  $200 \text{ m s}^{-1}$  (error bars smaller than the plotted symbols). The orbit (mass ratio, systemic velocity, velocity amplitudes, eccentricity and periastron passage) was fitted with a least-squares method to the measured velocities. The resulting parameters are presented in Supplementary Tables 2–9. The spectroscopic orbits, light curves and solutions for the remaining systems are of similar quality.

The systematic uncertainty in our distance measurement comes from the calibration of the SBCR and the accuracy of the zero points in our photometry. The root mean squared scatter in the current SBCR is 0.03 mag (ref. 13), which translates to an accuracy of 2% in the respective angular diameters of the component stars. Because the surface brightness depends only very weakly on metallicity<sup>16,17</sup>, this effect contributes to the total error budget at the level of only 0.3% (ref. 9). Both optical ( $V$ ) and near-infrared ( $K$ ) photometric zero points are accurate to 0.01 mag (0.5%). Combining these contributions quadratically, we determine a total systematic error of 2.1% in our present LMC distance determination.

The LMC contains significant numbers of different stellar distance indicators, and, being the second-closest galaxy to our own, offers us a unique opportunity to study these indicators with the utmost precision. For this reason, this galaxy has an impressive record of several hundred distance measurements<sup>2,3,19</sup>. Unfortunately, almost all LMC

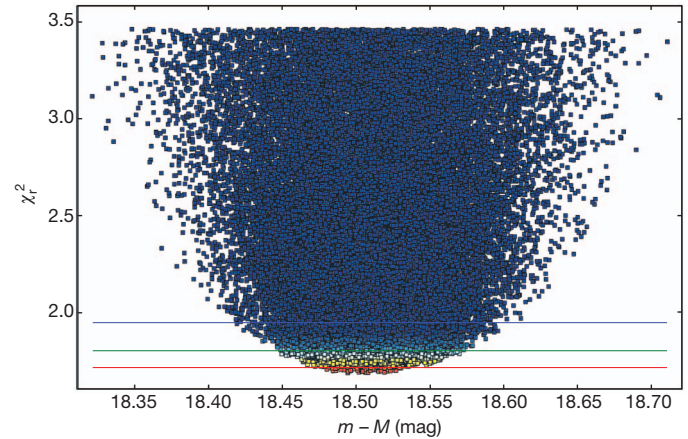


**Figure 2** | Error estimation of the distance for one of our target binary systems. The reduced  $\chi^2$  map (goodness of fit) for the system OGLE-LMC-ECL-15260 showing the dependence of the goodness of fit to the V-band and I-band light curves on the distance modulus of the primary component. This map was obtained from 110,000 models computed with the Wilson-Devinney code<sup>14,15</sup> within a broad range of the primary and secondary radii,  $R_1$  and  $R_2$ , the orbital inclination,  $i$ , the phase shift,  $\phi$ , the secondary's temperature,  $T_2$ , and albedo,  $A_2$ . In each case the distance,  $d$ , was calculated from the V-band surface-brightness/colour ( $V-K$ ) relation<sup>16</sup> and translated into distance modulus using  $m-M = 5\log(d) - 5$ , where  $m$  and  $M$  are the observed and absolute brightnesses, respectively. The horizontal lines correspond to the standard-deviation limits of the derived distance modulus, of 18.509 mag (50.33 kpc):  $1\sigma$ ,  $2\sigma$  and  $3\sigma$ , from bottom to top.

distance determinations are dominated by systematic errors, with each method having its own sources of uncertainties. This prevents a calculation of the true LMC distance by simply taking the mean of the

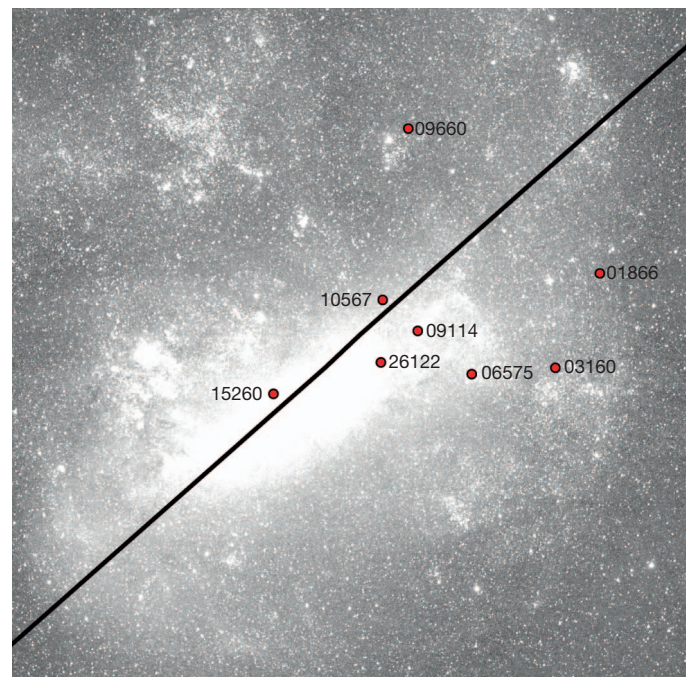


**Figure 3** | Location of the observed eclipsing systems in the LMC. Most of our eight systems (circles) are located quite close to the geometrical centre of the LMC and to the line of nodes (line), resulting in very small corrections to the individual distances for the geometrical extension of this galaxy (in all cases smaller than the corresponding statistical error in the distance determination). The effect of the geometrical structure of the LMC on the mean LMC distance reported here is therefore negligible. The background image has a field of view of  $8^\circ \times 8^\circ$  and is taken from the All Sky Automated Survey wide-field sky survey<sup>28</sup>.

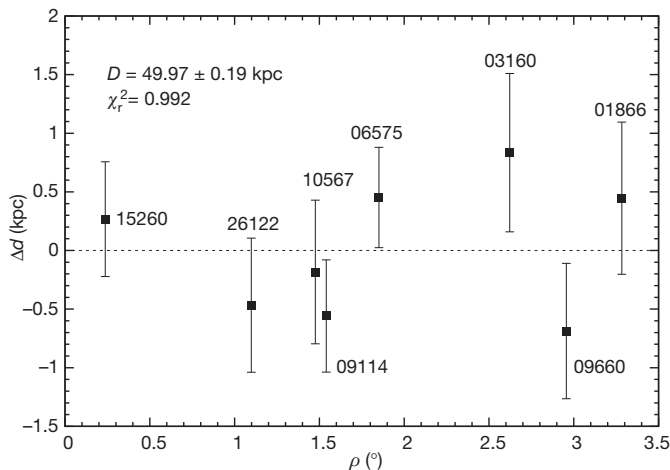


**Figure 4 | Consistency among the distance determinations for the target binary systems.** Distance offsets,  $\Delta d$ , between our particular eclipsing binary systems and the best-fitted LMC disk plane, plotted against the angular distance of the systems from the LMC centre,  $\rho$ . The identification of the systems is the same as in Fig. 3. The error bars correspond to  $1\sigma$  errors. We assumed the model of the LMC from ref. 18. We fitted one parameter, the distance to the centre of the LMC (RA = 5 h 25 min 06 s; dec. =  $-69^\circ 47' 00''$ ), using a fixed spatial orientation of the LMC disk (inclination,  $i = 28^\circ$ ; position angle of the nodes,  $\theta = 128^\circ$ ). The resulting distance to the LMC barycentre is  $49.97 \pm 0.19$  kpc, with a reduced  $\chi^2$  value very close to unity.

reported distances resulting from different techniques. Our present LMC distance measurement, of  $49.97 \pm 0.19$  (statistical)  $\pm 1.11$  (systematic) kpc (that is, a true distance modulus of  $18.493 \pm 0.008$  (statistical)  $\pm 0.047$  (systematic) mag), agrees well, within the combined errors, with the most recent determinations of the distance to the LMC<sup>19,20,21</sup>. Our purely empirical method allows us to estimate both statistical and systematic errors in a very reliable way, which is normally not the case, particularly in distance determinations relying in part on theoretical predictions of stellar properties and their dependences on environment. In particular, our result provides a significant improvement over previous LMC distance determinations made using observations of eclipsing binaries<sup>7,22</sup>. Those studies were based on early-type systems for which no empirical SBCR is available, and so had to rely on theoretical models to determine the effective temperature. Our present determination is based on many (eight) binary systems and does not resort to model predictions.

The classical approach to deriving the Hubble constant ( $H_0$ ) consists of deriving an absolute calibration of the Cepheid period–luminosity relation (CPLR), which is then used to determine the distances to nearby galaxies containing type Ia supernovae<sup>23</sup>. These supernovae are excellent standard candles that extend out to the region of unperturbed Hubble flow once their peak brightnesses are calibrated this way, and provide the most accurate determination of  $H_0$  (ref. 24). An alternative approach to calibrate the CPLR with Cepheids in the LMC is to calibrate it in our own Milky Way galaxy using Hubble Space Telescope (HST) parallax measurements of the Cepheids nearest to the Sun<sup>25</sup>. However, the CPLR that results from that approach is less accurate for two reasons. First, the Cepheid sample with HST parallaxes is very small (ten stars) relative to the Cepheid sample in the LMC (2,000 stars), which can be used to establish the CPLR once the LMC distance is known. Second, the average accuracy of the HST Cepheid parallaxes is 8% (ref. 25) and suffers from systematic uncertainties that are not completely understood, including Lutz–Kelker bias<sup>26,27</sup>. Therefore, at present the preferred route to determining the Hubble constant is that which uses the highly abundant LMC Cepheid population whose mean distance is now known, with the result of this work, to 2.2%. This result reduces the uncertainty in  $H_0$  to a very firmly established 3%.

We have good reason to believe that there is significant room to improve on the high-accuracy LMC distance determination reported here, by improving the calibration of the SBCR for late-type stars<sup>12,16</sup>, which is the dominant source of systematic error in our present determination. This work is in progress, and a determination of the distance to the LMC accurate to 1% should be possible once the SBCR calibration is refined. This will have a corresponding effect on further improving the accuracy of  $H_0$ . This is similar to the accuracy of the geometrical distance to the LMC, which is to be delivered by Gaia mission in around 12 years from now. The eclipsing-binary technique will then probably provide the best opportunity to check on the future Gaia measurements for possible systematic errors.

Received 19 August; accepted 20 December 2012.

- Komatsu, E. *et al.* Seven-year Microwave Anisotropy Probe (WMAP) observations: cosmological interpretation. *Astrophys. J. Suppl. Ser.* **192**, 18–65 (2011).
- Freedman, W. L. & Madore, B. F. The Hubble constant. *Annu. Rev. Astron. Astrophys.* **48**, 673–710 (2010).
- Schaefer, B. E. A problem with the clustering of recent measures of the distance to the Large Magellanic Cloud. *Astron. J.* **135**, 112–119 (2008).
- Lacy, C. H. Distances to eclipsing binaries: an application of the Barnes–Evans relation. *Astrophys. J.* **213**, 458–463 (1977).
- Paczynski, B. In *The Extragalactic Distance Scale* (eds Livio, M., Donahue, M. & Panagia, N.) 273–280 (Space Telescope Sci. Inst. Ser., Cambridge Univ. Press, 1997).
- Guinan, E. F. The distance to the Large Magellanic Cloud from the eclipsing binary HV 2274. *Astrophys. J.* **509**, L21–L24 (1998).
- Fitzpatrick, E. L., Ribas, I., Guinan, E. F., Maloney, F. P. & Claret, A. Fundamental properties and distances of Large Magellanic Cloud eclipsing binaries. IV. HV 5936. *Astrophys. J.* **587**, 685–700 (2003).
- Groenewegen, M. A. T. & Salaris, M. The LMC eclipsing binary HV 2274 revisited. *Astrophys. J.* **366**, 752–764 (2001).
- Graczyk, D. *et al.* The Araucaria project: an accurate distance to the late-type double-lined eclipsing binary OGLE SMC113.3 4007 in the Small Magellanic Cloud. *Astrophys. J.* **750**, 144–156 (2012).
- Udalski, A. *et al.* The Optical Gravitational Lensing Experiment: OGLE-III photometric maps of the Large Magellanic Cloud. *Acta Astron.* **58**, 89–102 (2008).
- Graczyk, D. *et al.* The Optical Gravitational Lensing Experiment: the OGLE-III catalog of variable stars. XII. Eclipsing binary stars in the Large Magellanic Cloud. *Acta Astron.* **61**, 103–122 (2011).
- Kruszewski, A. & Semeniuk, I. Nearby Hipparcos eclipsing binaries for color-surface brightness calibration. *Acta Astron.* **49**, 561–575 (1999).
- Pietrzyński, G. *et al.* The Araucaria project: determination of the Large Magellanic Cloud distance from late-type eclipsing binary systems. I. OGLE051019.64–685812.3. *Astrophys. J.* **697**, 862–866 (2009).
- Wilson, R. E. & Devinney, E. J. Realization of accurate close-binary light curves: application to MR Cygni. *Astrophys. J.* **166**, 605–620 (1971).
- Van Hamme, W. & Wilson, R. E. Third-body parameters from whole light and velocity curves. *Astrophys. J.* **661**, 1129–1151 (2007).
- Di Benedetto, G. P. Predicting accurate stellar angular diameters by the near-infrared surface brightness technique. *Mon. Not. R. Astron. Soc.* **357**, 174–190 (2005).
- Thompson, I. B. *et al.* Cluster AgeS Experiment. The age and distance of the globular cluster  $\omega$  Centauri determined from observations of the eclipsing binary OGLEC 17. *Astron. J.* **121**, 3089–3099 (2001).
- van der Marel, R. P., Alves, D. R., Hardy, E. & Suntzeff, N. B. New understanding of Large Magellanic Cloud structure, dynamics, and orbit from carbon star kinematics. *Astron. J.* **124**, 2639–2663 (2002).
- Mazzarella, J. M. NED for a new era. *Astron. Soc. Pacif. Conf.* **376**, 153–162 (2007).
- Walker, A. R. The Large Magellanic Cloud and the distance scale. *Astrophys. Space Sci.* **341**, 43–49 (2012).
- Monson, A. J. *et al.* The Carnegie Hubble Program: The Leavitt Law at 3.6 and 4.5  $\mu$ m in the Milky Way. *Astrophys. J.* **759**, 146–165 (2012).
- Bonanos, A. Z., Castro, N., Macri, L. M. & Kudritzki, R. P. The distance to the massive eclipsing binary LMC-SC1–105 in the Large Magellanic Cloud. *Astrophys. J.* **729**, L9–L15 (2011).
- Freedman, W. L. *et al.* Final results from the Hubble Space Telescope key project to measure the Hubble constant. *Astrophys. J.* **553**, 47–72 (2001).
- Riess, A. G. *et al.* A 3% solution: determination of the Hubble constant with the Hubble Space Telescope and Wide Field Camera 3. *Astrophys. J.* **730**, 119–137 (2011).
- Benedict, G. F. *et al.* Hubble Space Telescope fine guidance sensor parallaxes of galactic Cepheid variable stars: period–luminosity relations. *Astron. J.* **133**, 1810–1827 (2007).
- Lutz, T. E. & Kelker, D. H. On the use of trigonometric parallaxes for the calibration of luminosity systems: theory. *Publ. Astron. Soc. Pacif.* **85**, 573–578 (1973).
- van Leeuwen, F., Feast, M. W., Whitelock, P. A. & Laney, C. D. Cepheid parallaxes and the Hubble constant. *Mon. Not. R. Astron. Soc.* **379**, 723–737 (2007).
- Pojmański, G. The All Sky Automated Survey. *Acta Astron.* **47**, 467–481 (1997).

**Supplementary Information** is available in the online version of the paper.

**Acknowledgements** We acknowledge financial support for this work from the BASAL Centro de Astrofísica y Tecnologías Afines (CATA), the Polish Ministry of Science, the

Foundation for Polish Science (FOCUS, TEAM), the Polish National Science Centre and the GEMINI-CONICYT fund. The OGLE project has received funding from the European Research Council 'Advanced Grant' Program. We thank the staff astronomers at Las Campanas and ESO La Silla, who provided expert support in data acquisition. We thank J. F. Gonzalez for making the IRAF scripts *rvbina* and *spbina* available to us. We also thank O. Szewczyk and Z. Kolaczowski for their help with some of the observations.

**Author Contributions** G.P.: photometric and spectroscopic observations and reductions. D.G.: spectroscopic observations, modelling and data analysis. W.G.: observations and data analysis. I.B.T.: observations, RV determination, data analysis.

B.P.: spectroscopic observations and reductions, RV measurements. A.U., I.S. and S. K.: optical observations and data reductions. P.K., K.S., M.K., M.K.S., R.P., Ł.W., K.U., P.P., M.G. and P.K.: observations. G.B., P.G.P.M., N.N., F.B., R.P.K., J.S., A.G. and R.S.: data analysis. S.V.: analysis of the spectra. G.P. and W.G. worked jointly to draft the manuscript with all authors reviewing and contributing to its final form

**Author Information** Reprints and permissions information is available at [www.nature.com/reprints](http://www.nature.com/reprints). The authors declare no competing financial interests. Readers are welcome to comment on the online version of the paper. Correspondence and requests for materials should be addressed to G.P. ([pietrzyn@astrouw.edu.pl](mailto:pietrzyn@astrouw.edu.pl)).



# Porous materials with optimal adsorption thermodynamics and kinetics for CO<sub>2</sub> separation

Patrick Nugent<sup>1\*</sup>, Youssef Belmabkhout<sup>2\*</sup>, Stephen D. Burd<sup>1</sup>, Amy J. Cairns<sup>2</sup>, Ryan Luebke<sup>2</sup>, Katherine Forrest<sup>1</sup>, Tony Pham<sup>1</sup>, Shengqian Ma<sup>1</sup>, Brian Space<sup>1</sup>, Lukasz Wojtas<sup>1</sup>, Mohamed Eddaoudi<sup>1,2</sup> & Michael J. Zaworotko<sup>1</sup>

The energy costs associated with the separation and purification of industrial commodities, such as gases, fine chemicals and fresh water, currently represent around 15 per cent of global energy production, and the demand for such commodities is projected to triple by 2050 (ref. 1). The challenge of developing effective separation and purification technologies that have much smaller energy footprints is greater for carbon dioxide (CO<sub>2</sub>) than for other gases; in addition to its involvement in climate change, CO<sub>2</sub> is an impurity in natural gas, biogas (natural gas produced from biomass), syngas (CO/H<sub>2</sub>, the main source of hydrogen in refineries) and many other gas streams. In the context of porous crystalline materials that can exploit both equilibrium and kinetic selectivity, size selectivity and targeted molecular recognition are attractive characteristics for CO<sub>2</sub> separation and capture, as exemplified by zeolites 5A and 13X (ref. 2), as well as metal–organic materials (MOMs)<sup>3–9</sup>. Here we report that a crystal engineering<sup>7</sup> or reticular chemistry<sup>5,9</sup> strategy that controls pore functionality and size in a series of MOMs with coordinately saturated metal centres and periodically arrayed hexafluorosilicate (SiF<sub>6</sub><sup>2–</sup>) anions enables a ‘sweet spot’ of kinetics and thermodynamics that offers high volumetric uptake at low CO<sub>2</sub> partial pressure (less than 0.15 bar). Most importantly, such MOMs offer an unprecedented CO<sub>2</sub> sorption selectivity over N<sub>2</sub>, H<sub>2</sub> and CH<sub>4</sub>, even in the presence of moisture. These MOMs are therefore relevant to CO<sub>2</sub> separation in the context of post-combustion (flue gas, CO<sub>2</sub>/N<sub>2</sub>), pre-combustion (shifted synthesis gas stream, CO<sub>2</sub>/H<sub>2</sub>) and natural gas upgrading (natural gas clean-up, CO<sub>2</sub>/CH<sub>4</sub>).

Porous materials with unsaturated metal centres (UMCs)<sup>10</sup> or organic amines that chemically interact with CO<sub>2</sub> enhance selectivity for CO<sub>2</sub> in the presence of other gases. However, there are drawbacks: high energy costs associated with activation, regeneration and recycling of the sorbent material, especially for amines<sup>11</sup>; competition with water vapour, especially for UMCs<sup>12</sup>; and selectivity tends to monotonically decrease with increased loading of sorbate. Consequently, there remains a need for sorbents with favourable CO<sub>2</sub> sorption kinetics and thermodynamics over a wide range of CO<sub>2</sub> loading that would permit efficient CO<sub>2</sub> capture with low regeneration costs. MOMs are attractive in this context because they are inherently modular—that is, they consist of metals or metal clusters (‘nodes’ or ‘molecular building blocks’) coordinated to multi-functional organic ligands (‘linkers’)—and they offer extra-large surface areas, up to 7,000 m<sup>2</sup> g<sup>–1</sup> (ref. 6). However, although extra-large surface area facilitates high gravimetric uptake of gases at low temperature and/or high pressure, it is not necessarily conducive to efficient separations under practical conditions. Here we address how to optimize the thermodynamics and kinetics of gas adsorption through a class of MOMs that is amenable to crystal engineering or isorecticular chemistry in a manner that facilitates precise control over pore size and functionality: namely, ‘pillared square grids’, two-dimensional nets based on linked metal nodes

that are pillared via SiF<sub>6</sub><sup>2–</sup> anions (‘SIFSIX’) in the third dimension to form three-dimensional nets with primitive cubic topology<sup>13</sup>.

[Cu(4,4′-bipyridine)<sub>2</sub>(SiF<sub>6</sub>)]<sub>n</sub>, a prototypal primitive-cubic net that remains one of the best sorbents for CH<sub>4</sub> as measured by volumetric uptake<sup>14</sup>, exhibits highly selective CO<sub>2</sub> uptake versus both CH<sub>4</sub> and N<sub>2</sub> at 1 bar and 298 K (ref. 15). In the absence of UMCs or amine groups, we attributed this behaviour to favourable interactions between CO<sub>2</sub> and SIFSIX. This compound, which we call here SIFSIX-1-Cu, exhibits one-dimensional square channels (pore size 9.54 Å; here and throughout this Letter, pore sizes are given as diagonal dimensions) aligned by a periodic array of SIFSIX pillars, and is prototypal for a class of compounds that is amenable to pore-size tuning. In this Letter we report the synthesis, structure and sorption properties of three variants of SIFSIX-1-Cu with expanded and contracted pore sizes.

Reaction of 4,4′-dipyridylacetylene, dpa (ref. 16), with CuSiF<sub>6</sub> afforded purple rod-shaped crystals of [Cu(dpa)<sub>2</sub>(SiF<sub>6</sub>)]<sub>n</sub>, which we refer to as SIFSIX-2-Cu (see Supplementary Information for synthetic and crystallographic details for this and other compounds reported here). SIFSIX-2-Cu forms the expected primitive-cubic net with square channels of pore dimensions 13.05 Å (Fig. 1a). The interpenetrated polymorph, SIFSIX-2-Cu-i (Fig. 1b), is composed of doubly interpenetrated nets that are isostructural to the nets in SIFSIX-2-Cu. The independent nets are staggered with respect to one another, affording 5.15 Å pores (Fig. 1b). The isorecticular MOM based on pyrazine (pyr) SIFSIX-3-Zn, [Zn(pyr)<sub>2</sub>(SiF<sub>6</sub>)]<sub>n</sub>, was prepared according to published procedures<sup>17</sup> and is also a primitive-cubic net which encloses 3.84 Å channels (Fig. 1c). Pore sizes in this series therefore range from ultra-microporous to nanoporous. Bulk purity was confirmed using powder X-ray diffraction (PXRD) patterns (Supplementary Figs 1–3).

Activation of SIFSIX-2-Cu and SIFSIX-2-Cu-i (evacuation at 298 K for 12 h) afforded BET apparent surface areas of 3,140 and 735 m<sup>2</sup> g<sup>–1</sup>, respectively (corresponding Langmuir values, 3,370 and 821 m<sup>2</sup> g<sup>–1</sup>), from N<sub>2</sub> adsorption isotherms at 77 K. Micropore volumes are in good agreement with corresponding theoretical values (Supplementary Fig. 4 and Supplementary Table 3). SIFSIX-3-Zn adsorbs minimal amounts of N<sub>2</sub> at 77 K and thus its surface area (250 m<sup>2</sup> g<sup>–1</sup>) was determined from the CO<sub>2</sub> isotherm collected at 298 K (ref. 18).

Low-pressure CO<sub>2</sub>, CH<sub>4</sub> and N<sub>2</sub> sorption data were collected at 298 K (Supplementary Fig. 5a, Table 1). SIFSIX-2-Cu exhibited CO<sub>2</sub> uptake of 41.4 cm<sup>3</sup> g<sup>–1</sup> (equivalent to 1.84 mmol g<sup>–1</sup> or 81.3 mg g<sup>–1</sup>) at 298 K and 1 bar, but its denser polymorph, SIFSIX-2-Cu-i, exhibited substantially higher values of 121.2 cm<sup>3</sup> g<sup>–1</sup> (5.41 mmol g<sup>–1</sup>, 238 mg g<sup>–1</sup>). Such behaviour has also been observed in the context of hydrogen adsorption<sup>19</sup>. A review of the literature reveals that the gravimetric CO<sub>2</sub> uptake of SIFSIX-2-Cu-i at 298 K and 1 bar is among the highest yet reported in the context of MOMs (for example, Mg-dobdc (ref. 10), Co-dobdc (ref. 10), MIL-101 (ref. 20), [Cu(Me-4py-trz-ia)] (ref. 21) and partially hydrated HKUST-1 (ref. 22)). Notably, the above-mentioned

<sup>1</sup>Department of Chemistry, University of South Florida, 4202 East Fowler Avenue, Tampa, Florida 33620, USA. <sup>2</sup>Advanced Membranes and Porous Materials Center, Division of Physical Sciences and Engineering, 4700 King Abdullah University of Science and Technology (KAUST), Thuwal 23955-6900, Saudi Arabia.

\*These authors contributed equally to this work.

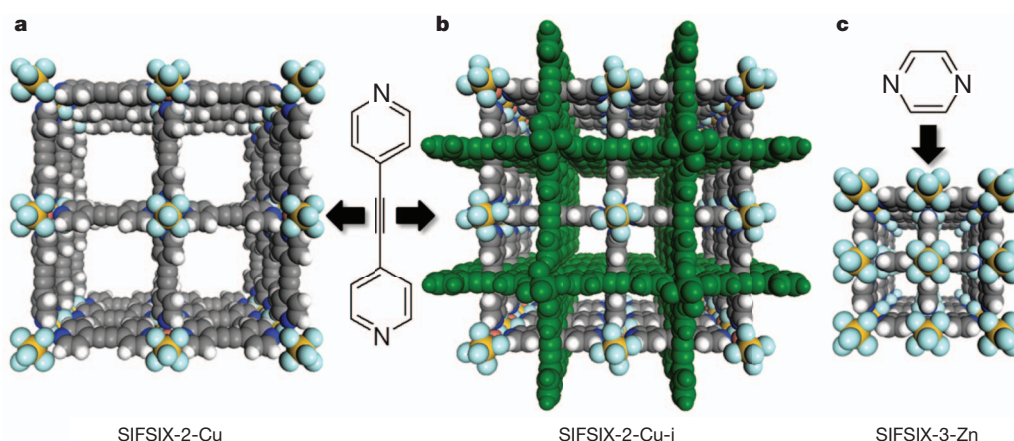


**Figure 1 | The variable pore size channel structures of SIFSIX-2-Cu, SIFSIX-2-Cu-i and SIFSIX-3-Zn.** **a**, SIFSIX-2-Cu; pore size 13.05 Å, BET apparent surface area ( $\text{N}_2$  adsorption)  $3,140 \text{ m}^2 \text{ g}^{-1}$ . **b**, SIFSIX-2-Cu-i; pore size 5.15 Å, BET apparent surface area ( $\text{N}_2$  adsorption)  $735 \text{ m}^2 \text{ g}^{-1}$ . **c**, SIFSIX-3-Zn; pore size 3.84 Å, apparent surface area (determined from  $\text{CO}_2$  adsorption

isotherm)  $250 \text{ m}^2 \text{ g}^{-1}$ . Colour code: C (grey), N (blue), Si (yellow), F (light blue), H (white). All guest molecules are omitted for clarity. Note that the green net represents the interpenetrated net in SIFSIX-2-Cu-i. The nitrogen-containing linker present in SIFSIX-2-Cu and SIFSIX-2-Cu-i is 4,4'-dipyridylacetylene (dpa) whereas that in SIFSIX-3-Zn is pyrazine (pyr).

benchmark MOMs possess higher surface area, are less dense than SIFSIX-2-Cu-i and contain UMCs. Volumetric  $\text{CO}_2$  uptake of SIFSIX-2-Cu-i at atmospheric pressure approaches that of Mg-dobdc (151 versus 163 v/v). Ideal adsorbed solution theory (IAST)<sup>23</sup> calculations indicate binary gas adsorption selectivity (Supplementary Fig. 5b) under practically relevant conditions (298 K;  $\text{CH}_4$  and  $\text{N}_2$  mole fractions equal to 0.5 and 0.9, respectively) to be dramatically higher for SIFSIX-2-Cu-i than SIFSIX-2-Cu for both  $\text{CO}_2/\text{CH}_4$  (33 versus 5.3) and  $\text{CO}_2/\text{N}_2$  (140 versus 13.7). These findings agree with the  $\text{CO}_2/\text{CH}_4$  (51) and  $\text{CO}_2/\text{N}_2$  (72) adsorption selectivity determined experimentally for SIFSIX-2-Cu-i using column breakthrough tests, a technique that determines the necessary time for a given volume of a gas to pass through a given sorbent bed column (Supplementary Fig. 6). To the best of our knowledge, the  $\text{CO}_2/\text{CH}_4$  and  $\text{CO}_2/\text{N}_2$  IAST selectivities exhibited by SIFSIX-2-Cu-i are the highest yet reported for a MOM without UMCs or amino groups. We attribute these observations to the enhanced isosteric heat of adsorption ( $Q_{\text{st}}$ ) of SIFSIX-2-Cu-i versus SIFSIX-2-Cu (45% higher at minimum loading, 71.5% greater at  $2.8 \text{ mmol g}^{-1}$ ,

Supplementary Fig. 5c). This increase is presumably attributable to better overlap of attractive potential fields of opposite walls in the relatively narrower pores of SIFSIX-2-Cu-i. SIFSIX-2-Cu-i is particularly suitable for  $\text{CO}_2$  separation from syngas, as shown by its selectivity (240) for  $\text{CO}_2$  over  $\text{H}_2$  in a  $\text{CO}_2/\text{H}_2$ :30/70 mixture, and as determined from column breakthrough experiments (Supplementary Fig. 6c).

The heart of pressure- and temperature-swing adsorption (PSA and TSA) processes for  $\text{CO}_2$  removal is the adsorbent bed: a recent study projected that a  $\text{CO}_2/\text{N}_2$  selectivity of  $>500$  combined with a capacity of  $2\text{--}4 \text{ mmol g}^{-1}$  for a  $\text{CO}_2/\text{N}_2$ :10/90 mixture would be required for practical utility (Supplementary Fig. 7)<sup>24</sup>. Figure 2a and b presents the  $\text{CO}_2$  adsorption isotherms of SIFSIX-2-Cu-i and SIFSIX-3-Zn, respectively, collected at sub-atmospheric pressures after activation at 298 K. Contraction of the pores led to a sharp increase in  $\text{CO}_2$  uptake at low  $\text{CO}_2$  loading, with nearly 11 wt% at 0.1 bar for SIFSIX-3-Zn versus 4.4 wt% at 0.1 bar for SIFSIX-2-Cu-i. Notably, the  $\text{CO}_2$  uptake for SIFSIX-3-Zn reached saturation at relatively low pressures ( $\sim 0.3$  bar; Supplementary Fig. 8), whereas the isotherm for  $\text{CO}_2$

**Table 1 | Gas adsorption/ $\text{CO}_2$  selectivity results and comparisons**

Property	Compounds				
	SIFSIX-2-Cu	SIFSIX-2-Cu-i	SIFSIX-3-Zn	Mg-dobdc*	13X†
Pore size (Å)	13.05	5.15	3.84	10.8	10
<b>Single-gas data</b>					
$Q_{\text{st}}$ for $\text{CO}_2$ at low $\text{CO}_2$ loading ( $\text{kJ mol}^{-1}$ )	22	31.9	45	47–52	44–54
$\text{CO}_2$ uptake at 298 K at 0.1 bar/1 bar ( $\text{mg g}^{-1}$ )	10/81.3	76/238	105/112	220/352	106/220
$\text{CO}_2$ uptake at 298 K at 0.1 bar/1 bar ( $\text{cm}^3 \text{ cm}^{-3}$ )	3/26	48/151	84/90	101/162	61/126
$\text{CH}_4$ uptake at 298 K at 1 bar ( $\text{mg g}^{-1}$ )	6.2	7.5	12.6	17.8	4.2
$\text{N}_2$ uptake at 298 K at 1 bar ( $\text{mg g}^{-1}$ )	4.9	4.2	6.4	NA	6.4
$\text{H}_2$ uptake at 298 K at 1 bar ( $\text{mg g}^{-1}$ )	NM	0.2	1.37	NA	NA
<b>Mixed-gas data</b>					
$\text{CO}_2$ uptake at 298 K in $\text{CO}_2/\text{N}_2$ :10/90 mixture at 1 bar ( $\text{mg g}^{-1}$ )	8.4‡	70‡/55§	99.9‡/104.4¶	NA	NA
$\text{CO}_2$ uptake at 298 K in $\text{CO}_2/\text{CH}_4$ :50/50 mixture at 1 bar ( $\text{mg g}^{-1}$ )	42.8‡	183‡/138§	108‡/110¶	NA	NA
$\text{CO}_2$ uptake at 298 K in $\text{CO}_2/\text{H}_2$ :30/70 mixture at 1 bar ( $\text{mg g}^{-1}$ )	NM	85§	112	NA	NA
Selectivity at 1 bar $\text{CO}_2/\text{N}_2$	13.7‡	140‡/72§	1,818‡/1,700¶	NA	420‡
Selectivity at 1 bar $\text{CO}_2/\text{CH}_4$	5.3‡	33‡/51§	231‡/350¶	137‡	103‡
Selectivity at 1 bar $\text{CO}_2/\text{H}_2$	NM	240§	$>1,800$	800*	NA

NA, not available; NM, not measured.

\* Ref. 29 (313 K data).

† Ref. 26 (298 K data).

‡ IAST.

§ Breakthrough experiments.

|| Mixture gravimetric (G) experiment.

¶ Mixture gravimetric-densimetric gas analysis (GDGA) experiment.

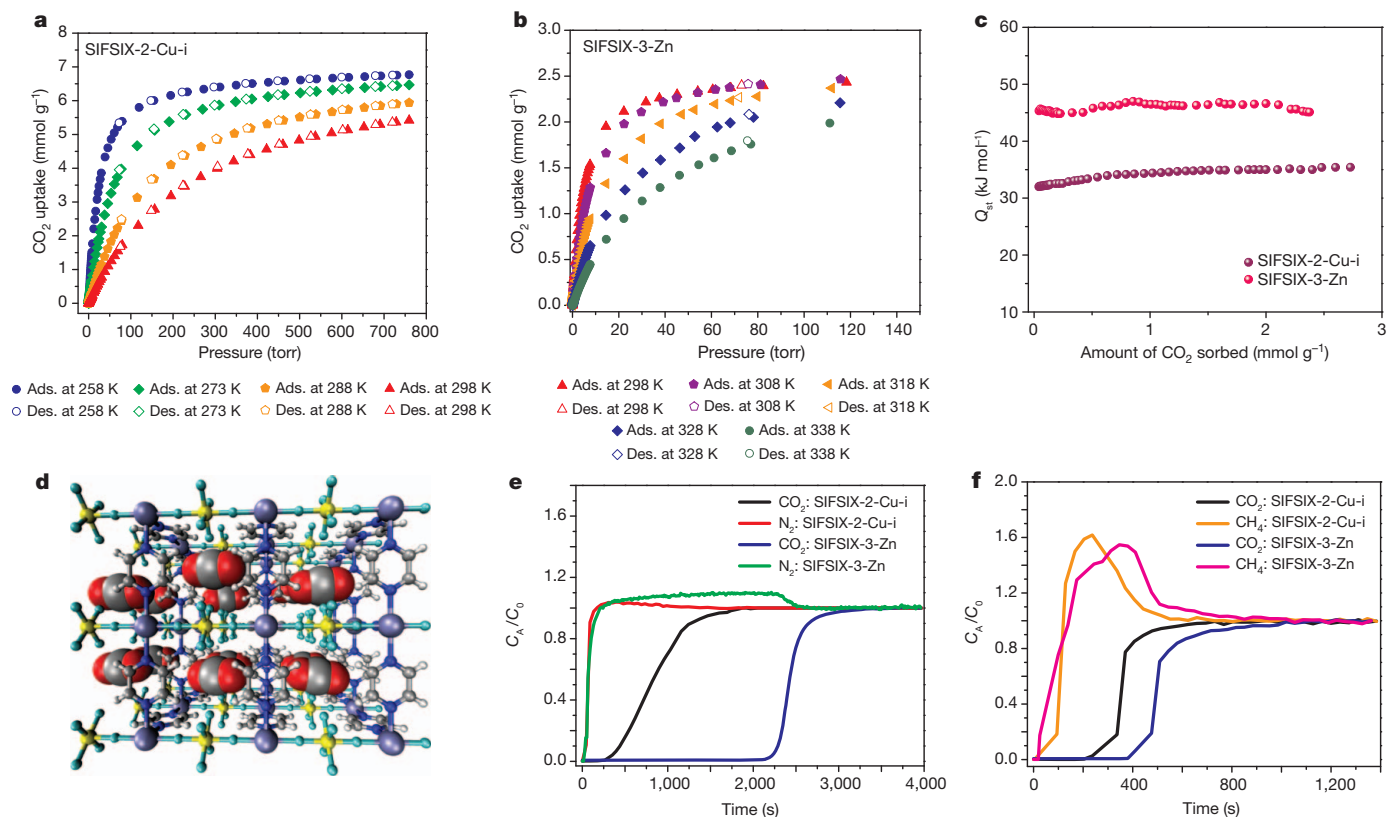


**Figure 2 | Pure gas adsorption, modelling and gas mixture breakthrough studies of SIFSIX compounds.** **a, b,** Variable temperature  $\text{CO}_2$  sorption isotherms for SIFSIX-2-Cu-i (**a**) and SIFSIX-3-Zn (**b**). **c,**  $Q_{\text{st}}$  of  $\text{CO}_2$  adsorption on SIFSIX-2-Cu-i and SIFSIX-3-Zn in the low pressure region. **d,** The modelled structure of a  $3 \times 3 \times 3$  box of unit cells of SIFSIX-3-Zn reveals close

adsorption on SIFSIX-2-Cu-i reached a plateau at relatively higher pressures (5–7 bar) (Supplementary Fig. 9b). As a result, SIFSIX-3-Zn exhibits high volumetric  $\text{CO}_2$  uptake that is comparable to those of Mg-dobdc (ref. 10) and UTSA-16 (ref. 25) at a  $\text{CO}_2$  partial pressure typical for post-combustion  $\text{CO}_2$  capture (Supplementary Fig. 23).

Figure 2c presents the  $Q_{\text{st}}$  of  $\text{CO}_2$  adsorption for SIFSIX-2-Cu-i and SIFSIX-3-Zn from variable temperature isotherms (Fig. 2a, b), and the  $Q_{\text{st}}$  of up to  $45 \text{ kJ mol}^{-1}$  is consistent with the steepness of the  $\text{CO}_2$  isotherms. The relatively constant  $Q_{\text{st}}$  indicates homogeneous binding sites over the full range of  $\text{CO}_2$  loading (Fig. 2c). These  $Q_{\text{st}}$  values are in the ‘sweet spot’ favourable for efficient, reversible adsorption–desorption—that is, strong but still reversible—and are supported by modelling studies (Fig. 2d, Supplementary Figs 25–27).

The  $\text{CO}_2$  selectivity of SIFSIX-3-Zn was investigated via column breakthrough tests using binary  $\text{CO}_2/\text{N}_2$ :10/90 (Fig. 2e) and  $\text{CO}_2/\text{CH}_4$ :50/50 gas mixtures (Fig. 2f) at 298 K and atmospheric pressure, and compared to the corresponding breakthrough tests on SIFSIX-2-Cu-i. Remarkably, SIFSIX-3-Zn showed much higher selectivity (495 and 109 for  $\text{CO}_2/\text{N}_2$ :10/90 and  $\text{CO}_2/\text{CH}_4$ :50/50, respectively) than SIFSIX-2-Cu-i, as  $\text{CO}_2$  was retained for longer times (for example,  $\sim 2000 \text{ s}$  versus  $300 \text{ s}$  for  $\text{CO}_2/\text{N}_2$ ). Notably,  $\text{N}_2$  and  $\text{CH}_4$  breakthrough occurred within seconds, indicative of high selectivity toward  $\text{CO}_2$ . To support and confirm the high selectivity derived from the breakthrough experiments, single-gas ( $\text{CO}_2$ ,  $\text{N}_2$ ,  $\text{CH}_4$  and  $\text{H}_2$ ) sorption isotherms were measured at low and high pressures and IAST calculations were used to predict adsorption equilibria for the following binary mixtures:  $\text{CO}_2/\text{CH}_4$ :05/95,  $\text{CO}_2/\text{CH}_4$ :50/50,  $\text{CO}_2/\text{N}_2$ :10/90 and  $\text{CO}_2/\text{H}_2$ :30/70. These mixtures mimic natural gas upgrading, biogas treatment, and post- and pre-combustion capture applications, respectively.

Figure 3a and b shows that the  $\text{CO}_2$  adsorption selectivity of SIFSIX-3-Zn calculated for binary gas separation versus  $\text{CH}_4$  and  $\text{N}_2$

interactions between the electropositive carbon atoms of  $\text{CO}_2$  molecules and fluorine atoms of SIFSIX anions. Colour code: C (grey), H (white), N (blue), O (red), Si (yellow), F (green), Zn (purple). **e,** Column breakthrough experiment for a  $\text{CO}_2/\text{N}_2$ :10/90 gas mixture (298 K, 1 bar) carried out on SIFSIX-2-Cu-i and SIFSIX-3-Zn. **f,** As **e** but for a  $\text{CO}_2/\text{CH}_4$ :50/50 gas mixture (298 K, 1 bar).

is unprecedented, outperforming Mg-dobdc (ref. 10), UTSA-16 (ref. 25) and zeolite 13X (ref. 26). Indeed, the selectivity of SIFSIX-3-Zn is comparable to that of amine-functionalized MOFs<sup>27</sup> and amine-bearing mesoporous silica<sup>28</sup>, particularly at low  $\text{CO}_2$  partial pressure. The calculated selectivity for  $\text{CO}_2/\text{N}_2$  (that is,  $1,539 \pm 307$  at 1 bar and 298 K) was validated by gas mixture gravimetric adsorption experiments at various pressures (Fig. 3c, d).

With regards to  $\text{CO}_2/\text{H}_2$  mixtures, adsorption isotherms of  $\text{CO}_2/\text{H}_2$ :30/70 were collected and showed similar shapes and uptakes to that obtained using pure  $\text{CO}_2$  (Supplementary Fig. 10). This indicates that SIFSIX-3-Zn adsorbs  $\text{CO}_2$  with very large selectivity over  $\text{H}_2$  (higher than 1,800), making it potentially suitable for pre-combustion capture or  $\text{H}_2$  purification. Because of the large error associated with  $\text{H}_2$  adsorption measurement (due to the relatively low uptake), quantitative measurements of  $\text{CO}_2/\text{H}_2$  selectivity were not possible. We note that calculated and measured selectivities exceeding 1,000 are often subject to uncertainties associated with measurement of the uptake of weakly adsorbed gases. Therefore, it would be inappropriate in this case to make quantitative comparisons between different adsorbents such as SIFSIX-3-Zn and Mg-dobdc<sup>29</sup> (800 at 1 bar and 313 K).

To confirm the synergistic nature of the thermodynamics and kinetics for  $\text{CO}_2$  capture, competitive adsorption kinetic studies of the above gas mixtures were conducted and are presented in Fig. 3e. We note that the  $\text{CO}_2$  non-equilibrium uptake at equal times for  $\text{CO}_2/\text{N}_2$ ,  $\text{CO}_2/\text{CH}_4$  and  $\text{CO}_2/\text{H}_2$  mixtures follows the behaviour of pure  $\text{CO}_2$ . In addition, at equilibrium the total  $\text{CO}_2$  uptake from the  $\text{CO}_2$ -containing gas mixtures agrees perfectly with the equilibrium uptake for pure  $\text{CO}_2$ . These distinctive findings show that when  $\text{CO}_2$ -containing mixtures are in contact with SIFSIX-3-Zn,  $\text{CO}_2$  adsorbs more strongly and faster than  $\text{N}_2$ ,  $\text{O}_2$ ,  $\text{CH}_4$  and  $\text{H}_2$ , thus occupying all the available space and sorption sites and consequently excluding other gases. Most



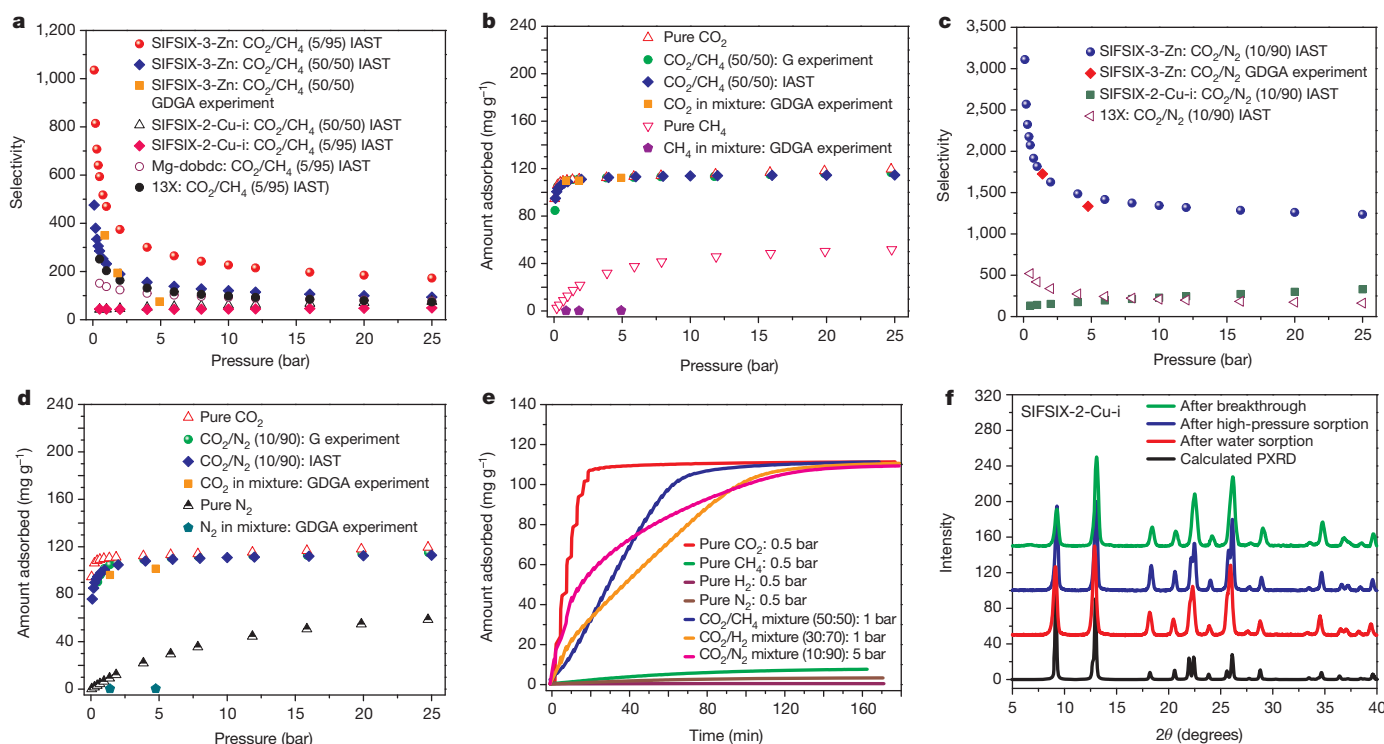


**Figure 3** | Gas mixture selectivity of SIFSIX compounds and the stability study of SIFSIX-2-Cu-i. **a**, Calculated (using IAST)  $\text{CO}_2$  adsorption selectivity for two different  $\text{CO}_2/\text{CH}_4$  mixtures on SIFSIX-2-Cu-i and SIFSIX-3-Zn compared to Mg-dobdc and 13X zeolite at 298 K. Experimental data using gravimetric-densimetric gas analysis (GDGA) are provided for comparison. **b**, IAST  $\text{CO}_2/\text{CH}_4$ :50:50 adsorption isotherm prediction compared to experimental pure  $\text{CO}_2$ ,  $\text{CH}_4$  and  $\text{CO}_2/\text{CH}_4$ :50:50 gas mixture adsorption isotherms collected using gravimetric (G) adsorption experiments for SIFSIX-3-Zn at 298 K. **c**,  $\text{CO}_2$  adsorption selectivity of SIFSIX-2-Cu-i, SIFSIX-3-Zn and

13X zeolite for  $\text{CO}_2/\text{N}_2$ :10:90 as calculated using IAST at 298 K. **d**, IAST  $\text{CO}_2/\text{N}_2$ :10:90 adsorption isotherm predictions compared to experimental pure  $\text{CO}_2$ ,  $\text{N}_2$  and  $\text{CO}_2/\text{N}_2$ :10:90 gas mixture adsorption isotherms collected using gravimetric (G) adsorption experiments for SIFSIX-3-Zn at 298 K. **e**, Kinetics of adsorption of SIFSIX-3-Zn for pure gases and gas mixtures containing various compositions of  $\text{CO}_2$ . **f**, PXRD patterns of SIFSIX-2-Cu-i after multiple cycles of breakthrough tests, high-pressure sorption, and water sorption experiments (compared to the calculated pattern).

importantly, SIFSIX-3-Zn fulfils the demanding attributes (Supplementary Fig. 7) required for economical and efficient  $\text{CO}_2$  post-combustion separation. Further, increasing the adsorption temperature did not significantly reduce the steepness of the  $\text{CO}_2$  adsorption isotherm for SIFSIX-3-Zn (Fig. 2b, Supplementary Fig. 8); this is a desirable feature in many  $\text{CO}_2$  separation and purification applications.

Whereas the sorbents reported here exhibit very good performance with respect to  $\text{CO}_2$  selectivity, their amenability to recycling and efficacy in the presence of moisture must also be addressed. The former was validated via adsorption–desorption cycle experiments conducted at 323 K and 0.15 bar (Supplementary Fig. 14). The latter—specifically, the effect of water vapour on the  $\text{CO}_2$  capacity and selectivity of SIFSIX-2-Cu-i and SIFSIX-3-Zn—was evaluated via a series of adsorption measurements. The water vapour adsorption isotherms are found to be of type I, with uptakes of 20 wt% and 11 wt%, respectively, at 74% relative humidity (Supplementary Fig. 24). Water adsorption affinity/capacity is reduced in the presence of  $\text{CO}_2$  gas mixtures, as shown by breakthrough experiments, especially for SIFSIX-3-Zn (Supplementary Figs 15b and 16b). Importantly, the presence of water in the given gas mixture had a negligible effect at elevated  $\text{CO}_2$  concentrations (Supplementary Fig. 15) in the case of SIFSIX-2-Cu-i. Regarding the  $\text{CO}_2/\text{H}_2$ :30/70 mixture,  $\text{CO}_2$  uptake and selectivity were only slightly reduced in the presence of moisture (1.61  $\text{mmol g}^{-1}$  and 191 at 74% relative humidity versus 1.99  $\text{mmol g}^{-1}$  and 237 at 0% relative humidity for SIFSIX-2-Cu-i, Supplementary Fig. 15b). Whereas SIFSIX-2-Cu-i was structurally unchanged by exposure to moisture (Fig. 3f), SIFSIX-3-Zn undergoes a reversible phase change at relatively high humidity (Supplementary Figs 19–22).

We have demonstrated how a crystal engineering or reticular chemistry approach to pore size control, coupled with favourable

electrostatic interactions provided by an array of inorganic anions, affords porous materials with exceptional selectivity, recyclability and moisture stability in the context of several industrially relevant  $\text{CO}_2$  separation applications. The structural features and exceptional mixed-gas sorption properties of the SIFSIX compounds reported here show that it is now possible to combine equilibrium<sup>10,11,26</sup> and kinetic<sup>30</sup> adsorption selectivity in the same porous material to facilitate effective  $\text{CO}_2$  separation and capture.

Received 3 July; accepted 20 December 2012.

Published online 27 February 2013.

1. Taylor, P. *Energy Technology Perspectives 2010 — Scenarios and Strategies to 2050* 74 (International Energy Agency, Paris, 2010).
2. Merel, J., Clausse, M. & Meunier, F. Experimental investigation on  $\text{CO}_2$  post-combustion capture by indirect thermal swing adsorption using 13X and 5A zeolites. *Ind. Eng. Chem. Res.* **47**, 209–215 (2008).
3. MacGillivray, L. R. *Metal-Organic Frameworks: Design and Application* (Wiley & Sons, 2010).
4. Li, H., Eddaoudi, M., O’Keeffe, M. & Yaghi, O. M. Design and synthesis of an exceptionally stable and highly porous metal-organic framework. *Nature* **402**, 276–279 (1999).
5. Eddaoudi, M. *et al.* Systematic design of pore size and functionality in isorecticular MOFs and their application in methane storage. *Science* **295**, 469–472 (2002).
6. Farha, O. K. *et al.* Metal-organic framework materials with ultrahigh surface areas: is the sky the limit? *J. Am. Chem. Soc.* **134**, 15016–15021 (2012).
7. Moulton, B. & Zaworotko, M. J. From molecules to crystal engineering: supramolecular isomerism and polymorphism in network solids. *Chem. Rev.* **101**, 1629–1658 (2001).
8. Kitagawa, S., Kitaura, R. & Noro, S. Functional porous coordination polymers. *Angew. Chem. Int. Edn* **43**, 2334–2375 (2004).
9. Yaghi, O. M. *et al.* Reticular synthesis and the design of new materials. *Nature* **423**, 705–714 (2003).
10. Caskey, S. R., Wong Foy, A. G. & Matzger, A. J. Dramatic tuning of carbon dioxide uptake via metal substitution in a coordination polymer with cylindrical pores. *J. Am. Chem. Soc.* **130**, 10870–10871 (2008).

11. Sumida, K. *et al.* Carbon dioxide capture in metal–organic frameworks. *Chem. Rev.* **112**, 724–781 (2012).
12. Kizzie, A. C., Wong Foy, A. G. & Matzger, A. J. Effect of humidity on the performance of microporous coordination polymers as adsorbents for CO<sub>2</sub> capture. *Langmuir* **27**, 6368–6373 (2011).
13. Subramanian, S. & Zaworotko, M. J. Porous solids by design — [Zn(4,4'-bpy)<sub>2</sub>(SiF<sub>6</sub>)<sub>2</sub>]-xDMF, a single framework octahedral coordination polymer with large square channels. *Angew. Chem. Int. Edn* **34**, 2127–2129 (1995).
14. Noro, S., Kitagawa, S., Kondo, M. & Seki, K. A new methane adsorbent, porous coordination polymer [CuSiF<sub>6</sub>(4,4'-bipyridine)<sub>2</sub>]<sub>n</sub>. *Angew. Chem. Int. Edn* **39**, 2081–2084 (2000).
15. Burd, S. D. *et al.* Highly selective carbon dioxide uptake by [Cu(bpy-n)(SiF<sub>6</sub>)] (bpy-1 = 4,4'-bipyridine; bpy-2 = 1,2-bis(4-pyridyl)ethene). *J. Am. Chem. Soc.* **134**, 3663–3666 (2012).
16. Coe, B. J. *et al.* Syntheses, spectroscopic and molecular quadratic nonlinear optical properties of dipolar ruthenium(II) complexes of the ligand 1,2-phenylenebis(dimethylarsine). *Dalton Trans.* (18), 2935–2942 (2004).
17. Uemura, K., Maeda, A., Maji, T. K., Kanoo, P. & Kita, H. Syntheses, crystal structures and adsorption properties of ultramicroporous coordination polymers constructed from hexafluorosilicate ions and pyrazine. *Eur. J. Inorg. Chem.* (16), 2329–2337 (2009).
18. Jagiello, J. & Thommes, M. Comparison of DFT characterization methods based on N<sub>2</sub>, Ar, CO<sub>2</sub>, and H<sub>2</sub> adsorption applied to carbons with various pore size distributions. *Carbon* **42**, 1227–1232 (2004).
19. Ma, S. *et al.* Framework-catenation isomerism in metal–organic frameworks and its impact on hydrogen uptake. *J. Am. Chem. Soc.* **129**, 1858–1859 (2007).
20. Llewellyn, P. L. *et al.* High uptakes of CO<sub>2</sub> and CH<sub>4</sub> in mesoporous metal-organic frameworks MIL-100 and MIL-101. *Langmuir* **24**, 7245–7250 (2008).
21. Lässig, D. *et al.* A microporous copper metal–organic framework with high H<sub>2</sub> and CO<sub>2</sub> adsorption capacity at ambient pressure. *Angew. Chem. Int. Edn* **123**, 10528–10532 (2011).
22. Yazaydin, A. O. *et al.* Enhanced CO<sub>2</sub> adsorption in metal-organic frameworks via occupation of open-metal sites by coordinated water molecules. *Chem. Mater.* **21**, 1425–1430 (2009).
23. Myers, A. L. & Prausnitz, J. M. Thermodynamics of mixed-gas adsorption. *Am. Inst. Chem. Eng. J.* **11**, 121–127 (1965).
24. Ho, M. T., Allinson, G. W. & Wiley, D. E. Reducing the cost of CO<sub>2</sub> capture from flue gases using pressure swing adsorption. *Ind. Eng. Chem. Res.* **47**, 4883–4890 (2008).
25. Xiang, S. *et al.* Microporous metal-organic framework with potential for carbon dioxide capture at ambient conditions. *Nature Commun.* **3**, 954 (2012).
26. Cavenati, S., Grande, C. A. & Rodrigues, A. E. Adsorption equilibrium of methane, carbon dioxide, and nitrogen on zeolite 13X at high pressures. *J. Chem. Eng. Data* **49**, 1095–1101 (2004).
27. Vaidhyanathan, R. *et al.* Direct observation and quantification of CO<sub>2</sub> binding within an amine-functionalized nanoporous solid. *Science* **330**, 650–653 (2010).
28. Belmabkhout, Y., Serna-Guerrero, R. & Sayari, A. Adsorption of CO<sub>2</sub>-containing gas mixtures over amine-bearing pore-expanded MCM-41 silica: application for gas purification. *Ind. Eng. Chem. Res.* **49**, 359–365 (2010).
29. Herm, Z. R., Swisher, J. A., Smit, B., Krishna, R. & Long, J. R. Metal-organic frameworks as adsorbents for hydrogen purification and precombustion carbon dioxide capture. *J. Am. Chem. Soc.* **133**, 5664–5667 (2011).
30. Han, S. *et al.* High-throughput screening of metal–organic frameworks for CO<sub>2</sub> separation. *ACS Combinat. Sci.* **14**, 263–267 (2012).

**Supplementary Information** is available in the online version of the paper.

**Acknowledgements** This publication is based on work supported by KAUST award number FIC/2010/06 (M.E. and M.J.Z.) and KAUST start up funds (M.E.). B.S. acknowledges computational resources made available by an XSEDE grant (number TG-DMR090028). Single-crystal diffraction experiments on SIFSIX-2-Cu-i were conducted at the Advanced Photon Source on beamline 15ID-B of ChemMatCARS Sector 15, which is principally supported by the National Science Foundation/Department of Energy under grant number NSF/CHE-0822838. Use of the Advanced Photon Source was supported by the US Department of Energy, Office of Science, Office of Basic Energy Sciences under contract number DE-AC02-06CH11357.

**Author Contributions** P.N., S.D.B. and M.J.Z. contributed to the conceptual approach to designing the materials synthetic experiments; P.N. and S.D.B. carried out the materials synthesis; L.W. and R.L. conducted and interpreted the crystallographic experiments; P.N., S.D.B., Y.B., S.M., M.E. and A.J.C. conducted and interpreted low-pressure sorption experiments; Y.B. and M.E. contributed to the initial ideas, conceptualizing, designing, conducting (Y.B.) and interpreting sorption experiments for gas separation of various industrially relevant gas mixtures (high-pressure single and mixed gas sorption experiments, sorption kinetics and breakthrough experiments) and IAST calculations; K.F., T.P. and B.S. conducted electrostatic models of gas sorption; and M.E. and M.J.Z. wrote the manuscript.

**Author Information** Supplementary crystallographic data for this manuscript has been deposited at the Cambridge Crystallographic Data Centre under deposition numbers CCDC 914600 and 914601. These data can be obtained free of charge from [http://www.ccdc.cam.ac.uk/data\\_request/cif](http://www.ccdc.cam.ac.uk/data_request/cif). Reprints and permissions information is available at [www.nature.com/reprints](http://www.nature.com/reprints). The authors declare no competing financial interests. Readers are welcome to comment on the online version of the paper. Correspondence and requests for materials should be addressed to M.E. (mohamed.eddaoudi@kaust.edu.sa) and M.J.Z. (xtal@usf.edu).

# Low-temperature aqueous-phase methanol dehydrogenation to hydrogen and carbon dioxide

Martin Nielsen<sup>1</sup>, Elisabetta Alberico<sup>1,2</sup>, Wolfgang Baumann<sup>1</sup>, Hans-Joachim Drexler<sup>1</sup>, Henrik Junge<sup>1</sup>, Serafino Gladiali<sup>3</sup> & Matthias Beller<sup>1</sup>

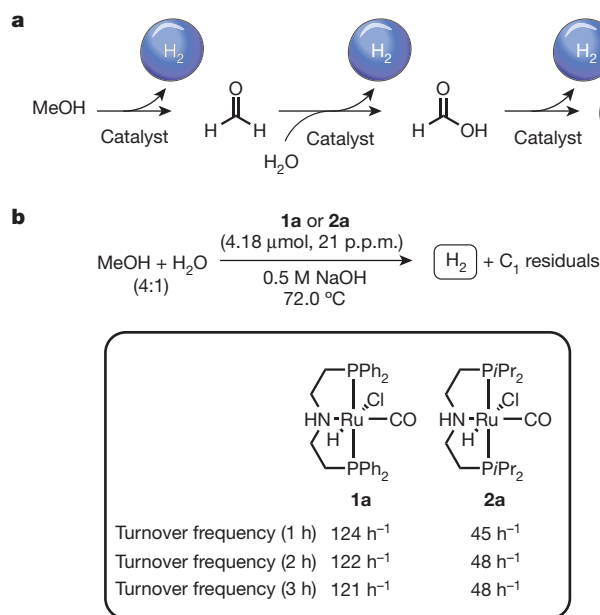
Hydrogen produced from renewable resources is a promising potential source of clean energy. With the help of low-temperature proton-exchange membrane fuel cells, molecular hydrogen can be converted efficiently to produce electricity<sup>1–5</sup>. The implementation of sustainable hydrogen production and subsequent hydrogen conversion to energy is called “hydrogen economy”<sup>2</sup>. Unfortunately, its physical properties make the transport and handling of hydrogen gas difficult. To overcome this, methanol can be used as a material for the storage of hydrogen, because it is a liquid at room temperature and contains 12.6 per cent hydrogen. However, the state-of-the-art method for the production of hydrogen from methanol (methanol reforming) is conducted at high temperatures (over 200 degrees Celsius) and high pressures (25–50 bar), which limits its potential applications<sup>6–8</sup>. Here we describe an efficient low-temperature aqueous-phase methanol dehydrogenation process, which is facilitated by ruthenium complexes. Hydrogen generation by this method proceeds at 65–95 degrees Celsius and ambient pressure with excellent catalyst turnover frequencies (4,700 per hour) and turnover numbers (exceeding 350,000). This would make the delivery of hydrogen on mobile devices—and hence the use of methanol as a practical hydrogen carrier—feasible.

Of the known hydrogen storage materials<sup>6–14</sup>, methanol represents a promising energy carrier. Its convenient properties (12.6% hydrogen and being liquid at room temperature) suggest that a “methanol economy” may be possible<sup>14</sup>. To combine the advantages of simple methanol transportation and the energy efficiency of proton-exchange membrane fuel cells, so-called ‘reformed methanol fuel cells’ have been developed. However, methanol-reforming processes are insufficient unless high temperatures (>200 °C) are used. Therefore, the state-of-the-art efficiency of reformed methanol fuel cells is only approximately 40%. Moreover, very low concentrations of carbon monoxide are tolerated in the fuel cell (<10 parts per million, p.p.m.), which is challenging for current catalytic systems. In general, methanol reforming occurs in the steam phase using heterogeneous catalysis and high temperatures<sup>6</sup>. Notably, Dumesic *et al.* have developed a Pt/Al<sub>2</sub>O<sub>3</sub>-based catalyst that allows for aqueous-phase methanol reforming at more acceptable temperatures (200–225 °C) and pressure (25–50 bar)<sup>7,8</sup>. In addition, the use of less expensive and more abundant Cu/Zn/Al<sub>2</sub>O<sub>3</sub> catalyst systems is also noteworthy, although they need higher temperatures than does the Pt/Al<sub>2</sub>O<sub>3</sub> catalyst<sup>6</sup>.

Our long-term interest in efficient low-temperature hydrogen generation<sup>15,16</sup>, led us to identify active molecular-defined catalysts for a low-temperature (<100 °C) aqueous-phase methanol dehydrogenation process. We envisioned a one-pot stepwise process including initial dehydrogenation of methanol to hydrogen and formaldehyde, water-promoted dehydrogenation of formaldehyde to formic acid and hydrogen, and final dehydrogenation of formic acid to hydrogen and carbon dioxide. This should lead to an overall yield of three molecules of hydrogen and one of carbon dioxide, thus resembling classic

methanol reforming (Fig. 1a). Either methanol (MeOH) or H<sub>2</sub>O could be in excess, depending on the potential applications.

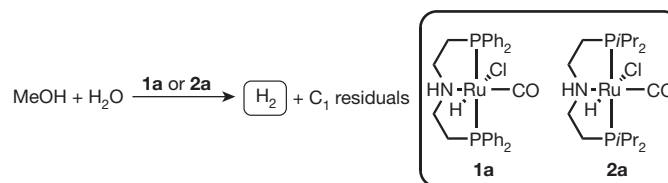
To the best of our knowledge, all known molecular-defined organometallic catalysts for alcohol dehydrogenation promote the liberation of only one molecule of hydrogen from each alcohol molecule<sup>17–24</sup>. Moreover, there exists no example of homogeneously catalysed dehydrogenations of aldehydes in the presence of water. Recently, organometallic complexes containing pincer-type ligands (capable of enabling cooperative metal–ligand catalysis) showed interesting activities in catalytic hydrogenation and dehydrogenation reactions<sup>18,21,22,25–29</sup>. Therefore, we envisioned that this type of catalyst might be suitable for selective methanol dehydrogenation, and possibly even for methanol reforming. To our delight, testing a variety of ruthenium-based pincer complexes (Supplementary Scheme 1 and Supplementary Table 2) in a 4:1 mixture of MeOH/H<sub>2</sub>O containing 0.5 M NaOH revealed significant catalyst activity for complexes **1a** and **2a** (the turnover frequency is the amount of hydrogen produced by each catalyst molecule per hour, 120 h<sup>–1</sup> and 45 h<sup>–1</sup>, respectively; Fig. 1b). Interestingly, in these reactions hydrogen generation had already occurred at 72.0 °C and all reactions produced very pure hydrogen gas.



**Figure 1 | Methanol reforming by homogeneous catalysis.** **a**, Schematic pathway for a homogeneously catalysed methanol reforming process via three discrete dehydrogenation steps. **b**, Best-performing catalysts among those tested (see Supplementary Information) for aqueous-phase methanol dehydrogenation performed with 0.5 M NaOH at 72.0 °C.

<sup>1</sup>Leibniz-Institut für Katalyse Eingetragener Verein an der Universität Rostock, Albert-Einstein Straße 29a, Rostock, 18059 Germany. <sup>2</sup>Istituto di Chimica Biomolecolare, CNR, traversa La Crucca 3, Sassari 07040, Italy. <sup>3</sup>Dipartimento di Chimica e Farmacia, Università di Sassari, Sassari 07100, Italy.

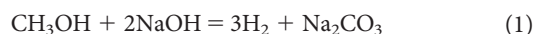


**Table 1 | Ru-catalysed aqueous-phase methanol dehydrogenation**

Entry	Catalyst amount ( $\mu\text{mol}$ , p.p.m.)	MeOH/H <sub>2</sub> O ratio	Reaction temperature (°C)	Turnover frequency, 1 h (h <sup>-1</sup> )	Turnover frequency, 2 h (h <sup>-1</sup> )	Turnover frequency, 3 h (h <sup>-1</sup> )
1	<b>1a</b> (4.18, 21)	4:1	89.0	754	819	860
2	<b>1a</b> (4.18, 19)	9:1	91.0	1,023	1,051	1,093
3	<b>2a</b> (22.2, 100)	9:1	91.0	1,281	1,250	1,151
4	<b>2a</b> (4.18, 19)	9:1	91.0	2,276	2,228	2,205
5	<b>2a</b> (1.58, 1.8)	9:1	91.0	2,668	2,687	2,670
6	<b>1a</b> (4.18, 28)	3:2	86.5	90	121	130
7	<b>2a</b> (4.18, 28)	3:2	86.5	732	719	711
8	<b>2a</b> (1.58, 16)	1:9	95.0	265	228	201
9	<b>2a</b> (1.58, 1.6)	neat MeOH	95.0	4,719	4,716	4,734

Investigation into the effect of MeOH/H<sub>2</sub>O ratio on catalyst activity. Performed with catalyst **1a** or **2a** (amounts are given in  $\mu\text{mol}$  and loading in  $\mu\text{mol mol}^{-1}$  of MeOH is stated as parts per million) in a 10–40 ml MeOH/H<sub>2</sub>O solution containing 8.0 M KOH (molarity based on total MeOH/H<sub>2</sub>O volume). For entries 1–7, the reaction mixtures were under reflux. The H<sub>2</sub>/CO<sub>2</sub> ratio, determined by gas-phase chromatography, was consistently >500:1. The gas evolution was determined by gas burette measurements. Each molecule of hydrogen is counted as resembling one turnover.

Under catalytic conditions (Supplementary Scheme 5) both formate and carbonate ions were observed in the nuclear magnetic resonance (NMR) as traces of the reaction mixtures, showing that the formate is an intermediate in this dehydrogenation sequence and that CO<sub>2</sub> is trapped as carbonate (Supplementary Figs 16 and 19). As shown in Fig. 1a, the first dehydrogenation step of methanol results in formaldehyde, which, however, we never detected in solution. The subsequent conversion to formate and hydrogen occurs rapidly under these conditions, but formate conversion is apparently more sluggish. Moreover, due to the alkaline character of the solution, any evolved CO<sub>2</sub> is initially trapped as carbonate. Hence, in the first phase of the reaction a base-mediated reforming sequence proceeds according to equation (1):



Although no bicarbonate (NaHCO<sub>3</sub>) was detected in the reaction mixtures, it should not be conclusively excluded as a possible product given the change in pH observed over time (as discussed below). Owing to the inherent complexity of the overall methanol reforming via dehydrogenation reactions, we assign turnover frequency and turnover number (the amount of hydrogen per catalyst molecule) as measures of the catalyst activity and productivity, respectively, for the production of each H<sub>2</sub> molecule. In fact, the successive production of three H<sub>2</sub> molecules and one CO<sub>2</sub> molecule gives a turnover number of 3.

Optimization of the reaction conditions demonstrates that several factors affect the catalyst activity: significant influences are seen by the nature of the base, its concentration, the water content, and the temperature. Exploring a range of bases and different base concentrations

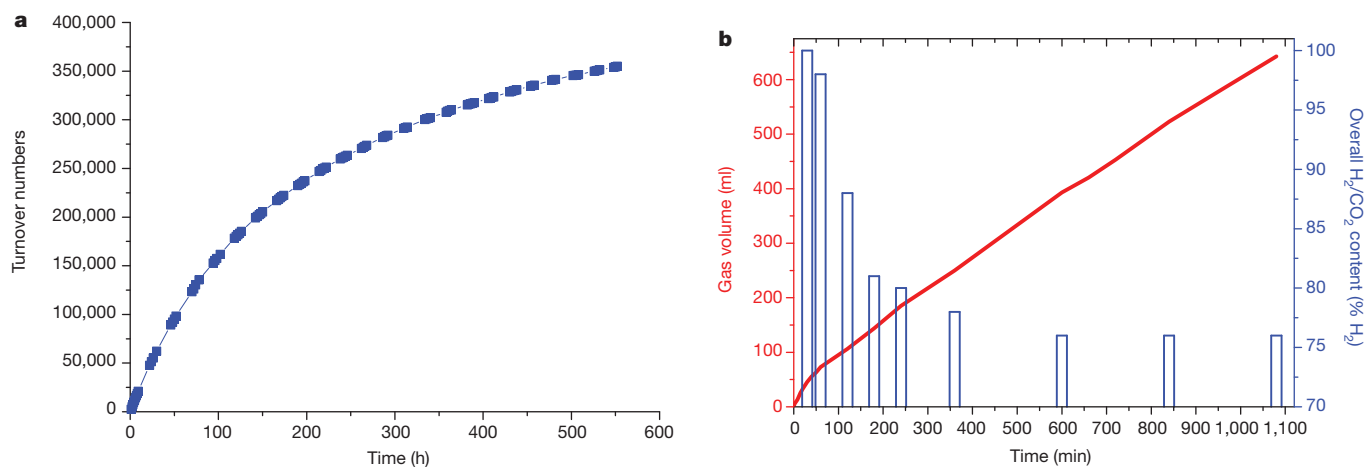


**Figure 2 | Approaching ‘real’ aqueous methanol reforming.** **a**, Aqueous methanol dehydrogenation using 1.0 p.p.m. of catalyst **2a** in a 9:1 ratio of MeOH/H<sub>2</sub>O containing 8.0 M KOH. **b**, Set-up for continuous aqueous methanol reforming using **2a**. Evolved gas volume (red line) and gas

composition (blue bars) as a function of time, with conditions as follows: MeOH/H<sub>2</sub>O 4:1 (10 ml), NaOH 0.1 M, **2a** 49.3  $\mu\text{mol}$ , 250 p.p.m. with respect to MeOH, 72 °C). For details, see Supplementary Table 4.

in a 4:1 MeOH/H<sub>2</sub>O solution led to the finding that 8.0 M potassium hydroxide (KOH) gave optimal results (Table 1, entry 1). It should be noted that the temperature increase due to such a high base concentration (salt effect) seems to be far more important than the high base concentration itself in boosting activity (Supplementary Scheme 2 and Supplementary Table 3). Using 8.0 M KOH, complex **2a** was more active than complex **1a** with a turnover frequency of up to 2,687 h<sup>-1</sup> (Table 1, entries 2–5). Not surprisingly, increasing the water content (MeOH/H<sub>2</sub>O = 3:2) had a detrimental effect on the catalytic activity. The poor solubility of **1a** explains the increase in activity over time because it is only slowly transformed into the catalytic active species (Table 1, entry 6). Again using **2a** instead of **1a** resulted in a more than fivefold improvement of activity (Table 1, entry 7). Even a highly diluted methanol system (MeOH/H<sub>2</sub>O = 1:9) still afforded significant hydrogen evolution, albeit with lower activity (Table 1, entry 8). From a practical point of view, this latter result is important because it allows the use of an aqueous methanol solution that may vary in methanol concentration over time. When performing an experiment simply with methanol and potassium hydroxide, a remarkable activity of approximately 4,720 h<sup>-1</sup> was obtained (Table 1, entry 9). Moreover, when the experiment in entry 4 of Table 1 was repeated in the presence of a large excess (>500 equivalents) of Hg, no decrease in activity was observed, which supports the homogeneous nature of the catalytic system.

To prove the stability of the catalyst system, a long-term experiment using 0.88 μmol of **2a** in 40 ml of a 9:1 MeOH/H<sub>2</sub>O solution, corresponding to a catalyst loading of 1 μmol mol<sup>-1</sup> of MeOH (1 p.p.m.),

was performed (Fig. 2a; Supplementary Scheme 3 and Supplementary Figs 13–15). In this case, MeOH is in excess and is thus taking the role of both the reactant and the solvent. The molecular catalyst was stable for more than three weeks and after 23 days, a total turnover number of 350,000 was achieved. Even after this time, the catalyst was still active with an instant turnover frequency of 200 h<sup>-1</sup>, measured as an average over the last 24 h. In this case, the hydrogen yield calculated for full methanol reforming was 27% (12% with respect to MeOH, Supplementary Equations (3) and (4)). The reaction showed almost constant activity for the last ten days. Importantly, less than 1 p.p.m. of both CH<sub>4</sub> and CO were observed by gas-phase gas chromatography throughout the reaction. By increasing the catalyst loading, the performance was easily improved. Hence, the same hydrogen yield is reached within 90 min when using 150 μmol mol<sup>-1</sup> (150 p.p.m.) of **2a**. Within 24 h, the yield of H<sub>2</sub> increases to 59% under these conditions and that of CO<sub>2</sub> approaches 43% (26% and 19%, respectively, if referring solely to MeOH). We did not perform any further optimizations towards higher conversion.

To show that a ‘real’ aqueous methanol-reforming process with a 3:1 H<sub>2</sub>/CO<sub>2</sub> gaseous content can be achieved, an experiment in the presence of low amounts of base (0.1 M of NaOH in a 4:1 MeOH/H<sub>2</sub>O) was performed (Supplementary Scheme 4). Under these conditions, the majority of CO<sub>2</sub> is released instead of being trapped as carbonate in solution. Indeed, in the presence of 250 p.p.m. of **1a**, the expected 3:1 H<sub>2</sub>/CO<sub>2</sub> gas composition was observed after approximately 5–6 h and then stayed constant until the reaction was stopped (Fig. 2b). We note

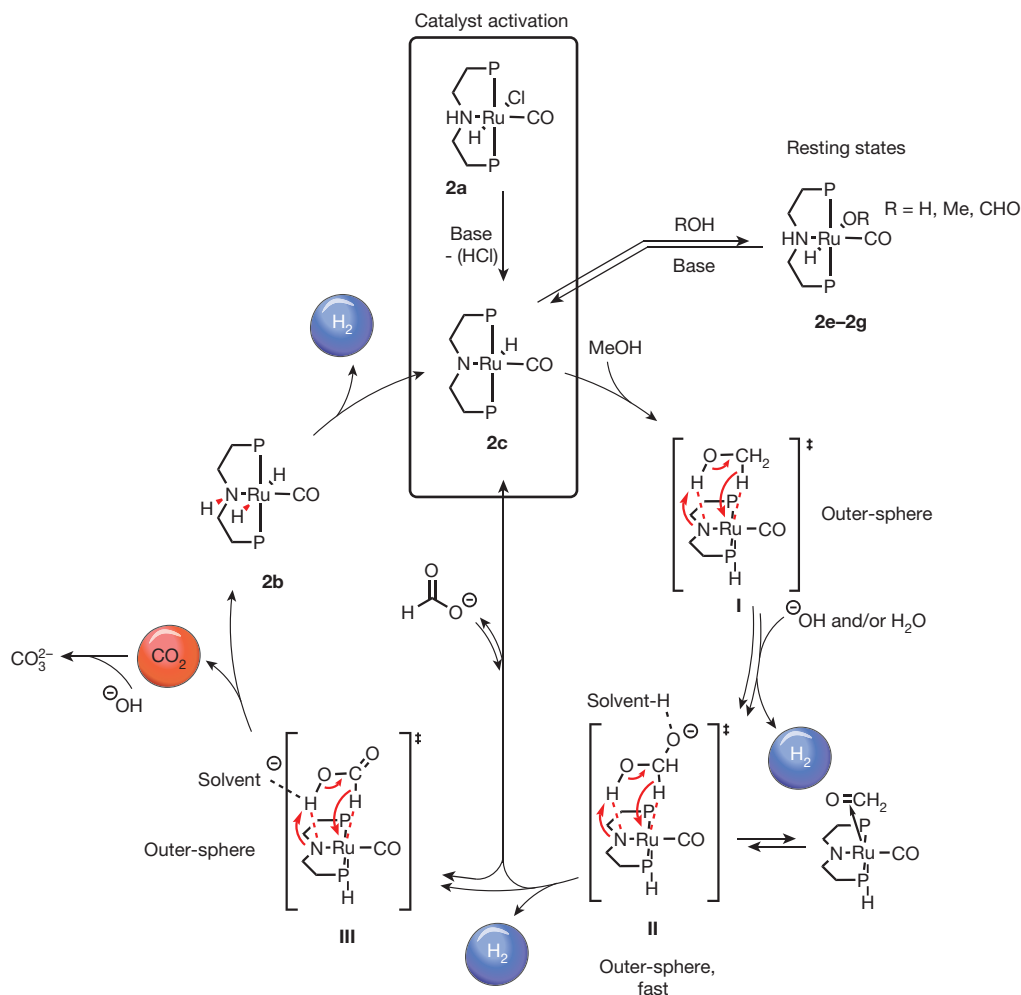


**Figure 3 | Proposed catalytic cycle for Ru-promoted aqueous-phase methanol dehydrogenation.** Proposed catalyst activation and catalytic cycle for low-temperature methanol reforming catalysed by **2c**, made *in situ* from

**2a**. The phosphorus *i*Pr substituents have been omitted for clarity. ‡ denotes transition state; solvent-H indicates a molecule of solvent involved in hydrogen bonding.

that a correlation between solution pH and gas composition is observed (Supplementary Table 4). The pH, initially at 13, dropped to approximately 10 over the first 4 h and then stayed constant for the rest of the reaction time. It seems that in the first phase of the reaction an equilibrium among hydroxide/(bi)carbonate/formate is approached, which then leads to a 'steady state' gas evolution, as would be expected if methanol reforming is taking place. The higher-than-expected content in  $H_2$  observed even after onset of the equilibrium is due to the fact that the hydrogen generated in the pre-equilibrium phase has not been discharged. Upon addition of aqueous HCl to a reaction mixture having pH 11 (Supplementary Table 4, entry 4), about 0.7 mmol of  $CO_2$  were evolved, proving that NaOH is actually consumed in the initial course of the reaction. Similar to the long-term reaction experiment, a stable gas evolution (activity) was reached; this time after 2–3 h.

Careful analysis of Fig. 2b shows that the overall process goes through three distinct reaction stages: In the first stage, corresponding to the first hour, the process is mediated by the base and a substantial amount of free hydroxide is still present in the reaction solution. Here, over 90% of the gas is  $H_2$  and the pH stays  $>12$ . The second stage is the equilibrating phase when the gas distribution, hydroxide consumption and pH are approaching a steady state. During this period, the activity changes at a slower rate while approaching the steady-state value as well. In the third stage (after 4–5 h and thereafter), steady-state conditions are established and the hydroxide/(bi)carbonate/formate concentration, gas evolution and distribution, and pH remain constant. Thus, the gas flux contains 3:1  $H_2/CO_2$ , and pH stays at about 10. Considering the observed general stability of the catalytic system (Fig. 2a), gas evolution can, under these conditions, last for weeks.

On the basis of *in situ* NMR experiments using **2a** as the pre-catalyst (Supplementary Figs 16–19), we propose the following catalytic cycle for our process (Fig. 3). Reaction of **2a** with base affords the more active species **2c**, which is able to dehydrogenate MeOH to yield hydrogen and formaldehyde. In agreement with previous observations<sup>16</sup>, we suggest that the generation of the first hydrogen molecule occurs through an outer-sphere concerted process as in **I**, that is, without direct coordination of methanol to the metal. Because formaldehyde itself as well as its hydrated species are barely detected in solution, HCHO might undergo a sequence of fast reactions while still coordinated to the metal centre. Attack of hydroxide gives the *gem*-diol(ate) **II**, which is probably further stabilized by a solvent-cage of the protic  $H_2O/MeOH$ . Again, outer-sphere dehydrogenation releases the second hydrogen molecule and formate is formed. At this point, the catalyst either restarts the catalytic cycle by losing formate and reacting with MeOH or it performs the final step of the catalytic cycle via **III**, leading to  $CO_2$  and the third molecule of  $H_2$ . Because free formate is actually detected in solution, its dehydrogenation through reaction with **2c** must be slow at low formate concentration in competition to MeOH. However, the fact that substantial  $CO_2$  formation is observed at a point where MeOH is still in large excess suggests that formate dehydrogenation might be relatively faster than MeOH dehydrogenation.

Notably, hydride species are observed in solution under catalytic conditions (Supplementary Fig. 17), most probably **2a** and **2e–g**. It seems that the need for base to keep the catalytic system active is related to the continuous formation of **2c** from such species and not to the deprotonation of methanol and formic acid. We may speculate whether the alkalinity of the medium might enhance reactivity by deprotonation of methanol. However, this would most probably require an inner-sphere mechanism, which has been questioned previously<sup>29</sup>.

In conclusion, we have demonstrated aqueous-phase methanol dehydrogenation and reforming at low temperature. Compared to previously known heterogeneous systems, we observe low amounts of contaminant gases CO and  $CH_4$  ( $<10$  p.p.m.). Key to success is the use of molecular-defined  $[RuHCl(CO)(HN(C_2H_4PPr)_2)]$  (where  $iPr \equiv CH(CH_3)_2$ ) catalysts, which exhibit high activities up to  $4,700\ h^{-1}$  and catalyst productivities of  $>350,000$ . The optimized system is stable under aqueous alkaline conditions and remains active for more than

three weeks. Once the relative concentrations of the reagents and possible intermediates competing for the catalyst have reached suitable steady-state values, the ratio of  $H_2$  to  $CO_2$  expected for MeOH aqueous reforming ( $H_2/CO_2$  3:1) is observed. Moreover, this system represents full conversion of all 'available' hydrogen atoms in the substrates to hydrogen by homogeneous catalysis. An intrinsic drawback is the base needed for this reaction to stay active. Nevertheless, using this system it might be possible to combine the advantages of methanol as the 'hydrogen carrier' and the superior efficiency of proton-exchange membrane fuel cells compared to methanol fuel cells.

## METHODS SUMMARY

All reactions were performed under inert atmosphere (argon) with exclusion of air. A solution of MeOH and  $H_2O$  in a given ratio, containing a defined amount of base, was heated to a certain temperature and let equilibrate for 30 min. Then an amount of one of five catalysts (**1–4**, and **5** (ref. 30)) was added to the solution. The amount of catalyst is reported in parts per million relative to MeOH. Gas evolution was measured by a gas burette (100-ml, 500-ml or 1-litre burette). Each molecule of hydrogen is counted as resembling one turnover. After the desired reaction time, the identity of the gas components and their ratio was determined by gas-phase chromatography.

Full Methods and any associated references are available in the online version of the paper.

Received 28 June 2012; accepted 7 January 2013.

Published online 27 February 2013.

- Stolten, D. (ed.) *Hydrogen and Fuel Cells* (Wiley-VCH, 2010).
- Muradov, N. Z. & Veziroglu, T. N. "Green" path from fossil-based to hydrogen economy: an overview of carbon-neutral technologies. *Int. J. Hydrogen Energy* **33**, 6804–6839 (2008).
- European Commission. *European Hydrogen and Fuel Cell Technology Platform "Implementation Plan – Status 2006"* [http://ec.europa.eu/research/fch/pdf/hfp\\_ip06\\_final\\_20apr2007.pdf](http://ec.europa.eu/research/fch/pdf/hfp_ip06_final_20apr2007.pdf) (European Technology Platform for Hydrogen and Fuel Cells, European Commission, 2007).
- United States Department of Energy. *A National Vision of America's Transition to a Hydrogen Economy — to 2030 and Beyond* [http://hydrogen.energy.gov/pdfs/vision\\_doc.pdf](http://hydrogen.energy.gov/pdfs/vision_doc.pdf) (United States Department of Energy, 2002).
- Pingwee, M., Jingguang, L. & Mytelka, L. *Hydrogen and Fuel-Cell Activities in China, 2007* <http://idl-bnc.idrc.ca/dspace/bitstream/10625/35673/1/127544.pdf> 295–308 (United Nations Univ. Press, 2008).
- Palo, D. R., Dagle, R. A. & Holladay, J. D. Methanol steam reforming for hydrogen production. *Chem. Rev.* **107**, 3992–4021 (2007).
- Cortright, R. D., Davda, R. R. & Dumesic, J. A. Hydrogen from catalytic reforming of biomass-derived hydrocarbons in liquid water. *Nature* **418**, 964–967 (2002).
- Shabaker, J. W., Davda, R. R., Huber, G. W., Cortright, R. D. & Dumesic, J. A. Aqueous-phase reforming of methanol and ethylene glycol over alumina-supported platinum catalysts. *J. Catal.* **215**, 344–352 (2003).
- Florusse, L. J. *et al.* Stable low-pressure hydrogen clusters stored in a binary clathrate hydrate. *Science* **306**, 469–471 (2004).
- Ashcroft, A. T., Cheetham, A. K., Green, M. L. H. & Vernon, P. D. F. Partial oxidation of methane to synthesis gas using carbon dioxide. *Nature* **352**, 225–226 (1991).
- Welch, G. C., San Juan, R. R., Masuda, J. D. & Stephan, D. W. Reversible metal-free hydrogen activation. *Science* **314**, 1124–1126 (2006).
- Denney, M. C., Pons, V., Hebden, T. J., Heinekey, D. M. & Goldberg, K. I. Efficient catalysis of ammonia borane dehydrogenation. *J. Am. Chem. Soc.* **128**, 12048–12049 (2006).
- Reece, S. Y. *et al.* Wireless solar water splitting using silicon-based semiconductors and earth-abundant catalysts. *Science* **334**, 645–648 (2011).
- Olah, G., Prakash, G. K. S. & Goepfert, A. Anthropogenic chemical carbon cycle for a sustainable future. *J. Am. Chem. Soc.* **133**, 12881–12898 (2011).
- Boddien, A. *et al.* Efficient dehydrogenation of formic acid using an iron catalyst. *Science* **333**, 1733–1736 (2011).
- Nielsen, M. *et al.* Efficient hydrogen production from alcohols under mild reaction conditions. *Angew. Chem. Int. Edn* **50**, 9593–9597 (2011).
- Morton, D. & Cole-Hamilton, D. J. Molecular hydrogen complexes in catalysis: highly efficient hydrogen production from alcoholic substrates catalysed by ruthenium complexes. *J. Chem. Soc. Chem. Commun.* **17**, 1154–1156 (1988).
- Nielsen, M., Junge, H., Kammer, A. & Beller, M. Towards a green process for bulk-scale synthesis of ethyl acetate: efficient acceptorless dehydrogenation of ethanol. *Angew. Chem. Int. Edn* **51**, 5711–5713 (2012).
- Baratta, W., Bossi, G., Putignano, E. & Rigo, P. Pincer and diamine Ru and Os diphosphane complexes as efficient catalysts for the dehydrogenation of alcohols to ketones. *Chemistry* **17**, 3474–3481 (2011).
- Fujita, K., Yoshida, T., Imori, Y. & Yamaguchi, R. Dehydrogenative oxidation of primary and secondary alcohols catalyzed by a Cp\*Ir complex having a functional C,N-chelate ligand. *Org. Lett.* **13**, 2278–2281 (2011).



21. Zhang, J., Leitus, G., Ben-David, Y. & Milstein, D. Facile conversion of alcohols into esters and dihydrogen catalyzed by new ruthenium complexes. *J. Am. Chem. Soc.* **127**, 10840–10841 (2005).
22. Spasyuk, D., Smith, S. & Gusev, D. G. From esters to alcohols and back with ruthenium and osmium catalysts. *Angew. Chem. Int. Edn* **51**, 2772–2775 (2012).
23. Kawahara, R., Fujita, K. & Yamaguchi, R. Dehydrogenative oxidation of alcohols in aqueous media using water-soluble and reusable Cp\*Ir catalysts bearing a functional bipyridine ligand. *J. Am. Chem. Soc.* **134**, 3643–3646 (2012).
24. Maenaka, Y., Suenobu, T. & Fukuzumi, S. Hydrogen evolution from aliphatic alcohols and 1,4-selective hydrogenation of NAD<sup>+</sup> catalyzed by a [C,N] and a [C,C] cyclometalated organoiridium complex at room temperature in water. *J. Am. Chem. Soc.* **134**, 9417–9427 (2012).
25. Gunanathan, C. & Milstein, D. Metal-ligand cooperation by aromatization-dearomatization: a new paradigm in bond activation and “green” catalysis. *Acc. Chem. Res.* **44**, 588–602 (2011).
26. Gunanathan, C., Ben-David, Y. & Milstein, D. Direct synthesis of amides from alcohols and amines with liberation of H<sub>2</sub>. *Science* **317**, 790–792 (2007).
27. Bertoli, M. *et al.* Osmium and ruthenium catalysts for dehydrogenation of alcohols. *Organometallics* **30**, 3479–3482 (2011).
28. Friedrich, A., Drees, M., Schmedt auf der Gönne, J. & Schneider, S. Highly stereoselective proton/hydride exchange: assistance of hydrogen bonding for the heterolytic splitting of H<sub>2</sub>. *J. Am. Chem. Soc.* **131**, 17552–17553 (2009).
29. Käb, M., Friedrich, A., Drees, M. & Schneider, S. Ruthenium complexes with cooperative PNP ligands: bifunctional catalysts for the dehydrogenation of ammonia–borane. *Angew. Chem. Int. Edn* **48**, 905–907 (2009).
30. Baratta, W. *et al.* Ruthenium(II) terdentate CNN complexes: superlative catalysts for the hydrogen-transfer reduction of ketones by reversible insertion of a carbonyl group into the Ru–H bond. *Angew. Chem. Int. Ed.* **44**, 6214–6219 (2005).

**Supplementary Information** is available in the online version of the paper.

**Acknowledgements** M.N. thanks the Alexander von Humboldt Foundation for financial support. We thank the BMBF and the Ministry of Science and Education of Mecklenburg-Western Pomerania for the basic funding of this project.

**Author Contributions** M.B., M.N. and H.J. designed the project on methanol dehydrogenation. M.N., E.A., H.J., S.G. and M.B. developed the project. M.N. and E.A. performed the catalytic experiments. E.A., W.B., M.N. and H.-J.D. performed mechanistic and analytic studies. M.N., E.A., H.J., S.G. and M.B. wrote the manuscript.

**Author Information** Reprints and permissions information is available at [www.nature.com/reprints](http://www.nature.com/reprints). The authors declare no competing financial interests. Readers are welcome to comment on the online version of the paper. Correspondence and requests for materials should be addressed to M.B. ([matthias.beller@catalysis.de](mailto:matthias.beller@catalysis.de)).

## METHODS

All reactions were performed under inert atmosphere (argon) with exclusion of air. Methanol was refluxed over magnesium and distilled under argon atmosphere. Water was distilled and degassed before use. NaOH and KOH were purchased and used as received.  $[\text{RuHCl}(\text{CO})(\text{PPh}_3)_3]$ ,  $[\text{RuHCl}(\text{CO})(\text{HN}(\text{C}_2\text{H}_4\text{PPh}_2)_2)]$  complex **1a** (Ru-MACHO),  $[\text{RuH}(\text{BH}_4)(\text{CO})(\text{HN}(\text{C}_2\text{H}_4\text{PPh}_2)_2)]$  complex **1b** (Ru-MACHO-BH),  $\text{HN}(\text{C}_2\text{H}_4\text{PiPr}_2)_2$ ,  $\text{HN}(\text{C}_2\text{H}_4\text{PiCy}_2)_2$  and carbonylchlorohydrido [6-(di-*t*-butylphosphinomethyl)-2-(*N,N*-diethylaminomethyl)pyridine] ruthenium(II) (complex **4**; see Supplementary Scheme 1) were purchased from STREM Chemicals Inc., stored under argon, and used as received.  $[\text{RuHCl}(\text{CO})(\text{HN}(\text{C}_2\text{H}_4\text{PiPr}_2)_2)]^{27}$  (complex **2a**),  $[\text{Ru}(\text{H})_2(\text{CO})(\text{HN}(\text{C}_2\text{H}_4\text{PiPr}_2)_2)]^{27}$  (complex **2b**; Supplementary Figs 6 and 7),  $[\text{RuH}(\text{CO})(\text{N}(\text{C}_2\text{H}_4\text{PiPr}_2)_2)]^{27}$  (compound **2c**; Supplementary Figs 8 and 9),  $[\text{RuHCl}(\text{CO})(\text{HN}(\text{C}_2\text{H}_4\text{PCy}_2)_2)]$  (compound **3**; Supplementary Figs 10–12), and complex **5** (ref. 30; see Supplementary Scheme 1) were prepared following or adapting procedures in the literature. Catalytic reactions for the measurement of hydrogen gas evolution were carried out in a thermostated double-walled three-necked flask equipped with a high-efficiency reflux condenser. The latter was connected via a three-way stopcock to a gas burette (see Supplementary Figs 4 and 5). At the beginning of each experiment, the reactor system (flask and condenser) was subjected to five consecutive vacuum–argon cycles, while isolated from the burette. Then the whole system,

including burette, was purged with argon for at least 15 min. A defined amount of water was then introduced in the flask, followed by the required amount of base and methanol. The system was then heated to the desired temperature by means of a thermostat. Once the temperature set in the thermostat had been reached, the system was allowed to equilibrate for 30 min, after which time a homogeneous solution had formed, even in those cases when a very high base concentration was used. The inner temperature reported for each experiment was measured with a ground-glass joint thermometer connected to the reactor (Supplementary Table 1). The desired amount of catalyst was weighed in a Teflon crucible and introduced into the reactor. The reaction solution was stirred at 700 r.p.m. To ascertain the composition of the evolved gas, a sample of the gas phase was withdrawn through a septum in the three-way stopcock with a gas-tight syringe and analysed by gas-phase chromatography using either HP Plot Q/flame ionization detector–hydrocarbons, carboxen/thermoconductivity detector–permanent gases, He carrier gas or carboxen/thermoconductivity detector/methanizer/flame ionization detector–permanent gases, He carrier gas (for representative gas-phase gas chromatography traces, see Supplementary Figs 1–3). The second gas-phase gas chromatography (see Supplementary Experimental Methods GC b) allows the detection of very low levels of  $\text{CH}_4$  and CO. The turnover number was calculated from the amount of hydrogen produced. Every hydrogen molecule represents one catalyst turnover number (see Supplementary Equations (1) and (2)).

# Dynamics of a Snowball Earth ocean

Yosef Ashkenazy<sup>1</sup>, Hezi Gildor<sup>2</sup>, Martin Losch<sup>3</sup>, Francis A. Macdonald<sup>4</sup>, Daniel P. Schrag<sup>4,5</sup> & Eli Tziperman<sup>4,5</sup>

Geological evidence suggests that marine ice extended to the Equator at least twice during the Neoproterozoic era (about 750 to 635 million years ago)<sup>1,2</sup>, inspiring the Snowball Earth hypothesis that the Earth was globally ice-covered<sup>3,4</sup>. In a possible Snowball Earth climate, ocean circulation and mixing processes would have set the melting and freezing rates that determine ice thickness<sup>5,6</sup>, would have influenced the survival of photosynthetic life<sup>4,5,7–9</sup>, and may provide important constraints for the interpretation of geochemical and sedimentological observations<sup>4,10</sup>. Here we show that in a Snowball Earth, the ocean would have been well mixed and characterized by a dynamic circulation<sup>11</sup>, with vigorous equatorial meridional overturning circulation, zonal equatorial jets, a well developed eddy field, strong coastal upwelling and convective mixing. This is in contrast to the sluggish ocean often expected in a Snowball Earth scenario<sup>3</sup> owing to the insulation of the ocean from atmospheric forcing by the thick ice cover. As a result of vigorous convective mixing, the ocean temperature, salinity and density were either uniform in the vertical direction or weakly stratified in a few locations. Our results are based on a model that couples ice flow and ocean circulation, and is driven by a weak geothermal heat flux under a global ice cover about a kilometre thick. Compared with the modern ocean, the Snowball Earth ocean had far larger vertical mixing rates, and comparable horizontal mixing by ocean eddies. The strong circulation and coastal upwelling resulted in melting rates near continents as much as ten times larger than previously estimated<sup>6,7</sup>. Although we cannot resolve the debate over the existence of global ice cover<sup>10,12,13</sup>, we discuss the implications for the nutrient supply of photosynthetic activity and for banded iron formations. Our insights and constraints on ocean dynamics may help resolve the Snowball Earth controversy when combined with future geochemical and geological observations.

The flow of thick ice over a Snowball Earth ocean (“sea glaciers”, characterized by dynamics very different from that of thinner sea ice<sup>14</sup>), has received significant attention over the past few years<sup>5–7,9,14,15</sup>. Similarly, the role and dynamics of atmospheric circulation and heat transport, CO<sub>2</sub> concentration, cloud feedbacks, and continental configuration have been studied<sup>16–18</sup>, as has the role of dust over the Snowball Earth’s ice cover<sup>17,19</sup>. In contrast, despite its importance, the ocean circulation during Snowball Earth events has received little attention. The few studies that used full-ocean General Circulation Models concentrated mostly on the ocean’s role in Snowball Earth initiation and aftermath<sup>20,21</sup>. No studies accounted for the combined effects of thick ice cover and flow, and driving by geothermal heating<sup>11,13,22,23</sup>, yet ref. 11 simulated an ocean under a 200-m-thick ice cover with no geothermal heat flux, and described a non-steady-state solution with near-uniform temperature and salinity, and vanishing Eulerian circulation together with strong parameterized eddy-induced high-latitude circulation cells.

To allow us to simulate the special circumstances during Snowball Earth events, we use a novel model that couples the ocean and thick ice flow (see Methods). We begin by exploring the Snowball Earth circulation using an easier-to-understand two-dimensional (2D,

latitude and depth) ocean model with no continents. The results point to the importance of ocean eddy motions, and given that these have never been studied for a Snowball Earth ocean, we investigate them using a high-resolution sector ocean model. Finally, we consider a near-global three-dimensional (3D) ocean model with reconstructed Neoproterozoic continental geometry to verify that our insights remain valid in this more realistic configuration.

We consider first the zonally averaged temperature, salinity and circulation, including the meridional overturning circulation (MOC). Figure 1 shows steady-state results from a 2D (latitude and depth) version of the ocean model coupled to a one-dimensional (1D, latitude) ice flow model, driven by geothermal heating (about 0.1 W m<sup>−2</sup>) that is enhanced over a prescribed bottom ridge (Supplementary Fig. 2). We assume the presence of land ice at a volume equivalent to about one kilometre of sea level (Methods), and our model predicts that the upper kilometre of the ocean is frozen as well. Concentrating salt in a significantly lower ocean volume resulted in ocean salinity that is significantly higher than that of the present day (Fig. 1b). The high salinity and high pressure at the bottom of the ice lowered the freezing temperature to approximately −3.5°C, explaining the cold temperature field (Fig. 1a). Variations in temperature and salinity are fairly weak<sup>11</sup>, as expected given the insulating thick ice cover and weak geothermal heat forcing.

The geothermal heat flux acts to create low-density water at the ocean bottom, and therefore leads to convective vertical mixing that makes the temperature and salinity effectively vertically uniform nearly everywhere, creating a water-mass pattern that is completely different from that expected during any other period in Earth history (Fig. 1a, b). Near the enhanced geothermal heating over the ridge, there is a weakly stable stratification due to meltwater production over the enhanced heating (bounded by the thick black contour in Fig. 1a, b).

The MOC (Fig. 1d) is surprisingly strong and is confined to around the Equator, very different from the high-latitude present-day MOC. The meridional velocity, which together with the vertical velocity composes the MOC, therefore decays very rapidly away from the Equator. The most prominent features in the zonal velocity field are the two strong jet-like flows near the Equator, flowing at opposite directions on the two sides of the Equator, and decaying slowly away from the Equator (Fig. 1c). The zonal velocity in the higher latitudes, away from the equatorial jet-like structures, is generally eastward throughout most of the water column apart from near the bottom. This eastward mid- to high-latitude velocity is in geostrophic equilibrium between the Coriolis force and the pressure gradient, and is driven by the large-scale meridional pressure and hence by the density gradient (which is a consequence of heating and melting over the ridge, lowering the density there; Methods).

To understand the equatorial zonal flows and MOC, we note that their dominant momentum balance is geostrophic in the north–south direction, and hydrostatic in the vertical, as is the case in the present-day ocean. The east–west momentum balance, however, is between the Coriolis force and eddy (turbulent) viscosity, which is negligible in most of the present-day ocean. The dominant momentum balances are therefore:

<sup>1</sup>Department of Solar Energy and Environmental Physics, The Blaustein Institutes for Desert Research, Ben-Gurion University of the Negev, Midreshet Ben-Gurion, 84990, Israel. <sup>2</sup>Institute of Earth Sciences, The Hebrew University of Jerusalem, Jerusalem, 91904, Israel. <sup>3</sup>Alfred-Wegener-Institut für Polar- und Meeresforschung, 27515 Bremerhaven, Germany. <sup>4</sup>Earth and Planetary Sciences, Harvard University, 20 Oxford Street, Cambridge, Massachusetts 02138, USA. <sup>5</sup>School of Engineering and Applied Sciences, Harvard University, 20 Oxford Street, Cambridge, Massachusetts 02138, USA.



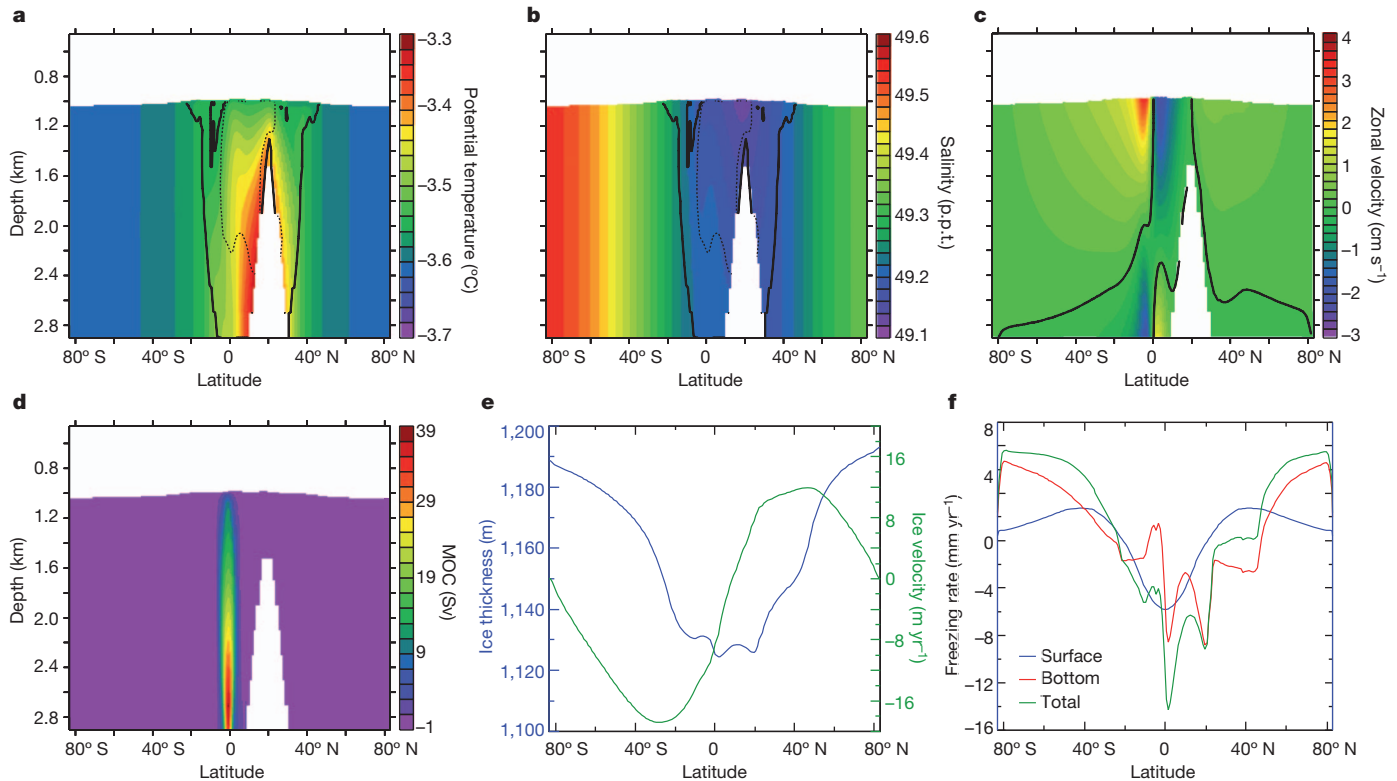


**Figure 1 | Results of a 2D (latitude and depth) ocean model coupled to a 1D (latitude only) ice flow model.** **a**, Potential temperature (colour scale; white area on top corresponds to the calculated ice cover thickness). **b**, Salinity (colour scale, in parts per thousands, p.p.t.), which varies due to freezing and melting (**f**) induced by spatially variable geothermal heating and heat flux through the ice owing to the latitude-dependent atmospheric temperature (Methods); salinity is somewhat lower in the Northern Hemisphere because of the ridge with enhanced geothermal heating and therefore enhanced melting

$$\begin{aligned} -fv &= v_h u_{yy} \\ fu &= -p_y / \rho_0 \\ p_z &= -g\rho \end{aligned}$$

where the east, north and vertical coordinates and velocities are denoted  $(x, y, z)$  and  $(u, v, w)$ ,  $g$  is gravitational acceleration,  $v_h = 2 \times 10^4 \text{ m}^2 \text{ s}^{-1}$  the horizontal eddy viscosity coefficient,  $f \approx \beta y$  is the Coriolis parameter, using the equatorial  $\beta$  plane approximation,  $\rho$  is the density,  $\rho_0$  a reference density, and  $p$  is the pressure. The meridional scale obtained from the zonal momentum equation is  $L \approx (v_h/\beta)^{1/3} \approx 100 \text{ km}$ , consistent with the extent of the MOC in the numerical solution. Assuming the meridional pressure gradient set by the differential geothermal heating to be approximately constant in latitude near the Equator, we can solve the above equations (Methods) to find:

$$\begin{aligned} u &\approx [g\rho_y(z + H/2)/(\beta\rho_0)](1/y) \\ v &\approx -[2v_h g\rho_y(z + H/2)/(\beta^2\rho_0)](1/y^4) \end{aligned}$$

where  $H$  is the ocean depth. The more rapid decay of the meridional velocity  $v$  as function of latitude  $y$  in these expressions explains why the MOC is restricted to the equatorial region, while the equatorial zonal flows  $u$  extend farther poleward. These solutions also predict that  $u$  changes sign across the Equator (where  $y = 0$ ) but  $v$  does not, and also that both horizontal velocities change sign with depth, at  $z = -H/2$ , all remarkably consistent with Fig. 1c, d.

The ice thickness in these solutions (Fig. 1e) is quite uniform, varying from 1,120 m to 1,200 m, owing to the homogenizing effect of the

there. **c**, Zonal velocity (colour scale). **d**, MOC stream function (colour scale;  $1 \text{ Sv} = 10^6 \text{ m}^3 \text{ s}^{-1}$ ), showing a strong equatorial MOC (35 Sv), compared to the present-day high-latitude North Atlantic MOC (about 20 Sv). **e**, Ice thickness and ice velocity as functions of latitude. **f**, Freezing rate (negative values imply melting) at the ice base together with prescribed sublimation/precipitation rates at the ice surface, showing that ocean contribution to setting the ice thickness is comparable to or larger than that of the atmosphere.

ice flow<sup>6</sup>, consistent with previous studies<sup>7,15</sup>. High-latitude basal freezing and low-latitude melting rates are balanced by an equatorward ice flow and are comparable to, if not larger than, the ice surface sublimation and precipitation rates (Fig. 1f). These rates are quite different from previous estimates that ignored ocean dynamics<sup>7</sup>, highlighting the important role of ocean dynamics.

The above 2D model predicts the ocean turbulent eddy field to have a dominant role in the momentum budget, via its parameterization by the horizontal eddy viscosity  $v_h$ . Snowball Earth eddy motions have not been studied before to our knowledge, and to examine them, we considered the results of a high-resolution model, shown in Fig. 2. This model demonstrated that the solution for the ocean circulation is surprisingly turbulent and time-dependent, far from the stagnant Snowball Earth ocean one might envision given the lack of wind forcing and air-sea fluxes. The zonal velocity field (Fig. 2c, f) shows several strong jets off the Equator, in addition to the two equatorial jets seen in the 2D solution. These jets, reminiscent of those seen in the atmosphere of Jupiter, arise from the action of the eddies. That is, the equatorial flows are unstable and generate eddies; the meridional convergence of eddy momentum fluxes  $\partial \overline{u'v'}/\partial y$  generates additional jets off the Equator (Fig. 2f), which again are unstable and feed back on the eddies that sustain the jets<sup>24</sup>.

The high-resolution run also shows a warm area to the northwest of the land mass, which leads to local melting rates of up to  $10 \text{ cm yr}^{-1}$  (Fig. 2e), about ten times larger than the maximum melting rates calculated by coarse model runs<sup>6,7</sup>. This warmer area is due to a concentrated coastal upwelling of deep water heated by geothermal heating. The upwelling occurs in response to the equatorial zonal flow away from the continent. This deep heating is allowed by a very weak

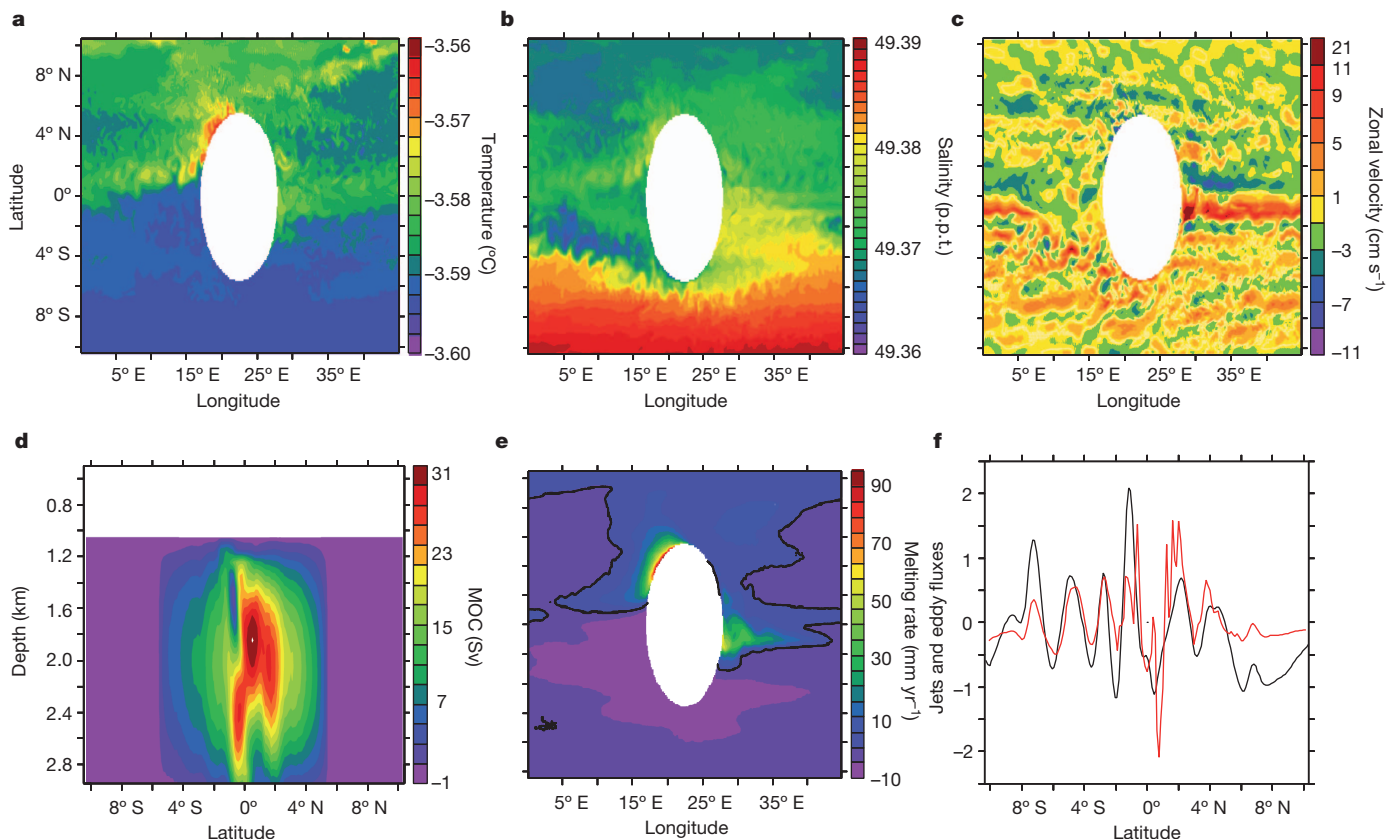


**Figure 2 | Results of a 3D high-resolution sector ocean model showing a rich time-dependent turbulent eddy field.** **a**, Snapshot of the temperature field (colour scale) at 1,150 m (that is, 125 m below the ice). **b**, As for **a**, but for salinity (colour scale). **c**, As for **a**, but for zonal velocity (colour scale). **d**, Time-averaged MOC (colour scale). **e**, Time-averaged melting rate (colour scale; zero

values marked by thick black contour). **f**, Zonal, depth and time means of zonal velocity (black), and of scaled convergence of eddy momentum fluxes  $-\partial \overline{u'v'}/\partial y$  (red), both as function of latitude. The close correspondence between the two demonstrates that eddy momentum flux convergence has a dominant role in the generation of the zonal jets.

local salinity-induced stratification due to geothermally driven ice melting (similar to that seen over the ridge in Fig. 1b). Although it is intriguing, the prescribed ice thickness in this model does not allow us to use this large melting rate conclusively to deduce the existence of thin ice or open water locally near continents, as suggested by some observations<sup>10</sup>, and to explain the survival of photosynthetic life during a global Snowball Earth<sup>8,9,15,25</sup>. The explicitly resolved eddy field can be used to estimate a mixing timescale from low to high latitudes of 500 years (Methods), which is not very different from present-day basin-scale mixing rates.

Finally, a 3D ocean solution with a realistic continental configuration supports the results of the 2D model (Fig. 3a, b and Supplementary Fig. 3). The zonally averaged fields (Supplementary Fig. 3), equatorial zonal jets, large-scale westward flows in the higher latitudes, the existence of an equatorial MOC, and the vertically uniform temperature, salinity and density in most areas away from the enhanced geothermal heating, are all consistent with the 2D solution discussed above. Differences from the 2D case include a weaker salinity range due to the concentrated geothermal heating region being confined and therefore weaker in the 3D case (spatial average is  $0.1 \text{ W m}^{-2}$  in both); the equatorial MOC is composed of two cells owing to the more complex continental and geothermal heating configuration. Like the high-resolution model discussed above, the global 3D solution in the presence of continents shows upwelling and downwelling wherever the equatorial zonal jets encounter continents. This upwelling is possibly due to the weak stratification of the Snowball Earth ocean, whereas in an ocean with present-day like stratification these jets would be diverted sideways via horizontal boundary currents.

The weakly stratified, convectively mixed ocean found here, as well as the strong coastal upwelling, strong equatorial MOC and well

developed eddy field, all imply that the deep and surface ocean are strongly linked in a Snowball Earth scenario, unlike in the well stratified present-day ocean. The well-mixed Snowball Earth ocean<sup>11</sup> has several interesting geochemical implications. First, if there are areas of photosynthesis under a local patch of thin ice, mixing or upwelling are needed to resupply limiting nutrients, because a weakly mixed ocean would lead to the exhaustion of the local nutrient pool and productivity would end. Second, the return of banded iron formations after a billion-year absence is an iconic feature of Neoproterozoic glaciation that is often attributed to stagnant Snowball Earth deep water<sup>3</sup>. Assuming that melt water was derived from land ice that contained air bubbles of an oxygenated atmosphere, one might expect that with enhanced melting and a strongly mixed ocean, iron concentrations could not rise sufficiently to deposit banded iron formations. However, Neoproterozoic banded iron formations, unlike Archean and Palaeoproterozoic ones, are not broadly distributed<sup>26</sup>. Instead, they form irregular lenticular bodies within glacial deposits, and are found predominantly in juvenile rift basins in close association with volcanic rocks, analogous to the Red Sea, where iron is supplied by hydrothermal fluids<sup>27</sup>. Such rift basins are somewhat isolated from the rest of the well-mixed ocean, allowing the build-up of iron levels and the development of banded iron formations, not inconsistent with our results showing a well-mixed ocean.

Our findings suggest that beneath the Snowball Earth ice cover, the Neoproterozoic oceans were dynamic, well mixed<sup>11</sup> and spatially and temporally variable: far from a stagnant pool. These ocean dynamics insights open the way to a reinterpretation of some geochemical, sedimentary and paleontological observations, possibly contributing to the debate on the existence of a global ice cover and to our understanding of the Neoproterozoic era.

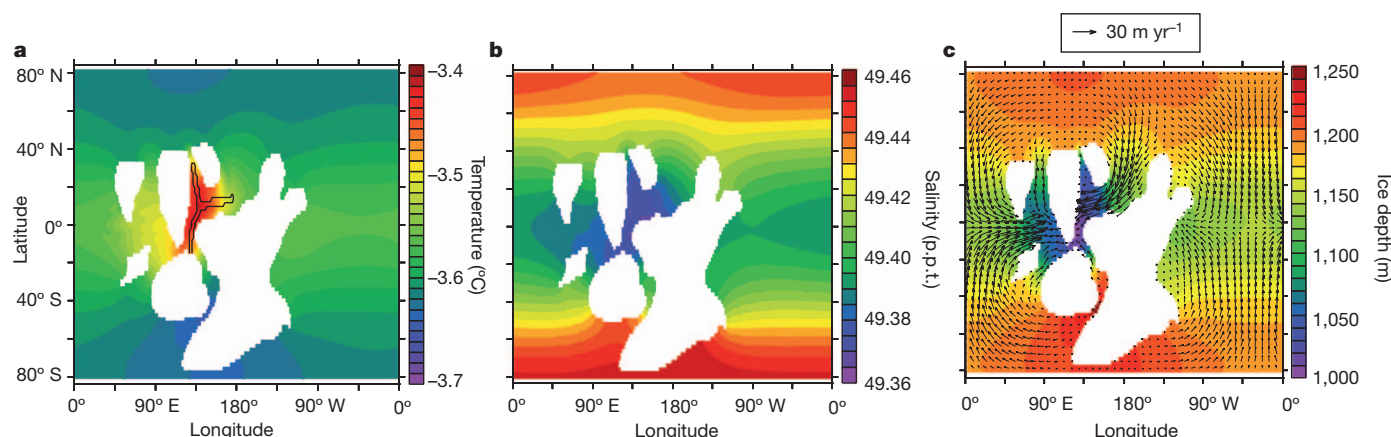


**Figure 3 | Results of the 3D ocean model coupled to a 2D (latitude and longitude) ice flow model, in the presence of reconstructed Neoproterozoic continental configuration.** **a**, Temperature at 1,200 m depth (colour scale), areas of enhanced geothermal heating (black contour lines) and land masses (white areas). **b**, Salinity at 1,200 m (colour scale). **c**, Ice thickness (colour scale), and ice velocity vectors (plotted every fourth grid point in the longitude

## METHODS SUMMARY

Our model couples the state-of-the-art ocean general circulation model, MITgcm<sup>28</sup>, which can simulate thick ice shelves<sup>29</sup>, with a recently developed 2D (latitude and longitude) ice flow model<sup>15</sup>, extending previous 1D flow models<sup>6,7</sup>. The model is run here in three configurations: 2D (latitude and depth) ocean model coupled to a 1D (latitude) ice flow model; a high-resolution (1/8°) sector model with prescribed uniform ice cover; and a 3D global model with reconstructed Neoproterozoic continental configuration coupled to a 2D ice flow model. A geothermal heat flux is prescribed in all three versions at the bottom of the ocean (Supplementary Fig. 2), with a spatial average of  $0.1 \text{ W m}^{-2}$ , and is spatially uniform except not far from the Equator (motivated by the Neoproterozoic continental reconstruction of ref. 30), where the geothermal flux is up to four times its background value. The 2D ocean model also prescribes a ridge over which the heating is enhanced, while the topography of the two other models is flat. Sensitivity experiments to the location and amplitude of the enhanced heating, and to the topography in both the 2D and 3D models, show our solution to be very robust.

**Full Methods** and any associated references are available in the online version of the paper.

Received 18 September 2012; accepted 8 January 2013.

- Harland, W. B. in *Problems in Palaeoclimatology* (ed. Nairn, A. E. M.) 119–149 (180–184 (John Wiley & Sons, 1964).
- Evans, D. A. D. & Raub, T. D. in *The Geological Record of Neoproterozoic Glaciations* (eds Arnaud, E., Halverson, G. P. & Shields-Zhou, G.) Vol. 36, 93–112 (London, Geological Society of London, 2011).
- Kirschvink, J. in *The Proterozoic Biosphere: A Multidisciplinary Study* (eds Schopf, J. & Klein, C.) 51–52 (Cambridge University Press, 1992).
- Hoffman, P. & Schrag, D. The snowball Earth hypothesis: testing the limits of global change. *Terra Nova* **14**, 129–155 (2002).
- McKay, C. Thickness of tropical ice and photosynthesis on a snowball Earth. *Geophys. Res. Lett.* **27**, 2153–2156 (2000).
- Goodman, J. & Pierrehumbert, R. Glacial flow of floating marine ice in “Snowball Earth”. *J. Geophys. Res.* **108**, doi:10.1029/2002JC001471 (2003).
- Pollard, D. & Kasting, J. Snowball Earth: a thin-ice solution with flowing sea glaciers. *J. Geophys. Res.* **110**, doi:10.1029/2004JC002525 (2005).
- Corsetti, F., Olcott, A. & Bakermans, C. The biotic response to Neoproterozoic snowball Earth. *Palaeogeogr. Palaeoclimatol. Palaeoecol.* **232**, 114–130 (2006).
- Campbell, A. J., Waddington, E. D. & Warren, S. G. Refugium for surface life on Snowball Earth in a nearly-enclosed sea? A first simple model for sea-glacier invasion. *Geophys. Res. Lett.* **38**, doi:10.1029/2011GL048846 (2011).
- Allen, P. A. & Etienne, J. L. Sedimentary challenge to Snowball Earth. *Nature Geosci.* **1**, 817–825 (2008).
- Ferreira, D., Marshall, J. & Rose, B. Climate determinism revisited: multiple equilibria in a complex climate model. *J. Clim.* **24**, 992–1012 (2011).
- Pierrehumbert, R. T., Abbot, D. S., Voigt, A. & Koll, D. Climate of the Neoproterozoic. *Annu. Rev. Earth Planet. Sci.* **39**, 417–460 (2011).
- Yang, J., Peltier, W. R. & Hu, Y. The initiation of modern “Soft Snowball” and “Hard Snowball” climates in CCSM3. Part II: Climate dynamic feedbacks. *J. Clim.* **25**, 2737–2754 (2012).

direction and every second grid point in the latitude direction). Results are generally consistent with the 2D solution (see also Supplementary Fig. 3), although some deviations from zonal symmetry occur owing to advection of temperature and salinity by ocean currents near continents, and owing to enhanced heating and freshening via ice melting in the area of enhanced geothermal heating between the continents.

- Warren, S., Brandt, R., Grenfell, T. & McKay, C. Snowball Earth: ice thickness on the tropical ocean. *J. Geophys. Res.* **107**, doi:10.1029/2001JC001123 (2002).
- Tziperman, E. et al. Continental constriction and sea ice thickness in a Snowball-Earth scenario. *J. Geophys. Res.* **117**, doi:10.1029/2011JC007730 (2012).
- Pierrehumbert, R. Climate dynamics of a hard snowball Earth. *J. Geophys. Res.* **110**, doi:10.1029/2004JD005162 (2005).
- Le Hir, G., Donnadieu, Y., Krinner, G. & Ramstein, G. Toward the snowball earth deglaciation. *Clim. Dyn.* **35**, 285–297 (2010).
- Donnadieu, Y., Godd  ris, Y., Ramstein, G., N  d  lec, A. & Meert, J. A snowball Earth climate triggered by continental break-up through changes in runoff. *Nature* **428**, 303–306 (2004).
- Abbot, D. S. & Pierrehumbert, R. T. Mudball: surface dust and Snowball Earth deglaciation. *J. Geophys. Res.* **115**, doi:10.1029/2009JD012007 (2010).
- Poulsen, C., Pierrehumbert, R. T. & Jacobs, R. L. Impact of ocean dynamics on the simulation of the Neoproterozoic “snowball Earth”. *Geophys. Res. Lett.* **28**, 1575–1578 (2001).
- Poulsen, C. & Jacob, R. Factors that inhibit snowball Earth simulation. *Paleoceanography* **19**, doi:10.1029/2004PA001056 (2004).
- Voigt, A., Abbot, D. S., Pierrehumbert, R. T. & Marotzke, J. Initiation of a Marinoan Snowball Earth in a state-of-the-art atmosphere-ocean general circulation model. *Clim. Past* **7**, 249–263 (2011).
- Le Hir, G., Ramstein, G., Donnadieu, Y. & Pierrehumbert, R. T. Investigating plausible mechanisms to trigger a deglaciation from a hard snowball Earth. *C. R. Geosci.* **339**, 274–287 (2007).
- Farrell, B. F. & Ioannou, P. J. Structural stability of turbulent jets. *J. Atmos. Sci.* **60**, 2101–2118 (2003).
- Runnegar, B. Palaeoclimate: loophole for snowball Earth. *Nature* **405**, 403–404 (2000).
- Bekker, A. et al. Iron formation: the sedimentary product of a complex interplay among mantle, tectonic, oceanic, and biospheric processes. *Econ. Geol.* **105**, 467–508 (2010).
- Young, G. M. Proterozoic plate tectonics, glaciation and iron-formations. *Sedim. Geol.* **58**, 127–144 (1988).
- Marshall, J., Adcroft, A., Hill, C., Perelman, L. & Heisey, C. A finite-volume, incompressible Navier Stokes model for studies of the ocean on parallel computers. *J. Geophys. Res.* **102**, 5753–5766 (1997).
- Losch, M. Modeling ice shelf cavities in a z coordinate ocean general circulation model. *J. Geophys. Res.* **113**, doi:10.1029/2007JC004368 (2008).
- Li, Z. X. et al. Assembly, configuration, and break-up history of Rodinia: a synthesis. *Precamb. Res.* **160**, 179–210 (2008).

**Supplementary Information** is available in the online version of the paper.

**Acknowledgements** We thank B. Rose for comments. This work was supported by the NSF Climate Dynamics P2C2 programme, grant number ATM-0902844 (to E.T. and Y.A.). E.T. thanks the Weizmann Institute for its hospitality during parts of this work. Y.A. thanks the Harvard EPS department for a most pleasant and productive sabbatical visit.

**Author Contributions** Y.A. and E.T. formulated the problem and performed the model runs and analysis. F.A.M. and D.P.S. contributed to the geological motivation and interpretation. M.L. and H.G. helped with the model set-up, and all authors contributed to the writing of the manuscript.

**Author Information** Reprints and permissions information is available at [www.nature.com/reprints](http://www.nature.com/reprints). The authors declare no competing financial interests. Readers are welcome to comment on the online version of the paper. Correspondence and requests for materials should be addressed to E.T. (eli@eps.harvard.edu) or Y.A. (ashkena@bgu.ac.il).



## METHODS

**Model description.** The model used here couples the Massachusetts Institute of Technology general circulation ocean model (MITgcm)<sup>28</sup> with its ice-shelf package<sup>29</sup> to a recently developed 2D (latitude and longitude) model of thick ice flow over a Snowball Earth ocean<sup>15</sup>, which is an extension of the 1D ice flow model of refs 6 and 7 and similar ones<sup>31–33</sup>. The ice flow model compensates for melting and sublimation at low latitudes and freezing/precipitation at high latitudes, with an equatorward ice flow calculated from ice-thickness gradients based on Glenn's law. The ice flow model employs the well known ice-shelf approximation in which the velocity is independent of depth<sup>34,35</sup>, together with an assumed linear vertical temperature profile within the ice<sup>6</sup>, which together make it possible to average over the vertical dimension rather than model it explicitly.

The coupling of the ice and ocean models is done asynchronously: the ocean model is run for 300 years and the ice model is then run for a similar period, and the process is repeated until a steady state is obtained. At each iteration the ocean model is given the ice thickness calculated by the ice model, while the ice model is driven by the melting and freezing rates calculated by the ocean model. The ice-surface meridional temperature, sublimation and snowfall are taken from ref. 7, with an Equator-to-pole temperature difference of 36°C (Supplementary Fig. 1). No-slip ocean boundary conditions are specified on side and bottom boundaries, and free-slip conditions are specified under the ice cover.

Turbulent convection is parameterized in our model experiments by an increased vertical diffusion where the vertical stratification is unstable. Eddy mixing and mixed-layer parameterizations developed for the present-day ocean<sup>36</sup> are probably not applicable for the very weakly stratified Snowball Earth ocean, and we use instead crude horizontal and vertical eddy diffusion. A different choice was made by ref. 11, who used an eddy parameterization tuned to present-day ocean eddies<sup>36</sup> and simulated a Snowball Earth ocean under 200-m-thick ice with no geothermal heating and therefore not at a thermodynamic equilibrium, but with a quasi-equilibrated circulation. They found a very weakly stratified ocean and described a vanishing Eulerian velocity field, yet with strong high-latitude parameterized eddy-driven meridional circulation cells, very different from the vigorous Eulerian equatorial overturning and jets we found here.

The 2D ocean model uses a horizontal diffusion coefficient of  $\kappa_h = 200 \text{ m}^2 \text{ s}^{-1}$  and viscosity of  $\nu_h = 2 \times 10^4 \text{ m}^2 \text{ s}^{-1}$ ; the 3D “realistic geometry” case uses different values of  $\kappa_h = 500 \text{ m}^2 \text{ s}^{-1}$  and  $\nu_h = 5 \times 10^4 \text{ m}^2 \text{ s}^{-1}$  required by its different resolution. The vertical viscosity in both models is set to  $\nu_v = 2 \times 10^{-3} \text{ m}^2 \text{ s}^{-1}$  and the vertical diffusivity to  $\kappa_v = 1 \times 10^{-4} \text{ m}^2 \text{ s}^{-1}$ . The high-resolution case uses a Leith eddy viscosity formulation<sup>37</sup>.

The 2D ocean model (latitude and depth, periodic in longitude) has a horizontal latitudinal resolution of  $1^\circ$  and 32 vertical levels, varying in thickness from 10 m adjacent to the ice to 200 m at depth (vertical grid spacing varies from 920 m at the top, entirely within the ice, followed by 15 levels of 10 m thickness each, and then 12 m, 17 m, 23 m, 32 m, 45 m, 61 m, 82 m, 110 m, 148 m, and seven levels of thickness 200 m at the bottom). The 2D ocean model is coupled to a 1D (latitude) version of the ice flow model. We performed sensitivity runs to the location and amplitude of the geothermal forcing and found the solution to be very robust.

The 3D near-global ocean model was run at a horizontal resolution of  $2^\circ$  from  $82^\circ \text{ S}$  to  $82^\circ \text{ N}$ , and with 73 vertical levels of varying thickness from 10 m near the ice to 200 m at depth (starting from the ocean surface, the first level is 550 m thick, followed by 57 levels whose thickness is 10 m, and then 14 m, 20 m, 27 m, 38 m, 54 m, 75 m, 105 m, 147 m, and finally seven levels of thickness 200 m; at steady state, the upper 33 levels are within the ice, and therefore inactivated, and the rest represent the ocean). Continental configuration is based on the 720-million-year-old Neoproterozoic reconstruction of ref. 30, and includes an estimated location of spreading ridges between the continents, where geothermal heating is probably enhanced (thick black contour in Fig. 3a; spreading ridges elsewhere are not included owing to the uncertainty in their location). Bathymetry reconstructions for the Neoproterozoic are not easy to come by, and we therefore specified a flat topography in the 3D case, relying on land masses to restrict zonal flows. We performed sensitivity runs with specified sills (1 km high) around the ocean constricted by the land masses, as well as with (1 km high) mid-ocean ridges specified in the open ocean, and found that these do not change the overall picture.

The high-resolution sector ocean model spans  $45^\circ$  longitude, from  $10.5^\circ \text{ S}$  to  $10.5^\circ \text{ N}$ , at a horizontal resolution of an eighth of a degree longitude and latitude and 20 vertical levels of thickness 100 m each. An ice cover with uniform thickness of 1,025 m is prescribed in this case rather than using the ice flow model (which would be prohibitive owing to the computational cost). A flat ocean topography is used, and enhanced geothermal heating is prescribed as a Gaussian centred around  $6^\circ \text{ N}$ , at up to four times the amplitude of the background geothermal flux. The surface temperature in this experiment is uniform (due to its relatively small meridional extent) and set to  $-44.4^\circ \text{ C}$ . This high-resolution run was integrated for over 100 years to reach an equilibrium of the eddy field, yet because its ice cover

is specified rather than evolving, the run is—unlike for the other two models—not at a complete thermodynamic equilibrium with its ice cover.

While geothermal heat can have some effect on the present-day ocean<sup>38</sup>, it is the dominant forcing in a Snowball Earth ocean. A hydrothermal heat flux is therefore prescribed here at the bottom of the ocean and is spatially uniform except where enhanced flux is prescribed to simulate the effect of spreading ridges. These enhanced geothermal areas are prescribed in the model runs shown in the paper to be not far from the Equator (motivated by the Neoproterozoic continental reconstruction of ref. 30), and the geothermal flux there is up to four times its background value. The observed background flux away from ocean ridges is about  $0.05 \text{ W m}^{-2}$ , and the flux observed at mid-ocean ridges is about four times larger, such that the average over ocean basins is estimated to be of the order of  $0.1 \text{ W m}^{-2}$  (see, for example, table 4 of ref. 39). We therefore prescribe a flux whose spatial average is  $0.1 \text{ W m}^{-2}$ , and which is larger locally over ridges. At a steady state the average flux escaping the ocean through the thick ice cover is therefore also  $0.1 \text{ W m}^{-2}$ . Supplementary Fig. 2 shows the hydrothermal forcing of all three models shown in the paper. The Neoproterozoic flux may have been slightly larger than that of the present day, but the difference is expected to be small relative to other uncertainties, so that modern values are used here.

Most ocean models cannot incorporate an ice cover thicker than their upper level, which is of the order of 5–50 m. It is, however, important to use a thick shelf ice formulation as done here, given that representing thick ice-shelves as thin sea ice is known to lead to biases in modelling present-day deep-water formation around Antarctica owing to the induced biases in freshwater fluxes due to melting/freezing<sup>40,41</sup>. An alternative to our thick ice-shelf formulation was used by ref. 11, which employed a dynamic rescaling of the vertical coordinate<sup>42</sup>.

**Derivation of the solution for the 2D flow field.** Consider the zonal equatorial jets seen (for example) in Fig. 1. Differentiate the hydrostatic equation in  $y$  and integrate in  $z$  to find  $p_y = g\rho_y z + F(y)$ , and assume this meridional pressure gradient set by the differential geothermal heating to be approximately constant in latitude  $y$  around the Equator. The meridional momentum equation then leads to an expression for  $u$ , and the zonal momentum equation to an expression for  $v$ . Requiring the vertically integrated meridional flow to vanish owing to mass conservation, we find  $F(y)$ , giving:

$$u \approx [g\rho_y(z + H/2)/(\beta\rho_0)](1/y)$$

$$v \approx -[2\nu_h g\rho_y(z + H/2)/(\beta^2\rho_0)](1/y^4)$$

If the geothermal heating and bathymetry are prescribed to be uniform, the MOC is weaker by about 75%, and if the ice-surface meridional temperature is also uniform, the MOC vanishes. This suggests that the atmospheric forcing via the ice-surface meridional temperature is responsible for about 25% of the MOC, in spite of the thick ice cover. The atmospheric driving of the Snowball Earth ocean, and of the MOC in particular, is through its effect on melting rates at high versus low latitudes. This difference mostly depends on the Equator-to-pole atmospheric temperature difference, and if the carbon dioxide is increased, for example, and if the meridional temperature difference is consequently lowered, then the atmospheric driving of the ocean circulation may be weaker. In addition to this, the sensitivity of the ice flow to surface temperatures derived from different carbon dioxide concentrations was explicitly discussed by ref. 15. When the geothermal forcing is uniform (but the ice-surface meridional temperature is still a function of latitude  $y$ ), or the ridge with enhanced heating is placed at the Equator, the north-south symmetry is still broken, and although the MOC is weaker and could be in either direction depending on initial conditions, the flows are qualitatively similar to the above.

**On the eddy field in the high-resolution model run.** The relatively strong zonal velocities that develop in the above 2D model near the Equator are characterized by a Reynolds number (based on molecular viscosity) that is much greater than one, of  $R = uL/\nu = (0.03 \text{ m s}^{-1})(2 \times 10^5 \text{ m})/(1.8 \times 10^{-6} \text{ m}^2 \text{ s}^{-1}) \approx 4 \times 10^9$ , anticipating a turbulent flow. In addition, the meridional gradient of vorticity ( $\beta - u_{yy}$ ) changes sign as function of latitude, indicating that eddies may develop owing to barotropic instability. It is also possible that the eddy field may be able to extract available potential energy from the (weak) meridional density gradient.

The eddy motions seen in our high-resolution run are characterized by a velocity scale of  $u' \approx 0.02 \text{ m s}^{-1}$  and a length scale of  $l \approx 100 \text{ km}$  (Fig. 2c). These scales can be used to estimate a mixing-length eddy viscosity of  $\nu_h \approx u'l \approx 2 \times 10^3 \text{ m}^2 \text{ s}^{-1}$ . A mixing timescale from low to high latitudes is therefore given by  $\tau \approx R^2/\nu_h \approx 500$  years, where  $R$  is the Earth's radius, not very different from present-day basin-scale mixing rates. This is a lower bound on mixing timescales, because one expects the snowball eddy field to be weaker at the higher latitudes where the mean flows and resulting eddy field are weaker. This is in contrast to the present-day ocean,

where eddy generation is strong at mid- to high latitudes near western boundary currents.

**Salinity uncertainties.** Estimating ocean salinity during the Neoproterozoic presents a challenge. We assume the pre-Snowball Earth salinity to be equal to that of the present day, but there is significant evidence that it varied significantly and may have been as high as twice that of the present day<sup>43</sup>; see also some recent reviews of evaporites through time<sup>44,45</sup>. Salinity may also have increased during Snowball Earth events if oceans continued to receive a supply of salts through both subglacial runoff and subglacial sediment transport, whereas evaporite deposition would have been nonexistent. The main effect of a higher ocean salinity on our simulation would have been the additional lowering of the freezing temperature, which is already quite low relative to modern values owing to both high pressure at the ice base and high salinity.

Another source of uncertainty in salinity is our assumed concentration of salt as a result of land-ice volume being equivalent to about 1 km of sea level. Modelling studies<sup>46,47</sup> estimate continental ice sheets to be a few kilometres thick after about 100,000 years, roughly comparable to the East Antarctic Ice-Sheet with a mean thickness of 2.15 km (ref. 48). In addition, geological relationships<sup>49</sup> estimated a post-glacial sea-level rise of 1.5 km, which is equivalent to melting 3.3-km-thick grounded ice sheets on all continents and oceanic platforms. We conclude that although no tight constraint on land ice exists, 1-km-thick ice sheets seem to be within the range of current estimates.

Yet another important salinity-related issue is the possibility of freshwater input from land-based subglacial flows. Such freshwater flow at the ocean surface, which may develop should there be any open coastal water, could be mixed down by the strong vertical convective mixing. Yet, if the fresh water input is strong enough, it could lead to a weak local coastal stratification (as seen in our solution) over the ridge due to melting there (Fig. 1b). This scenario remains speculative, given that it hinges on the existence of open coastal water, which our model does not explicitly predict.

31. Li, D. & Pierrehumbert, R. T. Sea glacier flow and dust transport on Snowball Earth. *Geophys. Res. Lett.* **38**, doi:10.1029/2011GL048991 (2011).
32. Goodman, J. C. Through thick and thin: marine and meteoric ice in a "Snowball Earth" climate. *Geophys. Res. Lett.* **33**, doi:10.1029/2006GL026840 (2006).
33. Pollard, D. & Kasting, J. F. Reply to comment by Stephen G. Warren and Richard E. Brandt on "Snowball Earth: A thin-ice solution with flowing sea glaciers". *J. Geophys. Res.* **111**, doi:10.1029/2006JC003488 (2006).
34. Morland, L. Unconfined ice-shelf flow. In *Dynamics of the West Antarctic Ice Sheet* (eds van der Veen, C. & Oerlemans, J.) 99–116 (D. Reidel, 1987).
35. MacAyeal, D. EISMINT: Lessons in ice-sheet modeling. Technical Report <http://geosci.uchicago.edu/pdfs/macayeal/lessons.pdf> (University of Chicago, 1997).
36. Gent, P. R. & McWilliams, J. C. Isopycnal mixing in ocean circulation models. *J. Phys. Oceanogr.* **20**, 150–155 (1990).
37. Leith, C. E. Stochastic models of chaotic systems. *Physica D* **98**, 481–491 (1996).
38. Adcroft, A., Scott, J. R. & Marotzke, J. Impact of geothermal heating on the global ocean circulation. *Geophys. Res. Lett.* **28**, 1735–1738 (2001).
39. Pollack, H., Hurter, S. & Johnson, J. Heat flow from the Earth's interior: analysis of the global data set. *Rev. Geophys.* **31**, 267–280 (1993).
40. Hellmer, H., Schodlok, M., Wenzel, M. & Schröter, J. On the influence of adequate Weddell Sea characteristics in a large-scale global ocean circulation model. *Ocean Dyn.* **55**, 88–99 (2005).
41. Thoma, M., Grosfeld, K. & Lange, M. The impact of the Eastern Weddell ice shelves on water masses in the Eastern Weddell Sea. *J. Geophys. Res.* **111**, C12010 (2006).
42. Campin, J., Marshall, J. & Ferreira, D. Sea ice–ocean coupling using a rescaled vertical coordinate  $z$ . *Ocean Model.* **24**, 1–14 (2008).
43. Knauth, L. Temperature and salinity history of the Precambrian ocean: implications for the course of microbial evolution. *Palaeogeogr. Palaeoclimatol. Palaeoecol.* **219**, 53–69 (2005).
44. Warren, J. Evaporites through time: tectonic, climatic and eustatic controls in marine and nonmarine deposits. *Earth Sci. Rev.* **98**, 217–268 (2010).
45. Evans, D. A. D. Proterozoic low orbital obliquity and axial-dipolar geomagnetic field from evaporite palaeolatitudes. *Nature* **444**, 51–55 (2006).
46. Donnadieu, Y., Fluteau, F., Ramstein, G., Ritz, C. & Besse, J. Is there a conflict between the Neoproterozoic glacial deposits and the snowball Earth interpretation: an improved understanding with numerical modeling. *Earth Planet. Sci. Lett.* **208**, 101–112 (2003).
47. Pollard, D. & Kasting, J. Climate-ice sheet simulations of Neoproterozoic glaciation before and after collapse to Snowball Earth. *Geophys. Monogr. Ser.* **146**, 91–105 (2004).
48. Lythe, M. *et al.* Bedmap: a new ice thickness and subglacial topographic model of Antarctica. *J. Geophys. Res.* **106**, 11335–11351 (2001).
49. Hoffman, P. F. Strange bedfellows: glacial diamictite and cap carbonate from the Marinoan (635) glaciation in Namibia. *Sedimentology* **58**, 57–119 (2011).

# Amphibious flies and paedomorphism in the Jurassic period

Diying Huang<sup>1</sup>, André Nel<sup>2</sup>, Chenyang Cai<sup>1</sup>, Qibin Lin<sup>1</sup> & Michael S. Engel<sup>3,4</sup>

The species of the Strashilidae (strashilids) have been the most perplexing of fossil insects from the Jurassic period of Russia and China<sup>1,2</sup>. They have been widely considered to be ectoparasites of pterosaurs or feathered dinosaurs, based on the putative presence of piercing and sucking mouthparts and hind tibio-basitarsal pincers purportedly used to fix onto the host's hairs or feathers<sup>1–6</sup>. Both the supposed host and parasite occur in the Daohugou beds from the Middle Jurassic epoch of China (approximately 165 million years ago)<sup>7,8</sup>. Here we analyse the morphology of strashilids from the Daohugou beds, and reach markedly different conclusions; namely that strashilids are highly specialized flies (Diptera) bearing large membranous wings, with substantial sexual dimorphism of the hind legs and abdominal extensions. The idea that they belong to an extinct order<sup>2</sup> is unsupported, and the lineage can be placed within the true flies. In terms of major morphological and inferred behavioural features, strashilids resemble the recent (extant) and relict members of the aquatic fly family Nymphomyiidae. Their ontogeny are distinguished by the persistence in adult males of larval abdominal respiratory gills, representing a unique case of paedomorphism among endopterygote insects. Adult strashilids were probably aquatic or amphibious, shedding their wings after emergence and mating in the water.

Order Diptera

*Strashila daohugouensis* sp. nov.

**Etymology.** The name refers to the locality of the type specimen.

**Holotype.** Nanjing Institute of Geology and Palaeontology (NIGP)155020, a complete male with details of head, associated with female allotype, without counterpart.

**Referred material.** Allotype NIGP156171; paratypes NIGP155017, NIGP155018, NIGP155019, NIGP155022, NIGP155023, NIGP155024, NIGP155025, NIGP155027 and NIGP156170.

**Locality.** The Xiayingzi outcrop of the Daohugou beds, Daohugou Village, Ningcheng County, Inner Mongolia, China. The exception is NIGP115019 (see Supplementary Information).

**Horizon.** Jiulongshan Formation, Middle Jurassic epoch.

**Diagnosis.** The new species greatly resembles the type species, *Strashila incredibilis*, except that it has shorter and more swollen male metafemora (see Supplementary Information for further details of the new species).

The enigmatic Jurassic-period insect *Strashila incredibilis* displays a hypognathous head with compact antenna and a short 'suctorial beak', an apterous thorax, prominent chelate hind legs, and fleshy lateral abdominal appendages<sup>1</sup>. Only a few strashilid males have been reported from the Late Jurassic epoch of Russia<sup>1</sup> and Middle Jurassic epoch of China<sup>2,9</sup>, and therefore knowledge of these enigmatic insects has been very limited. Recent descriptions add little critical information with regard to their functional morphology and systematic affinities, and attribute strashilids to an extinct, putatively ectoparasitic order<sup>2</sup>. The present study is based on 13 new specimens of 2 different

forms, *Strashila daohugouensis* sp. nov. (9 males, 2 females) and *Vosila sinensis* (2 males) (we demonstrate that *Vosila sinensis* and *Parazila saurica* are the same species; for details see Supplementary Information) from Daohugou. These specimens are rare among the 100,000 fossil insects recovered from Daohugou and among the collections of the Nanjing Institute of Geology and Palaeontology.

Although definitive Middle Jurassic ectoparasites (fleas) on vertebrates were reported recently from the Daohugou outcrops<sup>5,10</sup>, earlier speculation regarding strashilids as terrestrial ectoparasites can be rejected owing to an alternative hypothesis stemming from the discovery of hitherto unknown large membranous wings (Fig. 1i) and females of *Strashila*, in two cases preserved in copula (Fig. 1a, e). Males and females have identical head morphologies but differ strongly in the absence of the hind leg pincers in females, which excludes ectoparasitism on terrestrial vertebrates as these are reinterpreted as sex-related structures for grasping the female rather than a host's integument. In addition, unlike ectoparasitic insect lineages, the body is cylindrical in strashilids (Fig. 1e), rather than dorsoventrally or laterally flattened.

Male strashilids have genitalia of antiophoran type<sup>1,2,4</sup> that are thought to have terminalia characteristic of Holometabola and are close to those of Mecopteroidea, but with primitive volsellae (small accessory clasping sclerites)<sup>2</sup>. This has led to the suggestion that they are an extinct order and a sister group to the Mecoptera<sup>2</sup>. In fact, the male genitalia are virtually identical with those of the recent nematoceran flies<sup>11</sup> (for example, Chironomidae, Sciaridae or some Nymphomyiidae) rather than Mecoptera. Examination of the genitalia in finer detail reveals that they are clearly dipteran. The male tergite VIII shows a rounded anterolateral process (Figs 1c, f and 2c, and Supplementary Fig. 3i), and it has a volsella of typical dipteran morphology, gonocoxites articulated on the posterolateral sides of the transverse tergite, and gonostyli with terminal grasping hooks. The presence of these features in combination reinforces the placement of strashilids among basal lineages of the true flies<sup>12,13</sup> (Figs 1c, f and 2c, and Supplementary Figs 3i and 6a).

The relatively small, oval, prognathous head bears a pair of large compound eyes with numerous facets and a pair of lateral ocelli, which are not completely or virtually lost or reduced as in ectoparasitic insects (Fig. 1b, h and Supplementary Figs 1a–d, 2b, c, e, i and 3b). Together with the presence of short antennae, this supports further the affinity of the Strashilidae with true flies. The mouthparts are vestigial, remarkably reduced in both sexes (Fig. 1b, h and Supplementary Figs 2e and 3b), suggesting that the adults do not feed. The antennae have a scape and a pedicel, both of which are large, and a long flagellum with the main section annulated, comparable in critical details with those of nymphomyiids<sup>14</sup> (Fig. 1h and Supplementary Figs 2b, c, e, i and 3b).

The thorax of strashilids shows the typical subdivision of the thorax of true flies (Fig. 1a, g and Supplementary Fig. 2h). The male wings, large and membranous, are fringed with numerous long setae (Figs 1i, j and 3a, and Supplementary Figs 5a, e, f and 7b) and are similar to those of nymphomyiids, a primitive lineage of aquatic flies. The wings bear a

<sup>1</sup>State Key Laboratory of Palaeobiology and Stratigraphy, Nanjing Institute of Geology and Palaeontology, Chinese Academy of Sciences, Nanjing 210008, China. <sup>2</sup>CNRS UMR 7205, CP 50, Entomologie, Muséum national d'Histoire naturelle, Paris F-75005, France. <sup>3</sup>Division of Entomology, Natural History Museum, University of Kansas, Lawrence, Kansas 66045, USA. <sup>4</sup>Department of Ecology & Evolutionary Biology, University of Kansas, Lawrence, Kansas 66045, USA.



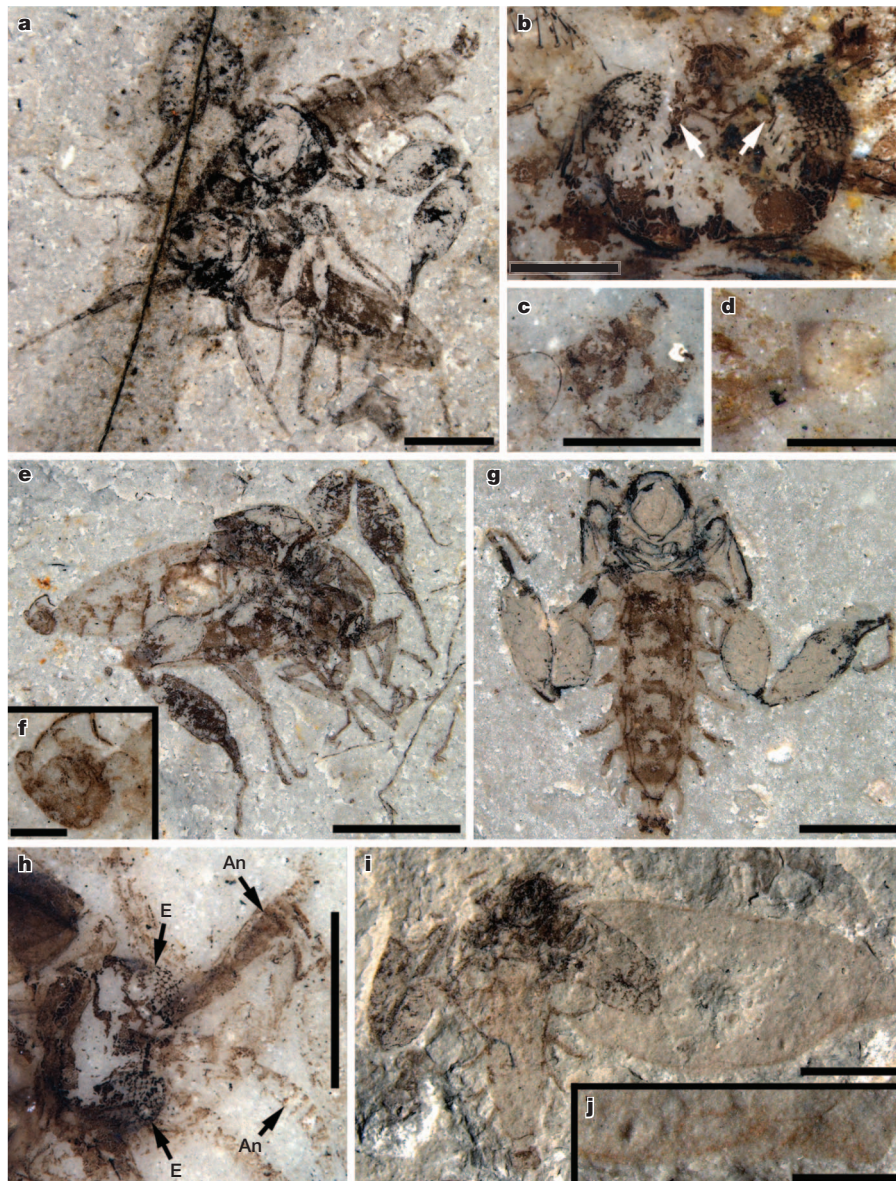


**Figure 1** | *Strashila daohugouensis* sp. nov. from the Middle Jurassic epoch of Daohugou, China. **a**, Mating pair, holotype (NIGP155020, male) and allotype (NIGP156171, female). **b**, Enlargement of the head of the male in **a**, white arrows indicate ocelli. **c**, Enlargement of the male genitalia in **a**. **d**, Enlargement of the female terminalia in **a**. **e**, Another mating pair, male

(NIGP155018a) and female (NIGP156170b). **f**, Enlargement of the male genitalia in **e**. **g**, Large male specimen (NIGP155017). **h**, Enlargement of the female head in **e**. An, antenna; E, eye. **i**, A male (NIGP155024) with wing. **j**, Enlargement of the marginal setae in **i**. Scale bars, 2 mm (**a**, **e**, **g**, **i**), 500 μm (**b**–**d**), 200 μm (**f**) and 1 mm (**j**).

few simple veins (Supplementary Fig. 5b, c) and closely resemble those of recent *Nymphomyia walkeri* in this respect<sup>15</sup>. The broadly separated coxae, a feature that is considered to be consistent with the hypothesis of ectoparasitism, is also found in species with an aquatic habit and

therefore cannot alone support attribution of the fossils with the former life-history scenario. The basitarsi of the fore and mid legs were armed with a row of small denticles (Supplementary Figs 1f, 2b, g, i and 4d), and were probably used for grasping. The strongly curved and sharply



**Figure 2** | *Vosila sinensis* from the Middle Jurassic epoch of Daohugou, China. **a**, Complete male (NIGP155026). **b**, Nearly complete male (NIGP155021a). **c**, Enlargement of the male genitalia in **b**. **d**, Enlargement of

the dorsoventrally compressed gills in **b**. **e**, Enlargement of the laterally compressed gills in **b**. Scale bars, 2 mm (**a**, **b**), 1 mm (**d**, **e**) and 500 μm (**c**).

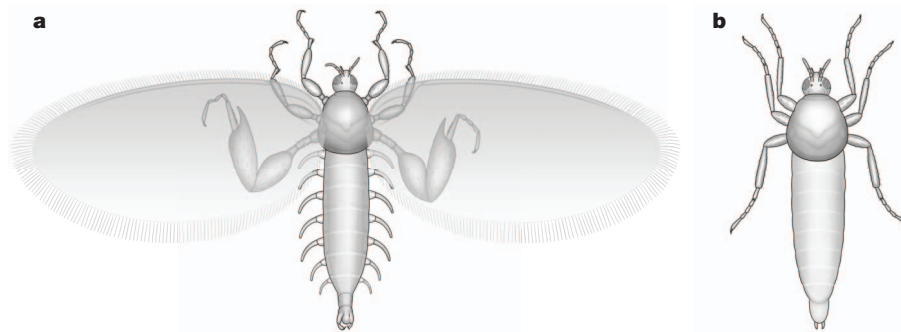


**Figure 3** | *Strashila daohugouensis* sp. nov. from the Middle Jurassic epoch of Daohugou, China. **a**, Reconstruction of the male. **b**, Reconstruction of the wing-shed female.

pointed pretarsal claws (Supplementary Figs 1g, 2b and 4d, e) correspond to adaptations for anchoring to fixed objects in the water column<sup>16</sup>. The male's swollen metafemur and metatibia, and its strong pincers (Figs 1a, e, g and 3a, and Supplementary Figs 2a, d, f, j, 3a, f, g and 5a), are sexually dimorphic as females have otherwise normal dipteran hind legs (Figs 1a, e and 3b and Supplementary Fig. 3a, f), and male pincers were used in either male–male competition or for holding the female during mating (Figs 1a, e and 4, and Supplementary Figs 3a, f, g and 7a), similar to some modern male oedemerid beetles<sup>17</sup>. The swollen legs also parallel the swollen tarsi of modern male dance flies (Empididae), and would have been used as visual signals to attract females<sup>18</sup>.

The most puzzling features of the strashilids are the pairs of lobes on the sides of the abdomen in males, which are inconsistent with terrestrial locomotion or ectoparasitism. Previous authors considered the function of these structures to be obscure<sup>1,2</sup> or thought that they were elaborate versions of the eversible abdominal glands of higher mecopterans<sup>4</sup>. These structures probably do not correspond to prolegs as in some dipteran larvae (for example, Nymphomyiidae and Empididae) because of their lateral insertion and absence of apical crochets. *Vosila* and *Strashila* display homologous abdominal extensions. *Vosila* have two series of lateral filamentous projections (Fig. 2a, b, d, e and Supplementary Fig. 4a, c), similar to those of *Hydrochara affinis*<sup>19</sup>, which correspond to gills typically used for aquatic respiration, such as in mayflies, many beetles, dobsonflies, caddisflies and some caterpillars<sup>20,21</sup>. In contrast, the tube-like extensions of *Strashila* (Figs 1g and 3a, and Supplementary Figs 2a, d, f, h, j, 3d, 5d and 6a–c) are comparable to those on segments V and VI of some male nymphomyiids, possibly also for grasping females<sup>22,23</sup>. Some Daohugou winged adult Ephemeroptera also have paired, slender, filamentous, lateral

abdominal gills (Supplementary Fig. 6a–g). Although similar gills occur in a few modern Ephemeroptera and Plecoptera, there is no record of adult Holometabola having well-developed and functional filamentous gills<sup>24,25</sup>. The presence of such gills indicates a continuation of larval structures into the adult stadium, representing a unique form of paedomorphism associated with this major biological function. To our knowledge, the very well preserved male NIGP155017 is the first strashilid fossil to show an abdominal tracheal system connected to spiracles (Fig. 1g and Supplementary Fig. 6a, b) that is similar to those of the aquatic larvae of the beetles *Hydrophilus*, *Hydrochara* and *Berosus*<sup>19</sup>, and the dobsonfly *Neuronemus*, in which the spiracles serve a respiratory function<sup>26</sup>.

These structures provide evidence that strashilids share several potential apomorphies with modern nymphomyiid flies, including the finer details of the antennae, ocelli, wings, terminalia and legs (see Supplementary Information for details). Their reduced mouthparts and wings are inefficient for feeding and active flight, respectively, and indicate an ephemeral life history, akin to modern nymphomyiid taxa. Similar to modern nymphomyiids, adult Strashilidae probably mated soon after emergence, shed their wings, crawled beneath the water, mated, and in some cases died in copula<sup>15,16,22,27</sup>, with the superposing male grasping the female below, thereby explaining the discoveries of females grasped by males, and both without their wings (Fig. 4).

The discovery of fossilized females and of several interesting characteristics of the wings resolves one of the long-standing questions of insect palaeontology and evolution—namely the biology and functional morphology of the enigmatic Strashilidae. We conclude that the Strashilidae were a highly specialized dipteran clade related to Nymphomyiidae, with an aquatic or amphibious life history. These new discoveries also aid our understanding of modern nymphomyiid



**Figure 4** | Ecological reconstruction of *Strashila daohugouensis* sp. nov. from the Middle Jurassic epoch of Daohugou, China. Two males are shown flying. A female with wings is shown crawling on land (top right), and two males and a female (top left) are shown searching for mates in water, having

shed their wings (isolated wings are also shown floating on the water). The illustration of the mating pair (front) shows how the male may have grasped the female.



morphology, suggesting that the abdominal extensions in males of some species may be a pedomorphic remnant, and emphasizing a unique developmental syndrome for future evolutionary developmental investigation. The Strashilidae were not parasitic. Ectoparasites of early mammals or feathered dinosaurs, principally fleas, were indeed present in the Daohugou fauna<sup>10</sup>, but the strashilids were not one of them.

## METHODS SUMMARY

The specimens are housed at the Nanjing Institute of Geology and Palaeontology, and were prepared using a sharp knife. Photographs were taken using a Zeiss Discovery V20 microscope system, with specimens moistened with 70% alcohol (Figs 1b–d, h and 2a, c–e, and Supplementary Figs 2b, c, e, g, i, j, 3a–f, h, i and 4b–e, g), and line drawings were made using a camera lucida on a binocular Olympus SZX7. Reconstructions were prepared with Corel Painter and Adobe Photoshop software. Finally, some specimens were examined with a LEO1530VP field emission scanning electron microscope.

Received 31 October 2012; accepted 10 January 2013.

Published online 20 February 2013.

- Rasnitsyn, A. P. *Strashila incredibilis*, a new enigmatic mecopteroid insect with possible siphonapteran affinities from the Upper Jurassic of Siberia. *Psyche (Stuttg.)* **99**, 323–334 (1992).
- Vršanský, P., Ren, D. & Shih, C. Nakridletia ord. n. – enigmatic insect parasites support sociality and endothermy of pterosaurs. *AMBA Projekty* **8**, 1–16 (2010).
- Labandeira, C. in *The Fossil Record of Predation* (eds Kowalewski, M. & Kelley, P. H.) 211–249 Paleontological Society Special Papers, Vol. 8 (Paleontological Society, Yale Printing Service, 2002).
- Grimaldi, D. A. & Engel, M. S. *Evolution of the Insects* (Cambridge Univ. Press, 2005).
- Gao, T.-P., Shih, C., Xu, X., Wang, S. & Ren, D. Mid-Mesozoic flea-like ectoparasites of feathered or haired vertebrates. *Curr. Biol.* **22**, 732–735 (2012).
- Poinar, G. O. Jr. Palaeontology: the 165-million-year itch. *Curr. Biol.* **22**, R278–R280 (2012).
- Wang, X., Zhou, Z., Zhang, F. & Xu, X. A nearly completely articulated rhamphorhynchoid pterosaur with exceptionally well-preserved wing membranes and 'hairs' from Inner Mongolia, northeast China. *Chin. Sci. Bull.* **47**, 226–230 (2002).
- Zhang, F., Zhou, Z., Xu, X., Wang, X. & Sullivan, C. A bizarre Jurassic maniraptoran from China with elongate ribbon-like feathers. *Nature* **455**, 1105–1108 (2008).
- Huang, D. Diversity of Jurassic insects—exemplified by Daohugou fauna. *Front. Earth Sci.* **17** (special issue), 149–150 (2010).
- Huang, D., Engel, M. S., Cai, C., Wu, H. & Nel, A. Diverse transitional giant fleas from the Mesozoic era of China. *Nature* **483**, 201–204 (2012).
- Wood, D. M. in *Proc. 2nd Int. Congress Dipterol* (eds Weismann, L., Országh, I. & Pont, A. C.) 255–284 (SPB Academic Publishing, 1991).
- Crampton, G. C. The genitalia of male Diptera and Mecoptera compared with those of related insects, from the standpoint of phylogeny. *Trans. Am. Entomol. Soc.* **48**, 207–225 (1922).
- Willmann, R. Das exoskelett der männlichen genitalien der Mecoptera (Insecta). 1. Morphologie. *Zeit. Zool. Syst. Evolutionsf.* **19**, 96–150 (1981).
- Courtney, G. W. Biosystematics of the Nymphomyiidae (Insecta: Diptera): life history, morphology, and phylogenetic relationships. *Smith. Cont. Zool. No. 550* (Smithsonian Institution, 1994).
- Kevan, D. K., McE. & Cutten-Ali-Khan, F. E. A. Canadian Nymphomyiidae (Diptera). *Can. J. Zool.* **53**, 853–866 (1975).
- Kevan, D. K., McE. & Cutten, F. E. A. in *Manual of Nearctic Diptera* Vol. 1 (eds McAlpine, J. F. et al.) 203–207 (Research Branch, Agricultural Canada Monograph, 1981).
- Furth, D. G. & Suzuki, K. The metatibial extensor and flexor tendons in Coleoptera. *Syst. Entomol.* **15**, 443–448 (1990).
- Daugeron, C., Plant, A., Winkler, I., Stark, A. & Baylac, M. Extreme male leg polymorphic asymmetry in a new empidine dance fly (Diptera: Empididae). *Biol. Lett.* **7**, 11–14 (2011).
- Richmond, E. A. Studies on the biology of the aquatic Hydrophilidae. *Bull. Am. Mus. Nat. Hist.* **42**, 1–94 (1920).
- Barclay, A., Portman, R. W. & Hill, P. S. M. Tracheal gills of the dobsonfly larvae, or hellgrammite *Corydalus cornutus* L. (Megaloptera: Corydalidae). *J. Kans. Entomol. Soc.* **78**, 181–185 (2005).
- Speidel, W. Studies on the phylogeny of the Acentropinae (Lepidoptera, Crambidae). *Mém. Soc. R. Belge Entomol.* **38**, 25–30 (1998).
- Ide, F. P. A fly of the archaic family Nymphomyiidae (Diptera) from North America. *Can. Entomologist* **97**, 496–507 (1965).
- Wagner, R., Hoffeins, C. & Hoffeins, H. W. A fossil nymphomyiid (Diptera) from the Baltic and Bitterfeld amber. *Syst. Entomol.* **25**, 115–120 (2000).
- Stys, P. & Soldan, T. Retention of tracheal gills in adult Ephemeroptera and other insects. *Acta Univ. Carol. (Biol.)* **1978**, 409–435 (1980).
- Marden, J. H. & Thomas, M. A. Rowing locomotion by a stonefly that possesses the ancestral pterygote condition of co-occurring wings and abdominal gills. *Biol. J. Linn. Soc.* **79**, 341–349 (2003).
- Cao, C.-Q. et al. Respiratory system and respiratory behaviors of the larva of *Neoneuromus ignobilis*. *Chin. J. Appl. Entomol.* **48**, 392–396 (2011).
- Cutten, F. E. A. & Kevan, D. K. McE. The Nymphomyiidae (Diptera), with special reference to *Palaeodipteron walkeri* Ide and its larva in Quebec, and a description of a new genus and species from India. *Can. J. Zool.* **48**, 1–24 (1970).

Supplementary Information is available in the online version of the paper.

**Acknowledgements** We are grateful to C. C. Labandeira for suggestions; A. P. Rasnitsyn for early discussions; and J. Sun for reconstructions. Financial support was provided by the National Basic Research Program of China (2012CB821903), the National Natural Science Foundation of China (9114201 and J1210006), the Outstanding Youth Foundation of Jiangsu Province (BK2012049), the Chinese Academy of Sciences (KZCX2-YW-QN104), and the US National Science Foundation (DEB-0542909).

**Author Contributions** D.H., A.N., C.C., Q.L. and M.S.E. participated in morphological studies, D.H. designed the program, D.H., A.N. and M.S.E. prepared the manuscript.

**Author Information** The LSID urn:lsid:zoobank.org:act:85DDCF37-C0D1-45C0-80B3-463E9D19ECE1 has been deposited in ZooBank. Reprints and permissions information is available at [www.nature.com/reprints](http://www.nature.com/reprints). The authors declare no competing financial interests. Readers are welcome to comment on the online version of the paper. Correspondence and requests for materials should be addressed to D.H. (dyhuang@nigpas.ac.cn).



# NFIB is a governor of epithelial–melanocyte stem cell behaviour in a shared niche

Chiung-Ying Chang<sup>1</sup>, H. Amalia Pasoli<sup>1</sup>, Eugenia G. Giannopoulou<sup>2</sup>, Géraldine Guasch<sup>3</sup>, Richard M. Gronostajski<sup>4</sup>, Olivier Elemento<sup>2</sup> & Elaine Fuchs<sup>1</sup>

Adult stem cells reside in specialized niches where they receive environmental cues to maintain tissue homeostasis. In mammals, the stem cell niche within hair follicles is home to epithelial hair follicle stem cells and melanocyte stem cells, which sustain cyclical bouts of hair regeneration and pigmentation<sup>1–4</sup>. To generate pigmented hairs, synchrony is achieved such that upon initiation of a new hair cycle, stem cells of each type activate lineage commitment<sup>2,5</sup>. Dissecting the inter-stem-cell crosstalk governing this intricate coordination has been difficult, because mutations affecting one lineage often affect the other. Here we identify transcription factor NFIB as an unanticipated coordinator of stem cell behaviour. Hair follicle stem-cell-specific conditional targeting of *Nfib* in mice uncouples stem cell synchrony. Remarkably, this happens not by perturbing hair cycle and follicle architecture, but rather by promoting melanocyte stem cell proliferation and differentiation. The early production of melanin is restricted to melanocyte stem cells at the niche base. Melanocyte stem cells more distant from the dermal papilla are unscathed, thereby preventing hair greying typical of melanocyte stem cell differentiation mutants. Furthermore, we pinpoint KIT-ligand as a dermal papilla signal promoting melanocyte stem cell differentiation. Additionally, through chromatin-immunoprecipitation with high-throughput-sequencing and transcriptional profiling, we identify endothelin 2 (*Edn2*) as an NFIB target aberrantly activated in NFIB-deficient hair follicle stem cells. Ectopically induced *Edn2* recapitulates NFIB-deficient phenotypes in wild-type mice. Conversely, endothelin receptor antagonists and/or KIT blocking antibodies prevent precocious melanocyte stem cell differentiation in the NFIB-deficient niche. Our findings reveal how melanocyte and hair follicle stem cell behaviours maintain reliance upon cooperative factors within the niche, and how this can be uncoupled in injury, stress and disease states.

Hair follicle stem cells and melanocyte stem cells remain quiescent within their hair follicle niche for weeks, a period known as telogen phase. With each new hair cycle, these two stem cell populations are coordinately activated. This happens when inhibitory signals are counteracted by activating cues that accumulate from Wnt and BMP/TGF- $\beta$  (bone morphogenetic protein/transforming growth factor  $\beta$ ) crosstalk with dermal papilla at the niche base<sup>6–8</sup>. Synchronized activity continues throughout the hair cycle. During the growth phase (anagen), melanocytes at the base of the mature hair follicle ('hair bulb') produce and transfer pigment to neighbouring committed hair follicle stem cell progeny ('matrix') as they differentiate into hair cells<sup>2,5</sup>. When destruction (catagen) ensues, melanocytes and matrix cells in the hair bulb apoptose, and the dermal papilla (enveloped by the hair bulb during anagen) retracts upward, returning the follicle to telogen. As anagen begins and a new hair bulb emerges, both hair follicle stem cells and melanocyte stem cells contain nuclear  $\beta$ -catenin, implicating canonical Wnt signalling in stem cell coordination<sup>6,8</sup>. These and several

other insights<sup>7,9,10</sup> suggest how local environmental signals synchronize proliferation and lineage progression of stem cells during hair cycling.

Uncoupling melanocyte and epithelial stem cell behaviours occurs under transient conditions, that is, in response to ultraviolet radiation, and in various disease and injury states<sup>11,12</sup>. Given the impact of Wnt and other signals on stem cells and their lineages, and current dogma that matrix cells must differentiate for melanocyte pigment to transfer<sup>10</sup>, the mechanisms by which melanocyte stem cells can be selectively mobilized from their niche without otherwise disrupting the normal hair cycle remains unknown.

Our venture into this study was prompted by our finding that relative to progeny, hair follicle stem cells express elevated nuclear factor I/B (NFIB)<sup>1</sup>. NFIB is required for lung and brain development and is often amplified and/or found at oncogenic chromosomal breakpoints in epithelial cancers<sup>13–15</sup>. NFIB was first detected in epidermis at embryonic day 14.5 (E14.5), concomitant with upregulation of established skin progenitors. Expression intensified as hair follicle stem cells emerged (Fig. 1a and Supplementary Fig. 1a–c).

In adult hair follicles, NFIB co-localized with hair follicle stem cells, whose niche in telogen is subdivided into an upper 'bulge' compartment and lower 'hair germ' (or secondary hair germ) adjacent to dermal papilla (Supplementary Fig. 1d). During anagen, NFIB-positive cells were also found within the upper outer root sheath (ORS), which in early catagen will form the new niche (bulge and hair germ) for the next hair cycle<sup>16</sup> (Fig. 1b). NFIB waned in transit-amplifying (TA) matrix progenitors (Fig. 1b and Supplementary Fig. 1e). NFIB was not detected in melanocyte stem cells marked by dopachrome tautomerase (DCT) and tyrosine kinase receptor KIT in the upper ORS and bulge/hair germ, nor in differentiated melanocytes within the hair bulb<sup>17</sup> (Fig. 1b, c). Overall, both inside and outside the niche, hair follicle stem cells and melanocyte stem cells showed synchronized behaviours but distinct expression patterns.

To address the function of NFIB, we conditionally induced *Nfib* ablation (cKO) in mouse hair follicle stem cells by using *Sox9-CreER* and *K15-CrePGR*. Unless specified, data are from *Sox9-CreER* mice, but both gave similar results. NFIB immunofluorescence verified that *Nfib* was efficiently targeted in hair follicle stem cells, consistent with *K15* and *Sox9* expression primarily in ORS/bulge/hair germ; furthermore, when *Rosa26<sup>fllox</sup>STOP<sup>fllox</sup>YFP* (*RosaYFP*; yellow fluorescent protein (YFP)) was used to mark and trace the progeny of Cre-induced cells, only hair follicle stem cells and their subsequent progeny, and not KIT<sup>+</sup> melanocytes or dermal cells, were fluorescently labelled<sup>18</sup> (Figs 1d, e and Supplementary Fig. 2a–c). Despite efficient targeting, however, *Nfib*-cKO hair coats and hair cycling appeared normal (Fig. 1f, g).

Equally surprising to the absence of hair follicle stem cell lineage defects were melanocyte lineage abnormalities. Fontana–Masson staining revealed atypical melanogenic cells at the niche base of telogen hair follicles (Fig. 2a and Supplementary Fig. 2d). Immunostaining

<sup>1</sup>Howard Hughes Medical Institute, Laboratory of Mammalian Cell Biology and Development, The Rockefeller University, New York, New York 10065, USA. <sup>2</sup>HRH Prince Alwaleed Bin Talal Bin Abdulaziz Alsaud Institute for Computational Biomedicine, Department of Physiology and Biophysics, Weill Cornell Medical College, Cornell University, New York, New York 10021, USA. <sup>3</sup>Division of Developmental Biology, Cincinnati Children's Hospital Medical Center, University of Cincinnati Medical School, Cincinnati, Ohio 45229, USA. <sup>4</sup>Department of Biochemistry, Developmental Genomics Group, NYS Center of Excellence in Bioinformatics and Life Sciences, State University of New York at Buffalo, Buffalo, New York 14203, USA.

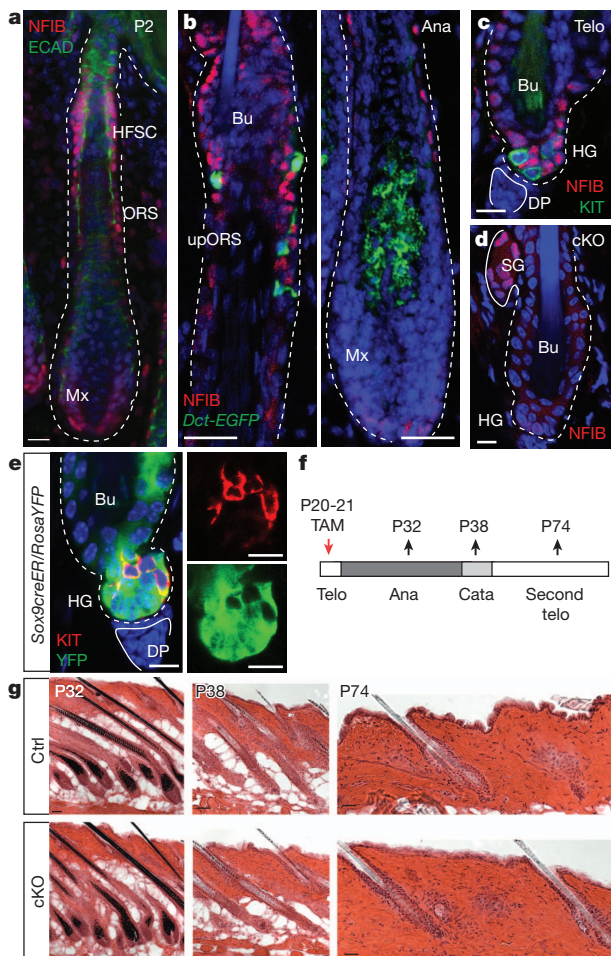


**Figure 1 | Conditional *Nfib* targeting in hair follicle stem cells does not perturb hair cycle or follicle architecture.** **a–c**, Immunofluorescence. **a**, Enrichment of nuclear NFIB in hair follicle stem cells and ORS of developing hair follicles. ECAD, E-cadherin; HFSC, hair follicle stem cells; Mx, matrix. **b**, NFIB in anagen hair follicles from adult *Dct-EGFP* BAC transgenic mice. NFIB is not seen in EGFP<sup>+</sup> melanocytes. Ana, anagen; Bu, bulge; upORS, upper ORS. **c**, Absence of NFIB in KIT<sup>+</sup> melanocyte stem cells of telogen hair follicles. DP, dermal papilla; HG, hair germ; Telo, telogen. **d–f**, Tamoxifen (TAM) was administered to *Sox9-CreER/Nfib<sup>fl/fl</sup>/RosaYFP*-cKO mice and analysed at various times thereafter. **d**, Note hair follicle stem-cell-specific *Nfib* targeting in bulge and hair germ. SG, sebaceous gland. **e**, Note YFP reporter activity in hair follicle stem cells but not in KIT<sup>+</sup> melanocyte stem cells. **f**, Schematic. Cata, catagen; P20, postnatal day 20. **g**, Haematoxylin- and eosin-stained back skins reveal normal hair cycle and follicle architecture upon NFIB loss. Ctrl, control. Scale bars: 50  $\mu$ m (P32, P38 in g); 25  $\mu$ m (a, b, P74 in g); 10  $\mu$ m (c–e).

showed increases in melanocytes (KIT<sup>+</sup>DCT<sup>+</sup>) throughout hair germ and bulge, and ectopic presence of differentiated melanocytes (KIT<sup>+</sup>DCT<sup>+</sup>TYRP1<sup>+</sup>MITF<sup>+</sup>TYR<sup>+</sup>) within hair germ (Fig. 2b, c and Supplementary Fig. 3a–c).

A priori, ectopic differentiated melanocytes in cKO hair germs might reflect hair bulb melanocytes that somehow escaped apoptosis during catagen. Alternatively, they could arise from precocious differentiation of niche melanocyte stem cells. To distinguish between these possibilities, we analysed melanocyte behaviour at each hair cycle stage (Fig. 2d and Supplementary Fig. 4). During anagen, TYRP1<sup>+</sup> cells dropped to wild-type levels in the bulge/upper ORS. As dermal papilla returned to the niche during late catagen, TYRP1<sup>+</sup> numbers again soared, persisting until the next anagen. By contrast, control stem cell niches displayed much more modest melanocyte stem cell differentiation, which occurred at telogen→anagen rather than catagen→telogen. The difference in this timing was >3 weeks for young adult mice.

Accompanying the disappearance of differentiated melanocytes within the anagen *Nfib*-cKO bulge/upper ORS, was their appearance

in the hair bulb (upper matrix) (Fig. 2e and Supplementary Fig. 4). Within the bulb, pigment transfer to differentiating hair cell recipients seemed normal. Additionally, at the start of catagen, TYRP1<sup>+</sup> melanocytes underwent apoptosis and were eliminated by mid-catagen in both control and cKO hair bulbs. In contrast to differentiated melanocytes, TYRP1<sup>+</sup> melanocyte stem cells remained elevated throughout cKO hair cycles, where they resided in the bulge/upper ORS. The only time at which melanocyte stem cells dropped transiently was during late catagen/telogen, when melanocyte stem cells near dermal papilla precociously differentiated.

These results pinpointed defects to the stem cell niche; furthermore, dermal papilla proximity seemed to affect primarily the uncoupling and premature differentiation of melanocyte stem cells rather than self-renewal (Fig. 2f). In addition, melanocyte stem cells in anagen stem-cell niches were still negative for TYRP1 even in 1-year-old *Nfib*-cKO hair follicles (Fig. 2d), indicating that ectopic differentiated melanocytes from telogen do not accumulate within the niche over hair cycles.

To test melanocyte stem cell activity further, we mated *Nfib*-cKO to *Dct-EGFP* mice and isolated EGFP<sup>+</sup> bulge cells from telogen hair follicles. Melanocyte differentiation markers, for example, *Kit*, *Mitf*, *Tyrb1*, *Tyr* and *Sox10*, were upregulated in EGFP<sup>+</sup> cells, whereas genes expressed by both melanocyte stem cells and differentiated melanocytes showed no change (Supplementary Fig. 3d). Finally, hair coats of ageing cKO mice were still pigmented, and melanocyte stem cell levels were sustained (Fig. 2e, g and Supplementary Fig. 3e). These data provided compelling evidence that NFIB-deficiency in hair follicle stem cells affects the timing of melanocyte differentiation without compromising melanocyte stem cell biology and/or function, which results in hair greying<sup>6,7,9,11</sup>.

Ultrastructural analysis unveiled new defects within the stem cell niche (Fig. 3a and Supplementary Fig. 5). Niche melanocytes closest to dermal papilla had pigment granules and immature melanosomes. Surprisingly, however, adjacent hair germ cells also had pigment granules. Their epithelial identity was shown by keratin filaments, desmosomes and hemidesmosomes. Although poorly understood, hair cell uptake of pigment from differentiated melanocytes is thought to depend on FOXN1<sup>10</sup>, expressed by differentiating matrix cells but not by hair follicle stem cells<sup>19</sup>.

Inappropriate accumulation of pigment proved calamitous for quiescent hair follicle stem cells in the telogen hair germ: it elicited their apoptotic death, typified by condensed chromatin, mitochondrial destruction, and cleaved caspase-3-immunolabelling (Fig. 3a, b and Supplementary Fig. 6). In addition, unaffected neighbouring K5-positive hair germ cells proliferated (Fig. 3c, d and Supplementary Fig. 6). Although hair germ proliferation is a normal sign of telogen→anagen<sup>8</sup>, precocious hair cycle entry was not observed.

Apoptotic and proliferative defects within the niche disappeared in anagen (Fig. 3b, d), concomitant with movement of differentiated melanocytes from niche to hair bulb (Fig. 2d–f). These results indicate that apoptosis and hyperproliferation of *Nfib*-null hair follicle stem cells depend upon precocious differentiation of neighbouring melanocyte stem cells. They also indicate that when differentiated melanocytes inappropriately bequeath pigment to hair follicle stem cells rather than their customary differentiated progeny (hair cells), pigment-laden hair follicle stem cells are unable to cope, whereas healthy hair follicle stem cell neighbours proliferate to restock the niche.

Notably, in older *Nfib*-cKO mice, black-pigmented dermal cells swarmed hair follicles and were even visible from the skin surface (Supplementary Fig. 7). Although dermal melanoblasts exist in certain skin regions such as the ear, and can differentiate under some conditions<sup>20</sup>, few TYRP1<sup>+</sup> melanocytes were found in cKO dermis. Rather, a number of cells encompassing this pigment were Mac1<sup>+</sup> with features of macrophages. Irrespective of whether pigment-laden vacuoles within dermal cells reflected engulfment of dying, pigmented cells, or direct pigment transfer from melanocytes, these defects made the normalcy of the hair coat of ageing cKO mice all the more remarkable.



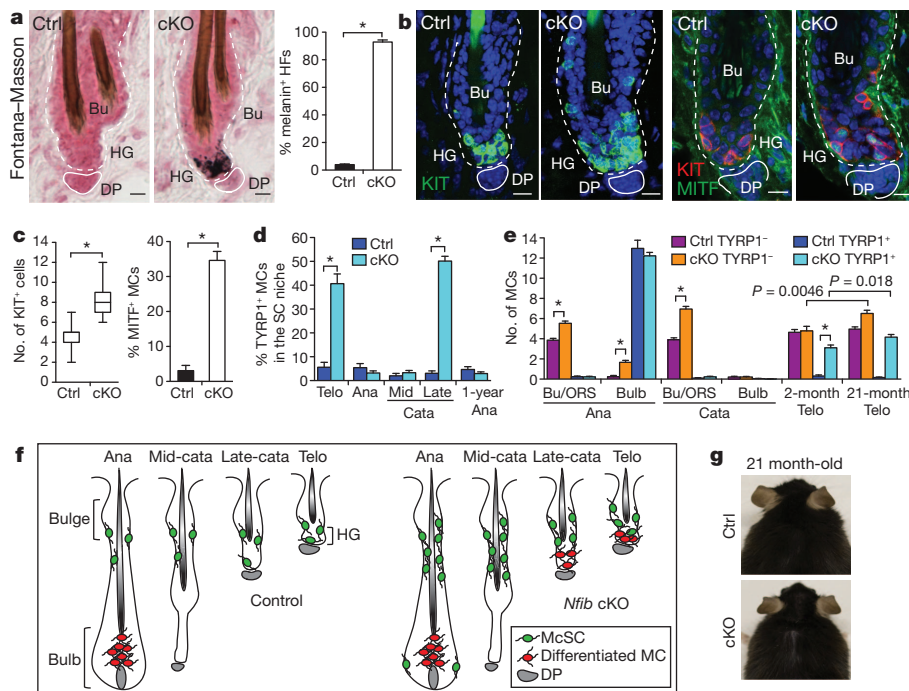


**Figure 2 | NFIB loss enhances melanocyte stem-cell self-renewal and perturbs melanocyte stem-cell activity in the hair follicle stem cell niche.** **a**, Ectopic pigmentation in telogen-phase cKO hair germ as detected by Fontana–Masson melanin staining and quantifications ( $n = 3$  mice per experiment,  $>40$  hair follicles per mouse). **b–e**, Immunofluorescence and quantifications. **b, c**, Increased melanocytes and ectopic differentiation in telogen cKO hair follicles (30–50 hair follicles; 2 mice per experiment). KIT marks melanocyte stem cells and differentiated melanocytes; MITF and TYRP1 are differentiation-specific melanocyte markers. MCs, melanocytes. **d**, Precocious melanocyte differentiation begins in the niche at late catagen. Quantifications of TYRP1<sup>+</sup> among KIT<sup>+</sup> or Dct-EGFP<sup>+</sup> melanocytes ( $>40$  hair follicles; 2 mice per experiment). Analyses shown start at second telogen. SC, stem cell. **e**, Quantifications of melanocyte stem cells (TYRP1<sup>+</sup>) and differentiated melanocytes (TYRP1<sup>+</sup>) at different hair follicle stages ( $>30$  hair follicles; 2 mice per experiment). **f**, Summary of data. McSC, melanocyte stem cell; MC, melanocyte. **g**, Lack of hair greying in ageing *Nfib*-cKO mice. Scale bars, 10  $\mu$ m (**a, b**). \* $P < 0.001$ . Error bars indicate s.e.m.

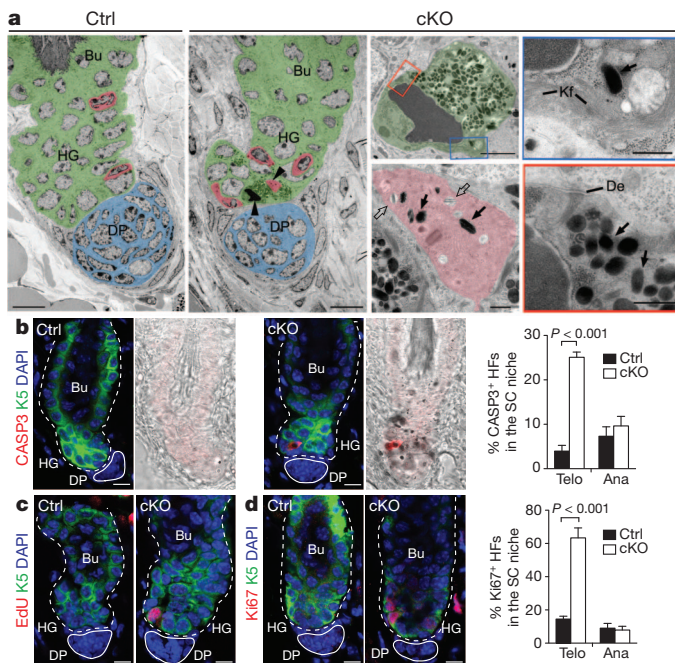


**Figure 3 | Premature transfer of pigment promotes apoptotic cell death in hair follicle stem cells in the NFIB-deficient niche.** **a**, Hair follicle ultrastructure. Pseudo-colouring highlights distinct stem cell niche cell types: green, hair follicle stem cell; red, melanocyte; blue, dermal papilla. Arrowheads mark cells shown at higher magnification. Open and solid arrows denote immature and mature melanosomes, respectively. Note pigment-laden apoptotic hair follicle stem cells whose boxed regions at higher magnification reveal condensed chromatin, degenerating mitochondrion, keratin filaments (Kf), desmosomes (De) and melanosomes. **b**, Activated caspase 3 antibody marks K5<sup>+</sup> apoptotic cKO hair follicle stem cells, seen in telogen but not anagen ( $n = 3$  mice;  $>30$  hair follicles per mouse). HFSCs, hair follicle stem cells; SC, stem cell. **c, d**, Increased hair follicle stem cell proliferation in telogen but not anagen *Nfib*-cKO hair follicles. Assessment was by EdU (5-ethynyl-2'-deoxyuridine) incorporation (administered twice, 24 h before analysis) and Ki67 immunostaining ( $n = 3$  mice;  $>30$  hair follicles per mouse). Scale bars: 10  $\mu$ m (low magnifications in **a** and **b–d**); 2  $\mu$ m (apoptotic hair follicle stem cell in **a**); 0.5  $\mu$ m (cytoplasmic segments and melanocyte in **a**). Error bars indicate s.e.m.

To dissect the molecular miscommunication between hair follicle stem cells and melanocyte stem cells in the niche, we used high throughput RNA-seq to transcriptionally profile bulge and hair germ hair follicle stem cells. Fluorescence activated cell sorting (FACS) of skins from *K15-CrePGR/RosaYFP/Nfib<sup>fl/fl</sup>* (cKO) and *Nfib<sup>fl/+</sup>* (het) mice were used for purifying CD34<sup>+</sup>-bulge and CD34<sup>+</sup>-hair germ cells (both YFP<sup>+</sup>Scal<sup>+</sup> $\alpha$ 6<sup>high</sup>CD200<sup>+</sup>) (Supplementary Figs 2a and 8a).

Of 800–1,000 messenger RNAs changed by  $\geq$  twofold in NFIB-deficient hair follicle stem cells relative to control, 145 were upregulated and 99 were downregulated (Supplementary Figs 8b and 9 and Supplementary Table 1). Quantitative PCR (qPCR) of independently purified samples validated the differences (Supplementary Fig. 8c, d). Notably absent from the list were *Foxn1*, *Fgf2*, *Nog*, *Egfr*, *F2r1* and derivatives of *Pomc*—all previously implicated in melanocyte differentiation and/or pigment transfer<sup>10,12,21</sup>. Also absent were genes involved in BMP/TGF- $\beta$  signalling, known to function in stem cell niche quiescence. Similarly, NFIB loss did not seem to affect canonical Wnt signalling, a key stimulus for stem cell activity and fate commitment: Wnt-sensitive target gene *Axin2* was unchanged in NFIB-deficient hair follicle stem cells, and upregulated genes included both negative and positive Wnt regulators.

These results were consistent with the normal hair cycle displayed by *Nfib*-cKO skin (Fig. 1g). Had any of these signalling pathways been perturbed, both stem cell populations—not just melanocyte stem cells—should have been affected. Moreover, hair follicle stem cells from mice genetically defective for Wnt, BMP and TGF- $\beta$  signalling still expressed NFIB protein and mRNA (Supplementary Fig. 10a, b). Thus at least within the quiescent stem cell niche, these signalling pathways seemed to be refractory to loss of NFIB, and NFIB seemed to be refractory to these signalling pathways.

To identify direct NFIB target genes, we performed chromatin-immunoprecipitation with high-throughput-sequencing (ChIP-seq) analysis on 10–15 million bulge hair follicle stem cells FACS-purified from 15–20 mice<sup>19</sup>. Applying immunoprecipitation-grade NFIB antibody to chromatin, we identified 1,449 genes that were directly and reproducibly bound by NFIB (Fig. 4a and Supplementary Table 2). NFIB-bound genes included *Krt5* (Supplementary Fig. 11a). Intriguingly, like *Krt5* and its transcription factor-AP2 family regulators, NFIB was absent in most areas of *Trp63*-null skin (Supplementary Fig. 10c). Additionally, *Nfib* is bound by p63 (ref. 22) and harbours TFAP2 binding motifs (data not shown), suggesting possible connections to these early stem cell markers.



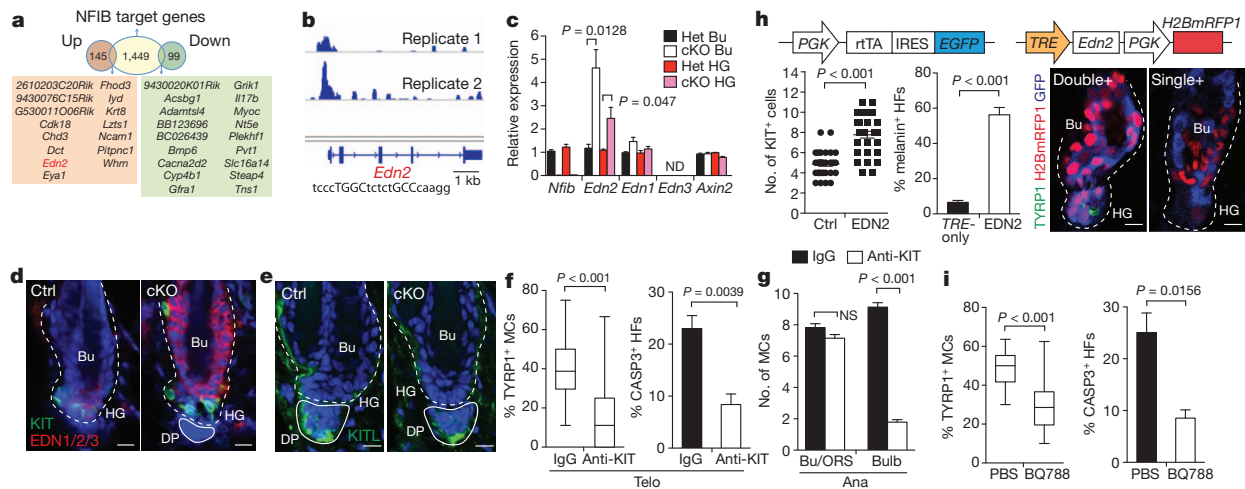


**Figure 4 | RNA-seq and ChIP-seq analyses identify *Edn2* as a direct NFIB-regulated gene mediating inter-stem cell crosstalk.** **a**, Identification of direct NFIB-regulated genes as those that bind NFIB (from ChIP-seq) and are up/downregulated in *Nfib*-cKO hair follicle stem cells (from RNA-seq). **b**, NFIB ChIP-seq profiles of *Edn2* promoter. NFIB palindromic-binding-sequence exists within the peak. **c**, qPCR on FACS-isolated populations confirm RNA-seq results (Het, normalizations to heterozygote values). **d**, Immunofluorescence shows ectopic endothelins in *Nfib*-cKO hair follicles. **e**, Immunofluorescence reveals KITL in dermal papilla. **f**, Reductions in TYR1<sup>+</sup> melanocytes (>60 hair follicles; 3 mice) and apoptosis ( $n = 4$  mice; >30 hair follicles per mouse) in cKO hair follicles after injecting anti-KIT blocking antibody (anti-KIT) during

catagen/telogen. IgG, control. **g**, Anti-KIT-mediated inhibition of KIT signalling during anagen (>45 hair follicles in two mice). **h**, Overhead schematic: lentiviral constructs. Quantifications show increased KIT<sup>+</sup> melanocytes (32 hair follicles; two mice per experiment) and melanin<sup>+</sup> hair follicles ( $n = 3$  mice; >60 hair follicles per mouse) upon EDN2 induction. Immunofluorescence shows TYR1<sup>+</sup> melanocyte differentiation in doubly- (*Edn2*) and not singly-transduced/uninfected (Ctrl) hair follicle stem cells. **i**, Reduced TYR1<sup>+</sup> melanocytes (>46 hair follicles in two mice) and apoptosis ( $n = 3$  mice; >25 hair follicles per mouse) in *Nfib*-cKO hair follicles after injection of EDNRB inhibitor BQ788. Scale bars: 10  $\mu$ m (**d**, **e**, **h**). ND, not determined; NS, not significant. Error bars indicate s.e.m.

NFIB peaks were enriched in  $\pm 2$  kilobases (kb; 12%) and 2–50 kb (29%) sequences proximal to gene transcription initiation sites (Supplementary Fig. 11b, c). A *de novo* motif search identified five sequences within these peaks (Supplementary Fig. 11d, e). Most common were TGGC<sup>A/T</sup> and <sup>A/T</sup>GCCA, which when combined, comprised a palindromic motif. Notably, NFIB protein self-dimerizes, and its preferred binding motif is a TTGGCANNNTGCCAA palindrome<sup>23</sup>. Moreover, in response to NFIB loss, 201 (~14%) NFIB target genes were differentially expressed relative to control hair follicle stem cells (Supplementary Fig. 12). Of these, 44% were upregulated whereas 56% were downregulated in NFIB-deficient hair follicle stem cells. NFIB's lack of apparent bias for hair follicle stem cell gene activation differed from the role of NFIC in cultured fibroblasts<sup>23</sup>.

Searching for candidates whose altered expression might enhance melanocyte stem cell proliferation and differentiation, we focused on the 33 NFIB-binding genes  $\geq$  twofold up- or downregulated in bulge and hair germ hair follicle stem cells when *Nfib* is ablated (Fig. 4a). Notable was the gene *Edn2*, encoding endothelin-2. Within the *Edn2* promoter was an NFIB-binding palindrome sequence containing an optimal spacer (Fig. 4b). In both ChIP-seq replicates, NFIB bound to this site.

Endothelins are secreted factors with the ability to mediate intercellular crosstalk. All three endothelins stimulate cultured melanocyte stem cells<sup>5</sup>. Although *Edn3* is required for neural crest migration and melanocyte specification during embryogenesis<sup>24</sup>, and *Edn1* has been implicated in Wnt-mediated melanocyte proliferation<sup>6</sup>, neither *Edn3* nor *Edn1* appeared on our list of hair follicle stem cell genes bound by NFIB. Moreover, as assessed by RNA-seq and qPCR, *Edn3* was not expressed in hair follicle stem cells, and *Edn1* showed low expression and little change upon NFIB loss (Fig. 4c and Supplementary Table 1). By contrast, at telogen $\rightarrow$ anagen, *Edn2* was transiently activated in wild-type hair follicle stem cells<sup>19</sup>, and in *Nfib*-null hair follicle stem cells, *Edn2* was upregulated more than twofold relative to controls. Pan anti-endothelin immunolabelling was also stronger in *Nfib*-null relative to control hair follicle stem cells (Fig. 4d). Finally, hair follicle stem cells express endothelial converting enzyme (ECE1) necessary to process/activate EDN2.

The *Edn2* changes were cell-autonomous, because *Edn2* mRNA was also upregulated in cultured *Nfib*-null keratinocytes (Supplementary

Fig. 13). Moreover, this difference depended upon NFIB, as it was rescued by expressing the main keratinocyte isoform, NFIB3. By contrast, even though KIT ligand (*Kitl*) mRNA seemed to be modestly induced in *Nfib*-null hair follicle stem cells (Supplementary Table 1), the levels were not influenced by NFIB3-rescue (Supplementary Fig. 13), nor did we observe NFIB binding to the *Kitl* promoter/enhancer in ChIP-seq analyses. Interestingly, however, whereas KITL was not detected in hair follicle stem cells, it was seen in dermal papilla<sup>17</sup> (Fig. 4e).

Together, these results indicated a model whereby *Edn2* induction by *Nfib*-null hair follicle stem cells enhances proliferation of neighbouring melanocyte stem cells and sensitizes them to precociously differentiate when they encounter KITL and possibly additional signals from dermal papilla. If true, then blocking KIT signalling should ameliorate precocious melanocyte stem cell differentiation in cKO hair follicles, whereas elevating EDN2 in wild-type hair follicle stem cells should generate phenotypic features of NFIB-deficiency.

We first tested this hypothesis by injecting a KIT-receptor-blocking antibody into the skins of cKO mice beginning in late catagen. By telogen, marked reductions were seen in TYR1<sup>+</sup> melanocytes and in activated-CASP3<sup>+</sup> hair follicle stem cells (Fig. 4f). Importantly and in agreement with previous findings<sup>17,25</sup>, KIT inhibition in anagen hair follicles only affected lineage-committed proliferation and differentiation: undifferentiated melanocyte stem cells remained elevated in the cKO niche (Fig. 4g and Supplementary Fig. 14).

We next induced EDN2 in wild-type adult skin by co-transducing E9.5 mouse embryos *in utero* with high-titre lentiviruses<sup>26</sup> harbouring: (1) a tetracycline-regulatable transactivator (*rtTA*) coupled in a bicistronic transcript to *EGFP*; and (2) *H2BmRFP1* and a tetracycline-inducible promoter driving either *Edn2* (*TRE-Edn2*) or nothing (*TRE-only*) (Fig. 4h). Following selective EDN2 induction (Supplementary Fig. 15), *rtTA/TRE-Edn2*-transduced hair follicle stem cell niches contained increased KIT<sup>+</sup> melanocytes, melanin<sup>+</sup> cells and TYR1<sup>+</sup> differentiated melanocytes (Fig. 4h). Notably, *de novo* melanogenesis was not detected in similarly transduced epidermis, indicating that EDN2's effects were confined to locations where pre-existing melanocyte stem cells reside (data not shown). Finally, premature melanocyte stem cell differentiation in *Nfib*-cKO niches

depended upon EDN2, because marked reductions in TYRP1<sup>+</sup> melanocytes and activated-CASP3<sup>+</sup> hair follicle stem cells were observed when an endothelin receptor inhibitor (BQ788) was injected intradermally into cKO skin from late-catagen (Fig. 4i).

In summary, our findings expose an unexpected gatekeeper, NFIB, which governs activity within the quiescent stem cell niche of hair follicles. Upregulation of a single NFIB target, *Edn2*, seemed to be sufficient to uncouple coordinated stem cell behaviour. In contrast to all known genetic pathways perturbing melanocyte stem cell function within hair follicles, precocious melanocyte differentiation and ensuing chaos was cyclical and did not compromise stem cell pools, hair pigmentation or growth, even in ageing animals. The mechanism underlying this unprecedented phenotype lends new importance to the two-tiered structure of the hair follicle stem cell niche, and to dermal papilla/KITL-independent and dependent steps in controlling the effects of EDN2.

Endothelin 2 has not been implicated hitherto in normal cutaneous melanocyte physiology. Moreover, whereas melanocyte specification during embryogenesis fails to occur without *Edn3* (ref. 27), melanogenesis is seemingly normal in *Edn1* knockout mice<sup>28</sup>. This has left it unclear as to whether endothelins function postnatally. Similarly to *Edn3*, elevating *Edn2* in epidermis did not promote melanogenesis<sup>20</sup>; however, our results show that when provided with the proper micro-environment and additional stimulatory signals, endothelins can influence adult melanocyte stem cells and their differentiation.

In closing, our findings add new understanding to how melanocyte stem cell and hair follicle stem cell behaviours maintain reliance upon cooperative factors within the niche. They also reveal how this communication might be selectively uncoupled in injury and disease states. Notably, *Edn2* is induced upon ultraviolet irradiation and other stress conditions associated with increased pigmentation<sup>29,30</sup>. Although beyond the scope of the present study, testing the possible role of NFIB in skin cancers, wound repair and stress responses merit investigation, as does removing possible redundancy from other NFI members expressed by hair follicle stem cells. In the future, it will be interesting to see the extent to which *Nfib* downregulation will tip the balance from coupled to uncoupled states in health and disease. Our studies here emphasize the importance of endothelins as important messengers to uncouple melanocyte and hair follicle stem cell synchrony.

## METHODS SUMMARY

*Nfib*<sup>fl/fl</sup> and *Nfib*<sup>-/-</sup> mice were engineered by R.M.G.'s laboratory. *Dct-EGFP* animals were generated by GENSAT. Histology and immunofluorescence were performed on cryosections (10–20 µm). For melanocyte markers, including DCT, TYRP1 and TYR, sections were permeabilized with 0.3% H<sub>2</sub>O<sub>2</sub> in cold methanol for 30 min at –20 °C. Melanin staining was performed using a Fontana–Masson stain kit (MarketLab). For NFIB ChIP-seq and RNA-seq analyses, hair follicle stem cells were isolated by FACS with indicated antibodies. For RNA extraction, cells were sorted directly into TRIzol LS Reagent (Life Technologies) and RNA was isolated using Direct-zol RNA MiniPrep (Zymo Research) with DNase treatment to remove residual genomic DNA. A detailed description of the ultrasound-guided lentiviral injection procedure and production of high-titre lentiviruses is described elsewhere<sup>26</sup>. Transduced mice were confirmed by genotyping with *EGFP* primers: forward 5'-AATGGCCACAAGTTCAGC-3', reverse 5'-TCGCCGATGGGG GTATTCT-3'. Positive mice were fed with doxycycline-containing chow from P21. Figures were prepared using ImageJ, Adobe Photoshop and Illustrator CS3. Graphing and statistical analyses were performed using Prism 5 (GraphPad Software).

**Full Methods** and any associated references are available in the online version of the paper.

Received 7 August; accepted 19 December 2012.

Published online 6 February 2013.

1. Tumber, T. *et al.* Defining the epithelial stem cell niche in skin. *Science* **303**, 359–363 (2004).
2. Nishimura, E. K. *et al.* Dominant role of the niche in melanocyte stem cell fate determination. *Nature* **416**, 854–860 (2002).
3. Blanpain, C. & Fuchs, E. Epidermal homeostasis: a balancing act of stem cells in the skin. *Nature Rev. Mol. Cell Biol.* **10**, 207–217 (2009).

4. Cotsarelis, G. Gene expression profiling gets to the root of human hair follicle stem cells. *J. Clin. Invest.* **116**, 19–22 (2006).
5. Hirobe, T. How are proliferation and differentiation of melanocytes regulated? *Pigment Cell Melanoma Res.* **24**, 462–478 (2011).
6. Rabbani, P. *et al.* Coordinated activation of Wnt in epithelial and melanocyte stem cells initiates pigmented hair regeneration. *Cell* **145**, 941–955 (2011).
7. Nishimura, E. K. *et al.* Key roles for transforming growth factor  $\beta$  in melanocyte stem cell maintenance. *Cell Stem Cell* **6**, 130–140 (2010).
8. Greco, V. *et al.* A two-step mechanism for stem cell activation during hair regeneration. *Cell Stem Cell* **4**, 155–169 (2009).
9. Tanimura, S. *et al.* Hair follicle stem cells provide a functional niche for melanocyte stem cells. *Cell Stem Cell* **8**, 177–187 (2011).
10. Weiner, L. *et al.* Dedicated epithelial recipient cells determine pigmentation patterns. *Cell* **130**, 932–942 (2007).
11. Inomata, K. *et al.* Genotoxic stress abrogates renewal of melanocyte stem cells by triggering their differentiation. *Cell* **137**, 1088–1099 (2009).
12. Fitch, K. R. *et al.* Genetics of dark skin in mice. *Genes Dev.* **17**, 214–228 (2003).
13. Gründer, A. *et al.* Nuclear factor I-B (*Nfib*) deficient mice have severe lung hypoplasia. *Mech. Dev.* **112**, 69–77 (2002).
14. Dooley, A. L. *et al.* Nuclear factor I/B is an oncogene in small cell lung cancer. *Genes Dev.* **25**, 1470–1475 (2011).
15. Steele-Perkins, G. *et al.* The transcription factor gene *Nfib* is essential for both lung maturation and brain development. *Mol. Cell. Biol.* **25**, 685–698 (2005).
16. Hsu, Y. C., Pasolli, H. A. & Fuchs, E. Dynamics between stem cells, niche, and progeny in the hair follicle. *Cell* **144**, 92–105 (2011).
17. Botchkareva, N. V., Khlgatian, M., Longley, B. J., Botchkarev, V. A. & Gilchrist, B. A. SCF/c-kit signaling is required for cyclic regeneration of the hair pigmentation unit. *FASEB J.* **15**, 645–658 (2001).
18. Rendl, M., Lewis, L. & Fuchs, E. Molecular dissection of mesenchymal-epithelial interactions in the hair follicle. *PLoS Biol.* **3**, e331 (2005).
19. Lien, W. H. *et al.* Genome-wide maps of histone modifications unwind *in vivo* chromatin states of the hair follicle lineage. *Cell Stem Cell* **9**, 219–232 (2011).
20. Aoki, H., Yamada, Y., Hara, A. & Kunisada, T. Two distinct types of mouse melanocyte: differential signaling requirement for the maintenance of non-cutaneous and dermal versus epidermal melanocytes. *Development* **136**, 2511–2521 (2009).
21. D'Orazio, J. A. *et al.* Topical drug rescue strategy and skin protection based on the role of *Mc1r* in UV-induced tanning. *Nature* **443**, 340–344 (2006).
22. McDade, S. S. *et al.* Genome-wide analysis of p63 binding sites identifies AP-2 factors as co-regulators of epidermal differentiation. *Nucleic Acids Res.* **40**, 7190–7206 (2012).
23. Pjanic, M. *et al.* Nuclear factor I revealed as family of promoter binding transcription activators. *BMC Genomics* **12**, 181 (2011).
24. Pla, P. & Larue, L. Involvement of endothelin receptors in normal and pathological development of neural crest cells. *Int. J. Dev. Biol.* **47**, 315–325 (2003).
25. Nishikawa, S. *et al.* *In utero* manipulation of coat color formation by a monoclonal anti-c-kit antibody: two distinct waves of c-kit dependency during melanocyte development. *EMBO J.* **10**, 2111–2118 (1991).
26. Beronja, S., Livshits, G., Williams, S. & Fuchs, E. Rapid functional dissection of genetic networks via tissue-specific transduction and RNAi in mouse embryos. *Nature Med.* **16**, 821–827 (2010).
27. Baynash, A. G. *et al.* Interaction of endothelin-3 with endothelin-B receptor is essential for development of epidermal melanocytes and enteric neurons. *Cell* **79**, 1277–1285 (1994).
28. Reid, K. *et al.* Multiple roles for endothelin in melanocyte development: regulation of progenitor number and stimulation of differentiation. *Development* **122**, 3911–3919 (1996).
29. Adur, J., Takizawa, S., Uchide, T., Casco, V. & Saida, K. High doses of ultraviolet-C irradiation increases vasoactive intestinal contractor/endothelin-2 expression in keratinocytes of the newborn mouse epidermis. *Peptides* **28**, 1083–1094 (2007).
30. Klipper, E. *et al.* Induction of endothelin-2 expression by luteinizing hormone and hypoxia: possible role in bovine corpus luteum formation. *Endocrinology* **151**, 1914–1922 (2010).

**Supplementary Information** is available in the online version of the paper.

**Acknowledgements** We thank Y.-C. Hsu, T. Chen, B. Keyes, S. E. Williams, A. Rodriguez-Folgueras and other Fuchs laboratory members for intellectual input and suggestions; L. Polak and N. Stokes for breeding of mouse lines and conducting *in utero* lentiviral injections; V. J. Hearing for providing anti-DCT, TYRP1 and TYR antibodies. We also thank Rockefeller facilities: Comparative Bioscience Center (AAALAC accredited) for care and husbandry care of mice in accordance with National Institutes of Health (NIH) guidelines; Bioimaging Center for advice on image acquisition; Flow Cytometry facility for FACS sorting. E.F. is an investigator of the Howard Hughes Medical Institute. This work was supported by grants from the NIH to E.F. (R01-AR050452 and R01-AR31737) and R.M.G. (R01-HL080624), and a CAREER grant to O.E. from the National Science Foundation (DB1054964).

**Author Contributions** C.-Y.C. performed all experiments; H.A.P. performed the ultrastructural analyses; E.G.G. and O.E. performed the bioinformatic analyses; G.G. carried out the initial characterization of NFIB expression during mouse development; R.M.G. provided the conditional *Nfib*<sup>fl/fl</sup> mice; E.F. supervised the project; E.F. and C.-Y.C. wrote the manuscript.

**Author Information** ChIP-seq data have been deposited in the Gene Expression Omnibus database under accession number GSE42900. Reprints and permissions information is available at [www.nature.com/reprints](http://www.nature.com/reprints). The authors declare no competing financial interests. Readers are welcome to comment on the online version of the paper. Correspondence and requests for materials should be addressed to E.F. ([fuchs@rockefeller.edu](mailto:fuchs@rockefeller.edu)).



## METHODS

**Mice.** P52–60 CD1 mice from Charles River laboratories were used for NFIB ChIP-seq experiments. *Nfib*<sup>fl/fl</sup> and *Nfib*<sup>+/+</sup> mice have been described<sup>15,31</sup>, as have transgenic *K15-crePGR*, knock-in *Sox9-creERT2* and *Rosa26<sup>lox</sup>STOP<sup>lox</sup>YFP* (*RosaYFP*) mice<sup>32–34</sup>. *Dct-EGFP* animals were generated by GENSAT project<sup>35</sup>. CreER was activated by intraperitoneal injection of P20–21 mice with 20 mg ml<sup>-1</sup> tamoxifen (Sigma) in corn oil (Sigma) (1 mg per 10 g body weight per day). CrePGR was induced by RU486 treatment: 5-day intraperitoneal injection of 10 mg ml<sup>-1</sup> RU486 (VWR) in sesame oil (Sigma) (0.75 mg 10 g body weight per day), together with 2-week topical application with 4% RU486 in ethanol.

All animals were maintained in an AAALAC-approved Comparative Bioscience Center (CBC) at The Rockefeller University and procedures were performed using IACUC-approved protocols that adhere to the standards of the National Institutes of Health.

**Histology and immunofluorescence.** Embryos (<E16.5) or back skins were embedded in OCT (Tissue Tek), frozen on dry ice and stored at -80 °C. Only in the case of *RosaYFP* reporter or lentiviral transduced mice, tissues were prefixed in 4% paraformaldehyde (PFA) for 30 min at room temperature before embedding in OCT in order to preserve the fluorescence signals. Un-prefixed frozen sections (10–20 µm) were fixed in 4% PFA for 10 min at room temperature. For histological analysis, sections were stained with haematoxylin and eosin. Melanin staining was performed using a Fontana–Masson stain kit (MarketLab Inc.) according to the manufacturer's directions. For immunofluorescence, sections were permeabilized in 0.3% Triton X-100 in PBS for 20 min and blocked for 1 h at room temperature in blocking buffer including 2.5% normal donkey serum, 2.5% normal goat serum (or 5% normal donkey serum alone when goat primary antibodies were used), 0.5% BSA and 0.1% Triton X-100 in PBS. For melanocyte markers, including DCT, TYRP1 and TYR, sections were permeabilized with 0.3% H<sub>2</sub>O<sub>2</sub> in cold methanol for 30 min at -20 °C<sup>36</sup>. MOM Basic kit (Vector Laboratories) was used for blocking when primary antibodies were generated from mouse. Primary antibodies were diluted in blocking buffer and sections were incubated overnight at 4 °C. After washing with PBS for 30 min at room temperature, sections were incubated for 1–2 h at room temperature with secondary antibodies conjugated to Alexa-488, Alexa-546, Alexa-647 (Molecular Probes), or RRX (Jackson Laboratories). EdU staining was performed using Click-iT EdU Alexa Fluor 594 Imaging Kit (Life Technologies) and following manufacturer's directions. Nuclei were stained using 4'6'-diamidino-2-phenylindole (DAPI). Imaging was performed on a Zeiss Axioplan 2, Zeiss Apotome, Zeiss Inverted LSM 510 laser scanning confocal microscope, or Zeiss Inverted LSM 780 laser scanning confocal microscope. Figures were prepared using ImageJ, Adobe Photoshop and Illustrator CS3.

The following antibodies and dilutions were used: NFIB (rabbit, 1:1,000, Active Motif); KIT (rat, 1:1,000, BD Pharmingen); P-cadherin (goat, 1:100, R&D); E-cadherin (rat, 1:500, Fuchs laboratory); K5 (guinea-pig, 1:500, Fuchs laboratory); CD34 (rat, 1:100, BD Pharmingen); Ki67 (rabbit, 1:300, Novocastra); cleaved-caspases 3 (rabbit, 1:300, R&D); GFP (chicken, 1:2,000, Abcam); EDN 1/2/3 (rabbit, 1:100, Santa Cruz); KITL (rat, 1:300, R&D); Mac-1 (rat, 1:100, eBioscience) MITF (mouse, 1:100, Abcam); DCT (rabbit, 1:500, gift from V. J. Hearing); TYRP1 (rabbit, 1:1,000, gift from V. J. Hearing); TYR (rabbit, 1:1,000, gift from V. J. Hearing).

**Electron microscopy.** Back skins were fixed in 2% glutaraldehyde, 4% PFA and 2 mM CaCl<sub>2</sub> in 0.05 M sodium cacodylate buffer, pH 7.2, at room temperature for >1 h, post-fixed in 1% osmium tetroxide, and processed for Epon embedding. Ultrathin sections (60–70 nm) were counterstained with uranyl acetate and lead citrate. Images were taken with a transmission electron microscope (Tecnai G2-12; FEI) equipped with a digital camera (model XR60; Advanced Microscopy Techniques).

**Isolation of hair follicle stem cells and FACS.** Subcutaneous fat was removed from skins with a scalpel. To isolate bulge hair follicle stem cells for NFIB ChIP-seq experiment, skins were placed on 0.25% trypsin (GIBCO) at 37 °C for 30 min with dermis side down. For isolation of bulge and hair germ hair follicle stem cells, skins were first incubated in 0.25% collagenase (Sigma) in HBSS (GIBCO) at 37 °C for 1 h to remove dermis. After gentle PBS washing, skins were treated with trypsin as described above. Single-cell suspensions were obtained by scrapping the skin gently and filtering through 70-µm strainers, followed by 40-µm strainers. Staining buffer (PBS with 5% FBS treated with BioRad Chelex to remove calcium) was added to inactivate Trypsin, and cells were collected by centrifugation for 5 min at 300g. Cell suspensions were incubated with the appropriate antibodies diluted in staining buffer for 30 min at 4 °C. The following antibodies were used: CD34–Alexa 660 (1:200, eBioscience); α6–phycoerythrin (1:500, eBioscience); SCA1–Alexa 700 (1:200, eBioscience); CD200–biotin (1:200, AbD Serotec); streptavidin–phycoerythrin–Cy7 (1:200, eBioscience). DAPI (100 ng ml<sup>-1</sup>) was used for death cell exclusion. Cell isolations were performed on BD FACSAria II sorters

equipped with BD FACSDiva software. For RNA extraction, cells were sorted directly into TRIzol LS Reagent (Life Technologies).

**RNA extraction and RNA-seq analysis.** Cells were isolated from *Nfib*<sup>fl/fl</sup>/*K15-crePGR/RosaYFP* (Het) and *Nfib* fl/fl/*K15-crePGR/RosaYFP* (cKO) mice. *Nfib* ablation was induced from second telogen (P50–60) with RU486 treatment, and mice were taken during third telogen (P120–130). The protocol of cell sorting was described above with antibodies: CD34–Alexa 660, CD200–biotin, α6–phycoerythrin, SCA1–Alexa 700 and streptavidin–phycoerythrin–Cy7. Cells were lysed with TRIzol LS Reagent (Life Technologies) and RNA was extracted using Direct-zol RNA MiniPrep (Zymo Research) with DNase treatment to remove residual genomic DNA. Isolated RNA samples were provided to the Genomics Resources Core Facility at Weill Cornell Medical College for quality control, library preparation, clustering and sequencing. RNA-seq reads were aligned to the mouse genome (mm9, NCBI Build 37) using TopHat<sup>37</sup> (<http://tophat.cbcb.umd.edu/>). Cufflinks<sup>38</sup> (<http://cufflinks.cbcb.umd.edu/>) was subsequently used to assemble the aligned reads into transcripts and then estimate the transcript abundances. Pathway analysis was performed using iPAGE<sup>39</sup> algorithm, included in the ChIP-seq framework<sup>40</sup>.

**Quantitative real-time PCR with reverse transcription.** RNA isolation was described above. Complementary DNA was synthesized from isolated RNA using SuperScript III First-Strand Synthesis System with oligo-dT primers (Invitrogen). cDNAs were mixed with indicated primers and Power SYBR Green PCR Master Mix (Applied Biosystems), and quantitative PCR (qPCR) was performed on a Applied Biosystems 7900HT Fast Real-Time PCR system for 40 cycles. Specificity was confirmed by subsequent melting curve analysis or gel electrophoresis. Levels of PCR product were expressed as a function of peptidylprolyl isomerase B (*PpiB*). Primers were designed through Primer 3 and amplified products encompassed exon/intron boundaries. The following primer sequences were used: *Nfib* forward 5'-ATGACCCATCCAGTCCCTCAA-3', reverse 5'-TTGAAGGAAAGGCTCTCCAA-3'; *Dct* forward 5'-AGAGAAACAACCCCTCCACAGA-3', reverse 5'-CCAATGACCACTGAGAGAGTTG-3'; *Kit* forward 5'-GGGCTAGCCA GAGACATCAG-3', reverse 5'-AGGAGAAGAGCTCCAGAGG-3'; *Mitf* forward 5'-TTGAAAACCGACAGAAGAAGC-3', reverse 5'-TGGATGGGATA AGGGAAAGTC-3'; *Tyrb1* forward 5'-GCCTCCAGTTACCAACACAGA-3', reverse 5'-AACGGATCAGACAAGAAGCA-3'; *Tyr* forward 5'-CCAGAAG CCAATGCACCTAT-3', reverse 5'-ATAACAGCTCCACCACTGC-3'; *Sox10* forward 5'-GACCACTACCTCACCCTCCA-3', reverse 5'-AGCCTCTCAGC CTCCTCAAT-3'; *Ednrb* forward 5'-CTCTGTGGCTTCCCCTTC-3', reverse 5'-CGATTGGATTGATGCAGGA-3'; *Pax3* forward 5'-GCCGAGAAAAGG CTAAACACA-3', reverse 5'-CGGAGCCTTCATCTGACTG-3'; *S100a1* forward 5'-CAAGGAAGGGGACAAATATAAGC-3', reverse 5'-CGTTTTCATCCAG TTCCTTCA-3'; *Edn1* forward 5'-TACTTCTGCCACCTGGACATC-3', reverse 5'-CCCTGAGTTCTTTTCTGCTT-3'; *Edn2* forward 5'-TTCTGCCATCGAA GACTG-3', reverse 5'-TGGCCTTCTTGTGACCTCT-3'; *Edn3* forward 5'-TGGGAAACAAGAGGACAAGG-3', reverse 5'-CTGGGAGCTTTCTGGAAC TG-3'; *Axin2* forward 5'-ACTGACCGACGATTCATGT-3', reverse 5'-CTGC GATGATCTCTCTCTG-3'; *Gpnmb* forward 5'-TGCTGCTGCTGTGTGAG AAG-3', reverse 5'-GGCAGTTTCTATTGGCTTG-3'; *Kitl* forward 5'-CAAG TCTTACAAGGGCAGTTGA-3', reverse 5'-ACAAGGTACGGGTAGCAAG-3'; *Chd3* forward 5'-ACTTTGATGAGCGTCTGAAG-3', reverse 5'-GGCTT GTCTTCTCATTTTCG-3'; *Whn* forward 5'-TGGCTTATAGACCTGATGGA GAA-3', reverse 5'-CTTCTGAGGGGATTGACAT-3'; *Acsbg1* forward 5'-AAGTTCTGTCCATGCTGCT-3', reverse 5'-TGGAGAAGTCACGTTGGAG A-3'; *Adamts14* forward 5'-GGCAACCAGACTCTCAGCTC-3', reverse 5'-CGGCAGCAGGTAGTTGTGTA-3'; *Cyp4b1* forward 5'-GCCTGATCTCTCTG CACATCA-3', reverse 5'-CACCTTCATCTCGTTTCATAGCA-3'; *Gfra1* forward 5'-TGCTGGCCCTCTAGATCCATAAC-3', reverse 5'-ACAGCGTCTT GGCAGTTGATA-3'; *Myoc* forward 5'-TCGGCTTTAGAGGAAGAGAAGA-3', reverse 5'-CATACTTGCCAGCGATTGTTT-3'; *Nt5e* forward 5'-ATGAA CATCTGGGCTACGA-3', reverse 5'-GTCCTTCCACACCGTTATCAA-3'; *Steap4* forward 5'-TGATTCCTATCCGTTACTATGTTTCG-3', reverse 5'-ATG GGCTGTCTTTATTAGTTAGGG-3'; *Tns1* forward 5'-TCTTACCATTGCC CTCAATGC-3', reverse 5'-CCACGAGCTCCACATAGCTC-3'; *PpiB* forward 5'-GTGAGCGCTTCCAGATGAGA-3', reverse 5'-TGCCGGAGTCGACAAT GATG-3'.

**NFIB ChIP-seq analysis.** All materials and methods for ChIP-seq experiments have been described<sup>19</sup>. For each independent NFIB ChIP experiment, 10–15 million bulge hair follicle stem cells were isolated by FACS (CD34–Alexa 660 and α6–phycoerythrin antibodies) from 15–20 CD-1 mice, and then used to isolate chromatin and incubated with anti-NFIB antibody (Active Motif) for ChIP-seq analysis. ChIP-seq reads were aligned to the mouse genome (mm9, build 37) with the Bowtie program<sup>41</sup> and the Illumina Analyzer Pipeline. ChIP-seq peak calling, genomic annotation of NFIB peaks, and comparison between NFIB targets and gene expression signature genes were



performed using ChIPseeqer<sup>40</sup>. Motif analysis was performed using FIRE<sup>42</sup> algorithm, included in the ChIPseeqer framework.

**Plasmid DNA constructions.** Plasmids encoding full-length *Nfib1* cDNA were obtained from ATCC (clone MGC-13959). Since NFIB3 is the major isoform present in epidermal keratinocytes, *Nfib3* cDNA was used in this study. *Nfib3* DNA fragment was amplified from *Nfib1* cDNA clone by PCR with primers: forward 5'-GTTGCGAGCTCTCATGATGTATTCTC-3', reverse 5'-GTCAACC CGGGCTAGCCCGAGGTACCAGGACTGGCTCGTTTGAGGA-3'.

For expression of EGFP-NFIB3, *Nfib3* DNA fragment was then inserted into *pEGFP-C1* between SacI and XmaI restriction sites. All lentiviral vectors (LV) were present in the *pLKO* lentiviral backbone (*pLKO-no-stuffer-PGK-MCS*, Addgene 10879). For construction of *LV-rtTA-IRES-EGFP*, DNA fragment of *rtTA-IRES-EGFP* was excised from *pMSCV-rtTA2S-M2-IRES-EGFP* with BglII and SalI restriction enzymes (RE) and cloned between BamHI and SalI sites of *pLKO* backbone. *rtTA2S-M2* (Tet-On Advanced) was cloned from *pUHD-rtTA2S-M2*. This was excised by digesting with BamHI and SacII, and blunting with Klenow. The blunted fragment was subcloned into *pMSCV-IRES-EGFP* digested with HpaI, and dephosphorylated with SAP. For construction of *LV-TRE-PGK-H2BmRFP1*, TRE promoter was first inserted into ClaI and AgeI sites of *pLKO* vector to replace U6 promoter (*pLKO-TRE-PGK*). The TRE promoter from Clontech's pTRE2 was amplified by PCR using primers flanked with ClaI and AgeI sites: forward 5'-CGTATATCGATGCCCTTTCGTCTCGA-3', reverse 5'-GAATTACCGGTGCGGAGGCTGGAT-3'.

*H2BmRFP1* DNA fragment was obtained from *pCR-H2BmRFP1* by BglII and NsiI restriction enzyme digestion<sup>26</sup>, which was then inserted between BamHI and NsiI sites of *pLKO-TRE-PGK*. *Edn2* cDNA were amplified from keratinocyte cDNA library with primers flanked with EcoRI site: forward 5'-CGCCAGAA TTCATGGTCTCCGCTGGT-3', reverse 5'-CGCCAGAATTCGGTGTTATC TCTTCTCCATC-3'.

Afterwards, DNA fragment was inserted into EcoRI site of *LV-H2BmRFP1-TRE* vector. All insertions were verified by DNA sequencing.

A detailed description of the ultrasound-guided lentiviral injection procedure and production of high-titre lentiviruses is described elsewhere<sup>26</sup>. Transduced mice were confirmed by genotyping with *EGFP* primers: forward 5'-AATGG CCACAAGTTCAGC-3', reverse 5'-TCGCCGATGGGGGTATTCT-3'. Positive mice were fed with doxycycline-containing chow from P21.

**Cell culture and *in vitro* Nfib overexpression.** Primary *Nfib*-null (KO) keratinocytes were isolated from epidermis of E18.5 *Nfib* knockout embryos (*Nfib*<sup>-/-</sup>) and control keratinocytes were from heterozygous *Nfib*<sup>+/-</sup> embryos. Keratinocytes were maintained in E-media supplemented with 15% serum and a final concentration of 0.05 mM Ca<sub>2</sub>. Experiments were performed using primary cells

with fewer than 15 passages. Plasmids expressing EGFP or EGFP-NFIB3 were introduced into control and KO keratinocytes with FuGENE 6 Transfection Reagent (Roche). After 24 h transfection, EGFP-positive cells were isolated by FACS for qPCR analysis.

**Intradermal injection of EDNRB receptor inhibitor BQ788 and anti-KIT blocking antibody.** To inhibit EDNRB receptor from late catagen, 100 µl BQ788 dissolved in PBS (1 mg ml<sup>-1</sup>, Tocris Bioscience) or PBS alone was injected intradermally into the back skin of mice on first catagen when skin colour turned from black to pink<sup>6</sup>. To inhibit KIT signalling, 100 µl anti-KIT antibody (BD Pharmingen, 1.0 mg ml<sup>-1</sup>, clone: ACK45 NA/LE) or control Rat IgG was used<sup>17</sup>. Injections were conducted every other day for 3 days (day 0, 2, 4), and mice were taken and analysed on day 5. For inhibition of KIT signalling during anagen, 100 µl anti-KIT antibody or control IgG was injected intradermally into back skin 1 day after depilation. Injections were conducted every other day for 5 days (day 0, 2, 4, 6, 8) and mice were taken and analysed on day 10.

**Statistics.** To determine significance between two groups indicated in figures, comparisons were performed in Prism 5 (GraphPad Software) with unpaired two-tailed student's *t*-test.

31. Hsu, Y. C. *et al.* Mesenchymal nuclear factor I B regulates cell proliferation and epithelial differentiation during lung maturation. *Dev. Biol.* **354**, 242–252 (2011).
32. Soeda, T. *et al.* Sox9-expressing precursors are the cellular origin of the cruciate ligament of the knee joint and the limb tendons. *Genesis* **48**, 635–644 (2010).
33. Morris, R. J. *et al.* Capturing and profiling adult hair follicle stem cells. *Nature Biotechnol.* **22**, 411–417 (2004).
34. Srinivas, S. *et al.* Cre reporter strains produced by targeted insertion of *EYFP* and *ECFP* into the *ROSA26* locus. *BMC Dev. Biol.* **1**, 4 (2001).
35. Heintz, N. Gene expression nervous system atlas (GENSAT). *Nature Neurosci.* **7**, 483 (2004).
36. Govender, D., Davids, L. M. & Kidson, S. H. Immunofluorescent identification of melanocytes in murine hair follicles. *J. Mol. Histol.* **37**, 1–3 (2006).
37. Trapnell, C., Pachter, L. & Salzberg, S. L. TopHat: discovering splice junctions with RNA-Seq. *Bioinformatics* **25**, 1105–1111 (2009).
38. Trapnell, C. *et al.* Transcript assembly and quantification by RNA-Seq reveals unannotated transcripts and isoform switching during cell differentiation. *Nature Biotechnol.* **28**, 511–515 (2010).
39. Goodarzi, H., Elemento, O. & Tavazoie, S. Revealing global regulatory perturbations across human cancers. *Mol. Cell* **36**, 900–911 (2009).
40. Giannopoulou, E. G. & Elemento, O. An integrated ChIP-seq analysis platform with customizable workflows. *BMC Bioinformatics* **12**, 277 (2011).
41. Langmead, B., Trapnell, C., Pop, M. & Salzberg, S. L. Ultrafast and memory-efficient alignment of short DNA sequences to the human genome. *Genome Biol.* **10**, R25 (2009).
42. Elemento, O., Slonim, N. & Tavazoie, S. A universal framework for regulatory element discovery across all genomes and data types. *Mol. Cell* **28**, 337–350 (2007).

# 'See-saw' expression of microRNA-198 and FSTL1 from a single transcript in wound healing

Gopinath M. Sundaram<sup>1\*</sup>, John E. A. Common<sup>1\*</sup>, Felicia E. Gopal<sup>1</sup>, Satyanarayana Srikanta<sup>2</sup>, Krishnaswamy Lakshman<sup>2</sup>, Declan P. Lunney<sup>1</sup>, Thiam C. Lim<sup>3,4</sup>, Vivek Tanavde<sup>1,5</sup>, E. Birgitte Lane<sup>1,6,7</sup> & Prabha Sampath<sup>1,7</sup>

Post-transcriptional switches are flexible effectors of dynamic changes in gene expression<sup>1</sup>. Here we report a new post-transcriptional switch that dictates the spatiotemporal and mutually exclusive expression of two alternative gene products from a single transcript. Expression of primate-specific exonic microRNA-198 (miR-198)<sup>2</sup>, located in the 3'-untranslated region of follistatin-like 1 (*FSTL1*)<sup>3</sup> messenger RNA, switches to expression of the linked open reading frame of *FSTL1* upon wounding in a human *ex vivo* organ culture system. We show that binding of a KH-type splicing regulatory protein (KSRP, also known as KHSRP) to the primary transcript determines the fate of the transcript and is essential for the processing of miR-198: transforming growth factor- $\beta$  signalling switches off miR-198 expression by downregulating KSRP, and promotes *FSTL1* protein expression. We also show that *FSTL1* expression promotes keratinocyte migration, whereas miR-198 expression has the opposite effect by targeting and inhibiting *DIAPH1*, *PLAU* and *LAMC2*. A clear inverse correlation between the expression pattern of *FSTL1* (pro-migratory) and miR-198 (anti-migratory) highlights the importance of this regulatory switch in controlling context-specific gene expression to orchestrate wound re-epithelialization. The deleterious effect of failure of this switch is apparent in non-healing chronic diabetic ulcers, in which expression of miR-198 persists, *FSTL1* is absent, and keratinocyte migration, re-epithelialization and wound healing all fail to occur.

Wound healing requires the regulated integration of complex biological events including cell migration, proliferation and extracellular

matrix remodelling<sup>4</sup>, globally stimulated by transforming growth factor- $\beta$  (TGF- $\beta$ ) and other growth factors<sup>5</sup>. Gene expression in this regenerative process is extensively regulated by non-coding microRNAs (miRNAs)<sup>6</sup>. We compared miRNA-expression profiling from cutaneous wounds, using a human skin *ex vivo* organ culture system sampled at 0 h and 24 h after injury, and found miR-198 to be a consistent and significant differentially expressed miRNA. Primate-specific miR-198 belongs to a small cohort of human exonic miRNA stem-loops (Fig. 1a and Supplementary Fig. 1) and is located within the eleventh exon of the protein-coding *FSTL1* (ref. 3) gene. At steady state, healthy epidermis expresses high levels of miR-198 (ref. 7), but upon injury, miR-198 levels plummet as early as 3 h after wounding and remain low for at least 24 h (Fig. 1b). *In situ* hybridization reveals expression of mature miR-198 in epidermal keratinocytes in normal skin, but not in epidermis 24 h after injury (Fig. 1c).

miR-198 lies within an exon of the *FSTL1* gene, therefore we investigated whether miR-198 and *FSTL1* were being co-regulated. In contrast to miR-198, *FSTL1* mRNA and protein were observed in the wound-edge epidermis 24 h after injury, but were not seen in unwounded epidermis (Fig. 1d, e and Supplementary Fig. 2). A reducing gradient of miR-198 intensity, and a corresponding appearance of *FSTL1* protein, was observed from the wound edge out to about 12 mm (Supplementary Fig. 3). A single transcript can therefore function either as a primary miRNA (pri-miRNA) transcript making miR-198 or as an mRNA<sup>8</sup> producing *FSTL1* protein, suggesting a

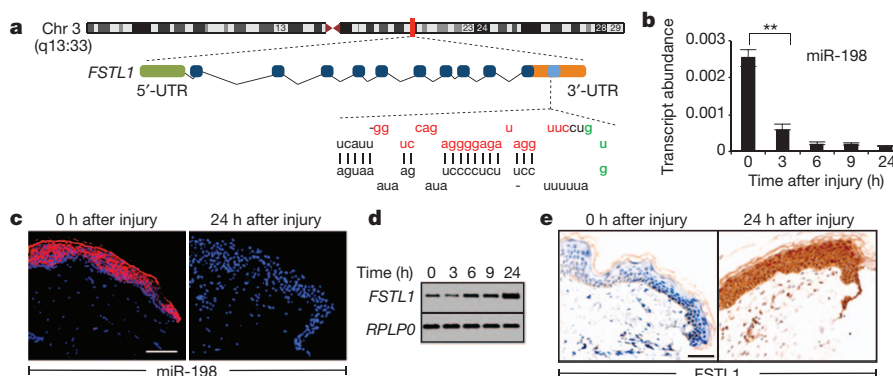


**Figure 1 | Expression of an exonic miRNA or linked open reading frame in context-specific physiological states.** **a**, Schematic diagram of the *FSTL1* gene on chromosome (chr) 3 (NM\_007085), showing the exon-intron boundaries and the 3'-UTR sequence encoding miR-198 (red indicates mature miR-198 sequence and green indicates the GUG motif in the terminal loop of the precursor miR-198 (pre-miR-198) sequence). **b**, miR-198 expression by qRT-PCR in organ culture explants at indicated time points after injury. Student's *t*-test was used to calculate the *P* value and error bars denote  $\pm$  s.e.m.

**\*\**P* < 0.001.** **c**, *In situ* hybridization with locked nucleic acid (LNA) probes specific for mature miR-198 on normal skin at 0 h (left) and 24 h (right) after injury (*n* = 5). miR-198 is stained red and nuclei are stained blue. **d**, Representative semiquantitative RT-PCR analysis of *FSTL1* mRNA in explant samples before and after injury at indicated time points. Ribosomal large subunit P0 (*RPLP0*) was used as a control. **e**, Immunohistochemical localization of *FSTL1* protein at 0 h (left) and 24 h (right) after wounding (*n* = 5). Scale bars, 100  $\mu$ m.

<sup>1</sup>Institute of Medical Biology, Agency for Science Technology & Research (A\*STAR), 138648, Singapore. <sup>2</sup>Jnana Sanjeevini Diabetes Center, Bangalore 560078, India. <sup>3</sup>Division of Plastic, Reconstructive & Aesthetic Surgery, National University Health System, 119074, Singapore. <sup>4</sup>Department of Surgery, Yong Loo Lin School of Medicine, National University of Singapore, 119228, Singapore. <sup>5</sup>Bioinformatics Institute, Agency for Science Technology & Research (A\*STAR), 138671, Singapore. <sup>6</sup>Department of Pathology, Yong Loo Lin School of Medicine, National University of Singapore, 119074, Singapore. <sup>7</sup>Department of Biochemistry, Yong Loo Lin School of Medicine, National University of Singapore, 117597, Singapore.

\*These authors contributed equally to this work.

post-transcriptional switch regulating context-specific expression of these diverse products of a single gene.

There was no significant change in expression of the precursor *FSTL1* mRNA (pre-*FSTL1* mRNA) synthesized from the DNA template after transcription, confirming that regulation was post-transcriptional (Supplementary Fig. 4a, b). Detection of low levels of *FSTL1* mRNA at 0 h after injury (Supplementary Fig. 4c), with transcript localization in the nucleus and absence of FSTL1 protein, indicated that *FSTL1* mRNA functions as a pri-miRNA transcript and is processed to form mature miR-198 (Supplementary Fig. 4d). Yet at 24 h after injury, the *FSTL1* transcript is functioning as an mRNA, as confirmed by the abundant FSTL1 protein (Supplementary Fig. 4d). The presence of the pre-miR-198 in the 3'-untranslated region (UTR) of *FSTL1* mRNA does not inhibit FSTL1 protein expression, as confirmed by chimaeric luciferase assays (Supplementary Figs 4e, f). In conclusion, if the *FSTL1* transcript is not processed to miR-198, the full-length transcript is exported to the cytoplasm and functions as *FSTL1* mRNA.

FSTL1, a member of the BM-40/SPARC/osteonectin family, is a glycoprotein originally cloned from an osteoblastic cell line as a TGF- $\beta$ 1-induced gene<sup>3,9</sup>. Expression of FSTL1 protein in the wound-edge epidermis (Fig. 1e) prompted us to study the role of *FSTL1* in wound healing. Keratinocytes transfected with small interfering RNA (siRNA) against *FSTL1* or control non-targeting siRNAs were grown to confluent monolayers and subjected to scratch-wounding. Knockdown of *FSTL1* (Supplementary Fig. 5a, b) significantly suppressed migration of keratinocytes (Supplementary Fig. 5c, d), demonstrating a new role for FSTL1 in promoting keratinocyte migration. Knockdown of *FSTL1* did not affect miR-198 expression (Supplementary Fig. 5e). Comparison of keratinocyte gene-expression profiles in the presence and absence of *FSTL1* revealed differentially expressed genes to include *CXCL10* (ref. 10) and *FERMT2* (ref. 11), both essential for migration, suggesting pathways by which FSTL1 may increase keratinocyte migration (Supplementary Fig. 5f).

By contrast, miR-198 expression in steady-state epidermis, and its downregulation in activated migrating epidermal keratinocytes<sup>12</sup> at the wound edge, suggests a function for miR-198 in inhibiting keratinocyte migration. Scratch-wound assays were therefore used to examine migration in keratinocyte monolayers overexpressing miR-198 (Supplementary Fig. 6a): these cells only closed 35  $\pm$  10% of the

scratch-wound area in 24 h, without affecting proliferation, compared to complete closure observed in controls (Supplementary Fig. 6b–d and Supplementary Videos 1 and 2). Although *FSTL1* mRNA itself has a binding site for miR-198, overexpression of miR-198 did not affect *FSTL1* expression (Supplementary Fig. 6e), as verified by luciferase assays (Supplementary Fig. 6f). Together, these results suggest that miR-198 inhibits keratinocyte migration independently of FSTL1.

We then sought to trace the miR-198 inhibitory regulatory network and identify specific regulators of keratinocyte migration by comparing cultured keratinocyte gene-expression profiles in the presence or absence of miR-198. Representation of selected array data as a heat-map revealed potential targets of miR-198, which were validated by quantitative reverse-transcriptase PCR (qRT-PCR) (Supplementary Fig. 6g, h). Further targets of miR-198 were analysed in a human skin organ culture model. At steady state, when epidermal keratinocytes express high levels of miR-198, these candidate target genes are down-regulated. Upon injury, expression of these target genes rises as miR-198 expression drops, supporting their potential regulation by miR-198 (Fig. 2a). Interrogation of the TargetScan v5.1 database and correlation with microarray data revealed direct targets, that is with at least one binding site each for miR-198, including urokinase-type plasminogen activator (*PLAU*), a serine protease that degrades extracellular matrix<sup>13</sup>; diaphanous homologue 1 (*DIAPH1*), involved in actin polymerization<sup>14</sup>; and laminin  $\gamma$ 2 chain (*LAMC2*), an essential component of the basement membrane protein laminin 332 (ref. 15). Significant downregulation of luciferase reporter activity with co-transfection of miR-198 and wild-type *PLAU*, *DIAPH1* and *LAMC2* 3'-UTRs, but not with mutant 3'-UTRs, confirmed these are direct targets of miR-198 (Fig. 2b and Supplementary Fig. 7). Knockdown of *DIAPH1*, *PLAU* and *LAMC2* using gene-specific siRNA (Supplementary Fig. 8a–f) significantly suppressed migration of keratinocytes, which only closed 46  $\pm$  16%, 59  $\pm$  8% and 40  $\pm$  6% of the scratch-wound area in 24 h, compared to complete wound closure seen in control-transfected keratinocytes, thus phenocopying the effect of miR-198 (Supplementary Fig. 8 g–j). Although we observed a moderate rescue of the effect of miR-198 with ectopic overexpression of individual targets, when taken in combination the rescue is highly significant (Supplementary Fig. 9).

Protein expression from these target genes was tested by immunohistochemistry in normal healthy skin. A substantial increase in

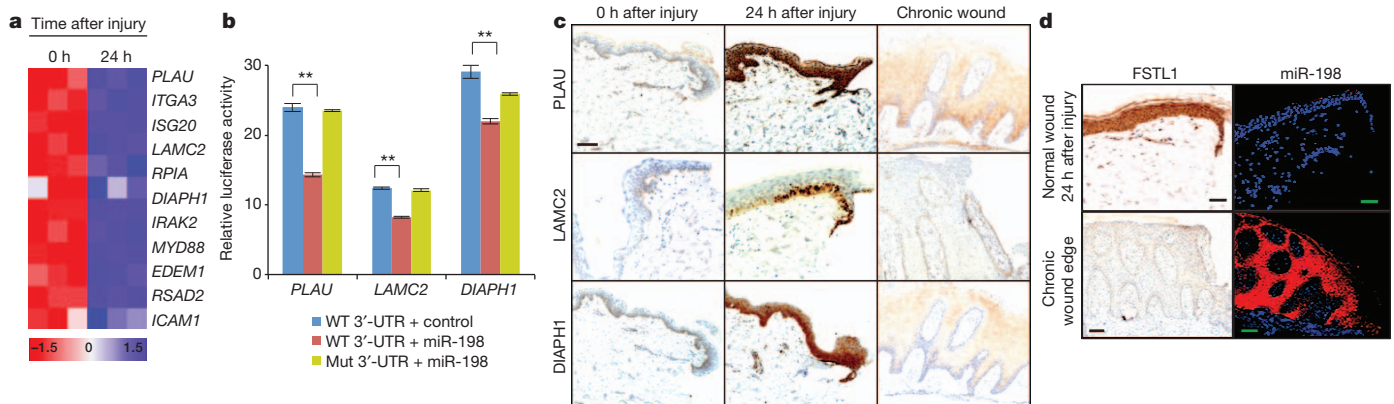


**Figure 2 | The regulatory switch is impaired in chronic wounds.** **a**, Heat-map of selected genes (putative targets) generated from microarray using RNA from skin (organ culture) at 0 and 24 h after injury. Expression values are displayed in shades of red (low) or blue (high) relative to the individual mean value of the gene in a linear scale. **b**, Validation of direct targets of miR-198 by luciferase reporter assays. Cells were co-transfected with wild-type (WT) or mutant (Mut) 3'-UTR luciferase reporter constructs as indicated, and either with miR-198 or non-targeting scrambled control. Normalized relative luciferase activities are shown as a bar diagram. Luciferase activity is expressed as mean relative to controls ( $n = 3$ ).  $**P < 0.001$ . Student's  $t$ -test was used to

calculate  $P$  value and error bars denote mean  $\pm$  s.e.m. **c**, Immunohistochemical analysis of PLAU, LAMC2 and DIAPH1, on sections from organ culture and chronic wounds. A substantial increase in protein expression of target genes is clearly observed at 24 h after injury (middle panels). However, in chronic wounds (right panels), the expression of target genes remains relatively low ( $n = 8$ ). **d**, Expression of FSTL1 protein and miR-198 detected by immunohistochemistry (left panels) and *in situ* hybridization (right panels) respectively, in normal wounds 24 h after injury or in chronic wounds ( $n = 8$ ). Scale bars, 100  $\mu$ m.



expression of these proteins was observed 24 h after wounding, validating the mRNA-expression profiles (Fig. 2c, left and middle panels). PLAUI, LAMC2 and DIAPH1 proteins were detected in epidermis at the wound edge, but not in unwounded epidermis (Fig. 2c). Thus we conclude that miR-198 restrains keratinocyte migration in steady-state epidermis by suppressing genes that are important for migration.

We then investigated expression of these targets in chronic non-healing ulcer wounds from patients with diabetes mellitus, in which wound healing is defective, and observed lower expression of PLAUI, DIAPH1 and LAMC2 (Fig. 2c, right panel) than in healing wounds. Persistent high levels of miR-198 were detected at the chronic-wound edge ( $n = 8$ ), suggesting an explanation for the absence or low levels of its target gene products (Fig. 2d). Furthermore, the absence of FSTL1 protein at the wound edge suggests that the FSTL1-miR-198 switch described above is non-functional in chronic wounds (Fig. 2d and Supplementary Fig. 10).

In an attempt to understand the regulation of the post-transcriptional switch that directs the transcript to function as a pri-miRNA or an mRNA, we analysed the sequence of the pre-miR-198 in the 3'-UTR of the *FSTL1* transcript. The presence of a GUG motif (Fig. 1a) within the terminal loop suggests that miR-198 belongs to a cohort of miRNAs processed by KSRP that binds to the specific G-rich motif<sup>16</sup>. RNA-binding-protein immunoprecipitation (RIP) (Fig. 3a and Supplementary Fig. 11a) and RNA gel retardation assays (Fig. 3b and Supplementary Fig. 11b) confirmed binding of KSRP to the GUG motif of pre-miR-198 in the 3'-UTR of *FSTL1* mRNA in normal epidermal keratinocytes. Formation of an RNA-protein complex with the wild-type probe (GUG motif), but not with a mutant probe (CUC motif), confirms the specificity of binding. Addition of recombinant KSRP to an *in vitro* miRNA processing assay yielded a significant increase in mature miR-198 with wild-type (GUG motif) but not with mutant (CUC motif) sequences, confirming the role of KSRP in miR-198 processing (Supplementary Fig. 12a, b).

In loss-of-function assays using a gene-specific siRNA against *KSRP*, detection of low levels of mature miR-198 with a corresponding increase in *FSTL1* mRNA supports the essential role of KSRP in switching on miR-198 processing (Fig. 3c). This suggests that the mere

presence of a miR-198 precursor stem-loop in *cis* cannot efficiently induce nuclear miR-198 processing. Adding another layer of complexity, we demonstrate that processing of exonic miR-198 is dependent on a *trans*-acting RNA-binding protein, KSRP<sup>16</sup>. In the absence of KSRP, miR-198 processing fails and *FSTL1* transcript now functions as an mRNA, resulting in expression of the FSTL1 protein.

TGF- $\beta$ 1 (but not FGF2 or PDGF-AB) can regulate this switch, suppressing miR-198 generation by downregulating KSRP production, to indirectly promote FSTL1 expression (Fig. 3d and Supplementary Fig. 13a-d). Increase in transcript abundance of miR-198 targets and *FSTL1* are independent of *de novo* transcription, as was confirmed by actinomycin-D inhibition of transcription (Supplementary Figs 14a, b and 15a, b). Thus TGF- $\beta$ 1 signalling promotes transcript stability of *FSTL1* and miR-198 targets.

Blocking the processing of miR-198 using siRNA against *DROSHA* leads to an increase in transcript abundance of miR-198 targets and *FSTL1* (Supplementary Figs 14c and 15c, d). Functional inhibition of miR-198 with anti-miR-198 results in increased protein expression of targets (Supplementary Fig. 14d). However, no change in FSTL1 expression with anti-miR-198 (Supplementary Fig. 15e) confirms that *FSTL1* is not a target of miR-198. In summary, TGF- $\beta$ 1 promotes the stability of *FSTL1* by downregulating KSRP, which is essential for miR-198 processing, providing a mechanism for post-transcriptional regulation of *FSTL1* and miR-198-target mRNAs.

The KSRP 3'-UTR has a highly conserved binding site for miR-181a<sup>17</sup>, a TGF- $\beta$ 1-induced miRNA (Supplementary Fig. 16a). A concomitant downregulation of KSRP suggests a link between TGF- $\beta$ 1 and KSRP mediated by miR-181a. Detection of miR-181a as early as 3 h after injury in explant wound assays suggested that repression of KSRP by TGF- $\beta$ 1 is potentially mediated by miR-181a (Supplementary Fig. 16b). Significant downregulation of luciferase activity upon co-transfection with miR-181a and wild-type (but not mutant) KSRP 3'-UTR confirmed that KSRP is a direct target of miR-181a (Supplementary Fig. 16c). This link between KSRP and TGF- $\beta$ 1 is further supported by the detection of KSRP in normal epidermal keratinocytes in the absence of TGF- $\beta$ 1 (Fig. 3e, upper panel). However, upon injury TGF- $\beta$ 1 downregulates KSRP (Fig. 3e, middle panel), thus facilitating

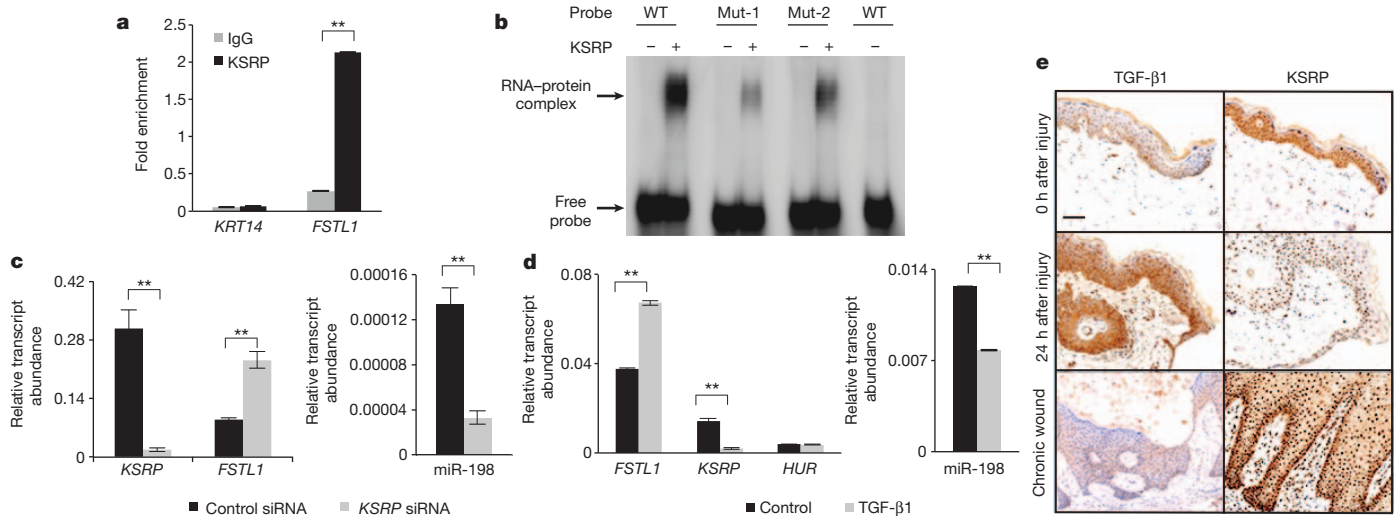


**Figure 3 | KSRP and TGF- $\beta$ 1 regulate the choice between expression of miR-198 or FSTL1.** **a**, RNA immunoprecipitation from keratinocyte lysates using anti-KSRP antibody or IgG control. qRT-PCR showing fold enrichment of transcripts reveals specific binding of KSRP protein to *FSTL1* mRNA but not to the most abundant mRNA species, *KRT14* ( $n = 3$ ). **b**, RNA gel retardation assay showing binding of KSRP to the GUG motif in the loop of the pre-miR-198 transcript and abrogation of binding with mutant CUC motif in this site (Mut-1). Mutation of the GG motif in the stem of the pre-miR-198 transcript to CC results only in a modest loss of binding (Mut-2). RNA-protein complex was

observed only with KSRP, not with a BSA control (last lane) ( $n = 3$ ). **c**, Histogram representing relative transcript abundance in keratinocytes transfected with control or gene-specific siRNA against KSRP ( $n = 3$ ). **d**, Histogram representing relative transcript abundance in keratinocytes treated with TGF- $\beta$ 1 or control ( $n = 3$ ). Student's *t*-test was used to calculate *P* value. Error bars denote mean  $\pm$  s.e.m. **e**, Immunohistochemistry with TGF- $\beta$ 1 (left panel) and KSRP antibody (right panel) on normal skin explants and chronic-wound sections ( $n = 5$ ). Scale bars, 100  $\mu$ m.

the expression of FSTL1. This suggests that the observed low levels of TGF- $\beta$ 1 and absence of TGF- $\beta$ 1 receptors in chronic wounds<sup>18,19</sup> may directly contribute to constitutive expression of miR-198. In support of this argument, we observe higher expression of KSRP and low levels of TGF- $\beta$ 1 in chronic wounds (Fig. 3e, lower panel). Thus the dysfunctional FSTL1-miR-198 switch that is the potential cause of impaired keratinocyte migration and loss of re-epithelialization culminating in non-healing chronic wounds may be a consequence of defective TGF- $\beta$  signalling.

Keratinocyte migration and re-epithelialization is essential for wound healing, when rapid wound closure is critical to restore barrier function and integrity of skin<sup>20,21</sup>. Data presented here describe a regulatory molecular switch that directly controls keratinocyte migration. At homeostasis a cohort of epidermal genes required for keratinocyte migration are kept suppressed by miR-198. Inappropriate expression of miR-198 may not only restrict migration<sup>22</sup> but could also contribute to decreased fibrinolysis and impaired matrix deposition in chronic diabetic ulcers<sup>23,24</sup> by inhibiting the expression of *PLAU* and *LAMC2*. At the non-healing edge of diabetic ulcers, keratinocytes proliferate<sup>25,26</sup> but fail to migrate. Our data suggest that failure to switch off miR-198 and absence of FSTL1 results in failure of these wounds to heal: by inhibiting multiple genes involved in various facets of keratinocyte migration, miR-198 may effectively prevent cell migration and re-epithelialization in chronic wounds (Supplementary Fig. 17).

The FSTL1-miR-198 'see-saw' seems to be a unique regulatory switch critical for wound healing, and in its elucidation we identify miR-198 as a potential molecular biomarker for non-healing wounds. Chronic wounds in patients with diabetes mellitus are a major global health burden and the most common cause of lower extremity amputations<sup>5,27,28</sup>. Targeting miR-198 and modulation of the defective switch in wound-healing disorders pose exciting possibilities as combinatorial topical therapeutics to improve patient outcomes.

## METHODS SUMMARY

**Human skin and ex vivo organ culture and injury assay.** *Ex vivo* injury assays were carried out using a human skin organ culture model system as described previously<sup>19</sup>. Tissue samples were processed for histology or RNA analysis at the indicated time points after injury. For immunohistochemistry, tissue samples were fixed before dehydration and embedded in paraffin blocks. Skin biopsies were excised from the margins of chronic non-healing ulcers of diabetic patients, before scheduled amputations. Samples were processed as above for immunohistochemistry. Chronic-wound biopsy samples were collected from patients ( $n = 8$ ) between the ages of 45 and 55 years old.

This study was approved by the local, domain-specific ethical review board in accordance with the Declaration of Helsinki. All participants gave written, informed consent.

**Full Methods** and any associated references are available in the online version of the paper.

Received 8 February 2012; accepted 3 January 2013.

Published online 10 February 2013.

- Anderson, P. Post-transcriptional regulons coordinate the initiation and resolution of inflammation. *Nature Rev. Immunol.* **10**, 24–35 (2010).
- Hinske, L. C., Galante, P. A., Kuo, W. P. & Ohno-Machado, L. A potential role for intragenic miRNAs on their hosts' interactome. *BMC Genomics* **11**, 533 (2010).
- Shibanuma, M., Mashimo, J., Mita, A., Kuroki, T. & Nose, K. Cloning from a mouse osteoblastic cell line of a set of transforming-growth-factor- $\beta$ 1-regulated genes, one of which seems to encode a follistatin-related polypeptide. *Eur. J. Biochem.* **217**, 13–19 (1993).
- Gurtner, G. C., Werner, S., Barrandon, Y. & Longaker, M. T. Wound repair and regeneration. *Nature* **453**, 314–321 (2008).

- Blakytyn, R. & Jude, E. The molecular biology of chronic wounds and delayed healing in diabetes. *Diabet. Med.* **23**, 594–608 (2006).
- Banerjee, J., Chan, Y. C. & Sen, C. K. MicroRNAs in skin and wound healing. *Physiol. Genomics* **43**, 543–556 (2011).
- Tan, S., Li, R., Ding, K., Lobie, P. E. & Zhu, T. miR-198 inhibits migration and invasion of hepatocellular carcinoma cells by targeting the HGF/c-MET pathway. *FEBS Lett.* **585**, 2229–2234 (2011).
- Cai, X., Hagedorn, C. H. & Cullen, B. R. Human microRNAs are processed from capped, polyadenylated transcripts that can also function as mRNAs. *RNA* **10**, 1957–1966 (2004).
- Hambrock, H. O. et al. Structural characterization of TSC-36/Flik: analysis of two charge isoforms. *J. Biol. Chem.* **279**, 11727–11735 (2004).
- Kroeze, K. L. et al. Autocrine regulation of re-epithelialization after wounding by chemokine receptors CCR1, CCR10, CXCR1, CXCR2, and CXCR3. *J. Invest. Dermatol.* **132**, 216–225 (2012).
- He, Y., Esser, P., Heinemann, A., Bruckner-Tuderman, L. & Has, C. Kindlin-1 and -2 have overlapping functions in epithelial cells implications for phenotype modification. *Am. J. Pathol.* **178**, 975–982 (2011).
- Freedberg, I. M., Tomic-Canic, M., Komine, M. & Blumenberg, M. Keratins and the keratinocyte activation cycle. *J. Invest. Dermatol.* **116**, 633–640 (2001).
- Lund, L. R. et al. Plasminogen activation independent of uPA and tPA maintains wound healing in gene-deficient mice. *EMBO J.* **25**, 2686–2697 (2006).
- Brandt, D. T. et al. Dia1 and IQGAP1 interact in cell migration and phagocytic cup formation. *J. Cell Biol.* **178**, 193–200 (2007).
- Frank, D. E. & Carter, W. G. Laminin 5 deposition regulates keratinocyte polarization and persistent migration. *J. Cell Sci.* **117**, 1351–1363 (2004).
- Trabucchi, M. et al. The RNA-binding protein KSRP promotes the biogenesis of a subset of microRNAs. *Nature* **459**, 1010–1014 (2009).
- Wang, B. et al. TGF $\beta$ -mediated upregulation of hepatic miR-181b promotes hepatocarcinogenesis by targeting TIMP3. *Oncogene* **29**, 1787–1797 (2010).
- Jude, E. B., Blakytyn, R., Bulmer, J., Boulton, A. J. & Ferguson, M. W. Transforming growth factor-beta 1, 2, 3 and receptor type I and II in diabetic foot ulcers. *Diabet. Med.* **19**, 440–447 (2002).
- Pastar, I. et al. Attenuation of the transforming growth factor  $\beta$ -signaling pathway in chronic venous ulcers. *Mol. Med.* **16**, 92–101 (2010).
- Usui, M. L. et al. Morphological evidence for the role of suprabasal keratinocytes in wound reepithelialization. *Wound Repair Regen.* **13**, 468–479 (2005).
- Ridley, A. J. et al. Cell migration: integrating signals from front to back. *Science* **302**, 1704–1709 (2003).
- Daniel, R. J. & Groves, R. W. Increased migration of murine keratinocytes under hypoxia is mediated by induction of urokinase plasminogen activator. *J. Invest. Dermatol.* **119**, 1304–1309 (2002).
- Marutsuka, K., Woodcock-Mitchell, J., Sakamoto, T., Sobel, B. E. & Fujii, S. Pathogenetic implications of hyaluronan-induced modification of vascular smooth muscle cell fibrinolysis in diabetes. *Coron. Artery Dis.* **9**, 177–184 (1998).
- Zorio, E. et al. Fibrinolysis: the key to new pathogenetic mechanisms. *Curr. Med. Chem.* **15**, 923–929 (2008).
- Usui, M. L., Mansbridge, J. N., Carter, W. G., Fujita, M. & Olerud, J. E. Keratinocyte migration, proliferation, and differentiation in chronic ulcers from patients with diabetes and normal wounds. *J. Histochem. Cytochem.* **56**, 687–696 (2008).
- Stojadinovic, O. et al. Molecular pathogenesis of chronic wounds: the role of beta-catenin and c-myc in the inhibition of epithelialization and wound healing. *Am. J. Pathol.* **167**, 59–69 (2005).
- Jeffcoate, W. J. & Harding, K. G. Diabetic foot ulcers. *Lancet* **361**, 1545–1551 (2003).
- Brem, H. & Tomic-Canic, M. Cellular and molecular basis of wound healing in diabetes. *J. Clin. Invest.* **117**, 1219–1222 (2007).

**Supplementary Information** is available in the online version of the paper.

**Acknowledgements** This work was supported by an A\*STAR Investigatorship award to P.S., the Biomedical Research Council of Singapore and the Skin Biology Cluster Platform, A\*STAR. We thank T. Kamala, S. Nama, M. Hisyam and C. Vaz for experimental support and B. Knowles for critical reading of the manuscript.

**Author Contributions** G.M.S. and J.E.A.C. performed most of the experiments; F.E.G. and D.P.L. helped with immunohistochemistry; K.L., T.C.L. and S.S. assisted in procurement of patient samples; V.T. helped in microarray data analysis; E.B.L. assisted in experimental design and contributed to writing the manuscript; and P.S. designed experiments, supervised this work and wrote the manuscript.

**Author Information** Microarray data are deposited in the Gene Expression Omnibus (GEO) under accession numbers GSE37967 and GSE41615. Reprints and permissions information is available at [www.nature.com/reprints](http://www.nature.com/reprints). The authors declare no competing financial interests. Readers are welcome to comment on the online version of the paper. Correspondence and requests for materials should be addressed to P.S. ([prabha.sampath@imb.a-star.edu.sg](mailto:prabha.sampath@imb.a-star.edu.sg)).

## METHODS

**Human skin and *ex vivo* organ culture and injury assay.** *Ex vivo* injury assays were carried out using a human skin organ culture model system as described previously<sup>19</sup>. Skin biopsies were excised from the margins of chronic non-healing ulcers of diabetic patients, before scheduled amputations. Chronic-wound biopsy samples were collected from patients ( $n = 8$ ) between the ages of 45 and 55 years old. **Cell culture.** N/TERT-1 keratinocytes derived from normal human epidermal keratinocytes and immortalized with the telomerase catalytic subunit were used for experiments. Cells were cultured in keratinocyte serum-free medium (Life Technologies) supplemented with  $0.2 \text{ ng ml}^{-1}$  of epidermal growth factor (EGF),  $25 \text{ } \mu\text{g ml}^{-1}$  of bovine pituitary extract,  $0.4 \text{ mM}$   $\text{CaCl}_2$  and penicillin/streptomycin. Cell cultures were maintained at low confluence to prevent differentiation and passaged before they reached 40% confluence.

Lenti-X 293T cells (Clontech) were cultured in DMEM with 10% fetal calf serum containing penicillin/streptomycin.

**Antibodies.** Antibodies used in this study are as follows: goat anti-FSTL1 antibody (Abcam), rabbit anti-DIAPH1 antibody (Cell Signaling), mouse anti-LAMC2 antibody (Santa Cruz Biotechnology), rabbit anti-PLAU (Abcam), mouse anti-TGF- $\beta$ 1 (Novocastra), rabbit anti-KSRP antibody (Bethyl Laboratories) and chicken anti-goat Alexa 488 (Molecular Probes, Invitrogen).

**RNA isolation from skin.** Total RNA from skin samples was isolated by a two-step RNA-isolation method. Skin biopsies were homogenized in TRIzol and RNA was extracted as per the manufacturer's protocol (Life Technologies). Precipitated RNA was further subjected to column purification (Exiqon) and subjected to quality-control analysis by NanoDrop (Thermo Scientific) and Bioanalyzer (Agilent Technologies) to assess the concentration and integrity of isolated RNA.

**Quantification of miRNA and mRNA.** Total RNA (50 ng) was reverse transcribed using miRNA-specific primers (Applied Biosystems, Life Technologies) according to TaqMan miRNA Reverse Transcription Kit (Life Technologies). Real-time analysis of miRNA expression was carried out using TaqMan probes. Cycle threshold (CT) values of miRNAs were normalized against *U6* small nuclear RNA internal control and values plotted as relative transcript abundance. Total RNA (500 ng) was reverse transcribed with Superscript III (Life Technologies) and anchored oligodT primer as per the manufacturer's instructions. Transcript levels were measured by qRT-PCR using SYBR Green PCR Master Mix (Applied Biosystems, Life Technologies) using gene-specific primers listed in Supplementary Table 1. CT values were normalized to endogenous *RPLP0* values, which have been specifically recommended for use in keratinocytes. For the detection of *FSTL1* mRNA by semiquantitative RT-PCR, the PCR amplification cycles were limited to 28. All experiments were performed in three biological replicates and representative figures are shown.

**Microarray analysis.** N/TERT-1 keratinocytes were transfected with 50 nM of negative control or miR-198 mimics using DharmaFECT transfection reagent according to manufacturer's protocol. Forty-eight hours after transfection, total RNA was isolated using the Exiqon miRCURY RNA Isolation Kit. Two-hundred-and-fifty nanograms of total RNA was converted into biotinylated antisense RNA (cRNA) using a TargetAmp Nano-g Biotin-aRNA Labelling Kit (Epicentre). Seven-hundred-and-fifty nanograms of biotinylated cRNA was hybridized to HT-12 v4 expression bead chip (Illumina) using samples in triplicate. Hybridization, washing and scanning were performed according to the manufacturer's protocol. Data extracted were normalized and analysed using Illumina BeadStudio. Similar global expression profiling by microarray was performed on N/TERT-1 keratinocytes transfected with siRNA against human *FSTL1* at 48 h after transfection. Microarray data have been deposited in the Gene Expression Omnibus database under accession numbers GSE37967 and GSE41615.

**In vitro scratch-wounding assays.** N/TERT-1 keratinocytes were transfected with miRIDIAN miRNA mimics at 50% confluence (Dharmacon). As a control, a non-targeting sequence-encoding *Caenorhabditis elegans* miR-239b with no known human targets was used. Cells were transfected with 50 nM miRNA mimic using Dharmafect 1 according to the manufacturer's protocol. Transfection efficiency was assessed on the basis of co-transfection of SiGLO Red transfection indicator. Using an IncuCyte wound maker, scratch wounds were made simultaneously in all culture wells 48 h after transfection and scratch area was monitored over 24 h using IncuCyte live-cell imaging system (Essen BioScience). Scratch-wound results were compiled from six wells with one scratch in each well. At the 24-h time point, closure of the control scratch wound was observed. To knock-down *FSTL1*, *DIAPH1*, *PLAU* and *LAMC2*, 50 nM of smart-pool siRNA against the open reading frame sequence (Dharmacon) was used to transfect keratinocytes. A non-targeting siRNA was transfected as a negative control. Transfection was performed using Dharmafect 1 transfection reagent. For rescue experiments using target gene overexpression, 100 ng of *DIAPH1*, *LAMC2* and *PLAU* open reading frame or an empty vector construct (Origene) was co-transfected along with miR-198 mimic using FuGENE 6 transfection reagent. Scratch wounds were

created 48 h after transfection and wound closure was measured by IncuCyte live-cell imaging system.

**Inhibition of miR-198/DROSHA and effect on target gene expression.** 5' fluorescein-labelled, phosphorothioate-modified power inhibitors against mature miR-198 (anti-miR-198), or a negative control inhibitor, were purchased from Exiqon. N/TERT-1 cells were transfected with 50 nM of the inhibitors using Dharmafect 1 transfection reagent. Forty-eight hours after transfection, target proteins were subjected to immunocytochemistry using respective antibodies. For the knockdown of *DROSHA*, N/TERT-1 cells were transfected with smart-pool siRNAs against human *DROSHA* and total RNA was isolated at 3 days after transfection.

**Proliferation assays.** N/TERT-1 keratinocytes were monitored by image analysis for 48 h after transfection. Cells were transfected at low density, and 24 h after transfection imaging was carried out in subconfluent states using IncuCyte live-cell imaging system (Essen BioScience). Proliferation was calculated by IncuCyte software algorithm to output a proliferation index corresponding to change in confluence of each well. These measurements are an average of six wells for each treatment.

**Immunohistochemistry.** Five-micrometre tissue sections were mounted on poly-L-lysine-coated glass slides (Thermo Scientific). After de-paraffinization, endogenous peroxidase was quenched by immersing the slides in 3% hydrogen peroxide in methanol. After incubation in 10% goat serum, slides were incubated with the primary antibody. Slides were subjected to thorough rinsing before incubation with species-matched secondary horseradish peroxidase (HRP)-labelled polymer antibodies (Dako). Chromogen 3,3'-diaminobenzidine (Dako) was used as substrate for colour development. Slides were counterstained with haematoxylin before dehydration and mounting with DPX (Sigma). Images were acquired on a Zeiss Axioimager microscope.

**Immunocytochemistry.** Keratinocytes cultured on coverslips were fixed using cold acetone/methanol. Coverslips were submerged in 5% BSA in PBS to block non-specific adherence and incubated with primary antibodies overnight at 4 °C. Cells were rinsed in PBS before incubation with species-matched secondary antibodies conjugated to Alexa probes (Molecular Probes, Invitrogen). After counterstaining with DAPI (4',6-diamidino-2-phenylindole;  $100 \text{ ng ml}^{-1}$ ), cells were mounted using FluorSave mounting media and image acquisition was done in Olympus FluoView FV1000.

**miRNA *in situ* hybridization.** Five-micrometre tissue sections were incubated with LNA probes (5'-DIG-labelled LNA probes specific for miR-198 or scrambled probe with no homology to known vertebrate miRNAs (Exiqon)) in hybridization buffer (Roche) at 51 °C for 4 h. After stringent washes, sections were blocked with 10% goat serum and further incubated with anti-DIG alkaline phosphatase (Roche) overnight at 4 °C. Sections were washed in PBS-T (0.1%) and miRNA-bound LNA probes were detected by Fast Red Substrate (Panomics). After counterstaining with DAPI, slides were mounted using FluorSave (Merck). Image acquisition was performed with Olympus FluoView FV1000 using TRITC filter. LNA probes designed for mature miRNAs do not recognize the precursor or primary miRNAs.

**Luciferase assay.** For the generation of chimaeric constructs with the target 3'-UTR linked to a firefly reporter gene, the 3'-UTR fragment spanning the miR-198-binding site was amplified from the parental 3'-UTR clone (GeneCopoeia) using specific primers and subcloned into the multiple cloning site of pmirGLO Dual-Luciferase miRNA-target expression vector.

The *FSTL1* 3'-UTR with (2.7-kb full-length 3'-UTR) and without pre-miR-198 stem-loop (0.9-kb truncated 3'-UTR) were amplified and subcloned from the parental full-length construct (Origene). The chimaeric constructs were co-transfected with miR-198 or a non-targeting negative control mimic using Effectene (Qiagen) in 293T cells. Firefly and Renilla luciferase activities were measured 48 h after transfection using a Dual-Luciferase reporter assay system (Promega). The firefly luminescence was normalized to Renilla luminescence values as an internal control for transfection efficiency. For the mutant 3'-UTRs in miR-198 targets, the miR-198 binding site, UCUGGAC, was converted to UUCAAGU using QuikChange Site-Directed Mutagenesis Kit (Stratagene) as per the manufacturer's instructions.

**RNA-binding-protein immunoprecipitation.** Keratinocytes, either treated with  $5 \text{ ng ml}^{-1}$  of TGF- $\beta$ 1 or mock treated, were lysed in radioimmunoprecipitation assay (RIPA) buffer. After clarifying the lysate at  $13,000g$  for 10 min, the cell extract was incubated with  $2 \text{ } \mu\text{g}$  rabbit KSRP antibody (Bethyl Laboratories) or control rabbit IgG, overnight at 4 °C. The antigen-antibody complex was pulled down with  $25 \text{ } \mu\text{l}$  (resin volume) of protein A sepharose pre-equilibrated with RIPA buffer at 4 °C for 1 h. The immunoprecipitated RNA bound to the resin was extracted using the Exiqon miRCURY RNA Isolation Kit. Reverse transcription of the immunoprecipitated RNA as well as the input extract RNA (10%) was carried out with Superscript III (Invitrogen) reverse transcriptase. Four microlitres of the complementary DNA was used in qRT-PCR using primers spanning



pre-miR-198 in the primary transcript. Results were normalized to input RNA levels and plotted as fold enrichment compared to the IgG control RIP.

For RIP with skin samples, biopsies were snap frozen immediately in liquid nitrogen at 0 h or 24 h after injury. The epidermis was peeled off from the dermis after disperse treatment overnight and homogenized in RIPA buffer, clarified and processed for RIP as above.

**In vitro precursor miRNA processing assay.** For preparation of pre-miR-198, pBluescript KS constructs containing pre-miR-198 sequence (obtained from miRBase) under the T7 RNA polymerase promoter were linearized and transcribed in the presence of radioactive [ $^{32}$ P]-UTP. Transcripts were resolved through 8% polyacrylamide gel, detected by autoradiography and gel purified in 0.3 M NaCl, overnight at 4 °C. The purified pre-miR-198 was denatured at 90 °C for 2 min and re-folded by slow cooling to room temperature (22 °C) in a buffer containing 25 mM Tris-Cl, pH 7.4, 100 mM NaCl, 5 mM MgCl<sub>2</sub> and 10% glycerol. The re-folded pre-miR-198 was stored in aliquots at -20 °C until further use. For the preparation of cytoplasmic extracts as the source of Dicer enzyme, subconfluent 293T cells were lysed in buffer containing 25 mM Tris-Cl, pH 7.4, 150 mM NaCl, 5 mM MgCl<sub>2</sub>, 0.25% NP-40 and protease inhibitor cocktail (Roche) for 10 min on ice. After clarifying the extract at 10,000g for 10 min, the protein concentration was measured using the BCA assay kit (Pierce Biotechnology).

*In vitro* precursor-miRNA processing assay was carried out with 50 µg of 293T extract and pre-miR-198 in the presence or absence of recombinant KSRP protein

(Origene) for 60 min at room temperature. Samples were processed with phenol-chloroform extraction and resolved through 8% denaturing poly acrylamide gel electrophoresis. To track the position of mature miR-198, the pre-miR-198 was treated with ShortCut RNase III (New England Biolabs) and processed as above. Low-range ssRNA ladder (New England Biolabs) and microRNA marker (New England Biolabs) were used to confirm the size of the reaction product. Reaction products were exposed to storage phosphor screens (GE Healthcare) and detected using Storm phosphorImager (GE Healthcare).

**Gel retardation assay.** The pre-miR-198 substrate for gel retardation assay was prepared as described above. Pre-miR-198 transcripts with mutated terminal loop and stem sequences (Supplementary Fig. 7b) were generated by mutating the parental plasmid (pBSKS) constructs using QuikChange Site-Directed Mutagenesis Kit (Stratagene). Recombinant KSRP protein (0.5 µM) was incubated with the wild-type or mutant pre-miR-198 transcripts in 20 µl of reaction buffer containing 30 mM Tris-HCl, pH 7.4, 5 mM MgCl<sub>2</sub>, 50 mM KCl, 0.5 mM DTT, 40 U ml<sup>-1</sup> RNaseOUT, 250 µg ml<sup>-1</sup> of yeast transfer RNA and 10% glycerol. After 30 min at room temperature, reaction products were resolved through 6% native polyacrylamide gel electrophoresis. The gel was dried and the protein-RNA complex and unbound RNA were visualized by phosphorimaging.

**Statistical analysis.** Values are reported as the mean ± the standard error. Statistical significance between two samples was determined with two-tailed Student's *t*-test using GraphPad InStat 3.0 software (GraphPad Software).

# MicroRNA-34a regulates cardiac ageing and function

Reinier A. Boon<sup>1\*</sup>, Kazuma Iekushi<sup>1\*</sup>, Stefanie Lechner<sup>2</sup>, Timon Seeger<sup>1,3</sup>, Ariane Fischer<sup>1</sup>, Susanne Heydt<sup>1</sup>, David Kaluza<sup>1</sup>, Karine Tréguer<sup>1</sup>, Guillaume Carmona<sup>1</sup>, Angelika Bonauer<sup>1</sup>, Anton J. G. Horrevoets<sup>4</sup>, Nathalie Didier<sup>5</sup>, Zenawit Girmatsion<sup>3</sup>, Peter Biliczki<sup>3</sup>, Joachim R. Ehrlich<sup>3</sup>, Hugo A. Katus<sup>6,7</sup>, Oliver J. Müller<sup>6,7</sup>, Michael Potente<sup>1,3,†</sup>, Andreas M. Zeiher<sup>3,7</sup>, Heiko Hermeking<sup>2</sup> & Stefanie Dimmeler<sup>1,7</sup>

Ageing is the predominant risk factor for cardiovascular diseases<sup>1</sup> and contributes to a significantly worse outcome in patients with acute myocardial infarction<sup>2</sup>. MicroRNAs (miRNAs) have emerged as crucial regulators of cardiovascular function and some miRNAs have key roles in ageing<sup>3,4</sup>. We propose that altered expression of miRNAs in the heart during ageing contributes to the age-dependent decline in cardiac function. Here we show that miR-34a is induced in the ageing heart and that *in vivo* silencing or genetic deletion of miR-34a reduces age-associated cardiomyocyte cell death. Moreover, miR-34a inhibition reduces cell death and fibrosis following acute myocardial infarction and improves recovery of myocardial function. Mechanistically, we identified PNUTS (also known as PPP1R10) as a novel direct miR-34a target, which reduces telomere shortening, DNA damage responses and cardiomyocyte apoptosis, and improves functional recovery after acute myocardial infarction. Together, these results identify age-induced expression of miR-34a and inhibition of its target PNUTS as a key mechanism that regulates cardiac contractile function during ageing and after acute myocardial infarction, by inducing DNA damage responses and telomere attrition.

To study the ageing process in the heart, we compared aged mice (18–20 months old) with young mice (6–8 weeks old). As expected, hearts of aged mice showed increased fibrosis (Fig. 1a), hypertrophy (Supplementary Fig. 2a), shorter telomeres (Fig. 1b) and increased cardiomyocyte apoptosis (Fig. 1c). Expression profiling of miRNAs isolated from the hearts of young and aged mice identified a number of dysregulated miRNAs that are known to have a role in cardiac (patho)physiology and in senescence (Fig. 1d and Supplementary Tables 1 and 2). For example, miR-21 and miR-574-5p are induced in the failing heart<sup>5,6</sup>, and miR-146a (ref. 7) and miR-29 (ref. 8) increase during senescence, whereas other previously described age-associated miRNAs were not regulated<sup>9</sup>. Interestingly, the entire miR-34 family (comprising miR-34a, b and c) (Fig. 1e) was significantly upregulated in aged hearts, whereas several cell-type enriched miRNAs were unchanged (Supplementary Fig. 2b). Furthermore, miR-34a levels, but not levels of the muscle-enriched miR-1 and miR-133, also significantly correlated with age in human heart biopsies ( $n = 21$ ), whereas levels of cardiac-enriched miR-208 declined (Fig. 1f, Supplementary Fig. 2c). As miR-34 is involved in apoptosis and senescence<sup>7,10,11</sup>, we focused on this miRNA family.

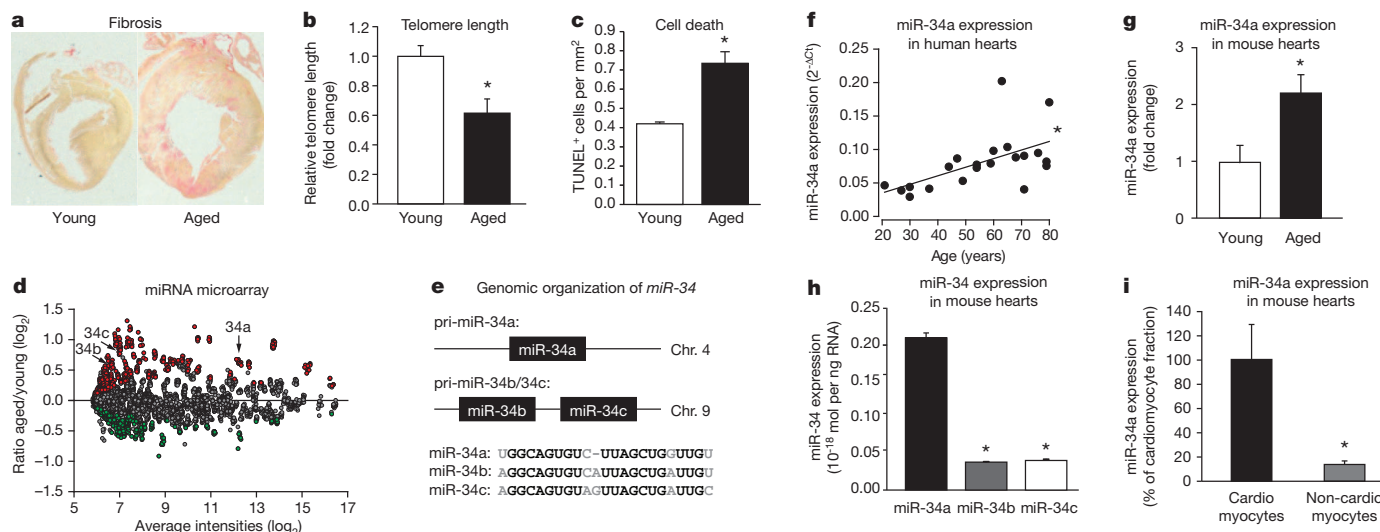


**Figure 1 | Ageing induces cardiac miR-34 expression.** **a**, Fibrosis staining of hearts from young (6–8 weeks old) and aged (18–20 months old) C57/Bl6 mice. **b**, Real-time PCR-based telomere length measurement of young and aged hearts (**b**) and cell death quantification using terminal deoxynucleotidyl transferase dUTP nick end labelling (TUNEL) (**c**). **d**, Microarray profiling results of miRNAs in aged and young hearts. **e**, Schematic representation of the primary transcripts encoding miR-34a, b, c, chromosomal location and

sequence homologies in mouse. **f**, RNA was isolated from human atrium biopsies and miR-34a expression was measured by real-time PCR. **g**, Real-time PCR expression analysis of miR-34a in aged and young mice hearts. **h**, Quantitative real-time PCR for miR-34a, b and c on RNA from total young mouse heart. **i**, Young heart cell-types were separated using Langendorff-perfusion digestion and miR-34a levels were measured by real-time PCR.  $n \geq 3$  for all experiments,  $*P < 0.05$ . Error bars depict s.e.m.

<sup>1</sup>Institute for Cardiovascular Regeneration, Centre of Molecular Medicine, Goethe University Frankfurt, 60590 Frankfurt, Germany. <sup>2</sup>Experimental and Molecular Pathology, Institute of Pathology, Ludwig-Maximilians-Universität München, 80337 Munich, Germany. <sup>3</sup>Department of Cardiology, Internal Medicine III, Goethe University, 60590 Frankfurt, Germany. <sup>4</sup>Department of Molecular Cell Biology and Immunology, VU University Medical Center, 1081BT Amsterdam, the Netherlands. <sup>5</sup>Myology Group, UMR S787 INSERM, Université Pierre et Marie Curie Paris VI, Institut de Myologie, Pitie-Salpêtrière, Paris Cedex, France. <sup>6</sup>Internal Medicine III, Heidelberg University Hospital, 69120 Heidelberg, Germany. <sup>7</sup>German Center for Cardiovascular Research DZHK, 13347 Berlin, Germany. <sup>†</sup>Present address: Max-Planck-Institute for Heart and Lung Research, 61231 Bad Nauheim, Germany.

\*These authors contributed equally to this work.

Quantitative real-time polymerase chain reaction (PCR) confirmed the upregulation of miR-34a in aged mice (Fig. 1g) and showed that miR-34a is the predominantly expressed miR-34 family member in the heart (Fig. 1h). Moreover, miR-34a levels were higher in isolated cardiomyocytes compared to non-cardiomyocytes (Fig. 1i). These data were further corroborated by miR-34a *in situ* hybridization in mouse heart sections (Supplementary Fig. 3).

As miR-34a has been shown to induce apoptosis in cancer cell lines<sup>11</sup> and apoptosis is a fundamental feature of ageing cardiomyocytes (Fig. 1c), we next assessed whether miR-34a has a role in cardiomyocyte apoptosis. Inhibition of miR-34a in rat neonatal cardiomyocytes reduced H<sub>2</sub>O<sub>2</sub>-induced apoptosis, whereas pre-miR-34a overexpression augmented this apoptosis (Supplementary Fig. 4). To study the role of miR-34a in apoptosis *in vivo*, we inhibited miR-34a by antisense oligonucleotides (antagomirs; Ant-34a)<sup>12</sup>, which reduced cardiac expression of miR-34a (Supplementary Fig. 5). To investigate whether miR-34a contributes to age-associated cell death in the heart, we treated 18-month-old mice with 8 mg kg<sup>-1</sup> Ant-34a, collected the hearts after 1 week and histologically quantified dead cells. Ant-34a treatment reduced the number of dead cells compared to controls (Fig. 2a). To further establish a role for miR-34a in cardiac ageing, we analysed cardiac contractile function by echocardiography in aged (73–83 weeks old) *miR-34a* knockout (*miR-34a*<sup>-/-</sup>) mice (Fig. 2b). Whereas cardiac function in young *miR-34a*<sup>-/-</sup> mice was comparable to wild-type littermates (Supplementary Fig. 6), the age-associated decline in cardiac function observed in the wild-type mice was prevented in *miR-34a*<sup>-/-</sup> mice (Fig. 2b). Furthermore, aged *miR-34a*<sup>-/-</sup> mice hearts were less hypertrophic and showed less cell death, compared to wild-type controls (Fig. 2c and Supplementary Fig. 6). To further substantiate a role of miR-34a in cardiac ageing phenotypes, we analysed *Ku80*<sup>-/-</sup> mice (*Ku80* is also known as *Xrcc5*), a genetic mouse model of accelerated ageing. In *Ku80*<sup>-/-</sup> mice cardiac miR-34a levels increased and pharmacological inhibition of miR-34a by locked nucleic acid (LNA)-based anti-miRs abolished deterioration of cardiac contractile function (Fig. 2d and Supplementary Fig. 7).

Because apoptosis and fibrosis are also hallmarks after an acute myocardial infarction (AMI) and age aggravates cardiac dysfunction after AMI, we next assessed the role of miR-34a in a mouse model of AMI. miR-34a expression was significantly upregulated in the border zone of the myocardial infarction (Fig. 2e). To test whether miR-34a contributes to cardiac dysfunction after AMI, we induced AMI in mice and injected antagomirs or LNA-based anti-miRs. Whereas the extent of myocardial infarction was similar at day 0, cardiac contractile function at two weeks after myocardial infarction was significantly better in antagomir Ant-34a or LNA-based anti-miRs treated mice compared to controls, as measured by wall motion score index and ejection fraction (Fig. 2f and Supplementary Fig. 8). These findings were confirmed by analysis of cell death and fibrosis on histological sections of the hearts (Fig. 2g–i). The reduction in the number of dead cells was not confined to cardiomyocytes, but also included non-cardiomyocytes (Supplementary Fig. 9). miR-34a was previously shown to induce senescence in endothelial cells<sup>13</sup> and to inhibit pro-angiogenic cell functions<sup>14,15</sup>. Therefore, we also investigated a potential impact of miR-34a inhibition on neovascularization. Indeed, Ant-34a treatment increased capillary density in the border zone of the infarct *in vivo* and miR-34a modulated angiogenic sprouting of human umbilical vein endothelial cells (HUVECs) *in vitro* (Supplementary Fig. 10). These findings indicate that miR-34a inhibition does not only improve cardiomyocyte survival but also has favourable effects on other cell types present in the heart, for example, endothelial cells.

To identify putative target messenger RNAs of miR-34a, we used three microRNA target prediction tools, miRanda, PicTar and Targetscan 5.1 (Supplementary Fig. 11a). The 49 targets, that were predicted by all three algorithms (Supplementary Table 3), were then compared to genes that were downregulated in aged mice (< 1.5-fold), as assessed in genome-wide mRNA expression profiles of aged and

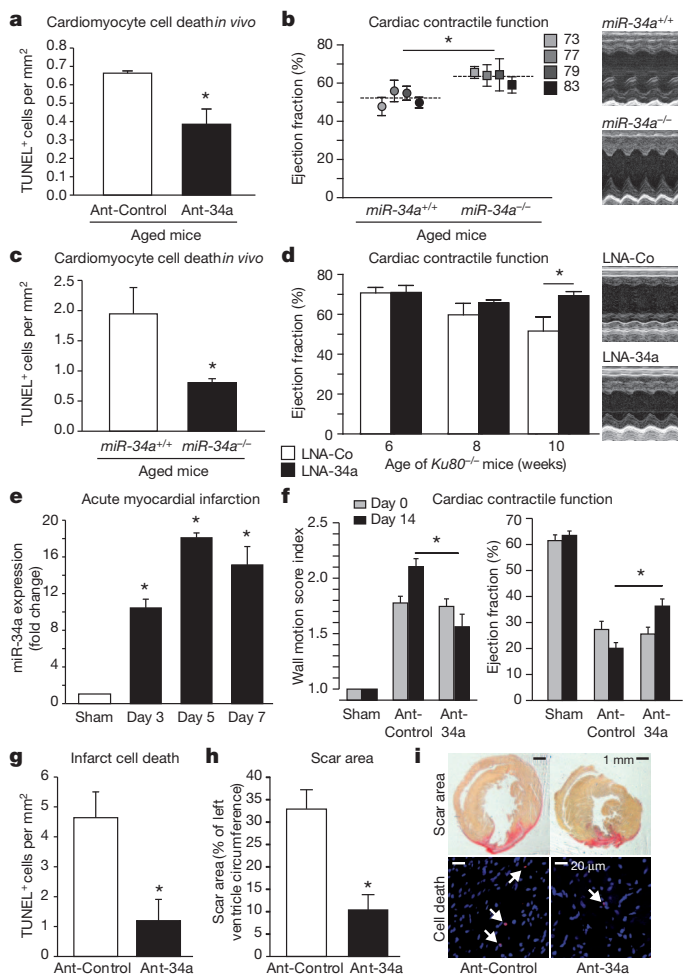


**Figure 2 | miR-34a reduction inhibits age-related and myocardial infarction-induced cardiomyocyte cell death and cardiac function.**

**a**, Cardiomyocyte cell death in aged mice (18 months old) treated with antagomir-34a or scrambled control antagomir. **b**, Echocardiography of *miR-34a*<sup>-/-</sup> mice and *miR-34a*<sup>+/+</sup> littermates at 73, 77, 79 and 83 weeks of age. Representative m-mode echocardiography images on the right. **c**, Cell death in hearts of *miR-34a*<sup>-/-</sup> and wild-type littermates. **d**, Echocardiography in *Ku80*<sup>-/-</sup> mice at 6, 8, and 10 weeks of age that received scrambled control locked nucleic acid modified anti-miRs (LNA-Co) and LNA-34a weekly subcutaneous from 4 weeks of age. Representative m-mode echocardiography images on the right. **e**, RNA was isolated from the border zone of the myocardial infarction at 3, 5 and 7 days after AMI (black bars) or from sham-operated animals (white bar). miR-34a levels were measured by real-time PCR. **f**, Echocardiography of mice subjected to AMI (day 0). After AMI, mice received control antagomir or antagomir-34a. Echocardiographic data are presented as wall motion score index and ejection fraction. **g**, **h**, Histological sections of infarcted hearts four weeks after AMI were analysed for TUNEL-positive cells (**g**) and scar area (**h**). **i**, Representative scar area and TUNEL stainings. White arrows indicate TUNEL-positive cells. *n* ≥ 4 per group for all experiments, \**P* < 0.05. Error bars depict s.e.m.

young mice (Supplementary Table 4). Only one gene was both a predicted target of miR-34a and downregulated by age on the mRNA level, *Ppp1r10* (also known as *Pnuts*; Supplementary Fig. 11b). In line with the post-transcriptional mechanism of action of miRNAs, PNUTS was even more profoundly downregulated at the protein level in aged hearts (Fig. 3a). PNUTS has a role in apoptosis of cancer cell lines<sup>16</sup>, interacts with the telomere regulator TRF2<sup>17</sup>, and is involved in DNA repair<sup>18</sup>, indicating a potential role in ageing. To assess whether PNUTS is a direct target of miR-34a, we generated luciferase reporter constructs, in which the miR-34a seed target or the PNUTS 3' untranslated region (3' UTR) is placed behind the luciferase gene. miR-34a inhibited luciferase activity, whereas no effect was observed when the



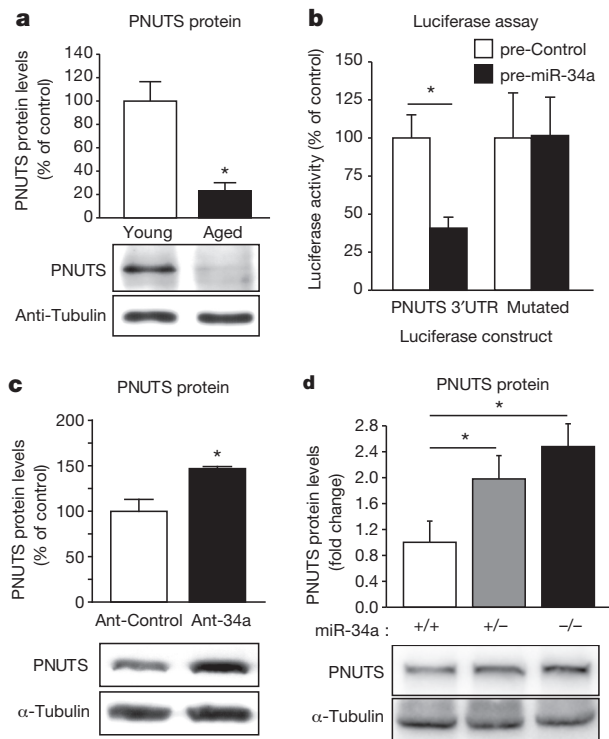


**Figure 3 | miR-34a directly targets PNUTS.** **a**, Western blot for PNUTS protein in aged (18–20 months) and young (6–8 weeks) mice hearts. **b**, Luciferase assay with wild-type PNUTS 3'UTR or PNUTS 3'UTR mutated in the predicted binding site of miR-34a, transfected with pre-miR-34a or control RNA. **c**, Mice were injected with antagomir-34a or control antagomir. Hearts were collected after 6 weeks and PNUTS protein levels were measured by western blot. **d**, PNUTS levels were measured by western blot in hearts of 19–21-week-old *miR-34a*<sup>+/+</sup>, *miR-34a*<sup>+/-</sup> and *miR-34a*<sup>-/-</sup> mice.  $n \geq 3$  for all experiments,  $*P < 0.05$ . Error bars depict s.e.m.

miR-34a target site was mutated (Fig. 3b and Supplementary Fig. 11). Conversely, inhibition of miR-34a induced luciferase activity (Supplementary Fig. 11c). A reverse-transcriptase-based assay confirmed that miR-34a also binds to the PNUTS 3'UTR (Supplementary Fig. 11e). *In vivo*, Ant-34a-mediated inhibition of miR-34a upregulated PNUTS in the heart (Fig. 3c) and genetic deletion of miR-34a also dose-dependently increased cardiac PNUTS levels (Fig. 3d). Together, these results demonstrate that miR-34a directly targets PNUTS.

Then, we determined whether PNUTS inhibits apoptosis of cardiomyocytes. In PNUTS-overexpressing cardiomyocytes,  $H_2O_2$ -induced apoptosis was significantly lower and the miR-34a-mediated enhancement of apoptosis was completely abrogated (Fig. 4a). To assess if PNUTS can also prevent cardiac contractile impairment *in vivo*, we generated adeno-associated virus (AAV9) to overexpress PNUTS under control of a cytomegalovirus-enhanced myosin light chain cardiac promoter (Fig. 4b and Supplementary Fig. 12). Cardiac PNUTS overexpression prevented the deterioration of cardiac contractile function after AMI in mice (Fig. 4b). PNUTS is known to interact with TRF2, and together these proteins have been described to play a role in DNA damage responses (DDR)<sup>18,19</sup>. DNA damage responses can be activated by bona fide DNA damage or by telomere dysfunction, when telomeres are aberrantly recognized as DNA damage, culminating in phosphorylation of CHK2 and apoptosis. Both telomere attrition and defects in DNA repair can cause cardiac dysfunction and cardiomyocyte apoptosis<sup>20–22</sup>. To assess whether inhibition of DNA damage responses could be a possible mechanism for the anti-apoptotic effects of PNUTS, we analysed phosphorylation of CHK2. CHK2 phosphorylation was diminished after ectopic expression of PNUTS in cardiomyocytes (Supplementary Fig. 13). Downregulation of TRF2 using specific small interfering RNAs showed that

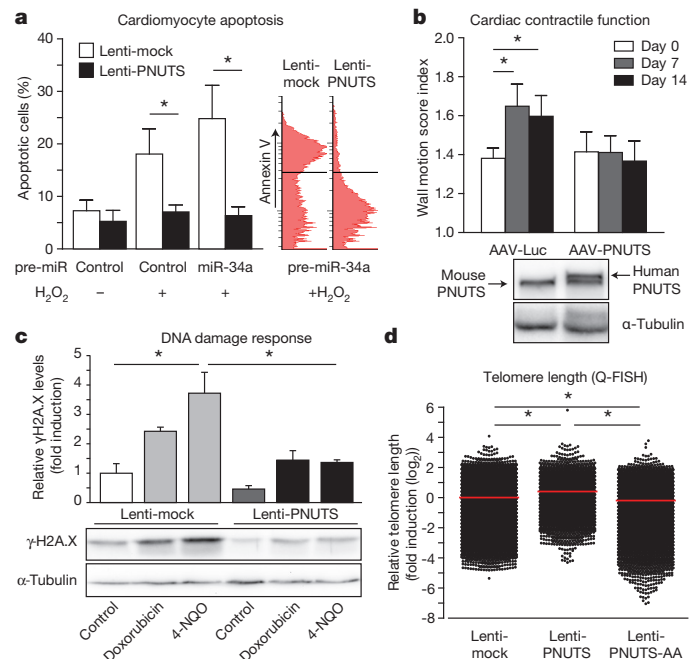


**Figure 4 | PNUTS inhibits apoptosis, telomere attrition and DNA damage response in cardiomyocytes.** **a**, Cardiomyocytes were transduced with mock or PNUTS overexpression lentivirus and, after 3 days, were transfected with pre-miR-34a or control RNA. Apoptosis was stimulated with 100  $\mu$ M  $H_2O_2$  on day 4 and quantified by flow cytometry on day 5. Histograms on the right represent total annexin V signal. **b**, Mice received adeno-associated virus (AAV9) to overexpress human PNUTS (AAV-PNUTS) or firefly luciferase (AAV-Luc) under the control of a cardiac-specific promoter 12–14 days before AMI. Heart function was assessed directly after AMI, after 7 and 14 days by echocardiography. PNUTS protein levels were assessed in hearts at 15 days after AMI. **c**, Cardiomyocytes were transduced with mock or PNUTS overexpression lentivirus and treated with doxorubicin (0.1  $\mu$ M) or 4-nitroquinoline 1-oxide (1  $\mu$ M) for 24 h or left untreated.  $\gamma$ -H2A.X and  $\alpha$ -tubulin were detected by western blot. **d**, Telomere length was assessed in human cardiomyocytes by quantitative fluorescent *in situ* hybridization at 6 days after lentiviral transduction with mock, PNUTS, or mutant PNUTS virus, lacking TRF2 binding capacity (PNUTS-AA). Red line depicts average telomere length per group.  $n \geq 3$  for all experiments,  $*P < 0.05$ . Error bars depict s.e.m.

inhibition of CHK2 activation by PNUTS does not occur in the absence of TRF2 (Supplementary Fig. 13). As DNA damage responses can be caused by DNA damage as well as telomere dysfunction, we assessed the DNA damage marker  $\gamma$ -H2A.X and telomere length in cardiomyocytes. PNUTS reduced DNA damage in cardiomyocytes, as measured by  $\gamma$ -H2A.X levels (Fig. 4c) and, consistently, inhibition of miR-34a also reduced cardiac DNA damage after AMI (Supplementary Fig. 14). Furthermore, PNUTS overexpression, but not TRF2-binding-deficient PNUTS, reduced telomere attrition *in vitro*, without affecting telomerase activity (Fig. 4d and Supplementary Fig. 15). Together these data show that PNUTS inhibits DNA damage response signalling and prevents AMI-induced cardiac contractile dysfunction, whereas deciphering its function during ageing deserves further studies.

In conclusion, our data demonstrate that inhibition of miR-34a reduces age-induced cardiac cell death and functional decline *in vivo*. Moreover, miR-34a is induced after acute myocardial infarction and inhibition of miR-34a enhances cardiac contractile recovery after acute myocardial infarction. miR-34a suppresses the expression of PNUTS, which inhibits telomere erosion, DNA damage response and apoptosis, thus providing a rationale for the pro-apoptotic effects of miR-34a in cardiomyocytes. In addition to PNUTS, miR-34a has other targets, such as SIRT1 (ref. 23), that confers protection against ischaemia reperfusion injury in the heart (Supplementary Fig. 16)<sup>24</sup>. Nevertheless, we demonstrate that the miR-34a–PNUTS axis has

profound effects on cardiac apoptosis, indicating that PNUTS is a key downstream effector of miR-34a. Moreover, our findings that PNUTS is reduced in ageing and regulates telomere maintenance and DNA damage responses provide a plausible mechanism, by which telomeres erode during ageing. Other targets of miR-34a<sup>25</sup> and functions in non-cardiomyocytes<sup>15</sup> could likewise contribute to its detrimental role in cardiac ageing and dysfunction. Finally, our results identify inhibition of miR-34a as a potential therapeutic strategy to improve cardiac contractile function after acute myocardial infarction.

## METHODS SUMMARY

**Laboratory animals, ethics and acute myocardial infarction model.** Male C57BL/6 mice were obtained from Charles River and Janvier. The animal experiments were approved by the Regional Board of the State of Hessen, Germany. Patient material was obtained under informed consent and according to the declaration of Helsinki. Acute myocardial infarction operations were performed as described<sup>26</sup>.

**RNA isolation, real-time PCR and transcriptional profiling.** Total RNA was isolated with miRNeasy kits from Qiagen and real-time PCR with Applied Biosystems microRNA assays run on an Applied Biosystems StepOnePlus. Quantification of real-time PCR was performed using synthetic microRNA sequences in a calibration curve. Transcriptional profiling was performed by DNAsion on the Agilent-v1 platform (570 miRNAs) or on the Affymetrix 430 v2.0 platform (mRNA, full genome).

**Statistical analysis.** Data were analysed with GraphPad Prism 5 using student's *t*-tests when comparing two conditions, or with an analysis of variance (ANOVA) with Bonferroni or Newman-Keuls correction for multiple comparisons. Probability values of less than 0.05 were considered significant and tests were performed two-sided. Data was tested for outliers using the Grubbs outlier test and, if outliers were present, they were removed. Data are presented as mean.

**Full Methods** and any associated references are available in the online version of the paper.

Received 13 April 2011; accepted 16 January 2013.

Published online 20 February 2013.

1. Lakatta, E. G. Age-associated cardiovascular changes in health: impact on cardiovascular disease in older persons. *Heart Fail. Rev.* **7**, 29–49 (2002).
2. Wellenius, G. A. & Mittleman, M. A. Disparities in myocardial infarction case fatality rates among the elderly: the 20-year Medicare experience. *Am. Heart J.* **156**, 483–490 (2008).
3. Small, E. M. & Olson, E. N. Pervasive roles of microRNAs in cardiovascular biology. *Nature*, **469**, 336–342 (2011).
4. Dimmeler, S. & Nicotera, P. MicroRNAs in age-related diseases. *EMBO Mol. Med.* <http://dx.doi.org/10.1002/emmm.201201986> (22 January 2013).
5. Thum, T. *et al.* MicroRNA-21 contributes to myocardial disease by stimulating MAP kinase signalling in fibroblasts. *Nature* **456**, 980–984 (2008).
6. van Rooij, E. *et al.* Dysregulation of microRNAs after myocardial infarction reveals a role of miR-29 in cardiac fibrosis. *Proc. Natl Acad. Sci. USA* **105**, 13027–13032 (2008).
7. Christoffersen, N. R. *et al.* p53-independent upregulation of miR-34a during oncogene-induced senescence represses MYC. *Cell Death Differ.* **17**, 236–245 (2010).
8. Boon, R. A. *et al.* MicroRNA-29 in aortic dilation: implications for aneurysm formation. *Circ. Res.* **109**, 1115–1119 (2011).
9. van Almen, G. C. *et al.* MicroRNA-18 and microRNA-19 regulate CTGF and TSP-1 expression in age-related heart failure. *Aging Cell* **10**, 769–779 (2011).
10. He, L. *et al.* A microRNA component of the p53 tumour suppressor network. *Nature* **447**, 1130–1134 (2007).
11. Hermeking, H. MicroRNAs in the p53 network: micromanagement of tumour suppression. *Nature Rev. Cancer* **12**, 613–626 (2012).

12. Krützfeldt, J. *et al.* Silencing of microRNAs *in vivo* with 'antagomirs'. *Nature* **438**, 685–689 (2005).
13. Ito, T., Yagi, S. & Yamakuchi, M. MicroRNA-34a regulation of endothelial senescence. *Biochem. Biophys. Res. Commun.* **398**, 735–740 (2010).
14. Zhao, T., Li, J. & Chen, A. F. MicroRNA-34a induces endothelial progenitor cell senescence and impedes its angiogenesis via suppressing silent information regulator 1. *Am. J. Physiol. Endocrinol. Metab.* **299**, E110–E116 (2010).
15. Xu, Q. *et al.* Micro-RNA-34a contributes to the impaired function of bone marrow-derived mononuclear cells from patients with cardiovascular disease. *J. Am. Coll. Cardiol.* **59**, 2107–2117 (2012).
16. De Leon, G., Sherry, T. C. & Krucher, N. A. Reduced expression of PNUTS leads to activation of Rb-phosphatase and caspase-mediated apoptosis. *Cancer Biol. Ther.* **7**, 833–841 (2008).
17. Kim, H. *et al.* TRF2 functions as a protein hub and regulates telomere maintenance by recognizing specific peptide motifs. *Nature Struct. Mol. Biol.* **16**, 372–379 (2009).
18. Landsverk, H. B. *et al.* The protein phosphatase 1 regulator PNUTS is a new component of the DNA damage response. *EMBO Rep.* **11**, 868–875 (2010).
19. Karlseder, J., Broccoli, D., Dai, Y., Hardy, S. & de Lange, T. p53- and ATM-dependent apoptosis induced by telomeres lacking TRF2. *Science* **283**, 1321–1325 (1999).
20. Sahin, E. *et al.* Telomere dysfunction induces metabolic and mitochondrial compromise. *Nature* **470**, 359–365 (2011).
21. Shukla, P. C. *et al.* BRCA1 is an essential regulator of heart function and survival following myocardial infarction. *Nature Commun.* **2**, 593 (2011).
22. Oh, H. *et al.* Telomere attrition and Chk2 activation in human heart failure. *Proc. Natl Acad. Sci. USA* **100**, 5378–5383 (2003).
23. Yamakuchi, M., Ferlito, M. & Lowenstein, C. J. miR-34a repression of SIRT1 regulates apoptosis. *Proc. Natl Acad. Sci. USA* **105**, 13421–13426 (2008).
24. Hsu, C. P. *et al.* Silent information regulator 1 protects the heart from ischemia/reperfusion. *Circulation* **122**, 2170–2182 (2010).
25. Bernardo, B. C. *et al.* Therapeutic inhibition of the miR-34 family attenuates pathological cardiac remodeling and improves heart function. *Proc. Natl Acad. Sci. USA* **109**, 17615–17620 (2012).
26. Bonauer, A. *et al.* MicroRNA-92a controls angiogenesis and functional recovery of ischemic tissues in mice. *Science* **324**, 1710–1713 (2009).

**Supplementary Information** is available in the online version of the paper.

**Acknowledgements** We thank M. Muhly-Reinholz, A. Knau, B. Zimmermann, N. Reinfeld and F. Gehring for technical assistance, F. W. Alt for providing SIRT1 mutant mice and D. Sassoon and G. Marazzi for conceptual advice. R.A.B. was supported by the Netherlands Organization for Scientific Research (NWO) and K.I. by a Research Grant Abroad of the Japanese Heart Foundation. This study was supported by a start-up grant of the Excellence Cluster Cardiopulmonary System (Exc 147-1) to R.A.B., by the European Research Council (Advanced grant "Angiomirs") and the German Center for Cardiovascular Research DZHK and the European Union FP7 project Endostem (Grant no. 241440) to S.D. H.A.K. and O.J.M. are supported by the German Centre for Cardiovascular Research (DZHK) and by the German Ministry of Education and Research (BMBF). M.P. is supported by the Max Planck Society, the Fondation Leducq (ARTEMIS) and an ERC Starting Grant (ANGIOMET). H.H. is supported by the DFG, the Deutsche Krebshilfe and the Rudolf-Bartling-Stiftung.

**Author Contributions** R.A.B. designed and performed experiments, analysed data and wrote the manuscript. S.L. and H.H. generated the *miR-34a*<sup>-/-</sup> mice. K.I., T.S., A.F., S.H., D.K., K.T., G.C. and A.B. performed experiments and analysed data. A.J.G.H. analysed microarray data. N.D., Z.G., P.B., J.R.E. and M.P. provided essential materials. H.A.K. and O.J.M. developed the AAV vectors. A.M.Z. wrote the manuscript. S.D. designed experiments, analysed data and wrote the manuscript. All authors have proofread the manuscript.

**Author Information** Data are available at the National Center for Biotechnology Information Gene Expression Omnibus (GEO) and are accessible through GEO Series accession number GSE43556. Reprints and permissions information is available at [www.nature.com/reprints](http://www.nature.com/reprints). The authors declare competing financial interests: details accompany the full-text HTML version of the paper at [www.nature.com/nature](http://www.nature.com/nature). Readers are welcome to comment on the online version of the paper. Correspondence and requests for materials should be addressed to S.D. ([dimmeler@em.uni-frankfurt.de](mailto:dimmeler@em.uni-frankfurt.de)).

## METHODS

**Laboratory animals, ethics and acute myocardial infarction model.** C57BL/6 mice were obtained from Charles River and Janvier. *Sirt1*<sup>+/-</sup> mice<sup>27</sup> and *Ku80*<sup>-/-</sup> mice were described previously<sup>28</sup>. *miR-34a*<sup>-/-</sup> mice (SV/C57BL6 background) were generated using homologous recombination with a vector containing *miR-34a* seed flanked with *loxP* sites and an intronic neomycin resistance (*Neo*) cassette flanked by *frt* sites. The *Neo* cassette was removed by crossing to *flp*-mice and *miR-34a* by crossing with CMV-Cre-mice. As a control, mice homozygous for *miR-34a* flanked with *loxP* sites were used. Generation of *miR-34a*<sup>-/-</sup> mice will be described in detail elsewhere (Hermeking *et al.*, in preparation). *miR-34a*<sup>-/-</sup> mice showed no obvious phenotype and were born at normal Mendelian ratio. The animal experiments were approved by the Regional Board of the State of Hessen, Germany. Patient material was obtained under informed consent and according to the declaration of Helsinki. Acute myocardial infarction operations were performed as described<sup>26</sup> and the mice were subsequently evaluated to assess the infarct size, after which mice received treatment. Echocardiography was performed using a Vevo-770 (Visualsonics) by a researcher blinded to the experimental conditions. Antagomirs (8 mg kg<sup>-1</sup>) were synthesized by VBC Biotech as described previously<sup>26</sup>. The following sequences were used in this study: Ant-Control: 5'-AAGGCAAGCUGACCCUGAAGUU-3' and Ant-34a: 5'-AC AACCAGCUAAGACACUGCCA-3'. LNA-Anti-miRs (LNA/DNA mixmers) (20 mg kg<sup>-1</sup> in *Ku80*<sup>-/-</sup> mice and 5 mg kg<sup>-1</sup> in wild-type mice) were from Exiqon and the sequences were LNA-Control: 5'-ACGTCTATACGCCA-3', *T<sub>m</sub>* 75 °C; and LNA-34a: 5'-AGCTAAGACACTGCC-3', *T<sub>m</sub>* 74 °C.

**Cell culture, transfection and flow cytometry.** Rat neonatal cardiomyocyte isolation was performed as described<sup>29</sup>. Human (GATA-4<sup>+</sup>/α-sarcomeric actin<sup>+</sup>) cardiomyocytes were purchased from Promocell. Separation of mouse cardiomyocytes and non-cardiomyocytes using Langendorff-perfusion-mediated digestion was performed as described<sup>26</sup>. Transfection of cardiomyocytes with pre-miR constructs (pre-miR-34a: 5'-GGCCAGCUGAGUGUUUCUUUGGCAGUGUCUUAGCUGGUUGUGAGCAUAAGUAAGGAAGCAUACAGCAAGUAUACUGCCCUAGAAGUGCUGCAGCUUGUGGGGCC-3'; pre-miR-control: Pre-miR Negative Control #1 from Life Technologies) and anti-miR hairpin inhibitors (miRIDIAN microRNA hsa-mir-34a hairpin inhibitor and miRIDIAN microRNA Hairpin Inhibitor Negative Control #1 from Thermo Fischer), both at 30 nM, as well as siRNA (mix of two sequences targeting *Trf2* (5'-CCC AAAGUACCCAAAGGCA-3' and 5'-GCUUCAGCGCCACCAUCCA-3', 20 nM each) or one negative control siRNA (5'-CGUACGCGGAUACUUCGA-3', 40 nM)) transfection was performed using HiPerfect reagent (Qiagen). Apoptosis was quantified using annexin V and 7-AAD staining and flow cytometry analysis using a CantoII (BD Biosciences). Annexin V-positive/7-AAD-negative cell populations were considered apoptotic.

**RNA isolation, real-time PCR and transcriptional profiling.** Total RNA isolation was performed with miRNeasy kits from Qiagen and real-time PCR with Applied Biosystems microRNA assays run on an Applied Biosystems Step-OnePlus. miRNA levels were normalized with *Rnu6* and *Sno202* expression and mRNA levels with *Rplp0*. Quantification of real-time PCR was performed using synthetic microRNA sequences in a calibration curve. Transcriptional profiling was performed by DNAvision on the Agilent-v1 platform (570 miRNAs) or on the Affymetrix 430 v2.0 platform (mRNA, full genome). Data was background-corrected and normalized by quantile normalization. Statistical comparisons were done using a Bayesian one-way ANOVA and probability values were corrected for multiple testing with the Benjamini–Hochberg false discovery rate method<sup>30</sup>. Data are available at the National Center for Biotechnology Information Gene Expression Omnibus (GEO) and are accessible through GEO Series accession number GSE43556.

**Microscopy, microRNA *in situ* hybridization, telomere assays and histology.** Confocal microscopy and *in situ* hybridization was performed as described before<sup>26</sup>, with the following modifications: miR-34a LNA-modified detection probe (5' and 3' DIG-labelled) was from Exiqon, hybridization temperature 57 °C. Telomere length was measured using real-time PCR, as described before<sup>31</sup>, as well as by quantitative fluorescence *in situ* hybridization (Q-FISH), using the

telomere PNA FISH Cy3 kit (Dako). Chromosome spreads were generated by addition of Colcemid (0.1 µg ml<sup>-1</sup>, 24 h) and after hybridization, images were captured with a Zeiss Axio Observer and ×63 objective. Telomere signals were quantified with TFL-Telo in a blinded manner<sup>32</sup>. Green fluorescent microspheres (Invitrogen) were used to normalize between slides. Telomerase activity was measured with the TRAPeze ELISA telomerase kit (Millipore). TUNEL (cell death) and Sirius red (fibrosis) staining was performed as described<sup>26</sup>. Fibrosis in infarcted hearts was quantified as described<sup>33</sup>.

**Luciferase assays, lentivirus, AAV and western blotting.** Luciferase constructs were made by inserting the full-length human *PNUTS* 3'UTR, obtained from Imagenes in the psiCheck2 vector (Promega), in which the putative miR-34a seed sequence binding site (5'-CACTGCC-3') was mutated to 5'-CTGTCGC-3'. Smaller UTR fragments were inserted using the following oligos: 2x-miR-34a: 5'-aagtcacacacatgcactgccttgaagtcacacacatgcactgcctt-3', 2x-miR-34a-mut: 5'-aagCTacacATcatgcTGTGCGcttgaagCTacacATcatgcTGTGCGctt-3', miR-34a-footprint: 5'-tgctggcctgaaagtcacacacatgcactgccttgggagtcagtcactccctgctcc-3', mut-footprint: 5'-tgctggcctgaaagCTacacATcatgcTGTGCGcttgggagtcagtcactccctgctcc-3'. Mutations are highlighted as uppercase. psiCheck2 plasmids were transfected in HEK293T cells using Genejuice (Merck) and pre-miR-34a and control RNA (Applied Biosystems), as well as LNA-Control and LNA-34a were transfected using Ribojuice (Merck). *PNUTS* cDNA was obtained in pDONR221 (Imagenes) and shuttled to the pLenti4 vector (Invitrogen). Lentiviral particles were generated as described<sup>34</sup>. Western blotting was carried out as described<sup>26</sup>. For adeno-associated virus vector generation, *PNUTS* complementary DNA flanked by BamHI and XbaI restriction sites was inserted into pUF-CMV/MLC0.26, a derivative of pUF-CMV/MLC0.26-µDys<sup>35</sup>. An AAV vector genome containing *Renilla* luciferase under control of the CMV/MLC0.26 promoter was used as control. AAV9 vectors were generated and titrated as described before<sup>35,36</sup>. Mice received 7 × 10<sup>11</sup> vector genomes. Anti-*PNUTS* antibodies were from R&D Systems, anti-γ-H2A.X, anti-P-CHK2 and anti-CHK2 antibodies were from Cell Signaling.

**Statistical analysis.** Data were analysed with GraphPad Prism 5 using student's *t*-tests when comparing two conditions, or an ANOVA with Bonferroni or Newman–Keuls correction for multiple comparisons. Probability values of less than 0.05 were considered significant and tests were performed two-sided. Data was tested for outliers using the Grubbs outlier test and, if outliers were present, they were removed. Data are presented as mean and error bars depict the standard error of the mean (s.e.m.).

- Cheng, H. L. *et al.* Developmental defects and p53 hyperacetylation in Sir2 homolog (SIRT1)-deficient mice. *Proc. Natl Acad. Sci. USA* **100**, 10794–10799 (2003).
- Vogel, H., Lim, D.-S., Karsenty, G., Finegold, M. & Hasty, P. Deletion of Ku86 causes early onset of senescence in mice. *Proc. Natl Acad. Sci. USA* **96**, 10770–10775 (1999).
- Koyanagi, M., Brandes, R. P., Haendeler, J., Zeiher, A. M. & Dimmeler, S. Cell-to-Cell Connection of Endothelial Progenitor Cells With Cardiac Myocytes by Nanotubes: A Novel Mechanism for Cell Fate Changes? *Circ. Res.* **96**, 1039–1041 (2005).
- Reiner, A., Yekutieli, D. & Benjamini, Y. Identifying differentially expressed genes using false discovery rate controlling procedures. *Bioinformatics* **19**, 368–375 (2003).
- Cawthon, R. M. Telomere measurement by quantitative PCR. *Nucleic Acids Res.* **30**, e47 (2002).
- Poon, S. S. S., Martens, U. M., Ward, R. K. & Lansdorp, P. M. Telomere length measurements using digital fluorescence microscopy. *Cytometry* **36**, 267–278 (1999).
- Tagakawa, J. *et al.* Myocardial infarct size measurement in the mouse chronic infarction model: comparison of area- and length-based approaches. *J. Appl. Physiol.* **102**, 2104–2111 (2007).
- Boon, R. A. *et al.* Kruppel-like factor 2 improves neovascularization capacity of aged proangiogenic cells. *Eur. Heart J.* **32**, 371–377 (2011).
- Schinkel, S. *et al.* Long-term preservation of cardiac structure and function after adeno-associated virus serotype 9-mediated microdystrophin gene transfer in *mdx* mice. *Hum. Gene Ther.* **23**, 566–575 (2012).
- Hauswirth, W. W., Lewin, A. S., Zolotukhin, S. & Muzyczka, N. Production and purification of recombinant adeno-associated virus. *Methods Enzymol.* **316**, 743–761 (2000).



# Non-optimal codon usage affects expression, structure and function of clock protein FRQ

Mian Zhou<sup>1</sup>, Jinhu Guo<sup>1†</sup>, Joonseok Cha<sup>1</sup>, Michael Chae<sup>1</sup>, She Chen<sup>2</sup>, Jose M. Barral<sup>3</sup>, Matthew S. Sachs<sup>4</sup> & Yi Liu<sup>1</sup>

Codon-usage bias has been observed in almost all genomes and is thought to result from selection for efficient and accurate translation of highly expressed genes<sup>1–3</sup>. Codon usage is also implicated in the control of transcription, splicing and RNA structure<sup>4–6</sup>. Many genes exhibit little codon-usage bias, which is thought to reflect a lack of selection for messenger RNA translation. Alternatively, however, non-optimal codon usage may be of biological importance. The rhythmic expression and the proper function of the *Neurospora* FREQUENCY (FRQ) protein are essential for circadian clock function. Here we show that, unlike most genes in *Neurospora*, *frq* exhibits non-optimal codon usage across its entire open reading frame. Optimization of *frq* codon usage abolishes both overt and molecular circadian rhythms. Codon optimization not only increases FRQ levels but, unexpectedly, also results in conformational changes in FRQ protein, altered FRQ phosphorylation profile and stability, and impaired functions in the circadian feedback loops. These results indicate that non-optimal codon usage of *frq* is essential for its circadian clock function. Our study provides an example of how non-optimal codon usage functions to regulate protein expression and to achieve optimal protein structure and function.

Eukaryotic circadian oscillators consist of autoregulatory circadian negative-feedback loops. In the core circadian oscillator of *Neurospora crassa*, FRQ protein is a central component that functions as the circadian negative element with its partner FRH<sup>7–9</sup>. Two transcription factors, WHITE COLLAR (WC)-1 and WC-2, form a heterodimeric complex that activates *frq* transcription<sup>10</sup>. The FRQ–FRH complex inhibits WC complex activity by interacting with the WC proteins<sup>11,12</sup>. The level and stability of FRQ have a key role in setting period length, phase and clock sensitivity to environmental signals<sup>7,8,13</sup>. In addition, FRQ promotes the expression of both WC proteins in an interlocked positive-feedback loop<sup>10,14</sup>.

The protein-coding genes of *Neurospora* exhibit strong codon bias (Supplementary Fig. 1a). The third position of almost every codon family in this filamentous fungus has the preference C>G>T>A. Codon optimization enhances the expression of a heterologous luciferase gene in *Neurospora*<sup>15,16</sup>. To establish that codon-usage bias regulates protein expression, we identified the most abundant *Neurospora* proteins in a whole-cell extract by mass spectrometry analyses. The genes encoding the top 100 most abundant proteins (Supplementary Table 1) exhibit much stronger codon bias than the rest of the protein-coding genes (Supplementary Fig. 1b).

We classified all predicted *Neurospora* transfer RNA genes and predicted the relative translation elongation rate for each codon on the basis of tRNA-gene copy numbers, which correlate with tRNA abundance, and the nature of anticodon–codon interactions<sup>4,17</sup>. The most preferred codon for each amino acid is always the codon with highest predicted translation elongation rate (Supplementary Table 2). Therefore, to ensure efficient translation of abundant proteins, selection

pressure favoured a bias for codons translated by highly abundant tRNA species.

Many *Neurospora* genes exhibit little or no codon bias (Supplementary Fig. 1a). FRQ is a low-abundance *Neurospora* protein. Its codon bias index<sup>18</sup> (CBI; in which CBI = 0 indicates completely random codon usage) value of 0.08 indicates that *frq* has little codon bias (Supplementary Fig. 1b). A codon-usage graph of the *frq* open reading frame (ORF) shows that many regions have non-optimal usage (Fig. 1a), whereas *frh* has good codon usage throughout its ORF.

We created two constructs in which the amino-terminal end (amino acids 1–164) of *frq* was codon optimized. In the m-*frq* construct, only the non-preferred codons were changed, whereas every codon was optimized in the f-*frq* construct. Predicted stability of RNA secondary structure was not notably affected by the optimization (Supplementary Table 3). These constructs and the wild-type *frq* (wt-*frq*) gene were transformed individually into a *frq* null strain (*frq*<sup>10</sup>). Both m-*frq* and f-*frq* strains have significantly higher levels of FRQ proteins in constant light than that of the wt-*frq* strain (Fig. 1b and Supplementary Fig. 2a). On the other hand, *frq* mRNA levels were comparable in these strains (Supplementary Fig. 2b). FRQ is known to upregulate WC protein levels<sup>10,14</sup>. The WC-1 and WC-2 levels, however, were similar in these strains despite the much higher levels of FRQ in the optimized strains (Fig. 1b and Supplementary Fig. 2a, c).

The wt-*frq* construct was able to fully rescue the arrhythmic conidiation rhythm of the *frq*<sup>10</sup> strain in constant darkness (Fig. 1c), but both of the optimized *frq* strains exhibited arrhythmic conidiation phenotypes; these are not due to the modest changes in the ratios of two alternatively translated FRQ forms, as either form of FRQ alone can support robust rhythms<sup>19,20</sup>.

We created two additional constructs (m1-*frq* and m2-*frq*), in which only the amino- or carboxy-terminal segments of the optimized region of m-*frq*, respectively, were optimized. The *frq*<sup>10</sup> transformants carrying either construct exhibited long-period conidiation rhythms and had FRQ levels between those of wt-*frq* and m-*frq* strains (Fig. 1c and Supplementary Fig. 3a). These results indicate that the severe conidiation rhythm phenotypes of the m-*frq* and f-*frq* strains are due to the cumulative effect of codon optimization and are not likely due to mutation of a DNA or RNA element.

To examine circadian phenotypes at the molecular level, we introduced a luciferase reporter construct that is under the control of the *frq* promoter<sup>16</sup> into wt-*frq*, m-*frq* and f-*frq* strains. As shown in Fig. 1d and Supplementary Fig. 3b, the robust rhythmic luciferase activity was abolished in the optimized strains. FRQ protein levels also lost molecular rhythmicity in the optimized strains (Fig. 1e, f and Supplementary Fig. 3c, d): the overall levels of FRQ were high and circadian changes in FRQ abundance and phosphorylation profile were abolished. In addition, FRQ stayed hyperphosphorylated in constant darkness in the optimized strains. Together, these results indicate that the non-optimal codon usage of *frq* governs FRQ expression level and is essential for clock function.

<sup>1</sup>Department of Physiology, The University of Texas Southwestern Medical Center, 5323 Harry Hines Boulevard, Dallas, Texas 75390, USA. <sup>2</sup>National Institute of Biological Sciences, 7 Life Science Park Road, Changping District, Beijing 102206, China. <sup>3</sup>Departments of Neuroscience and Cell Biology and Biochemistry and Molecular Biology, The University of Texas Medical Branch, Galveston, Texas 77555-0620, USA. <sup>4</sup>Department of Biology, Texas A&M University, College Station, Texas 77843-3258, USA. <sup>†</sup>Present address: State Key Laboratory of Biocontrol, School of Life Sciences, Sun Yat-sen University, Guangzhou 510275, China.

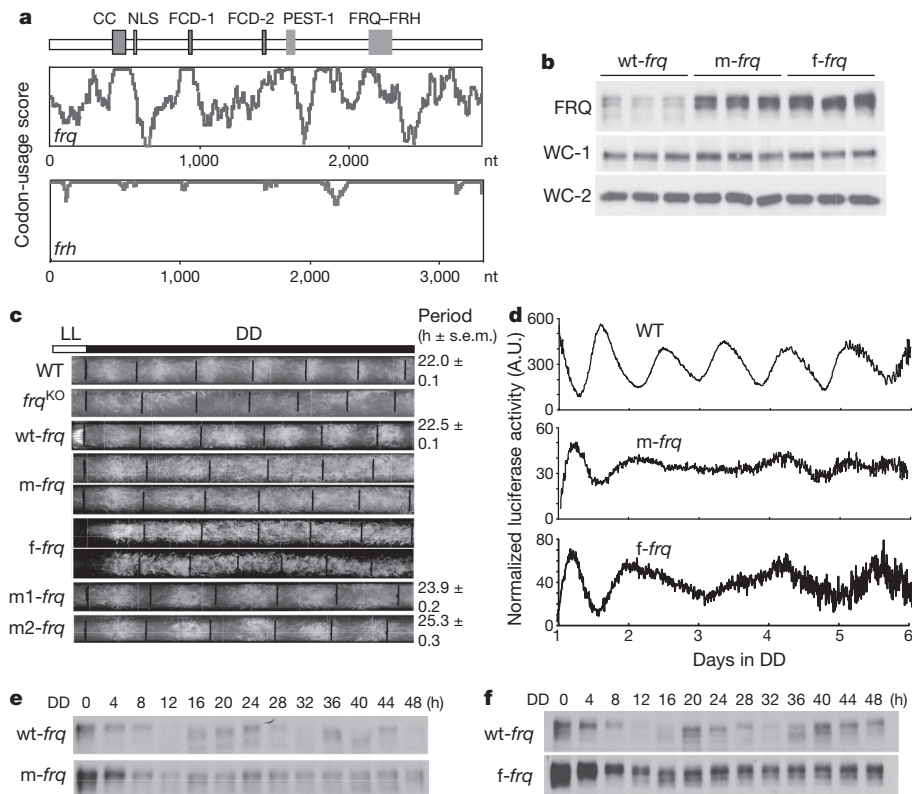


**Figure 1 | Codon optimization of *frq* results in high FRQ expression levels and loss of circadian rhythmicities.** **a**, Codon-usage score plots of *frq* and *frh* obtained using Codon Usage 3.5. CC, coiled-coil domain; FCD, FRQ–CK1 interaction domain; FRQ–FRH, FRQ–FRH interaction domain; NLS, nuclear-localization signal; nt, nucleotide; PEST, proline (P), glutamic acid (E), serine (S) and threonine (T) domain. **b**, Western blot showing the levels of FRQ and WC proteins in *wt-frq*, *m-frq* and *f-frq* strains. Three independent cultures in

constant light at 25 °C were used. **c**, Race tube analysis showing the conidiation phenotypes in constant darkness (DD). Black lines indicate the growth fronts every 24 h. LL, constant light. **d**, Luciferase reporter assay showing *frq* promoter activity of the indicated strains after 1 day in constant darkness. The measurement of luciferase activity was normalized to subtract the baseline luciferase signal. A.U., arbitrary units. **e**, **f**, Western blots showing loss of FRQ expression rhythms in the codon-optimized strains in DD.

The loss of circadian rhythms in the optimized strains is surprising, as we previously showed that high FRQ levels do not result in arrhythmicity<sup>10,21</sup>, suggesting that codon optimization causes defects in FRQ function. FRQ fulfils its function in the circadian negative-feedback loop through its interaction with WC proteins<sup>11</sup>. Immunoprecipitation assays showed that the relative amounts of FRQ associated with WC-2 were significantly decreased in both optimized strains

(Fig. 2a), suggesting that the FRQ function in the negative-feedback loop is impaired in the optimized strains.

FRQ also acts in a positive-feedback loop by promoting WC protein expression<sup>10,14</sup>. Constructs *qa-m-frq* and *qa-f-frq*, in which either *m-frq* or *f-frq* is under the control of a quinic-acid-inducible promoter, respectively, were introduced into the *frq* null strain. As expected, FRQ levels were higher in the *qa-m-frq* and *qa-f-frq* strains than the control

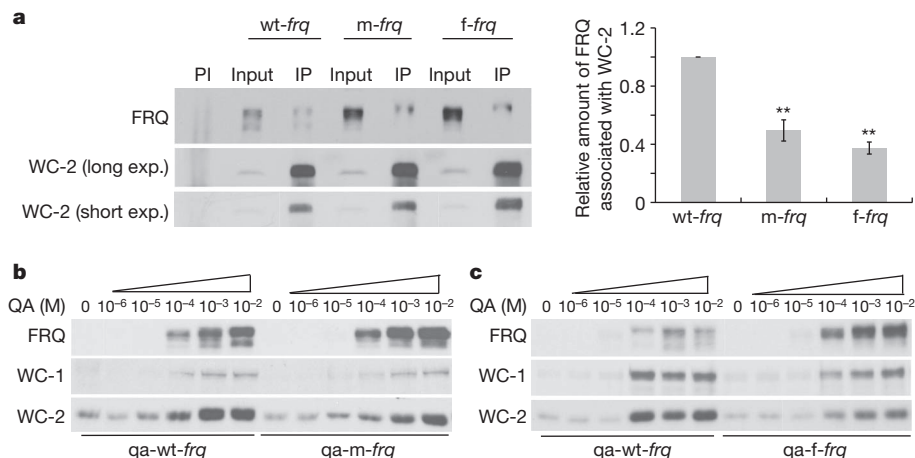


**Figure 2 | FRQ activities in circadian feedback loops are impaired in the *frq* codon-optimized strains.** **a**, Left, immunoprecipitation assay showing that FRQ has a decreased ability to interact with WC-2 in the codon-optimized strains. Two different exposures (exp.) of the WC-2 western blot were shown. Right, densitometric analyses of results from four independent experiments. IP, immunoprecipitation; PI, pre-immune serum. Error bars denote  $\pm$  s.e.m. ( $n = 9$ ). **b**, **c**, Western blots showing the levels of WC proteins and FRQ in the indicated strains at different concentrations of quinic acid (QA) in constant light.

densitometric analyses of results from four independent experiments. IP, immunoprecipitation; PI, pre-immune serum. Error bars denote  $\pm$  s.e.m. ( $n = 9$ ). **b**, **c**, Western blots showing the levels of WC proteins and FRQ in the indicated strains at different concentrations of quinic acid (QA) in constant light.

qa-wt-*frq* strain at a given quinic acid concentration (Fig. 2b, c and Supplementary Figs 4 and 5). Induction of FRQ resulted in increased levels of WC proteins, demonstrating the role of FRQ in the positive-feedback loop. At quinic acid concentrations higher than  $1 \times 10^{-4}$  M, however, the qa-m-*frq* and qa-f-*frq* strains had lower levels of WC-1 and WC-2 than the qa-wt-*frq* strain, despite having higher FRQ levels, indicating that FRQ function in the positive-feedback loop is also impaired in the codon-optimized strains.

The fact that FRQ function is impaired in codon-optimized strains despite higher FRQ protein levels suggests that the structural conformation of FRQ is altered. FRQ becomes progressively phosphorylated before its degradation<sup>7</sup>. Figure 3a shows that, in both m-*frq* and f-*frq* strains, FRQ was less stable than in the wild-type strain after the addition of cycloheximide (CHX). The difference in FRQ stability was most pronounced after 3 h of CHX treatment, a time when FRQ became hyperphosphorylated.

FRQ from the optimized strains was also less stable after protein extraction *in vitro* after freeze-thaw cycles. Although FRQ levels in freshly isolated samples were significantly higher in optimized strains, they decreased rapidly after freeze-thaw cycles (Fig. 3b). By contrast, expression of wt-*frq* in a *wc-2* knock-out strain to a level that is comparable to that of the optimized *frq* strains did not affect the freeze-thaw sensitivity of FRQ (Supplementary Fig. 6), indicating that the change in FRQ stability in the optimized strains is not due to high FRQ level or its reduced ability to interact with WC proteins. Furthermore, limited trypsin digestion showed that full-length FRQ in either optimized strain was more sensitive to trypsin digestion than in the control strain (Fig. 3c).

We reasoned that the changes in FRQ conformation in the optimized strains are due to an increase in the translation rate as a result of codon optimization. Thus, we examined whether FRQ in the f-*frq* strain can be rescued by the decreasing protein-translation rate at

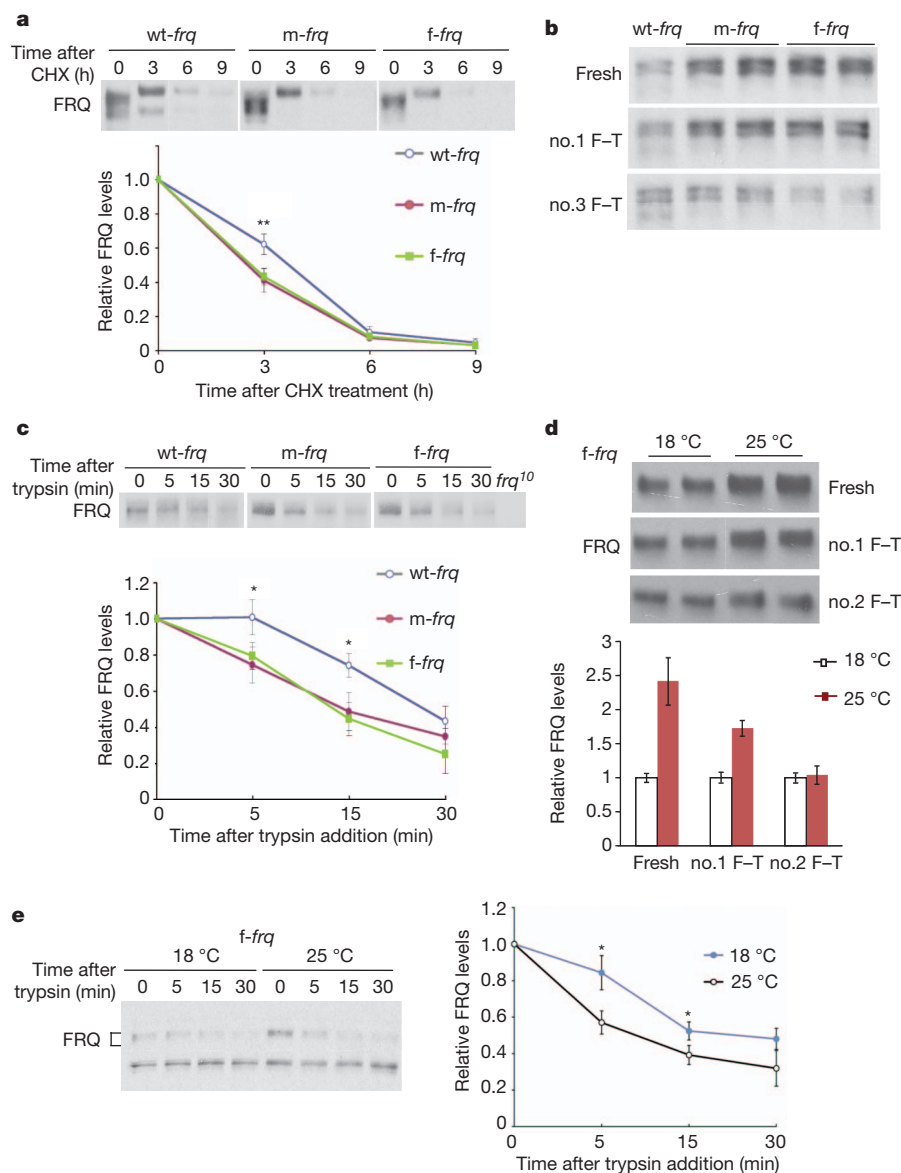


**Figure 3 | FRQ protein in the codon-optimized strains is less stable and more sensitive to trypsin digestion.** **a**, Top, western blots showing FRQ degradation after CHX treatment ( $10 \mu\text{g ml}^{-1}$ ). A longer exposure for the wt-*frq* strain was used so that the FRQ signals at time 0 are comparable between the three strains. Bottom, densitometric analyses of results of four independent experiments. **b**, **c**, Western blots showing sensitivity of FRQ from codon-optimized strains to freeze-thaw (F-T) cycles (**b**) and trypsin ( $1 \mu\text{g ml}^{-1}$ )

digestion (**c**, top). A longer exposure for the wt-*frq* strain was used in **c**. Densitometric analyses of FRQ levels of three independent experiments are shown (**c**, bottom). **d**, **e**, Western blots showing that FRQ from the f-*frq* strain grown at 18 °C is more resistant to freeze-thaw cycles (**d**;  $n = 2$ ) and to trypsin digestion (**e**;  $n = 4$ ) than that grown at 25 °C. \* $P < 0.05$ , \*\* $P < 0.01$ . For **d** and **e**, the densitometric analyses of the results are also shown. Error bars in **a**, **c**, **e** denote  $\pm$  s.d.



18 °C, as low temperature is known to reduce FRQ expression<sup>21</sup> (Fig. 4d). The low-temperature treatment was not successful in restoring the circadian conidiation rhythm of the *f-frq* strain (data not shown), which was not surprising because 18 °C is near the lower limit of temperature range permissive for rhythmicity<sup>22</sup>. FRQ in the *f-frq* strain at 18 °C, however, is much less sensitive to freeze–thaw cycles and to trypsin digestion than at 25 °C (Fig. 3d, e). These results suggest that *frq* codon optimization changes FRQ structure as a consequence of increasing translation rate.

To determine whether the codon-usage effect on FRQ is limited to the N terminus of FRQ, we created a *mid-frq* strain, in which the middle region (amino acids 185–530) of the *frq* ORF is optimized. This region contains two casein kinase 1 (CK1)-interaction domains and most of the phosphorylation sites that are important for FRQ stability and period determination<sup>23,24</sup>. Thus, changes of FRQ structural conformation in this region should affect FRQ phosphorylation and stability. As with *m-frq* and *f-frq* strains, the *mid-frq* strain exhibited arrhythmic conidiation (Fig. 4a). In the *mid-frq* strain, FRQ levels were high, and FRQ levels and phosphorylation profile were not rhythmic (Fig. 4b, c). No significant difference in *frq* mRNA was observed (Supplementary Fig. 7). Notably, in the *mid-frq* strain, FRQ accumulated in hypophosphorylated forms, was more stable after CHX treatment and was more resistant to trypsin digestion (Fig. 4b–e). In addition, the CHX-triggered rapid hyperphosphorylation of FRQ in the *wt-frq* strain was abolished in the *mid-frq* strain<sup>22</sup>. These results strongly indicate that the non-optimal codon usage of *frq* is important for FRQ structural

required for proper phosphorylation and stability. The opposite molecular phenotypes of *mid-frq* and the N-terminal-optimized strains indicate that changes in FRQ structural conformation in these strains are due to location-specific codon optimization.

In a companion study, codon optimization of *kaiBC* clock genes in cyanobacteria results in high Kai protein levels and impaired cell growth at cool temperatures<sup>25</sup>, suggesting that non-optimal codon usage is a shared adaptive mechanism in both prokaryotes and eukaryotes.

Our study suggests that codon usage regulates not only protein-expression level but also its structure and function. Protein folding, which occurs cotranslationally, requires protein chaperones and sufficient amounts of time<sup>17</sup>. Codon optimization results in increased translation rates and thus reduces the time available for folding. Bioinformatics analyses and heterologous protein-expression studies previously implicated codon usage as a factor that regulates protein folding<sup>26–28</sup>. In addition, a single rare codon in the human *MDR1* (also known as *ABCB1*) gene results in altered drug and inhibitor interaction<sup>29</sup>.

In sharp contrast with the cyanobacterial Kai proteins<sup>30</sup>, most of the FRQ protein is predicted to be disordered (Supplementary Fig. 8). Interestingly, the known domains of FRQ all have relatively low disorder tendencies and fall in regions where codon-usage scores are relatively high, suggesting that a fast translation rate in these well-structured regions does not interfere with protein folding. On the other hand, although the disordered regions may not form stable structures by themselves, they are critical for proper FRQ phosphorylation and

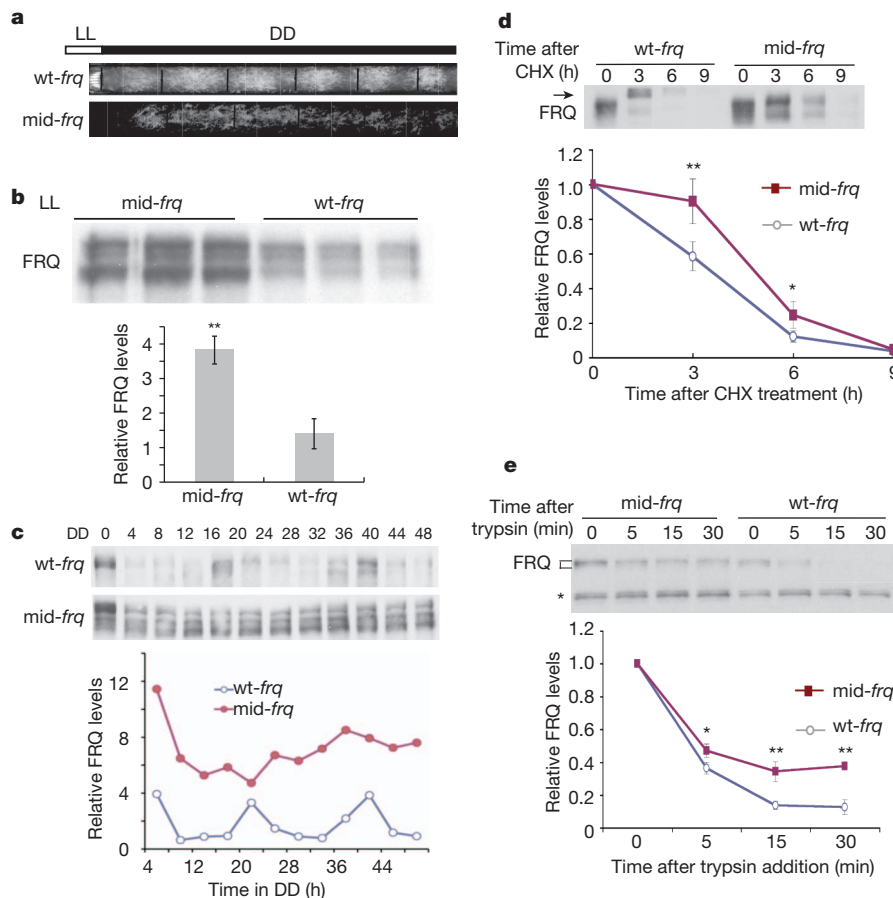


**Figure 4 | Codon optimization of the middle region of FRQ impairs FRQ phosphorylation and stabilizes FRQ.** **a**, Race tube analysis showing the conidiation phenotypes of indicated strains in constant darkness. **b**, Top, western blot showing FRQ expression profile in constant light. Bottom, densitometric analyses of three independent samples. **c**, Top, western blots showing FRQ expression profile in constant darkness. Bottom, densitometric analysis of the result. **d**, Top, western blot showing the degradation of FRQ after

CHX treatment. The arrow indicates the hyperphosphorylated forms of FRQ after the addition of CHX in the *wt-frq* strain. Bottom, densitometric analyses from four independent experiments. **e**, Top, western blot showing reduced sensitivity of FRQ from *mid-frq* to trypsin digestion (2 µg ml<sup>-1</sup>). Bottom, densitometric analyses of three independent experiments. Error bars denote s.d. \**P* < 0.05, \*\**P* < 0.01.

stability<sup>23,24</sup>. They may serve as platforms for inter- or intramolecular protein–protein interactions, which may require more time for protein folding than well-structured domains. Therefore, *frq* non-optimal codon usage should be a mechanism that allows the proper folding of FRQ by reducing translation rate in these predicted disordered regions.

## METHODS SUMMARY

Codons were optimized on the basis of *Neurospora* codon-usage frequency. Codon-usage score plot was obtained using software Codon Usage 3.5 (developed by Conrad Halling). CBI, frequency of optimal codons (Fop), ENC (effective number of codons) and GC (guanine-cytosine) content values were calculated by codonw (<http://mobyli.pasteur.fr/cgi-bin/portal.py#forms::codonw>). Optimized *frq* constructs were transformed into a *bd, frq<sup>10</sup>, his-3* strain.

**Full Methods** and any associated references are available in the online version of the paper.

**Received 31 May; accepted 11 December 2012.**

**Published online 17 February 2013.**

- Ikemura, T. Codon usage and tRNA content in unicellular and multicellular organisms. *Mol. Biol. Evol.* **2**, 13–34 (1985).
- Plotkin, J. B. & Kudla, G. Synonymous but not the same: the causes and consequences of codon bias. *Nature Rev. Genet.* **12**, 32–42 (2011).
- Drummond, D. A. & Wilke, C. O. Mistranslation-induced protein misfolding as a dominant constraint on coding-sequence evolution. *Cell* **134**, 341–352 (2008).
- Tuller, T. *et al.* An evolutionarily conserved mechanism for controlling the efficiency of protein translation. *Cell* **141**, 344–354 (2010).
- Gu, W., Zhou, T. & Wilke, C. O. A universal trend of reduced mRNA stability near the translation-initiation site in prokaryotes and eukaryotes. *PLoS Comput. Biol.* **6**, e1000664 (2010).
- Cannarozzi, G. *et al.* A role for codon order in translation dynamics. *Cell* **141**, 355–367 (2010).
- Heintzen, C. & Liu, Y. The *Neurospora crassa* circadian clock. *Adv. Genet.* **58**, 25–66 (2007).
- Baker, C. L., Loros, J. J. & Dunlap, J. C. The circadian clock of *Neurospora crassa*. *FEMS Microbiol. Rev.* **36**, 95–110 (2012).
- Cheng, P., He, Q., He, Q., Wang, L. & Liu, Y. Regulation of the *Neurospora* circadian clock by an RNA helicase. *Genes Dev.* **19**, 234–241 (2005).
- Cheng, P., Yang, Y. & Liu, Y. Interlocked feedback loops contribute to the robustness of the *Neurospora* circadian clock. *Proc. Natl Acad. Sci. USA* **98**, 7408–7413 (2001).
- He, Q. *et al.* CKI and CKII mediate the FREQUENCY-dependent phosphorylation of the WHITE COLLAR complex to close the *Neurospora* circadian negative feedback loop. *Genes Dev.* **20**, 2552–2565 (2006).
- Schafmeier, T. *et al.* Transcriptional feedback of *Neurospora* circadian clock gene by phosphorylation-dependent inactivation of its transcription factor. *Cell* **122**, 235–246 (2005).
- Huang, G., Wang, L. & Liu, Y. Molecular mechanism of suppression of circadian rhythms by a critical stimulus. *EMBO J.* **25**, 5349–5357 (2006).
- Lee, K., Loros, J. J. & Dunlap, J. C. Interconnected feedback loops in the *Neurospora* circadian system. *Science* **289**, 107–110 (2000).
- Morgan, L. W., Greene, A. V. & Bell-Pedersen, D. Circadian and light-induced expression of luciferase in *Neurospora crassa*. *Fungal Genet. Biol.* **38**, 327–332 (2003).
- Gooch, V. D. *et al.* Fully codon-optimized luciferase uncovers novel temperature characteristics of the *Neurospora* clock. *Eukaryot. Cell* **7**, 28–37 (2008).
- Spencer, P. S., Siller, E., Anderson, J. F. & Barral, J. M. Silent substitutions predictably alter translation elongation rates and protein folding efficiencies. *J. Mol. Biol.* **422**, 328–335 (2012).
- Bennetzen, J. L. & Hall, B. D. Codon selection in yeast. *J. Biol. Chem.* **257**, 3026–3031 (1982).
- Colot, H. V., Loros, J. J. & Dunlap, J. C. Temperature-modulated alternative splicing and promoter use in the circadian clock gene *frequency*. *Mol. Biol. Cell* **16**, 5563–5571 (2005).
- Diernfellner, A. *et al.* Long and short isoforms of *Neurospora* clock protein FRQ support temperature-compensated circadian rhythms. *FEBS Lett.* **581**, 5759–5764 (2007).
- Liu, Y., Merrow, M. M., Loros, J. J. & Dunlap, J. C. How temperature changes reset a circadian oscillator. *Science* **281**, 825–829 (1998).
- Liu, Y., Garceau, N., Loros, J. J. & Dunlap, J. C. Thermally regulated translational control mediates an aspect of temperature compensation in the *Neurospora* circadian clock. *Cell* **89**, 477–486 (1997).
- Tang, C. T. *et al.* Setting the pace of the *Neurospora* circadian clock by multiple independent FRQ phosphorylation events. *Proc. Natl Acad. Sci. USA* **106**, 10722–10727 (2009).
- Baker, C. L., Kettenbach, A. N., Loros, J. J., Gerber, S. A. & Dunlap, J. C. Quantitative proteomics reveals a dynamic interactome and phase-specific phosphorylation in the *Neurospora* circadian clock. *Mol. Cell* **34**, 354–363 (2009).
- Xu, Y., Ma, P., Shah, P., Rokas, A., Liu, Y. & Johnson, C. H. Non-optimal codon usage is a mechanism to achieve circadian clock conditionality. *Nature* <http://dx.doi.org/10.1038/nature11942> (this issue).
- Zhou, T., Weems, M. & Wilke, C. O. Translationally optimal codons associate with structurally sensitive sites in proteins. *Mol. Biol. Evol.* **26**, 1571–1580 (2009).
- Siller, E., DeZwaan, D. C., Anderson, J. F., Freeman, B. C. & Barral, J. M. Slowing bacterial translation speed enhances eukaryotic protein folding efficiency. *J. Mol. Biol.* **396**, 1310–1318 (2010).
- Komar, A. A., Lesnik, T. & Reiss, C. Synonymous codon substitutions affect ribosome traffic and protein folding during *in vitro* translation. *FEBS Lett.* **462**, 387–391 (1999).
- Kimchi-Sarfaty, C. *et al.* A “silent” polymorphism in the *MDR1* gene changes substrate specificity. *Science* **315**, 525–528 (2007).
- Johnson, C. H., Stewart, P. L. & Egli, M. The cyanobacterial circadian system: from biophysics to bioevolution. *Annu. Rev. Biophys.* **40**, 143–167 (2011).

**Supplementary Information** is available in the online version of the paper.

**Acknowledgements** We thank H. Yuan and Q. Ye for technical assistance, J. Dunlap for providing the *pdfq-luc-I* construct and M. Rosbash for suggesting the temperature experiments. We apologize to those colleagues whose studies we could not cite owing to space limitations. This work was supported by grants from the National Institutes of Health to Y.L. (GM068496 & GM062591) and M.S.S. (GM47498), and from the Welch Foundation (I-1560) to Y.L.

**Author Contributions** Y.L., M.Z. and J.G. designed the research. M.Z., J.G., J.C., M.C., S.C. and J.M.B. performed experiments. M.Z., J.G., J.M.B., M.S.S. and Y.L. analysed the results. Y.L. and M.Z. wrote the paper; J.G., J.M.B. and M.S.S. edited and commented on the manuscript.

**Author Information** Reprints and permissions information is available at [www.nature.com/reprints](http://www.nature.com/reprints). The authors declare no competing financial interests. Readers are welcome to comment on the online version of the paper. Correspondence and requests for materials should be addressed to Y.L. (Yi.Liu@UTsouthwestern.edu).

## METHODS

**Strains and growth conditions.** *Neurospora* strains used in this study were 87-3 (*bd a*; clock wild-type), 303-3 (*bd, frq<sup>10</sup>, his-3*)<sup>31</sup> and different *frq* N-terminal-codon-optimized strains created in this study. Strain 303-3 was used as the host strain for various *his-3*-targeting constructs. The *frq<sup>10</sup>, bd, wt-frq* (*frq<sup>10</sup>* containing a wild-type *frq* gene at the *his-3* locus) strain was used as the control in this study.

Growth conditions have been described previously<sup>32</sup>. Liquid cultures were grown in minimal medium (1 × Vogel's, 2% glucose). When quinic acid was used, liquid cultures were grown in (10<sup>-6</sup>–10<sup>-2</sup> M) quinic acid, pH 5.8, 1 × Vogel's, 0.1% glucose and 0.17% arginine. Race tube media contained 1 × Vogel's, 0.1% glucose, 0.17% arginine, 50 ng ml<sup>-1</sup> biotin and 1.5% agar. For rhythmic experiments, the *Neurospora* cultures were transferred from LL to DD at time 0 and were collected in DD at the indicated time (hours). Calculations of period length were performed as described<sup>22</sup>.

***frq* codon optimization, codon-usage score plot and indices calculation.** *frq* codon optimization was performed for the N-terminal part (1–498 nucleotides) or the middle region (553–1,590 nucleotides) of the ORF. The nucleotide sequences of the optimized *frq* are shown in Supplementary Figs 9 and 10. Codons were optimized on the basis of *N. crassa* codon-usage frequency and the predicted most efficient codon on the basis of tRNA copy numbers. In total, 65 codons were optimized in the *m-frq* construct, whereas 94 codons were optimized in the *f-frq* construct. Sequences surrounding an alternative *frq* 3' splice site in this region were not mutated.

Codon-usage score plot was obtained using Codon Usage 3.5 (developed by Conrad Halling) using a window size of 35 and logarithmic range of 3. The *N. crassa* codon-usage frequency table was obtained from <http://www.kazusa.or.jp/codon/>. To calculate the CBI, frequency of optimal codons (Fop), ENC (effective number of codons) and GC (guanine-cytosine) content, codonw in the Mobyale Portal website (<http://mobyale.pasteur.fr/cgi-bin/portal.py#forms:codonw>) was used<sup>18,33</sup>. CBI will equal 1.0 if a gene has extreme codon bias and will equal 0 if codon usage is completely random. If the number of optimal codons is less than expected by random change, the CBI value will be a negative value. *Neurospora* genome sequences were downloaded from the Broad Institute *N. crassa* database (<http://www.broadinstitute.org/annotation/genome/neurospora/MultiHome.html>). The top 100 most abundant proteins were identified by mass spectrometry analyses and ranked by their emPAI (exponentially modified protein abundance index) values<sup>34</sup> (Supplementary Table 1).

**Plasmid constructs and *Neurospora* transformation.** pKAJ120 (containing the entire wild-type *frq* gene including its promoter and a *his-3*-targeting sequence) and pBA50 (containing the wild-type *frq* gene under the control of the *qa-2* promoter and a *his-3*-targeting sequence) were used as the parental plasmids to create the optimized *frq* constructs<sup>32</sup>. Optimized *frq* sequences (synthesized by Genscript) were subcloned into parental plasmids to replace the wild-type *frq* gene to generate the *m-frq*, *f-frq* and *mid-frq* constructs. In the *m1-frq* construct, only the codons upstream of the predicted intron branch point were optimized as *m-frq*. For the *m2-frq* construct, only the codons downstream of the intron 3' end were optimized as *m-frq*. The resulting constructs were transformed into strain 303-3 by electroporation and targeted to the *his-3* locus<sup>35</sup>. Homokaryon strains were obtained by microconidia purification.

**Protein and RNA analyses.** Protein extraction, western blot analysis and immunoprecipitation assays were performed as previously described<sup>36–38</sup>. Equal amounts of total protein (50 µg) were loaded into each lane of SDS–PAGE gels (7.5% SDS–PAGE gels containing a ratio of 37.5:1 acrylamide/bisacrylamide). Densitometry of the signal was performed by using Image J.

RNA extraction and quantitative reverse transcriptase PCR (qRT–PCR) were performed as previously described<sup>39,40</sup>. For qRT–PCR, the primer sequences used for *frq* were 5'-GGAGGAGTCGATGTCAAGG-3' (forward) and 5'-CACTTC GAGTTACCATGTTGC-3' (reverse). The *Neurospora* gene coding for β-tubulin was used as an internal control. The primer sequences specific for β-tubulin were 5'-GCGTATCGGCGAGCAGTT-3' (forward) and 5'-CCTCACCAGTGTACCAAT GCA-3' (reverse).

*frq* mRNA secondary structure and folding energy was predicted by the mfold program (<http://mfold.rna.albany.edu/?q=mfold/RNA-Folding-Form>).

**Mass spectrometric analyses and database search.** The *Neurospora* proteins were separated on a 4–20% SDS–PAGE gradient gel. The whole-protein gel lane was sliced equally into 14 gel blocks from top to bottom. Each gel block was destained and then digested in-gel with sequencing grade trypsin (10 ng µl<sup>-1</sup> trypsin in 50 mM ammonium bicarbonate, pH 8.0) at 37 °C overnight. The resulting tryptic peptides from each gel block were extracted with 5% formic acid/50% acetonitrile and 0.1% formic acid/75% acetonitrile sequentially and then concentrated to ~20 µl in a CentriVap system (Labconco). The extracted peptides from each sample were separated by a home-made analytical capillary column (50 µm × 10 cm) packed with 5-µm spherical C18 reversed-phase material (YMC). An

Agilent 1100 binary pump was used to generate high-performance liquid chromatography gradient as follows: 0–5% B in 5 min, 5–40% B in 55 min, 40–100% B in 15 min (A = 0.2 M acetic acid in water; B = 0.2 M acetic acid/70% acetonitrile). The eluted peptides were sprayed directly into a LTQ mass spectrometer (Thermo Fisher Scientific) equipped with a nano-ESI ion source. The mass spectrometer was operated in data-dependent mode (MS scan mass range was 350–2,000 Da, the top-five most abundant precursor ions from each MS scan were selected for MS–MS scans, and dynamic exclusion time was 30 s). The mass spectrometric data from all 14 samples were combined and searched against *Neurospora* protein database on an in-house Mascot server (Matrix Science). The main search parameters were as below: protein N-terminal acetylation and methionine oxidation were included as variable modifications; two missed cleavage sites were allowed; precursor ion mass tolerance was set as 3 Da; fragment ion mass tolerance was 0.8 Da. Only peptides with *E* value above 0.01 were retained. The emPAI<sup>34</sup> was calculated for each protein by the Mascot software.

**Luciferase reporter assay.** The luciferase reporter construct (*frq-luc-bar*) was generated by insertion of the 4.7-kb BamHI–NotI fragment of *pfrq-luc-I* (a generous gift from J. Dunlap)<sup>16</sup> into the corresponding sites of pBARKS1. This construct, which contains the luciferase gene under the control of the *frq* promoter and the *bar* gene, was transformed into 87-3 (*bd a*), *wt-frq* (*frq<sup>10</sup>, bd, wt-frq*), *m-frq* (*frq<sup>10</sup>, bd, m-frq*) and *f-frq* (*frq<sup>10</sup>, bd, f-frq*) strains. Transformants were selected using the basta/ignite (200 µg ml<sup>-1</sup>) resistance conferred by the *bar* gene.

LumiCycle (Actimetrics) was used for the luciferase assay using a protocol similar to previously described<sup>16</sup>. The AFV (autoclaved FGS-Vogel's) medium contained 1 × FGS (0.05% fructose, 0.05% glucose, 2% sorbose), 1 × Vogel's medium, 50 µg l<sup>-1</sup> biotin and 1.8% agar. Firefly luciferin (L-8200 D-luciferin firefly (synthetic) potassium salt; BioSynth) was added to the medium after autoclaving (final concentration 50 µM). One drop of conidia suspensions in water were placed on AFV medium and grown in LL overnight. The cultures were then transferred to darkness, and luminescence was recorded in real time DD using a LumiCycle after 1 day in DD. The data were then normalized with LumiCycle analysis software by subtracting the baseline luciferase signal, which increases as cell grows. Therefore, the normalized luciferase signals reflect the amplitude of the rhythm and do not reflect the absolute luciferase signal. Under our experimental conditions, luciferase signals were highly variable during the first day in the LumiCycle and became stabilized afterwards, which is probably because of an artefact caused by the light–dark transfer of the cultures. Thus, the results presented were recorded after 1 day in DD.

**Protein-stability assay.** The liquid cultures of *Neurospora* strains were grown in LL for 1 day before the addition of CHX (final concentration 10 µg ml<sup>-1</sup>). Cells were collected at the indicated time points.

For the trypsin-sensitivity assay, protein extracts were diluted to a protein concentration of 2.5 µg µl<sup>-1</sup>. 100-µl extracts were treated with trypsin (final concentration 1 µg ml<sup>-1</sup>) at 25 °C. A 20-µl sample was taken from the reaction at each time point (0, 5, 15 and 30 min) after addition of trypsin. Protein samples were mixed with protein loading buffer and resolved by SDS–PAGE. To compare trypsin sensitivity of FRQ from different strains, experiments were performed side by side and the protein samples were transferred to the same membrane for western blot analysis.

- Cha, J., Yuan, H. & Liu, Y. Regulation of the activity and cellular localization of the circadian clock protein FRQ. *J. Biol. Chem.* **286**, 11469–11478 (2011).
- Aronson, B. D., Johnson, K. A., Loros, J. J. & Dunlap, J. C. Negative feedback defining a circadian clock: autoregulation in the clock gene *frequency*. *Science* **263**, 1578–1584 (1994).
- Wright, F. The 'effective number of codons' used in a gene. *Gene* **87**, 23–29 (1990).
- Ishihama, Y. *et al.* Exponentially modified protein abundance index (emPAI) for estimation of absolute protein amount in proteomics by the number of sequenced peptides per protein. *Mol. Cell. Proteomics* **4**, 1265–1272 (2005).
- Bell-Pedersen, D., Dunlap, J. C. & Loros, J. J. Distinct *cis*-acting elements mediate clock, light, and developmental regulation of the *Neurospora crassa* *eas* (*cgc-2*) gene. *Mol. Cell. Biol.* **16**, 513–521 (1996).
- Cheng, P., Yang, Y., Heintzen, C. & Liu, Y. Coiled-coil domain mediated FRQ–FRQ interaction is essential for its circadian clock function in *Neurospora*. *EMBO J.* **20**, 101–108 (2001).
- Garceau, N. Y., Liu, Y., Loros, J. J. & Dunlap, J. C. Alternative initiation of translation and time-specific phosphorylation yield multiple forms of the essential clock protein FREQUENCY. *Cell* **89**, 469–476 (1997).
- Guo, J., Cheng, P., Yuan, H. & Liu, Y. The exosome regulates circadian gene expression in a posttranscriptional negative feedback loop. *Cell* **138**, 1236–1246 (2009).
- Crosthwaite, S. K., Loros, J. J. & Dunlap, J. C. Light-Induced resetting of a circadian clock is mediated by a rapid increase in *frequency* transcript. *Cell* **81**, 1003–1012 (1995).
- Choudhary, S. *et al.* A double-stranded-RNA response program important for RNA interference efficiency. *Mol. Cell. Biol.* **27**, 3995–4005 (2007).



# Non-optimal codon usage is a mechanism to achieve circadian clock conditionality

Yao Xu<sup>1</sup>, Peijun Ma<sup>1</sup>, Premal Shah<sup>2</sup>, Antonis Rokas<sup>1</sup>, Yi Liu<sup>3</sup> & Carl Hirschie Johnson<sup>1</sup>

Circadian rhythms are oscillations in biological processes that function as a key adaptation to the daily rhythms of most environments. In the model cyanobacterial circadian clock system, the core oscillator proteins are encoded by the gene cluster *kaiABC*. Genes with high expression and functional importance, such as the *kai* genes, are usually encoded by optimal codons, yet the codon-usage bias of the *kaiBC* genes is not optimized for translational efficiency. We discovered a relationship between codon usage and a general property of circadian rhythms called conditionality; namely, that endogenous rhythmicity is robustly expressed under some environmental conditions but not others<sup>2</sup>. Despite the generality of circadian conditionality, however, its molecular basis is unknown for any system. Here we show that in the cyanobacterium *Synechococcus elongate*, non-optimal codon usage was selected as a post-transcriptional mechanism to switch between circadian and non-circadian regulation of gene expression as an adaptive response to environmental conditions. When the *kaiBC* sequence was experimentally optimized to enhance expression of the KaiB and KaiC proteins, intrinsic rhythmicity was enhanced at cool temperatures that are experienced by this organism in its natural habitat. However, fitness at those temperatures was highest in cells in which the endogenous rhythms were suppressed at cool temperatures as compared with cells exhibiting high-amplitude rhythmicity. These results indicate natural selection against circadian systems in cyanobacteria that are intrinsically robust at cool temperatures. Modulation of circadian amplitude is therefore crucial to its adaptive significance<sup>3</sup>. Moreover, these results show the direct effects of codon usage on a complex phenotype and organismal fitness. Our work also challenges the long-standing view of directional selection towards optimal codons<sup>4–7</sup>, and provides a key example of natural selection against optimal codons to achieve adaptive responses to environmental changes.

Most amino acids are encoded by several codons, and species vary in their preferences for specific codons for the same amino acid. This preference, or codon-usage bias, is thought to reflect a balance between mutational biases and selection for translational efficiency and accuracy<sup>4,6–9</sup>. Although the relative importance of various factors affecting codon usage is debated<sup>10,11</sup>, the degree of codon-usage bias is known to increase with higher gene expression<sup>12</sup>. In particular, genes under stronger selection for translational efficiency and/or accuracy show greater preference for using codons that have complementary transfer RNAs with higher abundances. Despite the fact that codon-usage bias is a strong indicator of selection on genes<sup>13</sup> and that the specific nature of codon bias can be changed by environmental factors such as temperature and hypersalinity<sup>14,15</sup>, its direct effect on a complex phenotype and organismal fitness remains largely unknown.

In the cyanobacterium *S. elongatus* PCC 7942, circadian rhythms confer a strong selective advantage in rhythmic environments<sup>3,16</sup>. Expression of the entire *S. elongatus* genome is controlled by the circadian pacemaker, as shown by rhythms of promoter activity<sup>17</sup>, messenger RNA abundance<sup>18–20</sup>, and the topology of the entire

chromosome<sup>19,21</sup>. The core circadian clock is composed of three components, KaiA, KaiB and KaiC, that are expressed as monocistronic *kaiA* and dicistronic *kaiBC* transcripts<sup>1</sup>. Both transcripts are expressed at very high levels, falling within the top 5% of mRNA abundances in *S. elongatus*<sup>18,19</sup>. Whereas initial examination of codon usage in *kaiBC* suggested an unusual codon bias (Supplementary Table 1 and Fig. 1a), further analyses indicated that amino acid-specific codon usage in *kaiB* and *kaiC* is not significantly different from that of the average codon usage in the rest of the genome (Fig. 1b). To quantify the degree of selection on the *kai* gene cluster, we focused on its codon adaptation index (CAI)<sup>13</sup> and the 5' mRNA folding energies of its transcripts. Given that *kaiBC* transcripts are highly abundant, it was surprising that the CAI for *kaiB* and *kaiC* is less than the average CAI value of all *S. elongatus* genes (Fig. 1b). Moreover, even though the folding energy of the *kaiB* transcript is less negative than that of most transcripts (Fig. 1c)—indicating that it has a relatively weaker secondary structure than most mRNAs in this organism and is therefore likely to initiate translation efficiently—the weak secondary structure of the *kaiB* transcript is insufficient to account for its high mRNA abundance given that the CAI is considerably below average. The *kaiC* portion of the *kaiBC* transcript has similar CAI (Fig. 1b) and folding energy (Fig. 1c) values to those of the *kaiB* portion.

To test whether the lower CAI of *kaiBC* might be adaptive in the core clock mechanism and/or in the output pathways controlled by the pacemaker in cyanobacteria, we generated two strains in which the endogenous *kaiBC* gene was replaced with modified versions of *kaiBC* where codon usage was 'optimized' to be similar to that of highly expressed genes<sup>18,19</sup>, thereby increasing their CAI values from 0.60 to 0.95 for *kaiB* and 0.61 to 0.82 for *kaiC* (Fig. 1a and Supplementary Tables 2 and 3). Changing the codon usage of a gene in its 5' region affects its folding energy and hence its rate of translation initiation<sup>8,22–24</sup>. Indeed, the optimized versions of *kaiB* and *kaiBC* also had significantly lower 5' folding energy than the *kaiBC* transcript (Fig. 1c, d). Because the *kaiBC* gene is transcribed as a single dicistronic mRNA with *kaiB* at its 5' end<sup>1</sup>, one optimized strain (optKaiB) replaced the entire wild-type *kaiB*<sup>WT</sup> gene with an optimized *kaiB*<sup>opt</sup> gene, whereas the other optimized strain (optKaiBC) replaced both the *kaiB*<sup>WT</sup> gene and the 5' half of the *kaiC*<sup>WT</sup> gene with optimized versions (*kaiB*<sup>opt</sup> and *kaiC*<sup>opt</sup>; Fig. 2a). Our initial hypothesis was that the 'non-optimal' codon bias of the endogenous *kaiBC* gene is essential for the expression of circadian rhythmicity, which would predict that the intrinsic rhythmicity of the optKaiB and optKaiBC strains would be poorer than that of wild type (as is true for the studies of the *Neurospora* FRQ protein<sup>25</sup>). Unexpectedly, the observed circadian rhythms of gene expression in the optKaiB and optKaiBC strains were as robust as those of the wild-type *S. elongatus* at the optimal growth temperature of 30 °C (Fig. 2b). However, to be adaptive, circadian clocks must be able to keep time accurately over the range of physiological temperatures for a given organism<sup>26</sup>, so we tested real-time gene expression profiles of the optimized strains relative to wild type at temperatures from 18 °C to 38 °C. Again, to our surprise the optKaiB and

<sup>1</sup>Department of Biological Sciences, Vanderbilt University, Nashville, Tennessee 37235, USA. <sup>2</sup>Department of Biology, University of Pennsylvania, Philadelphia, Pennsylvania 19104, USA. <sup>3</sup>Department of Physiology, The University of Texas Southwestern Medical Center, Dallas, Texas 75390, USA.

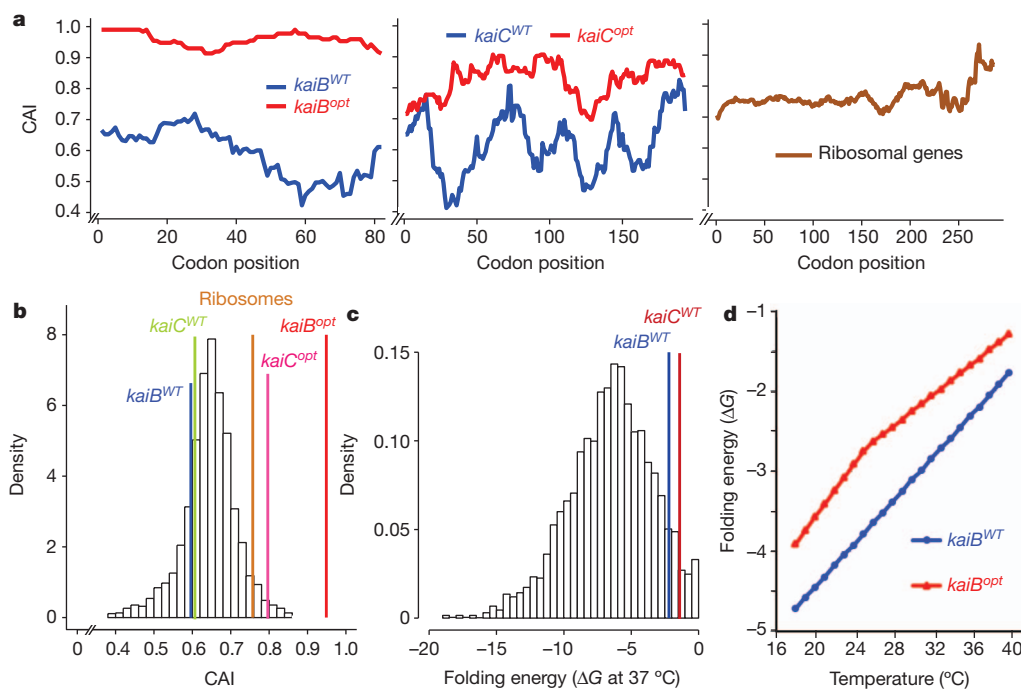


**Figure 1 | Non-optimal codon usage of cyanobacterial clock genes.** **a**, CAI values along the entire length of different genes at a sliding window of 20 codons. Left, *kaiB*<sup>WT</sup> versus *kaiB*<sup>opt</sup>. Middle, *kaiC*-I domain (encoded by the 5' half of the *kaiC* gene) of *kaiC*<sup>WT</sup> versus *kaiC*<sup>opt</sup>. Right, average of all ribosomal protein genes. **b**, Comparison of CAI values of the *kaiB*<sup>WT</sup>, *kaiB*<sup>opt</sup>, *kaiC*<sup>WT</sup>, *kaiC*<sup>opt</sup> and ribosomal genes in the CAI histogram distribution of the genome. **c**, Calculated 5' folding energy of the mRNA for all genes in the *S. elongatus* genome. **d**, Comparison of calculated minimum free energy of folding ( $\Delta G$ ) over a range of temperatures between *kaiB*<sup>WT</sup> and *kaiB*<sup>opt</sup>.

optKaiBC strains exhibited robustly rhythmic gene expression over a broad range of temperatures (Fig. 2b and Supplementary Table 4). By contrast, the rhythm of the wild-type strain damps within a few cycles

at cool temperatures (18–23 °C; Fig. 2b and Supplementary Table 4). There are no significant differences in the free-running period of the circadian rhythms between wild-type and optKaiB/optKaiBC at 18–20 °C and 26–32 °C, and only small differences at other temperatures in the 18–38 °C range (Fig. 2c). Overall, the temperature compensation of the optimized strains was slightly poorer ( $Q_{10} \approx 1.13$ ) over the range of 23–36 °C than that for wild type ( $Q_{10} \approx 1.10$  from ref. 27, and  $Q_{10} \approx 1.04$  from Fig. 2c and Supplementary Table 6), which might relate to the difference in mRNA folding energies (Fig. 1d).

We further confirmed that improved rhythmicity at lower temperatures of the optKaiB and optKaiBC strains (Fig. 2b) was due to higher protein production levels of KaiB and KaiC. First, we confirmed that KaiC levels are considerably higher in the optKaiBC strain than in the wild type (Fig. 3a and Supplementary Fig. 1), and showed that KaiB levels are similarly increased in both the optKaiB and optKaiBC strains (Fig. 3b and Supplementary Fig. 2). Interestingly, the amplitude of the KaiC phosphorylation rhythm is comparable between wild type and optKaiBC at 20 °C (Fig. 3a). Second, to validate that the augmented KaiB and/or KaiC levels were responsible for the improved rhythmicity at cool temperatures, we co-expressed the native (non-optimized) sequences of *kaiB* (strain KaiB<sup>WT</sup>/OX) or *kaiBC* (strain KaiBC<sup>WT</sup>/OX) from an isopropylthiogalactoside (IPTG)-inducible *trc* promoter to enhance endogenous production of KaiB and KaiC (Fig. 3c). Figure 3d shows that KaiB is overexpressed in the KaiB<sup>WT</sup>/OX and

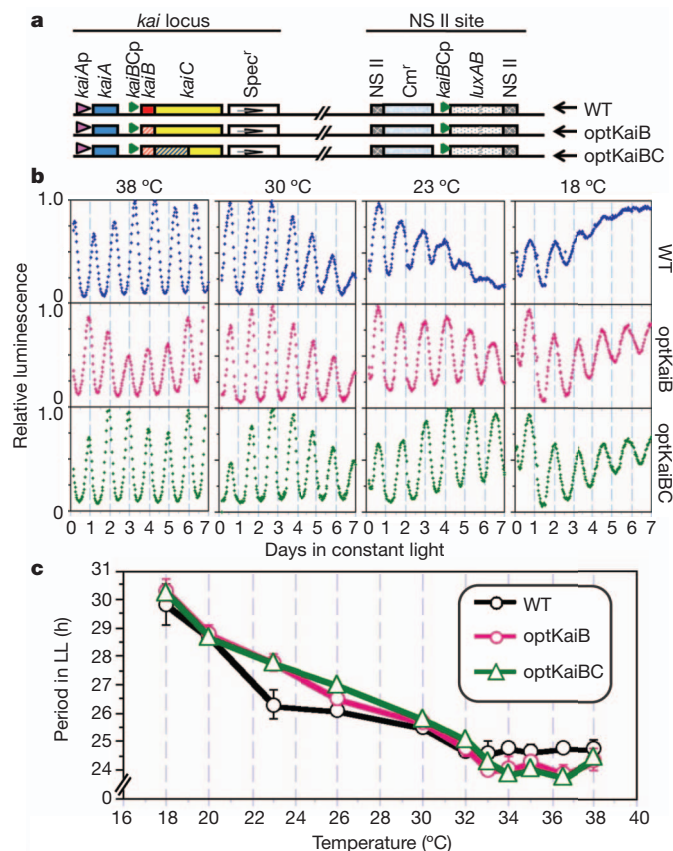


**Figure 2 | Conditional circadian phenotypes of the *kai*-optimized strains.** **a**, Diagrams of genes in the wild-type *kaiABC* (WT), *kaiB*-optimized (optKaiB) and *kaiBC*-optimized (optKaiBC) strains (see Methods for a detailed description). *Cm*<sup>r</sup>, chloramphenicol resistance; *kaiBCp*, *kaiBC* promoter; *luxAB*, reporter cassette containing the *luxA* and *luxB* genes; *NS II*, neutral site II; *Spec*<sup>r</sup>, spectinomycin resistance. **b**, Luminescence rhythms of wild-type and *kai*-optimized strains in constant light at the indicated temperatures. *In vivo* luminescence rhythms were monitored from a group of 12 colonies for each strain, and a representative example is shown for each group. **c**, Free-running periods of luminescence rhythms in constant light from different strains over a temperature range of 18–38 °C. Data are mean  $\pm$  s.e.m.

primarily by affecting KaiB and KaiC expression, thereby altering the relative levels of KaiB, KaiC and KaiA protein abundances in the cells. The stoichiometry among the Kai proteins is known to be crucial for expression of the cyanobacterial *in vitro* oscillator<sup>29</sup>, and it is therefore likely to be a key determining factor in the expression of rhythmicity *in vivo* that we report here.

**a**

WT optKaiBC

24 30 36 42 48 54 24 30 36 42 48 54

Ratio of hyper-P KaiC/total KaiC

Time in LL at 20 °C (h)

Relative total KaiC

Time in LL (h)

Total KaiC in LL24-54 (relative to WT)

Temperature

20 °C 25 °C 30 °C

**b**

WT optKaiBC optKaiBC

24 30 36 42 48 54 24 30 36 42 48 54 24 30 36 42 48 54

Time in LL (h)

Ratio of KaiB/NB

Time in LL at 20 °C (h)

Total KaiB in LL24-54 (relative to WT)

Temperature

20 °C 25 °C 30 °C

**c**

kai locus NS I NS II

kaiAp kaiA kaiBCp kaiB kaiC NS I Spec' luxAB NS I NS II Kmr' lacI<sup>q</sup> trpB<sup>+</sup> trpB<sup>+</sup> NS II

KaiB<sup>WT/OX</sup> KaiB<sup>WT/OX</sup> KaiB<sup>WT/OX</sup>

**d**

0 μM 5 μM IPTG

0 μM 5 μM

optKaiB optKaiBC WT KaiB<sup>WT/OX</sup> KaiB<sup>WT/OX</sup> KaiB<sup>WT/OX</sup>

KaiC KaiB KaiA NB

Relative Kai levels

KaiB KaiC KaiA

**e**

No IPTG 5 μM IPTG

WT optKaiBC optKaiBC KaiB<sup>WT/OX</sup> KaiB<sup>WT/OX</sup>

Relative luminescence

Days in constant light

constant light relative to wild type. **c**, Diagrams of the *kaiB*<sup>WT</sup>- or *kaiBC*<sup>WT</sup>-co-expressing strains. Km<sup>r</sup>, kanamycin resistance; *trcp*, *trc* promoter. **d**, Increase of KaiB and/or KaiC levels in *kaiB*<sup>WT</sup>- or *kaiBC*<sup>WT</sup>-co-expressing strains (KaiB<sup>WT</sup>/OX and KaiBC<sup>WT</sup>/OX) at 12 h constant light with/without 5 μM IPTG. Left panel shows immunoblot assays for KaiB, KaiC and KaiA; equal loading was confirmed by the nonspecific band. Right panel depicts the densitometry of relative KaiA, KaiB and KaiC protein abundances. **e**, Phenocopying of the cool-temperature rhythmicity of the *kaiB*- or *kaiBC*-optimized strains in the wild-type strain by increased expression of the *kaiB*<sup>WT</sup> and *kaiC*<sup>WT</sup> genes. Luminescence was recorded in constant light at 18 °C from cultures of wild-type, codon-optimized (optKaiB and optKaiBC), and *kai*-co-expressing (KaiB<sup>WT</sup>/OX and KaiBC<sup>WT</sup>/OX) strains in the presence or absence of IPTG (5 μM). Representative traces are shown for each case.



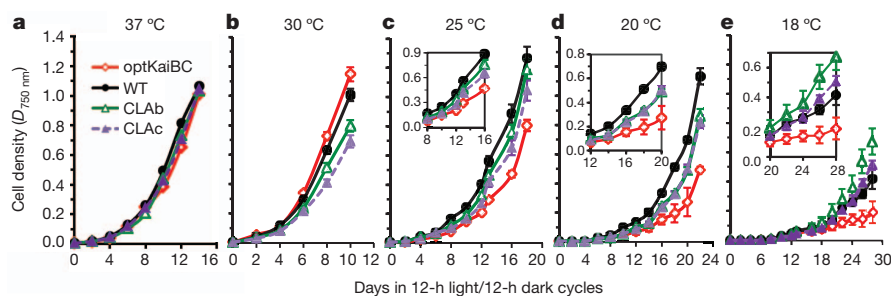


**Figure 4 | Optimizing the *kaiBC* sequence causes slower growth rate at cool temperatures.** **a–e**, Wild-type, optKaiBC, CLAb (arhythmic) and CLAc (damped oscillation) strains were grown in 12-h light/12-h dark cycles at 37 °C (**a**), 30 °C (**b**), 25 °C (**c**), 20 °C (**d**) or 18 °C (**e**), with constant air bubbling and shaking. Cell densities were monitored by measuring attenuance at 750 nm

( $D_{750\text{ nm}}$ ) every 2 days. Data are mean  $\pm$  s.e.m. from 2–6 independent experiments for each strain and condition. For a better comparison at 18, 20 and 25 °C, the insets are a magnified portion of the specified times. (For doubling time calculations, see Supplementary Table 7 and Supplementary Fig. 5.)

(Fig. 4d, e and Supplementary Table 7). Even the arhythmic CLAb and damped CLAc strains outperformed optKaiBC at 18–25 °C (Fig. 4c–e and Supplementary Table 7). Therefore, at cool temperatures in light–dark cycles, strains having damped (wild type and CLAc) or arhythmic (CLAb) phenotypes under free-running conditions outgrew the strain that expressed robust rhythms (optKaiBC).

Biases in codon usage are generally thought to be under directional selection for an optimal balance between translational efficiency and accuracy, in which a higher CAI is always better<sup>5,7</sup>. Other examples of selection for non-optimal codon usage (mediated by mRNA secondary structure and/or tRNA availability) are rare and poorly characterized<sup>8,30</sup>. Our study presents a counter-example to the standard view, and suggests the action of either selection against optimal codon usage, or stabilizing selection in which both low and high extremes in codon-usage bias have higher fitness costs. Indeed, the non-optimal codon usage seems to be a molecular mechanism in which post-transcriptional events allow *S. elongatus* cells to switch between circadian and non-circadian regulation of gene expression depending on the environmental conditions, and our results are reminiscent of earlier observations of such ‘conditionality’ for circadian rhythms<sup>2,31</sup>.

Why is conditionality an important characteristic of circadian rhythms? We tend to think of circadian clocks as rhythmic activators, but they are also rhythmic repressors. Under some conditions this repressor/activator balance may inhibit growth and circadian regulation may not be adaptive. At cooler temperatures, the free-running period of the circadian rhythm of *S. elongatus* can be as long as 30 h (Fig. 2c), suggesting that the coupling of gene expression and rhythmic regulation might be maladaptive for growth at lower temperatures. For example, we previously reported that *S. elongatus* mutant strains with 30 h period lengths can entrain to 24 h light–dark cycles, but they do so with a considerably later phase relationship that is maladaptive<sup>16</sup>; a result that fits with our current observations. As another example of conditionality, our previous competition experiments at 30 °C found that the arhythmic CLAb strain is more fit than wild type under constant illumination, but is rapidly outcompeted by wild type in light–dark cycles<sup>3</sup> (Fig. 4 shows that the growth of CLAb is poorer than wild type in light–dark cycles at 20–30 °C). Therefore, both illumination and temperature are environmental parameters that demonstrate the ‘conditional’ advantages of circadian regulation under some conditions but not others.

Our data show that optimizing the codon usage for the circadian *kaiBC* genes of *S. elongatus* does not disrupt endogenous circadian regulation (as in the case of the *Neurospora* FRQ protein<sup>25</sup>), but instead the sequence optimization enhances circadian regulation in a range of cool temperatures that are relevant for the ecology of this organism. Despite this enhancement of intrinsic rhythmicity, however, optimal codon usage at the *kai* locus impairs cell growth at cooler temperatures. Therefore, our data suggest selection against an optimal codon

usage because it is incompatible with a post-transcriptionally modulated conditional suppression of circadian rhythmicity at cool temperatures. In *S. elongatus*, circadian conditionality allows expression of robust endogenous rhythmicity in the range of temperatures that permit vigorous growth and suppress rhythmicity at temperatures in which growth of this species is minimal (Supplementary Fig. 5). Our observations provide a new example of post-transcriptional regulation of circadian clock genes that confers an adaptive response to different environmental conditions.

## METHODS SUMMARY

Frequencies of codon usage were analysed from all putative proteins in the whole genome of *Synechococcus elongatus* PCC 7942, all 59 ribosomal genes in the genome (Supplementary Table 2), and 16 highly expressed genes that show high microarray values from both data sets (Supplementary Table 3). The fractions of codon usage were based on usage frequencies per 1,000 codons (Supplementary Table 1). The overall relative synonymous codon usage (RSCU) values of the genome were calculated from 3,261 coding sequences from the genome (Supplementary Table 8), and infrequently used codons in *kaiB* or *kaiC* were changed to those coding for the specific amino acids with higher RSCU values (Supplementary Tables 9 and 10) or higher codon-usage fractions (Supplementary Table 1) in the genome. DNA fragments containing optimized *kaiB* or *kaiC* coding sequences (optKaiB or optKaiC) were synthesized and cloned into a plasmid containing the wild-type *kai* cluster DNA to replace the corresponding wild-type DNA sequences. The CAI values of all genes in the genome and the codon-optimized versions of the *kai* genes were calculated based on RSCU values.

**Full Methods** and any associated references are available in the online version of the paper.

**Received 29 May 2012; accepted 30 January 2013.**

**Published online 17 February 2013.**

- Ishihara, M. *et al.* Expression of a gene cluster *kaiABC* as a circadian feedback process in cyanobacteria. *Science* **281**, 1519–1523 (1998).
- Njus, D., McMurry, L. & Hastings, J. W. Conditionality of circadian rhythmicity: synergistic action of light and temperature. *J. Comp. Physiol.* **117**, 335–344 (1977).
- Woelfle, M. A., Ouyang, Y., Phanvijitsiri, K. & Johnson, C. H. The adaptive value of circadian clocks: an experimental assessment in cyanobacteria. *Curr. Biol.* **14**, 1481–1486 (2004).
- Drummond, D. A. & Wilke, C. O. Mistranslation-induced protein misfolding as a dominant constraint on coding-sequence evolution. *Cell* **134**, 341–352 (2008).
- Bulmer, M. The selection-mutation-drift theory of synonymous codon usage. *Genetics* **129**, 897–907 (1991).
- Plotkin, J. B. & Kudla, G. Synonymous but not the same: the causes and consequences of codon bias. *Nature Rev. Genet.* **12**, 32–42 (2011).
- Shah, P. & Gilchrist, M. A. Explaining complex codon usage patterns with selection for translational efficiency, mutation bias, and genetic drift. *Proc. Natl Acad. Sci. USA* **108**, 10231–10236 (2011).
- Eyre-Walker, A. & Bulmer, M. Reduced synonymous substitution rate at the start of enterobacterial genes. *Nucleic Acids Res.* **21**, 4599–4603 (1993).
- Akashi, H. Synonymous codon usage in *Drosophila melanogaster*: natural selection and translational accuracy. *Genetics* **136**, 927–935 (1994).
- Shah, P. & Gilchrist, M. A. Effect of correlated tRNA abundances on translation errors and evolution of codon usage bias. *PLoS Genet.* **6**, e1001128 (2010).
- Zhou, T., Weems, M. & Wilke, C. O. Translationally optimal codons associate with structurally sensitive sites in proteins. *Mol. Biol. Evol.* **26**, 1571–1580 (2009).

12. Ikemura, T. Correlation between the abundance of *Escherichia coli* transfer RNAs and the occurrence of the respective codons in its protein genes: a proposal for a synonymous codon choice that is optimal for the *E. coli* translational system. *J. Mol. Biol.* **151**, 389–409 (1981).
13. Sharp, P. M. & Li, W. H. The codon adaptation index—a measure of directional synonymous codon usage bias, and its potential applications. *Nucleic Acids Res.* **15**, 1281–1295 (1987).
14. Lynn, D. J., Singer, G. A. & Hickey, D. A. Synonymous codon usage is subject to selection in thermophilic bacteria. *Nucleic Acids Res.* **30**, 4272–4277 (2002).
15. Paul, S., Bag, S. K., Das, S., Harvill, E. T. & Dutta, C. Molecular signature of hypersaline adaptation: insights from genome and proteome composition of halophilic prokaryotes. *Genome Biol.* **9**, R70 (2008).
16. Ouyang, Y., Andersson, C. R., Kondo, T., Golden, S. S. & Johnson, C. H. Resonating circadian clocks enhance fitness in cyanobacteria. *Proc. Natl Acad. Sci. USA* **95**, 8660–8664 (1998).
17. Liu, Y. *et al.* Circadian orchestration of gene expression in cyanobacteria. *Genes Dev.* **9**, 1469–1478 (1995).
18. Ito, H. *et al.* Cyanobacterial daily life with Kai-based circadian and diurnal genome-wide transcriptional control in *Synechococcus elongatus*. *Proc. Natl Acad. Sci. USA* **106**, 14168–14173 (2009).
19. Vijayan, V., Zuzow, R. & O'Shea, E. K. Oscillations in supercoiling drive circadian gene expression in cyanobacteria. *Proc. Natl Acad. Sci. USA* **106**, 22564–22568 (2009).
20. Vijayan, V., Jain, I. H. & O'Shea, E. K. A high resolution map of a cyanobacterial transcriptome. *Genome Biol.* **12**, R47 (2011).
21. Woelfle, M. A., Xu, Y., Qin, X. & Johnson, C. H. Circadian rhythms of superhelical status of DNA in cyanobacteria. *Proc. Natl Acad. Sci. USA* **104**, 18819–18824 (2007).
22. Kudla, G., Murray, A. W., Tollervey, D. & Plotkin, J. B. Coding-sequence determinants of gene expression in *Escherichia coli*. *Science* **324**, 255–258 (2009).
23. Tuller, T., Waldman, Y. Y., Kupiec, M. & Ruppin, E. Translation efficiency is determined by both codon bias and folding energy. *Proc. Natl Acad. Sci. USA* **107**, 3645–3650 (2010).
24. Gu, W., Zhou, T. & Wilke, C. O. A universal trend of reduced mRNA stability near translation-initiation site in prokaryotes and eukaryotes. *PLOS Comput. Biol.* **6**, e1000664 (2010).
25. Zhou, M. *et al.* Non-optimal codon usage affects expression, structure and function of clock protein FRQ. *Nature* <http://dx.doi.org/10.1038/nature11833> (this issue).
26. Pittendrigh, C. S. On temperature independence in the clock system controlling emergence time in *Drosophila*. *Proc. Natl Acad. Sci. USA* **40**, 1018–1029 (1954).
27. Kondo, T. *et al.* Circadian rhythms in prokaryotes: luciferase as a reporter of circadian gene expression in cyanobacteria. *Proc. Natl Acad. Sci. USA* **90**, 5672–5676 (1993).
28. Xu, Y., Mori, T. & Johnson, C. H. Cyanobacterial circadian clockwork: roles of KaiA, KaiB and the *kaiBC* promoter in regulating KaiC. *EMBO J.* **22**, 2117–2126 (2003).
29. Nakajima, M., Ito, H. & Kondo, T. *In vitro* regulation of circadian phosphorylation rhythm of cyanobacterial clock protein KaiC by KaiA and KaiB. *FEBS Lett.* **584**, 898–902 (2010).
30. Konigsberg, W. & Godson, G. N. Evidence for use of rare codons in the *dnaG* gene and other regulatory genes of *Escherichia coli*. *Proc. Natl Acad. Sci. USA* **80**, 687–691 (1983).
31. Liu, Y., Garceau, N. Y., Loros, J. J. & Dunlap, J. C. Thermally regulated translational control of FRQ mediates aspects of temperature responses in the *Neurospora* circadian clock. *Cell* **89**, 477–486 (1997).

**Supplementary Information** is available in the online version of the paper.

**Acknowledgements** We are grateful for the suggestions of M. Woelfle and the technical assistance of D. Zelli and C. Chintanaphol. This research was supported by grants from the National Institute of General Medical Science to C.H.J. (R01 GM067152 and R01 GM088595) and to Y.L. (GM068496 and GM062591), the Welch Foundation (I-1560) to Y.L., and the National Science Foundation (DEB-0844968) and the Searle Scholars Program to A.R. P.S. acknowledges support from a Burroughs Wellcome Fund Career Award and a David & Lucille Packard Foundation Fellowship awarded to Joshua B. Plotkin.

**Author Contributions** Y.X. and P.M. collected data; Y.X., P.M. and Y.L. analysed the experimental data; Y.X., P.S. and A.R. analysed the bioinformatic data; Y.L. and C.H.J. designed the original conceptual basis for the study; Y.X. and C.H.J. designed the experimental bases for the study; Y.X., P.S. and C.H.J. wrote the manuscript. All authors discussed the results and commented on the manuscript.

**Author Information** Reprints and permissions information is available at [www.nature.com/reprints](http://www.nature.com/reprints). The authors declare no competing financial interests. Readers are welcome to comment on the online version of the paper. Correspondence and requests for materials should be addressed to C.H.J. ([carl.h.johnson@vanderbilt.edu](mailto:carl.h.johnson@vanderbilt.edu)).

## METHODS

**Evaluation of codon usage.** To evaluate the frequency of codon usage of the central clock genes *kaiABC*, we analysed coding sequences from different groups. One group is from 2,400,255 residue sequences from all putative proteins in the whole genome of *Synechococcus elongatus* PCC 7942. The second group is from all 59 ribosomal genes in the genome (Supplementary Table 2). We also analysed microarray data sets from two independent laboratories<sup>18,19</sup>. First, we calculated total microarray signals from one circadian cycle in constant light for each of these genes. Then, all of these genes were rearranged from strongest to weakest mRNA abundances based on the total microarray signal values in constant light. Finally, we selected the top 16 genes that show high microarray values from both data sets (Supplementary Table 3), and combined all of these coding sequences to the third group as putative highly expressed genes. The codon usage frequency was analysed with a web-based program from the Sequence Manipulation Suite of Bioinformatics.org (<http://www.bioinformatics.org>). The fractions of codon usage were based on usage frequencies per 1,000 codons (Supplementary Table 1).

**Codon optimization of *kai* genes.** Relative synonymous codon usage (RSCU) is defined as the ratio of the observed frequency of codons to the expected frequency, given that all the synonymous codons for the same amino acids are used equally<sup>13,32</sup>. In the absence of any codon-usage bias, the RSCU value would be 1.00. A codon that is used less frequently than expected will have a value of less than 1.00, and vice versa for a codon used more frequently than expected. The overall RSCU values of *S. elongatus* PCC 7942 were calculated from 3,261 coding sequences (990,021 codons) from the genome (Supplementary Table 8). Infrequently used codons in *kaiB* or *kaiC* coding sequences were changed to those coding for the specific amino acids with higher RSCU values (Supplementary Tables 9 and 10) or higher codon-usage fractions (Supplementary Table 1) in the genome. As shown in Supplementary Fig. 6 and Supplementary Table 9, 67 out of 102 codons were optimized for the entire *kaiB* coding region, whereas for the *kaiC* gene, the infrequently used codons were mainly optimized in the amino-terminal KaiC-I domain that is encoded by the 5' half of the *kaiC* gene (Supplementary Fig. 7 and Supplementary Table 10).

**Synthesis and construction of optimized *kai* genes.** DNA fragments containing optimized *kaiB* or *kaiC* coding sequences with wild-type flanking sequences were commercially synthesized and cloned into the SmaI site of pUC57 (EZBioLab) to produce pUCoptKaiB or pUCoptKaiC, respectively. On the basis of pUCoptKaiB or pUCoptKaiC templates, the *optKaiB* or *optKaiC* fragments were resynthesized using 12–18 thermal cycles with pfuUltra High-fidelity DNA polymerase (Stratagene) and primers containing the corresponding wild-type flanking sequences. After purification, the *optKaiB* or *optKaiC* fragments were EZcloned (Stratagene) into a plasmid containing the wild-type *kai* cluster DNA to replace the corresponding wild-type DNA sequences. After the unchanged parental plasmid was digested at 37 °C for 1 h with Dpn I (New England Biolabs), the circular, nicked optimized double-stranded DNA was transformed into *Escherichia coli* to generate pKai-optKaiB and pKai-optKaiC, respectively. To optimize the *kaiB* and *kaiC* genes, the resynthesized *optKaiB* fragment was EZcloned into the pKai-optKaiC plasmid to replace the corresponding wild-type *kaiB* coding sequences and produce pKai-optKaiBC. All of these *kai*-optimized constructs were confirmed by DNA sequencing analysis. In case of direct comparison, the wild-type versions of the *kaiB*, *kaiC* and *kaiBC* genes or coding sequences are indicated as *kaiB*<sup>WT</sup>, *kaiC*<sup>WT</sup> and *kaiBC*<sup>WT</sup>, whereas the codon-optimized versions are denoted as *kaiB*<sup>opt</sup>, *kaiC*<sup>opt</sup> and *kaiBC*<sup>opt</sup>, respectively.

**Computation of CAI and 5' mRNA folding energy.** To calculate CAI values of genes, we began by calculating the RSCU of all ribosomal genes<sup>13</sup> (Supplementary Table 2). Using these RSCU values, we calculated the CAI values of all genes in the *S. elongatus* genome and the codon-optimized versions of the *kai* genes. Using a sliding window of 20 codons, Fig. 1a shows that optimized versions of both *kaiB* (*kaiB*<sup>opt</sup>) and *kaiC* (*kaiC*<sup>opt</sup>) genes have higher CAI values along the entire length of the genes than the wild-type versions, and higher than the average CAI of ribosomal genes. The CAI of the wild-type *kaiB* and *kaiC* genes is less than the average CAI of the genome, in spite of their high abundance in the transcriptome. As expected, the average CAI of ribosomal genes is much higher than the average. As an example, the CAI of *kaiB*<sup>opt</sup> was optimized to 0.95 as shown by the red line in Fig. 1b by adding the RSCU of ribosomal genes.

In addition to codon usage as it relates to the relative expression of various tRNA genes, the translational efficiency of the production of a protein depends on the 5' folding energy of its mRNA. To calculate the minimum free energy ( $\Delta G$ ) of folding of the 5' region of mRNAs, we used the first 40 nucleotides of the coding sequences (1–40 nucleotides). In addition, we used the RNA folding algorithm in RNA fold of the Vienna RNA package 2.0 (ref. 33). We calculated  $\Delta G$  at 37 °C for each gene in the *S. elongatus* genome using default parameters. Then, to calculate the effect of temperature on folding energy for the *kai* genes (wild-type and optimized versions), we varied the temperature from 18 to 40 °C. The folding energy of the

*kaiB*<sup>WT</sup> and *kaiC*<sup>WT</sup> genes is much higher than the rest of the genome, indicating selection for faster translation initiation (Fig. 1c). Because the folding energy of an mRNA depends on the temperature, calculation of the minimum free energy of folding ( $\Delta G$ ) at varying temperatures showed that  $\Delta G$  for both *kaiB*<sup>WT</sup> and *kaiB*<sup>opt</sup> increases with temperature, and that optimizing codon usage also increases the  $\Delta G$  of the *kaiB*<sup>opt</sup> gene at all temperatures (Fig. 1d).

**Generation of *kai*-optimized and *kai*-co-expressing cyanobacterial strains.** *S. elongatus* PCC 7942 was used as the cyanobacterial host strain. A *kaiBCp::luxAB* luminescence reporter of clock-controlled gene expression was integrated into either neutral site I (NS I) with a spectinomycin selection marker (or in other experiments, into NS II with a chloramphenicol selection marker), in which the expression of the *Vibrio harveyi* luciferase structure gene cassette *luxAB* is driven by the promoter of the *kaiBC* genes (*kaiBCp*) and serves as a real-time reporter of promoter activity<sup>1,27,28</sup>. The *kaiABC*-null strain was created by replacement of the *kaiABC* DNA region with a kanamycin-resistance gene<sup>1</sup>. The wild-type *kaiABC* cluster or codon-optimized *kaiABC* cluster containing a *kaiB*<sup>opt</sup>, *kaiC*<sup>opt</sup> or *kaiBC*<sup>opt</sup> coding region and a spectinomycin-resistance cassette was reintroduced into the endogenous *kai* locus by replacing the kanamycin-resistance gene of the *kaiABC*-null strain to give rise to transgenic strains with either the wild-type or the optimized version of the *kaiABC* cluster. This replacement was done in such a way that the *kaiABC* cluster was recreated to be exactly the same as the wild-type cluster with no insertions or deletions except a selection marker downstream of the genomic *kaiC* sequence. The transgenic cyanobacterial strain containing the wild-type version of the *kai* cluster was named the wild-type strain, whereas the strains containing codon-optimized versions of the *kai* cluster with *kaiB*<sup>opt</sup>, *kaiC*<sup>opt</sup> or *kaiBC*<sup>opt</sup> were called optKaiB, optKaiC or optKaiBC, respectively (Fig. 2a). For co-expression of wild-type *kaiB*, *kaiC* or *kaiBC* genes *in vivo*, the *trc*::*kaiB*<sup>WT</sup>, *trc*::*kaiC*<sup>WT</sup> or *trc*::*kaiBC*<sup>WT</sup> constructs with a kanamycin-resistance marker<sup>28</sup> were transformed into the NS II region of a wild-type luminescence reporter strain to generate *kai*-co-expressing strains KaiB<sup>WT</sup>/OX, KaiC<sup>WT</sup>/OX or KaiBC<sup>WT</sup>/OX (Fig. 3c), in which the co-expression of wild-type *kaiB*, *kaiC* or *kaiBC* genes from NS II was under the control of an IPTG-derepressible heterologous *trc* promoter, and the original *kaiABC* cluster remains at the original wild-type site. These codon-optimized strains containing *kaiB*<sup>opt</sup>, *kaiC*<sup>opt</sup> or *kaiBC*<sup>opt</sup> and *kai*-co-expressing strains were confirmed by PCR, DNA sequencing, immunoblotting and luminescence analyses. As indicated in Fig. 2a, the wild-type coding region of the *kaiB* gene was replaced with *kaiB*<sup>opt</sup> coding sequences in the optKaiB strain, whereas the *kaiBC* coding region was replaced with both the *kaiB*<sup>opt</sup> and *kaiC*<sup>opt</sup> (that is, *kaiBC*<sup>opt</sup>) coding sequences in the optKaiBC strain. At NS II, a *kaiBC* promoter-driving *luxAB* expression cassette with a chloramphenicol selection marker was integrated to function as a luminescence reporter of clock-controlled promoter activity. In the *kaiB*<sup>WT</sup>- or *kaiBC*<sup>WT</sup>-co-expressing strains in Fig. 3c, three sites in the chromosome are depicted: (1) the wild-type *kaiABC* cluster (*kaiABC*<sup>WT</sup>); (2) the *luxAB* luminescence reporters in NS I; and (3) an IPTG-derepressible promoter driving expression of *kaiB*<sup>WT</sup> (KaiB<sup>WT</sup>/OX strain) or *kaiBC*<sup>WT</sup> (KaiBC<sup>WT</sup>/OX strain) in NS II.

**Measurement of luminescence rhythms.** Cyanobacterial strains were grown in modified BG11 (ref. 34) liquid media with air bubbling or BG11 agar plates supplemented with appropriate antibiotics (20 µg ml<sup>-1</sup> spectinomycin; 10 µg ml<sup>-1</sup> kanamycin; 7.5 µg ml<sup>-1</sup> chloramphenicol) at 30 °C under continuous cool-white illumination (constant light; 40–50 µE m<sup>-2</sup> s<sup>-1</sup>). Before the cells were released into constant light for the luminescence assay, a 12-h dark exposure was given to synchronize the rhythms of the individual cells in the population. For induction of co-expressed *kaiB*, *kaiC* or *kaiBC* genes, the *trc* inducer IPTG was added at the beginning of constant light to final concentrations of 0, 2, 5, 10, 100 or 1,000 µM. Luminescence was measured with the *kaiBCp::luxAB* reporter of clock-controlled gene expression that serves as a real-time reporter of promoter activity<sup>1,27,28</sup>. For measurement of *in vivo* luminescence rhythms at different temperatures (18–38 °C), at least 12 independent colonies for each condition were monitored as previously described<sup>28,35</sup>. Our standard light intensity for the luminescence rhythm assay was 40–50 µE m<sup>-2</sup> s<sup>-1</sup>, but we observed that the rate of damping in the wild type was influenced by both the temperature (as described in this paper) and light intensity (as tested under a range of light intensities).

**Calculation of free-running period,  $Q_{10}$  value, and damping rate of luminescence rhythms.** The period of luminescence rhythms was analysed with ChronoAnalysis II, version 10.1 (courtesy of T. Roenneberg), and the  $Q_{10}$  value for evaluation of temperature compensation over a wide range of temperatures was calculated with the following equation:  $Q_{10} = [(1/\tau_2)/(1/\tau_1)]^{10/(T_2-T_1)}$ ; in which  $\tau_1$  denotes period at the lower temperature ( $T_1$ ), and  $\tau_2$  denotes period at the higher temperature ( $T_2$ )<sup>36</sup>. Damping rate is the number of days required for the amplitude of the rhythm to decrease to 1/e of the starting value. The damping rates were calculated with the LUMICYCLE data analysis program (Actimetrics;



courtesy of D. Ferster). The program fits the data to a sine wave multiplied by an exponential decay factor<sup>37</sup>.

**Immunoblot assays for Kai abundance.** After two 12-h light–dark cycles, liquid cultures at  $D_{750\text{ nm}} = 0.3$  were released to constant light at indicated temperatures. About 30 ml of cells were collected at different time points and an appropriate amount of fresh medium was added to the culture flask to maintain an equal cell density during the time-course experiment. For *kaiB*- or *kaiBC*-co-expressing strains, the cultures were treated with/without 5  $\mu\text{M}$  IPTG at constant light time zero, for 12 h before cell collection. Total proteins were extracted as previously described<sup>35</sup>. Total extracts were separated by SDS–PAGE (15% gel for KaiB and 10% gel for KaiA and KaiC) and transferred onto nitrocellulose membranes. Proteins were transferred to nitrocellulose for immunoblotting using polyclonal rabbit antisera raised against KaiA or KaiB<sup>35</sup> or using polyclonal mouse antisera raised against KaiC<sup>28</sup>. Equal loading of extracts was confirmed by Coomassie blue staining in the gel, Ponceau red staining on the membrane, and/or by the density of nonspecific bands on the immunoblots. The immunoblot signals for relative Kai protein density/abundance were analysed with National Institutes of Health Image J software.

**Determination of growth rate and doubling time.** Growth rates of cyanobacterial strains, including wild type, optKaiBC, as well as two arrhythmic/damped *kaiC* mutants (CLAb and CLAc)<sup>1,3</sup>, were measured in parallel at 18, 20, 25, 30, 34 and 37 °C. Initial cultures were grown in liquid BG-11 medium at 30 °C under constant illumination (50  $\mu\text{E m}^{-2} \text{ s}^{-1}$ ) in a shaking water bath at 100 r.p.m. and with air bubbling into the cultures. Cell densities were monitored by measuring the attenuation at 750 nm ( $D_{750\text{ nm}}$ ). When cell densities reached  $D_{750\text{ nm}} = 0.8$ , cultures were diluted to  $D_{750\text{ nm}} = 0.005$ , and grown in 12-h light–dark cycles (12 h light (50  $\mu\text{E m}^{-2} \text{ s}^{-1}$ ) followed by 12 h darkness) in water baths set to 18, 20, 25, 30, 34 or 37 °C with shaking (100 r.p.m.) and air bubbling. Cell densities were

determined at  $D_{750\text{ nm}}$  over a time course as indicated. When  $D_{750\text{ nm}}$  values of cell cultures exceed 0.9, the attenuation measurement is not linear with cell density. Therefore, for samples with a  $D_{750\text{ nm}}$  that was larger than 0.9, the samples were diluted to a  $D_{750\text{ nm}}$  that was within the linear range before attenuation determination (and the plotted  $D$  value is then corrected for the dilution). Two-to-six independent experiments were performed for each strain, and the growth curves were plotted as average  $D_{750\text{ nm}}$  values over time in light–dark. Doubling time was calculated by fitting exponential curves to the growth curves. Growth rate was generated by fitting growth data to exponential curves (cell density at a specific time = initial cell density  $\times e^{(\text{growth rate} \times \text{time})}$ ) (see <http://mathworld.wolfram.com/LeastSquaresFittingExponential.html>). Doubling time was calculated as: doubling time (h) =  $(\ln(2)/\text{growth rate}) \times 24$ .

**Statistical analyses.** A two tailed Student's *t*-test was used for statistical analyses. \* $P < 0.05$ ; \*\* $P < 0.01$ .

32. Sharp, P. M. & Li, W. H. An evolutionary perspective on synonymous codon usage in unicellular organisms. *J. Mol. Evol.* **24**, 28–38 (1986).
33. Schuster, P., Fontana, W., Stadler, P. F. & Hofacker, I. L. From sequences to shapes and back: a case study in RNA secondary structures. *Proc. R. Soc. Lond. B* **255**, 279–284 (1994).
34. Bustos, S. A. & Golden, S. S. Expression of the *psbDII* gene in *Synechococcus* sp. strain PCC 7942 requires sequences downstream of the transcription start site. *J. Bacteriol.* **173**, 7525–7533 (1991).
35. Xu, Y., Mori, T. & Johnson, C. H. Circadian clock-protein expression in cyanobacteria: rhythms and phase setting. *EMBO J.* **19**, 3349–3357 (2000).
36. Xu, Y. et al. Intramolecular regulation of phosphorylation status of the circadian clock protein KaiC. *PLoS ONE* **4**, e7509 (2009).
37. Izumo, M., Johnson, C. H. & Yamazaki, S. Circadian gene expression in mammalian fibroblasts revealed by real-time luminescence reporting: temperature compensation and damping. *Proc. Natl Acad. Sci. USA* **100**, 16089–16094 (2003).

# CPEB1 coordinates alternative 3'-UTR formation with translational regulation

Felice-Alessio Bava<sup>1</sup>, Carolina Eliscovich<sup>2†\*</sup>, Pedro G. Ferreira<sup>2\*</sup>, Belen Miñana<sup>2</sup>, Claudia Ben-Dov<sup>2</sup>, Roderic Guigó<sup>2</sup>, Juan Valcárcel<sup>2,3</sup> & Raúl Méndez<sup>1,3</sup>

**More than half of mammalian genes generate multiple messenger RNA isoforms that differ in their 3' untranslated regions (3' UTRs) and therefore in regulatory sequences<sup>1</sup>, often associated with cell proliferation and cancer<sup>2,3</sup>; however, the mechanisms coordinating alternative 3'-UTR processing for specific mRNA populations remain poorly defined. Here we report that the cytoplasmic polyadenylation element binding protein 1 (CPEB1), an RNA-binding protein that regulates mRNA translation<sup>4</sup>, also controls alternative 3'-UTR processing. CPEB1 shuttles to the nucleus<sup>5,6</sup>, where it co-localizes with splicing factors and mediates shortening of hundreds of mRNA 3' UTRs, thereby modulating their translation efficiency in the cytoplasm. CPEB1-mediated 3'-UTR shortening correlates with cell proliferation and tumorigenesis. CPEB1 binding to pre-mRNAs not only directs the use of alternative polyadenylation sites, but also changes alternative splicing by preventing U2AF65 recruitment. Our results reveal a novel function of CPEB1 in mediating alternative 3'-UTR processing, which is coordinated with regulation of mRNA translation, through its dual nuclear and cytoplasmic functions.**

Alternative 3'-UTR processing to produce mRNA isoforms can occur by either alternative splicing of terminal exons and/or alternative polyadenylation (APA). APA, which is significantly more frequent than alternative splicing<sup>7</sup>, usually occurs by activation of 'weaker' polyadenylation signals (PAS) located 5' of 'stronger' PAS, the latter tending to be used by default<sup>8</sup>. In general, longer 3' UTRs display reduced translation, for example, due to microRNA target sites present in longer transcripts but not in shorter variants<sup>2,3</sup>. Transcripts encoding proto-oncogenes and other cell proliferation proteins tend to have longer 3' UTRs in non-proliferative tissues and shorter variants in transformed cells or highly proliferative tissues<sup>9–11</sup>.

Nuclear polyadenylation requires two core sequence elements<sup>1</sup>: the canonical PAS, recognized by the cleavage and polyadenylation specificity factor (CPSF), and a G/U-rich element, bound by the cleavage-stimulating factor. Other upstream accessory sequence elements modulate the use of suboptimal or non-consensus sites. Specific cytoplasmic mRNAs undergo elongation of their poly(A) tails in a cleavage-independent manner. Cytoplasmic polyadenylation uses the same PAS as in nuclear polyadenylation as well as an upstream cytoplasmic polyadenylation element (CPE)<sup>4</sup>. Cytoplasmic polyadenylation is mediated by a CPE-binding protein (CPEB1), which recruits CPSF to the PAS<sup>12</sup>; they then jointly recruit the cytoplasmic poly(A) polymerase GLD2<sup>13</sup>. CPE-mediated translational control targets 10–20% of the genome, particularly transcripts encoding cell cycle and cell differentiation regulators<sup>14–17</sup>. CPEB1 complexes are, at least in part, preassembled in the nucleus before their transport to the cytoplasm<sup>5,6</sup>. Although the nucleo-cytoplasmic distribution of CPEB1 varies (Supplementary Fig. 1a), in the stage IIIb Hodgkin's lymphoma-derived cell line (HD-MyZ) CPEB1 is mainly nuclear and

largely co-localizes with the splicing factor SRSF2<sup>18</sup>; this suggests a potential functional link between nuclear CPEB1 and pre-mRNA processing (Fig. 1a). The specificity of CPEB1 signal was confirmed by transfection with an inducible CPEB1 short hairpin (sh)RNA<sup>17</sup>, which resulted in a strong reduction of CPEB1 protein levels and of the nuclear fluorescent signal (Supplementary Fig. 1a, b). We found that this nuclear CPEB1 interacts with CPSF by cross-coimmunoprecipitation in RNase-treated and CPEB1-supplemented HeLa nuclear extracts (Supplementary Fig. 1c).

To address whether CPEB1 could regulate alternative splicing, we compared transcripts from control and CPEB1-knockdown (CPEB1-KD) HD-MyZ cells using a splicing-sensitive microarray covering >1,800 alternative splicing events in almost 500 genes important for cell proliferation, cancer progression and pre-mRNA splicing, including 113 events affecting 3' terminal exons<sup>19,20</sup>. We identified 139 CPEB1-dependent changes affecting 81 genes (Supplementary Table 1). Of those, 17 events were in 3' terminal exons for 6 genes. In five of the cases, a tandem CPE/alternative PAS was found in the proximity of an alternative 3' splice site that becomes more used after CPEB1 knockdown. In others, CPEB1-enhanced cleavage eliminated the most distal alternative 3' splice site and in the last the CPEs/alternative PAS were upstream of an alternative 5' splice site that is more used upon CPEB1 knockdown (Supplementary Fig. 2a). The changes in alternative splicing were confirmed by reverse transcription followed by quantitative PCR (RT-qPCR) using splice junction-specific oligonucleotides (Supplementary Fig. 2b).

3'-UTR processing of *BUB3* mRNA results in five possible alternative 3' UTRs generated from a combination of two alternative 3' splice sites and four alternative PAS (Fig. 1b). Expressed-sequence-tag evidence supports the tissue-specific expression of these variants, and *BUB3* mRNA has been proposed to be translationally regulated by CPEB1<sup>16</sup>. Indeed, *BUB3* pre-mRNA contains two CPEs immediately downstream of the first 3' splice site and PAS. We determined the *BUB3* 3'-UTR variants generated in the presence or absence of CPEB1 by RT-PCR, with oligonucleotide primers for the constitutive exon 7 and the poly(A) tail, followed by Southern blot for the common exon 7. To identify each of the 3'-UTR variants, the blots were re-hybridized with junction-probes complementary to the two possible splice sites (3' SS1 and 3' SS2 in Fig. 1c) and with probes complementary to sequences just upstream of the four possible cleavage sites (PAS1 to PAS4 in Fig. 1c). Quantification of the different UTRs labelled with exon 7 (Fig. 1d; see Methods for the quantification procedure) confirmed a small but reproducible increase in the use of 3' SS1 relative to 3' SS2 on CPEB1 knockdown (Fig. 1b, lanes 1 and 2 for PAS and 3 to 6 for alternative splicing). Independent quantification using splicing specific RT-qPCR (Fig. 1d and Supplementary Fig. 3a) showed a similar increase in the 3'-SS1/3'-SS2 ratio on CPEB1 knockdown. In addition, the quantification of each variant labelled with the 3' SS1

<sup>1</sup>Institute for Research in Biomedicine (IRB Barcelona), Baldori Reixac 10, 08028 Barcelona, Spain. <sup>2</sup>Centre for Genomic Regulation (CRG), UPF, Dr. Aiguader 88, 08003 Barcelona, Spain. <sup>3</sup>Institució Catalana de Recerca i Estudis Avançats (ICREA), Passeig Lluís Companys 23, Barcelona, 08010, Spain. <sup>†</sup>Present address: Albert Einstein College of Medicine, Department of Anatomy and Structural Biology, Bronx, New York 10461, USA.

\*These authors contributed equally to this work.

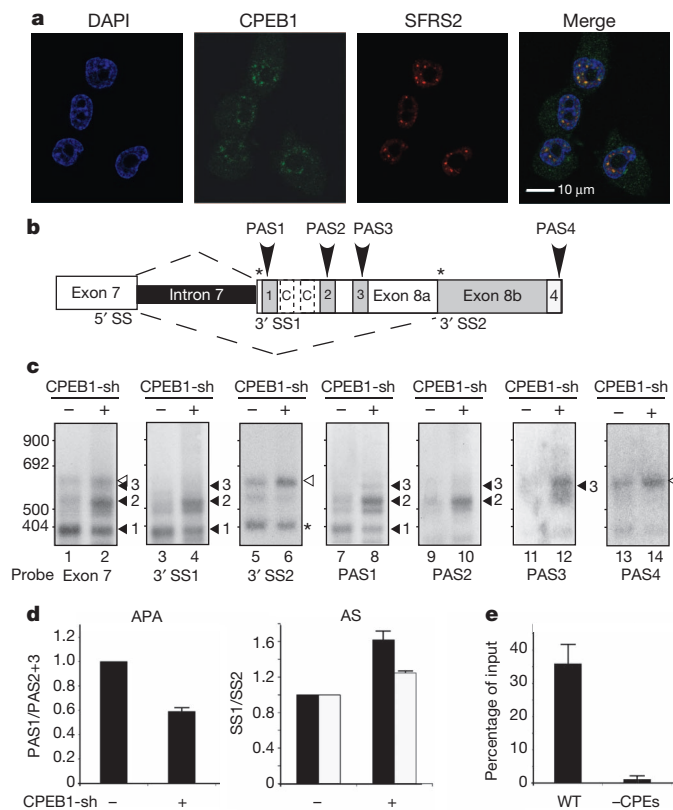


**Figure 1 | Nuclear CPEB1 co-localizes with SFRS2 and regulates the alternative 3'-UTR formation of *BUB3* mRNA.** **a**, Immunofluorescence of CPEB1 and SFRS2 in HD-MyZ cells. DNA staining (DAPI) in blue, CPEB1 staining in green, SFRS2 staining in red and the merged signals are shown. Scale bar, 10  $\mu$ m. **b**, Schematic representation of *BUB3* 3' UTR. Two alternative 3' splice sites (3' SS1 and 3' SS2), four PAS (PAS1, 2, 3, 4) and two CPEs (C) are indicated. The asterisks indicate stop codons. **c**, HD-MyZ cells were induced (CPEB1-sh+) or not (CPEB1-sh-) with doxycycline. Total RNA was isolated and 3' UTRs from endogenous *BUB3* mRNA were amplified by 3' RACE. The cDNA products were analysed by Southern blot using the indicated  $^{32}$ P-labelled probes. 3'-SS1-derived 3' UTRs (solid arrowheads; numbers indicate PAS1, PAS2 or PAS3) and 3' SS2/PAS4 3' UTR (white arrowheads) are indicated. The asterisks indicate unspecific products. **d**, Quantifications of APA or alternative splicing from c (black bars, see Methods) or by RT-qPCR (white bars). Error bars, s.d.;  $n > 3$ . ( $P = 0.00016$  for alternative splicing endogenous *BUB3* mRNA in control versus KD cells). **e**, WT or CPE-mutated *BUB3* pre-mRNAs coimmunoprecipitated with CPEB1 were detected by intron-specific RT-qPCR. Error bars, s.d.;  $n = 6$ .

or PAS1 probes unveiled a significant increase in the use of the PAS2 and PAS3 relative to PAS1 in absence of CPEB1 (Fig. 1d). CPEB1 depletion also had an effect on total *BUB3* mRNA levels, but not in other 'housekeeping' transcripts (Supplementary Fig. 3b). These results, confirmed with two other shRNAs (Supplementary Fig. 4a, b), indicate that CPEB1 on one hand promotes use of the 3' SS2/PAS4 over UTRs using 3' SS1, and on the other hand promotes 3' SS1/PAS1 at the expense of the 3' SS1/PAS2 and 3' SS1/PAS3 variants.

To determine if these effects were direct, we transfected a minigene containing a tagged-exon 7, intron 7 and exon 8a/b and the corresponding variants with inactivating mutations either in the CPEs (Fig. 2a) or in alternative PAS1 and PAS2 (Supplementary Fig. 5). Accordingly, the unprocessed pre-mRNAs generated by the wild type, but not by the CPE mutant-minigene, coimmunoprecipitated with CPEB1 (Fig. 1e and Supplementary Fig. 6). We then analysed the 3'-UTR variants generated from the minigenes in control or CPEB1-KD cells. Transcripts from the minigene were processed as the endogenous *BUB3* transcript and responded equally to CPEB1 depletion (Figs 1c and 2a). Quantification of the alternative 3' UTRs, generated

by the wild-type and mutant minigenes and in the presence or absence of CPEB1 (Fig. 2b), showed that either inactivation of the CPEs or knockdown of CPEB1 changed the selection of the PAS from PAS1 to a distributive use of all three PAS1–3 sites (Fig. 2a, b). Interestingly, the effects of knocking down CPEB1 or mutating the CPEs on alternative PAS selection were similar and non-additive (Fig. 2b, left panel), suggesting that the selection of PAS1 is directly driven by CPEB1 binding to the CPEs. For the selection of the 3' splice acceptor site, mutation of the CPEs or CPEB1 knockdown caused a shift from the use of 3' SS2 to 3' SS1 (Fig. 2a, b). Independent quantification using splice junction-specific RT-qPCR showed a similar increase in the 3' SS1/3' SS2 ratio on CPEB1 knockdown or CPE mutations (Fig. 2b).

For alternative splicing the effect of CPE mutation was partially additive to the effect of CPEB1 knockdown, suggesting that CPEB1 has both direct and indirect effects on *BUB3* alternative splicing. The observed changes were not due to mRNA stability differences (Supplementary Fig. 7a) or to nonsense-mediated decay (Supplementary Fig. 7b). Mutation of alternative PAS1–2 increased the use of 3' SS2 over 3' SS1 (Supplementary Fig. 5), consistent with competition between cleavage and downstream splicing, as the use of PAS1 and PAS2 will remove 3' SS2. Additionally, mutation of the CPEs or knock-down of CPEB1 resulted in the generation of an additional splice variant (S3/PAS4) from a cryptic 5' splice site (Fig. 2a and Supplementary Fig. 5a, splice junction probe (S3)). To circumvent the complexity generated by the combination of APA and alternative splicing, we generated a simplified construct containing only the three tandem alternative PAS and the CPEs, which was then transfected in control or CPEB1-KD cells (Fig. 2c). This simplified processing confirmed that CPEB1 promoted the use of PAS1 over PAS2–3, independently of splicing. Finally, we used HeLa nuclear extracts without or supplemented with recombinant CPEB1 to assess *in vitro* cleavage. Indeed, cleavage was both CPE- and CPEB1-dependent, indicating a direct effect of CPEB binding (Fig. 2d and Supplementary Figs 8 and 9).

To test the mechanism by which CPEB1 regulates splicing, we performed ultraviolet crosslinking-immunoprecipitation for the U2 small nuclear ribonucleoprotein particle auxiliary factor 65 kDa (U2AF65)<sup>21</sup> (Fig. 3a, b and Supplementary Fig. 10), to test its specific binding to the polypyrimidine tract (Supplementary Fig. 10d). U2AF65 showed a stronger crosslinking to the distal 3'-SS2 site than to the proximal 3'-SS1 site, even without CPEs. When the 3'-SS1 probe was extended to include the CPEs and PAS1, crosslinking of U2AF65 was undetectable, suggesting that CPEs negatively affect the recruitment of U2AF65 to the 3' SS1. Accordingly, inactivating mutation of the CPEs<sup>14</sup> (–CPEs in Fig. 3a, b) in the extended probe reduced CPEB1 crosslinking and restored U2AF65 crosslinking. Mutation of PAS in the extended probe (–PAS1 in Fig. 3a, b) also increased U2AF65 crosslinking, suggesting that CPEB1-mediated recruitment of the polyadenylation machinery to PAS1 negatively affects the recruitment of the splicing machinery to 3' SS1. Interestingly, increasing the distance between 3' SS1 and the CPEs/PAS1 (Spacer in Fig. 3a, b) restored U2AF65 crosslinking to the same levels as mutation of PAS, pointing to steric hindrance between the splicing and polyadenylation machineries. Taken together, these results indicate that CPEB1 negatively affects recognition of the proximal 3' SS1 by splicing factors through the recruitment of the polyadenylation machinery to PAS1. However, CPEB1 also had additional 'indirect' functions in splicing by modulating the levels of several splicing factors (Supplementary Fig. 11) encoded by CPE-regulated mRNAs<sup>14</sup>, a known mechanism of alternative splicing regulation<sup>22</sup>.

We next explored the biological relevance of alternative 3'-UTR processing of *BUB3* pre-mRNA. First, we analysed whether different 3' UTRs could mediate different translational efficiencies. We generated chimaeric transcripts with the Renilla luciferase open reading frame (ORF) fused to each of the five 3' UTRs identified and co-expressed



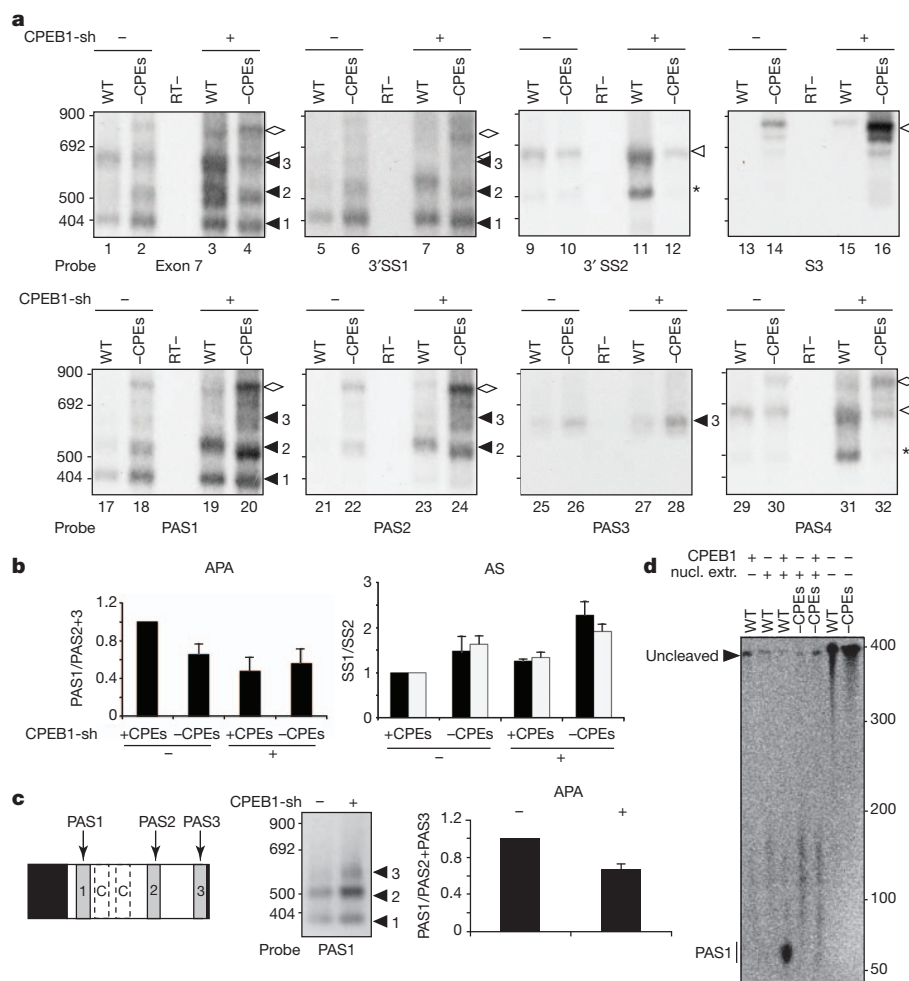


**Figure 2 | CPEs and CPEB1 directly regulate the alternative 3'-UTR formation of *BUB3* mRNA.** **a**, HD-MyZ cells, stably transfected with a doxycycline-inducible CPEB1 shRNA vector, were treated (CPEB1-sh+) or not (CPEB1-sh-) with doxycycline and then transfected with *BUB3* minigene containing WT or mutated CPEs. The minigene-derived 3' UTRs and the negative control (RT-) were analysed and labelled as in Fig. 1c. S3/PAS4 3' UTR (white diamond) is indicated. Asterisks indicate unspecific products. **b**, Quantifications of APA or alternative splicing from **c** (black bars, see Methods) or by RT-qPCR (white bars). Error bars, s.d.;  $n > 3$ . (For alternative splicing;  $P = 0.00037$  for WT vs (-CPEs) minigene in control cells and  $P = 0.00030$  for

them with Firefly luciferase as a control. To avoid nuclear processing of the reporters (Supplementary Fig. 12), any PAS upstream from the one being tested were inactivated. After normalizing for transcript levels (see Supplementary Fig. 12 for unnormalized luciferase activities and mRNA levels), all three variants generated from the 3' SS1 (PAS1, PAS2 and PAS3) and S3/PAS4 showed less efficient translation than the 3'-SS2 variant (Fig. 3c). Thus, the *BUB3* transcript variants generated in the presence of CPEB1 resulted in higher translation. Indeed the level of endogenous *BUB3* protein synthesized in the presence of CPEB1 was significantly higher than in CPEB1-KD cells (Fig. 3d), even though the level of *BUB3* mRNA increased in the knockdown (Supplementary Fig. 3b). *BUB3* is an essential component of the spindle-assembly checkpoint<sup>23</sup>, so CPEB1-KD cells failed to activate the spindle-assembly checkpoint (Supplementary Fig. 13).

Next, we examined how general the nuclear function of CPEB1 is in alternative pre-mRNA processing. We purified RNA from control and CPEB1-KD HD-MyZ cells and analysed 3' UTRs by high-throughput sequencing of the poly(A)-containing RNA fragments, identifying CPEB1-dependent APA changes (Fig. 3g and Supplementary Fig. 14). For 4,442 3' UTRs (out of 13,039; see Supplementary Information), we could estimate the transcript end. Control cells

WT minigene in control versus KD cells). **c**, Schematic representation of a simplified *BUB3* 3' UTR. PAS1, 2, 3 and two CPEs (C) are indicated (left panel). HD-MyZ cells were induced with doxycycline as in **a**, the simplified minigene was transfected and the derived 3' UTRs characterized as in **a** (middle panel). Quantifications of APA are plotted (right panel). Error bars, s.d.;  $n > 3$ . **d**, HeLa nuclear extract (nucl. extr.), supplemented or not with recombinant CPEB1, were incubated with the indicated radiolabelled RNAs transcribed from the minigene shown in **c**, either WT or with mutated CPEs. Then, RNA was extracted and resolved in a denaturing acrylamide gel, together with the free probes as controls. The cleaved product (PAS1) and the uncleaved product are indicated.

showed statistically significant shorter 3' UTRs than CPEB1-KD cells, but only for RNAs containing a CPE near the proximal alternative PAS (Supplementary Figs 6a, 11 and Supplementary Tables 2, 3 and 4). 868 UTRs were shorter in control cells, as opposed to 16 cases that were shorter in the knockdown. Of the former, 61% had a CPE motif near the APA site ( $P < 10^{-10}$ , Supplementary Table 4). Thus, we observed a correlation between the presence of CPEs in the proximity of an alternative PAS and the use of this site when CPEB1 was present, but not in its absence, to produce shorter 3' UTRs (Supplementary Figs 15–19). This was also the case of *BUB3* 3' UTR, for which the reads confirmed the results obtained by Southern blot and RT-qPCR experiments (Fig. 3h). For a few randomly selected candidates, we performed 3' RACE (rapid amplification of cDNA ends) RT-PCR followed by Southern blot in HD-MyZ cells expressing or not the CPEB1 shRNA. In all three cases, we observed an increase in the long versus short 3'-UTR ratio on depletion of CPEB1 (Fig. 3e). Moreover, the change in 3'-UTR length had a direct effect on the final accumulation of the encoded proteins (Fig. 3f). As is the case for cytoplasmic polyadenylation<sup>14</sup>, gene ontology analysis revealed that transcripts with CPEB1-regulated APA are enriched in cell cycle/growth/adhesion proteins and oncogenes (Supplementary Table 5). We performed

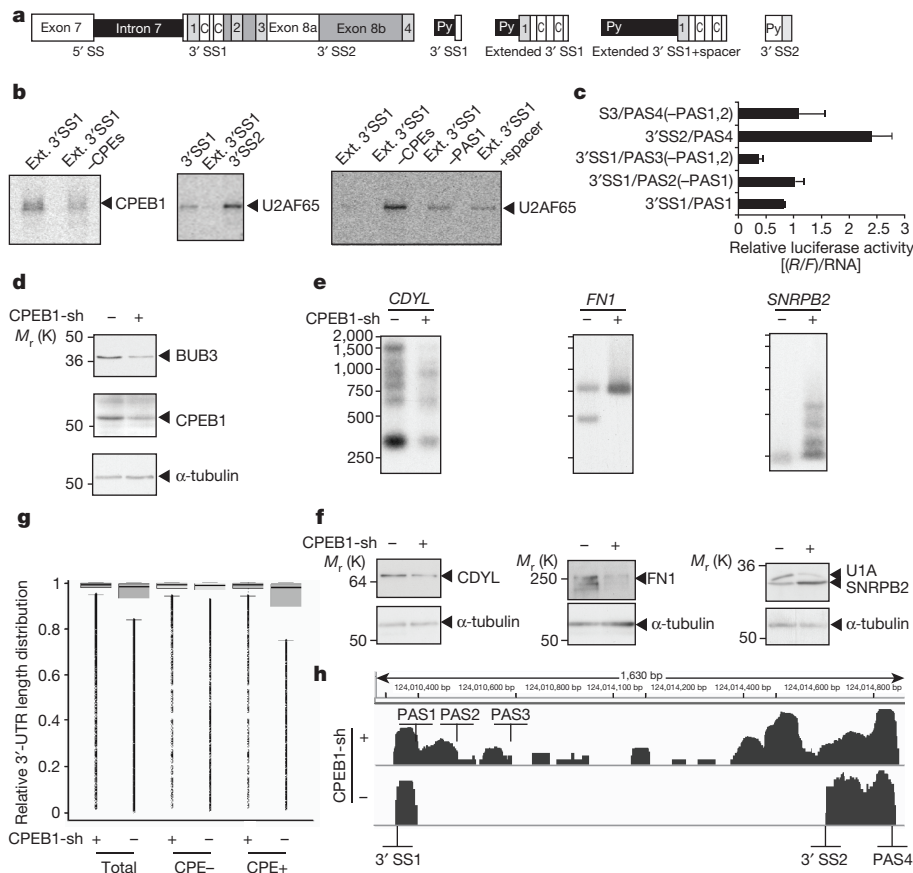


**Figure 3 | CPEB1 regulates recruitment of U2AF65, the use of proximal polyadenylation sites and *BUB3* mRNA translational control.** **a**, Schematic representation of radiolabelled RNA probes derived from *BUB3* 3' UTR. **b**, The indicated radiolabelled RNA probes were incubated with HeLa nuclear extract, ultraviolet-crosslinked and digested with RNase. U2AF65 or CPEB1 were immunoprecipitated and detected by autoradiography after 10% SDS-PAGE. **c**, HD-MyZ cells were transfected with vectors containing the Renilla luciferase ORF fused to the indicated *BUB3* 3' UTRs. Firefly luciferase ORF was used as a control. The relative levels of Renilla to Firefly activities, normalized by their mRNA levels, are shown ( $R/F$ ). Error bars, s.d. **d**, HD-MyZ, as in Fig. 2, cells

were treated (CPEB1-sh+) or not (CPEB1-sh-) with doxycycline and the levels of BUB3, CPEB1 and  $\alpha$ -tubulin were analysed by Western blot. Total RNA was purified and analysed by 3'-RACE-Southern-blot using specific probes for the indicated genes (**e**) or by deep sequencing (**g**). The distribution of relative 3'-UTR length for KD and control, with and without occurrence of CPE motif, is plotted (see Methods). **f**, Extracts from **e** were analysed by Western blot, with  $\alpha$ -tubulin as control. **h**, mRNA sequencing coverage for *BUB3* (NM\_004725 and NM\_001007793). The read coverage densities on a log scale for KD (upper) and WT (lower) are indicated. The PAS and 3' SS are indicated.

RNA-immunoprecipitation for CPEB1, but the large fraction of CPEB1-bound mature mRNAs masked the association with pre-mRNAs (see Supplementary Methods).

We found a general, but tissue-specific, trend towards shorter 3' UTRs in CPE-containing mRNAs (Supplementary Fig. 20; Supplementary Tables 6 and 7). Thus in low differentiated tissues or in tumoral samples, the correlation between shorter 3' UTRs and the presence of CPEs was highly significant, whereas differentiated tissues expressed the longest possible 3' UTR. This differential effect is consistent with the distribution of cis-acting elements in their 3' UTRs, (Supplementary Figs 21 and 22; Supplementary Table 3). Finally, we performed a 'naïve' motif enrichment analysis in the regions surrounding the polyadenylation sites in control and CPEB1-KD cells (Supplementary Tables 12–15). The pair PAS/CPE is the most significantly enriched pair of motifs linked to CPEB1-mediated APA events.

These results support a general model in which nuclear CPEB1 promotes alternative 3'-UTR formation by a dual mechanism (Fig. 4). First, CPEB1 helps to recruit CPSF to upstream suboptimal PAS that have CPEs closer than 100–150 nucleotides, either upstream or downstream. In the absence of CPEB1, these transcripts are processed in the strong and more 3' PAS, thus generating a long 3' UTR with greater potential for containing regulatory elements. When CPEB1 is present it promotes the use of an upstream APA site, thus generating shorter 3' UTRs that exclude the regulatory elements. In addition, when the CPEs

are upstream of the cleavage site (Supplementary Table 8), the resulting transcripts include a CPE at an optimal distance of the PAS for their regulation by CPEB1 in the cytoplasm<sup>14</sup>. Second, when the CPE-driven alternative PAS is present in the proximity of an alternative splice site, the CPEB1–CPSF complex interferes with the recruitment of the splicing machinery. Alternative 3'-UTR formation is mediated by a combination of these two mechanisms, APA and alternative splicing, including cases where the kinetics of cleavage eliminate downstream competing splicing sites, exons or polyadenylation sites. Conversely, kinetic competition can favour splice site selection and thus eliminate alternative polyadenylation sites. In addition to these effects *in cis*, CPEB1 indirectly modulates alternative splicing by changing the relative levels of splicing factors, possibly by regulating the translation and/or the alternative 3' UTRs of their mRNAs.

Thus, the function of CPEB1 is to recruit CPSF to a PAS, thereby promoting cleavage and polyadenylation in alternative PAS in the nucleus and poly(A) tail elongation and translational regulation in the cytoplasm. This dual function of CPEB1 provides transcript-specific coordination of pre-mRNA processing and translation control at two levels. First, the cytoplasmic polyadenylation complex would be preassembled during CPEB1-mediated pre-mRNA processing. Second, the same CPE that promotes the use of the alternative PAS will be then placed at the appropriate distance to promote translational activation in the cytoplasm. In the longer 3'-UTR variants, generated

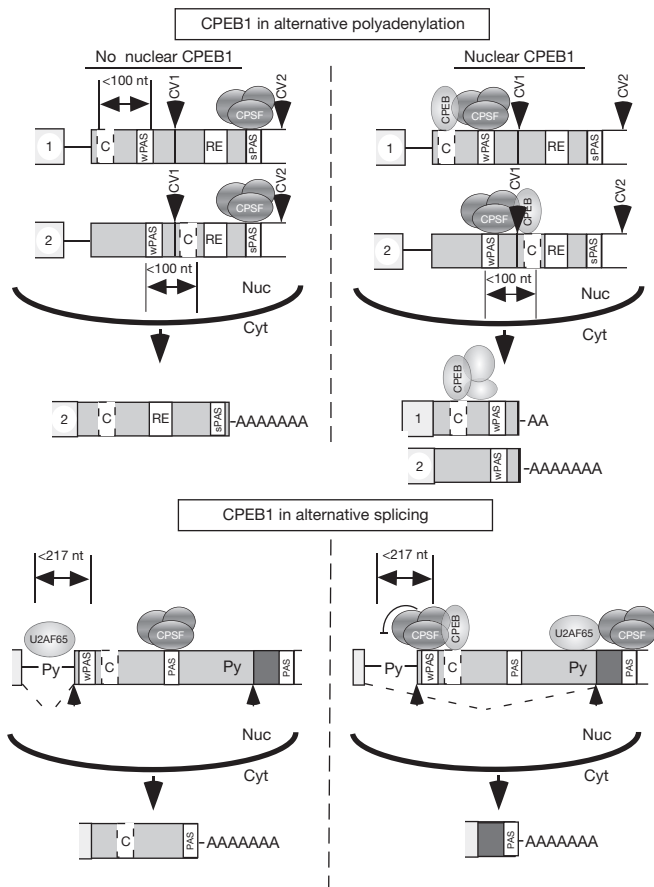


**Figure 4 | Model for CPEB1-mediated regulation of the alternative 3'-UTR formation.** Schematic representation of alternative polyadenylation (top) and alternative splicing (bottom) and in the absence (left) and presence (right) of CPEB1. Abbreviations: C, CPE; wPAS, weak PAS; sPAS, strong PAS; RE, regulatory element; CV1, cleavage 1; CV2, cleavage 2; Nuc, nucleus; Cyt, cytoplasm; Py, polypyrimidine tract; SS1, 3' splicing site 1; SS2, 3' splicing site 2; CPSF, cleavage and polyadenylation specificity factor; CPEB, cytoplasmic polyadenylation element binding protein 1; and U2AF65, U2 small nuclear ribonucleoprotein auxiliary factor.

in the absence of CPEB1 from the more 3' consensus PAS, the resulting CPEs would be too far from the PAS to assemble the cytoplasmic polyadenylation complex<sup>14</sup>. This dual function of CPEB1—as a translational regulator and as a pre-mRNA processing factor—provides a platform from which to coordinate nuclear and cytoplasmic gene expression regulation.

## METHODS SUMMARY

CPEB1-KD cell lines were generated as described<sup>17</sup>. For 3' RACE and Southern blot analysis, total RNA was extracted, retro-transcribed using a 3'-RACE oligo and amplified using specific primers. After electrophoresis, the agarose gel was treated with a denaturation solution and then with a neutralization solution. The DNA transferred and cross-linked to a nylon membrane, which was then pre-hybridized with Church buffer and hybridized with each <sup>32</sup>P-labelled probe. For luciferase-reporter assays, HD-Myc cells were transfected with each *BUB3* 3' UTR fused downstream of Renilla luciferase ORF, together with the control plasmid (Firefly luciferase). Luciferase activity was detected and normalized to RNA content. Ultraviolet cross-linking and immunoprecipitation <sup>32</sup>P-labelled RNAs were incubated with HeLa nuclear extract under *in vitro* splicing conditions, ultraviolet-crosslinked and digested with RNase A. U2AF65 or CPEB1 was immunoprecipitated and loaded on 10% SDS-polyacrylamide gels. Gels were dried and exposed to a PhosphorImager screen. For mRNA sequencing, DNase-treated total RNA was fragmented and poly(A)-positive fragments were reverse-transcribed to construct the libraries. The samples were then analysed on a Genome Analyzer IIx.

**Full Methods** and any associated references are available in the online version of the paper.

Received 13 January 2012; accepted 11 January 2013.

Published online 24 February 2013.

- Di Giammartino, D. C., Nishida, K. & Manley, J. L. Mechanisms and consequences of alternative polyadenylation. *Mol. Cell* **43**, 853–866 (2011).
- Sandberg, R. *et al.* Proliferating cells express mRNAs with shortened 3' untranslated regions and fewer microRNA target sites. *Science* **320**, 1643–1647 (2008).
- Mayr, C. & Bartel, D. P. Widespread shortening of 3' UTRs by alternative cleavage and polyadenylation activates oncogenes in cancer cells. *Cell* **138**, 673–684 (2009).
- Weill, L. *et al.* Translational control by changes in poly(A) tail length: recycling mRNAs. *Nature Struct. Mol. Biol.* **19**, 577–585 (2012).
- Ernault-Lange, M. *et al.* Nucleocytoplasmic traffic of CPEB1 and accumulation in Crm1 nucleolar bodies. *Mol. Biol. Cell* **20**, 176–187 (2009).
- Lin, C. L. *et al.* The nuclear experience of CPEB: implications for RNA processing and translational control. *RNA* **16**, 338–348 (2010).
- Wang, E. T. *et al.* Alternative isoform regulation in human tissue transcriptomes. *Nature* **456**, 470–476 (2008).
- Tian, B. *et al.* A large-scale analysis of mRNA polyadenylation of human and mouse genes. *Nucleic Acids Res.* **33**, 201–212 (2005).
- Licatalosi, D. D. *et al.* HITS-CLIP yields genome-wide insights into brain alternative RNA processing. *Nature* **456**, 464–469 (2008).
- Ji, Z. & Tian, B. Reprogramming of 3' untranslated regions of mRNAs by alternative polyadenylation in generation of pluripotent stem cells from different cell types. *PLoS ONE* **4**, e8419 (2009).
- Ji, Z. *et al.* Progressive lengthening of 3' untranslated regions of mRNAs by alternative polyadenylation during mouse embryonic development. *Proc. Natl Acad. Sci. USA* **106**, 7028–7033 (2009).
- Mendez, R. *et al.* Phosphorylation of CPEB by Eg2 mediates the recruitment of CPSF into an active cytoplasmic polyadenylation complex. *Mol. Cell* **6**, 1253–1259 (2000).
- Barnard, D. C. *et al.* Symplekin and xGLD-2 are required for CPEB-mediated cytoplasmic polyadenylation. *Cell* **119**, 641–651 (2004).
- Piqué, M. *et al.* A combinatorial code for CPE-mediated translational control. *Cell* **132**, 434–448 (2008).
- Belloc, E. & Mendez, R. A deadenylation negative feedback mechanism governs meiotic metaphase arrest. *Nature* **452**, 1017–1021 (2008).
- Eliscovich, C. *et al.* Spindle-localized CPE-mediated translation controls meiotic chromosome segregation. *Nature Cell Biol.* **10**, 858–865 (2008).
- Novoa, I. *et al.* Mitotic cell-cycle progression is regulated by CPEB1 and CPEB4-dependent translational control. *Nature Cell Biol.* **12**, 447–456 (2010).
- Fu, X. D. & Maniatis, T. Factor required for mammalian spliceosome assembly is localized to discrete regions in the nucleus. *Nature* **343**, 437–441 (1990).
- Corrionero, A., Minana, B. & Valcarcel, J. Reduced fidelity of branch point recognition and alternative splicing induced by the anti-tumor drug spliceostatin A. *Genes Dev.* **25**, 445–459 (2011).
- Paronetto, M. P., Minana, B. & Valcarcel, J. The Ewing sarcoma protein regulates DNA damage-induced alternative splicing. *Mol. Cell* **43**, 353–368 (2011).
- Ruskin, B., Zamore, P. D. & Green, M. R. A factor, U2AF, is required for U2 snRNP binding and splicing complex assembly. *Cell* **52**, 207–219 (1988).
- Chen, M. & Manley, J. L. Mechanisms of alternative splicing regulation: insights from molecular and genomics approaches. *Nature Rev. Mol. Cell Biol.* **10**, 741–754 (2009).
- Li, M. *et al.* Bub3 is a spindle assembly checkpoint protein regulating chromosome segregation during mouse oocyte meiosis. *PLoS ONE* **4**, e7701 (2009).

**Supplementary Information** is available in the online version of the paper.

**Acknowledgements** We thank A. Nebreda, R. Gomis, T. Yates, M. Fernandez, V. Giangarrà, J. P. Tavanéz, F. Lai, I. Novoa, J. La Cava and members of the Valcarcel and Mendez laboratories for comments on the manuscript and other contributions. We also thank the Ultrasequencing Units (CRG, IRB) and the Microscopy Units (CRG, IRB) for technical assistance. This work was funded by research grants as follows: from Consolider, MICINN and Generalitat de Catalunya to J.V., R.G. and R.M.; from RNAREG to J.V. and R.M.; from AICR to R.M.; from EURASNET and Fundación Marcelino Botín to J.V.; and from the National Institutes of Health and Instituto de Salud Carlos III to R.G. F.-A.B. holds a “la Caixa” predoctoral fellowship, and P.G.F. was supported by a FCT-Portugal postdoctoral grant and by a Spanish MICINN Consolider grant.

**Author Contributions** R.M., J.V. and F.-A.B. performed the experimental design and data analysis. C.E. contributed to the initial project development, initial experiments, experiment design and analysis. C.B.-D. contributed to the initial stages of the project, with the microarray design and cloning of the *BUB-3* minigene. B.M. performed the microarray experiments. F.-A.B. performed the rest of the experiments. P.G.F. performed the bioinformatic analysis. R.G. contributed to the design and interpretation of the bioinformatic analysis. R.M. prepared the manuscript with the help of F.-A.B., P.G.F. and J.V.

**Author Information** Sequencing data are available at the European Nucleotide Archive (ERP001603). The MIAME-complying microarray data have been deposited in the GEO database (GSE32440). Reprints and permissions information is available at [www.nature.com/reprints](http://www.nature.com/reprints). The authors declare no competing financial interests. Readers are welcome to comment on the online version of the paper. Correspondence and requests for materials should be addressed to R.M. ([raul.mendez@irbbarcelona.org](mailto:raul.mendez@irbbarcelona.org)).



## METHODS

**Antibodies.** Anti-CPEB1 antibody was from Proteintech (13274-1-AP). Anti-U2AF65 was an MC3 monoclonal antibody hybridoma supernatant<sup>21</sup>. Anti-BUB3 was from Abcam (ab-4180). Anti-SFRS2 was from Sigma (S4045). Anti-FNI was from Abcam (ab-2413). Anti-CDYL was from Abcam (ab-3999). Anti-SNRPB2 was from Proteintech (13512-1-AP). Anti-SF3a-60, anti-SF3a-66, anti-SF3a-120 and anti-SF3b-155 were kind gifts from A. Krämer. Anti-U1-70Kda was from Santa Cruz (sc-9569). Anti-CPSF100 was from Abcam (Ab126760). Anti-CPSF160 was from Abcam (Ab81552). Anti-UPF1 was from Abcam (Ab10510). Anti- $\alpha$ -tubulin was from Sigma (T902-6).

**Oligonucleotides. For 3' RACE:** 5'-TAATACGACTCACTATAGGGCGG ATCCTTTTTTTTTTTTTTTTTTTTTTTTNN-3' For *BUB3* pre-mRNA RT after PCR: 5'-TATCGAGCAGGCATCAACA-3'.

**For RPP:** sense primers: BUB3, 5'-ATTGGCCACAGGTGGTCTG-3' (endogenous) or 5'-GTCGACGACACTTGCTCAAC-3' (minigene); FNI, 5'-GACA GAGAAGATTCCCGAGAGTA-3'; CDYL 5'-TGCAGAGGAAGATCGATG AG-3', SNRPB 5'-CAAGAAATAACATTGGGATAGTCG-3'. Antisense primer: 5'-GTAATACGACTCACTATAGGGC-3'.

**For Southern-blot probes:** BUB3 Exon7, 5'-ATGATGGGACTACGCTTGCA-3'; BUB3 PAS1, 5'-TGGGGAGTACGAATTGTTTT-3'; BUB3 PAS2, 5'-GCA CTTAAGAAGGTGTTTATAATT-3'; BUB3 PAS3, 5'-GAAACAAAAATC ATCAAGGTC-3'; BUB3 PAS4, 5'-CAAGGGTCTGCATCTCG-3'; BUB3 3'SS1, 5'-GTACATGGTGACTTGGGTTTG-3', BUB3 3'SS2, 5'-GATTAGG TGGACTTGGGTTTG-3'; BUB3 S3, 5'-GATTAGGTGGACCTTTAATG CAG-3'; FNI 5'-TCCAATCCAGAGGAACAAGC-3'; CDYL 5'-TTCCCTGA TCCATTCTCAC-3', SNRPB2 5'-CAGTGTGTTTGTGATAACATTGG-3'.

**For RT-qPCR:** FMR1ex16 gene expression 5'-CCCGAACAGATAATCGTCCA-3' (sense) and 5'-TGAAGGGATCCATCTGTTGTT-3' (antisense); FMR1ex16 inclusion 5'-AAGAAGACATGATAGGATTGTGAGTTT-3' (sense) and 5'-CT TTAAGTGAACACACTGGTCA-3' (antisense); FMR1ex16 Skipping 5'-CAGA TGGATCCCTTCAGATCA-3' (sense) and 5'-CATTCACGAGTGGTGTGTA-3' (antisense); MKNK2 gene expression 5'-CCCCGGAGAACACCTTG-3' (sense) and 5'-CTGCAGGACCATGGGAGT-3' (antisense); MKNK2 inclusion 5'-AA CAGCTGTGCCAAAGACCT-3' (sense) and 5'-ACTGGAGGGTGGAGA CAG-3' (antisense); MKNK2 skipping 5'-AGAACACCTTGCCCACTCC-3' (sense) and 5'-GGAAGTGACTGTCCACCTC-3' (antisense); SNRPB gene expression 5'-CCACCTCCTGGTATGAGACCT-3' (sense) and 5'-CATTGGA GTCCCTCTCCAG-3' (antisense); SNRPB inclusion 5'-ACCTTGGCCACAG AGTATG-3' (sense) and 5'-CCATGAGACTCCACGAACA-3' (antisense); SNRPB skipping 5'-CTGGGATGCGAGGGC-3' (sense) and 5'-AGGAGGGC CAAGATGAGTCT-3' (antisense); BUB3 exon7, 5'-CGCATCACTTGCCCT TCAGTA-3' (sense) and 5'-TGTCACCTTGGCGAATGAAGA-3' (antisense); BUB3 inclusion #1, 5'-GTCGACGACACTTGCTCAAC-3' (sense) and 5'-CAAGTACATGGTGACTTGGGTTT-3' (antisense); BUB3 skipping #1 5'-GT CGACGACACTTGCTCAAC-3' (sense) and 5'-TGATTAGGTGGACTTGGG TTTT-3' (antisense); BUB3 inclusion #2, 5'-GCAGAAACAAAACCCAAG TCA-3' (sense) and 5'-ATCCACCATTGGGGAGTACG-3' (antisense); BUB3 skipping #2 5'-CAGAAACAAAACCCAAGTCCA-3' (sense) and 5'-GACA GAAAACAGAGAAATCCACA-3' (antisense); FMR1ex9 gene expression 5'-AGCTTGCTCGAGATTTCAT-3' (sense) and 5'-CAATAGCAGTGACCCC AGGT-3' (antisense); FMR1ex9 inclusion 5'-CACCATCACCATCGAAA-3' (sense) and 5'-TTTCAGCCTCAATCCTCACC-3' (antisense); FMR1ex9 skipping 5'-TTCCAAGGAAGTATAGGCAAA-3' (sense) and 5'-TTTCAGCCTCAAT CCTCACC-3' (antisense); TRA2B gene expression 5'-GCGTCACATCCGG TAGAGTT-3' (sense) and 5'-CAACCTCTTGACCTTCCTT-3' (antisense); TRA2B inclusion 5'-AAGGAAAATGCGGAAGTCGT-3' (sense) and 5'-CAT TTTCTTCTTCAACATTAACC-3' (antisense); TRA2B skipping 5'-AAGGAAG GTGCAAGAGGTTG-3' (sense) and 5'-GGAAGCAGACGGGATTC-3' (antisense); SFRS2 gene expression 5'-GGTCCAGGTCCCGGTCTC-3' (sense) and 5'-TTGGATTCCCTCTTGGACAC-3' (antisense); SFRS2 inclusion 5'-CTTGG TTATTGGCCAGGAA-3' and 5'-CACAAAGGCTACCATCAGCA-3' (anti-sense); SFRS2 skipping 5'-GGTCCAGGTCCCGGTCTC-3' (sense) and 5'-TGCT TGCCGATACATATTT-3' (antisense); GAPDH 5'-GAGTCAACGGATTTT GGTCGT-3' (sense) and 5'-TTGATTTTGGGAAGGATCTCG-3' (antisense); MRPL19 5'-CAGTTTCTGGGGATTGTCAT-3' (sense) and 5'-TATTCAGGA AGGGCATCTCG-3' (antisense); GLA 5'-CAGAAATCCGACAGTACTGCAA-3' (sense) and 5'-CATATCTGGGTCAATCCAACC-3' (antisense).

**For mutagenesis:** CPEs, 5'-CCAGGGAAAAATATTAATTGGATATTATA ACAACC-3' and 5'-GGTGTGTTATAATATCAAAATTAATATTTTCCCTGG-3', 5'-TAAATAAACACCTTCTTAAGTGCATGAG-3' and 5'-CCTCTTTT CCATTATTTTCAGG-3'; PAS1, 5'-GTGCCATGTTGATGATAAGGAAACA ATTCGTAATCCCC-3' and 5'-GGGGAGTACGAATTGTTTCCTTATCATC AACATGGCAC-3'; PAS2, 5'-GGTTTTGAATTTTTTTTTTAAATGGGCA

CCTTCTTAAGTGC-3' and 5'-GCACCTTAAGAAGGTGCCCATTTAAAAA AAAAAATTCAAAAACC-3'; polypyrimidine tract, 5'-TTGATCTCATGCT GTTCTGTGTGTCCCGGAACCTGTAGGTCACC-3'.

**Plasmid constructions.** BUB3 exon7, intron7 and exon8 were subcloned into pCMV56<sup>24</sup>. Each of the five BUB3 3' UTRs were subcloned downstream of the Renilla luciferase (pRL-SV40 from Promega). The SV40 poly(A) signal of these constructs was then removed by HpaI digestion.

**Cell cultures, DNA transfections and RNA purification.** Exponentially growing HD-Myz cells grown in Roswell Park Memorial Institute medium (RPMI-1640 + glutaMAX-I), 10% FCS (fetal calf serum) and 1% penicillin/streptomycin were transfected at 80% confluence with 0.2  $\mu$ g of plasmid DNA using Effectene transfection reagent (Qiagen), following the manufacturer's instructions. Cells were incubated 24 h before RNA purification and total RNA was isolated using the RNeasy Mini Kit (GE Healthcare). An additional treatment with DNase was performed using the Turbo DNA-free Kit (Ambion).

**CPEB1-KD cell line.** The CPEB1-KD HD-MyZ cell line was generated as described previously<sup>17</sup>. Briefly, HeLa cells or HD-MyZ cells, stably transfected with a doxycycline-inducible CPEB1 shRNA vector, were induced (CPEB1shRNA+) or not (CPEB1shRNA-) with doxycycline for 4 days for subsequent analysis. Transient CPEB1-KD were performed transfecting sh vectors against the following target sequences: 5'-GCACUUGCUGAAUCUGUCUUU-3' and 5'-GCAGG UCUCUUGGUUUCAUU-3' Transient UPF1-KD was performed by siRNA transfection using lipofectAMINE 2000 (Invitrogen). The target sequence of each siRNA is: 5'-GAGAUAGCCUGCGGUACA-3', 5'-GGUCCGGCUCUUUUU AAUG-3' 5'-GAUGCAGUCCGCUCAUU-3'.

**Immunofluorescence.** Cells were plated on poly-lysine pre-coated glass coverslips. 12 h later, cells were fixed in PBS/formaldehyde 4% (30 min) and permeabilized at room temperature for 5 min in 0.1% Triton/PBS. They were then blocked with 1% BSA for 1 h and incubated with primary antibodies against CPEB1 alone or in combination with the SFRS2, washed, and then labelled with the matching secondary antibodies. Images were obtained on an inverted Leica TCS SP5 confocal microscope with a 63 $\times$  1.4 NA PLAN APO objective.

**Cell extracts and Western-blot analysis.** HD-MyZ or HeLa cells were lysed in Triton buffer (20 mM HEPES pH 7.0, 150 mM NaCl, 1% Triton X-100, 10% glycerol, 1 mM EDTA, 1 mM phenylmethylsulphonyl fluoride, 1 $\times$  protease inhibitors (Sigma). The lysates were sonicated using Bioruptor (Diagenode) and centrifuged at 16,000g and supernatants were resolved by 10% SDS-PAGE. 30  $\mu$ g of lysate was loaded onto each lane.

**Immunoprecipitation.** HeLa nuclear extracts were incubated at 30 °C for 30 min in cleavage conditions (see 'in vitro cleavage assay' section below) in the presence of protease inhibitors. Extracts were precleared, incubated at 37 °C for 30 min with RNase A 50  $\mu$ g ml<sup>-1</sup> and immunoprecipitated with anti-CPEB1 antibody or with rabbit IgG for 4 h at 4 °C. Immunoprecipitates were washed in cold lysis buffer (1.5 mM MgCl<sub>2</sub>, 20 mM HEPES pH 7.5, 150 mM NaCl, 1% NP40, 1 mM EDTA, 10% glycerol, 0.1 mM DTT, 1 mM PMSF, 1 $\times$  proteases inhibitor) and the beads were resuspended in loading buffer 1X, boiled at 60 °C for 20 min and resolved by SDS-PAGE together with the inputs.

**RNA immunoprecipitation.** HD-MyZ cells were transfected with the WT or CPE-mutated minigenes. After 15 h they were washed with PBS, cross-linked with 1% formaldehyde for 10 min at 30 °C and treated with glycine 1 M. After washing twice with PBS, cells were lysed in lysis buffer (1.5 mM MgCl<sub>2</sub>, 20mM HEPES pH 7.5, 150 mM NaCl, 1% NP40, 1 mM EDTA, 10% glycerol, 0.1 mM DTT, 1 mM PMSF, 1X proteases inhibitor, 1X RNase inhibitor). Lysates were precleared, immunoprecipitated with anti-CPEB1 antibody or with rabbit IgG for 4 h at 4 °C. Immunoprecipitates were washed in cold lysis buffer supplemented with RNase inhibitors. Beads were resuspended in lysis buffer with 0.1% SDS, 3 mg of proteinase K and incubated for 30 min at 55 °C and RNA was extracted for RT-qPCR analysis.

**3' RACE and Southern blot analysis.** RT-PCR was carried out using the SuperScript II reverse transcriptase kit (Invitrogen), following the manufacturer's instructions, starting with 500 ng of DNase-treated total RNA and the 3' RACE primer.

After PCR using each couple of specific primers, the samples were loaded in a 1.5% agarose gel and run for 2 h at 90 V. The gel was then treated with a denaturation solution (1.5 M NaCl, 0.5 M NaOH) for 30 min and then with a neutralization solution (1 M Tris, 1.5 M NaCl pH 7.4) for 45 min. After transfer, the DNA was cross-linked to the nylon membrane (254 nm; 0.12 J); the membrane was pre-hybridized with Church buffer for 3 h, hybridized with each <sup>32</sup>P-labelled probe for 12 h and washed with SSC 1X, 0.1% SDS three times.

For Southern-blot 'APA quantifications', 3'-SS1 and PAS1 probes detected all the 3'-SS1-derived 3'-UTR-cDNAs allowing for direct comparison between PAS1, PAS2 and PAS3. For Southern-blot 'Splicing quantifications' common exon7 probes detected all the possible *BUB3* 3'-UTR variants. For all the variants, except

the doublet 3'-SS1/PAS3-SS2/PAS4, quantification can be directly derived from exon7 signal. 3'-SS1/PAS3 migrated very close to SS2/PAS4, detected as a doublet with exon 7 probe. As Southern-blots were performed by successive re-probing of the same membrane with the different splicing and cleavage probes, a comparison between lanes, expressed always as ratios for each probe, was made.

Therefore, the ratio 3' SS1/PAS3- SS2/PAS4 in each doublet was calculated as in the following example. Let  $X$  be the signal of 3' SS1/PAS3 in WT conditions (either cells or minigene),  $X_i$  the signal of 3' SS1/PAS3 in mutant conditions (either cells or minigene),  $Y$  the signal of SS2/PAS4 in WT conditions (either cells or minigene) and  $Y_i$  the signal of SS2/PAS4 in mutant conditions (either cells or minigene) and in the above example. Then,  $X + Y / X_i + Y_i = 0.91$  (Fig. 3, lanes 1 and 2);  $X/X_i = 0.38$  (Fig. 3, lanes 25 and 26) and  $Y/Y_i = 1.6$  (Fig. 3, lanes 9 and 10). Thus,  $X/Y = 0.3$  and  $X_i/Y_i = 1.3$ . Factors from which the ratio of 3' SS1/PAS3 and SS2/PAS4 could be derived form the signal of the doublet in each line.

In these equations, there are two groups of errors. One is derived from the origin of the sample: in the example from Fig. 3a, lanes 1, 25 and 9 are derived from reprobings the same membrane three times (that is, they are the same sample, RT-PCR, gel, and so on), which will all have the same error (sample 1 error,  $\alpha$ ) derived from loading (in the case of the minigene, transfection), RT-PCR, and so on. The same is true for lanes 2, 26 and 10, which will have all the same error (sample 2 error,  $\beta$ ). The second source of differential errors is derived from using three different probes: exon7 (lanes 1, 2), PAS3 (lanes 25, 26) and 3' SS2 (lanes 9, 10) (probe errors  $a$ ,  $b$  and  $c$  respectively).

Now, if we include the errors we can generate the following set of equations with multiple variables: to determine the relative composition of the doublet band corresponding to SS1/PAS3 + SS2/PAS4, quantifications from lane 1 will have to be corrected by the error factors  $a$  and  $\alpha$ , whereas the same band quantified from lane 2 would have to be corrected by factors  $a$  and  $\beta$ . Quantification of both bands will produce a ratio where:  $\alpha(X + Y)/a\beta(X_i + Y_i) = 0.91$ , and neutralizing the errors from the probe:

$$\alpha(X + Y)/\beta(X_i + Y_i) = 0.91$$

For the quantification with the probe PAS3 (lanes 25 and 26) that detects only SS1/PAS3, but not SS2/PAS4, UTR variant, we can derive the following equation:  $b\alpha X/b\beta X_i = 0.38$ , and neutralizing the errors from the probe:

$$\alpha X/\beta X_i = 0.38$$

In the same way, for the quantifications with the 3'-SS2 probe (lanes 9 and 10) that detects only 3' SS2/PAS4, but not 3' SS1/PAS3, UTR variant, we can derive  $c\alpha Y/c\beta Y_i = 1.6$ , and then:

$$\alpha Y/\beta Y_i = 1.6$$

Now, if we start solving the multiple equations by substituting in the first one we get:

$$\alpha X + \alpha Y = 0.91\beta X_i + 0.91\beta Y_i$$

$$\beta X_i = \alpha X/0.38$$

$$\beta Y_i = \alpha Y/1.6$$

Substituting the last two equations in the first:

$$\alpha X + \alpha Y = 0.91\alpha X/0.38 + 0.91\alpha Y/1.6$$

and then  $a$  can be simplified and we are left with  $X/Y = 0.3$ .

In a similar way, if we substitute instead  $\alpha X$  and  $\alpha Y$  we obtain  $X_i/Y_i = 1.3$ .

As shown, with these normalizations the errors derived both from the two different origins of the samples and from the use of three different probes are neutralized, demonstrating that the samples can be compared.

**Analysis of the translational control by BUB3 3' UTRs.**  $0.2 \times 10^6$  HD-MyZ cells were transfected with 300 ng of each BUB3 3'-UTR-Renilla luciferase, together with 30 ng of the control plasmid (Firefly luciferase). After 24 h, the RNA was extracted for quantification by qPCR. Luciferase activity was detected using the Dual-Luciferase Reporter Assay System (Promega), following the manufacturer's instructions.

#### **In vitro transcription, ultraviolet cross-linking and immunoprecipitation.**

Transcription templates were generated by PCR from the different plasmids, with a T7 promoter included in the upstream primer. Radiolabelled pre-mRNAs were transcribed for 2 h at 37 °C by using approximately 1 µg of template DNA in 25 µl of transcription reactions containing final concentrations of 40 mM Tris-HCl, pH 7.9, 10 mM NaCl, 6 mM MgCl<sub>2</sub>, 2 mM spermidine, 0.8 mM dithiothreitol, 0.5 mM ATP, CTP and GTP, 0.05 mM UTP, 30 µCi [ $\alpha$ -<sup>32</sup>P]UTP, and 60 units of T7 or 42 units of SP6 RNA polymerases (Promega). The transcripts were isolated by gel purification followed by phenol/chloroform/isoamylalcohol (25:24:1) extraction and ethanol precipitation.

<sup>32</sup>P-labelled RNAs were incubated under *in vitro* splicing conditions with HeLa nuclear extract in a total volume of 27 µl. After incubation for 30 min at 30 °C, mixtures were irradiated with ultraviolet light (254 nm; 0.4 J). After incubation with 1 mg ml<sup>-1</sup> RNase A at 37 °C for 30 min, U2AF65 was immunoprecipitated with the MC3 monoclonal antibody hybridoma supernatant. After incubating for 60 min at 4 °C, 30 µl of a 50% slurry of protein A/G sepharose beads were added and the mixture was incubated under rotation for another 60 min. Beads were sedimented by centrifugation and washed 4 times with 800 µl of high salt buffer (500 mM NaCl, 50 mM Tris-HCl pH 8.0, 1% NP-40) and once with the same buffer with 100 mM NaCl. Sedimented beads were resuspended in 4 × SDS loading dye, heated at 95 °C for 5 min, and briefly centrifuged. The supernatant was then loaded on 10% SDS-polyacrylamide gels. Gels were dried and exposed to a PhosphorImager screen.

**In vitro cleavage assay.** *In vitro* cleavage assay was performed as previously described<sup>7</sup>, incubating HeLa nuclear extract with the probes as in Fig. 3d in the presence or not of 0.1 µM recombinant CPEB1.

**Flow cytometry.** DNA content was measured by staining with Hoechst as indicated and analysed by flow cytometry with an LSR machine (Becton Dickinson). Flow cytometry data were analysed with FlowJo software.

**Microarray analysis.** Cy3- and Cy5-labelled cRNAs were generated from 500 ng of total RNA using the Quick-Amp Labelling Kit, No Dye (cat. no. 5190-0447) and Cy3 and Cy5-CTP from Perkin-Elmer (NEL580 and NEL581). 6 µg of each cRNA was hybridized in our custom oligo microarray platform (Agilent) in an Agilent rotating oven at 60 °C for 18 h. After hybridization, the arrays were washed, and scanned images were analysed. Statistical analyses were carried out with LIMMA package (Bioconductor). Microarray results have been deposited in the GEO database (GSE32440).

**qPCR.** PCR was carried out in a LightCycler 480 (Roche) using SYBRGreen I Master (Roche) and the primers indicated in 'oligonucleotides' section above. Three sets of primers were used for each alternative splicing event analysed; one pair monitored gene expression by amplifying a constitutive exon, and the other two pairs specifically amplified each single isoform (inclusion versus skipping).

**mRNA sequencing.** DNase-treated total RNA was fragmented to about 400 nt. Poly(A)-positive fragments were captured, reverse-transcribed and used to construct the libraries. The samples were then analysed on the Genome Analyzer II x. Data are available at the European Nucleotide Archive (ERP001603).

24. Gebauer, F. *et al.* Mouse cytoplasmic polyadenylation element binding protein: an evolutionary conserved protein that interacts with the cytoplasmic polyadenylation elements of c-mos mRNA. *Proc. Natl. Acad. Sci. USA* **93**, 14602–14607 (1996).

## CORRIGENDUM

doi:10.1038/nature11848

## Corrigendum: Global quantification of mammalian gene expression control

Björn Schwanhäusser, Dorothea Busse, Na Li, Gunnar Dittmar, Johannes Schuchhardt, Jana Wolf, Wei Chen & Matthias Selbach

*Nature* **473**, 337–342 (2011); doi:10.1038/nature10098

Mark Biggin of the Lawrence Berkeley National Laboratory contacted us, noting that our mass-spectrometry-based protein copy number estimates are lower than several literature-based values. We therefore re-analysed the scripts used for data processing, and found a scaling error that occurred during the conversion of normalized protein intensity values into absolute copy number estimates. As described in the original Article, slope and offset for scaling were calculated by linear regression based on an in-solution digest with spiked-in

proteins of known concentrations. We erroneously used the slope and the offset from an unrelated experiment to scale protein levels, resulting in a systematic underestimation of protein levels and derived translation rate constants. We apologize for this error and any confusion it may have caused.

When the error was corrected, the median levels of detected proteins increased about threefold and the ratio of average protein to messenger RNA increased from 900 to 2,800. The median and apparent maximum translation rate constants increased from 40 to 140 and from 180 to 1,000 proteins per mRNA per hour, respectively. Consequently, the estimated maximum translation rate constant in sea urchin embryos at 15 uC (140 proteins per mRNA per hour) is lower than our corrected prediction for mouse fibroblasts (1,000 proteins per mRNA per hour). All our conclusions about global gene expression control (correlations between mRNA and protein levels and half-lives, predominant control of protein abundance at the level of translation, functional properties of genes with specific half-life

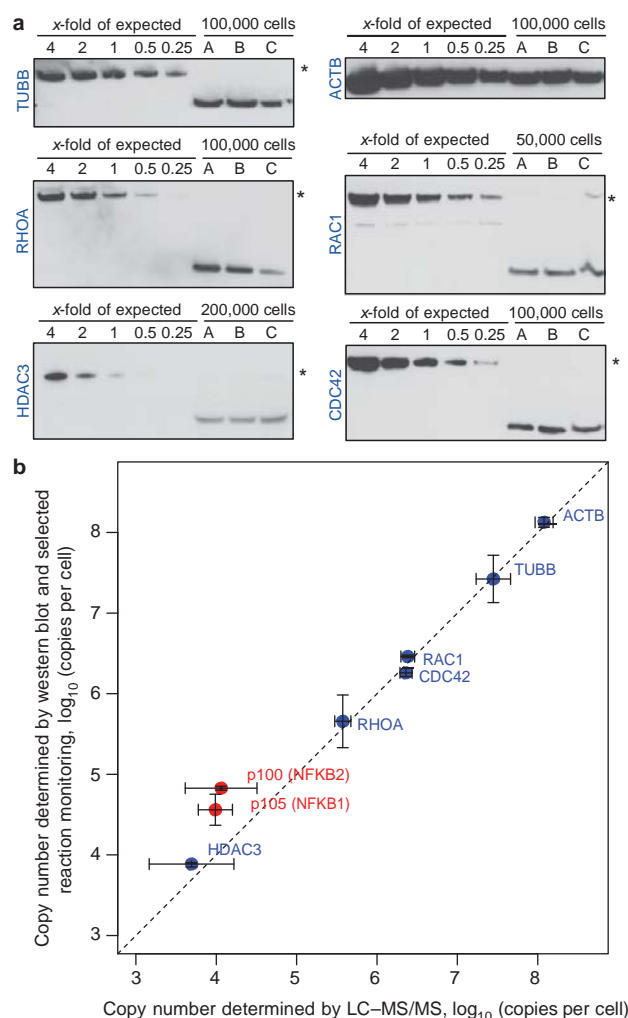


**Figure 1** | Comparison of LC-MS/MS-based protein copy number estimates in NIH3T3 cells with alternative methods. **a**, Representative western blots of cellular proteins with dilution series of purified protein standards. Standards were diluted in a way that one-fold corresponds to the amount expected from the average of the LC-MS/MS-based estimates. The asterisks indicate the position of the GST-fusion proteins. **b**, Comparison of estimates based on western blots (blue,  $n = 3$ ) and selected reaction monitoring (red,  $n = 3$ ) with our LC-MS/MS data ( $n = 52$ ). Error bars show standard deviations.

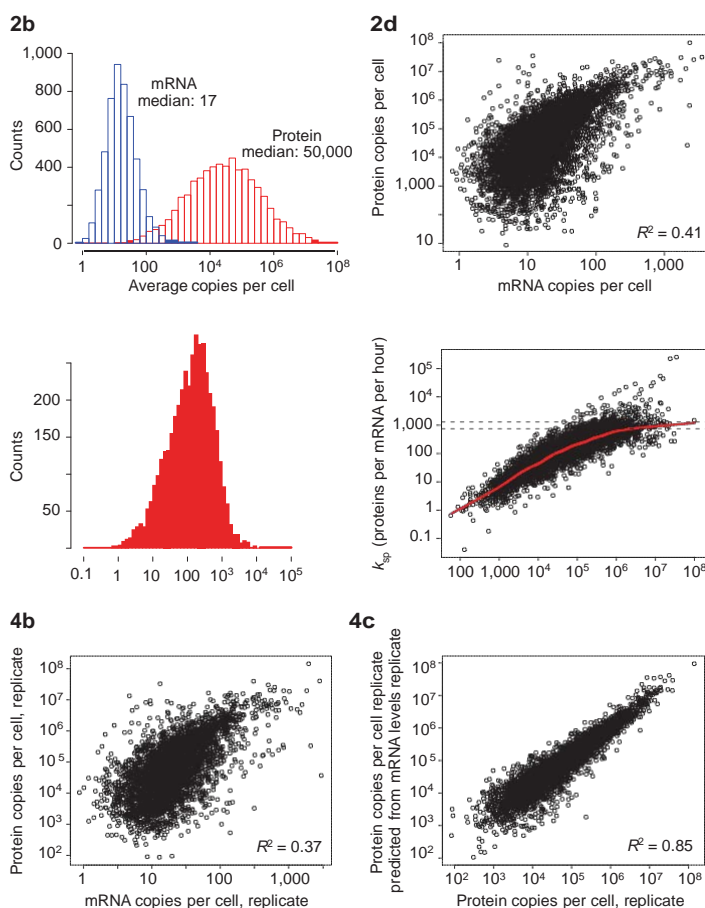


**Figure 2** | This figure shows the corrected panels for Figs 2b and d, 3c and d and 4b and c of the original Article. We note that although the distribution of data in the original and corrected figures appears very similar, the axes are different.



combinations and so on) are unaffected. Figure 2 of this Corrigendum shows the corrected Figs 2b and d, 3c and d and 4b and c. Supplementary Figs 5a and b, 6d and f, 8f, 12a and b, and Supplementary Tables 1 and 3 of the original Article have been corrected. Protein copy numbers and translation rate constants in the text and figures in the HTML and PDF versions of the original Article have been corrected.

To further validate copy numbers in NIH3T3 cells we performed western blots with a dilution series of purified human proteins as standards (Fig. 1a of this Corrigendum). Briefly, cells were washed, harvested by trypsinization, counted independently by two persons, lysed in radioimmunoprecipitation assay buffer (containing 1% SDS) and separated by SDS–polyacrylamide gel electrophoresis (PAGE). As standards, defined amounts of human glutathione-S-transferase (GST)-tagged HDAC3, TUBB (Abnova), RHOA, RAC1 or CDC42 (purified in house and quantified spectrophotometrically) or purified ACTB (Biotrend) were diluted in SDS sample buffer containing 0.07 mg Escherichia coli lysate per microlitre to minimize protein loss during dilution. Antibodies against HDAC3 (2632), CDC42 (2466) and Rac1/2/3 (2467) were from Cell Signalling; the ACTB (A5441)

and TUBB (T8328) antibodies were from Sigma and the anti-RHOA antibody (SC-418) was from Santa Cruz. Protein abundance in NIH3T3 cells was estimated densitometrically, based on the dilution series as a standard curve (Scion Image). We also used selected reaction monitoring to quantify two additional proteins (p100 and p105). To this end, cells were lysed (6 M urea, 2 M thiourea) and lysates mixed with synthetic-stable-isotope-labelled proteotypic peptides (SpikeTides, JPT Peptide Technologies). Samples were digested and analysed on a Q-Trap 5500 system (AB Sciex) in three technical replicates monitoring three transitions per peptide. Quantification was performed using Multiquant 1.2 (AB Sciex) based on the two most intense transitions. Overall, copy number estimates of the eight proteins obtained by alternative approaches correlated well with our data derived from liquid chromatography and tandem mass spectrometry (LC-MS/MS) (Fig. 1b of this Corrigendum), even though the two measurements based on selected reaction monitoring lie above the diagonal. The data are in good agreement with the expected precision and reproducibility of our large-scale absolute protein quantification approach (see Supplementary Figs 6d and 8b of the original Article).

## CORRIGENDUM

doi:10.1038/nature11977

# Corrigendum: Structure-based prediction of protein–protein interactions on a genome-wide scale

Qiangfeng Cliff Zhang, Donald Petrey, Lei Deng, Li Qiang, Yu Shi, Chan Aye Thu, Brygida Bisikirska, Celine Lefebvre, Domenico Accili, Tony Hunter, Tom Maniatis, Andrea Califano & Barry Honig

*Nature* **490**, 556–560 (2012); doi:10.1038/nature11503

In this Letter, one of the points shown in Fig. 2 and Supplementary Figs 8, 9 and Supplementary Table 4 reflects the presence of interactions that had been erroneously deposited from a previous publication<sup>1</sup> into the IntAct database. We have now used the MINT database to retrieve these interactions, and Fig. 2 is corrected here (shown below as Fig. 1). The error in IntAct was corrected on 9 November 2012 in consultation with the original authors of the paper. We thank S. Michnick for bringing this to our attention. We also thank M. Maletta for pointing out that Supplementary Fig. 10C was mislabelled and erroneously indicated that NKX2-2 protein was not included in the experiment. See Supplementary Information to the original paper for corrected versions of Supplementary Figs 8–10C and Supplementary Table 4. These errors do not affect the results or conclusion of the paper, and have been corrected in the HTML and PDF of the original paper.

1. Tassavov, K. et al. An in vivo map of the yeast protein interactome. *Science* **320**, 1465–1470 (2008).

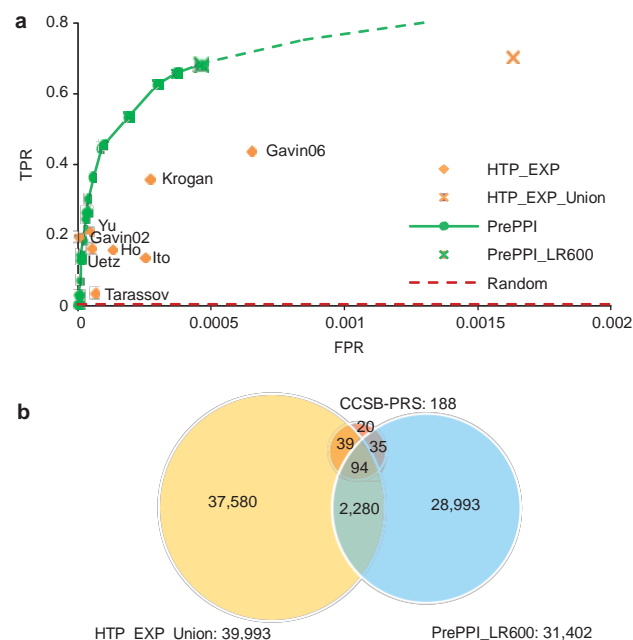


Figure 1 | This is the corrected Fig. 2.

# CAREERS

**TURNING POINT** Accelerated training helps ecologist to land major grant **p.131**

**@NATUREJOBS** Follow us on twitter for the latest news and features [go.nature.com/e492gf](http://go.nature.com/e492gf)

**NATUREJOBS** For the latest career listings and advice [www.naturejobs.com](http://www.naturejobs.com)

BJORN RUNE LIE/GETTY



## EDUCATION

# A sense of community

*US scientists passionate about teaching can find rewarding work at community colleges.*

BY NEIL SAVAGE

Chad Knights used to see his professional future laid out before him, and it basically involved cancer research. Then a colleague told him about a part-time teaching position at Northern Virginia Community College in Alexandria, not far from Washington DC, where Knights was doing a postdoc at Georgetown University. He took the job for extra money, and ended up falling in love with the work.

Despite the objections of his principal

investigator and his thesis adviser, Knights took a full-time job at the community college in 2007. "The ability not just to teach the students but to inspire them to share in my love of science gave me a new purpose," he says, recalling a student from Ghana who told him what a privilege it was to attend college, and a woman in her forties who teared up when she first saw a cell through a microscope.

Teaching at a community college may not be a career option that occurs to many scientists. It certainly wasn't on Knights' radar. But it can be a rewarding choice for scientists passionate

about teaching who enjoy working with students from a wide variety of educational, cultural and socioeconomic backgrounds.

In the United States, community colleges are generally publicly funded institutions offering a wide range of educational programmes, from remedial work to job training or associate's degrees. Some students are recent high-school graduates, or those who did not finish high school but took a test to earn the equivalent of a high-school diploma. Others are adults who want retraining in a specific field such as nursing, or military ►

► veterans trying to join the civilian workforce. Some plan to transfer to a university after completing their programme. And some are immigrants for whom English is a second language.

Faculty members spend most of their time teaching; they rarely run research programmes and are not required to publish. Tenure is possible: review committees look for effective teaching and participation in other aspects of the college, such as serving on committees. However, the US Department of Education found that in 2009 only 12% of community-college teachers were tenured, full-time faculty members; another 4% were on the tenure track. By comparison, 26% of faculty members at conventional universities were tenured, with 12% on the tenure track.

In the 2011–12 academic year, average pay at community colleges ranged from US\$45,894 for a lecturer to \$73,333 for a full professor, according to the latest *Annual Report on the Economic Status of the Profession* by the American Association of University Professors in Washington DC. At universities that grant doctorates, the average pay ranged from \$56,891 for a lecturer to \$130,803 for a full professor.

## INTO THE CLASSROOM

Community-college science teachers are in demand. The United States has 1,132 community colleges with a total of 13 million students, many of whom will take science courses for an associate's degree or a certificate in a technical field. Others plan to transfer to a bachelor's degree with a science major elsewhere, or are working on business or humanities majors and need a science course such as astronomy or introductory biology to fulfil requirements.

Part-time adjunct faculty members fill many of the teaching slots, allowing college administrators to add or subtract course sections on the basis of student demand. Nearly 69% of community-college faculty members were part-time in 2009, the latest year for which figures are available, compared with 41% in universities, according to the US Department of Education. Some adjuncts are graduate students earning extra money or exploring teaching as a career option. Others are successful business people willing to share their expertise. And some commute between part-time jobs at several schools to effectively create a full-time job.

One benefit of teaching at a community college rather than a high school is that the students are adults, who tend to be more focused and driven than teenagers. It can also appeal to teachers who prefer the shorter academic calendar of a college. "I feel it gives you a lot of the benefits of working in the college environment, while at the same time focusing on teaching," says Jeff Schinske, a biology teacher at De Anza College in Cupertino, California.

The required educational qualifications

vary by state, but in general a community-college teacher needs a master's degree or higher. "We like to have PhD-level credentials," says Donald Brady, assistant dean of science, technology, engineering and mathematics at Middlesex Community College in Lowell, Massachusetts. Mary Rittling, president of Davidson County Community College in Thomasville, North Carolina, says that faculty members need the same educational background as they would to teach undergraduates at a university. The qualifications of their teachers can affect whether a community-college student can transfer their course credits to a university programme.

Applicants should demonstrate currency in their field with, for example, recent graduate study or a publication record, says Brady. "When we look at applications for full-time positions, it's good to see a CV with what the individual has published," he says. However, he adds, the most important criterion is proven teaching ability.

Knights, who sits on his college's hiring committee, says that experience as a university teaching assistant does not help candidates, because it does not generally involve managing a class alone. Teachers



***"The first couple of years, it's well understood that your primary responsibility is learning on the job."***

Scott Schultz

to get to know their prospective colleague.

Unlike primary and secondary schools in the United States, community colleges do not require their teachers to be certified. However, varying levels of educational training are available, usually through universities. Northern Arizona University in Flagstaff, for example, offers a master of arts in science teaching, which is open to science graduates who want to teach at community colleges. George Mason University in Fairfax, Virginia, offers a doctor of arts in community-college education. And North Carolina State University in Raleigh offers a doctorate, a master's degree and a graduate certificate in community-college teaching. The certificate caters mostly to those who already have a master's degree in their field, says Chad Hoggan, who runs the programme.

Participants learn concepts such as differences in learning styles and how to work with them, and how to teach online courses, which are becoming common. Such skills are important, says Hoggan, but he does not promise anyone that a certificate will land them a job. "It might set you apart from an applicant pool of 60 people," he says.

Mentoring support can be thin at smaller community colleges and novice teachers can feel as if they have been thrown in at the deep end, says Scott Schultz, chair of the science division at Delta College in University Center, Michigan. "If you go to a larger school, there's often somebody who's going to take you under their wing," he says. But at small institutions, a new faculty member might receive little more than a list of class objectives and a copy of the textbook used by the previous instructor. "The first couple of years, it's well understood that your primary responsibility is learning on the job," says Schultz.

## TEACHER TRAINING

To help newcomers to cope, Schultz leads the Two-Year College New Faculty Training Experience, an 18-month programme run by the American Association of Physics Teachers in College Park, Maryland. The experience includes online discussions and two weekend conferences: this year, one is at Delta, and the other at the University of Minnesota in Minneapolis. The programme covers teaching strategies and introduces new teachers to more-experienced faculty members. It is important to build such networks, says Schultz. Of the community-college campuses that teach physics, 58% have only one physics teacher, or only part-time ones, according to a survey conducted last year by Susan White, a researcher at the American Institute of Physics in College Park.

The population of biology teachers across community colleges is much larger, but the job can still get lonely, says Schinske. In primary and secondary schools, teachers form communities of peers by grade level. In universities, those in the same research area collaborate and attend conferences. But such organizing forces do not exist at community colleges. So Schinske and Kimberly Tanner, who studies biology education at San Francisco State University in California, used a US National Science Foundation grant to launch Community College Biology Faculty Enhancement Through Scientific Teaching, a programme held at local colleges and San Francisco State University that runs monthly workshops and a week-long summer institute on teaching strategies and techniques. It also partners biology instructors with their peers to help them to become better teachers.

The difficult economy has actually boosted demand for community-college science teachers, as some students look for educational options that are cheaper than universities and



others want to retrain. A 2009 study by the American Association of Community Colleges in Washington DC found that enrolment in for-credit courses had increased by 16.9% between autumn 2007 — before the economic downturn — and autumn 2009. “You see a surge when the economy goes down, mainly because we provide access and affordability,” says Rittling. “The change in the economy has really impacted us in science,” agrees Sarah Quast, a professor of chemistry at Middlesex Community College. “Our science courses, if they haven’t doubled, are close to doubling.”

Although the US national unemployment rate remains high — at 7.9% as of January this year — there is a need for ‘middle-skill jobs’ with community-college training, says Matthew Meyer, associate vice-president for science, technology, engineering and mathematics innovations in the North Carolina Community College system, based in Raleigh. Nurses, for example, are always in demand, and many get their training at community colleges, where they take courses such as anatomy, physiology and microbiology. Dental hygienists, radiology technicians and lab technicians all take biology, engineering or physics courses. Meyer also sees a growing need for employees with training in aeronautics, nanotechnology, advanced manufacturing and life sciences such as pharmaceuticals.

Those trends will mean more openings for science teachers, as will demographic changes. “Our faculty on average are in their upper forties or fifties,” says Meyers. “We’re going to have to be able to replace them.”

Although teaching at a community college is not research-oriented, scientists can still use their training. Schultz says that it is not uncommon for community-college instructors to publish in educational-research journals. “Although we are not doing research on subatomic particles, we are constantly collecting data and doing research on how to improve learning in our classroom,” he says.

Teaching appeals to the researcher in Schinske. Assessing his class involves gathering data from students about what they know at the beginning of the course, getting feedback on what concepts they understand and which ones they struggle with, and measuring how they have changed by the end. In some ways, he says, the experience is not unlike his graduate work in monitoring fish populations to study their evolution. “There are times when I view my students very similarly to my study organisms,” he says, “and I mean that in only the most respectful way.” ■

**Neil Savage** is a freelance writer based in Lowell, Massachusetts.

## TURNING POINT

# Jörg Wiedenmann

*Jörg Wiedenmann, head of the Coral Reef Laboratory at the UK National Oceanography Centre, Southampton, won a €1.29-million (US\$1.7-million) European Research Council (ERC) Starting Grant in December. He will use the money to investigate how nutrient starvation influences coral bleaching, in which the symbiotic microbes that give corals their colour are damaged.*

### Did you have an aquarium as a child?

Yes. My grandmother took me to the local aquarium, where I became fascinated with corals and saltwater invertebrates. Eventually I got my own seawater aquarium. This childhood hobby developed into an important skill set: I am one of the few people in the field who can maintain long-term coral collections and use them as experimental models in an aquarium.

### Describe your first research finding.

It was for my senior thesis at the University of Ulm in Germany. I came across anemones in the Mediterranean Sea that had red fluorescent proteins, even though they were non-luminescent. I realized that, as an ecologist, I would need to gain skills in biochemistry, genetics and structural biology to study these proteins.

### How did that set your research direction?

I was lucky. I worked with open-minded biomedical researchers who taught me techniques that opened up a new horizon — exploring the use of fluorescent proteins in biomedical applications. It was very exciting, collaborating with experts in different disciplines.

### You have moved through your career quickly.

#### What motivated you?

I finished my PhD in three and a half years when colleagues were taking four to five. I realized that moving on would help me to further my career. After my PhD, the head of the department offered me a group-leader position at Ulm. One is expected to move around and gain experience, but having worked in an interdisciplinary environment gave me the confidence to lead a group. In 2005, I got my habilitation, the prerequisite to become a professor in Germany; I was three and a half years younger than average. Trying to complete tasks in a short time was probably an important decision in my career.

### Do you think skipping a postdoc helped you to get established?

I do. It is instructive to have early independence, but it can be hard. I needed to get my own funding; I could not rely on a senior figure with



a grant. As a result, I applied for, and got, many prestigious fellowships. I think demonstrating independence helped my ERC application.

### How has moving to Southampton helped you?

I needed a change. The move allowed me to explore questions about coral biology — such as what drives stress responses. In my first years there, I got a number of small grants, but after three and a half years, my lab needed a big proposal to continue to do good science.

### How did you put together your ERC proposal?

I was convinced that I had a very exciting idea that would fit perfectly into the ERC funding scope. My collaborators and I collected data to convince a sceptical scientific community that we could combine lab experiments with field-based approaches to get useful answers for coral-reef management (J. Wiedenmann *et al.* *Nature Clim. Change* 3, 160–164; 2013).

### What did it feel like to get the grant?

It is a game changer. It gives me the freedom to do science and produce papers that would otherwise be delayed. I am happy to invest this time in science instead of another proposal.

### What part does outreach play in your job?

We have a strong outreach culture at the National Oceanography Centre. I built a coral aquarium in the reception area, to educate visitors and students. Researchers can use it to explain how the coral changes with light level. Pressing a button changes the illumination of the tank from white to blue to bring out the fluorescence of the corals, which gives us the opportunity to explain the biomedical applications for those proteins. ■

INTERVIEW BY VIRGINIA GEWIN

# CANOPY OF SKULLS

*When two worlds collide.*

BY BETH CATO

Medea trod the patchwork shadow and light beneath the canopy of skulls. Set high on poles, the white bones had turned varying shades of grey and green. Some wore full skins of verdant flora. These were the colony elders, the first generation on Rikyu. Almost 50 skulls, their soulless eye sockets staring at the stars from whence they had come.

As a child, Medea had yearned for her own skull to belong among the canopy. She had come to accept that she was generations too late for such an honour, and now she no longer belonged on Rikyu at all.

Within hours, a shuttle would deliver the 11 surviving colonists to an orbiter. Medea was the youngest at 15, and she itched with restlessness. She had no desire to stay, not since Mama had died the previous winter. And yet, she ached with a need to pay homage to the only home she knew, to these skulls she had adored since childhood.

"Give me a sign," she whispered to her great-great-grandparents above. She was even wearing her furs one final time, so they'd recognize her. "Show me how to honour you."

Birdlings and slither-slips rustled among the ferns. Gnarled vines draped from pole to pole brushed her cheeks. She knew each elder's name as a mantra: Kazuo Uematsu, Mary Brown, Jorge Jimenez and down the line. A few poles were empty, their bones swallowed by the forest.

Her bare feet, callused to stiff leather, paced the familiar furrows below the canopy. Something smooth slid beneath her toe. She paused and picked up a white rock. Odd, to find such a rounded stone so far from the river.

"Forty-nine skulls. Your precious elders. A century on this rock, and these are the most valuable things here. Pathetic."

Medea whirled around. It was Mr Dale, the researcher. He had come down on the shuttle and intended to stay and study the remains of their colony. Her brow furrowed as she struggled to understand him. They both spoke English, but the ship's crew used strange words and formed their tongues in peculiar ways.

"Yes. Forty-nine," she said with a smile, pleased at his interest in the canopy.

He stopped about ten feet away. His pale skin gleamed like sickness, though she knew it was from a lack of natural light. Strange, to think of her own skin turning so pale while travelling through space.



"This is my favourite place," Medea said. "I will miss it most." She blinked back tears.

He tilted an ear as he tried to decipher her words, then shook his head.

"You're not even worth the effort of turning on my translator. Well, you'll be gone soon enough, and those lucky bastards on the ship get to work on civilizing you." He snorted. "Though it'd be funny to see you lot learning about hot showers and ready food, all that. No more hunting, not unless you're going to pelt rocks at a refrigerator." He pointed at her. "Where... are... your... clothes?"

His words and accent tumbled together like mating coati, but the last bit was indeed easier to understand. "At my house. I needed to wear my furs to come here and say good-bye."

Medea did love how her new clothes fit — soft as otterette skin, though strange in how they covered her from neck to ankle.

The processed protein nuggets they expected her to eat were not as welcome.

She rubbed the

smooth stone in the well of her palm and wondered what the elders wanted of her.

"Ah, little barbarian. It's quite understandable when alien races engage in such practices, but for humans to degrade to ancient meat-eating-and-wearing days? That's repulsive." He sighed and jerked his hand overhead at the skull of Aamina Mukherjee. "And no concept of money, no concept of worth. This lot crashed on this uncharted, un-terra-formed slag heap, and you may as well have landed in the Mesozoic."

Medea couldn't help but perk up. "That's Aamina! She was a botanist. She cultivated the vines we use for thatching and snares, and genetically tweaked them to reduce skin allergies. Isn't she beautiful with her draping flowers? You're lucky to see her in bloom."

Homesickness knotted in her gut, even though she had yet to leave home. She was so excited to see other worlds, and yet — she envied this man for staying here. She thought on something Mr Dale said — the ship's crew being "lucky bastards". They thought as highly of him. She'd heard the captain say that Mr Dale was a "crooked bastard" who deserved to stay on a planet like Rikyu.

"Look at you," said Mr Dale, laughing. "You're daft. You'll probably end up whoring on Janero. You have no idea that something like this — this bone on a stick — will sell for a million genny-slips because of the story and tragedy of this place. You're a new-fangled Donner Party. I'll make my fortune here." He gripped a vacant pole, grinning.

Here. The depth of meaning in that one word resonated. Sunlight sliced through the opening in the canopy and illuminated his bare head. Birdlings hushed. Medea smiled acknowledgment to the skulls and to Mr Dale's fervent request.

The rock flew from her hand. His skull cracked, sound reverberating through the canopy. Mr Dale tumbled backwards with a crackle of underbrush.

"You are a first generation to come here! If I could stay with the elders, I would. You are lucky to belong here!"

Tears filled her eyes as she unsheathed her knife. She had just enough time to set him on a pole. Medea gazed up at the heavens, like the skulls around her, and watched for the glint of the orbiter above. ■

➔ **NATURE.COM**  
Follow Futures:  
@NatureFutures  
go.nature.com/mtoodm

Beth Cato resides in Arizona. Her work can be found in *Daily Science Fiction* and *Flash Fiction Online*. For information on her latest projects, please visit [www.bethcato.com](http://www.bethcato.com).